TURKU AMK
TURKU UNIVERSITY OF
APPLIED SCIENCES

Juha Kontio, Meiju Keinänen,
Tarja Åberg & Elina Asukas (eds.)

ISATE – International Symposium on Advances in Technology Education Conference proceedings

August 17th–20th, Turku, Finland – part 3

Juha Kontio, Meiju Keinänen, Tarja Åberg & Elina Asukas (eds.)
ISATE – International Symposium on Advances in Technology Education
Conference proceedings
August 17th–20th, Turku, Finland – part 1
ISBN 978-952-216-794-1

Juha Kontio, Meiju Keinänen, Tarja Åberg & Elina Asukas (eds.)
ISATE – International Symposium on Advances in Technology Education
Conference proceedings
August 17th–20th, Turku, Finland – part 2
ISBN 978-952-216-795-8

Juha Kontio, Meiju Keinänen, Tarja Åberg & Elina Asukas (eds.)
ISATE – International Symposium on Advances in Technology Education
Conference proceedings
August 17th–20th, Turku, Finland – part 3
ISBN 978-952-216-796-5

Research Reports from Turku University of Applied Sciences 51
Turku University of Applied Sciences
Turku 2021

ISBN 978-952-216-796-5 (pdf)
ISSN 1796-9964 (electronic)
http://julkaisut.turkuamk.fi/isbn9789522167941.pdf

Turku UAS' publications: turkuamk.fi/julkaisut

Table of Contents

Health Technology and Medical Engineering

Research and activities on medical data analysis and medical diagnosis support system
Miyori Shirasuna

Development of Flood Hazard Map for the Visually Impaired
Tomohiro Kiyotaki, Taisei Miyasaka, Hikonosuke Aizu, Yoshinori Fujisawa

Development of Wearable Braille Reader
Akiha Yanagisawa, Shoichi Ito

Evaluation of Prep-n-GoTM Buffer for DNA extraction in urine sample
Cheung Kuen Wan, Ka Po Ngai

Development of Communication Tools for People with Speech Difficulties
Daichi Matsuzawa, Yoshinori Fujisawa

Technical Exchange Between Thai and Japanese Students Working on a Mekong River Joint Project
Tomonari Masuzaki, Supachai Prainetr, Tomonori Tabusa, Hidetsugu Hukuda, Toshio Mukai, Ganbat DAVAA

Infection capability of materials using graphene film and its impedance characteristics.
Hideyuki Kanematsu, Ryoichi Nakagawa, Yuki Torisawa, Hidekazu Miura, Masato Ishihara, Masahito Ban, Dana M. Barry, Stefan Zimmermann

Development of a transfer aid which can be used by a wheelchair user without assistance
Yusuke KOBAYASHI, Daisuke MIYASHITA

Evaluation of iEMG Focusing on Trunk Muscles During One-Handed Wheelchair Driving
Satoshi Ohashi, Akira Shionoya, Keiu Harada

Toward EMG estimation of wheelchair operation with neural network
Shimpei Aihara, Ryusei Shibata, Ryosuke Mizukami, Takara Sakai, Akira Shionoya

Oxygen Intake Estimation in Wheelchair Driving by Machine Learning
Akira Shionoya, Ryousuke Mizukami, Syogo Asanuma, Masahito Nagamori, Hisashi Uchiyama, Satoshi Ohashi

Exploration of an inflection point of Ventilation Parameters with Anaerobic Threshold by the Strucchange
Akira Shionoya, Takenori Aida, Hirofumi Nonaka, Kouji Hayami, Hisashi Uchiyama, Masahito Nagamori, Satoshi Ohhashi, Mai Kobayashi, Tsugumi Takayama, Shinji Kimura

Effects of Wave Images on Standing Posture of Ship Crew
Takanori Sakamaki, Renon Doine

Estimating the Emotional Information of the Songs using Search Engines
Jin Akaishi, Masaki Sakata, Mitsutaka Nakano, Kazuhiro Koshi, Kimiyasu Kiyota

Development of Remote Support System to Improve Physical Activity Habits of Elderly Patients with COPD
Chisato Ohashi, Shunsuke Akiguchi, Mineko Ohira

Practical education for advanced engineers of KOSEN based on assistive technology for a sustainable society
Kimiyasu Kiyota, Koichi Watanabe, Keijiro Araki, Akira Shionoya, Mitsuteru Inoue

Technology-enhanced Exercise is Effective in Improving Balance and Happiness Level among Healthy Elders – Pilot Study
Evelyn KO, Wollo WU, Florence MOK

Consideration of Tablet Application for Special Needs Children with Multiple Support Functions
Shunsuke Akiguchi, Chisato Ohashi

Case Study of Curriculum Design of Computer Programming related to Assistive Technology
Manabu Shimakawa, Chiharu Okuma, Kimiyasu Kiyota

CDIO Approach based Educational Project of Sensor Fusion for Assistive Technology
Kosei Nojiri, Hirofumi Ohtsuka, Daichi Arai, Etsuo Horikawa

Image Correction Methods of Cirrhosis Liver Classification on CNNs
Yoshihiro Mitani

Development of a High Repetition Impulse Power Supply for Sterilization by High Electric Fields
Takahisa Ueno, Kyohei Asami, Takashi Furukawa, Takashi Sakugawa

Assistive Technology in Education for Self-Monitoring with an Optical Wearable Heart Rate Monitor
Masahito Nagamori, Miwako Fukuda, Hajime Takano, Nao Shinoda, Akira Shionoya, Satoshi Ohhashi, Tatuya Susukida, Masaki Nagasawa, Hitoshi Miyake

Improvement of Gaze Input Communication System with Predictive Conversion
Katsumi Hama, YU Jia Xin, Manabu Suzuki, Takahiko Nakamura

Development of a Smartphone Operation Support System Based on Inclusive Design
Yeoh Wei Loon, Ryuto Handa, Isamu Matsuno, Hidetoshi Nakayama, Shinya Suzuki

Functional Engineering Materials

Mechanical Property of Low-Melting Sn-Bi Lead-Free Solder Alloys
Akira Yamauchi

Low-temperature sintering of ZnAl2O4 ceramics containing Cu3Nb2O8 additive and their dielectric and thermal properties
Koichi Shigeno, Takuma Yano, Hirotaka Fujimori

Fabrication of flexible magneto-optical indicator with KOSEN students for engineering education of non-destructive inspection
Ryosuke Hashimoto, Yuya Funaki, Toshiya Itaya

Quantitative evaluation of Biofilms formed on various materials using crystal violet
Hideyuki Kanematsu, Kei Sakurai, Ryo Satoh, Dana M. Barry, Nobumitsu Hirai, Toshihiro Tanaka

Evaluation for anti-viral characteristics of various metallic materials using Influenza A and feline calicivirus
Hideyuki Kanematsu, Dana M. Barry, Takeshi Kogo, Risa Kawai, Ryo Satoh

On-site characterization of impurities in gypsum from waste plasterboards for circular economy system
Masamoto Tafu, Juna Nakamura, Momoka Tanii, Saori Takamatsu, Atsushi Manaka

A concrete example of societal Implementations based on GEAR Material Project
Takaya Sato, Hideyuki Kanematsu, Hitoshi Wake

MORPHOLOGY CONTROL OF MONOMER-POLYMER HYBRID ELECTRON ACCEPTOR FOR BULK-HETEROJUNCTION SOLAR CELL
Takehito Kato, Yuki Kurokawa, Kei Nishii, Yasuyuki Ueda, Fuminobu Imaizumi, Daisuke Kawagoe, Shin-nosuke Suzuki, Hideyuki Kanematsu, Tadashi Fukumoto

Development of biomass-based plastics with biodegradability and thermoplasticity.
Ryo Satoh, Michiko Konno, Saika Honma, Takashi Morinaga, Toshio Kamijo, Takaya Sato

Tensile Examination and Strength Evaluation of Latewood in Japanese Wood
Akihiro Takahashi

Fracture Behavior and Strength Degradation in Over-Aged Maraging Steel
Akihiro Takahashi

Behavior of polysiloxane films in contact with aqueous solutions or biofilm simulating solutions
Nobumitsu Hirai, Masaya Horii, Nanako Sugawara, Himeka Kato, Katsuhiko Sano, Akira Suzuki, Yoshiaki Sawada, Takeshi Kougo, Akiko Ogawa, Daisuke Kuroda, Hideyuki Kanematsu

Synthesis and Properties of Graphene Oxide Composite Electrolyte Membrane with Single Ion Conductivity
Ryo SHOMURA, Ryota TAMATE, Takashi MORINAGA, Takaya SATO, Kazunori TAKADA

Characterization of a double network ion gel formed by one pot synthesis
Hiroyuki Arafune, Kenta Miura, Sachiho Inoue, Yuto Tsuchida, Yuma Watarai, Takashi Morinaga, Toshio Kamijo, Takaya Sato

Characteristics of Powder Discharge by Vibrating Fluidization
Koichiro Ogata, Tsutomu Harada, Riho Abe, Hideo Kawahara, Eiji Mitani, Koji Mitani

Mechanical joining of two ultra-high-strength steel and one aluminium sheets using pre-punched middle sheet
Yohei Abe, Ken-ichiro Mori

BROAD EXCITATION BAND OF SPIN WAVE USING MICROSTRIP LINE FOR MAGNONIC DEVICE
Kanta Mori, Taichi Goto, Toshiaki Watanabe, Pang Boey Lim, Mitsuteru Inoue

Development of multiferroic composite films for voltage-driven magneto-optic special light modulators
Yuichi Nakamura, Naohide Kamada, Ryo Hasumi, Taichi Goto, Pang Boey Lim, Hironaga Uchida, Mitsuteru Inoue

MAGNETOOPTICAL PROPERTIES OF CERIUM SUBSTITUTED YTTRIUM IRON GARNET FILMS FOR SPIN CONTROLLED LASERS
Yuki Yoshihara, Pang Boey Lim, Mitsuteru Inoue, Taichi Goto

SPIN CONTROLLED LASER USING MAGNETIC GARNET FILM
Taichi Goto, Ken Aoki, Hibiki Miyashita, Yuki Yoshihara, Takumi Koguchi, Pang Boey Lim, Mani Mina, Mitsuteru Inoue

SIMULATION OF MAGNETIC DOMAIN FOR SPIN WAVE LOGIC DEVICE
Takumi Koguchi, Tadashi Ataka, Pang Boey Lim, Mitsuteru Inoue, Taichi Goto

Mechanical Property Changes of Austenitic Stainless Steels by Severe Plastic Deformation and Subsequent Aging
Frank Jaksoni Mweta, Yoshikazu Todaka, Nozomu Adachi

Formation mechanism of micro-arc and coating by plasma electrolytic oxidation of titanium
Toshiaki Yasui, Katsuki Hayashi, Masahiro Fukumoto

Evaluation of electrode design of a microfluidic impedance biosensor for DNase assay
Kanta Nishibayashi, Seimei Oku, Takahiro Himuro, Masanori Eguchi

Health Technology and Medical Engineering

Research and Activities on Medical Data Analysis and Medical Diagnosis Support System

Miyori Shirasuna

National Institute of Technology, Tsuruoka College / Department of Creative Engineering, Course of Mechanical Engineering, Assistant professor, Yamagata, Japan

m-shirasuna@tsuruoka-nct.ac.jp

Abstract

In collaboration with medical institutions, we are engaged in research concerning medical data analysis and diagnostic support using simple and straightforward statistical analysis methods from an engineering standpoint and perspective. Currently, Japanese medicine is more regressive than that in other developed countries in terms of technology, knowledge sharing, and succession planning. Additionally, the shortage of doctors, a declining birthrate, and an aging population have been noted as future problems in Japan that need to be addressed. To this end, we have analyzed data on Sleep Apnea Syndrome (SAS) and assisted with likelihood discrimination, including the use of preliminary groups, to assist with subtyping of pediatric Orthostatic Dysregulation (OD). Because tailor-made data analysis systems and tools are often difficult to maintain following their delivery, we use the simplest and clearest analysis methods possible. Moreover, because the data are standardized and stored in a database, the analytical results are uniform, ensuring that the analytical findings are accurate consistent, even if the diagnosticians are different. Furthermore, we have considered devising methods for presenting diagnostic results in a manner understandable to patients.

Our medical diagnostic support is essentially based on the experience of a physician that has developed multiple sensory indicators. We believe that a visual and quantitative embodiment of this remains a field with substantial room for exploration in Japanese medicine, and that this will be even more necessary in the future. For example, our proposal for likelihood determination of SAS enabled a ~40-fold reduction in the time required for diagnosis at medical institutions and was accompanied by a 100% determination rate. In the case of OD disorder, we succeeded in systematizing the experiential side of the physician and quantifying the discrimination criteria to obtain a positive discrimination rate >90%.

Keywords: *Medical Assistance, Sleep Apnea Syndrome, Orthostatic Regulation Disorder, Wavelet Transformation, Multivariate Analysis*

Introduction

From an engineering standpoint and perspective, we research medical data analysis and diagnostic support using simple statistical analysis methods, data mining, and signal processing such as wavelet transform in collaboration with medical specialists. Although Japan's medical care is technologically at the forefront of the world, it is lagging behind other developed countries in terms of technology, knowledge sharing, and succession planning. Also, a shortage of doctors, a declining birthrate, an aging population, and a declining population have been pointed out as future challenges for Japan [1][2]. This problem is not to be taken lightly, but it is not an easy one to solve. To address these issues, we have analyzed data on Sleep Apnea Syndrome (SAS) to support likelihood discrimination, including the use of a reserve group to support subtyping of Orthostatic Dysregulation (OD) in children. Custom-made data analysis systems and tools, not only for medical data analysis, are often difficult to maintain after they are provided, so we try to use simple and easy to understand analysis methods as much as possible [3][4]. Also, because the data is standardized and databased, the results of our analysis are uniform, and the results of the analysis are accurate and consistent even if the diagnosticians are different. Besides, we are considering ways to present the results of the diagnosis to patients in a way that is easy to understand. Our medical diagnostic support is essentially based on the experience of physicians who have developed multiple sensory indicators. The visual and quantitative embodiment of this is a field that still has a lot of room to explore in Japanese medicine, and we believe it will be even more necessary in the future to solve the problems mentioned earlier. Our medical diagnostic support is essentially based on the experience of physicians who have developed multiple sensory indicators. The visual and quantitative embodiment of this is a field that still has a lot of room to explore in Japanese medicine, and we believe it will be even more necessary in the future to solve the problems mentioned earlier.

The structure of this paper is as follows. In Chapter 2, we describe our approach to medical data analysis. Chapter 3 describes our collaboration with physicians.

Chapter 4 describes our work on SAS as example 1, and Chapter 5 describes pediatric orthostatic dysregulation (OD) as example 2. Chapter 6 describes the focus of teaching engineering students research concepts using our studies, and Chapter 7 provides a summary of this paper.

Medical data analysis

Medical data analysis is a field of medical engineering that is currently being applied for the analysis of multiple diseases. Recent rapid progress in machine learning and artificial intelligence (AI) techniques has allowed scientists to conduct research using these methods. These methods can be used to analyze voice, images, and/or a combination of these, with additional applications expected in the future. However, these technologies have issues. First, machine learning and AI require extremely large volumes of data. Second, analytical results show that even when accuracy is good, the underlying analytical process represents a "black box." Third, the accuracy of these is highest at the time of delivery (i.e., at the time of initial analysis and creation), and there is a concern that this accuracy will decline later, requiring continued maintenance [3][4]. Fourth, because many of these analytical methods are difficult to understand, only the analyst or others in these areas will be able to interpret the results, leaving many of those presented with the findings neglectful of or unable to translate the findings [5]. There are numerous reports of the advancement of AI in medicine, as well as reports of problems with its use (e.g., automated blood pressure monitors reported as medically unreliable) [6][7][8]. We currently analyze medical data but are unable to apply machine learning or AI due to the absence of a necessary amount of data. The ideal form of medical data analysis is "white open," which describes support and empirical replication based on the opinions and requests of physicians.

Cooperation between doctors and data scientists

Doctor experience and expertise are very important, which makes automating the diagnostic responsibility of doctors difficult. During our interviews, we found that the capabilities of many of the medical devices and/or those used for analysis were unclear. Knowledge of these devices is sometimes not passed onto user, including doctors, due to corporate interests; therefore, doctors in the medical field, especially those not participating in a large project or research group, are often required to delay data analysis using this equipment due to a lack of the time and tools required for independent analysis of the data. This is a common issue for physicians in small- and medium-sized medical institutions in Japan.

We have worked with systems engineers prior to their joining a university, finding that they experienced a substantial divide between customers requesting analytical support and the analysts. On issue is that analysts tend to attempt new or complicated analytical methods. Naturally, customers who are presented with results obtained from these methods are often confused, which is a common problem associated with medical data analysis using machine learning and AI. Although these methods are useful, a disadvantage is that even analysts cannot visualize the analytical process. Therefore, we are focusing our research on a method that allows both the analyst and the client (in this case, the physician) to understand, share, and discuss the analytical method and the meaning of the results. These initiatives and specific examples are discussed in Chapters 4 and 5.

SAS analysis

SAS is a disease present in many countries and a frequent cause of accidents due to dozing or distraction in patients. An SAS diagnosis requires multiple steps, including a patient making an appointment at the hospital, requesting an interview, and renting a measurement device for the first visit. The patient then requests the results of a second round of analysis, requires overnight hospitalization for a third round, and again requests the results. This process can take >1 month and often take time away from work, which is difficult for salaried workers in Japan. Because SAS is not a painful disease and there are no subjective symptoms, individuals suspected of having SAS often do not have a sense of crisis. Therefore, many do not receive a diagnosis, and even those attempting to receive a diagnosis find the process tedious and cease going to the hospital. Naturally, this is also a problem for medical institutions. Additionally, an SAS diagnosis is inefficient, as a sleep medicine specialist spends ~6 hours per subject performing manual visual analysis of data obtained from a polygraph examination, which involves hospitalization for one night [9][10].

We have assessed the possibility of SAS discrimination using only audio data. Voice data is not used in the current SAS diagnosis for multiple reasons, including the long, noisy, and heterogeneous breathing sounds during 6 to 8 hours of sleep, which makes data retention and analysis difficult. The World Health Organization has established criteria for SAS diagnosis, but they do not include breathing sounds during sleep. Therefore, in the interests of both subjects and analysts, we believe that a method allowing subjects to perform SAS diagnosis at home using a simple integrated circuit (IC) recorder, which will also shorted the study time required by analysts. Additionally, this method eliminates the potential problem of subjects not being able to sleep in a different sleep environment.

We have attempted to diagnose SAS using IC recorders and improve efficiency, followed by statistical analysis to determine SAS probability. The results are promising, and our future work will investigate an analytical method that combines previous methods with machine learning. We believe that better analytical results can be obtained by applying various the strengths of multiple methods. This will be supported by a Japanese grant for scientific research for 3 years starting in 2020.

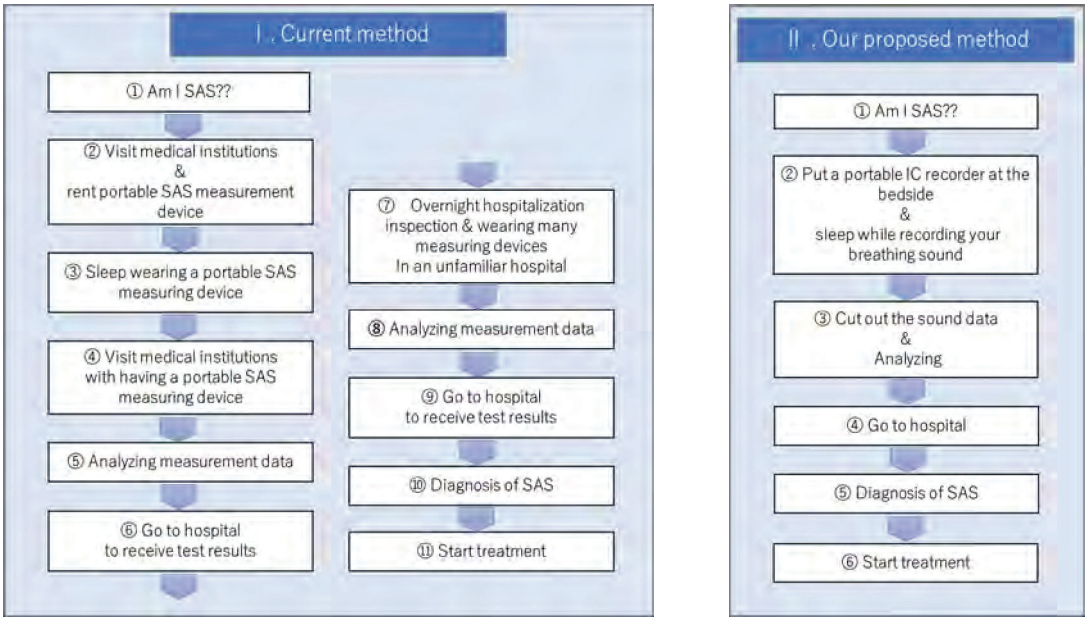

Figure 1 The current SAS diagnostic steps and the diagnostic steps that incorporate our proposed method.

Figure 1 shows the current SAS diagnostic steps and the diagnostic steps that incorporate our proposed method. On the left is the diagnostic step that is currently primarily performed in healthcare facilities, and on the right is the step that would be taken if our proposed method were incorporated. We can see that our proposal is simpler than the current steps.

OD analysis

Approximately 700,000 Japanese elementary to high school students are afflicted with autonomic dysautonomia. Because the population of the relevant age group is ~10 million people, this makes the incidence rate ~7%. OD is a disorder in which blood pressure and the pulse are not well regulated, with the consensus view that the autonomic nervous system is a strong factor, and that symptoms are often overlooked or neglected by parents and schools. Because the main symptoms of OD include a hard time waking up in the morning, headache, nausea, and lack of motivation, the affected person is more likely to be truant, which can cause multiple problems in their social life [11][12].

However, because OD is a disease that patients can recover from with the appropriate treatment, it is important that they are diagnosed at an early stage and become well-informed of the issues. OD has attracted the attention of Japanese medical societies, and research has been conducted ahead of other countries; however, a lack of specialists remains a major challenge. There are four main OD subtypes, each of which is treated differently. The experience of the specialist physician is important for this classification. The current guidelines for OD diagnosis were established by the Japanese Society of Pediatric Psychosomatic Medicine in 2006 and are based on a time-dependent variation in blood pressure and heart rate according to changes in body posture from the prone state to the upright state (called the questioning and standing tests).

However, this classification is often not in line with guidelines and used independently by physicians. We have attempted to replicate the observational role of physicians to present a quantitative measurement of the diagnosis. Additionally, we have attempted to provide a "white open" analysis environment for physicians in order to allow them to check the progress of the analysis (i.e., data consistency and the state of the distribution while performing the analysis). We have obtained a discrimination rate of >90% for subtype assignment and are focusing on presenting simple but reliable analytical results using basic statistical methods. Application of this method can potentially allow physicians to obtain insight into new subtypes and enable them to train other physicians by sharing data.

OD research is performed mainly in Japan, although the disease afflicts children worldwide. Therefore, our goal is that this research will promote diagnostic support for OD specialists worldwide and health support for children in the future.

Figure 2 shows the Finometer MIDI by Finapres Medical Systems [13], a non-invasive blood pressure meter used by OD specialists during a new orthostatic test. In general, blood pressure is not a continuous value in medical institutions as it is in the home, but in this crisis, blood pressure can be measured continuously. There are still very few medical institutions in Japan that use this continuous blood pressure monitoring device. Therefore, we are using the results from this device to make an accurate diagnosis of OD and its subtypes based on the results measured with a common blood pressure measuring device (not a continuous blood pressure measuring device).

Figure 2: Non-invasive blood pressure monitoring devices used by OD specialists during the new orthostatic test

(OD) as example 2. Chapter 6 describes the focus of teaching engineering students research concepts using our studies, and Chapter 7 provides a summary of this paper.

Guidance to engineering students

Engineering students are good at using mathematical formulas and natural laws as tools but somewhat more likely to rely on the tools. For example, students can use a library of data analysis software but have little control or understanding of the meaning of the library or the interpretation of the results. This is called "file/folder thinking" and a common trait of engineering students. This approach is similar to translating written Japanese into English using an automatic translator, followed by transferring the passage into a report without verifying that the meaning is consistent with the original Japanese. Therefore, students with whom I perform research are involved in extensive discussions and are frequently asked to explain in their own words why a method was used and why they think they received a given result. This allows them to think about what needs to be done for subsequent problems and represents a kind of repetition that encourages them to think for themselves. Additionally, because each student presents a different personality and level of expertise, assignments are presented according to their strengths, which can be very difficult. However, the hope is that this repetition will lead to a process of cultivating a trusting relationship between the students and the instructor and help them overcome problems they might experience as students before graduating.

Figure 3 shows an example of a medical support system for OD created by a student. Time series data, measured with non-invasive continuous sphygmomanometers and heart rate measuring instruments, are cleansed and various statistics (e.g., mean, variance, kurtosis, and skewness) are presented as a result. Based on these results, blood pressure and heart rate histograms can also be created, so doctors can visually capture information from measurements that were previously only numerical.

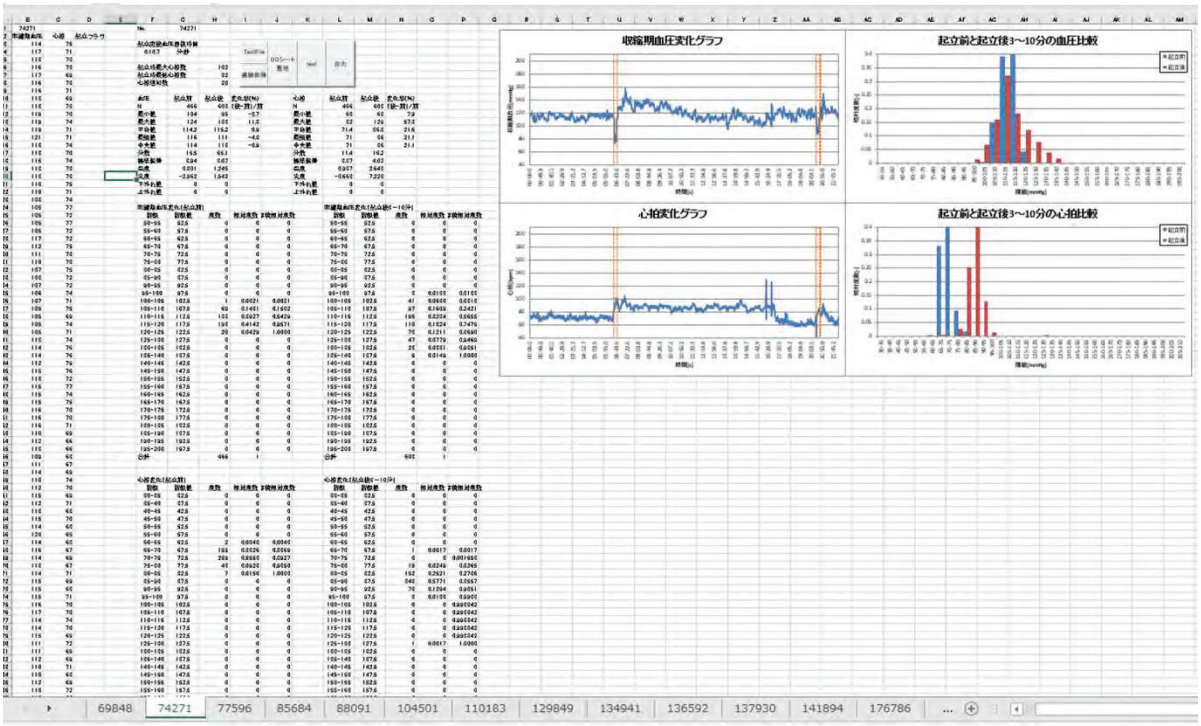

Figure 3 An interactive OD medical support system - created by students.

Conclusions

This report briefly describes our approach to medical data analysis, our collaboration with specialist physicians, two practical examples of our activities, and the teaching and research guidance of engineering students concerning these studies and activities. It is difficult to visually represent or quantify the experience of a specialist, Moreover, as engineers, we understand that medical and medical engineering methods useful for data analysis continue to advance daily. Therefore, we will continue to study and follow-up on these methods and work closely with doctors to help improve the healthcare in Japan and around the world. Furthermore, we will continue to educate engineering students and support the broadening of their perspectives and flexibility of their critical thinking skills to support their future roles in the global arena.

Acknowledgements

This work was supported by JSPS KAKENHI Grant Number 20K20220.

We are grateful to MD Norio KAZUMA (KAZUMA KODOMO Clinic, Saitama, Japan), MD YASUHIRO ISHKAWA (ISHIKAWA Clinic, Saitama, Japan) and Prof. SHO Tadashi (Hiroshima Institute of Technology, Hiroshima, Japan) for their efforts in this research.

References

AI: Artificial Intelligence Specialized Media (2020) from https://ledge.ai/medical-comparison/.

Nippon Jimuki Co. (2020) from https://carnas.njc.co.jp/column/crisis-increasing-elderly-population-2025/.

Net One (2020) from https://www.netone.co.jp/knowledge-center/netone-blog/20191107-1/.

Nikkei XTECH (2018) from https://xtech.nikkei.com/atcl/nxt/mag/sys/18/00041/092600004/.

Cope, B., Kalantzis, M. & Searsmith, D. (2020). Artificial intelligence for education: Knowledge and its assessment in AI-enabled learning ecologies. Journal, Educational Philosophy and Theory, Doi https://doi.org/10.1080/00131857.2020.1728732. Vol.19, No. 3, pp. 1-3.

WIRED, (2020) AI 'diagnosis' risks exacerbating medical problems from https://wired.jp/membership/2020/04/07/ai-makes-bad-medicine-even-worse/.

Japanese Cardiovascular Society, (2012), Guidelines for Diagnosis and Treatment of Sleep and Respiratory Disorders in Cardiovascular Diseases.

Coldewey, D. (2020) from https://jp.techcrunch.com/2020/05/04/2020-04-27-google-medical-researchers-humbled-when-ai-screening-tool-falls-short-in-real-life-testing/.

Oe, K. (2017) The future use of AI in medicine and its challenges, Jpn J. Drug Inform,

Diagnosis and Treatment of Cardiovascular Diseases, Report of the 2008-2009 Joint Research Group, pp.968--970.

Sato, K., (2016), Method of treating sleep apnea - multidisciplinary treatment of sleep-disordered breathing, Chugai Igaku-Sya, pp. 5, 8-14, 23-36.

Tanaka, H., (2013), A book on orthostatic dysregulation, a disease of children who can't get up in the morning, Kodan-Sya, pp.1-24.

Japanese Society of Pediatric Psychosomatic Medicine, (2015), Guidelines of the Society of Pediatric Psychosomatic Medicine - Five guidelines for daily practice, Nanko-Do, pp.26-41.

Finapres Medical Systems, from Finometer MIDI, http://www.finapres.com/Products/Finometer-MIDI

Development of a Flood Hazard Map for the Visually Impaired

Tomohiro Kiyotaki[a], Taisei Miyasaka[a], Hikonosuke Aizu[a] and Yoshinori Fujisawa [*a]

[a] National Institute of Technology, Nagano College,
Dept.of Electoronics and Computer Science, Nagano, Japan

*fujix@nagano-nct.ac.jp

Abstract

In October 2019, a large typhoon (HAGIBIS) hit Japan and caused heavy damage to our city due to heavy rains. Due to the flooding of the river, the residents near the river were evacuated. Hazard maps showed the depth of inundation by floods in five different colors. However, the visually impaired people cannot use these maps, and there are currently no hazard maps for the visually impaired. Also, it is difficult to use normal hazard map data for the visually impaired.

There is a modified point map, which uses five different patterns of point maps according to the color information of the five levels of inundation areas. However, there was a problem in that it was difficult to understand the differences in the patterns and the information was not readable. In response to a request from a visually impaired person who wanted a solution to this problem, we are developing a flood hazard map for the visually impaired so that they can grasp the inundation area even though they cannot see.

We propose a method of representing the flooded area by cutting material such as an acrylic sheet in the depth direction, instead of using a point map pattern. We think that this will allow us to intuitively know the inundation level with our fingertips. We have found that adding ordinary map details (buildings, roads, etc.) to the inundation area details (depth direction) is too much information and is difficult to comprehend, so we have separated the map particulars from the inundation area details and the two maps can be compared.

The flooded area data is cut in the depth direction to solve the problem of point maps, but the map information does not have a unified mark corresponding to the map symbols that indicate details such as buildings, roads, and landmarks. In the future, we will propose marks corresponding to map symbols that can be identified by touching with a fingertip. In addition, we aim to adopt these symbols in both our proposed maps and the standard hazard maps for the visually impaired in Japan.

Keywords: *visually impaired people, hazard map,*

Introduction

On October 12, 2019, heavy rains from Typhoon No.19 (HAGIBIS) that landed in Japan, caused extensive damage to Nagano city. The heavy rains forced many areas to be evacuated due to the threat of river flooding. Many residents living near the river evacuated to nearby evacuation shelters based on a hazard map published by the local government. However, it was very difficult for the visually impaired people to evacuate because they could not read the commonly used hazard maps. Therefore, a hazard map specifically for the visually impaired is needed. Braille translation volunteers for the visually impaired people tried to create a hazard map with point maps as shown in Figure 1.

Figure1: Hazard Map with Point Maps

The point map shows a picture and a diagram represented by patterns of dots that are felt with fingertips and it used to help visually impaired people understand the map by touching it. In the hazard map with point maps, railroad tracks or roads and so on are represented by a series of points, and the inundation level is represented by changing the density or pattern of the points, and other buildings and area names are

represented in Braille. Since the point map is a familiar expression for visually impaired people, we thought the hazard map with point maps was a very good idea.

However, the hazard map with point maps is difficult for visually impaired people to understand even if they touch it because there are too many patterns to represent. So, visually impaired people asked us to solve this problem. Then, we proposed to replace the point map with a hazard map in which flat plates are cut according to inundation levels. In this map, the higher the inundation level, the deeper the flat plate is cut, and the more steps that are added to represent inundation levels. We thought that this method could convey the inundation level more intuitively by touch than the hazard map with point maps method.

In this paper, the method of making the hazard map is described, and the explanation of the constructed hazard map is given. Finally, we describe the evaluation of the effectiveness of the hazard maps we made for the visually impaired people.

How to Make a Hazard Map

The procedure for making a hazard map is as follows.

1. edit the original map image data
2. convert to grayscale image
3. convert to points group data
4. meshing
5. output to file for cutting
6. sharpen materials

In this section, these procedures are explained in detail.

The image data of the original map used in this study is the area around “Sansai Station” on the "Nagano City Disaster Prevention Map" on the official website of Nagano City. Image data of the original map is shown in Figure 2.

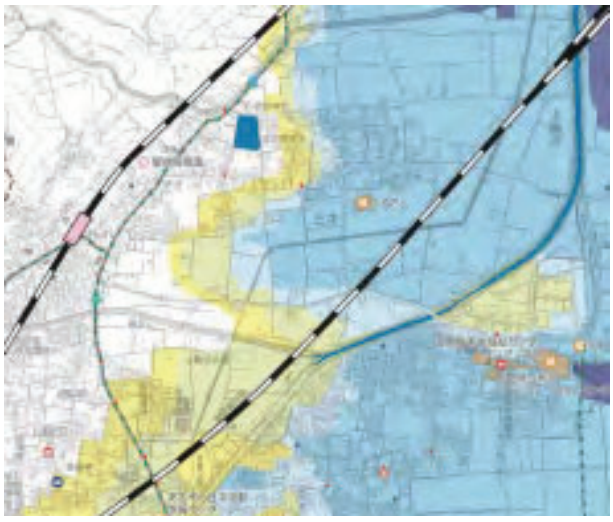

Figure2: Original Hazard Map

In the hazard map shown in Figure 2, the inundation areas on the general map are painted with colors corresponding to the inundation level. This hazard map contains so much information about buildings or roads and other features that visually impaired people cannot understand, even if they touch the map that has been cut as it is. Therefore, it is necessary for users to edit the original image data to retain only the necessary information. Figure 3, 4, and 5 are the edited versions based on Figure 2.

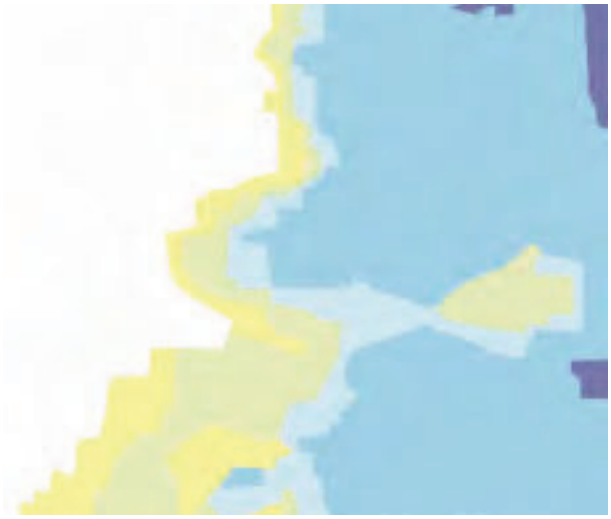

Figure3: Image Data of Inundation Level

Figure4: Image Data of Road, Building, etc

Figure5: Image Data of River, Railroad, etc

Figure6: Image Data of Inundation Level with grayscale

Figure 3 shows only the inundation level information. Figure 4 shows roads, buildings, a station, and a part of the railroad tracks, and Figure 5 shows a river and a part of the railroad tracks. Figure 3 is the source data for the hazard map of inundation level, and Figures 4 and 5 are the source data for the hazard map of geographic information.

After the original image data has been edited, we first convert the image to a 256-grayscale image. Here, we make a one-to-one correspondence between RGB values and grayscale values. For example, when converting the image data of the inundation level in Figure 3 to grayscale, the color of the original image and the grayscale value have a correspondence relationship as shown in Table 1.

Table1: Correspondence between Color and Grayscale Values

Inundation Level	Full Color Value	Depths [mm]	Grayscale Color Value
1	#FFF697	0.30000	239
2	#E9EEB8	0.66000	221
3	#D0EAF4	1.09200	119
4	#9FD5EC	1.61040	172
5	#787AB3	2.23248	140

Naturally, we will not cut areas that do not flood.

Figure 6 shows the color image in Figure 3 converted to a grayscale image using Table 1.

The cutting depths in Table 1 were calculated based on Fechner's law.

The next step is to convert the grayscale image in Figure 6 into three-dimensional points group data. The position of each pixel in the grayscale image is defined as the x and y coordinates, and the color information of the 256 gray levels is defined as the z coordinate.

The three-dimensional points group data has no surface, so it cannot be cut. Therefore, it is necessary to create a surface based on the point group data, which is called “meshing”. As for meshing software, we used MeshLab. The results of meshing with MeshLab are output as a file for a cutting machine and input to the cutting machine to make a hazard map.

Hazard Maps we Created

In this study, we have repeatedly "made", "evaluated", and "improved" the hazard maps. Therefore, there have been 31 prototypes so far, and instead of introducing all of them, we will introduce the ones with significant changes and the prototypes that were used in the meeting for the visually impaired people.

Figure 7 shows the first hazard map that was cut.

Figure7: First Prototype of Hazard Map

This is an unedited cutting of the image data of the color hazard map shown in Figure 2. There are no inundation levels, and all geographic information is included. The size is 100 mm square, and the thickness is 10 mm.

Figure 8 shows the second prototype.

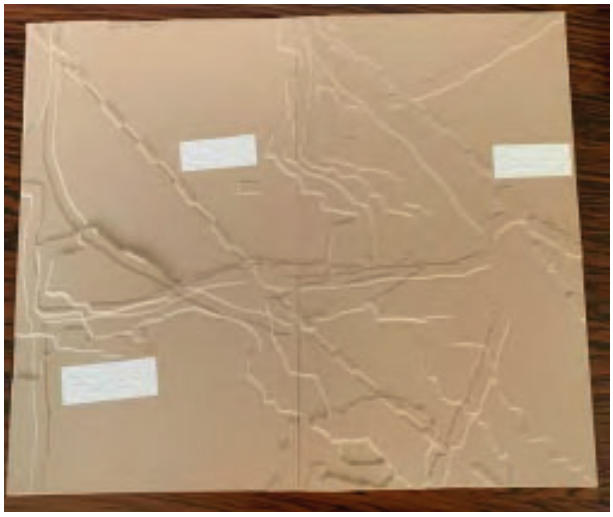

Figure8: Second Prototype of Hazard Map

Unlike the first prototype, only the addition of steps according to the inundation level and necessary geographic information had been retained. The five steps are implemented based on Fechner's law. The material is chemical wood, the size is 225x220 mm, and the thickness is 5 mm.

Figures 9 and 10 show the hazard map of the third prototype. From the third prototype, the maps are separated into two categories. One of them is a map with geographic information only and the other one is a map with inundation levels only. By touching and comparing the different maps of the same area, the user can understand the information of the inundation area. From this prototype, we used acrylic plates as the material. The advantage of this material is that it is transparent, so when it is placed on the map, the color information can be taken in.

Figure9: Third Prototype of Map around “Sansai Station”

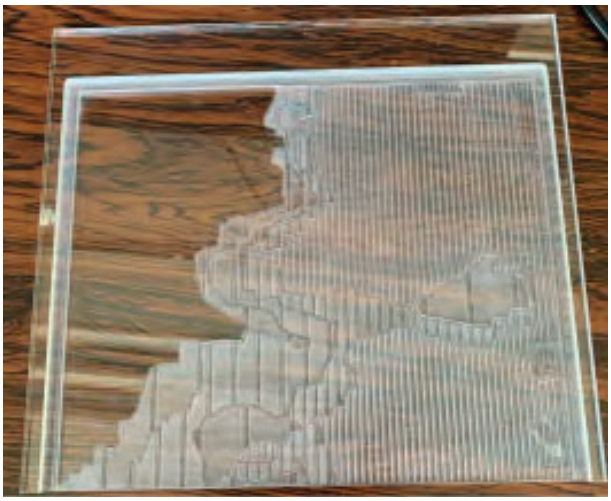

Figure10: Inundation Level Map of Same area to Figure9

The map of the area around “Sansai Station” in Figure 9 has been cut down to leave the main roads, buildings, station, railroad tracks, river, and pond. Roads are represented by convex lines, rivers are represented by concave lines, and railroad tracks are represented by alternately concave and convex lines. The map of inundation levels in Figure 10 has the following two features.

- Difference in steps per flooding level
- Pattern for each flooding level

In order to make it easier to notice changes in the inundation level, each inundation level is marked with a step, and in this prototype data, the deeper the step, the higher the inundation level. Fechner's law was used to make the changes in the steps more perceptible.

We made it possible to grasp the inundation level of the place users are touching by making a difference in the tactile sensation according to the inundation level through the pattern of each inundation level. In this

prototype data, a vertical stripe pattern is adopted, and the narrower the distance between the stripes, the higher the inundation level, and this pattern also represents the north and south.

Evaluation

We had visually impaired people actually touch the prototype hazard maps (Figure 11) that we had made and received a lot of feedback. In the first and second prototypes, many people commented that there was too much information on the map. Some people thought it would be better to have a pattern for each inundation level, so we added a pattern in the third prototype.

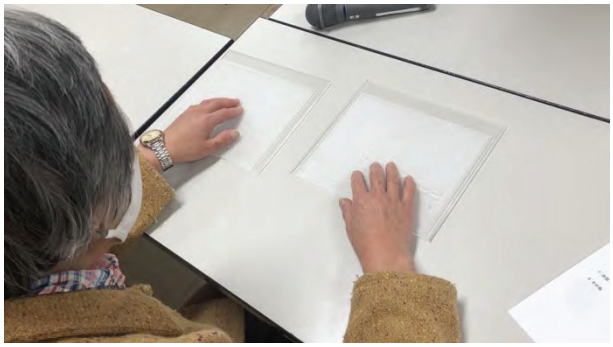

Figure11: A visually impaired person touching the maps

In the third prototype, by separating the map with geographic information and the map with inundation levels, we were able to reduce the amount of information in each map. By touching and comparing these maps, visually impaired people will be able to recognize the inundation level in their living area and know how to get to the nearest evacuation shelter.

Conclusions

In response to a request from visually impaired people, this study proposed a three-dimensional hazard map that expresses changes in inundation level with steps instead of a point map, and the map was repeatedly "made", "evaluated", and "improved". As a result, it was found that it is effective to express the change of inundation level as a step, which is the main feature of this study. The amount of change in the step was decided by using Fechner's law. It was also decided to make hazard maps separately for inundation levels and geographic information. In the hazard map of the inundation level, it was decided to express the inundation level by adding a vertical stripe pattern and changing the interval in addition to the steps. For the geographic information maps, the specification is to add major buildings, roads, and other geographic information that the user deems necessary.

As a future issue, the geographic information maps need to be improved in the way they represent buildings. Currently, we are making several perceptible marks to make a one-to-one mapping between buildings and marks like Figure 12. The goal is to make it common throughout our country.

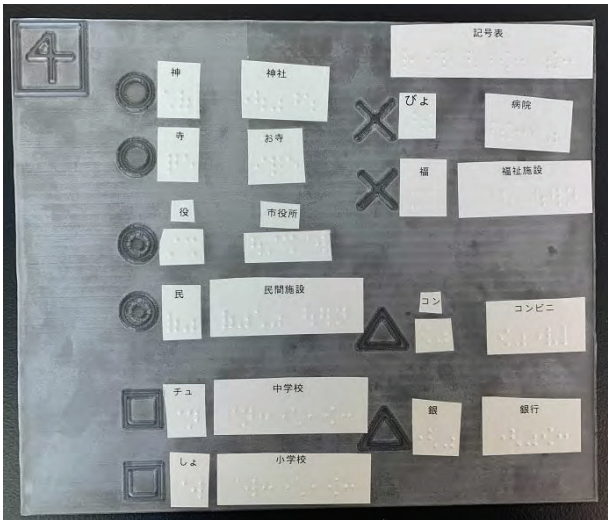

Figure12: Some marks

Acknowledgements

We would like to express our gratitude to the members of the Kita-Nagano Area UD Study Group for their many comments on this research.

References

Nagano City, Nagano City Disaster Prevention Map. Retrieved from https://www.city.nagano.nagano.jp/uploaded/attachment/49974.pdf

Seiichiro NAMBA, Psychophysics and tone quality. Retrived from https://www.jstage.jst.go.jp/article/tja/71/2/71_53/_artic ar/-char/ja/

Tetsuya Watanabe, Hirotsugu Kaga, Makoto Kobayashi, Kazunori Minatani, Surveys on Tactile Graphic Conversion Service for the Blind. Retrived from https://www.jstage.jst.go.jp/article/his/20/2/20_147/_arti cle/-char/en

DEVELOPMENT OF WEARABLE BRAILLE READER

Akiha Yanagisawa [*,a] and Shoichi Ito [a]

[a] National Institute of Technology, Nagano College, Nagano, Japan

*21908@g.nagano-nct.ac.jp

Abstract

Braille is the most universal tactile language for visually impaired people. It is inferred that about 90% of visually impaired people in Japan cannot read Braille. If they can easily read Braille text with some devices, they will improve their quality of life. We are developing a new wearable device which enables visually impaired people to read Braille with their finger. Users of this device attach a pressure sensor onto their fingertips. Users trace the Braille text with the sensor, then they can hear the voice which translate texts from Braille into Japanese. This device also implements spell correction mechanism which is specialized for Braille. It corrects wrong spelling of Braille texts which originates from lack or excess of Braille dots. Pressure sensor is used to read an arrangement of Braille dots as a distribution of pressure. However, the development of the pressure sensor has not reached the stage of completion. This pressure sensor is 1.2cm square, combined with 15cm square circuit board. We need to separate these two components in order to be attached onto the fingertip. This study has already completed the whole software system and some experiments have been done on a set of pressure distribution data into Braille text conversion engine, high-precision Braille to Japanese translation engine, and speech synthesis system. We report on the current state of wearable Braille reader with a plan for adjusting the size of the sensor.

Keywords: *Braille, visually impaired people, pressure sensor, wearable device, spell corrector*

Introduction

Braille is the most universal tactile language for visually impaired people. It was invented by a French, Louis Braille in 1825 and prevailed around the world. This tactile system is useful in terms of receiving information (e.g. Braille guide plate at the station) as well as reading books and writing text. This allows them to go outside on their own.

In Japan, the number of visually impaired people is approximately 320,000, and it is estimated that about 10% of them are Braille users. They must learn Braille grammar, a complex system of special characters and letter combinations, and train themselves to read many small dots of its letters. Learning Braille is said to be difficult to achieve after the age of 14, which means that people who lose their sight later in their life find difficulty in their learning of it.

The purpose of this study is to develop a new wearable device that supports visually impaired people who need Braille and have trouble in its learning. The device named “wearable Braille reader” is equipped with a very small size pressure sensor, a microcomputer with a rechargeable battery and a Bluetooth earphone. Users trace Braille text with the pressure sensor attached onto their index fingers. The microcomputer of the system converts pressure distribution data into Braille texts, then users can hear Japanese-translated text with the Bluetooth earphone.

System Overview and Typical Use

The picture of the whole system is shown in Figure 1.

Figure 1: System Overview

A pressure sensor (the left in Figure 1) is connected to a mobile computer via USB. It does not need its own battery because it works with USB bus power supply from the mobile computer. We use Raspberry Pi 4 model B (RPi) as a mobile computer (the right top in Figure 1). A 3.5inch touch control LCD screen is directly connected onto RPi. RPi and LCD is driven with power supply from a rechargeable mobile battery

(the right bottom in Figure 1). A set of earphones (the bottom center in Figure 1) is connected to the mobile computer via Bluetooth wireless connection. In Figure 1, our system software is displayed on the LCD. The system software is written in C++ language and Qt framework. It can be run on three operating systems (i.e., Windows/mac OS/Linux) without any modifies since its source codes of the software has very high portability. Of course, visually impaired people cannot control the software with touch control interface. Therefore, we are planning to implement physical tactile switches to RPi to control the software without touch control.

Typical use of this system is as follows: We assume that users of the system attach the pressure sensor onto their fingertips, put the earphone on their ears, and put the mobile computer and the battery into a pocket. Users trace Braille text with their index fingers, then the pressure sensor detects existence of dots of Braille texts as a pressure distribution. The mobile computer analyses an arrangement of the dots from pressure distribution data and translates them into a text of spoken language. Current version of the system can translate Braille of Japanese style grammar into Japanese. Translated texts are read out by a built-in speech synthesis system. Users can hear the Braille texts as a voice with Bluetooth earphone.

Figure 2 shows a flow of data and processing. The dashed line frame in the figure means the operations which are processed by the mobile computer and its built-in system software.

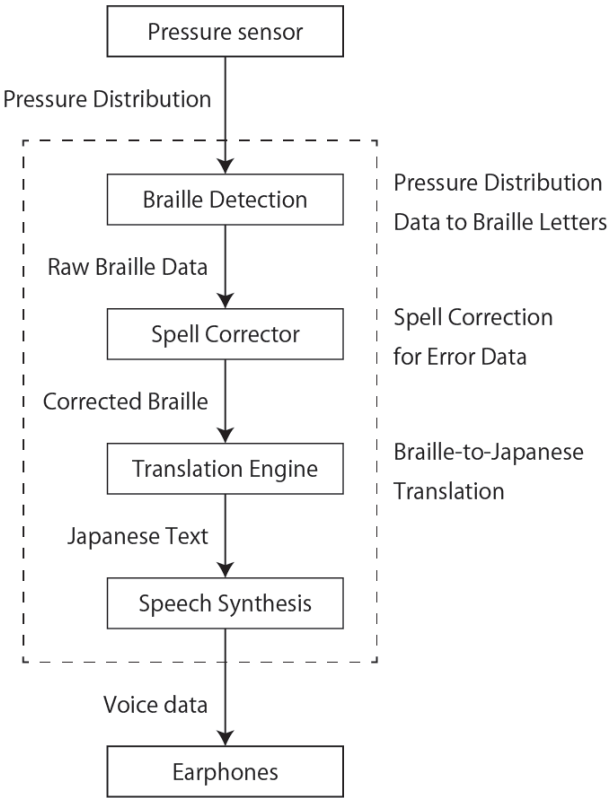

Figure 2: Flow of data and processing

Pressure Sensor and Detecting Braille

Pressure sensor is a key device of our system. It detects an arrangement of Braille dots as a pressure distribution data. We use YP-USP01A pressure sensor board by Inaba Rubber Co. ltd. which is shown in Figure 3.

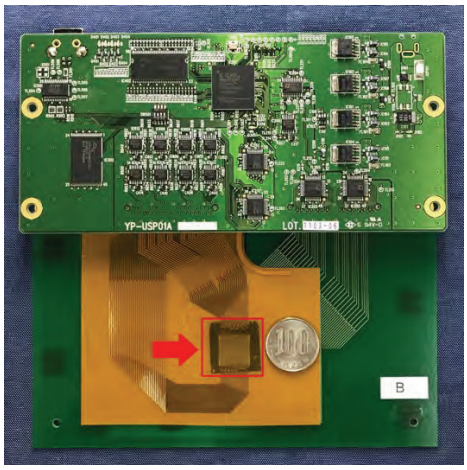

Figure 3: Pressure sensor and its circuit board

The pressure sensor of this product has 60 by 60 sensor cell within 1.2cm square conductive rubber tip (arrowed in Figure 3, we placed a coin in the right of the tip to compare the size). This pressure sensor tip is small but tightly bonded with a 15cm square circuit board. This fact makes our device unwearable. In order to attach the sensor tip onto the fingertip of a user, it should be separated from the circuit board in the future work.

The side view of one Braille dot is dome form as shown in Figure 4. The diameter of one Braille dot, i.e., variable *d* in Figure 4, is about 1.5mm. The height of one Braille dot (*h* in Figure 4) is about 0.5mm. Since only the apex of Braille dot can contact a sensor cell, the resolution of the pressure sensor must be very high. The size of each sensor cell of YP-USP01A is 0.2mm square, and each of the cell can distinguish the strength of pressure in 65536 steps. This size is enough to detect isolated Braille dots as pressure distribution.

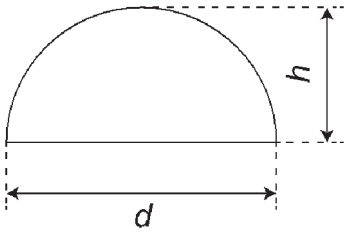

Figure 4: Side view of one Braille dot

A set of pressure distribution data obtained by the pressure sensor will sent into a mobile computer. A set of Pressure distribution data for one Braille phrase consists

of 50 to 300 frames. System software on the mobile computer reconstructs an arrangement of Braille dots from a pressure data set and separates these dots into isolated Braille letters.

Spell Corrector for Braille

As explained before, a set of Pressure distribution data for one Braille phrase consists of 50 to 300 frames. Each frame may contain error data, such as a lack of Braille dot or the ghost of dot which appears accidentally. Users may get wrong Braille texts if we convert these error-containing pressure distribution data into Braille mechanically. As a result, users of our system will get meaningless translated sentences. We show an example in Figure 5. The left in Figure 5 shows a word "dog" in Braille. If one dot in the second letter of this word is lost while users of our system traces this Braille dots, the system will translate it as "dkg".

Figure 5: A lack of Braille dot

We have implemented a spell correction system which is specialized for Braille to correct these read errors. Our spell corrector searches the word for which the arrangement of the Braille dots is the closest to "dkg", and finds out "dog" as its solution.

In addition to the case of read errors, we must consider an inversely traced Braille. Let us consider a Braille text which is printed on the lid of round shape bottles. Visually impaired people don't know which is the correct direction to trace because they cannot see which is the upward direction of letters. Figure 6 shows an example of Braille in a correct direction and the same rotated in 180 degrees. The left in Figure 6 means a word of "hint". If users trace this Braille in a reversed direction, they will get a meaningless word "ti." as shown in the right in Figure 6. Our spell corrector generates the rotated dot arrangement internally, and searches from the dictionary the words corresponding to the inputted dot arrangement as well as the rotated dot arrangement. As a result, the system finds the word “hint” and detects that there is no word "ti." It recognizes "ti." as the reversely traced word of the inputted dot arrangement for "hint", and corrects it. The spell dictionary of the system includes 2,170,000 Japanese words, most of which are nouns.

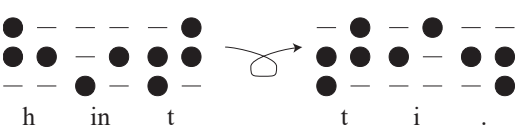

Figure 6: Rotated Braille text

Braille-to-Japanese Translation Engine

We have implemented a high precision Braille-to-Japanese translation engine for the wearable Braille reader. It recognizes almost all grammars of Japanese Braille system, and it can translate generic Braille texts into Japanese.

Table 1 shows the physical dimensions of Braille in some countries (if value takes a range, we show its median). The units in the table are millimeter. Variables *a*, *b*, *p* and *q* are corresponding to the same symbol in Figure 7. Fortunately, since the physical dimensions of Braille are almost the same between many countries (e.g., The Accessible Design Foundation of Japan, 2017; UK Association for Accessible Formats 2017; National Library Service for the Blind and Physically Handicapped of the Library of Congress 2014; Australian Braille Authority 2014), it is possible to switch to the other language version of wearable Braille reader simply replacing the translation engine. We are working on Braille-to-UEB translation engine. Unified English Braille, or UEB, is a commonly used Braille system in English spoken countries.

Table 1: Physical dimensions of Braille in each country

	a	*b*	*p*	*q*
Japan	2.40	2.25	5.70	13.00
UK	2.50	2.50	6.00	10.00
US/Canada	2.34	2.34	6.22	10.16
Australia	2.40	2.40	6.50	10.50

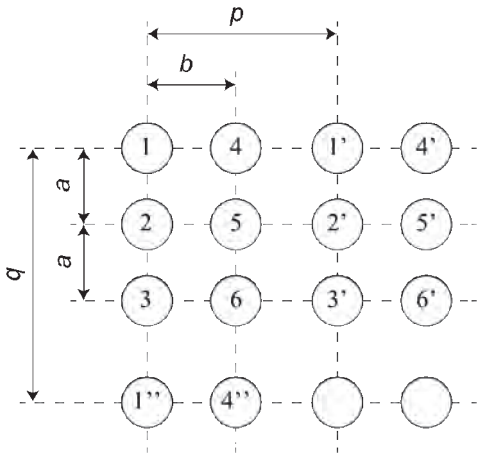

Figure 7: Physical dimensions of Braille

Test of the System

We show the results of a reading test of Braille with our device. We cannot trace Braille text with this sensor since the pressure sensor tip is tightly bonded with its circuit board as shown in Figure 3. Therefore, we made "Braille plates" to input Braille into the sensor. An Example of Braille plates is shown in Figure 8. The top in the figure is a Braille plate which means "Stairs" in

Japanese and its corresponding Braille dots. The bottom is "Book" and its Braille dots in English Braille grammar. A simple word and corresponding Braille dots are printed on a sticker. We put it on 70mm by 30mm acrylic plate. We placed them onto the sensor and slowly slides them in a horizontal direction. This operation mimics the tracing Braille with a pressure sensor attached onto user's index finger.

Figure 8: Braille plates

We have scanned 28 Braille plates with our system. The system could read 14 of 28 Braille plates correctly. Translated results were also correct. The system could read 5 of 28 Braille plates with errors within 2 dots. Even in this case, users could hear correct voice since the built-in spell correction system corrected these errors.

As for other nine cases, our system could not reconstruct an arrangement of Braille dots correctly. It is difficult to slide the Braille plate horizontally right over the sensor tip due to the Braille plate covering the sensor tip. This may be solved if we separate the sensor and its circuit board and attach the sensor onto the fingertip.

We also measured battery duration time of this system. We started from fully charged 10,000mAh mobile battery and measured its duration time until its power is going down. We turned on all functionality of RPi (i.e., LCD, Bluetooth and Wi-Fi) and played MP4 movie repeatedly. No operations were done by its user while the test. We measured 10 times, and the system worked 600 minutes on average.

Summary and Future Works

We explained the status of our wearable Braille reader in this paper. Current version of this device can read about 50% of the Braille text correctly. It seems that the spell correction system works well. The sensor of this device, however, is too large to be attached onto user's fingertip. We must separate the pressure sensor from its circuit board to be attached onto the fingertip.

The operation of the current system requires touch control of LCD panel. For visually impaired people, it is impossible to operate our system. We need to add some physical switches for operation of our system.

Keeping these problems in mind, we will consider modifying the whole hardware set of the system to become more suitable to wear.

On the software side, Braille to non-Japanese language translation engine is also considered. We are developing UEB engine and a spell correction system equipped with UEB. We will increase the kinds of languages applied to UEB.

Acknowledgements

We would like to thank Yoshinori Fujisawa for useful discussions. This work was supported by JSPS KAKENHI Grant Number JP19K12917.

References

Australian Braille Authority (2014). *Physical Specifications for Braille*. Retrieved from https://brailleaustralia.org/about-braille/physical-specifications-for-braille/.

National Library Service for the Blind and Physically Handicapped of the Library of Congress (2014). *Specification 800:2014 Braille Book and Pamphlets* (Section 3.2). Retrieved from https://www.loc.gov/nls/wp-content/uploads/2019/09/Spec800.11October2014.final_.pdf.

The Accessible Design Foundation of Japan (2017). *JIS T 0921:2017 Accessible design -- Application of braille on signage, equipment and appliances*. Retrieved from https://webdesk.jsa.or.jp/books/W11M0090/index/?bunsyo_id=JIS+T+0921%3A2017.

UK Association for Accessible Formats (2017). *Standard dimensions for the UK Braille Cell*. Retrieved from https://www.ukaaf.org/wp-content/uploads/2020/03/Braille-Standard-Dimensions.pdf.

EVALUATION OF PREP-n-GO™ BUFFER FOR DNA EXTRACTION IN URINE SAMPLE

K.P. Ngai[a] and C.K. Wan[*,a]

[a] Department of Health and Life Sciences, Hong Kong Institute of Vocational Education (Sha Tin), Hong Kong

*ckwan@vtc.edu.hk

Abstract

Various human samples are used for DNA analysis. Prep-n-Go has long been used for the extraction of DNA in buccal swabs and blood samples. It is a convenient and reliable method by using an extraction buffer for direct PCR amplification without DNA qualification. This study aims at evaluating Prep-n-Go for the extraction of DNA in urine sample, with collecting urine considered to be advantageous due to its non-invasive sampling method. In this study, urine samples with different volume (100µL, 200µL and 400µL) were mixed with 400µL Prep-n-Go Buffer. Samples were then amplified directly using the VeriFiler™ Express PCR amplification Kit (Applied Biosystems™). Each PCR reaction comprised 20µL master mix and 5µL template DNA. Capillary electrophoresis was carried out on the Seqstudio Genetic analyzer and alleles were determined using the GeneMapper ID-X v 5 software (Applied Biosystems™). A total of four urine samples were collected from two males and two females with informed consent. Urine sample of 100µL achieved significantly stronger signal (i.e., higher peak height of relative fluorescence units (RFUs)) than those of 200µL and 400µL samples. Moreover, the efficacy of two extraction methods: room temperature and heat protocols from the same sample was also investigated. The results showed that the average peak heights from room temperature protocol were significantly higher than in the heat protocol. It took less than 1h for DNA extraction from the urine samples. Apart from buccal swabs and blood samples, this study showed that the Prep-n-Go Buffer can extract DNA from urine samples directly. It is an efficient method for obtaining DNA profiles from urine samples, which greatly shortened the duration for DNA qualification and reduced the turnaround time.

Keywords: *DNA extraction; urine samples; Prep-n-Go*

Introduction

The non-invasive buccal swabs method has been considered as a convenient and efficient alternative to the conventional invasive DNA sampling of blood samples (Hanselle et al., 2003). The application of the new approach in DNA analysis, however, might still has short-comings such as the relatively long extraction time (approximately 1 to 2 hours). It also involved multiple sample transfer between container tubes, which results in higher risk of contamination.

Prep-n-Go™ buffer has shown promising results in reducing the extraction time and lower the risk of contamination. Previous studies demonstrated successful extraction of DNA from buccal swabs and blood samples, respectively (Gomes et al., 2017). In this study, the feasibility of using the Prep-n-Go™ to extract DNA from urine samples was evaluated. The performance of two extraction protocols: room temperature and heat protocols was also investigated.

Materials and Methods

Sample collection and DNA extraction

A total of four urine samples were collected from two males and two females with informed consent. Urine samples with different volume (100µL, 200µL and 400µL) were mixed with 400µL Prep-n-Go Buffer.

PCR amplification

Samples were amplified using the VeriFiler™ Express PCR amplification Kit (Applied Biosystems™). It is a 6-dye short tandem repeat (STR) multiplex assay that amplifies 23 autosomal STR loci. Each PCR reaction comprised of 20µL master mix and 5µL template DNA. The components of the PCR mixtures are shown in Table 1. The program included (1) an initial incubation step at 95°C for 1 minutes, and (2) a denature step at 94°C for 3 seconds, 59°C for 16 seconds, followed by 65°C for 29 seconds and 60°C for 5 minutes. The reaction was

performed using the Veriti™ Thermal Cyclers (Applied Biosystems, Foster City, CA) with 27 cycles.

Table 1. PCR assay Mix Component.

Component	Volume/Sample
DNA template	5 µL
Primes Set	10 µL
Master Mix	10 µL

Electrophoresis and analysis

Capillary electrophoresis was carried out on the Seqstudio (Applied Biosystems™) and alleles were determined using the GeneMapper ID-X v 5 software (Applied Biosystems™). The components for genetic analyser are shown in Table 2. All data were analyzed using the SPSS statistical package (version 21.0). One-way ANOVA results suggested the significant differences between the means of different samples.

Table 2. Component for Capillary electrophoresis

Component	Volume/Sample
PCR product	1 µL
600 LIZ® Size Standard	0.4 µL
Hi-Di formamide	9.6 µL

Results and Discussion

Blood samples have been traditionally used to produce DNA profiles. The invasive sample collection method has been widely replaced by non-invasive buccal swabs. Urine could be another potential candidate of non-invasive sample. But there are still concerns on the time-consuming extraction step. Various extraction methods took approximately several hour to extract DNA from the samples and involved several tube transfers. Developing new method to speed up the extraction process with simple procedure could reduce the risk of contamination and enhance the precision of the analysis.

The results of this study showed that the Prep-n-Go approach can effectively extract DNA from the urine sample. Figure 1 showed the good quality DNA profiles from the 100 µL urine samples. Gomes et al. (2017) and Iyavoo et al. (2019) obtained similar results.

The signal peak heights (i.e., relative fluorescence units (RFUs)) of extracting DNA from various volume of urine samples are shown in Figure 2. The extraction has been performed under room temperature. The signal peak heights of the 100µL urine sample remained higher than that of the 200µL and 400µL samples. The significantly weaker signal for the 200µL and 400µL samples may be due to the presence of more PCR inhibitor.

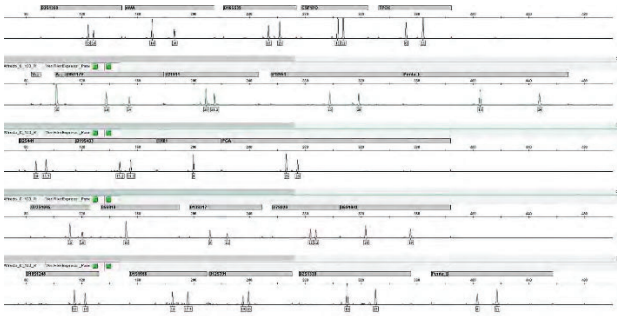

Figure 1. The relative fluorescence units (RFUs) of urine samples.

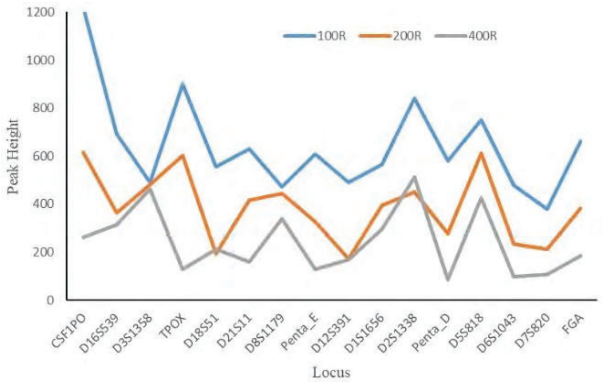

Figure 2. The relative fluorescence units (RFUs) of urine samples with different urine volumes under room temperature extraction.

Table 3. Turnaround time (TAT) of urine samples by using Prep-n-Go Buffer.

		Time
Room temperature Protocol	DNA extraction	5 mins
	Amplification	45 mins
	Separation and Detection	45 mins
	Total TAT time	**95 mins**
Heat Protocol	DNA extraction	20 min
	Amplification	45 min
	Separation and Detection	45 min
	Total TAT time	**110 mins**

Iyavoo et al. (2019) reported that the heat protocol could achieve better extraction results than the room temperature protocol by using buccal swabs samples. However, the heat protocol took longer time to obtain DNA profile. Our results showed that by using the Prep-n-Go Buffer, either with the room temperature or the heat protocol, the turnaround time (TAT) is much shorter than other extraction protocols (Table 3). However, the presence of inhibitors in the urine sample is unpredictable. As PCR is an enzymatic reaction, the presence of various inhibitors would be unfavourable for PCR. There is no standardized method to remove PCR inhibition. Further studies are required to adopt external

DNA as an internal control to detect the presence of inhibitors.

Conclusions

The results of this study showed that the Prep-n-Go Buffer can extract DNA from urine samples directly. It is an efficient and non-invasive method for obtaining DNA profiles, which greatly shortened the duration for DNA qualification and reduced the turnaround time. The Prep-n-Go approach has a potential to minimize the risk of cross-contamination and thus enhance the precision of the analysis.

Acknowledgements

The work described in this paper was fully supported by the Department of Health and Life Sciences, Hong Kong Institute of Vocational Education (Sha Tin), Hong Kong.

References

Gomes, C., Martínez-Gómez, J., Díez-Juárez, L., Díaz-Sánchez, S., Palomo-Díez, S., Arroyo-Pardo, E., Cano-López, M., & Fernández-Serrano, J. (2017). Prep-n-Go™: A new and fast extraction method for forensic blood samples. Forensic Science International: Genetics Supplement Series, 6, e265–e266.

Hanselle, T., Otte, M., Schnibbe, T., Smythe, E., & Krieg-Schneider, F. (2003). Isolation of genomic DNA from buccal swabs for forensic analysis, using fully automated silica-membrane purification technology. Legal Medicine, 5, S145–S149.

Iyavoo, S., Knights, S., Mavrommatis, M., & Haizel, T. (2019). Implementation of Prep-n-Go™ Buffer for DNA extraction from buccal swabs. Forensic Science International: Genetics Supplement Series, 7(1), 211–213.

VeriFiler™, Express PCR Amplification Kit User Guide, Thermo Fisher Scientific, 2017.

Development of communication tools for people with speech difficulties

Daichi Matsuzawa[a], Yoshinori Fujisawa[*,a]

[a] National Institute of Technology, Nagano College/Department of Electronics and Computer Science, Nagano, Japan

*fujix@nagano-nct.ac.jp

Abstract

We are currently researching a request from a special-needs school to develop a device that can help children communicate effectively. These needs are related to communication, such as "I want to help the children communicate their thoughts and feelings better" and "I want to help the children communicate with others better". These children are troubled by the fact that they cannot speak well, or that they speak in a way that is difficult to understand and are repeatedly asked to repeat back. These children can speak. However, because it is difficult for others to hear them, they may be made to speak the same thing repeatedly and eventually give up speaking. As a means for people with such pronunciation difficulties to communicate effectively. We can use a computer to recognize the speech of a person with pronunciation difficulties, and the computer can recognize the content of this speech. If the computer can recognize the speech of a person with pronunciation difficulties and visualize it so that others can understand the content of the recognized speech, it will be helpful in communication. We are currently working on a visualization method using sign language and fingerspelling, in addition to transcribing the speech as it is. Since there are people with various kinds of disabilities in special needs schools, it is thought that visualization using sign language and fingerspelling, which are familiar to people with hearing disabilities, is of significance. At present, we first recognized the speech of a normal person without disabilities and visualized it. Since the speech style of people with pronunciation difficulties is different from that of normal people, it is difficult to use speech recognition software to recognize their speech. However, if we create a special acoustic model for people with pronunciation difficulties, the recognition accuracy will be improved. For this reason, we are planning to sample the voices of people with pronunciation difficulties, examine the phonemes, and develop speech recognition software optimized for them.

Keywords: *speech recognition, Julius, speech difficulties, fingerspelling, sign language*

Introduction

We have been consulted by a special-needs school on the development of a device that will enable children with disabilities to communicate effectively. This consultation was based on the special-needs school staff's desire to help the children better communicate their thoughts and feelings, and to help the children better communicate with their surroundings. Children with speech difficulties are troubled by their inability to speak well, or by the fact that they speak in a way that is difficult to understand and are heard repeatedly. The children are capable of speak. However, when the children speak, it is difficult for others to understand them, so they are often heard repeatedly, and eventually they give up speaking. We investigated the number of people with disabilities who have such communication and other problems. According to the results of the 2006 Survey of Physically Handicapped Children and Persons published by the Ministry of Health, Labor and Welfare, the estimated number of physically handicapped persons in Japan is 3,483,000. Of these, 343,000 (9.8% of the total number of physically disabled persons) are classified as having hearing or speech impairment, which is defined as having problems with communication related to speech. In addition, the estimated number of physically handicapped children in Japan is 93,100,000. Of these, 15,800,000 (18.6% of the total number of children with physical disabilities) are classified as having hearing or speech impairment. Thus, it is likely that a large number of people have hearing and speech impairments that are considered to be problems with speech-related communication. Among such people with disabilities, the disability that is the subject of this research is called dysarthria. Dysarthria is a disorder in which the ability to pronounce words normally and clearly is lost. The main symptoms are awkward speech, choppy, muffled breathing, irregular, obscure, or monotonous. However, dysarthric people are able to understand and use language correctly. The direct cause of dysarthria is believed to be a problem with muscle movement. These muscle movement problems are believed to be caused mainly by abnormalities in the brain. Stuttering, in which the speech does not come out smoothly, is also considered to be a type of dysarthria. People with these symptoms are referred to as those with

speech difficulties in this research. At present, people with speech difficulties often use boards with letters and pictures on them or computer equipment with a keyboard and screen to communicate. The purpose of this research is to develop a device that enables people with speech difficulties to communicate smoothly by making their speech the axis of communication and making it easier for the other person to understand what they are saying.

Differences between similar researches

There are several similar researches to this one. We describe the purpose of this research is described in comparison with those researches. Supporting the hearing impaired with sign language CG in television is considered to be similar to this study in that it attempts to use sign language CG to communicate to the hearing impaired. Figure 1 shows an example of sign language CG used in television and other applications.

Figure 1 Example of sign language CG

The difference between our research and this one is that we visualize the words of people with speech difficulties. Unlike normal people, people with speech difficulties generally find it difficult to use speech recognition technology. Therefore, the purpose of this research is to improve the recognition accuracy and speed of speech recognition for people with speech difficulties to the same level as for healthy people.

A communication support board is a communication support device that may be used by people with current speech difficulties to communicate. Instead of speaking, they communicate by pointing to pictures. Figure 2 shows an example of a communication support board. These communication support boards are used by people with speech difficulties to communicate their intentions and what they want to say to others by pointing to pictures. Compared to the communication support board, this research assumes that spoken words are used for communication, which is expected to broaden the range of expression and make communication more accurate. In addition, since voice is used for communication, the system can be used hands-free, which is an advantage for people with hand disabilities.

Figure 2 Example of a communication support board

Solution to the problem

One of the challenges for people with speech difficulties is that it is difficult for the person with whom they are conversing to understand what the person with speech difficulties is saying. As a solution to this problem, we came up with a method that allows a computer to recognize and visualize speech. In this method, speech is input to a computer, and speech recognition software on the computer is used to recognize the content of the speech. We thought it would be good if we could create a communication aid that would visualize the recognized content so that the person with whom we were talking could understand it. As for the visualization method, we are considering the use of sign language and fingerspelling in addition to the transcription method. This is because it is thought to be effective when communicating with hearing-impaired people in special needs schools.

Building the system

We describe the system that actually performs the visualization. Figure 3 shows a schematic diagram of the system.

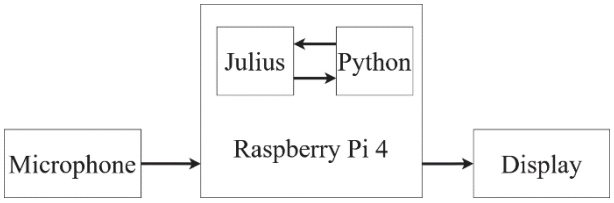

Figure 3 Schematic diagram of the system

Figure 3 shows how the visualization system works. First, we use a microphone as an input. This time, we used a USB microphone. From this microphone, audio is input to the computer. The computer used is a Raspberry Pi 4. The reason for using the Raspberry Pi 4 is to make it possible for many people to use it when it is actually used in special needs schools. On the computer, a speech recognition software called Julius is running. Julius is an open-source, high-performance, general-purpose, large-vocabulary continuous speech recognition engine for the development and research of speech recognition systems. By using Julius, speech can be recognized as characters. In this system, start Julius as module mode. This allows data to be retrieved from other programs using socket communication. The acquired data is processed using Python. The system displays characters, images, and video depending on the recognized character content. The display of text is a method of visualization as a transcription. The image is supposed to be displayed as a fingerspelling. The video is supposed to be displayed as the movement of the sign language. For these displays, the Python image libraries Pillow and OpenCV were used. The output from the computer will be on a display.

Proprietary dictionary

Julius uses a dictionary for speech recognition. This dictionary is distributed, but you can also make your own. By creating a dictionary, it will be able to recognize only the words that you specify. This makes it easier to recognize words that are expected in a conversation. In this research, we also worked on creating our own dictionary. In order to create Julius's original dictionary data, files corresponding to the four elements of "reading", "phonemes", "syntax", and "vocabulary" are required. The extensions for each file are listed below.

- "reading" file extension ".yomi"
- "phonemes" file extension ".phone"
- "syntax" file extension ".grammar"
- "vocabulary" file extension ".voca"

These files are described below. We created a dictionary based on seven words: "ohayou," "konnichiha," "konbanha," "oyasumi," "hare," "kumori," "ame," and "a". These words are words with meanings as shown in Table 1.

Table 1 Words and their meanings

Words	Meaning
ohayou	good morning
konnichiha	hello
konbanha	good evening
oyasumi	good night
hare	sunny
kumori	cloudy
ame	rainy
a	vowel

To learn the words shown in Table 1, create a file of the elements of each of the words shown in the previous section. Listing 1 shows the "read" file.

Listing 1 "read" file

```
おはよう　おはよう
こんにちは こんにちは
こんばんは こんばんは
おやすみ　おやすみ
晴れ　はれ
曇り　くもり
雨 あめ
あ あ
```

The "read" file defines the "read" of words to be registered in the dictionary. As shown in Listing 1, write the word to be recognized on the left side and the reading in hiragana on the right side. The words on the left may be defined by Kanji characters, etc. Listing 2 shows the "phoneme" file.

Listing 2 "phoneme" file

```
おはよう　　o h a y o u
こんにちは　　k o N n i ch i h a
こんばんは　　k o N b a N h a
おやすみ　　o y a s u m i
晴れ　h a r e
曇り　k u m o r i
雨　　a m e
あ　　a
```

The "phoneme" file is created by using the "read" file. Use the script (yomi2voca.pl) included in Julius to create it. Listing 3 shows the "syntax" file.

Listing 3 "syntax" file

```
S : NS_B WORD NS_E
WORD : OHAYOU
WORD : KONNICHIWA
WORD : KONBANHA
WORD : OYASUMI
WORD : HARE
WORD : KUMORI
WORD : AME
WORD : A
```

The “S” in the first line of the “syntax” file indicates the syntax definition. NS_B means the start of the sentence and NS_E means the end of the sentence. The second and subsequent lines are strings to be recognized, and are used by capitalizing the reading of the “phoneme” file in List 2. Listing 4 shows the “vocabulary” file.

Listing 4: “vocabulary” file

```
% OHAYOU
おはよう o h a y o u
% KONNICHIWA
こんにちは k o N n i ch i h a
% KONBANHA
こんばんは k o N b a N h a
% OYASUMI
おやすみ o y a s u m i
% HARE
晴れ h a r e
% KUMORI
曇り k u m o r i
% AME
雨 a m e
% A
あ a
% NS_B
[s] silB
% NS_E
[/s] silE
```

Save these files from List 1 to List 4 in the same directory, and run the script (mkdfa.pl). This will generate three files with the extensions ".dfa", ".dict", and ".term". By using this, speech recognition can be performed using an original dictionary.

System execution

We have built a system and verified that it can recognize speech correctly using our own dictionary. What we confirmed this time was the recognition of speech by healthy people. Depending on the content of the speech, the computer will process it. When we say the word "sunny", it recognizes it and shows "the weather is sunny now" on the display. Likewise, if we say the word "cloudy", it will display "the current weather is cloudy", and if we say the word "rainy", it will display "the current weather is rainy". Also, when we say the word "a", it recognizes it and displays an image with the word "a" written in hiragana. It is designed to display 3DCG, which means "A" in finger fingerspelling. Also, when we say the word "hello," it will recognize it, and a video will be played and displayed. It is designed to display 3DCG with movement, which means "hello" in sign language.

We show a screenshot of the actual result of the run. First, Figure 4 shows what happens when the computer recognizes a word and displays the corresponding word.

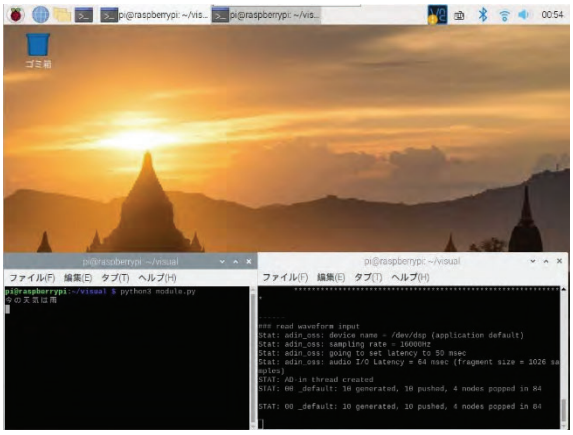

Figure 4 Showing the recognized word

In Figure 4, this is what happens when we say "rainy". In the console on the right, Julius is running in module mode, connecting to the program and returning the results of speech recognition. On the left side of the console, a Python program is running, displaying words according to what Julius has recognized in speech. In the future, we are considering registering more words in a dictionary and transcribing the conversation as it is. Next, Figure 5 shows how the computer recognizes a word and displays the corresponding image.

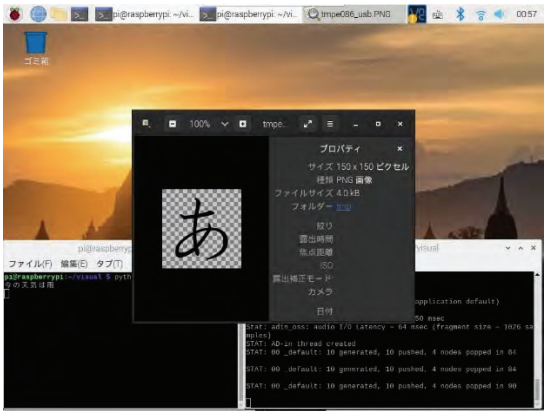

Figure 5 Showing the image of the recognized word

Since we spoke the word "a", an image with the word "a" written in hiragana will be displayed. This is displayed for the purpose of displaying fingerprints, as shown in Figure 6. In the future, we are considering to display the fingerprint image after recognizing each Japanese syllable. Finally, Figure 7 shows what happens when the computer recognizes a word and plays and displays the corresponding video.

Figure 6 Fingerspelling that means "a"

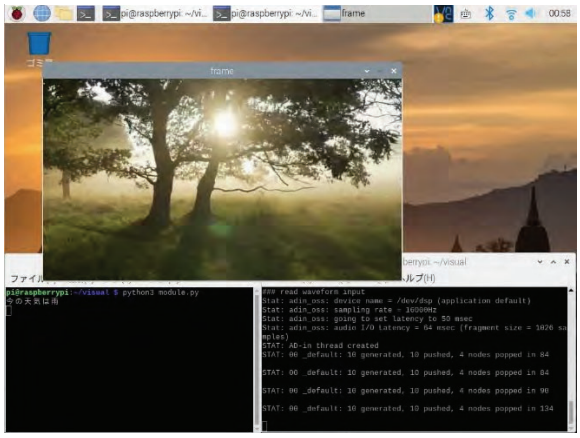

Figure 7 Showing the movie of the recognized word

We say, "Hello," and the video is played and displayed. In the future, we are considering playing a video of a sign language with movement that means "hello".

Acoustical model

The voice recognition system mentioned earlier worked normally when used by healthy people. However, previous studies have shown that people with speech difficulties have a different speech style from normal people. If people with speech difficulties uses the current system, he or she may not be able to recognize it properly. This is because the speech recognition software is expected to be less accurate due to the difference in speech styles. This is not practical for practical use, so ingenuity is required.

As a method of devising, we are considering creating an acoustic model optimized for people with speech difficulties. Acoustic models are used in speech recognition software to determine what a voice is by analyzing its frequency components and time variation. The type of acoustic model we are considering is the Hidden Markov Model, which represents the acoustic features of phonemes. To create an acoustic model, it is necessary to create a phoneme model, which is the basis of the acoustic model. For this reason, the voices of people with speech difficulties are sampled and the phonemes are examined. We are considering using a toolkit called Hidden Markov Model Tool Kit to build the model. The use of a special acoustic model for people with speech difficulties is expected to improve the recognition system.

JuliusLib

Python, which is currently used for image and video display, has execution speed problems. This is probably due to the fact that Python is an interpreted language. If the execution speed is slow, the tempo of visualizing the content of the utterance will be slow, and the flow of the conversation will be halted. The ideal system should be able to immediately display the content of speech. In order to achieve this, it is necessary to consider the construction of a system using a fast executing language such as C Langage. One possible way to achieve this is to use the JuliusLib mechanism. This is a library that contains the main body (engine) of the recognition processing part of speech recognition. By using this library, it is possible to create your own speech recognition applications that incorporate the Julius engine. The embedded engine and the application communicate using callbacks.

Conclusions

We are currently working on a communication aid for people with speech difficulties. This is a device that recognizes the speech of a person with speech difficulties and conveys it to the other person in a way that is easily understood. We have been able to implement mechanisms that lead to communication support through the speech of healthy people. This is because of the improved accuracy of speech recognition, such as the use of a proprietary dictionary, and the use of methods such as transcription and image display to convey speech to the other party. In the future, we would like to improve the accuracy of recognition by creating acoustic models for people with speech difficulties, and challenge the recognition speed by using JuliusLib. And we would like to further improve this system by having it reviewed and used by students in special needs schools.

References

Results of the 2006 Survey of Physically Challenged Children and Persons. Retrieved from https://www.mhlw.go.jp/toukei/saikin/hw/shintai/06/dl/01.pdf.

Dysarthria - 09. Diseases of the Brain, Spinal Cord, and Peripheral Nerves - MSD Manual Home Edition. Retrieved from https://www.msdmanuals.com/ja-jp/%E3%83%9B%E3%83%BC%E3%83%A0/09-%E8%84%B3%E3%80%81%E8%84%8A%E9%AB%84%E3%80%81%E6%9C%AB%E6%A2%A2%E7%A5%9E%E7%B5%8C%E3%81%AE%E7%97%85%E6%B0%97/%E8%84%B3%E3%81%AE%E6%A9%9F%E8%83%BD%E9%9A%9C%E5%AE%B3/%E6%A7%8B%E9%9F%B3%E9%9A%9C%E5%AE%B3.

Supporting the Hearing Impaired with Sign Language CG in Television. Retrieved from https://www.jstage.jst.go.jp/article/itej/69/7/69_526/_article/-char/ja/.

NHK Sign Language CG. Retrieved from https://www2.nhk.or.jp/signlanguage/index.cgi.

Communication Support Board - Meiji Yasuda Foundation for Mental Health. Retrieved from https://www.my-kokoro.jp/communication-board.

Julius a large-vocabulary continuous speech recognition engine. Retrieved from https://julius.osdn.jp.

Takiguchi, Tetsuya Iida, Akemi Speech Disorders and Speech Technology Journal of the Institute of Electronics, Information and Communication Engineers = The journal of the Institute of Electronics, Information and Communication Engineers 91(12), 1019-1023, 2008-12-01 The Institute of Electronics, Information and Communication Engineers

HTK Speech Recognition Toolkit. Retrieved from https://htk.eng.cam.ac.uk

JuliusLib. Retrieved from https://julius.osdn.jp/juliusbook/ja/desc_juliuslib.html

INFECTION CAPABILITY OF MATERIALS USING GRAPHENE FILM AND ITS IMPEDANCE CHARACTERISTICS

H.Kaneamtsu[*,a], R.Nakagawa[a], Y. Torisawa[a], H.Miura[b]. D.M.Barry[c]
M.Ishihara[d], M.Ban[e], R.Kawai[a], T.Kogo[a], A.Ogawa[a], N.Hirai[a], M.Yoshitake[f], and S.Zimmermann[g]

[a] National Institute of Technology (KOSEN), Suzuka College, Suzuka, Mie, Japan
[b] Suzuka University of Medical Science, Suzuka, Mie, Japan
[c]Department of Electrical & Computer Engineering, Clarkson University, Potsdam, NY, 13699, the USA./SUNY Canton, Canton, NY, 13617, the USA.
[d]National Institute of Advanced Industrial Science and Technology, Tsukuba, Ibaraki, Japan
[e]Nippon Institute of Technology, Miyashiro, Saitama, Japan
[f]National Institute of Materials Science, Tsukuba, Ibaraki, Japan
[g]Leibniz Universität Hannover, Institute of Electrical Engineering and Measurement Technology, Appelstr. 9A, 30167 Hannover, Germany

*kanemats@mse.suzuka-ct.ac.jp

Abstract

Biofilms form on materials by bacterial activities. Bacteria existing in biofilms generally have a high resistance to the human immune system and antibiotics. Therefore, bacteria can survive more in biofilms, which leads to healthcare-acquired infection, chronic diseases, etc. Also, many problems exist in our surrounding environment such as scales within pipes, contamination on material surfaces in the kitchen, toilet, bathtub, etc. are caused by bacterial activities. Therefore, the effective countermeasures against biofilm formation and growth should be established urgently. For fulfilling this purpose, we need to find an effective sensing device and system. In this experiment, we focused on graphene films. In our laboratory, we found graphene's high sensitivity to biofilm formation. If we could find a suitable probe and signal to detect the sensitivity of graphene, we would get a chance to produce a good sensor. The problem is what kind of signals we would use and how we would get the signals from graphene. In this experiment, we measured the impedance of graphene films using copper and polymer substrates, when biofilms formed on graphene films. We include a discussion about the application of graphene's impedance characteristics for biofilm sensing.

Keywords: *graphene, 2D materials, Impedance, biofilms, EPS*

Introduction

Since COVID-19's outbreak and pandemic, people have been sensitive to infection. Since then, we have learned a lot about infection not only as professionals, but also as regular citizens. Infections are often classified according to the organisms that cause them. Bacterial infection is one of them. On the other hand, infection is caused by viruses. In both cases, materials could intervene the infection from human to human.

Usually, bacteria do not survive very long, since they need nutrition (carbon compounds) to survive. However, most materials do not provide bacteria with a continuous supply of nutrition. Biofilms form on materials' surfaces in most practical cases. Biofilms are composed of water, polymeric substances, and bacteria themselves at the beginning stage of their growth. In biofilms, bacteria could have high resistance to biocides and antibiotics due to some reasons. Therefore, biofilms could serve as a reservoir for bacteria, so that bacteria could survive without the existence of human beings.

As for viruses, there have been no concrete documents between their activities and biofilms. It should be the future task for us to demonstrate it. However, viruses could keep their activity in humid environments for a while. Since biofilms contain water components, they might provide viruses with humid environments even on materials.

From the viewpoint, biofilms might be a key for materials' infectious capabilities. In this paper, we tentatively define materials' infectious capability as the capability of biofilm formation. For this project, we measured it using graphene as one of the advanced 2D materials.

Graphene and biofilm formation capability

Biofilms form on materials' surfaces by bacterial activities. As already described, they are basically composed of water (more than 80% at the initial stage,

but the contents decrease with time.), polymeric substances derived from bacteria (called EPS: extracellular polymeric substances), and bacteria themselves (including live and dead bacteria). The growing process is basically composed of three stages. The first stage is the formation of conditioning film as a prior condition for biofilm formation. Carbon compounds are potential nutrition for most of bacteria and they tend to absorb on materials' surfaces as inhomogeneous thin film. That is called "conditioning film".

The second stage is the approaching of bacteria to materials' surfaces and attachment process. Bacteria and materials' surfaces have their electric double layers, respectively. When the two substances having electric double layers approach each other, the repulsive force between them is produced due to the osmotic pressures. The components and kinds of forces between them vary, depending on materials. To attach onto materials' surfaces, bacteria need to have a special component to overcome the repulsive force. The component is biofilms. Concretely speaking, EPS interacts with materials' surfaces to produce attraction forces. As a result, bacteria could attach to materials' surfaces.

The third stage is a signal deduction process called quorum sensing. Overcoming the repulsive force between bacteria and materials, bacteria increase their numbers on materials' surfaces. When the number reaches a threshold value, the signal deduction substances called auto inducer increases and reaches a threshold value. Then the substances enter the bacterial cells and stimulate a part of DNA. Then the excretion of polysaccharide occurs for all affected bacteria simultaneously. As a result, bacteria and materials' surfaces are surrounded by polymeric substances. At this point, biofilms form on materials' surfaces.

The sensing of infection is equivalent to monitor biofilms. Conventionally, biofilms have been evaluated in various ways. Mainly, the expensive apparatuses, such as optical microscopes, fluorescent microscopes, scanning electron microscopes, transparent electron microscopes, confocal laser microscopes, Raman spectroscopy, mass spectroscopy, AFM, STM, etc. However, those types of apparatus are not always suitable for in-situ and quantitative analyses. On the other hand, some of the authors investigated the utilization of staining so far. Even though this method is quantitative, it is not available for in-situ measurement and sensing.

Therefore, in this investigation, we focused on electrochemical methods. Electrochemical methods for the purpose are classified into potentiometry, amperometry and impedance measurements. They have been investigated by us and other researchers. When we focus on the final market products, the requirements are miniaturization, user-friendliness, rapidness for measurement, etc. The key for the realization and satisfaction is the electrode materials. It is the ideal complete situation that biofilms form on the electrode material with suitable sensitivity, formation rate, intensity of signals, response rate and quantities, etc. Therefore, the searching for the electrode materials should be the first important mission.

We, authors, have been searching for the suitable electrode materials. In 2016, we asked a venture company to make mono-layer graphene and five -layered graphene films on glass specimens. Then we checked the biofilm formation behaviours, using Raman spectroscopy. As a control, we used graphite, one of the same carbon materials. And then, we found graphene was very sensitive to biofilm formation. At the same time, we also found that the five-layered graphene films had almost the same sensitivity to that of graphite. Therefore, we presume that the sensitivity to biofilm formation decreases with increasing layer numbers, since the characteristics of graphene would be lost with increasing the layer numbers. Why is graphene so sensitive to biofilm formation?

It is well- known that pie electron clouds stand out in the normal direction. On the other hand, biofilms are composed of bacteria and EPS. Therefore, the mutual overlap of electric clouds for both sides is easy to occur, when both phases are approached. The overlap produces repulsive forces due to the osmotic pressure. However, the high affinity between graphene and EPS/bacteria in biofilm (due to the pie electron clouds) promotes the formation and growth of biofilms.

The authors already confirmed the high capability of graphene to form biofilms. However, it is the future mission and task for us to get the electric signals for biofilm formation. In this study, we introduce some of our results to achieve the purpose.

Experimental

Fig.1 The appearance of the impedance measurement system.

The monolayer graphene film was formed on copper substrate by a chemical vapor deposition. The thickness was confirmed as 10 micro-meters. Using a static biofilm formation method, we produced biofilms on those graphene film specimens. The bacteria used for biofilm formations were *E.coli* (K-12, G6). The bacteria were inoculated on the LB liquid culture and incubated at 37 degrees Celsius for 24 hours with vibrational culturing. Then the bacterial solution was poured into each of 6 plastic wells where specimens were already put in

advance. They were incubated at 25 degrees Celsius for 72 hours to form biofilms on each specimen.

After biofilm formation, specimens were taken out of the plastic wells and dried naturally in ambient air for 10 minutes. Then the impedance measurement was made. The measurement system is shown in Fig.1

The specimens were put between two thin insulated plates and closely attached by the external pressure. Then the impedance between the two electrodes was measured by an impedance analyzer (HIOKI, IM3590). The results were shown as a frequency-impedance curve.

Results and discussion

Fig. 2 shows some of the results for specimens without biofilms. As shown in the figures, impedance values decreased with increasing frequencies gradually.

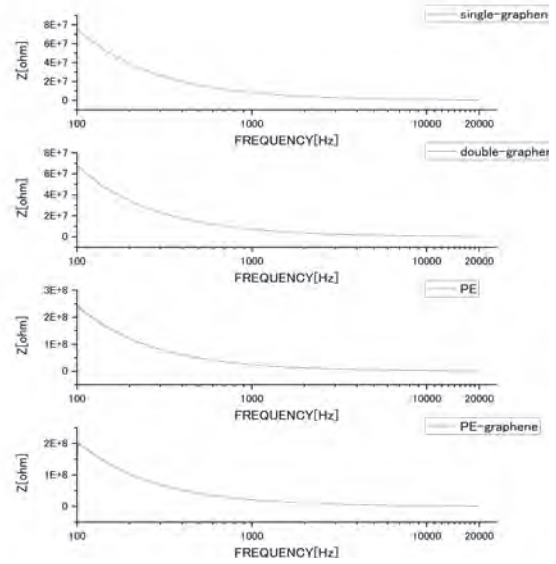

Fig. 2 Impedance behaviours of specimens without biofilms.

In the diagrams, not only the result for monolayered graphene (single layer -graphene), those of double layer graphene, PE, and graphene film specimen on PE were also shown. The tendencies were the same among those specimens. However, the absolute values differed from case to case because the extent of biofilm formation and growth was different in these cases.

On the other hand, the impedance for the specimen with biofilms for monolayered graphene specimen is shown in Fig.3.

As shown in Fig.3, the impedance curve showed two peaks, one at 200 Hz and the other one at 10kHz. The two peaks could be attributed to the formation of biofilms.

The appearance of peaks could be attributed to the existence of biofilms. Fig.4 shows the mechanism schematically. This figure illustrates the cross- sectional biofilm schematically. Conductive water components dominate the inside of biofilms. However, insulative

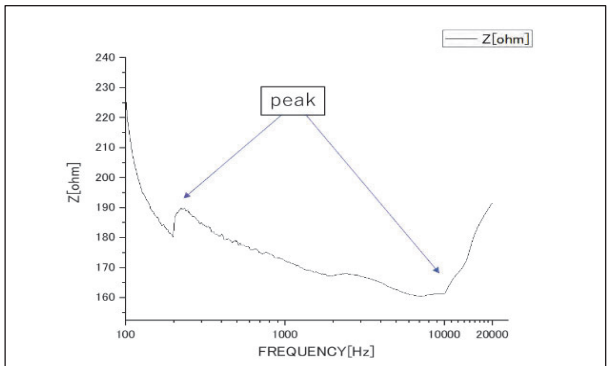

Fig. 3 The impedance behaviour for the monolayer graphene film specimen with biofilms.

polymer derived from bacteria (EPS) increases with the biofilm formation. At the lower frequencies, the current tends to flow through conductive phases (in this case, the liquid solution in biofilms.). However, when the frequencies are increased, the current flows more through the insulated phases. This corresponds to EPS and bacteria in this case. Therefore, the peaks appear when biofilms are developed with EPS.

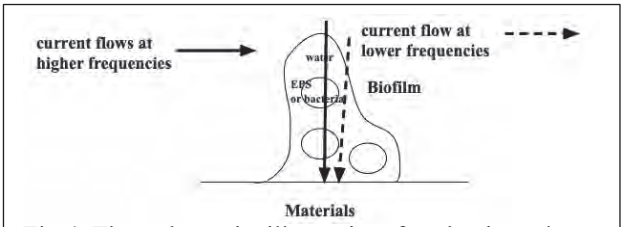

Fig.4 The schematic illustration for the impedance peaks obtained in this study.

Whatever the mechanism might be, the phenomena (the appearance of peaks) could be utilized for the sensing and monitoring of biofilm formation and growth.

In this paper, we introduced the results only for monolayer graphene film specimens. However, we will show other results for multi-layer graphene specimens and those on other substrates. At any rate, in order to develop practical sensors utilizing the phenomenon, we have to accumulate more data and discussion in the future. That will be our next mission and step in the near future.

Conclusions

In this experiment, we measured the impedance of graphene films formed using copper and polymer substrates, when biofilms formed on graphene films. We also discussed applications of graphene's impedance characteristics to biofilm sensing.

As a result, we found that the impedance peaks appeared at some frequencies discretely, when biofilms formed and developed on the specimen's surfaces. The phenomenon must be related to the biofilm formation and growth. We expect that the relation and phenomenon would be applied to sensing and monitoring of biofilms in the future.

Acknowledgements

This work was supported by JSPS KAKENHI (Grants-in-Aid for Scientific Research from Japan Society for the Promotion of Science, Grant Number 20K05185 and 21K12739. A part of this work was supported by GEAR 5.0 Project of the National Institute of Technology (KOSEN) in Japan.

References

Characklis, W.G. Fouling biofilm development: a process analysis. *Biotechnology and bioengineering* **1981**, *23*, 1923-1960

Characklis, W.G. Fouling biofilm development: a process analysis. *Biotechnology and bioengineering* **1981**, *23*, 1923-1960.

J.W.Costerton; K.J.Cheng; Geesey, G.G.; I.Timothy; J.Ladd; Nckel, C.; Dasgupta, M.; Marrie, T.J. Bacterial biofilms in nature and disease. *Annual reviews in Microbiology* **1987**, *41*, 435-464.

Lappin-Scott, H.M.; Costerton, J.W. Bacterial biofilms and surface fouling. *Biofouling* **1989**, *1*, 323-342, doi:https://doi.org/10.1080/08927018909378120.

Characklis, W.G.; Marshall, K.C. *Biofilms*; John Wiley & Sons, Inc., New York, the USA: New York, 1990.

Lawrence, J.; Korber, D.; Hoyle, B.; Costerton, J.W.; Caldwell, D. Optical sectioning of microbial biofilms. *Journal of bacteriology* **1991**, *173*, 6558-6567.

Lewandowski, Z.; Walser, G.; Characklis, W.G. Reaction kinetics in biofilms. *Biotechnology and bioengineering* **1991**, *38*, 877-882.

Mattila-Sandholm, T.; Wirtanen, G.J.F.r.i. Biofilm formation in the industry: a review. **1992**, *8*, 573-603.

Lappin-Scott, H.M.; J., J.; Costerton, J.W. Mmicrobial biofilm formation and characterisation. *Society for Applied Bacteriology technical series, Society for Applied Bacteriology Symposium* **1993**, *30*.

Lee, W.; Lewandowski, Z.; Morrison, M.; characklis, W.G.; Avci, R.; Nielsen, P.H. Corrosion of mild steel underneath aerobic biofilms containing sulfate - reducing bacteria part II: at high dissolved oxygen concentration. *Biofouling* **1993**, *7*, 217-239, doi:0.1080/08927019309386255.

Lewandowski, Z.; Altobelli, S.A.; Fukushima, E. NMR and Microelectrode Studies of Hydrodynamics and Kinetics in Biofilms. *Biotechnology progress* **1993**, *9*, 40-45.

Quesnel, L.B.; Gilbert, P.; Handley, P.S. *Microbial cell envelopes : interactions and biofilms*; Blackwell Sci. Pubs.: Oxford ; Boston, 1993; pp. vii, 160 p.

Stewart, P.S.; Peyton, B.M.; Drury, W.J.; Murga, R. Quantitative observations of heterogeneities in Pseudomonas aeruginosa biofilms. *Appl. Environ. Microbiol.* **1993**, *59*, 327-329.

Beer, D.d.; Stoodley, P.; Roe, F.; Lewandowski, Z. Effects of biofilm structures on oxygen distribution and mass transport. *Biotechnology and bioengineering* **1994**, *43*, 1131-1138.

De Beer, D.; Stoodley, P.; Roe, F.; Lewandowski, Z. Effects of biofilm structures on oxygen distribution and mass transport. *Biotechnology and bioengineering* **1994**, *43*, 1131-1138.

Flemming, H.-C. *Biofilme, Biofouling und mikrobielle Schädigung von Werkstoffen*; Oldenbourg, München, Germany: München, 1994; pp. xvi, 277

Fletcher, M. Bacterial biofilms and biofouling. *Current opinion in biotechnology* **1994**, *5*, 302-306.

Jiang, H.; Bishop, P. Aerobic biodegradation of azo dyes in biofilms. *Water Science and Technology* **1994**, *29*, 525.

Jiang, H.; Bishop, P. Aerobic biodegradation of azo dyes in biofilms. *Water Science and Technology* **1994**, *29*, 525.

Abrahamson, M.T. Development of Artificial Biofilms for Use in Mass Transport Studies. Montana State University, Bozeman, Montana, the USA, 1995.

Busscher, H.; Bos, R.; Van der Mei, H. Initial microbial adhesion is a determinant for the strength of biofilm adhesion. *FEMS microbiology letters* **1995**, *128*, 229-234.

Percival, S.L.; Walker, J.T.; Hunter, P.R. *Microbiological aspects of biofilms and drinking water*; CRC Press: Boca Raton, 2000; pp. 229 p.

Donlan, R.M. Biofilms and Device-Associated Infections. *Emerging Infectious Diseases* **2001**, *7*, 277-281.

Murga, R.; Miller, J.; Donlan, R. Biofilm formation by gram-negative bacteria on central venous catheter connectors: effect of conditioning films in a laboratory model. *Journal of clinical microbiology* **2001**, *39*, 2294-2297.

Harrison, J.J.; Turner, R.J.; Marques, L.L.R.; Ceri, H. Biofilms - A new understanding of these microbial communities is driving a revolution that may transform the science of microbiology. *American Scientist* **2005**, *93*, 508-515, doi:10.1511/2005.56.977.

Bjarnsholt, T.; Kirketerp-Moller, K.; Kristiansen, S.; Phipps, R.; Nielsen, A.K.; Jensen, P.O.; Hoiby, N.; Givskov, M. Silver against Pseudomonas aeruginosa biofilms. *APMIS* **2007**, *115*, 921-928, doi:10.1111/j.1600-0463.2007.apm_646.x.

Eboigbodin, K.E.; Seth, A.; Biggs, C.A. A review of biofilms in domestic plumbing. *American Water Works Association. Journal* **2008**, *100*, 131.

Shirtliff, M.; Leid, J.G. The role of biofilms in device-related infections. In *Springer series on biofilms v. 3.*, Springer: Berlin, 2009; pp xii, 269 p.

Kurisserya, S.R.; Kanavillila, N.; Leungb, K.T.; Chenc, A.; Daveyb, L.; Schraftb, H. Electrochemical and microbiological characterization of paper mill biofilms. *Biofouling* **2010**, *26*, 799 - 808, doi:10.1080/08927014.2010.519025.

Lobelle, D.; Cunliffe, M. Early microbial biofilm formation on marine plastic debris. *Marine pollution bulletin* **2011**, *62*, 197-200.

Kanematsu, H.; Ikigai, H. Alloy Plating and Biofilm Formation. *Proceedings of 14th International Congress Marine Corrosion and Fouling (ICMCF)* **2008**, 38 (29A-32-33).Kanematsu, H.; Ikigai, H.; Campbell, S.A.; Beech, I.B. Sn-Ag Alloy Plating Films Mitigating Biofilm Formation. *Sur/Fin 2009* **2009**, 406-415.

Kanematsu, H.; Ikigai, H.; Yoshitake, M. Evaluation of Various Metallic Coatings on Steel to Mitigate Biofilm Formation. *International Journal of Molecular Science* **2009**, *10*, 559-571, doi:10.3390/ijms10020559.

Miyano, Y.; Kanematsu, H.; Hirai, N.; Hirai, T.; Kamiya, O. The Study of Biofilm Formation and the Electrochemical Behavior of Some Metals. In Proceedings of The 15th International Congress on Marine Corrosion and Fouling. 2010, The Sage Gateshead, UK, July 28, 2010; p. 60.

Kogo, T.; Hideyuki, K.; Daisuke, K.; Itoh, H. Biofilm Formation Derived from Ambient Air and the Characteristics of Apparatus. In Proceedings of The Asia-Pacific Interdisciplinary Research Conference (AP-IRC 2012), Irago Sea-Park & Spa Hotel, Tahara, Aichi, Japan; p. 77.

Kanematsu, H.; Hihara, T.; Ishihara, T.; Imura, K.; Kogo, T. Evaluation for Corrosion Resistance of Nano-Cluster Layer and Biofilm Formation. *International Journal of Engineering Sciences & Research Technology* **2013**, *2*, 2424-2432.

Kanematsu, H.; Hirai, N.; Miura, Y.; Itoh, H.; Kuroda, D.; Umeki, S. Biofilm Leading to Corrosion on Material Surface and the Moderation by Alternative Electro-magnetic Field. In Proceedings of Materials Science and Technology (MS & T), Montreal, Quebec, Canada, 0ctober 27-31, 2013; pp. 2761-2767.

Kanematsu, H.; Kogo, T.; Noda, M.; Hirai, N.; Ogawa, A.; Miura, Y.; Itoh, H.; Yoshitake, M. Composite Coating to Control Biofilm Formation and MIC. In Proceedings of 17th International Congress on Marine Corrosion and Fouling (ICMCF). Stephen Riady Centre, National University of Singapore, Singapore, 6-10, July 2014; p. 101.

Barry, D.M.; Kanematsu, H. Physical Removal of Biofilm. In *Biofilm and Materials Science*, 2015; 10.1007/978-3-319-14565-5_20pp 163--167.

Hirai, N.; Mun, M.K.; Masuda, T.; Itoh, H.; Kanematsu, H. Atomic force microscopy analysis of biofilms formed on different plastics. *Materials Technology* **2015**, *30*, 57-60, doi:10.1179/1753555714y.0000000238.

Kanematsu, H.; Barry, D.M. New Evaluation Techniques for Biofilm in Materials Science. In *Biofilm and Material Science*, Kanematsu, H., Barry, D.M., Eds. Springer: New York, 2015; pp. 187-192.

Kanematsu, H., & Barry, D. M. (2015). Conditioning Films. In H. Kanematsu & D. M. Barry (Eds.), *Biofilm and Materials Science* (1st ed., pp. 9-15). New York, USA: Springer.

Kanematsu, H., et al. (2016). Verification of effect of alternative electromagnetic treatment on control of biofilm and scale formation by a new laboratory biofilm reactor. *Ceramic Transactions* **259**: 199-212.

Kanematsu, H. (2017). A New International Standard for Testing Antibacterial Effects. *Advanced Materials & Processing, 175*(4), 26-29.

Hideyuiki, K.; Barry, D.M.; Ikegai, H.; Yoshitake, M.; Mizunoe, Y. Nanofibers and Biofilm in Materials Science. In *Handbook of Nanofibers - Fundamental aspects, experimental setup, synthesis, properties and physicochemical characterization*, Barhoum, A., Bechelany, M., HamdyMakhlouf, A.S., Eds. Springer International Publishing AG: Switzerland, 2018; Vol. 1, pp. 1-21.

Kanematsu, H.; Kanesaki, S.; Kudara, H.; Barry, D.M.; Ogawa, A.; Mizunoe, Y. Biofilm Formation on Titanium Alloy Surfaces in a Laboratory Biofilm Reactor. In *Ceramic Transactions - Advances in Ceramics for Environmental, Functional, Structural, and Energy Applications*, Mahmoud, M.M., Sridharan, K., Colorado, H., Bhalla, A.S., J.P.Singh, Gupta, S., Langhorn, J., Jitianu, A., Manjooran, N.J., Eds. John Wiley & Sons Inc: New York, the United States, 2018; Vol. 265, pp. 221-228.

Kanematsu, H.; Maeda, S.; Barry, D.M.; Umeki, S.; Tohji, K.; Hirai, N.; Ogawa, A.; Kogo, T.; Ikegai, H.; Mizunoe, Y. Effects of Elastic Waves at Several Frequencies on Biofilm Formation in Circulating Types of Laboratory Biofilm Reactors. In *Ceramic Transactions - Advances in Ceramics for Environmental, Functional, Structural, and Energy Applications*,

Mahmoud, M.M., Sridharan, K., Colorado, H., Bhalla, A.S., J.P.Singh, Gupta, S., Langhorn, J., Jitianu, A., Manjooran, N.J., Eds. John Wiley & Sons Inc: New York, the United States, 2018;
Vol. 265, pp. 43-51.

Kanematsu, H.; Oizumi, A.; Sato, T.; Kamijo, T.; Honma, S.; Barry, D.M.; Hirai, N.; Ogawa, A.; Kogo, T.; Kuroda, D., et al. Biofilm Formation of a Polymer Brush Coating with Ionic Liquids Compared to a Polymer Brush Coating with a Non-Ionic Liquid. *Coatings* **2018**, *8*, 398-412, doi:http://dx.doi.org/10.3390/coatings8110398.

Kanematsu, H.; Oizumi, A.; Sato, T.; Kamijo, T.; Honma, S.; Barry, D.M.; Hirai, N.; Ogawa, A.; Kogo, T.; Kuroda, D., et al. Polymer Brush Made By Ionic Liquids and the Inhibition Effects for Biofilm Formation. *ECS Transactions* **2018**, *85*, 1089-1095, doi:10.1149/08513.1089ecst.

Kanematsu, H.; Shindo, K.; Barry, D.M.; Hirai, N.; Ogawa, A.; Kuroda, D.; Kogo, T.; Sano, K.; Ikegai, H.; Mizunoe, Y. Electrochemical Responses of Graphene with Biofilm Formation on Various Metallic Substrates by Using Laboratory Biofilm Reactors. *ECS Transactions* **2018**, *85*, 491-498, doi:10.1149/08513.0491ecst.

Kanematsu, H.; Shindo, K.; Barry, D.M.; Hirai, N.; Ogawa, A.; Kuroda, D.; Kogo, T.; Sano, K.; Ikegai, H.; Mizunoe, Y. Electrochemical Responses of Graphene with Biofilm Formation on Various Metallic Substrates by Using Laboratory Biofilm Reactors. *ECS Transactions* **2018**, *85*, 491-498, doi:10.1149/08513.0491ecst.

Kanematsu, H.; Nakagawa, R.; Sano, K.; Barry, D.M.; Itoh, R.; Yamada, H.; Hirai, N.; Miura, H.; Ogawa, A.; Kogo, T., et al. Biofilms by *E.coli* & *S.epidermidis* and Its Sensing Possibility by Graphene-Dispersed Silane Coating. In Proceedings of ECS Meeting Abstracts for the 235th annual convention, May, 2019; pp. 3-4.

Kanematsu, H.; Nakagawa, R.; Sano, K.; Barry, D.M.; Ogawa, A.; Hira, N.; Kogo, T.; Kuroda, D.; Wada, N.; Lee, S.-H., et al. Graphene Dispersed Silane Compound Used as a Coating to Sense Immunity from Biofilm Formation. *Medical Devices & Sensors* **2019**, *1*, 1-16, doi:https://doi.org/10.1002/mds3.10043.

Development of a transfer aid which can be used by a wheelchair user without assistance

Y.Kobayashi[*,a] and D.Miyashita [a]

[a] National Institute of Technology, Nagano College, Nagano, Nagano, Japan

*koba@nagano-nct.ac.jp

Abstract

Transferring to a chair or bed from a wheelchair is difficult for wheelchair users without assistance. Because they must lift their bodies up and move from a wheelchair to bed by themselves. So transfer without assistants puts a strain on them and is associated with a risk of fall. However, it is something indispensable in living a life for wheelchair users. Some lifts or assist systems called transfer aids are developed to help transfer, nevertheless they need assistance. Lifts need large space to use and it is hard to carry. To attach the transfer aids, a wheelchair needs to be modified. The aim of our study is to develop a transfer aid which can be used by a wheelchair user without assistance. This transfer aid can attach to a wheelchair easily without improvement. And it can be carried easily so wheelchair users can use it everywhere. The user can freely adjust the height and angle of the transfer aid. The developed transfer aid has the spread mechanism that users feel trouble-free to spread the transfer aid. Only by the simple motion of two axes, wheelchair users can spread the transfer aid. Because of the developed transfer aid was made of metal, it had high rigidity and less deformation. And it makes users stable to transfer. To confirm the safety and stress distribution of the transfer aid, the pressure of the transfer aid caused by the load of the user was analyzed by CAE. As a result of the CAE, a factor of safety was larger than 1.0 at almost any location. The developed transfer aid succeeded in users transfer themselves. And users could transfer more safely and quickly because the developed transfer aid was attached firmly to a wheelchair. The three subjects were able to complete the transfer with the developed transfer aid in about 15 seconds. One user could transfer by cross direction by using developed transfer aid who usually transfers by forward direction. Based on the test results, an arc-shaped sheet shape was also proposed.

Keywords: *wheelchair, transfer aids, welfare tools, transfer, welfare engineering*

Introduction

Transferring to a chair or bed is an important operation for wheelchair users in their daily life. However, these transferring operations are difficult for wheelchair users without assistance. Because they must lift their bodies up and move from a wheelchair to bed by themselves. So transfer without assistants puts a strain on them and is associated with a risk of fall. Some lifts or assist systems called transfer aids are developed to help transfer, nevertheless they need assistance. And lifts need large space to use and it is hard to carry. Therefore, a board type transfer aid, called a transfer board, is often used. A transfer board is a board that is inserted under the hips of the person being transferred, passed between the wheelchair and the target of the transfer, and then slid over the hips for the transfer. Transfer boards are often used because they are simple in mechanism, not very expensive, and lightweight. It also decreases the burden on the assistants because they do not have to lift the transfers. When using the transfer board, the armrests on the sides of the wheelchair need to be removed. Additionally, if the board moves during the transfer, there is a risk of the user falling. For these reasons, even though the transfer board can be used by oneself, it is better to use it with an assistant. As described above, existing transfer aids are often avoided because they often require an assistant or are large. In this study, we propose the development of a transfer aid that enables wheelchair users to transfer easily by themselves and can be carried easily.

Mechanism of a developed transfer aid

We try to develop the transfer aid with the following functions:
- Users can transfer themselves without assistance.
- Users can attach the transfer aid to the wheelchair without modification for the wheelchair.
- No need to carry it around.
- Users can use transfer aid on the go.
- The transfer aid can attach to the wheelchair without inhibiting the folding mechanism for the wheelchair.

We propose an overview of a mechanism of a transfer aid as shown in Figure 1. The transfer aid is placed under the seat of a wheelchair while the user is driving the wheelchair. The extended seat is spread from under the seat to the front of the wheelchair for

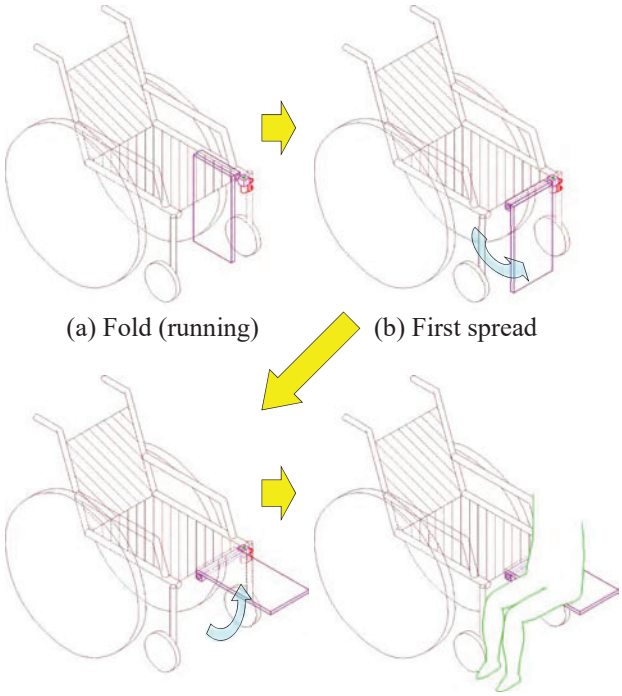

(a) Fold (running) (b) First spread

(c) Second spread (d) Complete (Transferring)

Figure 1: Mechanisms for spreading transfer aid

transfer. The spread of the transfer aid is done by rotating the two axes.

An overview of the designed transfer aid is shown in Figure 2. The size of the extended seat is 150 mm in width and 400 mm in length. A wider extended seat is better, but if it is too wide, it will bump against the legs when spread, causing problems in the transfer operation. Also, if it is too long, it will be difficult to fold up, but if too short, not only will the transfer distance be shortened, but also the part to be placed on the transfer target will be shortened and stability will be decreased. Therefore, we designed the extended seat as a two-piece folding system.

Safety and stress distribution while transferring

To confirm the safety and stress distribution of the transfer aid, the pressure of the transfer aid caused by the load of the user was analyzed by CAE. The analysis was performed by ANSYS based on the 3D data of Solidworks used in the design. As constraint conditions, the edge of the extended seat of the transfer aid was specified as the rotation fulcrum, the parts holding the extended seat and the link axis as the rotation fulcrum, and the links holding the transfer aid and the parts fixed to the wheelchair as the fixed fulcrum. The analysis was done by changing the following factors that would affect usage: the size of the load, the position of the load, and the load area. We assumed that the weight of the user was 70 kgf and that the load was 350 N (half weight), 690 N (full weight), and 1130 N (1.5 times) as the impact load. The position of the load was assumed to be the wheelchair side, the center, and the transfer destination side of the extended seat. The load area was assumed to be the palm area (90mm x 90mm square), the hips area(Rounded rectangle with width 180mm and length 120mm), and half of the extended seat surface (width 150mm, and length 220mm at the wheelchair side and 180mm at the destination side).

The results of the analysis are shown in Table 1 for the loading on the extended seat half surface, the loading on the palm area is shown in Table 2, and the loading on the hips area is shown in Table 3. Examples of the analysis results are shown in Figures 3 and Figures 4. The safety factor was greater than 1.0 under almost all conditions. However, the safety factor was 0.9, which was lower than 1.0, only when 1130 N was loaded on the central part of the transfer aid with one hand. This means that 115 kgf is loaded on one hand. In the analysis, the safety factor was calculated based on the elastic limit, so the transfer aid did not break immediately under these conditions, and only plastic deformation occurred in a part of the parts. In the case of actual transfer, it is unlikely that a load of more than 100 kgf will be applied to one hand. However, a safety factor of less than 1.0 should be avoided for safety reasons when considering impact loads. Therefore, we modified the size of the parts with the smallest safety factor to improve the rigidity.

The parts where the load was concentrated were around the seat parts shown in Figure 5 and around the fixed parts shown in Figure 6. The place where the stress

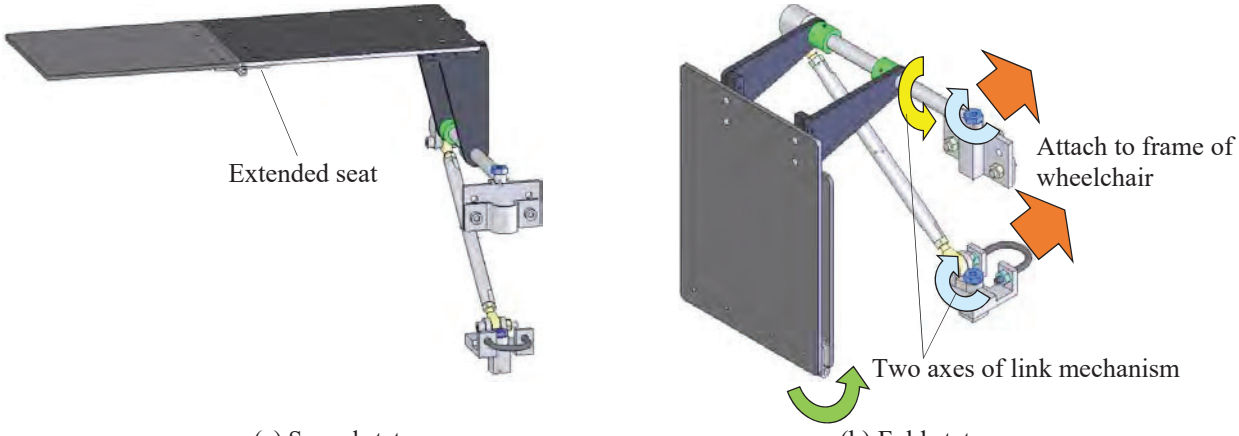

(a) Spread state (b) Fold state

Figure 2: Design of developed transfer aid

Table 1: Analysis result about load on half plate area

Load area	Half plate area					
Load position	Destination side			Wheelchair side		
Number of elements	21563			21563		
Load [N]	350	690	1130	350	690	1130
Maximum equivalent stress [MPa]	17.4	34.3	56.1	50.6	99.7	163.2
Maximum displacement [mm]	0.10	0.20	0.32	0.19	0.37	0.61
Minimum safety factor	11.9	6.0	3.7	4.4	2.2	1.4

Table 2: Analysis result about load on palm area

Load area	Palm area								
Load position	Destination side			Center			Wheelchair side		
Number of elements	24200			24200			24200		
Load [N]	350	690	1130	350	690	1130	350	690	1130
Maximum equivalent stress [MPa]	7.1	14.0	23.0	84.1	165.8	277.2	62.3	122.9	234.9
Maximum displacement [mm]	0.01	0.03	0.04	0.36	0.71	1.17	0.24	0.47	0.76
Minimum safety factor	15.0	14.8	9.0	3.0	1.5	0.9	3.7	1.9	1.1

Table 3: Analysis result about load on hip area

Load area	Hip area								
Load position	Destination side			Center			Wheelchair side		
Number of elements	21629			24780			24374		
Load [N]	350	690	1130	350	690	1130	350	690	1130
Maximum equivalent stress [MPa]	8.5	23.7	27.9	57.6	113.5	185.9	55.5	109.3	179.0
Maximum displacement [mm]	0.02	0.06	0.07	0.17	0.34	0.56	0.11	0.22	0.35
Minimum safety factor	15.0	8.7	7.4	4.3	2.2	1.3	4.5	2.3	1.4

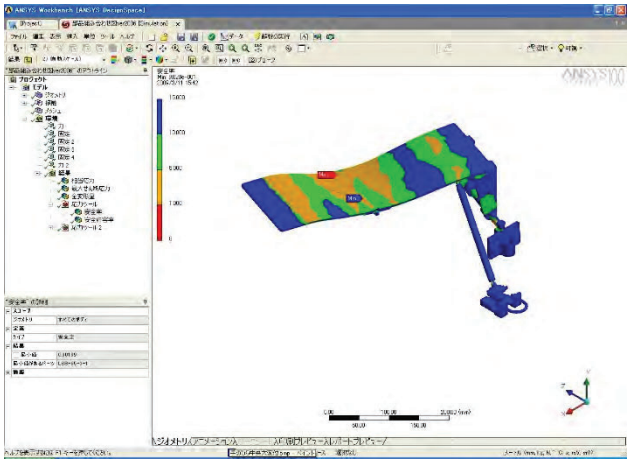

Figure 3: Analysis result of safety factor
(Palm area, Center, 1130 N)

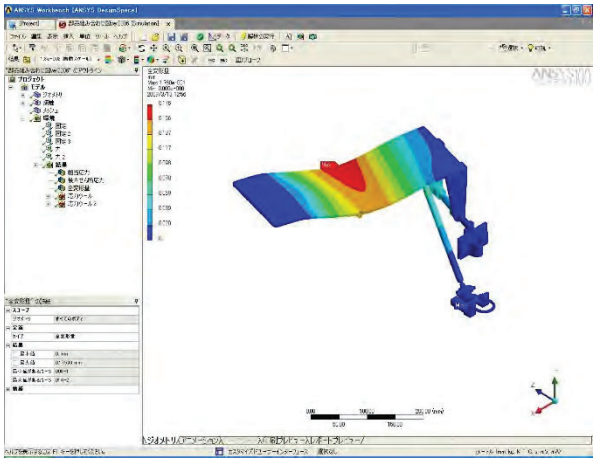

Figure 4: Analysis result of displacement
(Hip area, Center, 350 N)

was highest in the seating part in Figure 5 was the same as the place where the stress was highest in both ends supported beam. For the part in Figure 6, there was no problem when the extended seat surface was horizontal, but when the extended seat surface was angled upward or downward even slightly, stress concentration occurred at the edge of the fixed part. The safety factor was greater than 1.0, but the stress concentration was not good, so the parts were redesigned and the contact area was increased to prevent stress concentration.

Prototype and Confirmation

The prototype of the designed transfer aid attached to a wheelchair is shown in Figure 7. The material was stainless steel for the shaft of the movable part and aluminium for the extended seat. The size when folded (Figure 7(b)) was 230 mm in height and 115 mm in thickness. When spread out (Fig. 7(a)), the seat surface was 150 mm in width and 400 mm in length. The two folded extended seating surfaces were fixed by magnets. The two folded seats were fixed by magnets so that they

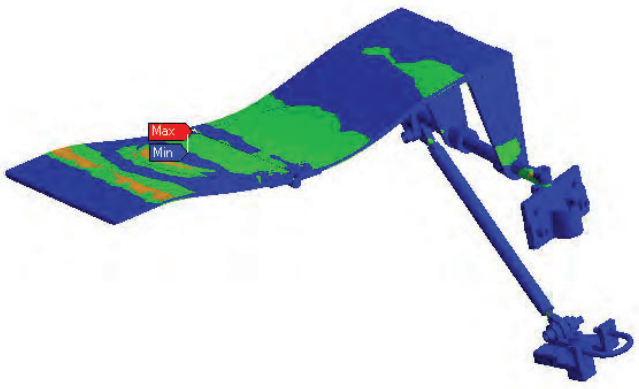

Figure 5: Stress concentration at the plate

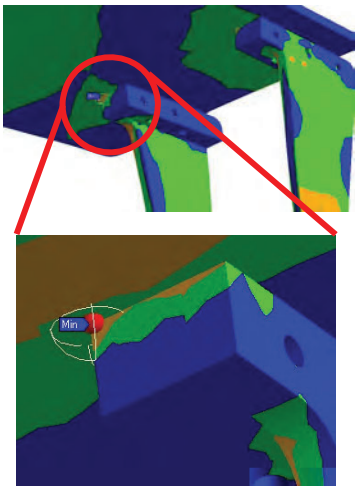

Figure 6: Stress concentration at the attachment parts

(a) Spread

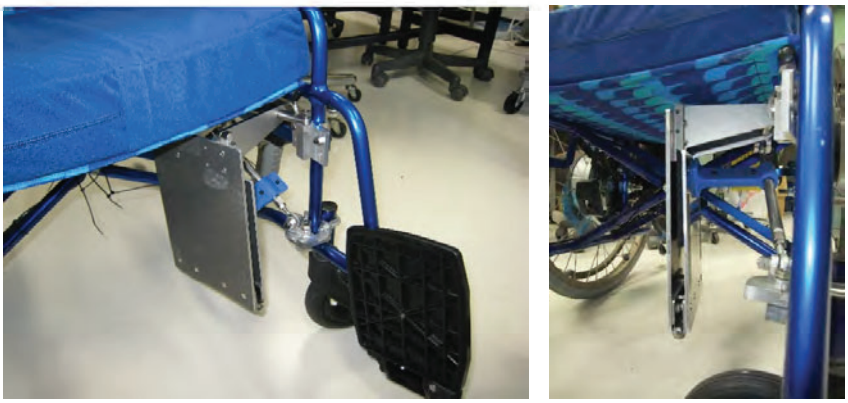

(b) Fold

Figure 7: Developed transfer aid

were kept in the folded state when stored and could be easily spread out without any mechanism.

The developed transfer aid was attached to a wheelchair and tested. As mentioned above, the transfer aid was attached to the frame of the wheelchair without any modification. Then, we tested whether the transfer aid could be spread out and stored while it was attached to the wheelchair. The operation is shown in Figure 8.

The operation from the stored state to the finished spread out was successfully done. Also, the wheelchair could be folded with the transfer aid attached without problems. There was no trouble in the mechanical strength of the transfer aid, as it did not deform when the user rode on it and shook it with weight.

Besides, we tested the transfer movements by wheelchair users using developed transfer aid. As a comparison, transfer with a transfer board was also measured. By using the developed transfer aid, we confirmed that the transfer time could be decreased and the user could transfer stably by themselves. The results of the measurements are shown in Table 4. Subject B was not stable even when transferred with the transfer board, and was not transferred with the developed transfer aid for safety reasons. The three subjects were able to

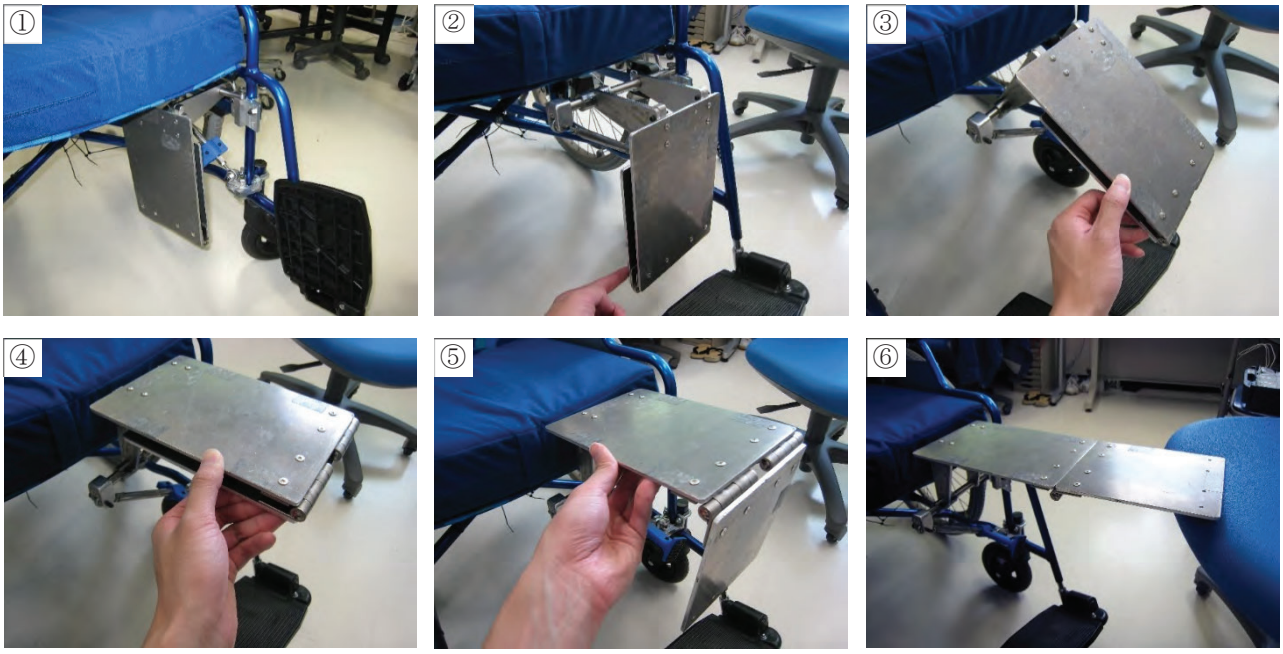

Figure 8: Motion of spread about developed transfer aid

Table 4: Results of measurement

Subjects	Transfer board				Developed transfer aid			
	Time [s]		Transfer direction	Stability	Time [s]		Transfer direction	Stability
	Bed → Wheelchair	Wheelchair → Bed			Bed → Wheelchair	Wheelchair → Bed		
A	33	19	Cross	Unstable	15	9	Cross	Stable
B	91	65	Forward	Incomplete	—	—	—	—
C	6	5	Cross	Stable	15	16	Cross	Stable
D	7	19	Forward	Unstable	10	13	Cross	Stable

complete the transfer with the developed transfer aid in about 15 seconds. Three of the four subjects were able to transfer with the developed transfer aid. In particular, subject A was able to complete the transfer in less than half the time compared to the transfer board. Subject D who usually transferred forward direction because they could not transfer crosswise with general transfer aid could transfer cross direction when using the developed transfer aid.

Results and Discussion

The subject in this test was able to transfer stably even though he had not practiced transferring with the developed transfer aid much. It can be expected that more practice will enable more stable transfers in a shorter time.

In the discussion after the test, some users said that it was difficult to support the body with their hands and to keep a stable posture when transferring with the transfer board because of its flexibility. The material of the transfer board was polyethylene, which was plastic and easily deformed. Although it did not break or deform plastically during the transfer operation, it deformed greatly when sitting in the center with both ends supported, as shown in Figure 9. This may cause deformation at the point where the hand or hip was placed during the transfer operation, making the posture unstable. On the other hand, since the seat of the developed transfer aid was made of aluminium, it was not deformed much and can be transferred stably even when a high load was applied. Therefore, it is considered that the developed transfer aid is more stable than the transfer board because the seat is not easily deformed, and it also decreases the time for transferring.

For the seat width of the transfer aid, some comments were suggested that the seat width of the transfer aid was narrower than that of the transfer board. The width of the transfer board used in this study was 325 mm, while the seat width of the developed transfer aid was 150 mm. The wider width gives more space to place hands during transfer, psychologically increasing the feeling of safety. It makes users transferring not only for cross direction but also forward direction. However, the wider the seat, the narrower the space for the legs, and the more difficult the transfer operation becomes. One solution to this problem, the shape of the seat design can make more space for the legs and increase the seat width.

Shape of the Seat exchange mechanism

To increase the seat width and space for the legs, an arc-shaped seat aid was designed, as shown in Figure 10.

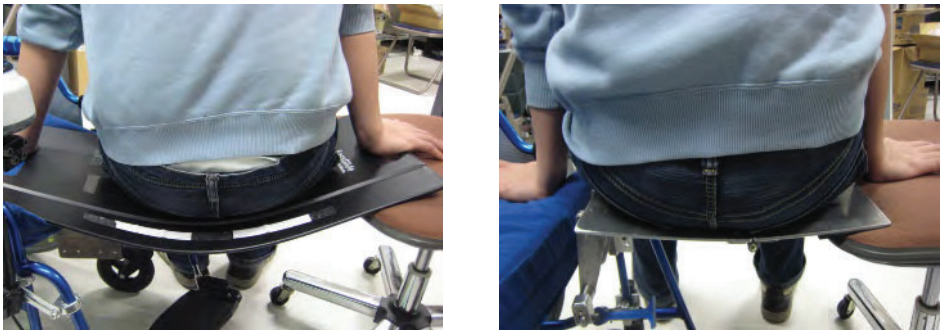

(a) Transfer board (b) Developed transfer aid

Figure 9: Deformation of transfer aid by the load

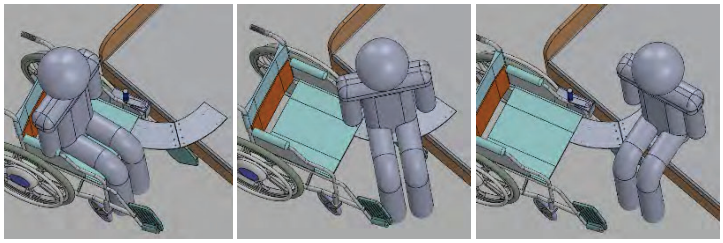

(a) Spread (b) Transferring (C) Complete

Figure 10: Transfer using arc-shaped seat

For the sheet part, the arc-shaped plate and the rectangular-shaped plate can be easily exchanged according to the user's requirements. This function will make it possible for more users to use it.

Conclusions

We have developed a transfer aid that allows wheelchair users to transfer by themselves. The transfer aid is fixed to the wheelchair, so it does not need to be carried. It can also be attached easily to a wheelchair without modification. It is compact and does not inhibit the folding function of the wheelchair, since it can be folded under the wheelchair seat when driving and spread out when transferring. We also confirmed that users who could only transfer to the forward direction could transfer to the cross direction using developed transfer aid. By using aluminum as the material for the seat, the flexibility caused by body weight was greatly decreased, and the stability was greatly increased. As a result, we confirmed the effectiveness of the proposed transfer aid. We proposed not only a rectangular shape but also an arc shape for the seat. By designing the seat in the shape of an arc, it is possible to increase the width of the seat and provide space for the legs.

References

Aono, M., Tanaka, O., Iijima, H., Miyamoto, A., Arai, T., Ohta, K., Miyata, T. & Nakajima, H., The development of the new transfer aid that used a “KOMAWARISAN” as a base, Proceedings of The 17th Japanese Conference on the Advancement of Assistive Rehabilitation Technology (2002), pp. 415-418.

Health and Welfare Information Association, Welfare toll guidebook 2011, (2011), p. 125.

Inoue, T. & Yamazaki, N., Physical loads during using transfer aids, Journal of the Society of Biomechanisms, Vol.25, No.3 (2001), pp.123-129.

Japanese Standards Association, JIS handbook 38 welfare (2001), pp. 132-133.

Katsuhira, J., Tomita, S., Haraguchi, T., Harada, S., Ishikawa, E., Kubo, K. & Maruyama, H., Effect of use and type of assistive devices and posture while using them on the low back load in transferring tasks, The Japanese journal of ergonomics, Vol.46, No.2 (2010) , pp.157-165.

Kinoshita, K., & Koizumi K., Study on transfer instrument (Theoretical consideration on lift up motion of transfer operation), Journal of the Japan Society of Mechanical Engineers, Vol.73, No.730 (2007), pp.1661-1666.

Kobayashi. Y., Research of transfer system for disabled by self-help, Report of the Health Labour Sciences Research Grant Comprehensive Research on Disability Health and Welfare (2010), pp.1-41.

Motegi, N., Yasuda, S. & Misawa, T., Experimental study of assistant aids and a new nursing method in nursing care work, The journal of science of labour, Vol.88, No.3 (2012), pp.81-93.

Evaluation of iEMG Focusing on Trunk Muscles During One-Handed Wheelchair Driving

Satoshi Ohashi[*,a], Akira Shionoya[b] and Keiu Harada[a]

[a] National Institute of Technology, Tomakomai College, Tomakomai, Hokkaido, Japan
[b] Nagaoka University of Technology, Nagaoka, Niigata, Japan

*ohashi@tomakomai.kosen-ac.jp

Abstract

In the field of sports for the disabled, assistive devices are specially designed and adjusted according to the presence or absence of disabilities, the degree of disability, the physique of the athlete, and the type of competition. We have developed a wheelchair that can be driven by one hand, which is designed for use by athletes who are hemiplegic or have lost one arm. The wheelchair can also be operated with both hands. The wheelchair is also expected to improve the quality of life (QOL) because of the advantage of using it with one hand. However, the effects on the physical load and the posture when operating the wheelchair are still unknown.

The purpose of this study is to collect information on the physical load of passengers and the effects on seating, assuming that the wheelchair can be used in sports competitions, and to evaluate these data. Moreover, we focused on the Muscles of Arm, Muscles of Shoulder Joint, and Trunk Muscle used for driving movements during wheelchair operation. The purpose of this paper is to measure the Trunk Muscles during one-handed wheelchair operation and to unveils the relationship between the passenger's body axis and posture. We used surface EMG sensors to measure the muscle activity of flexor digitorum profundus, triceps brachii, deltoid, pectoralis major, latissimus dorsi, flexor digitorum profundus, and pectoralis major, which are mainly used when operating a wheelchair. We used the iEMG to evaluate changes in muscle activity due to differences in wheelchair operation methods and biases in left and right muscle activity. The results showed that the operation of a one-handed wheelchair was found that heavily use the external oblique abdominis on the hand rim side of the wheelchair. Because the operation of a one-handed wheelchair requires a different operating posture than two-handed wheelchairs.

Keywords: *wheelchair, disability, assistive technology, QOL, iEMG, muscle activity, physical load*

Introduction

In recent years, Assistive Technology (AT) has been researched and developed worldwide as one of the solutions to improve the quality of life (QOL) in the fields of medical care, nursing care, and welfare (e.g., Boatman et al., 2020; Garip et al., 2017; Pettersson, Hagberg, Fredriksson, & Hermansson, 2016). However, these assistive technologies for daily life have not been widely disseminated until they are generally available to everyone, and many people cannot benefit from these technologies. On the other hand, in the field of sports for the physically challenged (Hill, Scarborough, Berkson, & Herr, 2014; Kasitinon et al., 2020), it has the advantage that the assistive devices can be specially designed and adjusted for each individual, depending on the disability of the athlete, the degree of disability, the physique, and the athletic events, but it also has the disadvantage that the cost is very high. In sports for people with disabilities, as represented by the Paralympics, many competitions involve the use of wheelchairs. Various types of competition wheelchairs have been developed according to the degree of physical handicap of the athlete and the characteristics of the competition (Berger, Van Nieuwenhuizen, Van Der Ent, & Van Der Zande, 2012). We have developed a wheelchair that can be driven by one hand, which is designed for use by athletes who are hemiplegic or have lost one arm. The wheelchair can also be operated with both hands. We believe that the wheelchair can be applied to the competitions where athletes who still have the function of both hands can use one hand free to handle a racket or other objects.

The purpose of this study is to support athletes in their athletic activities by using our one-handed drivable wheelchair. However, the effects on the physical load and the posture when operating the wheelchair are still unknown. This study is to collect information on the physical load of passengers and the effects on seating, assuming that the wheelchair can be used in sports competitions, and to evaluate these data. Moreover, we focused on the Muscles of Arm, Muscles of Shoulder Joint, and Trunk Muscle used for driving movements during wheelchair operation. In this paper, we measure the muscle activity during one-handed and two-handed

wheelchair manipulation and evaluate the relationship with posture during manipulation.

Materials and Methods

Figure 1 shows the competition wheelchair used in this study, which has a mechanism that allows the wheelchair to move straight ahead with one hand. Ordinary wheelchairs are equipped with independent wheels on both sides, so passengers cannot drive straight ahead with one-handed operation. Therefore, we developed a driving force transmission axle (DFTA) to transmit a driving force from one wheel to the other. The DFTA was made by a standard iron of which a specific gravity was 7.87 g/cm3 and a young's modulus was 192.08 GPa. Sports competition wheelchairs have camber angles on the left and right wheels. For this reason, the DFTA is equipped with two steel universal joints of the same standard. Wheelchairs equipped with this DFTA can move straight ahead with a one-handed operation (Hirano, Hoshino, Kenmotsu, & Shionoya, 2015; Kudo, Kenmotsu, & Shionoya, 2016; Shionoya, & Kenmotsu, 2012; Shionoya, & Kenmotsu, 2018). On the other hand, the one-hand drive wheelchair developed for bowling competitions, shown in Figure 2, is designed without a camber angle because it needs to specialize in straight-line performance according to the characteristics of the competition. The two one-handed wheelchairs used in this experiment were manufactured by Ox Engineering Co., Ltd.

In this study, we use surface EMG sensors to observe the muscle activity of Muscles of Arm, Muscles of Shoulder Joint, and Trunk Muscles, which are mainly used when operating a wheelchair. The results of these EMGs will be used to evaluate the relationship between the passenger's body axis and their posture while operating a wheelchair that can be driven with one hand. For this purpose, two experiments will be conducted. The first experiment evaluates the electromyogram of the Muscles of Arm and Muscles of the Shoulder Joint. The second experiment evaluates the electromyogram of the trunk muscles. The surface EMG of the passenger is measured using a PolymatePro MP6000 biological signal system manufactured by Miyuki Giken Co., Ltd. (Figure 3). Its specifications are shown in Table 1. This study and the experimental data have been approved by the Ethics Committee of Nagaoka University of Technology.

Evaluation of the Muscles of Arm and Shoulder Joint

In this experiment, we will focus on the Muscles of Arm and Muscles of the Shoulder Joint used for driving movements during wheelchair operation. The purpose of this experiment is to observe and evaluate the changes in the muscle activity of Muscles of Arm and Muscles of the Shoulder Joint of a passenger depending on the driving method used during wheelchair operation. From the measurement results, we will evaluate the difference in muscle activity between one-handed and two-handed driving to maintain wheelchair operation.

Figure 1
A wheelchair for sports competition

Figure 2
A wheelchair for a bowling competition

Figure 3
PolymatePro MP6000

Table 1
Specifications of PolymatePro MP6000

Model Number	MP6000
Input Channel	VERSATILE: 13 SENSOR: 5 AUX: 3 PULSE: 1 EXT: 2
Impedance	250 GΩ
Sampling Frequency	200 - 2000 Hz
Size	H60×W116×D185 mm
Weight	570 g

In this experiment, we will use a right-handed, one-handed wheelchair developed by the Shionoya Laboratory at Nagaoka University of Technology (Figure 1). The surface EMG during the wheelchair operation is measured with a PolymatePro MP6000 (Figure 3). As shown in Figure 4, The surface EMG measurements are taken at five muscle sites on the upper part of the body: (a) flexor digitorum profundus (the little finger side), (b) triceps brachii, (c) deltoid, (d) pectoralis major, and (e) latissimus dorsi. The research participants were two healthy adult males. The height and weight of the research participants are 173.5 ± 1.5 cm and 70.5 ± 2.5 kg. Their dominant hand is on the right side. The conceptual diagram of the experiment is shown in Figure 5. The procedure of this experiment is shown below.

1. Before running, maintain the condition (a) and (b) shown in Figure 6 with a load of 5 kg for 30 seconds each.
2. The start is at a standstill, and then all-out running is performed at 1 drive per second (for 1 rotation) for a total of 8 drives (for 8 rotations).
3. After running, keep the condition (a) and (b) with a load of 5 kg for 30 seconds each, in the same way as before running.
4. The research participant should take enough rest to recover from fatigue.
5. Perform steps 1. through 4. three times for one-handed driving and three times for two-handed driving, alternating between the two.

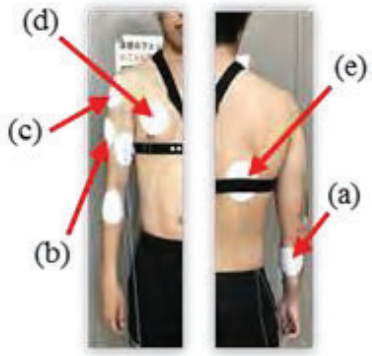

Figure 4
Measurement points for surface EMG

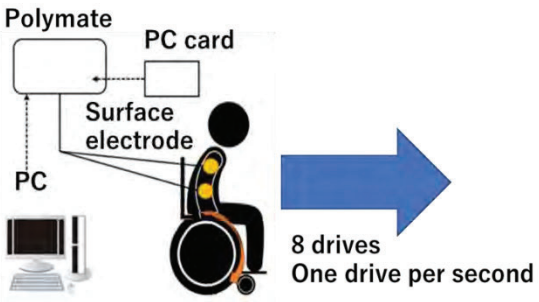

Figure 5
The conceptual diagram of the experiment

Condition (a) Condition (b)

Figure 6
Load applied to the upper arm

Based on the measurement results of the surface EMG, we calculated the iEMG, which quantifies the amount of muscle activity due to a single drive. The iEMG is a quantification of the total workload of the electrical activity of a muscle. It is called an integral electromyogram. Figure 7 shows the results of iEMG for the triceps muscle in two research participants A and B. This result is the transition per one drive of one-hand drive and two-hand drive and is the average value of iEMG for the number of trials.

Similar to the triceps shown in Figure 7, the flexor digitorum profundus (Figure 8) and the pectoralis major (Figure 9) also showed a monotonic decreasing trend. The amount of muscle activity in these muscles decreased as the speed of the wheelchair increased, indicating that muscle activity is activated during the driving motion to start the wheelchair. The results suggest that these muscles are the main driving muscles that play an important role in the starting motion from a stopped state. In the triceps brachii muscle shown in Figure 7, the amount of muscle activity increased by about 14 % in the one-handed driving operation compared to the two-handed driving operation. For the pectoralis major muscle shown in Figure 9, the amount of muscle activity in the one-handed driving motion increased by approximately 20 %. However, for the flexor digitorum profundus muscle shown in Fig. 8, the amount of muscle activity decreased by about 13 % in the one-hand drive operation compared to the two-hand drive operation. The flexor digitorum profundus during driving is also the strength to grip the wheelchair hand rim. Comparing research participant A and research participant B, there is a large 21 % difference in the iEMG results between one-handed and two-handed driving. When two-handed driving was used as the standard, research participant A showed a 20 % decrease in one-handed driving. On the other hand, research participant B increased by 1 %. In other muscle areas, the average difference was 8 %. Consequently, It was found that individual differences have a great influence on the flexor digitorum profundus.

The amount of muscle activity calculated in this experiment increased in the one-handed drive compared to the two-handed drive. The wheelchair that we developed can be driven by one hand, and the driving force must be transmitted to the wheel on the opposite

side by the driving action of one hand. Therefore, the wheelchair needs to use 10% more muscle power than the two-handed wheelchair.

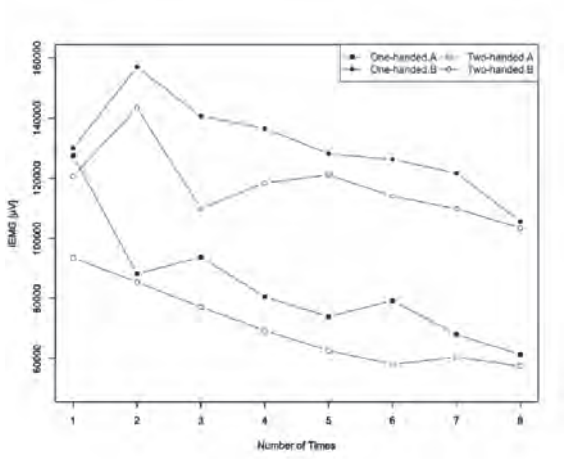

Figure 7
iEMG of the triceps brachii

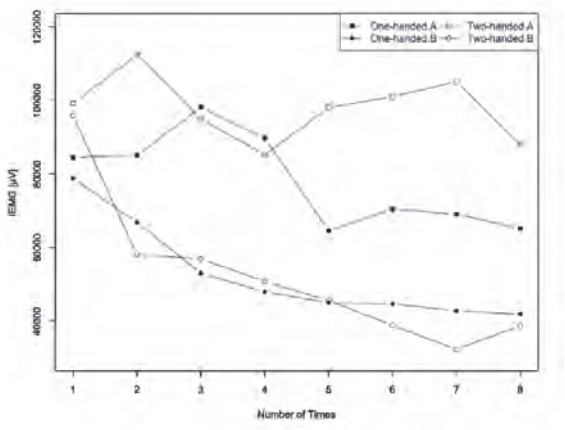

Figure 8
iEMG of the flexor digitorum profundus

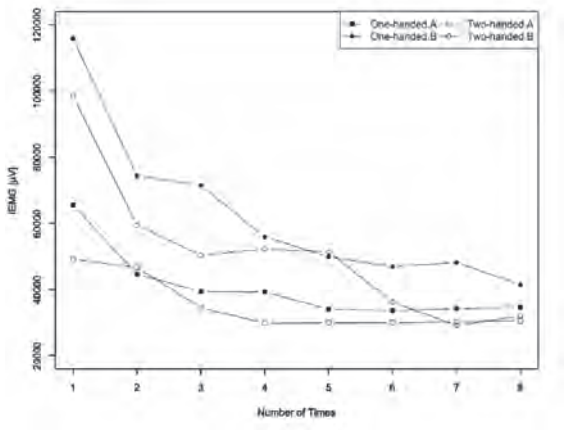

Figure 9
iEMG of the pectoralis major

Evaluation of the Trunk Muscles

In this experiment, we will focus on the effects of different wheelchair drive methods on the operator's posture. The purpose of this experiment is to observe and evaluate how the muscular activity of the passenger's trunk muscles changes according to the driving method used when operating the wheelchair. From the measurement results, we will evaluate the difference in muscle activity between one-handed and two-handed driving to maintain wheelchair operation.

In this experiment, we will use a left-handed, one-handed wheelchair developed by the Shionoya Laboratory at Nagaoka University of Technology (Figure 2). The surface EMG during the wheelchair operation is measured with a PolymatePro MP6000 (Figure 3). As shown in Figure 10, the surface EMG is measured at a total of six locations, including the right and left sides of (a) erector spinae, (b) external oblique abdominis, and (c) triceps brachii. The research participants were seven healthy adult males. The height and weight of the research participants are 173.1 ± 4.2 cm and 65.4 ± 5.6 kg. Their dominant hand is on the right side. The conceptual diagram of the experiment is shown in Figure 11. The experimental procedure is the same as the one described above.

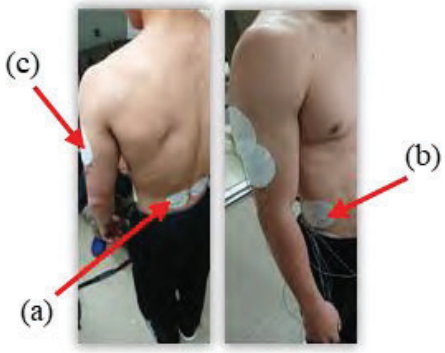

Figure 10
Measurement points for surface EMG

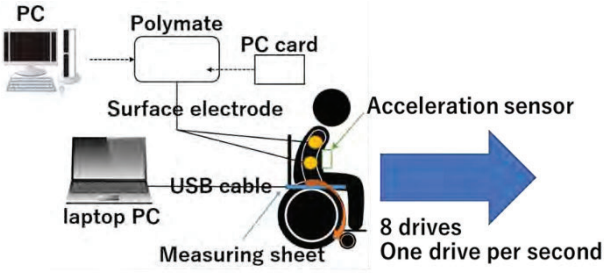

Figure 11
The conceptual diagram of the experiment

Based on the measurement results of the surface EMG, we calculated the iEMG, which quantifies the amount of muscle activity due to a single drive. Figure

12 shows the variation in iEMG average of the triceps brachii measured with seven research participants, left and right separately. Similarly, Figure 13 shows the results for the external oblique abdominis and Figure 14 shows the results for the erector spinae. These results are the transition per one drive of one-hand drive and two-hand drive and is the average value of iEMG for the number of trials.

In the triceps brachii shown in Figure 12, the percentage of muscle activity in the one-handed drive based on the two-handed drive was 103% for the left triceps brachii on the side of hand rim side and 17% for the right triceps brachii with no activity. There was no significant difference in muscle activity of the triceps brachii related to wheelchair hand rim manipulation between one-handed and two-handed driving. It was found that the triceps brachii was able to clearly distinguish between wheelchair hand rim manipulation and non-manipulation.

In the external oblique abdominis shown in Figure 13, the percentage of muscle activity during one-handed drive relative to two-handed drive was 279 % for the left external oblique abdominis on the hand rim side of the wheelchair and 126 % for the right external oblique abdominis on the right side without hand rim manipulation. There was significant difference in the muscle activity of the external oblique abdominis related to wheelchair hand rim manipulation between one-handed and two-handed driving. The muscle activity of the left side external oblique abdominis in one-handed driving was more than double that in two-handed driving. In addition to the muscle activity of the triceps brachii shown in Figure 12, it was found that the manipulation posture during one-handed driving was found to heavily use the left side external oblique abdominis on the hand rim side of the wheelchair. Because the oblique abdominis a major role in the turning motion of the body, the driving posture in one-handed driving involves more twist motion toward the hand rim side.

In the erector spinae shown in Figure 14, the percentage of muscle activity in the one-handed drive based on the two-handed drive was 94 % for the left erector spinae on the hand rim side of the wheelchair and 91 % for the on the right side without hand rim manipulation. The muscle activity of the erector spinae muscles by one-handed driving decreased by about 10% compared to that by two-handed driving. The operation of a one-handed wheelchair uses the triceps brachii and external oblique abdominis more than a two-handed wheelchair, so it is assumed that the muscle activity of the erector spinae was reduced. Next, we focus on the posture of the passenger. The operating posture of a one-handed wheelchair is to twist the upper limbs in an oblique direction toward the left side hand rim. On the other hand, the operating posture of a two-hand drive wheelchair involves repeated forward and backward bending motions of the upper limbs. In the correct operating posture of the two-hand drive, the body axis is not tilted in the left-right direction. Therefore, the muscle activity of the erector spinae, which constitutes the trunk, is not greatly biased to either the left or right side. However, unlike the results for the triceps brachii and external oblique abdominis shown in Figure 12 and Figure 13, the muscle activity of the right-side erector spinae increased approximately twofold in the two-handed driving. The reason for this may have been a problem with the experimental method. In the running experiment, one-handed driving and two-handed driving were measured alternately. Therefore, it is possible that the research participants unconsciously tilted their body axis toward the hand rim side even during two-handed driving, which is necessary for left-handed hand rim operation in one-handed driving. For three of the seven research participants, the muscle activity of the right side of the erector spinae increased more than twice as much as that of the left side during both one-handed and two-handed driving. Since the iEMG results of the erector spinae showed a large variation among the research participants, we speculate that individual differences may also have influenced the results.

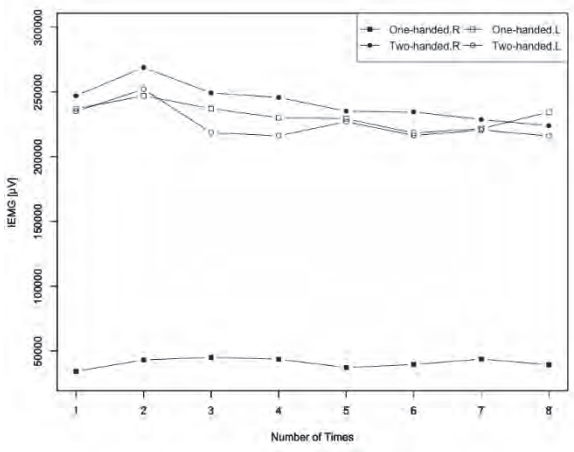

Figure 12
iEMG of the triceps brachii

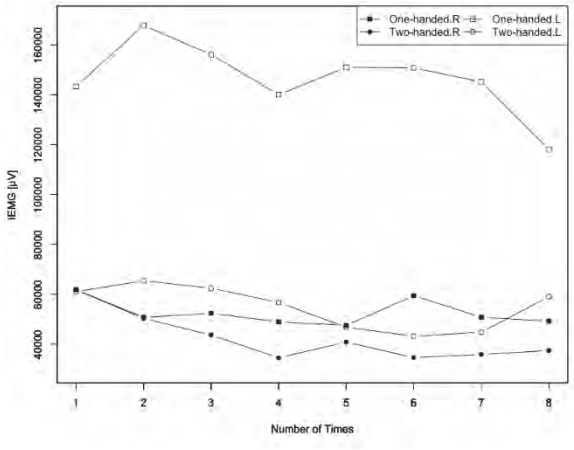

Figure 13
iEMG of the external oblique abdominis

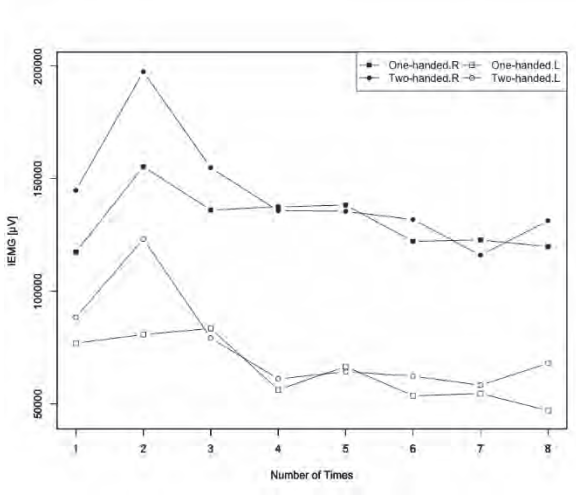

Figure 14
iEMG of the erector spinae

Conclusions

In conclusion, we have obtained the following from experiments:

1. The operation of a one-handed wheelchair requires a different operating posture than two-handed wheelchairs. The operating posture is to twist the upper limbs in an oblique direction twist motion the hand rim.
2. The operation of a one-handed wheelchair was found that heavily use the external oblique abdominis on the hand rim side of the wheelchair. The muscle activity of the left side external oblique abdominis in one-handed driving was more than double that in two-handed driving.
3. The operation of a one-handed wheelchair requires about 10 % more muscle power of the triceps brachii on the operating side than a two-handed wheelchair.

In the future, the number of research participants should be increased, and quantitative evaluation should be conducted. The experiments need to minimize the influence of the research participants on the driving operation. In addition to the surface electromyogram measurement, detailed data on the posture of the passenger will be obtained by using acceleration sensors.

Acknowledgements

This work was supported by JSPS KAKENHI Grant Number 18K11890 and Nagaoka University of Technology (NUT) grant. We gratefully acknowledge the work of past and present members of our laboratory.

References

Berger, M.A.M., Van Nieuwenhuizen, M., Van Der Ent, M., & Van Der Zande, M. (2012). Development of new wheelchair for wheelchair basketball players in the Netherlands. *Procedia Engineering*, 34, 331-336. https://doi.org/10.1016/j.proeng.2012.04.057

Boatman, F., Golden, M., Jin, L., Kim, Y., Law, S., Lu, A., Merriam, N., & Zola, S. (2020). Assistive technology: Visual mapping combined with mobile software can enhance quality of life and ability to carry out activities of daily living in individuals with impaired memory. *Technology and Health Care*, 28, 2, 121-128. https://doi.org/10.3233/thc-191980

Garip, Y., Ozel, S., Tuncer, O.B., Kilinc, G., Seckin, F., & Arasil, T. (2017). Fatigue in the mothers of children with cerebral palsy. *Disability and Rehabilitation*, 39, 8, 757-762. https://doi.org/10.3109/09638288.2016.1161837

Hill, D., Scarborough, D.M., Berkson, E., & Herr, H. (2014). Athletic Assistive Technology for Persons with Physical Conditions Affecting Mobility. *Journal of Prosthetics and Orthotics*, 26, 3, 154-165. http://dx.doi.org/10.1097/JPO.0000000000000034

Hirano, T., Hoshino, N., Kenmotsu, Y., & Shionoya, A. (2015). Development of the sport-typed wheel-chair, which can drive straight by either one-handed or both-handed operation. *Proc. Jpn. Soc. Mech. Eng. Meet.*, G2300104 in CD-R Proceedings. https://doi.org/10.1299/jsmeshd.2014._B-25-1_

Kasitinon, D., Royston, A., Wernet, L., Garner, D., Richard, J., & Argo, L.R. (2020). Health-Related Incidents among Intercollegiate Wheelchair Basketball Players. *2020 American Academy of Physical Medicine and Rehabilitation*, 1-10. https://doi.org/10.1002/pmrj.12474

Kudo, F., Kenmotsu, Y., & Shionoya, A. (2016). Development and drive performance evaluation of wheelchair for competition with a function to drive on ahead by one-hand operation. *Proc. Jpn. Soc. Mech. Eng.*, G2300103 in CD-R Proceedings.

Pettersson, I., Hagberg, L., Fredriksson, C., & Hermansson, L.N. (2016). The effect of powered scooters on activity, participation and quality of life in elderly users. *Disability and Rehabilitation: Assistive Technology*, 11, 7, 558-563. https://doi.org/10.3109/17483107.2015.1027301

Shionoya, A., & Kenmotsu, Y. (2012). Development and Evaluation of the Sport-Type Wheel-Chair can Drive Straight Using Either One-Handed or Both-Handed Operation. *DESCENTE Sport Sci*., 33, 93–103. https://doi.org/10.1299/jsmeshd.2014._B-25-1_

Shionoya, A., & Kenmotsu, Y. (2018). Development of New Wheelchair for Sports Competition. *Proceedings of The 12th Conference of the International Sports Engineering Association*, 2, 6, 257-262. https://doi.org/10.3390/proceedings2060257

TOWARD EMG ESTIMATION OF WHEELCHAIR OPERATION WITH NEURAL NETWORK

S. Aihara [a, b], R. Shibata [c], R. Mizukami [c], T. Sakai [c] and A. Shionoya [c]

[a] Japan Institute of Sports Sciences, Department of Sport Science, Tokyo, Japan
[b] Waseda University, School of Creative Science and Engineering, Tokyo, Japan
[c] Nagaoka University of Technology, Graduate School of Information and Management Systems Engineering, Niigata, Japan

*shimpei.aihara@jpnsport.go.jp

Abstract

Paralympic competitions are recently drawing attention. Majority of events held in the Paralympic Games use wheelchairs, and wheelchair sports are recognized as international competition. There are active engagements in motion analysis, performance evaluation, and content evaluation to improve competitiveness. A widely used tool for these evaluations is the electromyography (EMG), which monitors muscular activities. However, attaching electrodes is cumbersome and limits the activities due to wiring cables and measuring devices; thus, EMG is generally used under controlled conditions. Therefore, it is difficult to obtain data in the same environment as the actual competition environment.

Aim of this study is to develop a method for estimating myopotential that can easily be used in competitive environments without restricting physical movements. We constructed a neural network model that acquires images of the movements of a human captured by a camera and measured values of inertial sensors mounted on the wheelchair as inputs and myopotential as output. The key point coordinates of human were derived and used from the captured images. The inertial sensors were installed under the wheelchair seat and at the center of the wheels. The sensor installed under the wheelchair seat measured acceleration and the ones positioned at the center of the wheels measured angular velocity. The model we designed was a neural network model based on convolution integrals. It learns the designed model using a dataset obtained from this study and estimates myopotential of forearms, biceps, rear deltoids, and pectoralis major muscle.

Myopotential was estimated when they operated wheelchairs to move straight, make turns, rotate, and zigzag. When the estimated and measured myopotentials with the EMG were compared, we found a strong correlation between them (correlation coefficient was 0.7 or above). Thus, we were successful in constructing a neural network that can estimate myopotential corresponding to a wide variety of wheelchair operations.

Keywords: *myopotential, neural network, wheelchair sports, camera, inertial sensor*

Introduction

In recent years, there has been an improvement in the competitiveness of parasports, increasing awareness of social interest in a convivial society where everybody, including the disabled, can participate, and the Paralympic Games continued to attract attention and interest. Majority of the events held in the Paralympic Games use wheelchairs, and wheelchair sports are recognized as international competition. There have been active engagements in motion analysis, performance evaluation, and content evaluation to improve competitiveness. Focusing on muscular activities is a useful approach, and electromyography (EMG), which makes it possible to observe muscular activities, is widely used. Surface EMG measured with EMG can be used as a noninvasive way of capturing the activity of individual muscles during physical activities (Sözen, 2010). Studies on the analysis of walking action (Winter and Yack, 1987), running action (Hunter, Seeley, Hopkins, Carr, and Franson, 2014), jumping action (Wulf, Dufek, Lozano, and Pettigrew, 2010), and cycle-pedaling skills (Cannon, Kolkhorst, and Cipriani, 2007) have been reported. In the case of wheelchair sports, pushing action (Vanlandewijck, Theisen, and Daly, 2001) and fatigue evaluation (Uzun, Pourmoghaddam, Hieronymus, and Thrasher, 2012) are reported.

However, in many cases, EMG is used undercontrolled conditions because of the limitations of physical actions and discomfort due to attaching electrodes, devices, and cables to the body (Howard, 2016). In addition, electrodes may move during intense sporting activities, greatly increasing the noise (Lee, Yoon, Lee, Seong, Lee, Jang, Choi, Yu, Kim, Lee, and Son, 2020).

Progress has been made in developing more compact devices, wireless EMGs (Wonkeun and Jung, 2009), and electrodes that do not come off easily when a conductive gel is used (Lee, Yoon, Lee, Seong, Lee, Jang, Choi, Yu, Kim, Lee, and Son, 2020). However, such EMGs are extremely expensive; hence, the people who can own and use these devices are limited (Felici and Del Vecchio, 2020). Under these circumstances, there are limited number of cases in which these advanced EMGs are used for real actions in competitive settings.

Therefore, we investigated into a method for estimating myopotential in competitive settings. In this study, we developed a method for estimating myopotential with a neural network using a video camera and inertial sensors. It was reported that these measuring devices have been widely used in competitions (Reilly, 2001; Camomilla, Bergamini, Fantozzi, and Vannozzi, 2018). Furthermore, because the video camera is a completely contactless device and the inertial sensor is compact, lightweight, and attached to a wheelchair, they do not interfere in the competitive activities. Therefore, if we can estimate myopotential using the video camera and inertial sensor, it can be used to estimate myopotential, which would be a revolutionary approach.

Methods

Figure 1 shows the steps we followed to develop the myopotential estimation model. In this section, dataset construction, i.e., data acquisition, data pre-processing, and dataset creation, are described. Further, the model we designed to estimate myopotential is described. Finally, model learning is explained.

Data Collection

We conducted synchronous data acquisition of myopotential, camera images, and inertial sensors while the wheelchair was operating. The test subject was one healthy male and university student. The subject did not use wheelchairs on daily basis, but received sufficient training before participating in the test. The used wheelchair type was wheelchair tennis. The measurement was taken in a gymnasium with a wooden floor. The measuring devices used were the camera (Pocket Cinema Camera 4K, Blackmagic Design Pty. Ltd.), inertial sensor (IMS-SD, Tec Gihan Co., Ltd.), and EMG (Polymate Pro MP6000, Miyuki Giken Co., Ltd.). Three cameras were used, and they were placed at certain places to capture the images of the entire measurement field (10 m × 10 m). Recording was conducted at a sampling frequency of 60 Hz and resolution of 4 K (7,680 pixel × 4,320 pixel). The three cameras used an external trigger as input and performed synchronous measurements. Examples of images taken with three cameras using synchronous measurement are shown in Figure 2.

Figure 3 shows the installation locations of the inertial sensors. The inertial sensor was equipped with a three-axis acceleration sensor, three-axis angular velocity sensor, and three-axis geomagnetic sensor. Sensor A was located at the center of the wheel axis. The forward direction of the wheelchair was set to the positive X-axis direction, and the upward vertical direction, to the positive Z-axis direction. Sensors B and C were placed at the center of the right and left wheels, respectively. The upward direction perpendicular to the wheel surface was set to the positive Z-axis direction. The sampling frequency was 1,000 Hz. The resolution of the inertial sensors was set to 12 bits and dynamic range to ±16 G. The angular velocity sensor had a resolution of 16 bits and dynamic range of ±2,000 dps.

Figure 4 shows the position where the myopotential electrodes were attached. Five measurement points were used, i.e., flexor digitorum profundus on the right hand, biceps brachii, triceps brachii muscle, rear deltoid, and right pectoralis major. The sampling frequency was 1,000 Hz.

The target movements chosen, based on an interview with experts in wheelchair sports, covered the important movements involved in chair work of wheelchair sports. Those were forward move at three intensities, zigzag move, backward move, 90° turn and 180°turn. Test subject was asked to mix up these moves and operate wheelchair.

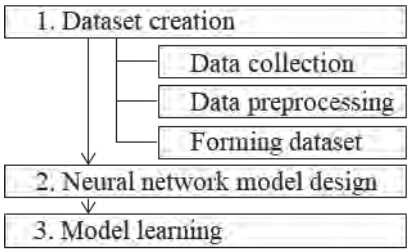

Figure 1 Steps to develop the myopotential estimation model

Figure 2 Example of measured camera image

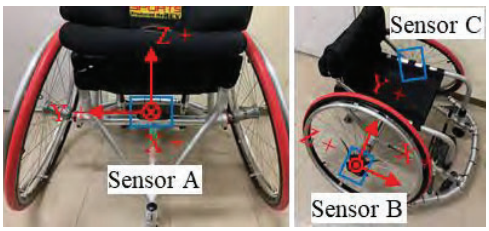

Figure 3 Positions of inertial sensors

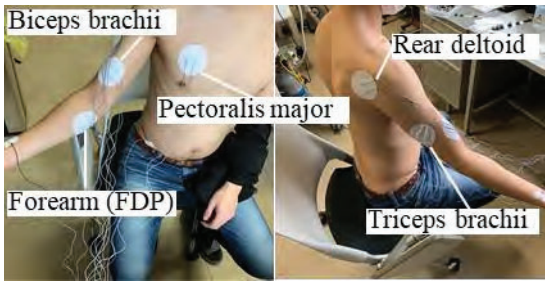

Figure 4 Attachment position of myopotential

Data Preprocessing

Figure 5 shows the procedure for creating the dataset. Figure 6 shows the sample data of the preprocessing and formation of datasets. Firstly, the data from each measuring device were time-synchronized using the external trigger signal input at the time of data collection.

Processing of images captured by video camera. To start with, the 2D coordinates of the body joints of the human shown in the image were calculated using the open pose (Cao, Hidalgo, Simon, Wei, and Sheikh, 2021) was used. Among the three synchronously measuring video cameras, the camera in which the test subject was displayed the largest within the same timeframe was used. In this study, the upper body key point coordinates thought to affect the rowing motion of the wheelchair were calculated. The joint parts used in this study are shown in Figure 7. Next, we calculated the 3D coordinates based on the calculated body joint 2D coordinates using the pose-baseline (Julieta, Rayat, Javier, and James, 2017). Finally, the calculated body joint 3D coordinates and key points on the pelvis were normalized by converting them to local coordinates. With the point of origin as pelvis, the upward direction perpendicular to the floor was set to the positive Z-axis direction. The plane horizontal to the ground and passing through the point of origin was set as the XY plane. The line that projects the line connecting the right and left hips on the XY plane was set as the Y-axis, and the direction toward the left hip from the right hip was set as the positive direction. The coordinate system was a right-hand system. The above process was repeated for each frame.

Processing of data recorded with inertial sensors. In this study, we used the three-axis acceleration data for inertial sensor A to express the acceleration of the wheelchair movement, and the three-axis angular velocity data from inertial Sensors B and C to express the wheel rotation. For the acceleration and angular velocity data, a low-pass filter with a cutoff frequency of 60 Hz was employed to reduce high-frequency element noise. Finally, down-sampling to 60 Hz was performed to standardize the sampling frequency for each measuring device.

Processing of data recorded with EMG. As full-wave rectification smoothing processing, the absolute value of the amplitude was sought, and a low-pass filter with a cutoff frequency of 2.6 Hz was employed. The cutoff frequency was adopted from the report by Yoshida and Terao (2003). We then normalized the maximum myopotential for the myopotential data for each test subject, %MVC (percent maximum voluntary contraction).

Finally, we performed down-sampling at 60 Hz to standardize the sampling frequency of each measuring device.

Forming Dataset

The input data (predictor variables) were the 3D coordinates (48 dimensions) of 16 body joint parts, the 3D acceleration data of the wheelchair (3D), the three-axis angular velocity data (6 dimensions) of the left/right wheels, making a total of 57 dimensions. The output values (response variables) were set to various myopotential data. The data configuration of the timepoint t was set to data in the input value data cut out from the timepoint t to w units (w: window width) prior to t and output value data cut out from timepoint t data.

Next, time, t, was slid by slide width, p, and the input and output data were cut out again. By repeating these processes, the dataset was formed. The window width w was set to 6, and the slide width was set to 6. The formed dataset has a total of 4,502 data.

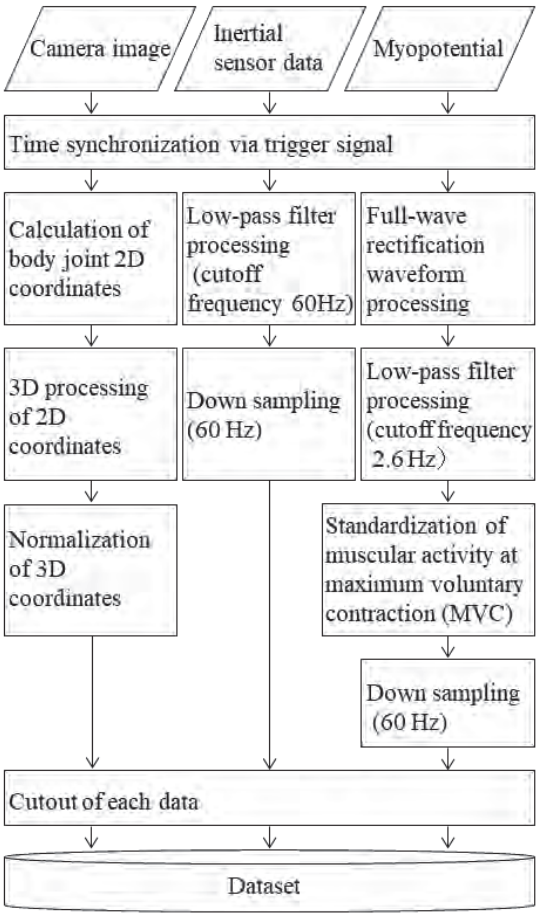

Figure 5 Procedure for preprocessing and formation of datasets

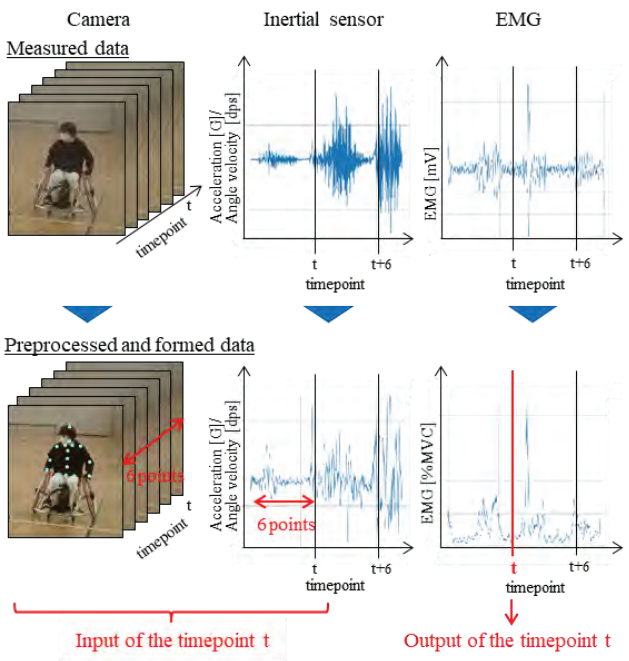

Figure 6 Sample data of the preprocessing and formation of datasets

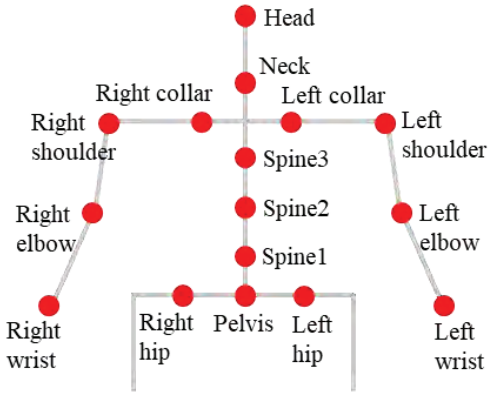

Figure 7 Body joints calculated from the camera image

Neural Network Model Designed to Estimate Myopotential

Figure 8 shows the architecture of the designed model. The input is a 6 × 57 grid. It connects to the convoluted layers to extract features. The Relu function was adopted as the activation function.

Next, output of the previous process connects to the max-pooling layer to acquire the maximum value within the kernel. Then, to avoid over-learning, it connects to the dropout layer with a dropout rate of 0.5 (Srivastava, Hinton, Krizhevsky, and Salakhutdinov, 2014). The above process was repeated twice. Then, the kernel size was set to 1 × 2 and 1 × 3. The number of channels was changed to 128 and 256. After reshaping, it connects to a fully convoluted layer. The Relu function was adopted as the activation function. The fully connected layer was repeated three times and, finally, a 1D value was the output. The value of the output indicates the myopotential for one target part.

Model Learning

The designed model was learned using data for divided at random at a ratio of 8:2 for learning and evaluation data, respectively. When learning, the optimization function used was that of Adam (Kingma and Ba, 2015), the learning ratio was 0.01, and the number of learning times was 3000. Model learning was performed for each myopotential part.

Results and Discussion

The learned model was applied to the evaluation data to verify the accuracy of the myopotential estimation. Figure 9 shows the measured EMG values and the proposed model estimation value distribution diagram for all evaluation data. The coefficient of determination R2 for the regression line was 0.53. The root-mean-square error relative to the EMG-measured values was 12.96 %MVC.

Next, we examined the correlation (Spearman's correlation coefficient) between the EMG-measured

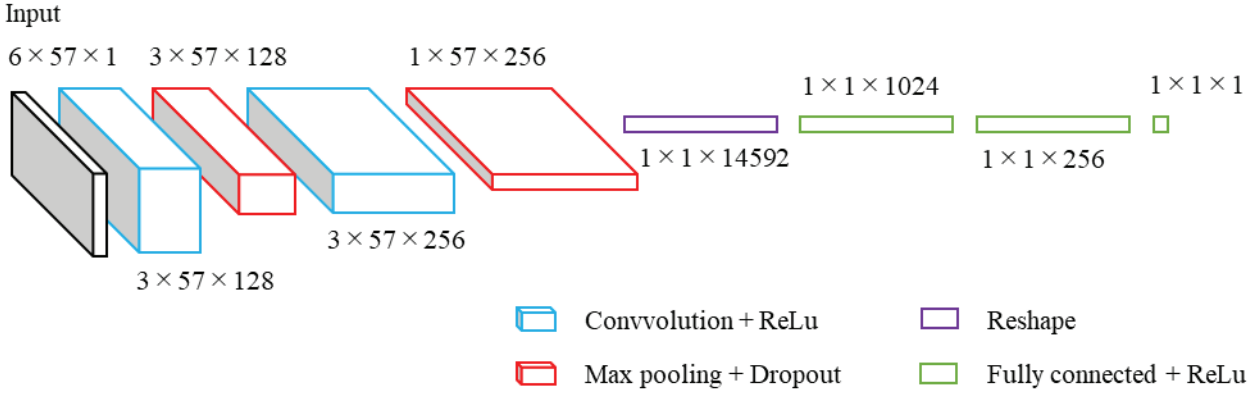

Figure 8 Architecture of the designed model (not to scale)

values for each myopotential area and the estimated values. We further evaluated the significance of the correlation coefficient. The correlation coefficient between the measured and estimated values for each myopotential area is shown in Table 1. All correlation coefficients in the table are significant at a level of 0.1%. The correlation coefficient for all evaluation data was 0.73 ($p < 0.001$). It was confirmed that the proposed model could estimate values with a positive correlation to the myopotential measured value. As the evaluation data were various chair work movements observed during wheelchair sports, the model is said to have general significance for all movement types. In addition, comparing the estimated results for each myopotential area, the correlation coefficient was 0.6 or above ($p < 0.001$). The proposed model can support differences in myopotential areas.

In the previous study (Dickerson, Hughes, and Chaffin, 2008), myopotential during dynamic weight tasks was estimated by solving the reverse dynamics and optimization problem using the measured values from optical motion capture and electromagnetic tracker as inputs. It was reported that with deltoid muscles there was a correlation coefficient accuracy of 0.53 was reported using EMG, and with biceps brachii, the accuracy was 0.61. In this study, a similar accuracy was achieved using simple measuring devices.

To estimate myopotential, muscular activity, muscular strength, and joint torque with high accuracy, it is necessary to use kinematic data (for example, the 3D posture data of a human) acquired from a motion-capture system and the mechanical data resulting from exercise (Dao, 2019). To acquire mechanical data during wheelchair operations, it is necessary to measure the wheelchair data using a built-in torque meter (Asato, Cooper, Robertson, and Ster, 1993). In this study, it is considered that the wheelchair moves as a result of the wheelchair operation, and so, we use the wheelchair acceleration and angular velocity data obtained from inertial sensors (pseudo-mechanical data) instead. Thus, it is considered that the designed model can learn myopotential estimation by obtaining the human kinematic data during wheelchair operations and the pseudo-mechanical data resulting from this movement as input values.

However, when performing movements unrelated to wheelchair operations, such as swinging a tennis racket or shooting a basketball, no change occurs in the wheelchair acceleration or angular velocity data obtained from the inertial sensors. Thus, the myopotential may be erroneously estimated.

Further, as the objective of this study is to develop a simple measurement method, we used a method of calculating the human 3D postural data from a camera image (e.g., Cao, Hidalgo, Simon, Wei, and Sheikh, 2021; Julieta, Rayat, Javier, and James, 2017). Compared to the optional motion capture, the 3D posture position data have lower accuracy. Therefore, improving the method of calculating 3D postural data from captured images and the positional accuracy, the accuracy of myopotential estimation is improved.

Furthermore, the model developed in this study estimates the data for one test subject ignoring individual differences. Using datasets with more test subjects and increased learning data and learning the proposed model, the model could consider individual differences.

Conclusions

The purpose of this study was to develop a method to estimate the myopotential when operating wheelchairs. A simple method to measure myopotential based on a camera image and inertial sensors attached to the wheelchair was proposed. By designing a neural network model using convolution neural network, model learning was performed using the collected data. Further, we developed a model that estimated myopotential correlated to the measured myopotential values (correlation coefficient 0.7 or above). We thus realized a method of estimation that uses only a video camera and inertial sensors without an EMG.

In future studies, we aim to develop a model that estimates myopotential with higher accuracy and considers individual differences.

This study was conducted with the approval of the Human Research Ethics Review Board of Nagaoka University of Technology (approval number: 2017-38). A study participant provided informed consent.

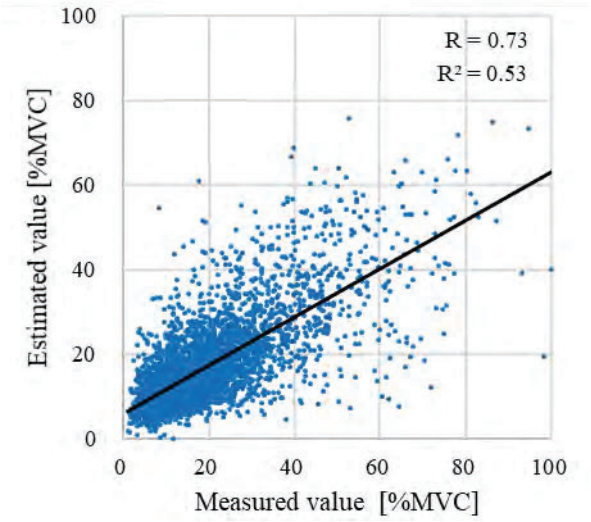

Figure 9 Relationship between the EMG measured and proposed model estimated values

Table 1 Correlation coefficient between measured EMG values and proposed model estimated values. All correlation coefficients in the table are significant at a 0.1% level.

Forearms	Biceps	Triceps	Rear deltoid	Pectoralis	All parts
0.69	0.64	0.69	0.61	0.86	0.73

Acknowledgements

We gratefully acknowledge the work of past and present members of our laboratory.

References

Asato, K.T., Cooper, R.A., Robertson, R.N., & Ster, J.F. (1993). SMART Wheels: Development and Testing of a System for Measuring Manual Wheelchair Propulsion Dynamics. *IEEE Transactions on Biomedical Engineering, 40(12), 1320-1324.*

Camomilla, V., Bergamini, E., Fantozzi, S., & Vannozzi, G. (2018). Trends Supporting the In-Field Use of Wearable Inertial Sensors for Sport Performance Evaluation: A Systematic Review. *Sensors, 18(3), 873.*

Cannon, D.T., Kolkhorst, F.W., & Cipriani, D.J. (2007). Effect of pedaling technique on muscle activity and cycling efficiency. *European Journal of Applied Physiology, 99(6), 659-664.*

Cao, Z., Hidalgo, G., Simon, T., Wei, S.E., & Sheikh, Y. (2021). OpenPose: Realtime Multi-Person 2D Pose Estimation Using Part Affinity Fields. *IEEE Transactions on Pattern Analysis and Machine Intelligence, 43(1), 172-186.*

Dao, T.T. (2019). From deep learning to transfer learning for the prediction of skeletal muscle forces. *Medical and Biological Engineering and Computing, 57(5), 1049-1058.*

Dickerson, C.R., Hughes, R.E. & Chaffin, D.B. (2008). Experimental evaluation of a computational shoulder musculoskeletal model. *Clinical Biomechanics, 23(7), 886-894.*

Felici, F., & Vecchio, A.D. (2020). Surface Electromyography: What Limits Its Use in Exercise and Sport Physiology?. *Frontiers in Neurology, 11(11).*

Howard, R. (2016). Wireless Sensor Devices in Sports Performance. *IEEE Potentials, 35(4), 40-42.*

Hunter, I., Seeley, M.K., Hopkins, J.T., Carr, C., & Franson, J.J. (2014). EMG activity during positive-pressure treadmill running. *Journal of Electromyography and Kinesiology, 24(3), 348-352.*

Julieta, M., Rayat, H., Javier, R., & James, J.L. (2017). A simple yet effective baseline for 3d human pose estimation. *Proceedings IEEE International Conference on Computer Vision, 2640-2649.*

Kingma, D.P., & Ba, J.L. (2015). Adam: A method for stochastic optimization. *3rd International Conference on Learning Representations.*

Lee, S., Yoon, J., Lee, D., Seong, D., Lee, S., Jang, M., Choi, J., Yu, K.J., Kim, J., Lee, S., & Son, D. (2020). Wireless Epidermal Electromyogram Sensing System. *Electronics, 9(2), 269.*

Reilly, T. (2001). Assessment of sports performance with particular reference to field games. *European Journal of Sport Science, 1(3), 1-12.*

Sözen, H. (2010). Comparison of muscle activation during elliptical trainer, treadmill and bike exercise. *Biology of Sport, 27(3), 203.*

Srivastava, N., Hinton, G., Krizhevsky, A., & Salakhutdinov, R. (2014). Dropout: A Simple Way to Prevent Neural Networks from Overfitting. *Journal of Machine Learning Research, 15(56), 1929-1958.*

Turker, H., & Sze, H. (2013). Surface Electromyography in Sports and Exercise. *Electrodiagnosis in New Frontiers of Clinical Research, 5, 175-194.*

Uzun, S., Pourmoghaddam, A., Hieronymus, M., & Thrasher, T.A. (2012). Evaluation of muscle fatigue of wheelchair basketball players with spinal cord injury using recurrence quantification analysis of surface EMG. *European Journal of Applied Physiology, 112(11), 3847-3857.*

Vanlandewijck, Y., Theisen, D., & Daly, D. (2001). Wheelchair propulsion biomechanics: Implications for wheelchair sports. *Sports Medicine, 31(5), 339-367.*

Winter, D.A. & Yack, H.J. (1987). EMG profiles during normal human walking: stride-to-stride and inter-subject variability. *Electroencephalography and Clinical Neurophysiology, 67(5), 402-411.*

Wonkeun, Y. & Jung, K. (2009). Development of a compact-size and wireless surface EMG measurement system. *2009 ICCAS-SICE, 1625-1628.*

Wulf, G., Dufek, J.S., Lozano, L., & Pettigrew, C. (2010). Increased jump height and reduced EMG activity with an external focus. *Human Movement Science, 29(3), 440-448.*

Yoshida, M. & Terao, M. (2003). Suitable Cutoff Frequency of Low-pass Filter for Estimating Muscle Force by Surface Eectromyogram. *Annual International Conference of the IEEE Engineering in Medicine and Biology- Proceedings, 2, 1709-1711.*

Oxygen Intake Estimation in Wheelchair Driving using Machine Learning

Ryosuke. Mizukami [a] , Syogo Asanuma [a], Masahito Nagamori [a], Hisashi Uchiyama [a], Satoshi Ohashi [b] and Akira Shionoya [a]

[a] Nagaoka University of Technology, Niigata, Japan
[b] National Institute of Technology, Tomakomai College, Hokkaido, Japan

*s193373@stn.nagaokaut.ac.jp

Abstract

Recently, it has become easier to acquire and analyze various sensor data with development of new wearable devices and the deep learning. On the field of sports or healthcare, there has been a lot of research for supporting a human exercise using these data. Most of these studies, however, have been conducted on wholesome people, and there are few studies on people with disabilities. Although the estimating heart rate using the machine learning have been reported in wheelchair driving, the estimation of an exercise work load especially the oxygen intake has not been performed. If it becomes possible to estimate the oxygen intake during wheelchair manipulating, it will be possible to know the oxygen intake easily without using the respiratory metabolic measurement device. The purpose of this study was to develop the model for estimating the oxygen intake of wheelchair users by the machine learning of accelerometers and heart rate sensors data. An accelerometer was installed onto the undercarriage of the wheelchair and a heart rate sensor and a wearable respiratory metabolism measurement device were attached to each subject. Subjects were 6 wholesome males. An acceleration, heart rate and oxygen intake were measured during a 5-minute lap around a 20-meter square course at 7.2 km/h and 9.0 km/h. The estimation model consisted of an input layer with inputs for acceleration in the direction of wheelchair motion, acceleration in the left-right direction, and the heart rate which has been reported to be highly correlated with the oxygen intake, an intermediate layer with 16 units of LSTM (activation function was the ReLu function) and a layer with 1 unit of total coupling (activation function was a linear function) to output the predicted values of an oxygen intake. For the LSTM, the data up to one minute ago was used as the historical data. When the proposed model was applied, it was possible to estimate the oxygen intake within a mean absolute error of 1.83 ml/ml/kg, and confirmed that the oxygen intake estimation model constructed by this study could estimate the oxygen intake with high accuracy.

Keywords: *Wheelchair, Oxygen intake, 3-axis Acceleration Sensor, Heart rate sensor, Machine Learning, Neural network*

Introduction

Recently, the spread of wearable devices makes the measurement and analysis of various sensors data easily. Furthermore, with the development of the AI or the deep learning, studies have been actively performed using the data effectively obtained from such devices. In the field of sports or health care, studies using a human behavior data measured by these devices are performed actively for the purpose of a human exercise or health assisting. For example, a simulation model has been suggested for estimating an exercise level using an acceleration data measured by a device attached to subject. Most studies are, however, for healthy subject and few for disabled subject (Ohnishi et.al, 2015). Furthermore, the heart rate estimation models in walking for healthy subjects (Sumida et.al, 2014) and that estimation models in driving a wheelchair (Asanuma et.al.,2020., Kamibayashi et.al, 2019) have been already reported. However, the oxygen intake estimation model in driving a wheelchair has not been reported. The oxygen intake is very important as an indicator for health(ACSM.,2013). Being able to estimate oxygen uptake while driving in a wheelchair eliminates the need to use expensive and difficult-to-measure respiratory metabolizers.

The purpose of this study is to suggest a simulation model to estimate the oxygen intake using a data detected by a wearable device in driving a wheelchair.

Materials and Methods

Experimental protocol

In order to construct and evaluate an oxygen uptake estimation model, the acceleration data, the heart rate, and the oxygen intake during wheelchair manipulating were measured in the experiment. Figure 1 shows the state of experimental. In the experiment, the subjects were asked to go around a 20m square course set up in the gymnasium in a wheelchair at 7.2km/h and 9.0km/ h for 5 minutes, and the acceleration data, heart rate, and oxygen uptake were measured. In the experiment, the measurement of each parameter was started after confirming that the subject's heart rate was at rest. The subjects were 6 healthy men (age: 22.2 ± 1.07 years, height: 172.0 ± 3.32 cm, weight: 63.7 ± 5.09 kg) shown in Table 1, and all of whom did not ordinarily use a wheelchair. The wheelchair used in this experiment was a basketball competition wheelchair (manufactured by OX Engineering Co., Ltd.) shown in Fig. 2.

Measurement data

The measured data were 3-axis acceleration (G), heart rate (bpm), and oxygen uptake (ml/min/kg). Accelerometer was a 3-axis accelerometer (Fig. 3: Slick, G-MEN DR-01, sampling cycle 100 Hz) attached onto a wheelchair, oxygen intake was measured using a portable respiratory and metabolic measurement system (Fig. 4: AE100i, Minato Medical Science Co., Ltd.). The heart rate was measured by a heart rate sensor (Fig. 5: POLARH10, sampling time 1s) attached to the subject's chest.

Data processing

Measurement data were smoothed by a half overlap with 24 seconds window size. Therefore, the data after smoothing becomes 12 s interval. Next, in order to make all samples have the same data size, zero padding was performed so that all samples had the largest size. For heart rate data, the value obtained by subtracting the initial value of each sample was used. Thus, these data represent the fluctuation values from the initial heart rate of each sample.

Estimate model construction and evaluation

Figure 6 shows the model constructed in this study. The estimation model consists of input layer (the acceleration toward a driving direction, the transverse acceleration, and Heart rate), the

Figure 1 The state of experiment

Figure 2 The wheelchair used in this experiment

Table 1 The physical characteristics of subjects

Subject	Age (years)	Height (cm)	Weight (kg)
A	22	174	63
B	21	172	72
C	24	165	59
D	23	175	63
E	21	174	68
F	22	172	57

intermediate layer of the LSTM with 16 units (the activation function is the ReLu function) and fully connected layer that outputs predicted heart rate. LSTM used data up to 1 minute ago as past data. Using 5 out of 6 subjects (of which 20% are validation data) as learning data and applying the remaining 1 subject's sample as test data, each subject is used as test data Cross validation was performed and six models were constructed. Adam is used as the optimization algorithm. Batch size is 4. The parameter update was performed at 50 epochs, and the parameter model with the smallest verification error was adopted. Prediction error of estimation models constructed was the mean absolute error (MAE) of the measured and predicted values of the Oxygen Intake. In addition, the estimation of the constructed estimation model starts 1 minute after the start of driving because the data of 1 minute before is used for LSTM.

Results and Discussions

Table 2 shows the MAE obtained using the model constructed in the previous chapter. Figure 7 shows an example of the comparison results between the predicted and measured values of oxygen uptake. Here, Route 1 traveled at 7.2 km / h, and Route 2 traveled at 9.0 km / h.

From Table 1, it can be seen that the result with the smallest MAE is F2 (Route 2 of subject C), and the result with the largest MAE is A2 (Route 2 of subject F). As a result, it is possible to realize an estimation with an error smaller than the estimation error of 4.2 kg/min/kg (1.2 METs) obtained by the previous study that estimated the exercise load during walking in a healthy person. From these,

Figure 3 3-axis accelerometer used in this study

Figure 4 Portable respiratory and metabolic measurement system used in this study

Figure 5 Heart rate sensor used in this study

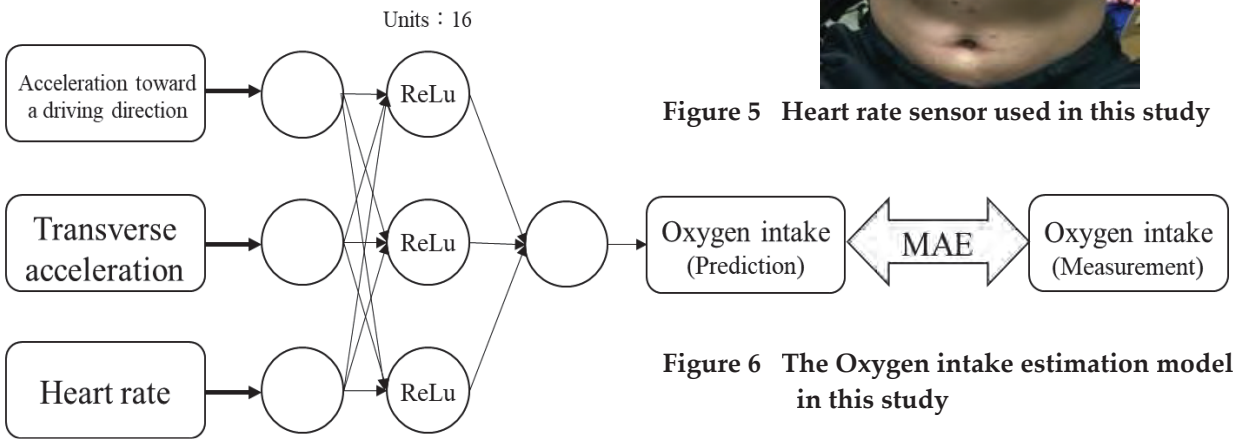

Figure 6 The Oxygen intake estimation model in this study

it is considered that the oxygen intake estimation model constructed by this study can realize the estimation with high accuracy.

Furthermore, paying attention to the result of Fig. 7 (Route 2 of subject C), it can be seen that the prediction of oxygen uptake is realized by following the measured value. However, in the result of Fig. 8 (Route 2 of subject F), although the approximate trend of oxygen intake is captured, the predicted value is lower than the measured value as a whole, and the prediction error becomes large. It is considered that the reason for this is that subject F had lower physical ability than other subjects, so the increase in oxygen uptake was larger than that of other subjects. In addition, there were cases in which the trend of oxygen uptake was not fully captured in other results. This is thought to be due to the lack of subjects and routes number for machine learning. For the future study, it is considered that the estimation accuracy will be improved by increasing the number of subjects and routes, categorizing the subjects according to the exercise experience, and introducing parameters related to the exercise experience and physical ability of each subject.

Conclusions

In this study, we constructed an estimation model of oxygen uptake when driving a wheelchair using sensory data obtained from an accelerometer and a heart rate sensor. As a result, the estimation error was 1.83 ml / min / kg (0.52 METs). This is an estimation error of the exercise load during walking of a healthy person of 4.2 ml / min / kg (1.2 METs) or less, and it is considered that the estimation with high accuracy was realized. Therefore, it was suggested that the estimation model constructed in this study can estimate the oxygen intake when driving a wheelchair. However, some results did not fully capture the trend of oxygen uptake, so it is necessary to increase the number of subjects and routes in the future. In addition, in situations where higher estimation accuracy is desired, such as in sports scenes, it is possible to introduce parameters that represent the physical abilities of each individual in addition to the input data used this time, and to categorize them according to the exercise experience of the subject. It is expected that the estimation accuracy will be improved. In addition, in order to improve the estimation accuracy, it is considered possible to realize highly accurate oxygen uptake estimation in various situations by incorporating wheelchair-specific movements such as dashing and turning movements into the route.

Table. 2 Mean absolute error of each subjects

subject	Route		mean
	1	2	
A	1.37	0.98	1.18
B	1.49	1.36	1.43
C	1.62	0.73	1.18
D	2.98	3.46	1.98
E	2.36	1.10	1.73
F	1.34	3.15	2.25
mean	1.86	1.80	1.83

(ml/min/kg)

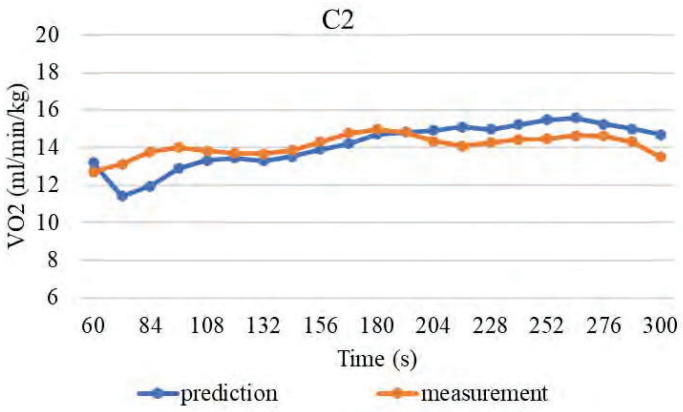

Figure 7 Prediction and measurement of the Oxygen intake variation (Route 2 of subject C)

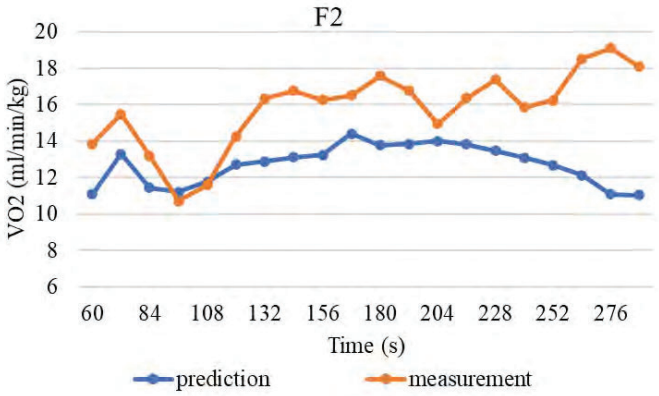

Figure 8 Prediction and measurement of the Oxygen intake variation (Route 2 of subject F)

References

American College of Sports Medicine (ACSM). (2013) ACSM's Guidelines for Exercise Testing and Prescription NINTH EDITION, 9th ed., Lippincott Williams & Wilkins

Asanuma, S., Kamibayashi, Y. & Shionoya, A (2020) Model for Heart Rate Estimation in Driving Wheelchair using Wearable Device. 13th Conf. Int. Sports Eng. 49(1), https://doi.org/10.3390/proceedings2020049052

Kamibayashi, Y., Nagamori, M., Uchiyama, H. & Shionoya, A. (2019) A proposal of model for heart rate estimation while using wheelchair with 6-axis sensor. JSME Symposium: Sports engineering and Human Dynamics 2019, 19-306

Madgwick, S.O.H. (2010) An efficient orientation filter for inertial and inertial/magnetic sensor arrays. Report x-io and University of Bristol (UK)

Ohnishi, K., Ito, N., Kobayashi, Y., Kaji, K., Naito, K., Mizuno, T. & Nakajo, N. (2015) A consideration for the estimation of momentum using both heart rate sensor and acceleration sensor - Preliminary experiment for health assist system - [Translated from Japanese.]. The Special Interest Group Technical Reports of IPSJ, 2015-MBL-77

Sumida, M., Mizumoto, T., & Yasumoto. (2014) A method for estimating heart rate during walking with smartphone. Journal of Information Processing Society of Japan, 55(1), 399-412

EXPLORATION OF AN INFLECTION POINT OF VENTILATION PARAMETERS WITH ANAEROBIC THRESHOLD BY THE STRUCCHANGE

Akira Shionoya [a], Takenori Aida[*a], Hirofumi Nonaka[a], Kouji Hayami[b], Hisashi Uchiyama[a]
Masahito Nagamori[a], Satoshi Ohhashi[c], Mai Kobayashi[d], Tsugumi Takayama[e]
and Shinji Kimura[e]

[a] Nagaoka University of Technology, Nagaoka, Japan
[b] Data dock Ltd., Nagaoka, Japan
[c] National Institute of Technology, Tomakomai College, Tomakomai,Japan
[d] Seiryou, Junior College of Rehabilitation, Nagaoka, Japan
[e] Niigata University Medical and Dental Hospital, Niigata, Japan

* s165042@stn.nagaokaut.ac.jp

Abstract

Anaerobic threshold (AT), widely used as an index of safe and effective exercise workload in exercise therapy, is defined as the workload or O_2 consumption level at which metabolic acidosis and associated changes in pulmonary gas exchange occur. To determine AT, a blood lactate measurement via sampling or a ventilation measurement using a respiratory metabolic measurement device is needed. Blood sampling can only be performed by a licensed medical doctor or a nurse, and ventilation measurement requires expensive equipment. With a ventilator during a gradual incremental workload exercise, AT is measured based on ventilation parameter inflection points as follows: rapid increase in ventilation expired gas volume (VE); excess CO_2 production (VCO_2); increase in respiratory quotient (VCO_2/VO_2); increase in the O_2 equivalent (VE/VO_2) without a change in CO_2 equivalent (VE/VCO_2); and increase in the end tidal O_2 concentration (ETO_2) without a change in the end tidal CO_2 concentration ($ETCO_2$). We focus on these ventilation parameter inflection points. The purpose of this study is to explore the inflection points of ventilation parameters alongside AT using the *strucchange* feature of statistical machine learning and to determine *easy* and *inexpensive* AT. Subjects included 10 healthy males. Each wore a metabolic measurement device. The expired gas was sampled by this device during an incremental workload exercise using a bicycle ergometer. The VE and the VCO_2 contained in the sampled expired gas were sampled for 10 s on average. The data were analysed using a three-point moving average via *strucchange*. Specifically during exercise, the inflection points of VE vs. workload and CO_2 production vs. workload were explored. As a result, we succeeded in automatically locating the inflection points of the ventilation expired gas volume and CO_2 production.

Keywords: *Anaerobic threshold, inflection-point exploration, strucchange, ventilation expired gas volume, excess CO_2 production*

Introduction

Japan currently has the highest rate of aging among developed countries, and according to a United Nations (2019) report, Japan's proportion of people over the age of 65 is predicted to increase to greater than 30 % by 2040. According to a report by Toshima (1994), heart disease has become the second leading cause of death since 1985, owing to changes in the living environment and eating habits of Japanese people following rapid economic growth. Additionally, Wannamethee, Shaper and Walker (2000) reported that maintaining quality of life after suffering from heart disease leads to extension of healthy life expectancy and heart-disease prevention. The anaerobic threshold (AT) proposed by Wasserman, (1984) is used as a reference to prevent exercise overwork. AT reflects exercise intensity and O_2 uptake immediately prior to anaerobic metabolism occurring alongside aerobic metabolism during load-incremental exercise, when the associated change in gas-exchange parameters occurs (Figure 1). Yabe, Kono and Moriyama (2016) recommended exercising at the AT level as an effective index considering safety, even for people with a medical history.

According to Wasserman (1984), AT reflects the maximum exercise intensity that can be performed without a continuous increase in blood lactate concentration during incremental load exercise. The parameters in Figure 1 are described as follows: ① non-linear increase in ventilation volume (VE: L/min): ② non-linear increase in CO_2 emission (VCO_2: ml/kg/min);

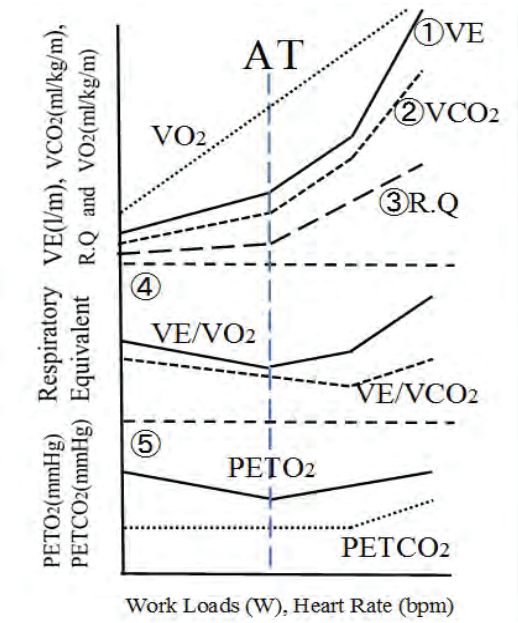

Figure 1 Wasserman classification

③ non-linear increase in respiratory quotient (RQ); ④ increase in O_2 (equivalent VE/VO_2) without a change in CO_2 (equivalent VE/VCO_2) and ⑤ increase in the end tidal O_2 concentration ($PETO_2$: mmHg) without a change in the end tidal CO_2 concentration ($PETCO_2$: mmHg). To determine AT, methods of analysing gas in exhaled breath and measuring blood lactate concentration via sampling are used. In particular, the latter method is invasive and expensive. Furthermore, practitioners rely on 'rule-of-thumb' guidance. In a previous study on AT determination, Tsubusadani, Hayashi, Sekikawa, Kawaguchi, Taisei and Kobayashi (2001) proposed a method called 'heart-rate threshold', which identifies AT based on non-invasive data, such as heart rate. However, there is room for improvement in measurement accuracy, owing to the influence of respiration on heart rate variability. Shionoya, Fukumoto and Miyake (1993) and Shionoya, Hasegawa and Miyake (1998) developed an AT approximate estimation system using the Fourier transformation of the respiratory curve, based on which a dilated ergometer for heart rate and respiration control is being developed. Kimoto and Shinoya (2016) reported the utility of simple AT identification that focuses on frequency analysis of the respiratory curve under respiratory restriction. The V-slope method, a conventional analogue, (Figure 2) is also used as an AT identification method. Sue, Wasserman, Moricca and Casaburi (1988) simplified AT derivation by assigning the point of increase in the slope from the slope θ45° of the plotted straight line at the change point when plotting the amount of change in VCO_2 with respect to VO_2 in exhaled breath. However, this method assumes complete decomposition of glucose $C6H12O6+6O2 \rightarrow 6CO2+6H2O$ as AT's premise, which has not been theoretically identified. Furthermore, even with the AT determination process of Beaver and Wasserman (1986),

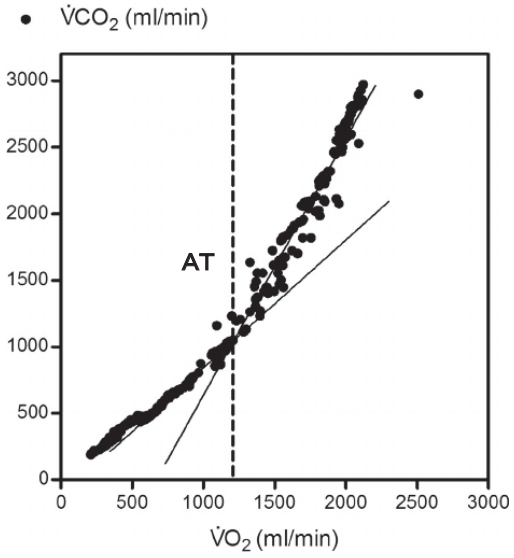

Figure 2 AT using V-slope method

the subjectivity of the examiner is strong in the determination of the change point.

In summary, a method that can objectively determine AT has not yet been established, even with sophisticated equipment. Therefore, this study aims to develop a more objective method of identifying AT inflection points by using the *strucchange* function of machine learning.

Materials and Methods

Subjects: The subjects included 15 healthy males and two healthy females, 17 persons total (age 21±1.4 years, body-mass index 21±1.9) who exercised daily. The purpose of measurement was fully explained to the subjects prior to the experiment, which was conducted after obtaining consent. The experiment was conducted at the Sports Engineering Laboratory of Nagaoka University of Technology and in the Laboratory of Seiryou,Junior College of Rehabilitation.

Experiment protocol: After a subject performed stretching exercises, the height of a stationary ergometry bicycle saddle (AEROBIKE EZ101, COMBIWELLNESS Corp.) was adjusted, the pedals were fixed, and an exhaled-gas mask was applied for the duration. A resting state (rest) was held for 3 min on the bicycle, and a warm-up pedalling exercise of 50 rpm was performed for 3 min at a load of 20 W. Then, while maintaining 50 rpm, a load incremental exercise (exercise) was performed using the ramp-load method in which the load increases by 20 W every minute. After exercising for 9 min, 30 s, a 3-min cool down was performed. The detailed experimental protocol is shown in Figure 3. The Vmax 29S manufactured by SensorMedics Corp. was used as the respiratory metabolism measuring device, and analysis was performed using the breath-by-breath method.

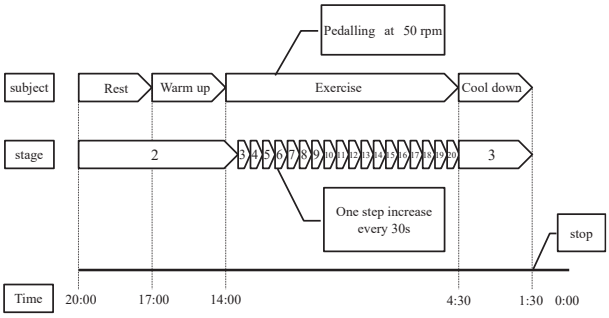

Figure 3 Experiment protocol

Ventilation parameters (e.g., ventilation volume (VE: L/min), O_2 uptake (VO_2) and CO_2 emission (VC O_2: ml/kg/min)) were measured from the exhaled gas of the subjects during exercise and analysed (Figure 4). Each ventilation parameter was recorded on a computer built into the analyser and digitized. Data were then sampled at every 10 s on average and smoothed using a simple moving average (three points). After smoothing, the data were saved on a portable universal serial-bus device and analysed using the R language *strucchange* package (Achim & Friedrich, 2011). The analysis interval was 12 min, 30 s from the warm-up to the end of the exercise. This is consistent with the protocol of the exercise load incremental exercise, which has four stages: warm-up (steady state) → AT → respiratory compensation point → cool-down. The respiratory metabolism analyser does not have a change-point extraction function. Hence, additional tools (e.g., *strucchange* and V-slope) are needed. According to Farnsworth (2008), *strucchange* is used to extract structural changes in the fields of statistics and econometrics, and it is possible to estimate confidence intervals for structural change points using the Bayesian information criterion. The AT was thus determined using the respiratory metabolism measuring device and the built-in V-slope analysis function. The AT of each subject was then calculated and reflected as a vertical solid line on the graph (time axis) of each ventilation parameter.

Results and Discussion

Results from Strucchange and respiratory metabolism analysis: Figure 5 shows the results of a typical example (subject E) in which the VE after smoothing was modified using *strucchange*. Similarly, Figure 6 shows the results (subject E) of VCO_2 after *strucchange* and smoothing. The vertical dashed line indicates the change point identified by *strucchange*, and the red H shape indicates the confidence interval, which was calculated in the range of 95 %. With the increase of VE and VCO_2, the four change points are clearly displayed. For all subjects, there were at least three and at most five change points for both VE and VCO_2.

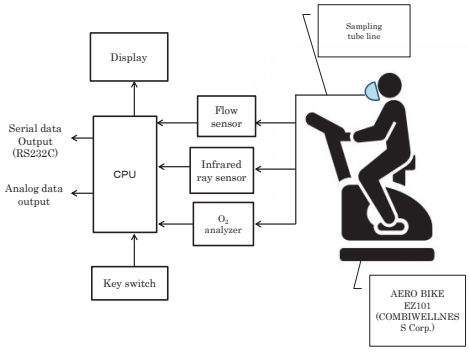

Figure 4 Experimental setup

Results from V-slope method and Strucchange, respiratory metabolism analysis: Figure 7 shows the change point of subject E by the V-slope method, which was compared to the change point derived from *strucchange*. Figure 7 shows an AT (black circle) obtained by the author using the conventional V-slope method alongside each AT via *strucchange* (red circle) and respiratory metabolism analysis (black circle) using the same coordinates.

Table 1 AT by Strucchange, V-slope method, respiratory metabolism analysis in VE (numbers in table converted to W)

Subject	*strucchange*	V-slope Method	respiratory metabolism analysis
A	110	120	100
B	100–110	110	110
C	80–90	100	90
D	70–80	110	80
E	80–90	120	80
F	120–130	100	120
G	120–130	130	120
H	90–100	120	90
I	70–90	90	90
J	120–130	130	120
K	90–100	145	100
L	100	120	Undetectable
M	90–100	90	Undetectable
N	100–110	120	Undetectable
O	100	115	Undetectable
P	80–100	135	Undetectable
Q	100–110	89	Undetectable

Table 2. AT by Strucchange, V-slope method, respiratory metabolism analysis in VCO_2 (numbers in table converted to W)

Subject	*strucchange*	V-slope method	respiratory metabolism analysis
A	110–120	120	100
B	110–130	110	110
C	90	100	90
D	70–80	110	80
E	80–90	120	80
F	120–130	100	120
G	120–130	130	120
H	90–100	120	90
I	100–110	90	90
J	120–130	130	120
K	90–105	145	100
L	95–105	120	Undetectable
M	90–105	90	Undetectable
N	100–110	120	Undetectable
O	95–105	115	Undetectable
P	80–95	135	Undetectable
Q	100–115	89	Undetectable

Discussion

Comparison between Strucchange and Respiratory Metabolism Analysis: From Figure 5&6, each change point was detected for VE and VCO_2 during the exercise load incremental exercise using *strucchange*. From Table 1.2, the analysis results for AT from *strucchange* using the respiratory metabolizer to measure VE and VCO_2

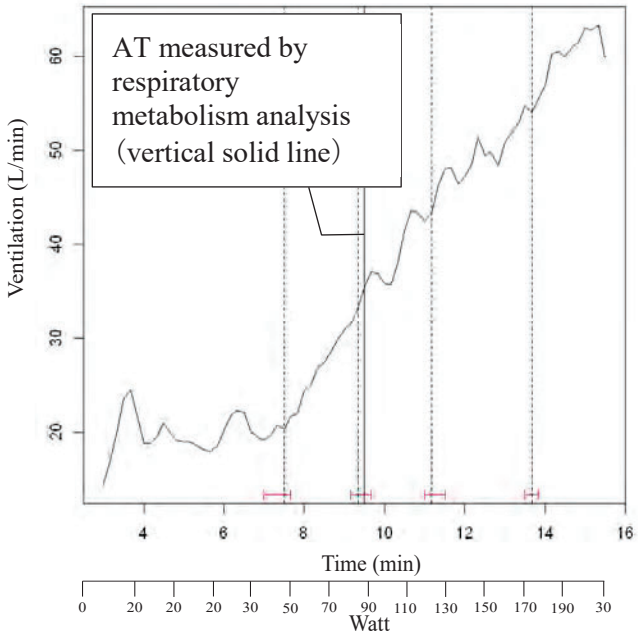

Figure 5 Subject E (post strucchange)

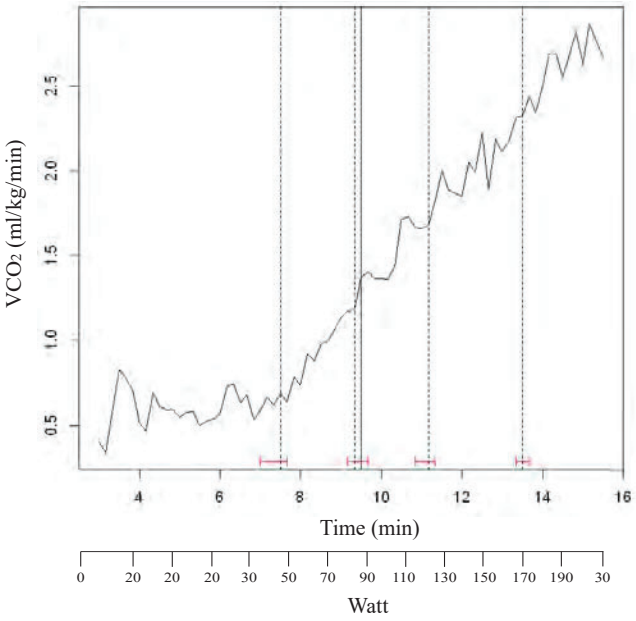

Figure 6 Subject E (post *strucchange*)

were in the same range for 10 (B–K) out of 17 persons. The possibility that AT could not be detected via device analysis was considered to be the reason why it became undetectable when using the respiratory metabolism analyser. The reason is that the detection algorithm used by the respiratory metabolism device is based on the V-slope method, inferring that AT detection is insufficient when using the slope of the increase in VCO_2 with respect to VO_2. When the slope of the increase in VCO_2 with respect to VO_2 is θ45° or greater, it becomes more difficult to detect AT. This phenomenon is reflected in the experimental results of this study. Hence, V-slope AT detection is deemed insufficient for respiratory

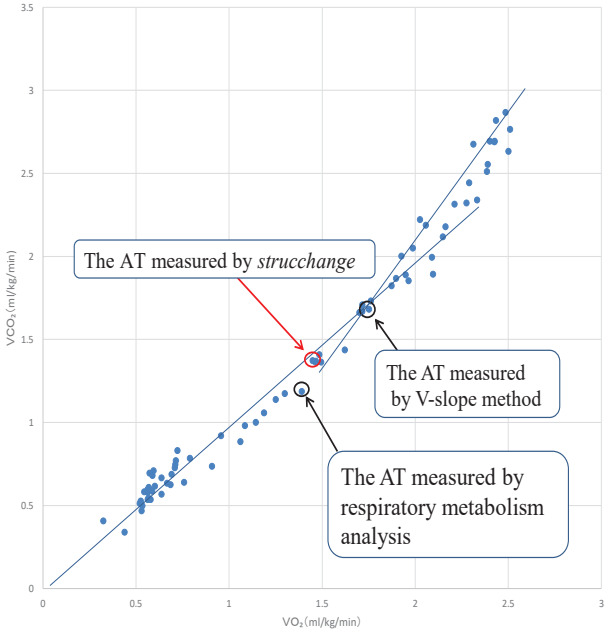

Figure 7 Subject E (Comparison of each AT by V-slope method, *strucchange* and respiratory metabolism analysis)

metabolism analysis. Hence, *strucchange* is the preferred tool.

Comparison between V-slope method and Strucchange and respiratory metabolism analysis: From Tables 1 and 2, *strucchange* and respiratory metabolism analysis were suitable to capture AT results, which were nearly the same in some subjects. However, the results differed when using the V-slope method. The AT determination threshold of *strucchange* tended to be lower than that of the V-slope method, which is considered to be the cause of examiner subjectivity when the slope increases past θ45° when using the V-slope method. Therefore, *strucchange* is physiologically significant, and Figure 5 shows the non-linear increase in VE (Wasserman, 1984). Hence, *strucchange* is now believed to present a good solution to the conventional AT identification problem left behind by V-slope.

Conclusions

In this study, incremental load tests were conducted using a bicycle ergometer, and AT change points based on ventilation parameters were identified using *strucchange*. The findings of the study are summarized as follows:

1. It is possible to detect AT change points for each ventilation parameter (i.e., VE and VCO_2) using *strucchange*.
2. The confidence intervals of the *strucchange* results match those of VE and VCO_2 respiratory metabolism analysis. However, the detection method by respiratory metabolism analysis was based on the V-slope method, for which AT detection became nearly impossible.

From the results, the accuracy of AT detection when using the conventional V-slope method is inferior to those obtained using the *strucchange* of each ventilation parameter. Going forward, future studies should adapt this method so that AT detection can be further refined by accounting for past exercise habits. Because there are individual differences in subjects and errors in analysis from various RQ methods, it is necessary to elucidate the causes. In the future, we plan to develop a medical-engineering cooperative system that makes diagnoses based on engineering methods and physiological ventilation parameters.

Acknowledgements

This study was conducted as joint research based on the Comprehensive Medical and Engineering Cooperation Agreement between Niigata University Medical & Dental Hospital and Nagaoka University of Technology. We would like to express our gratitude to everyone involved.

References

Achim, Z. & Friedrich, L. (2011). Package 'strucchange', Retrieved from https://cran.r-project.org, pp. 11-13.

Akira, S. & Ichirou, F. & Hitoshi, M. (1993). Approximate estimation of ventilatory threshold by Fourier transform of ventilatory information. *The Japanese Journal of Ergonomics*, 29, 548-549.

Akira, S. & Mitsuhiko, H. & Hitoshi, M. (1998). Development of ergometer controlling exercise workload by the combination of heartrate and respiratory frequency with several functions for at estimation. *The Journal of the society of Biomechanisms Japan*, 14, 81-93.

Beaver, W. L. & Wasserman, K. (1986). A new method for detecting anaerobic threshold by gas exchange, *The American Physiological Society*, 2021.

Voorn, E. L., Gerrits, K. H., Koopman, F. S., Nollet, F. & Beelen, A. (2014). Determining the Anaerobic Threshold in Postpolio Syndrome: Comparison with Current Guidelines for Training Intensity Prescription. *Archives of physical Medicine and Rehabilitation*, 95, 935-940.

Farnsworth, G. V. (2008). *Econometries in R*. Retrieved from https://www.fsb.miamioh.edu/lij14/672_Rbook2.Pdf, pp. 1-50.

Hironori, T. (1944). Coronary artery disease trends in Japan. *Japanese Circulation Journal*, 58, 166-172.

Hiroyuki, Y. & Kenichi, K. & Yoshifumi, M. (2016). Prediction of Anaerobic Threshold cardiovascular surgery in hemodialysis patients. *The Japanese Journal of Physical Therapy*, 43, 397-403.

Mitsuru, T., Yukiko, H., Kiyokazu, S., Koutaro, K., Kiyoshi, O. & Kazunori, K. (2001). Relationship between Heart-rate variability during exercise and ventilatory threshold. *The Japanese Journal of Physical Fitness and Sports Medicine*, 50, 185-192.

Rika. K. & Akira, S. (2016). The anaerobic threshold (AT) determination experimental system and the movement of ventilation expire in limited respiratory. The Institute of Electronics, *Information and Communication Engineers of Japan (IEICE)*, Technical Report 116 (170), 7-12.

Sue, D. Y., Wasserman, K., Moricca, R. B. & Casaburi, R. (1988). Metabolic acidosis during exercise in patients with chronic obstructive pulmonary disease. *Chest*. 94, 931-938.

United Nations (2019). *World Population Prospects: The 2019 Revision*. Retrieved from https://population.un.org/wpp/.

Wannamethee, S. G., Shaper, A. G. & Walker, M. (2000). Physical activity and mortality in old men with diagnosed coronary heart disease. *Circulation*, 102, 1358-1363.

Wasserman, K. (1984). The anaerobic threshold measurement to evaluate exercise performance. *American Review of Respiratory Disease*, 129(2), 2.

Effects of Wave Images on Standing Posture of Ship Crew

T. Sakamaki*[,a], and R. Doine[b]

[a] National Institute of Technology, Toba College, Mie, Japan
[b] Tohto University, Chiba, Japan

*takanori@toba-cmt.ac.jp

Abstract

Fatigue due to ship environments is often experienced by ship crew members and has been reported as a cause of marine accidents. Therefore, it is necessary to clarify the causes of fatigue. Previously, we hypothesized that crew postural motion owing to posture control is one such cause. We examined the standing postural motions and exercise loads of crew members in a small marine craft. As a result, the exercise loads of the crew members while standing in the craft at a heave acceleration of 1.00–1.39 m/s ^{2} were similar to those while stepping at a rate of 30–40 steps/min on land, indicating postural motion to be a possible cause of fatigue. Most crew members, except for navigators, cannot see the ocean waves and tilt of a ship because they work in confined spaces; consequently, they control their postures against ship motion using equilibrium and somatic sense. It is necessary to reveal the effects of visual information on the standing postures of crew members to determine the causes of their fatigue. Accordingly, in this study, we aim to measure and evaluate the effects of wave images projected by a ship handling simulator on the standing postures of crew members. We used four types of images, namely, images without waves and images with wave directions of 180°, 135°, and 90°, for eight participants. The standing postures of the participants were evaluated based on the motion of the center of gravity (COG), exercise load determined by energy expenditure, and root mean square of linear and angular accelerations at the head and hip. Significant differences were observed in the total length of the COG motions between the cases of images without waves and with waves ($p < 0.05$). Additionally, the COG motions of the participants in response to the aforementioned wave directions were observed. The results of this study indicate that visual sense is a crucial factor for human posture control. If crew members can recognize ship motion using their visual senses, equilibrium, and somatic senses simultaneously, their fatigue can be reduced, as they would be able to control their postures predictively.

Keywords: *crew, fatigue, wave image, standing posture, center of gravity*

Introduction

The fatigue of crew members has been reported to be one of the causes of marine accidents. Thus, to mitigate such accidents, it is necessary to reduce crew fatigue.

In our previous study, we found that the standing postural motions of passengers, such as motions of the head and hip, can cause physical fatigue because the energy expenditure is increased in standing postural motions in a small marine craft. Resultantly, the exercise loads of the crew members while standing in the craft at a heave acceleration of 1.00–1.39 m/s^2 are similar to those while stepping at a rate of 30–40 steps/min on land; this indicates that postural motion is a possible cause of fatigue.

It has also been reported that standing postural motions of human are affected by visual stimuli. Therefore, it is necessary to analyze standing postural motions affected by visual stimuli to clarify the causes of physical fatigue for passengers. Most crew members, except for navigators, cannot see the ocean waves and the tilt of a ship, because they work in confined spaces; consequently, they control their postures against ship motion using equilibrium and somatic sense. Accordingly, it is necessary to determine the effects of visual information on the standing postures of crew members to determine the causes of their fatigue.

The purpose of this study was to measure and evaluate the effects of wave images projected by a ship-handling simulator on the standing postures of crew members.

Materials and methods

Measurement system

The measurement system consisted of three orientation sensors, a calorimeter, and a Wii balance board (Fig. 1). The orientation sensors were placed on the head and waist of each participant and on the floor of the ship handling simulator. These sensors measured linear and angular accelerations. The calorimeter functioned based on the mixing chamber method and measured the energy expenditure. The energy expenditure was calculated from the respiratory volume, O_2 concentration, and frequency of respiration. The balance board measured the center of gravity for each participant.

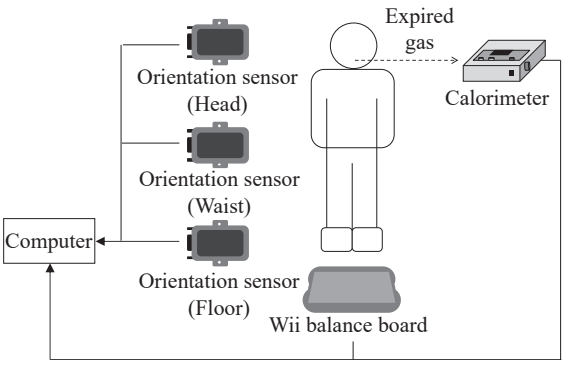

Figure 1 System configuration diagram

The linear and angular acceleration signals were sampled at 100 Hz. The energy expenditure over every 10 s was recorded. The center of gravity signals were sampled at 100 samples per second.

Experimental environment

(1) Ship handling simulator

This experiment was performed with approval from the research ethics committee of the National Institute of Technology, Toba College, Mie, Japan, and a ship handling simulator at the college was used (Figure 2). The horizontal and vertical viewing angles of the simulator were 225° and 30°, respectively, centered on the gyro compass installed at the center of the wheelhouse at a distance of 3 m from the screen.

(2) Specifications of the simulated ship and wave images

The experimental conditions included four wave image patterns (Table 1). A high-speed boat (length: 39.8 m, breadth: 9.00 m) was used for the entire pattern. The course and speed were 0° and 15 kn, respectively. The sea-wind speed was set to zero. Pattern 1 was set as an image without waves. In Patterns 2, 3, and 4, the wave directions were set as 180°, 135°, and 90°, respectively, and the wave height and wave length were set as 3 m and 8 s, respectively. Figure 3 shows the wave directions with respect to the participant's position.

Table 2 lists the motions of the simulated high-speed boat. In Pattern 2, the pitch motion (rotational motion about the x-axis) was the largest. In Pattern 4, the roll motion (rotational motion about the y-axis) was the largest.

(3) Participants and experimental protocols

Table 3 shows the details of eight participants involved in the experiment. Before the start of the experiment, we explained the procedures to the participants, and they gave written informed consent about this experiment. To prevent the effects of eating, exercising, and sleeping on energy expenditure, the participants were instructed to get sufficient sleep the night before the experiment and to abstain from eating, drinking anything other than water, and intense exercise for four hours before the start of the experiment.

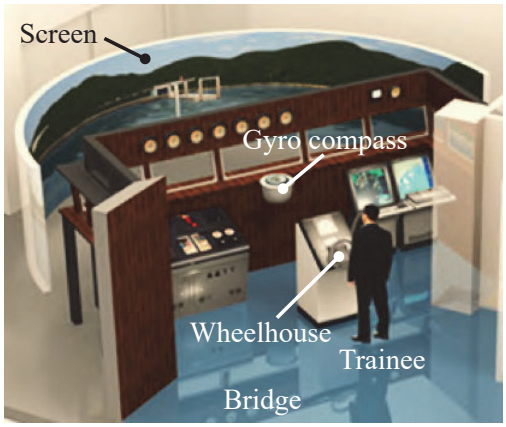

Figure 2 Ship handling simulator

Table 1 Experimental conditions

		Pattern 1	Pattern 2	Pattern 3	Pattern 4
High speed boat	Course [°]	0	0	0	0
	Speed [kn]	0	15	15	15
Wave	Direction [°]	0	180	135	90
	Height [m]	0	3	3	3
	Length [s]	0	8	8	8

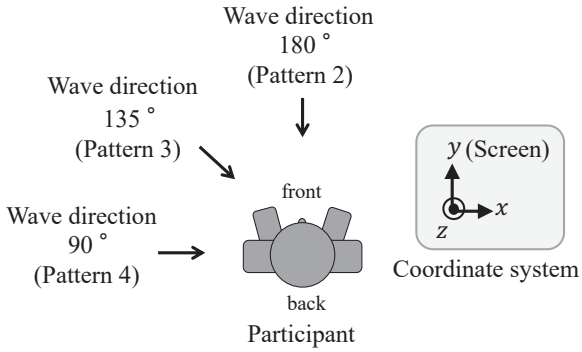

Figure 3 The wave directions with respect to the participant 's position

Table 2 Motions of the simulated high-speed boat

	Pattern 1	Pattern 2	Pattern 3	Pattern 4
Roll [°]	0.00	-1.56～1.55	-9.47～9.09	-13.20～12.69
Pitch [°]	0.00	-10.78～10.26	-8.77～7.50	-5.93～5.87
Yaw [°]	0.00	-0.02～0.02	-0.11～0.11	-0.13～0.13

Table 3 Participants involved in the experiment

Participant	Sex	Age	Height [cm]	Weight [kg]
A	male	23	165	66
B	male	22	177	76
C	female	21	161	85
D	male	21	180	65
E	male	22	185	92
F	male	20	178	78
G	male	20	161	48
H	male	20	180	77

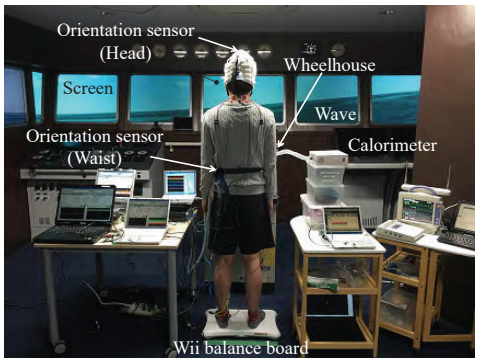

Figure 4 Experimental setup

Figure 4 shows the experimental setup. The standing position of the participants was behind the steering wheel, which was installed at a distance of 2.2 m from the gyro compass located at the center of the screen. The participants were instructed to look at the screen (bow side). The experimental protocol was as follows: sitting for 15 min under Pattern 1, standing for 15 min under Pattern 1, sitting for 15 min under Pattern 1, standing for 15 min under Pattern 3, sitting for 15 min under Pattern 1, standing for 15 min under Pattern 2, sitting for 15 min under Pattern 1, and standing for 15 min under Pattern 4. In the standing position, the participants were instructed to space their feet about the width of their shoulders and stand naturally. Figure 5 shows the simulated wave images used under each experimental condition.

Evaluation indicators

The standing postural motion was evaluated in terms of the root mean square (RMS) values of the linear and angular acceleration, the exercise load, and the motion of the center of gravity (COG).

(1) RMS values of linear and angular acceleration

The participants experienced motion with six degrees of freedom. These motions are referred to as surge (x-axis, longitudinal motion), sway (y-axis, sideways motion), heave (z-axis, vertical motion), roll (rotational motion about the x-axis), pitch (rotational motion about the y-axis), and yaw (rotational motion about the z-axis). The frames of the orientation sensors were transformed to a fixed coordinate system using the following coordinate transformation, to compare the motion of the floor with the body motion of the participants:

$$\begin{bmatrix}\alpha_{xe}\\ \alpha_{ye}\\ \alpha_{ze}\end{bmatrix}=\begin{bmatrix}cos\psi & -sin\psi & 0\\ sin\psi & cos\psi & 0\\ 0 & 0 & 1\end{bmatrix}\begin{bmatrix}cos\theta & 0 & sin\theta\\ 0 & 1 & 0\\ -sin\theta & 0 & cos\theta\end{bmatrix}\begin{bmatrix}1 & 0 & 0\\ 0 & cos\phi & -sin\phi\\ 0 & sin\phi & cos\phi\end{bmatrix}\begin{bmatrix}\alpha_x\\ \alpha_y\\ \alpha_z\end{bmatrix} \quad (1)$$

$$\begin{bmatrix}\omega_{xe}\\ \omega_{ye}\\ \omega_{ze}\end{bmatrix}=\begin{bmatrix}cos\psi & -sin\psi & 0\\ sin\psi & cos\psi & 0\\ 0 & 0 & 1\end{bmatrix}\begin{bmatrix}cos\theta & 0 & sin\theta\\ 0 & 1 & 0\\ -sin\theta & 0 & cos\theta\end{bmatrix}\begin{bmatrix}1 & 0 & 0\\ 0 & cos\phi & -sin\phi\\ 0 & sin\phi & cos\phi\end{bmatrix}\begin{bmatrix}\omega_x\\ \omega_y\\ \omega_z\end{bmatrix} \quad (2)$$

where α_x, α_y, and α_z are the surge, sway, and heave in the coordinate systems of each orientation sensor at the head, waist, and floor of the simulator, respectively. α_{xe}, α_{ye}, and α_{ze} are the surge, sway, and heave, respectively, in the fixed coordinate system.


(a) Pattern 1 (images without waves)

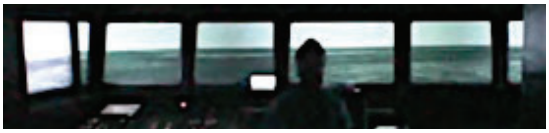
(b) Pattern 2 (wave direction: 180°)

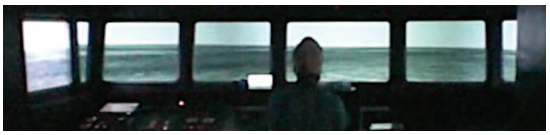
(c) Pattern 3 (wave direction: 135°)

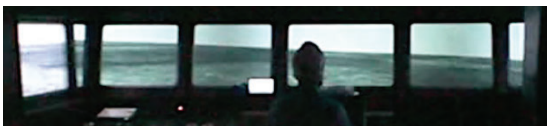
(d) Pattern 4 (wave direction: 90°)

Figure 5 Simulated wave images

ω_x, ω_y, and ω_z are the roll, pitch, and yaw in the coordinate systems of each orientation sensor at the head, waist, and floor of the simulator, respectively. ω_{xe}, ω_{ye}, and ω_{ze} are the roll, pitch, and yaw, respectively, in the fixed coordinate system.

The RMS value is defined as

$$RMS=\sqrt{\frac{1}{N}\sum_{i=0}^{N-1}(f_i)^2} \quad (3)$$

where f_i is the linear or angular acceleration, and N is the number of data points which were collected for 10 min after 5 min had elapsed from the participants assuming the standing posture. N was set as 60,000. Linear and angular acceleration frequencies of 0–15 Hz were observed at the head and waist. A low-pass filter with a cut-off frequency of 15 Hz was applied to the linear and angular accelerations to remove noise.

The characteristics of the RMS values were analyzed based on the mean RMS values of the eight participants. Analysis of variance (ANOVA) and the Tukey method were used to examine the differences in the RMS values between Pattern 1 and the other patterns. The significance level was set to 0.05.

(2) Exercise load

The exercise loads of the participants were calculated with reference to the metabolic equivalent, by dividing the 10 min mean energy expenditure in the standing posture by that in the sitting posture.

$$\text{Exercise load}=\frac{\text{Energy expenditure in standing posture}}{\text{Energy expenditure in sitting posture}} \quad (4)$$

The aforementioned 10 min mean energy expenditures were calculated from the energy expenditures 5 min after the participants had assumed the standing posture.

The characteristics of the exercise loads were analyzed based on the mean value of the exercise loads of the eight participants. ANOVA was performed to examine the differences in the exercise loads between Pattern 1 and the other patterns. The significance level was set to 0.05.

(3) Motion of COG

A low-pass filter with a cut-off frequency of 1 Hz was applied to the COG data to remove noise. The motions of the COG were evaluated in terms of the total, longitudinal, and sideways lengths of the COG. Figure 6 shows a conceptual diagram of the COG length. The coordinate value $C_n(x_n,y_n)$ is the nth COG sample, and $C_{n-1}(x_{n-1},y_{n-1})$ represents the n−1th COG sample. L_n is the distance from C_{n-1} to C_n. The total length of the COG is denoted as L_N, which is calculated as follows:

$$L_N = \sum_{n=1}^{N} L_n = \sum_{n=1}^{N} \sqrt{(x_n - x_{n-1})^2 + (y_n - y_{n-1})^2} \quad (5)$$

L_{xn} is the distance from x_{n-1} to x_n. The sideway lengths of the COG are denoted as L_{xN}, which is calculated as

$$L_{xN} = \sum_{n=1}^{N} L_{xn} = \sum_{n=1}^{N} |x_n - x_{n-1}| \quad (6)$$

L_{yn} is the distance from y_{n-1} to y_n. The longitudinal length of the COG is denoted as L_{yN}, which is calculated as

$$L_{yN} = \sum_{n=1}^{N} L_{yn} = \sum_{n=1}^{N} |y_n - y_{n-1}| \quad (7)$$

N is the number of data points which were collected for 10 min after 5 min had elapsed from the participants assuming the standing posture. N was set as 60,000. Some sampled data corresponding to the participants changing the position of their feet on the balance board were excluded.

The characteristics of the total COG lengths were analyzed using the mean value for the eight participants. ANOVA and Tukey method were employed to examine the differences in the total length between Pattern 1 and the other patterns. The significance level was set to 0.05. The characteristics of the longitudinal and sideways lengths of COG were analyzed using scatter diagrams and regression lines.

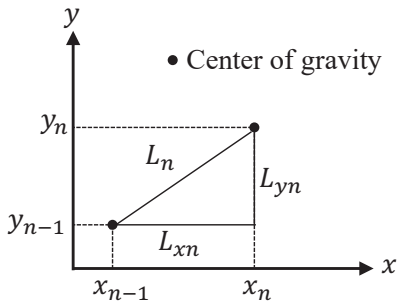

Figure 6 Conceptual diagram of the COG length

Results

RMS values of linear and angular acceleration

Figure 7 shows the mean RMS values of the linear acceleration at the head and waist, and Figure 8 shows the values of the angular acceleration. Each value in these graphs represents the mean and standard deviation for the eight participants. N is the number of data points. No significant differences were detected in the RMS values of linear acceleration between Pattern 1 and the other patterns ($p > 0.05$). A similar result was obtained for the RMS values of angular acceleration.

Exercise loads

Figure 9 shows the mean values and standard deviations of the exercise loads under each experimental condition. No significant differences were detected in the exercise loads between Pattern 1 and the other patterns ($p > 0.05$).

Motions of COG

Figure 10 shows an example of the locus of the COG. The longitudinal and sideways lengths of the COG under Patterns 2–4 were greater than those under Pattern 1. Figure 11 shows mean values and standard deviations of the total COG length for the eight participants under each

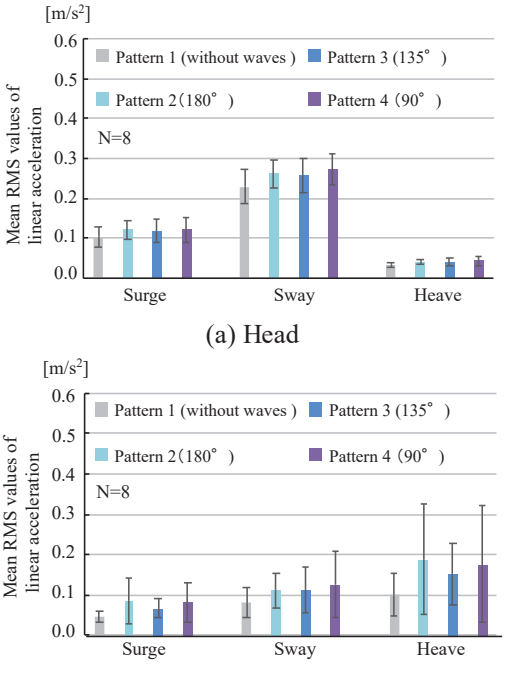

Figure 7 Mean RMS values of linear accelerations

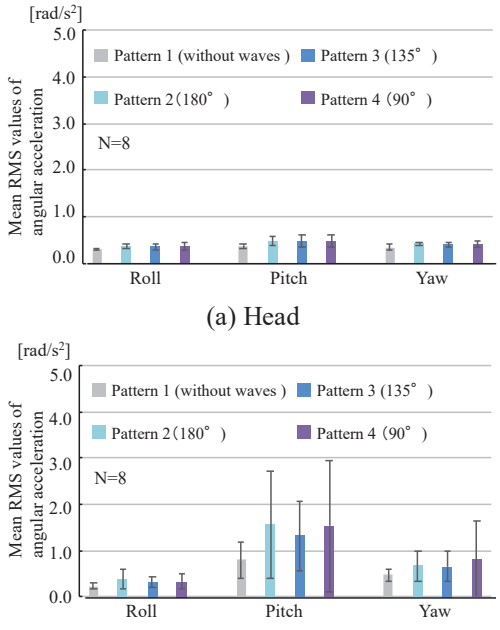

Figure 8 Mean RMS values of angular accelerations

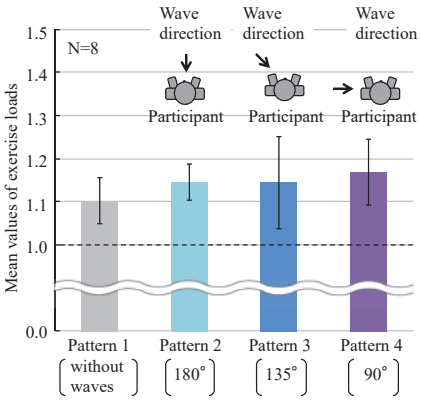

Figure 9 Mean values of exercise loads

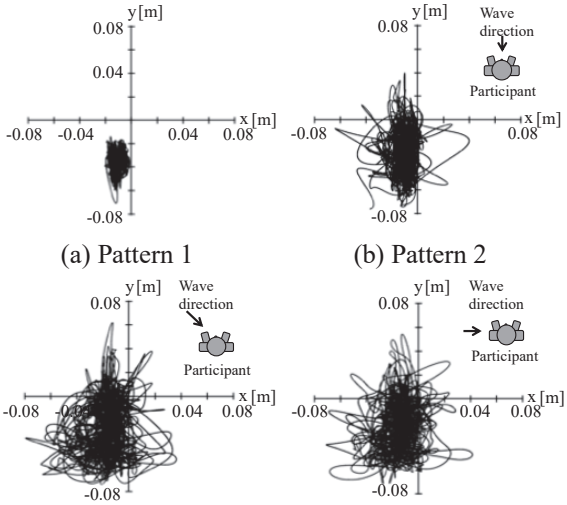

Figure 10 An example of the locus of the COG (participant A)

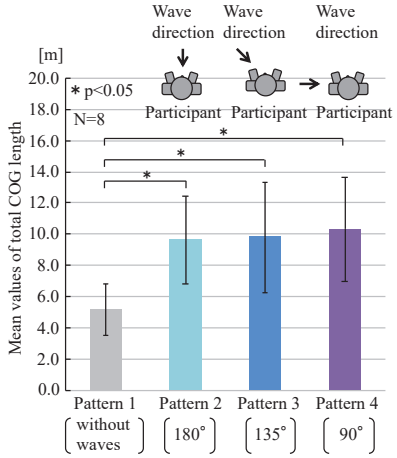

Figure 11 Total COG length (*: $p < 0.05$)

experimental condition. N is the number of data points. The asterisk (*) in Figure 11 indicates that a significant difference was detected. Significant differences were detected in the total length of the COG between Pattern 1 and the other patterns ($p < 0.05$).

Figure 12 shows scatter diagrams and regression lines of the longitudinal and sideways lengths of the COG for the eight participants. N is the number of data points. The slope of the regression line under Pattern 1 was larger than that under the other patterns. The longitudinal lengths of the COG were greater than the sideways lengths. In Patterns 2–4, more lateral length components were included in the wave image, and the sideways lengths of the COG were greater than the longitudinal lengths.

Discussion

The standing postures of the participants were evaluated based on the RMS of the linear and angular accelerations at the head and hip, the exercise load (determined based on the energy expenditure), and the COG motion.

In our experiments, most participants experienced slight motions in the standing posture by viewing the wave images. These motions were not evaluated in terms of the RMS of linear and angular accelerations at the head and hip or the exercise load. These visual stimuli-induced motions were marginal and are different from the standing postural motions on ships. These motions were evaluated based on the COG motion. Significant differences were observed in the total length of the COG motions between the cases of images with and without waves ($p < 0.05$). In addition, standing postural motion occurred as a visual response to the direction of the wave projected by the simulator.

The standing posture was controlled by information from the sense of equilibrium, somatic sensation, and vision. In particular, information obtained through vision may be effective for predictive control of standing postures.

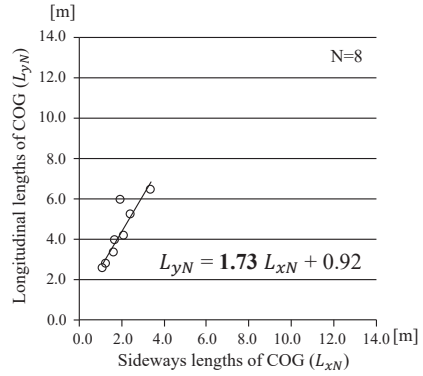

(a) Pattern 1

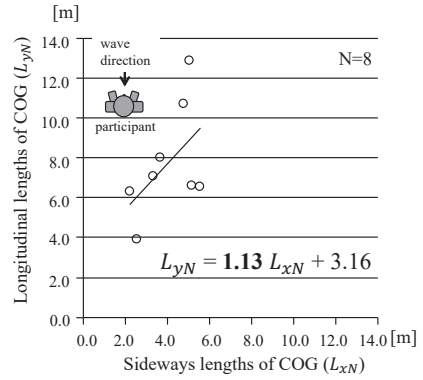

(b) Pattern 2 (wave direction: 180°)

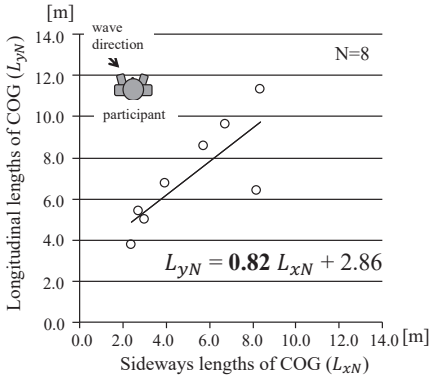

(c) Pattern 3 (wave direction: 135°)

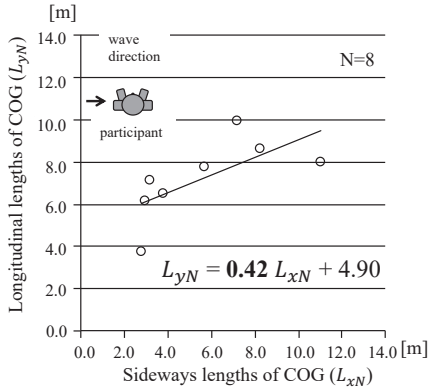

(d) Pattern 4 (wave direction: 90°)

Figure 12 Relationship of sideways lengths of COG and longitudinal lengths of COG

Most crew members, except for navigators, cannot see the ocean waves and the tilt of the ship, because they work in confined spaces; consequently, they control their postures against ship motion using the sense of equilibrium and somatic sense, without relying on vision. Thus, fatigue may increase if predictive control of standing postures based on the sense of vision is not performed.

Conclusions

The standing postural motions induced by visual stimuli were minor and were different from the standing postural motions on ships. These motions were evaluated based on the COG motion. Significant differences were observed in the total length of the COG motions between the cases of images with and without waves ($p < 0.05$). In addition, standing postural motion occurred as a visual response to the direction of the wave projected by the simulator.

The results indicate that visual sense is a crucial factor in human posture control. If crew members can recognize ship motion using their visual senses, equilibrium, and somatic senses simultaneously, their fatigue can be reduced as they would be able to control their postures predictively.

Acknowledgements

This study was supported by Grants-in-Aid for Scientific Research 17H02056, 18K13951, and 21K04575. We wish to thank Dr. Hiroaki Seta for the experiment using the ship-handling simulator.

References

Amir D. A. and Jayavel S. (2006). Complete business statistics. New York: McGraw-Hill.

Renon D., Takanori S., Hiroaki S., Masamitsu I., Akihiko H. and Yasuhiro F. (2015). The exercise load of passengers' postural control against ship motion using human energy expenditure. *Journal of Advanced Biomedical Engineering*, 4, 164-169.

Renon D., Hiroaki S., Akihiko H. and Takanori S. (2019). Effects of wave direction difference projected by a ship handling simulator on human standing postural motion. *Journal of Japan Institute of Navigation*, 141, 39-46.

Renon D., Fujio M., Hiroaki S. and Takanori S. (2019). Effects of passengers' standing postural motions on their energy expenditures in a small marine craft. *Journal of Japan Institute of Navigation,* 140, 124-132.

Sébastien J.V., Moira B.F., Gina M. A. and Thomas A. S. (2008). Postural instability and motion sickness in a virtual moving room, *Journal of the Human Factors and Ergonomics Society*, 50, 2, 332-345.

ESTIMATING THE EMOTIONAL INFORMATION IN SONGS USING SEARCH ENGINES

Jin Akaishi[*,a], Masaki Sakata[b], Mitsutaka Nakano [a], Kazuhiro Koshi [a] and Kimiyasu Kiyota [a]

[a] Department of Human-Oriented Information Systems Engineering, National Institute of Technology, Kumamoto College, Koshi, Japan
[b] School of Engineering, Hokkaido University, Sapporo, Japan

* jin@kumamoto-nct.ac.jp

Abstract

It has been found that music has various positive effects on people's psychological and body condition, such as improvement of concentration, and reduction of fatigue and stress. Some studies have shown that listening to sad music at a very sad time reduces the feeling of sadness. Similarly, when feeling angry, it has become clear that listening to music that expresses anger alleviates the feeling of anger. Therefore, a system that automatically recommends songs that heal negative emotions according to the mood of the listener is considered effective in reducing stress. In this research on song recommendation, we apply a technique of guessing the emotions of sentences and build a new system that automatically estimates the emotional value of songs based on the lyrics with high accuracy. We adopt a method of searching for and processing related words in text using Web mining. This method is based on the idea that emotions contained in the lyrics can be inferred by extracting emotional words that co-occur from the large amount of text information existing on the Web. This makes it possible to infer emotions for a phrase even if there is no expression in the phrase that matches the emotion dictionary. In the experiment, we first constructed a sentiment analysis system using the proposed Web search method. We then analysed the lyrics of 50 Japanese songs and inferred the emotions that the lyrics evoke. Next, we performed a questionnaire survey involving 10 men and women about those lyrics and classified the results into seven types of emotions. Finally, we compared the emotions in the lyrics automatically estimated by the system with the questionnaire results. It was found that the agreement between the automatic system and real human emotions was 61%, as indicated by the F-score. From the results, the proposed method showed a slight improvement over a previous method.

Keywords: *music therapy, emotion tagging, mood management, Japanese song lyrics, search engine*

Introduction

Recent studies have shown that music has positive effects on a person's psychological state and physical health, such as improving concentration, and reducing fatigue and stress (e.g., Arnett, 1991; Wells and Hakanen, 1991). It is becoming clear that negative emotions can be alleviated by listening to music that reminds people of a particular emotion. Matsumoto (2002) found that when a subject has very sad emotions and listens to sad music, the feeling of sadness decreases. Similarly, a study by Sharman and Dingle (2015) revealed that listening to intense music when a subject is feeling angry can alleviate the anger. Based on these research results, system that propose songs according to the mood of the listener has been proposed (Yamada, 2001).

One of the important functions in the song proposal system is to automatically estimate the emotions evoked by the song with higher accuracy. A system that automatically classifies the emotions in a song is indispensable for processing a certain request from a huge number of songs. Music and lyrics can be considered as elements that evoke emotions contained in songs. Mechanisms for inferring the emotions expressed in songs based on the lyrics has been proposed, and its performance has been evaluated (e.g., Hu, 2009).

Several methods have been put forward for extracting emotional information. One conventional method focuses on surface expression and processes emotions using a valence pattern using an emotion dictionary, ML-Ask, which was developed by Pataszynski et al. (2009), An emotion evaluation system with more complex functions, such as consideration of negative sentences in Japanese, has also been used. Furthermore, a method has been proposed by Shi et al. (2008) to search for related words in text using Web mining. This method improves the accuracy of estimating the emotional value contained in text. By extracting emotional words that co-occur from a large amount of text on the web for an input phrase and performing emotional estimation, even if there is no

direct emotional expression in the song phrase, it is possible to infer the emotion.

There have been many studies aimed at extracting emotional information from sources such as news items, conversations, and song lyrics (e.g., Pataszynski et al. 2009). There have also been many attempts at emotional guessing for lyrics, including a study by Yamada (2001). However, research on estimating the emotions in Japanese lyrics using a Web search engine is extremely limited. Quantitative estimations of emotions using Web search for sentences that are different from ordinary sentences, such as Japanese lyrics, is interesting from the viewpoint of Japanese emotion estimation and musical healing.

The purpose of this study is as follows. As part of the song proposal method, we use a Web search engine to build a system that can classify the emotions that a song evokes based on Japanese lyric information. We then compare the accuracy of this system with that for conventional methods. We clarify the processing characteristics that need to be taken into consideration when performing sentiment analysis of Japanese lyrics, which use a style that differs from ordinary sentences.

It is expected that the accuracy of the emotion estimation system can be improves by using such a Web search. Analysing a large number of search sentences and related sentences on the Web is likely to reflect the feelings of the majority. Therefore, it is considered that the accuracy of emotional estimation of the text for conveying the message to the masses represented by the song, which is not the personal text represented as in a diary, will be further enhanced.

Research method

First, we selected 50 recently popular Japanese songs, and extracted the lyrics for testing. Next, the lyrics decomposed into morphemes were input into a system that infers the emotions that the lyrics recall to humans, and the results were output.

The central system used in this study is a combination of a classification method that combines a Web search engine and ML-Ask. The ML-Ask system is used for sentiment analysis of lyrics. If the lyrics do not have a word that corresponds to the dictionary of emotional words, the Web engine is used for analysis.

In addition to the above method, we also perform emotion estimation using two methods to compare the accuracy of emotion evaluation with that for conventional methods. We evaluate the input data using three methods: the most standard classification method using only the extended dictionary based on the "Emotion Expression Dictionary" as in Yamada's method (hereafter referred to as Method A), a method using only the emotion estimation system ML-Ask (hereafter referred to as Method B), and a method that combines the Web engine and ML-Ask (hereafter referred to as Method C).

Next, as correct answer data to be used as a basis for evaluating the emotions evoked by the song, we presented the lyrics of 50 songs to 10 people, performed a questionnaire survey, and recorded the emotions recalled when reading the lyrics.

Finally, the accuracy of the emotions of the lyrics classified by each system was evaluated using an F-score, with the emotions that emerge when reading the lyrics obtained by the questionnaire as the correct answer.

The emotion dictionary used in this study was the dictionary of Yamada et al., which is an extension of the standard emotion word dictionary in Japanese, "Emotion Expression Dictionary". In addition to the 1,097 words in the emotional expression dictionary, synonyms for emotional words have been added from the "Must-have Synonyms Practical Dictionary" published by Sanseido. The total number of emotional words after expansion is 1,930.

Seven emotion categories are dealt with in this study: joy, relief, sadness, anger, like, dislike, and excitement. There are 10 types of classifications widely used in Japanese sentiment analysis in the "Sentiment Expression Dictionary". However, because of Yamada's research, when Japanese lyrics are presented to subjects, the emotions that the subjects feel from the lyrics are frequently five types: "joy, like, relief, sadness, and excitement." It has become clear that the five types of emotion, "dislike, fear, anger, shame, and surprise", rarely appear. Based on the above results, in order to reduce the processing burden, this study deals with seven categories by adding two emotions that appeared relatively frequently.

System for classifying lyrics emotions

We describe in detail a method (method C) that uses a Web search engine to infer the emotions evoked by the lyrics we propose this time. An outline of the system is shown in Fig. 1. In the proposed method, emotions are first estimated using ML-Ask. Here, we use a method for inferring emotions from sentence-ending expressions and emotional expressions contained in the sentence itself using a superficial expression of the sentence. If the emotion expression cannot be extracted, an emotion estimation using a search engine, "emotion estimation by causal relationship on the Web" is performed. Here, we used a method of acquiring sentences that have a causal relationship with sentences from the Web and recognizing emotions.

1 Divide the lyrics into morphemes with MeCab.
2 Analyze the lyrics divided into morphemes
  2.1 Outputs the emotion value for the matching classification when the morpheme matches the emotion word in the dictionary of the system.
  2.2 If there is no emotional word in the sentence, analyze the sentence that holds the causal relationship that exists on the Web.

2.2.1 Morphological analysis of short sentences obtained from the Web, comparison with an emotion dictionary, and if they match, the emotion value of that classification is output.

3 Aggregate the output emotional value

The following is an example of the process. For example, if a lyric contains an emotional word such as "happy", the word "joy" is judged. If the lyrics do not contain emotion words, such as "I played baseball," the system uses a search engine to retrieve sentences on the Web that are related to the lyrics. For example, if the sentence retrieved is "I had fun playing baseball," the co-occurrence of the emotion word "fun" is judged as “joy”.

Emotion estimation using search engine

This section describes the detailed procedure for emotion estimation using a search engine. When a lyric phrase does not contain a word with an emotion in the dictionary, the phrase in the lyric is extracted and a conjunction is added to the end of the sentence to create a search query. The search query is input and the resulting short sentences are saved. The search query is created based on the rules used by Shi et al., and some modifications are made according to the emotion estimation of the lyrics. The following is a description of these modifications.

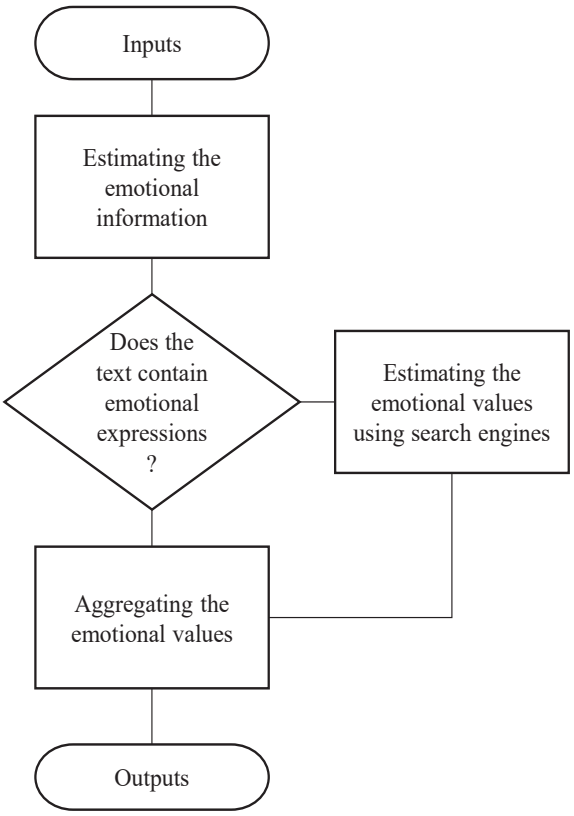

Figure 1. System flowchart

- Creating phrases from 3-gram
  - If the following conditions are not met, lengthen it to 4-gram, 5-gram…
- The beginning of the phrase is not a particle or conjunction
  - Do not make phrases from particles or conjunctions
- The end of the phrase is a verb or adjective
- Ignore codes and emoticons
- Change the end of a sentence to a non-past terminal form
  - Make the phrase grammatically correct when a conjunction is added

Next, to make it easier for emotional words to co-occur, the Japanese conjunctions "*-te, -to, -node*" are added to the end of the created phrase. A search query is a combination of these three conjunctions with a phrase. Shi et al. revealed that by including some adjunct words in the search query, more search results including emotion words can be obtained. Based on the results, we adopted the above three conjunctions, which had a high probability of acquiring emotion words. The reason for limiting the number of conjunctions to three is to limit the amount of searching.

We obtained snippets from a search engine using a query with the conjunctions described above. In this study, we used Microsoft Bing as the search engine. Forty snippets obtained for each query were saved as text data. In other words, one phrase saves 120 snippets. From the acquired snippets, the sentences following the input phrase were saved for use in emotion estimation. However, if the sentence following the phrase contains a conjunction such as "but", the sentence was not saved. Table 1 shows an example of the above process.

Analysis of text data

Morphological analysis was performed on the saved text data, and matching processing was carried out using a dictionary that is an extension of Yamada's "Emotional Expression Dictionary". Similar to Shi's research, the number that matched each emotion was used as the score for that emotion category, and sorting was performed in descending order. The scores for all emotions were totalled, and the category in the top 60% was taken as the emotion value for the song. There can be multiple emotions output. However, those with a small number of hits are likely to be emotions that have nothing to do with the emotional value for the song. So, even if a certain emotion category occupies the top 60%, if it is less than 10% of the total emotions, the value is not output. For example, in the case of "Sorrow 51%, Joy 9%, and the other five emotions are 8% each", Joy is in the top 60%, but only sad emotions are output.

Aggregation of emotional value

The evaluations for each emotion category obtained by the emotion evaluation by ML-Ask and the emotion evaluation by the causal relationship on the Web are aggregated. The evaluation using ML-Ask, which is processed in the first stage, performs advanced processing, such as directly analysing the lyrics and considering negative sentences. Therefore, it is considered to be more accurate than emotion estimation using a search engine. Therefore, in order to improve the accuracy, the output of the emotion category when emotional expression by ML-Ask is included is weighted. Five types of weights (1-5 times), were tried, and three times, which had a high F-score overall, was adopted. In other words, in this system, the evaluation by ML-Ask was three times heavier than the evaluation using the Web.

Table 1. Example of inputting Japanese lyrics to saving the sentence to be analyzed when estimating emotions by Web search

	Romanized transcription / English translation
Input sentence	*Harukaze ga fuite ita.* / Spring breeze was blowing.
Phrase	*Harukaze ga fuku* / Spring breeze blows
Search query	*Harukaze ga fukuto* / When the spring breeze blows
Snippet	*Hito wa harukazegafuku to haru no torai wo shiri, atatakaku naru to omotte yorokobu* / People are pleased to know the arrival of spring when the spring breeze blows and think that it will be warm.
Saved sentence	*Haru no torai wo shiri, atatakaku naru to omotte yorokobu* / (People are) happy to know the arrival of spring and think it will be warm

Emotional classification of lyrics by questionnaire

Data were collected from the subjects regarding their feelings toward the lyrics of the song in the form of a questionnaire. Ten subjects (eight males and two females, in their teens to 40s, mean age: 22.4 years) read the lyrics of 50 songs and tagged each song with the emotions they deemed appropriate from the seven emotions (multiple answers allowed).

The questionnaires were tabulated and divided into cases in which the emotions of the top two were used as the correct answer for the song and cases in which the emotions of the top three were used as the correct answer for the song.

Results

The accuracy was compared by calculating the F-score (F_1) for the emotion estimation results for the three systems, using the emotion tags for the 50 songs obtained in the questionnaire as the correct answers. The results of the experiment are shown in Tables 2 and 3. Table 2 shows the results for the correct answer ranked in the top two. Table 3 shows the results of the correct answer in the top three.

In the results, when the correct answer data shown in Table 2 is ranked in the top two of the questionnaire, the F-score for method A is 53, the F-score of method B is 46, and the F-score of method C is 57.

In the results shown in Table 3 when the correct answer data was ranked in the top three in the questionnaire, the F-score for method A was 54, that for method B was 48, and that for method C was 61.

As a concrete example of the results, Table 4 shows an example in which method C was more effective than method A. Table 5 shows an example in which method

Table 2. Results when the correct answer data is in the top two estimated emotions by Web search

	precision [%]	recall [%]	F-score [%]
Method A	55	54	53
Method B	56	43	46
Method C	56	62	57

Table 3. Results when the correct answer data is in the top three estimated emotions by Web search

	precision [%]	recall [%]	F-score [%]
Method A	63	50	54
Method B	66	40	48
Method C	67	58	61

Table 4. Successful example of method C

Song name	Evaluation by humans	Method A	Method C
Yozora no mukou	Sadness, Dislike	Liking	Sadness, Dislike, Liking

Table 5. Failure example of Method C

Song name	Evaluation by humans	Method A	Method C
Idea	Joy, Relief	Dislike, Joy	Dislike, Sadness

C was not effective.

Discussion

Here, we focus on the cases in which the correct answer data up to the top three is adopted. Comparing the F-values for method C and method B, method C is 13% higher than method B. Therefore, emotional estimation using causal relationships on the Web is effective. Comparing method C and method A, the recall rate improved by 8% and the F-score improved by 7%. Therefore, the accuracy improved slightly.

The reason why Method A has a higher F score than Method B, even though the procedure is simpler, is considered to be because the emotion dictionary is larger than that for Method B. The dictionary used in Method A has 1930 emotion words, and Method B has 907 emotion words. The emotion dictionary used in method C that evaluates sentences from the Web is the same as the dictionary in method A.

There is a study by Pataszynski using a Web search for emotion estimation, which was the basis of this study. In their study, the F-score was 54% to 53% when the emotions of conversational sentences were estimated by a similar method. It is difficult to make a simple comparison with the results of the present study because the analysis target, the number of emotion categories, and the types of search engines are different. However, the emotion estimation of the lyrics in this study is about 7% better than the case for conversational sentences. This indicates that the use of a Web search engine may be more suitable than the analysis of conversational sentences in estimating emotions in lyrics.

It was shown that method C in this study improves the accuracy of emotion evaluation. However, the improvement was limited by computational and network costs, such as using a search engine.

As a method for improving the accuracy, it is conceivable to change the lyrics using the word-stopping and inversion methods into normal sentences in advance by pre-processing. Table 6 shows an example of lyrics expressed using three types of methods, i.e., a normal sentence, a word stop, and an inversion method, and phrases generated from the sentence. Since the three original sentences in Table 6 do not contain emotion words, emotion inference based on causal relationships on the Web is applied. Therefore, phrase creation for the search query is performed. The phrases generated based on the phrase creation rules are shown on the right-hand side of Table 6.

As can be seen in the generated phrases in Table 6, the word "meteor shower" is omitted from the phrases generated based on the sentences using the word-stopping and inversion methods. This is because the phrase creation rule "the end of the phrase is a verb or an adjective" is applied. By eliminating the word "meteor shower" in the search query, the resulting snippet becomes more abstract and the estimated emotion value can be different from that in the original lyrics. Therefore, it is considered that the accuracy of emotion classification can be improved by judging the sentence using the word stop and inversion methods in advance and returning it to a declarative sentence.

Conclusions

In this study, we constructed a system that can classify the emotions that a song evokes from Japanese lyric information using a Web search engine as part of a song proposal system that suits the mood of the listener. We also performed a quantitative evaluation using a method that combines emotion estimation using a superficial expression of sentences and emotion estimation using a search engine. The method using a search engine improved the accuracy by 4% compared to the method using a conventional dictionary. However, when considering the cost of using a network and search engine, no significant performance improvement was observed to match the cost. It was pointed out that the accuracy may be improved by considering the inversion method and stopping a sentence with a noun.

Since all the subjects in this study were Japanese, 50 Japanese songs were selected for the emotion analysis. As a result, it is expected that the results obtained in this study are biased toward Japanese people. In the future, it is expected that more general results will be obtained by studying a wider range of music, including linguistic diversity.

The search results fluctuate depending on the query and time, and frequently contain noise. Therefore, it is possible that the results obtained in this study may be limited in time. It is also possible that the results may differ depending on the lyrics. In the future, it is necessary to verify the results by expanding the timing of the search and the range of song selection.

Table 6. Effect of inversion and ending a sentence with a noun in generated phrases

	Original sentence	Generated phrases
	Romanized transcription / English translation	
Normal sentence	*Ryuseigun ga yozora ni kiete itta.* / The meteor shower disappeared into the night sky.	*Ryuseigun ga yozora ni kieru.* / Meteor shower disappears in the night sky. *Yozora ni kieru.* / Disappear in the night sky
Ending a sentence with a noun	*Yozora ni kiete itta ryuseigun* / A meteor shower that disappeared in the night sky	*Yozora ni kieru.* / Disappear in the night sky
Inverted sentence	*Yozora ni kiete itta, ryuseigun ga.* / The meteor shower that disappeared in the night sky.	*Yozora ni kieru.* / Disappear in the night sky

As a future task, it is conceivable to introduce a search query creation method that modifies the word-stopping and inversion methods into ordinary sentences.

References

Arnett, J. (1991). Adolescents and heavy metal music: From mouth to metalheads. *Youth and Society*, 23, 76-98.

Goto, M. (2002). A Real-time Music Scene Description System: A Chorus-Section Detecting Method. *Information Processing Society of Japan SIG Notes*, 47, 27-34.

Hu, Y., Chen, X. & Yang, D. (2009). Lyric-based song emotion detection with affective lexicon and fuzzy clustering method. *10th International Society for Music Information Retrieval Conference (ISMIR 2009)*, 123-128.

Matsumoto, J. (2002). Why People Listen to Sad Music: Effects of Music on Sad Moods. *Japanese Journal of Educational Psychology*, 50, 23-32.

Ptaszynski, M., Dybala, P., Shi, W., Rzepka, R. & Araki, K. (2009). A System for Affect Analysis of Utterances in Japanese Supported with Web Mining. *Journal of Japan Society for Fuzzy Theory and Intelligent Informatics*, Vol. 21, No. 2, 30-49 (194-213).

Sharman, L. & Dingle, G. A. (2015). Extreme metal music and anger processing, *Frontiers in Human Neuroscience*, 9:272. doi: 10.3389/fnhum.2015.00272.

Shi, W., Rzepka, R. & Araki, K. (2008). Emotive Information Discovery from User Textual Input Using Causal Associations from the Internet. *Forum on Information Technology 2008*, 267-268.

Wells, A., & Hakanen, E. A. (1991). The emotional use of popular music by adolescents. *Journalism Quarterly*, 68, 445-454.

Yamada, A. (2011). *Proposal of song emotion extraction method using lyrics information.* Retrieved from http://www.nadasemi.ii.konan-u.ac.jp/publication/research/2011/final/yamada.pdf

Development of Remote Support System to Improve Physical Activity Habits of Elderly Patients with COPD

Chisato Ohashi[*,a], Shunsuke Akiguchi[b] and Mineko Ohira[c]

[a] National Institute of Technology, Toyama College/ Department of General Education Toyama, Japan
[b] National Institute of Technology, Toyama College/ Department of Electronics and Computer Engineering, Toyama, Japan
[c] National Hospital Organization East Nagano Hospital/ Internal Medicine, Nagano, Japan

*c-ohashi@nc-toyama.ac.jp

Abstract

Chronic obstructive pulmonary disease (COPD) was previously described as chronic bronchitis or emphysema of the lungs resulting from a past smoking habit. COPD can cause depression and social handicaps due to limitations of physical activity (PA) in daily life, and thereby, a decline in quality of life. The rate of exercise therapy implementation among elderly patients with COPD is low. One of the reason for this is suspected to be their decreased motivation to participate in exercise therapy at home because of feeling of alienation from society or the community.

The purpose of the present study was to develop a remote physical activity support system that utilizes information communication technology for fostering exercise therapy habits in elderly patients with COPD, and then to carry out a clinical trial to verity its effectiveness.

First, we developed a smartphone app equipped with a network server that health care providers can use to monitor the PA of patients with COPD and communicate results to them daily via e-mail for fostering exercise therapy habits in patients. The smartphone app also measures walking distance using the global positioning system and the number of steps taken using an accelerometer. The app then displays of the patients' PA using graphs and maps.

Next, we obtained the consent of a 77-year-old male patient with COPD to carry out a clinical trial. This patient had been receiving home oxygen therapy, but was not having any trouble carrying out daily PA. We found that the patient's PA time/day of the term of using the system was significantly longer compared with the pre-term of using the system (85.7 ± 14.2 min/day vs 63.2 ± 9.2 min/day, $p<0.05$). Moreover, the patient's duration of moderate intensity PA time/day of the post-term of using the system was significantly longer compared with the term and the pre-term of using the system and (11.2 ± 6.6 min/day vs 1.1 ± 0.9 and 1.2 ± 0.6 min/day, respectively; $p<0.05$). These results suggest that our system using a smartphone app is effective for an elderly patient's PA time/day, and expected fostering elderly patient's exercise habits.

Keywords: *COPD, Physical activity, Elderly patient, Exercise habits, Remote health support*

Introduction

Respiratory disease is a concerning physical limitation in daily life, and can lead to psychological problems such as depression and social handicaps because of reduced endurance. In addition, this situation can lead to a decline in quality of life (QOL) and foster disease progression as part of a vicious circle[1]. Chronic obstructive pulmonary disease (COPD) is the general term used to describe respiratory diseases such as chronic bronchitis or emphysema of the lungs resulting from a past smoking habit. COPD is known to cause depression and social handicaps due to limitations of physical activity (PA) in daily life, leading to a decline in quality of life (QOL).

The following targets have been identified to manage COPD: 1) improve the patient's symptoms and QOL; 2) maintain and improve exercise and PA capacity; 3) prevent acute exacerbation; 4) halt the progression of COPD; 5) preserve and treat pulmonary complications; and 6) improve vital prognosis. Breathing exercises, exercise therapy, and nutritional care are the central non-pharmacotherapeutic interventions for patients with COPD. However, home oxygen therapy (HOT) is used in cases of progressing hypoxemia[2]

Exercise therapy is known to improve the exercise tolerability, respiratory strength, respiratory distress, activities of daily living (ADL), QOL, and depression in patients with COPD[3]. In terms of exercise therapy, vigorous intensity exercise has shown clearer positive effects, but also carries an increased risk of respiratory

distress. In addition, vigorous intensity exercise should be performed with an attending care worker or monitor. On the other hand, light intensity exercise carries fewer risks, and is easy to continue at home independently. The adaptability of light intensity exercise in elderly patients with COPD has also been demonstrated[4]. The positive effects of home health care exercise have been verified in patients with COPD, even in respiration rehabilitation[4]. However, the rate of exercise therapy implementation among elderly patients is low. One of the reasons for this is thought to be decreased motivation to carry out exercise therapy because of feelings of alienation from society or the community.

Purpose

To improve the habituation of exercise therapy among elderly patients with COPD, a comprehensive rehabilitation system that enables family doctors and visiting nurse to share patient data and follow up with patients quickly is needed. Therefore, using information and communication technology (ICT), we developed a PA support system to assess and manage PA in patients with COPD, as well as to maintain or improve their QOL remotely.

The purpose of the present study is to report the results of a clinical trial on behavior modifications in daily life and changes in QOL in an elderly male patient with COPD who was receiving HOT using our newly developed PA monitoring and support system.

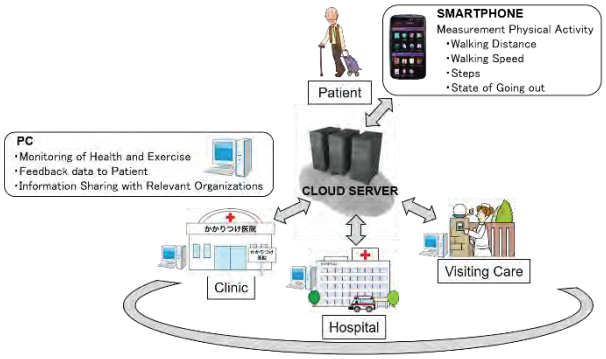

Figure 1: Remote Physical Activity Monitoring and Support Home Health Care System for Elderly Patients with Chronic Obstructive Pulmonary Disease

Development of the PA Monitoring and Support System

We developed a PA monitoring and support home health care system for elderly patients with COPD to improve their exercise therapy habits, help prevent their condition from worsening, and help avoid their social and community isolation, which could lead to other health problems such as frailty or sarcopenia. We decided to use a smartphone as the system device, and thus, developed a smartphone app. In recent years, the advancement of smartphone technology has progressed rapidly and enjoys widespread use by all generations. Next, we built a network server for the smartphone app to save and to share data among family doctors and visiting nurses. Figure 1 shows an overview of the system.

1. Measurement of Physical Activity

The operating system used to develop the smartphone app, which we called "Tekuteku-chan", was Android 4.0. Android JAVA IDE, Eclipse (Luna Release 4.4.0) programming language was used for software development. Our app has the following app functions.

1) User authentication
2) Walking distance measurement using the Global Positioning System (GPS)
3) Step counting using an accelerometer
4) Camera function for taking photographs

Walking distance is measured using the smartphone's GPS. First, the app acquires location information using GPS, and then it calculates the speed and distance. An original algorithm is used to count steps with an accelerometer. Although these PA data can be displayed in the foreground by scrolling (Figure 2), the app can continue to function in the background. The app icon appears in the notification bar to save battery resources. Moreover, the app allows users to take photographs and examine nutrition data about their meals. Photographs are uploaded with location information. All data collected by the app are uploaded automatically to a network server. Reattempts are made at 30-s intervals if no network connection is available.

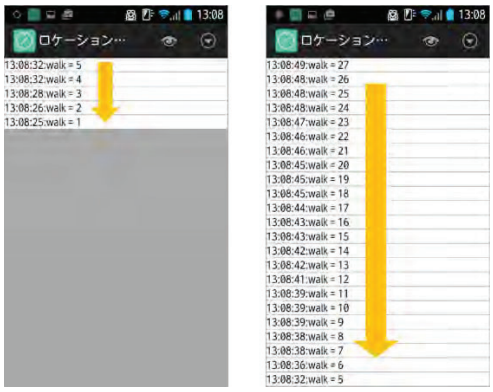

Figure 2: Data, Time, and Steps are Displayed in the Foreground of the Smartphone App by Scrolling

2. Network Server for Saving Data

Next, we set about building a network server that could be used by doctors and visiting nurses to monitor and check patients' PA and nutrition data on a web browser. Before using the server software, the person attending to or monitoring a patient must register as a

user. The following information is required for registration.

1) Patient ID number, name, and address (the address is necessary to show the base point on the server software map)
2) Account and password for app certification
3) Target walking distance per day
4) Target time zone for collecting data
5) Upper and lower limits of walking speed (to avoid the conversion of data collected during movement in vehicles)

The web software presents the patient's PA status, total walking distance, average walking speed, a graph of steps and time series walking distance, and photographs every day. In addition, the patient's movement points are shown on a Google map (Google Inc.) on the same web page. Data can be exported as a spreadsheet file (Excel; Microsoft Corp.) from the server to a PC (Figure 3). After a doctor checks the data, he/she sends messages of encouragement from a remote PC to the patient's smartphone. This is the key point to maintain patients' motivation to get plenty of PA and exercise therapy. Figure 3 shows the PC display.

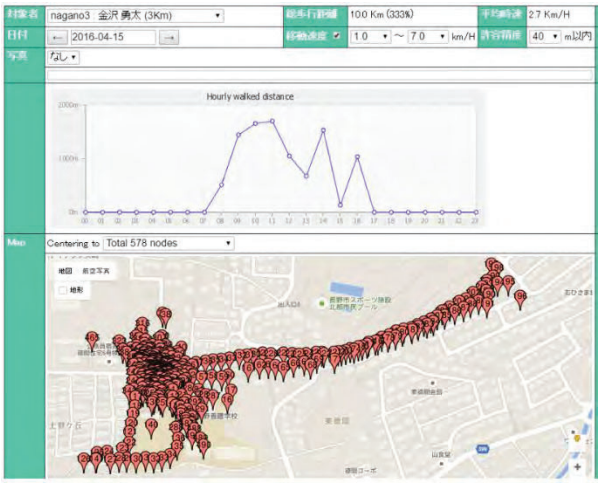

Figure 3: PC Software Shows a Graph and Map of the Patient's Physical Activity Data

3. Self-estimation of Physical Activity

We also developed another app, called "Hanamaru-system", that patients can use to estimate their PA data by themselves. The app has two functions. The first is to check their own target achievement rate through a variety of animations. The display shows a boy with apples. When patients engage in more PA, the animation changes step-by-step, e.g., the boy has a happier expression and the number of apples increases. We adopted this function so that patients could enjoy the system in a similar mindset as that when playing a game. Another function is to notify the patient of messages from their doctor. Figure 4 shows these functions.

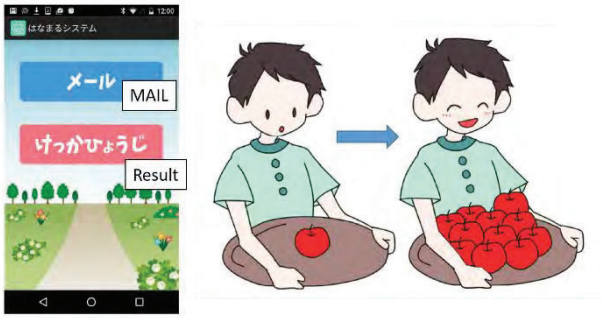

Figure 4: The "Hanamaru-system" Smartphone App Shows Physical Activity Data Using Animation for Self-Estimation

Clinical Trial

After explaining this information to a 77-year-old male patient with COPD at National Hospital Organization East Nagano Hospital (ENH), he provided written consent to participate in a clinical trial for 15 months, from September 2017 to October 2018, in collaboration with ENH. Although this patient regularly visits the hospital for HOT, his condition is stable and does not interfere with his daily life. For the present trial, we prepared a smaller and lighter smartphone that he could carry easily. His physical characteristics are shown in Table1.

Table 1: Characteristics of the Participant

Subject	Age	Height [cm]	Weight [kg]	BMI
male	73	164.2	59.4	22.0

1. Methods

The trial to evaluate our newly developed remote PA monitoring and support app was carried out for 15 months, from September 2017 to October 2018. To establish remote communication with the patient, we checked his data on a PC and used Gmail (Google Inc.) to send messages from a PC in Toyama Prefecture to his smartphone in Nagano Prefecture two or three times a week. The smartphone display shows only three apps, Tekuteku-chan, Hanamaru-system, and Gmail, because putting too many icons on the display was considered to make operation of the smartphone less user-friendly. In addition, we went to ENH to visit the patient face-to-face and meet his family doctor to report his recent status once a month.

To estimate his PA data and behavior modification for improving PA habits accurately, we asked the patient to wear an activity monitor (Lifecorder [LC]; Suzuken Co. Ltd., Japan) for three different 1-week measurement periods: the remote support term and both the pre- and post-terms. Figure 5 shows the measurement protocol.

The LC technology uses medical-grade sensors and filters out motion and vibration, only counting actual steps. It also measures the intensity (light, moderate, or vigorous) of PA. Kumahara reported that light intensity is approximately <3 metabolic equivalents (METs), a physiological measure expressing the energy cost of PA, moderate intensity is approximately 3–6 METs, and vigorous intensity is approximately >6 METs. METs are defined as a ratio of the metabolic rate [5]. Data on steps/day, total time of light/moderate/vigorous intensity PA (LMVPA)/day, and duration of LMVPA/time were collected using the LC. We also summed the duration time of LMVPA or moderate/vigorous intensity PA (MVPA)/time in the following 10 stages: <4 s, 8–12 s, 16–28 s, 1 32–56 s, 60-116s, 120-176s, 180-296s, 300-416s, and >420s.

We applied a nonparametric test to compare the amounts of PA using SPSS software (SPSS 16.0 Family; IBM Co.).

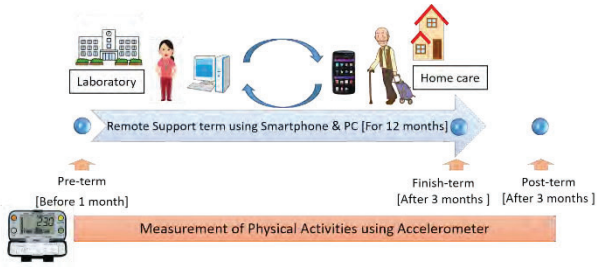

Figure 5: Measurement Protocol of Physical Activity to Verify the Effectiveness of the Remote Support System

2. Results

The number of steps/day and the time of the respective PA (light/moderate/vigorous) were estimated three times using the LC. Table 2 shows that the number of steps/day and duration of PA/day were significantly higher in the remote monitoring and support term and post-term than in the pre-term (6988±1264 and 6458±933 vs 5500±812, respectively; both $p<0.05$ and 85.7±14.2 min and 72.3±10.0 min vs 63.2±9.2 min, respectively; both $p<0.05$). Moreover, the duration of light intensity PA was significantly lower in the pre- and post-term than in the remote monitoring and support term (62.0±9.2 min and 61.1±9.9 min vs 84.6±14.5 min, respectively; both $p<0.05$). It is very interesting that the duration of moderate intensity PA was significantly longer in the post-term than in the remote monitoring and support and pre-term (11.2±6.6 min vs 1.1±0.9 min and 1.2±0.6 min, respectively; both $p<0.05$).

Next, we compared the total duration time of LMVPA in each term at each of the 10 stages. The remote monitoring and support term was significantly longer than the pre- and post-term for the 300–416 s duration time (5.6±4.5 min vs 0.0±0.0 min and 0.0±0.0 min, respectively; both $p<0.05$). No significant difference was seen in the other stages (Table 3). We also compared each term for the total duration time of MVPA, which is known to affect health promotion greatly. The duration of MVPA/day was almost 1 min/day for both the remote monitoring and support and pre-term. On the other hand, the post-term was higher, by about 11 min/day. Moreover, the division of all duration time of MVPA was under-12s (1.1min/day, 100%) for the remote monitoring and support and pre-term, but the division of over-16 s of all duration time of MVPA was 5.2 min/day (46.4%) for post-term.

Table 2: Comparison of Steps and Amount of Physical Activity in the Three Terms

Term	The Amount of Physical Activity				
	Step Step/day)	light (min/day)	moderate (min/day)	Vigorous (min/day)	Total (min/day)
Pre term	5500 ± 8123	62.0 ± 9.2#	1.2 ± 0.6	0.0 ± 0.0	63.2 ± 9.2
Support term	6988 ± 1264*	84.6 ± 14.5	1.1 ± 0.9	0.0 ± 0.0	85.7 ± 14.2*
Post term	6458 ± 934*	61.1 ± 9.9#	11.2 ± 6.6*#	0.0 ± 0.0	72.3 ± 10.0*

Average ± S.D.
*; vs Pre-term
#; vs Remote support term, $p<0.05$

Table 3: Comparison of the Total Duration Time of Physical Activity per Day in the Three Terms

The duration time of physical activity [second]	The sum time/day		
	Pre-term	Remote support term	Post-term
Under 4	14.5 ± 2.9 (22.9%)	16.5 ± 3.5 (19.2%)	12.5 ± 1.8 (17.3%)
8-12	21.4 ± 2.7 (33.8%)	23.0 ± 4.9 (26.8%)	22.0 ± 2.7 (30.5%)
16-28	9.8 ± 2.4 (15.6%)	13.8 ± 3.3 (16.1%)	14.6 ± 3.4 (20.2%)
32-56	3.3 ± 2.0 (5.2%)	6.4 ± 6.2 (7.5%)	3.2 ± 1.9 (4.5%)
60-116	4.2 ± 2.9 (6.7%)	6.6 ± 2.8 (7.7%)	6.8 ± 3.7 (9.4%)
120-176	8.9 ± 4.0 (14.1%)	8.0 ± 6.4 (9.4%)	10.3 ± 6.0 (14.2%)
180-296	1.1 ± 1.8 (1.7%)	5.7 ± 5.1 (6.7%)	2.8 ± 3.4 (3.9%)
300-416	0.0 ± 0.0# (0.0%)	5.6 ± 4.5 (6.5%)	0.0 ± 0.0# (0.0%)
Over 42	0.0 ± 0.0 (0.0%)	0.0 ± 0.0 (0.0%)	0.0 ± 0.0 (0.0%)
Total	63.2 ± 9.2 (100%)	85.7 ± 14.3 (100%)	72.3 ± 10.0 (100.0%)

Average ± S.D.
#; vs Remote support term, $p<0.05$

Table 4: Comparison of the Total Duration Time of Moderate Intensity Physical Activity per Day in the Three Terms

The duration time of moderate intensity physical activity [second]	The sum time/day		
	Pre-term	Remote support term	Post-term
Under 4	1.1 ± 0.6 (91.7%)	1.0 ± 0.6 (90.9%)	3.2 ± 1.3 (28.6%)
8-12	0.1 ± 0.2(8.3%)	0.1 ± 0.3 (9.1%)	2.8 ± 1.4 (25.0%)
16-28	0.0 ± 0.0 (0.0%)	0.0 ± 0.0 (0.0%)	3.1 ± 2.5 (27.7%)
32-56	0.0 ± 0.0 (0.0%)	0.0 ± 0.0 (0.0%)	1.8 ± 1.9 (16.0%)
60-116	0.0 ± 0.0 (0.0%)	0.0 ± 0.0 (0.0%)	0.3 ± 0.6 (2.7%)
120-176	0.0 ± 0.0 (0.0%)	0.0 ± 0.0 (0.0%)	0.0 ± 0.0 (0.0%)
180-296	0.0 ± 0.0 (0.0%)	0.0 ± 0.0 (0.0%)	0.0 ± 0.0 (0.0%)
300-416	0.0 ± 0.0 (0.0%)	0.0 ± 0.0 (0.0%)	0.0 ± 0.0 (0.0%)
Over 42	0.0 ± 0.0 (0.0%)	0.0 ± 0.0 (0.0%)	0.0 ± 0.0 (0.0%)
Total	1.2 ± 0.6 (100%)	1.1 ± 0.8 (100%)	11.2 ± 6.2(100.0%)

Discussion

Respiratory disease is a concerning physical limitation in daily life, and can cause psychological problems such as depression and social handicaps such as difficulties living a normal life because of reduced endurance. For this reason, we developed a remote monitoring and support system to improve the PA habits of elderly patients with COPD and prevent conditions such as frailty, which can lead to the development of lifestyle-related diseases, reduced QOL, or a bedridden status.

We carried out a clinical trial on one elderly male patient with COPD to examine the effectiveness of our smartphone app. The amount of PA in the M & S term increased 20 min/day compared with the pre-term. Furthermore, >3-min duration time of PA/day increased from 1.7% to 13.2%. We continued to contact the elderly male patient with COPD two or three time a week using a smartphone in remote places, from Toyama to Nagano Prefectures, and visited him once a month at ENH for 1 year. The results suggest that the app improved his PA habits. Based on the results we checked on the PC, he took a walk in the early morning almost every day. The duration of LMVPA/day decreased significantly in the M & S and post-term compared with the remote monitoring and support term. However, the duration of MVPA and >3 min duration time were significantly longer for the post-term than for these terms.

When patients with COPD perform exercises or PA, an important point is the prevention of disease exacerbation, such as respiratory distress. Therefore, patients should control the intensity of PA. Nevertheless, in the present study, the amount of MVPA increased in the patient who joined the trial. Accordingly, we thought there were two reasons for this. First, his exercise tolerability improved, so no exacerbations appeared while he was performing MVPA. Actually, in interviews, he did not complain of disease exacerbation. Second, his improved exercise tolerability gave him more confidence to conduct exercises or PA. Decreases in mental and social QOL are a concern in patients with COPD. In this clinical trial, we purposed improving the patient's exercise habits at first, but then we considered the possibility of improving not only PA,but also mental and social QOL.

Conclusions

Communication between health care providers and patients is extremely important for increasing PA in elderly patients with COPD. To prevent frailty resulting from decreased opportunities to go out in public, it is necessary to maintain or improve QOL in elderly patients.

As the next stage of this study, we plan to develop another app for use with a tablet PC that allows patients with COPD to check their own data collected by the smartphone app and relay their health condition to doctors or nurses. We believe that such a system that can enable patients with COPD to connect with health care providers more easily should be implemented in the future.

Acknowledgements

I would like to thank the members of East Nagano hospital and Municipal Iizuna hospital for supporting and collaboration on this research.

This study was supported by a grant from The First Bank of Toyama, Ltd.(2018.4-2019.3) and JSPS KAKENHI Grant Number JP 19K11316 (2019.4-2022.3).

References

[1]Nakamura, Y., Tanaka, K., Shigematsu, R., Inoue, M., Homme, T. & Sekizawa K. (2018), Assessment of physical activities from functional physical fitness tests research for patients with chronic obstructive pulmonary disease. *Annals of the Japanese Respiratory Society*, 39(4), 231–237.

[2]Respiratory disease, COPD (2014). *The Japanese Respiratory Society*, http://www.jrs.or.jp/uploads/uploads/files/disease_qa/disease_b01.pdf

[3]Satake, M., & Shioya, T. (2007), Verification of walking-based therapeutic exercise. *The Journal of the Japan Society for respiratory Care and Rehabilitation*, 17(2), 89-92.

[4]Kozuki M. (2004), Does exercise therapy improve the physical fitness in the elderly patients with cardiopulmonary diseases. *The Japanese Association of Rehabilitation Medicine*, 41(6), 393-397.

[5]Kumahara, H., Schutz, Y., Ayabe M., & Yoshioka, M. (2004), The use of uniaxial accelerometer for the assessment of physical-activity-related energy expenditure: a validation study against whole body indirect calorimetry. *British Journal of Nutrition*, (91), 393-397.

PRACTICAL EDUCATION FOR ADVANCED ENGINEERS OF KOSEN BASED ON ASSISTIVE TECHNOLOGY FOR A SUSTAINABLE SOCIETY

K. Kiyota[*,a], K. Watanabe[a], K. Araki[a], A. Shionoya[b] and M. Inoue[c]

[a] National Institute of Technology (KOSEN), Kumamoto College, Koshi, Japan
[b] Nagaoka University of Technology, Niigata, Japan
[c] National Institute of Technology (KOSEN), Tokyo, Japan

*kkiyota@kumamoto-nct.ac.jp

Abstract

Assistive technology (AT) is any item, device, software, or product system used to enhance, maintain, or improve the functional abilities of people with disabilities. There are many people around the world with severe physical disabilities, such as ALS and spinal cord injury patients. People living with ALS, also known as Lou Gehrig's disease, lose their ability to walk, talk, eat, and eventually breathe.
To support these disabled and elderly people, we formed the National KOSEN Support Equipment Development Network (KOSEN-AT) with faculty members of technical colleges 10 years ago. Many support systems for people with disabilities have been developed in KOSEN-AT. Among them, we also developed a teaching material production environment using prototyping methods for children with severe and multiple disabilities who can hardly move their bodies. Our developed teaching material production environment was inexpensive and easy to program and was supported by teachers of ICT at a special school for physical disabilities.
In parallel with the above background, In Japan, the National Institute of Technology (KOSEN), started its new research project called GEAR 5.0 in May 2020. The AT and medical engineering are one of those key disciplines selected as GEAR 5.0 project. In this session, we will discuss the mission of KOSEN-AT in the GEAR 5.0 project, our newly proposed concept of Extended AT and the engineering curriculum of AT skills for developing advanced future engineers.

Keywords: *Assistive technology, Disability support, Education of engineers*

Introduction

Recently, the enhancement of welfare and medical care for the super-aging society has become an issue not only in Japan but also on a global scale. Recently, the Ministry of Health, Labour and Welfare (MHLW) has imposed an obligation on all employers to employ people with disabilities at a rate higher than the legal employment rate, to promote "people with disabilities to live and work together as members of the community. In response to this social situation, the Ministry of Education, Culture, Sports, Science, and Technology (MEXT) has taken the lead in promoting policies for the early realization of an inclusive society based on rational consideration in various schools. Under these circumstances, the demand for AT devices for the disabled and elderly is increasing in the welfare equipment industry and educational institutions, and there is an urgent need to train AT engineers who can develop assistive devices.

However, national colleges of technology (NCTs) are higher education institutions that accept graduates of junior high schools and provide an integrated education for five years (five and a half years for merchant marine technical colleges) to train engineers required by society. NCTs have produced a large number of engineers specializing in mechanical, electrical, information, biochemical, architectural, and civil engineering. However, the development of AT devices requires not only conventional specialized skills but also new technical skills (AT skills) that consider the needs of the people (disabled and elderly users). In other words, it is desirable to introduce technical education that uses a social implementation model (needs-oriented) for the development and evaluation of devices and orthotics in cooperation with specialists from different fields such as medical and welfare care. In response to such requests from special support schools and medical institutions in each prefecture, the faculty members of 13 NCTs took the lead in establishing the National KOSEN Assistive Technology (AT) Development Network (KOSEN-AT Net).

Activities of the KOSEN-AT Network

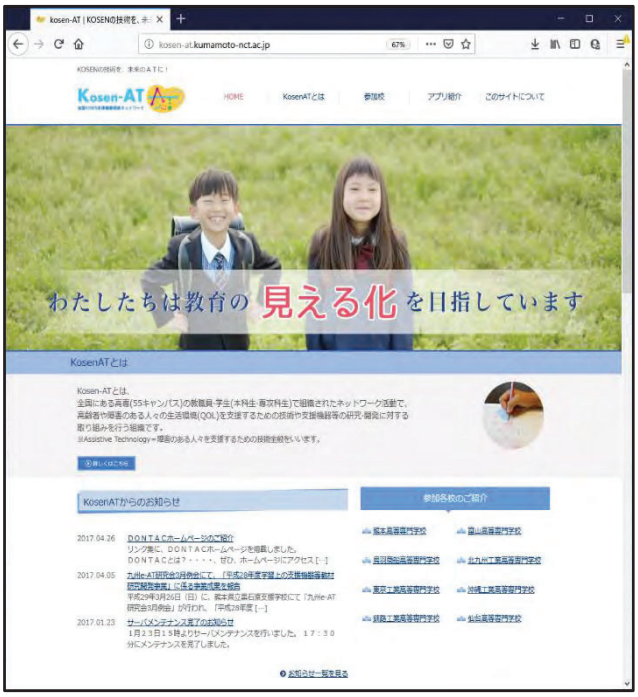

Figure 1 Website of the National KOSEN Support Equipment Development Network

Figure 1 shows the website of the National KOSEN Assistive Technology Development Network (http://kosen-at.kumamoto-nct.ac.jp/). The KOSEN-AT network has been conducting research and development to feedback the opinions of people with disabilities and people in the fields of education, welfare, and medical care that have been cultivated at each technical college to research activities. As part of the results, the project "Development of ICT education support materials using cloud computing to visualize the educational effects of learning" (representative school: Kumamoto National College of Technology) was adopted as a contracted project for special support education by the Ministry of Education, Culture, Sports, Science and Technology from 2014 to 2016. In this project, we proposed a framework to visualize the effects of learning by recording information such as the operation time of tasks, the percentage of correct answers, and the time taken to answer questions when students use iPads and tablets in class, etc., on the terminals and saving the information on a cloud server when they are connected to the Internet in a Wi-Fi environment to maintain the learning process. We propose a framework to realize "visualization of learning effects. Special support education is an educational program that provides appropriate guidance and necessary support for young children with disabilities to understand their educational needs, enhance their abilities, and improve or overcome their difficulties in life and learning, from the perspective of supporting their independent efforts and social participation. The KOSEN-AT Net is an educational program that identifies the educational needs of each individual and provides appropriate guidance and necessary support to enhance their abilities and improve or overcome difficulties in life and learning.

Figure 2 Examples of welfare support equipment and applications by the KOSEN support equipment development network (in Japanese)

KOSEN-AT Net developed teaching materials and assistive devices to be used in special support schools, etc., based on the assistive devices and applications developed by each technical college in this project. Figure 2 shows an example of the support applications developed in this project, including a system for training tablet operation and a system for reading out colors for visually impaired students and children (developed by Kushiro National College of Technology: Touch Color). The upper part of Fig. 3 shows a prototype of the Touch Color system being tested by visually impaired students. Initially, the color sensor was controlled by a microcomputer, and the color was determined by RGB signals, and then read aloud by a smartphone application using Bluetooth. However, during the evaluation of students at a school for the blind, the teacher in charge asked if the system could be used without a smartphone. In response to these requests, we improved the final commercialization kit to include the device in a small pendant-shaped case and directly read out the colors using the built-in speech synthesis IC (lower part of Figure 3).

Figure 3 Commercialization kit for “touch color”

Education for AT Technicians

In the process of the project commissioned by MEXT, we compiled the “Welfare Information Education Research Seeds and Needs Collection,” which summarizes the requests (needs) of the people involved in the field and the specialized technologies (seeds) possessed by NCTs to date. In addition, by referring to the opinions of experts, keyword searches and classification of basic assistive technologies were conducted so that the book can be used at special support schools. This book collects 19 research seeds of NCTs and 62 needs from special support schools, etc. (105 pages), and has been used for research and development of new AT devices, such as matching seeds and needs and feedback of evaluation devices to special support schools since 2015 (Fig. 4).

Figure 4 Seeds and Needs of Welfare Information Education Research

AT Technician Skills for Technical College Students

To cope with the aging society and to support people with disabilities, there is an urgent need for early training of AT engineers who are responsible for the development of AT devices in the welfare equipment industry and educational institutions. To meet these social needs, it is necessary to have not only conventional specialized knowledge but also new specialized skills to collaborate with specialists in different fields and to absorb the opinions of the people concerned (hereinafter referred to as AT skills).

The KOSEN-AT Net has studied the introduction of active learning education based on a social implementation model that incorporates these skills into the model core curriculum of NCTs. In addition, the Nagaoka University of Technology, Toyohashi University of Technology, and the National Institute of NCTs have collaborated and cooperated to develop the KOSEN-AT Net, based on practical education in AT device development that has been promoted in the graduation research of the main course students (five-year course: associate degree course) and the special research of the major course students (two-year course after graduation: bachelor degree course) to which the members of the collaborating NCTs belong. Based on practical education in AT equipment development that has been promoted in the special research of the second-year course after graduation (bachelor’s course), we have developed a skill map for AT skill standardization in the AT domain project of the education reform project (three-machine collaboration project), in which Nagaoka University of Technology, Toyohashi University of

Technology, and the National Institute of Technology have collaborated and cooperated.

The basic concept of the skill standard for AT engineers in technical colleges is defined as follows.

In the educational program for AT super engineers (super engineers with AT mind*), the purpose is to define the learning contents and achievement targets to acquire the abilities and qualities that engineers in all fields should have.

* "AT-mind" is a spirit (mind) that aims to support people with disabilities, and to contribute by acquiring the necessary skills to achieve this goal from the perspective of the people concerned.

Enhancement of Technical College Education (AT Future Technology Human Resource Development Model for a Sustainable Society)

In Japan, the National Institute of Technology (KOSEN) started its latest research project, called GEAR 5.0, in May 2020. The AT and medical engineering are key disciplines selected as the focus of the GEAR 5.0 project.

This project aims to realize the next generation AT (extended-AT (eAT)) that combines AT and digital (AI, IoT, robotics, big data, and mobility, etc.) to realize Society 5.0. Figure 5 shows the conceptual idea of the eAT (extended-AT) project in GEAR 5.0. We will promote market-creating research that will lead to the expansion of employment for people with disabilities, the improvement of quality of life for patients and people with disabilities, and the extension of healthy life expectancy for the elderly. At the same time, students at the college of technology will participate in the process of social implementation, and through problem-solving activities and the development of prototype devices and services, they will acquire practical knowledge of advanced technologies and develop engineers with an AT mindset who can solve problems from the perspective of people with disabilities.

To promote the above research and education, we will accumulate and share the know-how of the design data and customization of the next generation ATs developed by the GEAR 5.0 participating technical colleges as an AT library that can be shared by all technical colleges in Japan, to improve the development efficiency of AT devices and services and promote the social implementation of ATs. In addition, we will establish a joint research network with medical and welfare institutions, companies, local governments, etc., to share the voices of AT users, on-site needs, and issues, and jointly create better AT devices and services, and build a research system for industry-academia-government collaboration.

The ultimate goal of this project is to produce AT engineers from technical colleges across the country who can realize "the creation of a symbiotic society by using eAT even for people with disabilities."

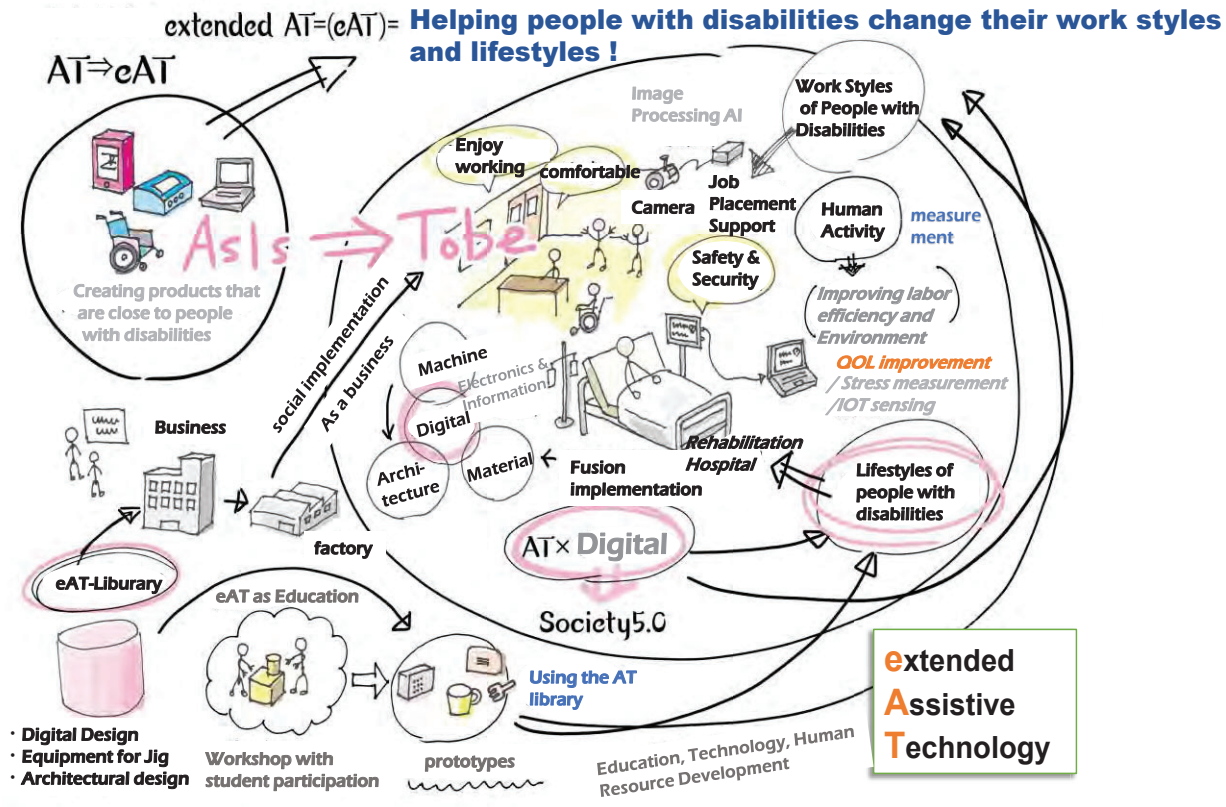

Figure 5 conceptual diagram of the eAT (extended-AT) in GEAR 5.0 project

Figure 6 shows the concept of the mission of research issues related to AT and the advancement of technical college engineer education in this GEAR 5.0 project (nursing care and medical engineering fields), in which five technical colleges from all over Japan are collaborating. As shown in Fig. 5, conventional AT is a technology that focuses on the manufacturing of assistive devices that accompany people with disabilities to overcome and complement their disabilities. In other words, it is a customized industry with high-mix, low-volume production that must accommodate various disabilities. Therefore, it is a gap market where no major companies have been able to enter. Until now, the technical colleges collaborating in the nationwide KOSEN-AT network have been working individually with local special needs schools, NPOs in Japan, and medical institutions to develop and research assistive devices.

Therefore, in GEAR 5.0, each base technical college will be in charge of the following missions to promote the project. In 2023, by sharing the results of each base school with each collaborating technical college, all base technical colleges will implement these functions and act as a nationwide organization as a branch of AT.

Introduction of AT Technician Education

(1) Case of NIT, Kumamoto College

In 2014, an educational program on AT skills was introduced in the "Creative Technology Design Practice," a two-credit seminar course for first-year students of the advanced course at NIT, Kumamoto College. This course is jointly taught by two faculty members, and after lectures and exercises on basic issues related to AT design, each group (consisting of three to four members) is given a theme as an assignment and is required to

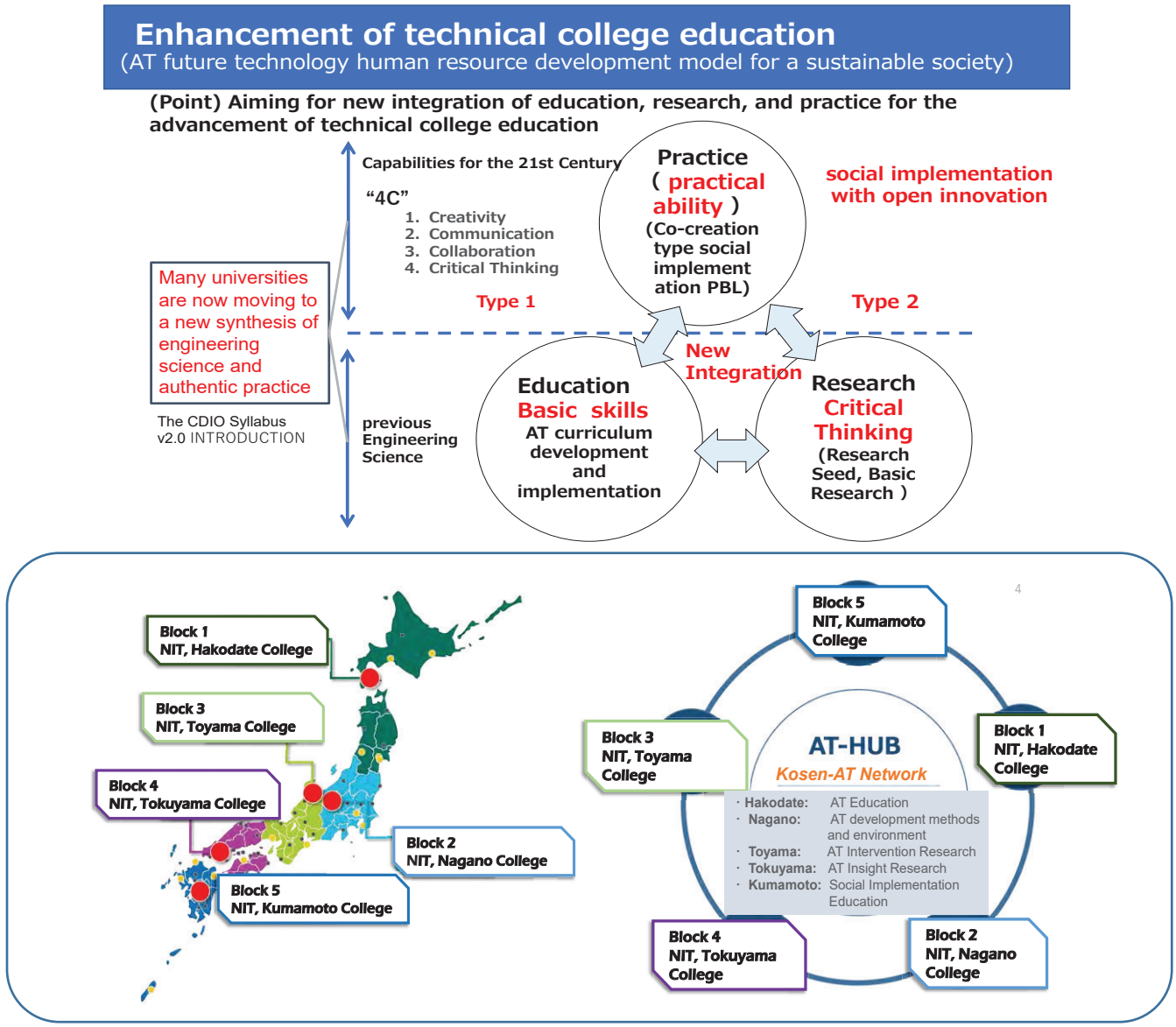

Figure 6 Enhancement of technical college education with the Kosen-AT Network in GEAR 5.0 project and Mission of the five partner technical colleges

generate ideas (planning) and materialize them, i.e., design and manufacture a demonstration machine, under a limited budget. The theme of the project is based on the examples of needs in the welfare field contained in the "Welfare Information Education and Research Seeds and Needs Vol. 2," which is a collection of seeds and needs conducted as part of a project by MEXT.

(2) Case of NIT, Hakodate College

In 2013, NIT, Hakodate college reorganized its departments and established the "Robotics Course" as one of the courses for fourth-year students in the Department of Production Systems Engineering. Particularly, this course covers "Robotics Experiments" and "Creative Experiment II" in the fourth year, and "Introduction to Medical Welfare Engineering" and "Graduation Project" in the fifth year. In the robotics experiments, the achievement goals for the learning content related to the basics of bioengineering are "to understand the functions (structure) of the body and be able to create simple mechanical models," "to understand the basics of measurement and evaluation techniques for physiological phenomena," and "to understand the basics of biological information processing. The themes specialized in the AT field include "measurement of muscle action potential" and "biological motion experiments.)

In addition, since 2007, in the "Creative Experiment" (second semester of the first year) for each major and the "Combined Creative Experiment" (first semester of the second year) across majors, project-based learning has been conducted by setting the needs of local companies as the theme and assigning retired engineers (special professors) as educational staff. Some themes are related to AT. In this course, various abilities, including the ability to set and solve problems and the ability to apply complex technologies, have been acquired based on engineering design education and collaborative education from the beginning, and these are also indispensable for AT engineer education. Specific

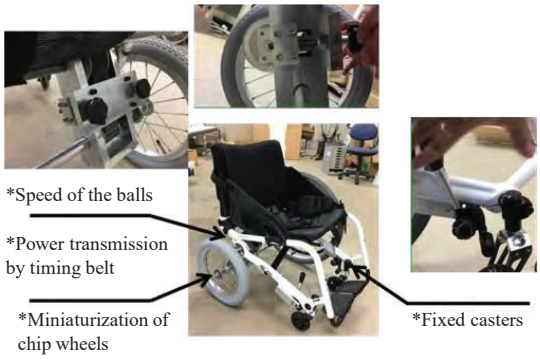

Figure 7 Appearance of the developed wheelchair for bowling.

The examples so far include the "development of hair washing equipment for home care" for use in various situations and the "developments of a bowling wheelchair" (Fig. 7) that can drive straight ahead with one hand.

Conclusions

This report describes the activities of the KOSEN-AT network at the National College of Technology and an overview of the GEAR 5.0-AT project that started in FY2020. Therefore, AT skills and techniques are necessary to communicate with people with disabilities, share their sense of trouble, and lead to concrete products. We are planning to further study the acceptability and introduction methods for this purpose, and develop a social implementation model of introduction case study in cooperation with a special subsidiary in the future.

Acknowledgements

We would like to express our deepest gratitude to the companies, teachers, and staff of special needs schools, and medical professionals who understand and cooperate with the GEAR 5.0-AT project.

References

Kiyota, K. (2018). Efforts to train AT engineers by the nationwide KOSEN-AT network. Information processing Society of Japan. *Journal of Information Processing Society of Japan*, 645, 939-942.

Uesugi, K., Dachi, A., Shintani, H., Koshi, K., Tsunoda, I., & Kiyota, K. (2018). Development of a gait training system that realizes resuction of lumbago by improving walking posture and correcting bowlegs. *Journal of International Society of Life Information Science*, 8-14.

Shimakawa, I., Taguchi, C., Okuma & . Kiyota, K. (2019). Smartphone application program of obstacle detection for visually impaired people. *ICIC Express, Part B: Applications*, 10, 219-226.

Technology-enhanced Exercise is Effective in Improving Balance and Happiness Level among Healthy Elders – Pilot Study

Evelyn Y.C. KO, Wollo W.S.Wu, Florence P.S. Mok

Department of Health & Life Sciences,
Hong Kong Institute of Vocational Education (Kwai Chung)
Vocational Training Council, Hong Kong

wollo@vtc.edu.hk

Abstract

Falls and depressed mood are common problems encountered among the elderly. Although evidence from systematic literature review suggested that exercise could reduce the risk of fall and enhance happiness level, traditional exercise training regime composes of regular training in terms of hourly training for two to three sessions weekly for months, those outcomes from the training program are often reduced by poor exercise adherence and high dropout rate from long-term participation. The objective of this study is to evaluate the effectiveness of a low dose short duration exercise training program using a playware device – Moto Tiles (MT) in improving the functional balance status and happiness level among healthy elders in Hong Kong community.

14 community-dwelling healthy elders (13 female & 1 male; mean age = 73.6 ± 6.6 years old) who met the inclusion criteria were voluntarily recruited from a local District Elderly Community Center to participate in a 6-week MT exercise programme (45-minute exercise on MT) designed by the physiotherapist. Standardized clinical measures, 1) Timed-Up and Go Test (TUGT), 2) Functional Reach (FR), 3) Single-Leg Stance (SLT) were used to assess the subjects' functional balance abilities, and their happiness level was assessed by 4) Oxford Happiness Questionnaire (OHQ). Pre and post-program comparisons were used to evaluate the change in their functional statuses among subjects.

Significant improvement on all outcome measures for those elderly was demonstrated. Improvement on functional balance ability was reflected by shorter time spent in TUGT (mean change = 13%; p=0.003), better trunk elongation in FR (mean change = 24.3%; p=0.001), and increased in the duration of SLS for both dominant leg (mean change = 41.7%; p=0.001) and non-dominant leg (mean change = 104.9%; p=0.001). Besides, those elderly also showed greater happiness level as shown in OHQ (mean change = 25 %; p=0.007).

Results from this pilot study illustrate that significant improvement in the elders' functional balance and happiness statuses could be attained by a short-duration MT program. It shed lights on the feasibility of implementing a shorter duration of the technology-enhanced exercise training program on fall prevention for elders in the community setting to enhance cost-effectiveness.

Keywords: *Community-dwelling, Elderly, Exercise, Moto Tiles, Balance, Happiness level*

Introduction

Falls is a considerable common problem encountered among the elderly. It is one of the significant causes of morbidity and mortality in elderly populations. World Health Organization (2012) predicted around 424,000 people died from falls globally. Chu *et al* (2007) stated around 20% of community-dwelling elderly aged ≥ 65 having at least one fall at a year in Hong Kong. About 75% of them sustained an injury including serious ones such as fractures. Fong *et al* (2011) reported the incidence of falls among community-dwelling elderly in Hong Kong was 26%. Fallers would experience a loss of confidence, a decline in abilities and independence in their daily functions. Those fallers with fear of fall and depressed mood would also negatively affected their psychological and social situations.

It was noted that muscle strength of knee extensors, weak dynamic balance, slow gait speed as well as previous fall history were associated with falls (Chu *et al* 2007). However, Centre and Health Protection (2013) indicated individuals mistakenly treated that fall as a normal part of ageing. In fact, Fall prevention could be achieved by early management of risk factors and implementation of a healthy lifestyle, together with targeted multi-disciplinary interventions.

Positive effects on fall prevention were demonstrated by Mittaz Hager *et al* (2019) with home-based exercise programme for the elderly. Improvement was found in

balance and gait speed. Exercise adherence/ compliance of these participants was also crucial to the outcomes. However, Mailloux *et al* (2006) reported fair adherence was noted due to loss of interest and if they felt that those exercises did not alleviate their problems.

A recent study by Collado-Mateo *et al* (2021) identified fourteen key factors to enhance the adherence to physical exercise including use of technology, enjoyment, social support and relatedness, integration in daily living, active role of participants as well as communication and feedbacks etc.

Various exercise gaming and technology-enhanced training have been introduced gradually. Smaerup *et al* (2017) offered computer-assisted home training (Mitii) for elders with vestibular dysfunction. Some positive feedback from the elderly were received. However, adjustment on the system could be considered to facilitate the effects for rehabilitation. e.g. feedbacks on the quality of performance; better understanding of the relevance of the exercise as well as more interactions with the therapist.

Moto Tiles has been selected for balance training as Lund and Jessen (2014) reported positive effects on physical abilities, static and dynamic balance, agility and endurance of elderly users.

In Hong Kong, Moto Tiles is only implemented at few venues for exercise or rehabilitation. In our study, the effectiveness of a low dose short duration exercise training program using a play-ware device would be assessed – Moto Tiles on the improvement of the functional balance status and happiness level among community healthy elders in Hong Kong.

Materials and Methods

Subjects

Fourteen community-dwelling elders (13 female and 1 male), the mean age of 73.6 $\pm$ 6.6 were recruited voluntarily from one of the local District Elderly Community Centre. They were classified as "Outdoor walker" in the Modified Functional Ambulatory Category. They were able to communicate and follow instructions.

Program with Technology-enhanced exercise

The Moto Tiles exercise programme was carried out from mid-October to the end of November 2020 at one of the elderly centre of a non-governmental organization (NGO) in Hong Kong. Moto Tiles was implemented as a 6-week program of one session weekly. Each session composed of 15 to 20 minutes of warm-up & cool down, with 40 to 45 minutes of Moto Tiles training. Each session lasted for 60 minutes.

Moto Tiles is a playware technology that composed of 10 tiles and the tablet installed with apps of various games. Tablet connects those 10 tiles through Bluetooth. Interactive games could carry out by this playful set to individuals with various age groups. Candidates would challenge their abilities in balance and coordination through stepping on those tiles in forward, backward, lateral and diagonal directions. Furthermore, each game is designed with various levels to suit the different physical abilities of the users. As two sets of Moto Tiles were operated in our study, the elderly were divided into two groups. The elderly participated in this playful training in the form of one person or two. Competitions were offered between them to enlighten the atmosphere.

Games named "Paint", "Color Race", "Reach", "Show the pattern" & "Concentration Color" and "Final countdown" were selected in the training program. Each game lasts approximately 60 seconds 2 to 3 repetitions at each session.

Outcomes measurement

Pre-post program comparison was evaluated on the functional balance and happiness level among those elderly. "Time up & Go test"- TUGT, "Functional reach"-FR and "Single leg Stance"-SLS were adopted on the evaluation of the functional balance. The happiness level was evaluated by the "Oxford Happiness Questionnaire" (OHQ).

Hills and Argyle (2002) developed the Oxford Happiness Questionnaire to assess personal happiness. This consists of 29 statement related to happiness. Macini *et al* (2012) and Hadinezhad & Zaree (2009) reported excellent reliability (ICC = 0.84) for OHQ.

Shamway-Cook *et al* (2000) established Timed up & Go test for measurement on the risk of fall-related to functional balance for elderly. Time was counted during the transfer from sit to stand, walking 6 meters with turning in between as well as return to sitting. Time spent with 10 seconds or less is classified as normal while high fall risk for those with $\geq$ 14 seconds.

Functional Reach was adopted to assess the dynamic balance on stable Base of Support (BOS) (Duncan *et al*, 1990). It also implies the fall risk according to the extent of trunk elongation. Williams *et al* (2017) concluded that Functional Reach Test had an excellent reliability level (ICC= 0.93-0.99)

Single leg stance test (SLS) was used to test static balance on a narrow based BOS. Michikawa *et al* (2009) reported the correlation of SLS with fall risk. Springer *et al* (2007) found excellent reliability of the single leg stance test (ICC= 0.90).

Statistical Analysis

Data collections were made on 12 Oct 2020 (First session) and 23 Nov 2020 (last session) of the Moto Tiles Exercise Program. Personal demographic data and pre-post program measurement for functional balance and happiness level would be recorded.

Software PSPP version 26 was used to analyse the data. Wilcoxon signed-rank test was adopted to evaluate the statistical difference on the pre- and post-program comparison on those outcome measurements after the Moto Tiles exercise program. Mean & standard deviation was calculated. The mean change was also assessed

Results

Significant statistical differences were noticed in all outcome measures for those elderly. Their functional balance was improved by shorter time spent in TUGT (mean change = 13%; p=0.003), better trunk elongation in FR (mean change = 24.3%; p=0.001), and increase in duration of SLS for both dominant leg (mean change = 41.7%; p=0.001) and non-dominant leg (mean change =104.9%; p=0.001). Besides, those elders also improved in happiness level with OHQ (mean change = 25 %; p=0.007).

Post-program evaluation for each outcome measure was illustrated in form of mean and standard deviation. They were shown from figure 1 to 5 respectively as Timed up & Go test, Functional reach, Single leg stance (Dominant leg), Single leg stance (Non-Dominant leg) and the Oxford Happiness Questionnaire.

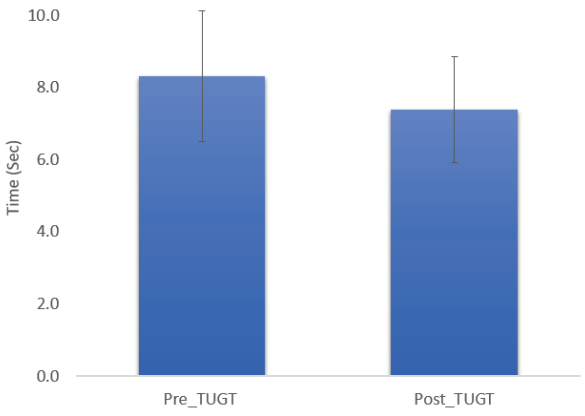

Figure 1: Changes in Timed up & Go Test

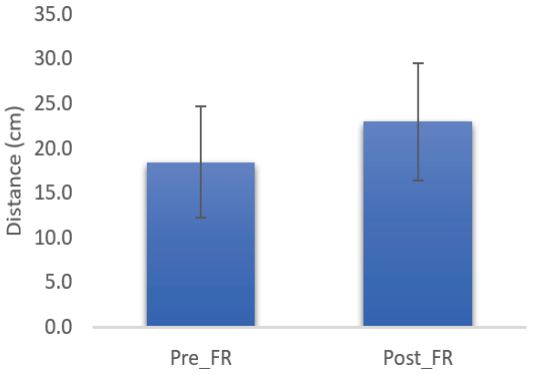

Figure 2: Changes in Functional Reach

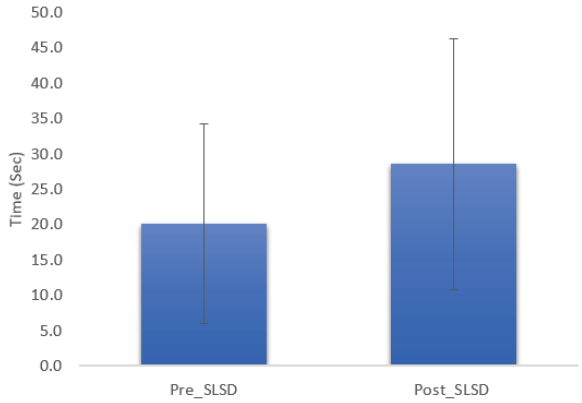

Figure 3: Changes in Single Leg Stance (Dominant)

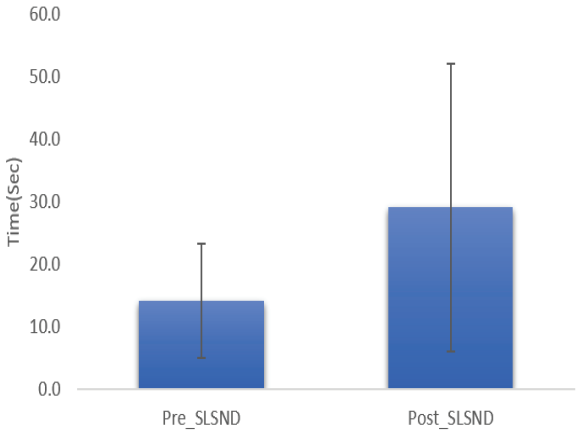

Figure 4: Changes in Single Leg Stance (Non-dominant)

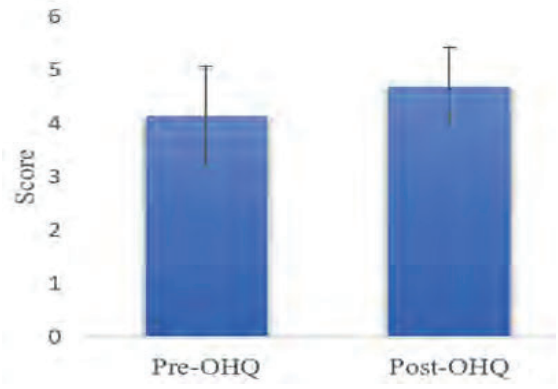

Figure 5: Changes in Oxford Health Questionnaire

Discussion

Exercise adherence and Amusement

Good exercise adherence was demonstrated with 13 out of 14 elders with > 80 % attendance. 7 elderly completed the program with full attendance. Most of them was absence only due to medical follow up or sickness. As the Moto Tiles is a play ware technology, exercises were offered in form of various games from the Moto Apps from the tablet with 10 tiles. Elderly showed joyful feelings & got excited especially during group format or competitions. Their social support and relatedness could also enhance as the agreement with Collado-Mateo *et al* (2021).

Effects from Moto Tiles Exercise

After the completion of the Moto Tiles exercise program, positive effects on functional balance status and happiness level of those elderly were resulted. These were well illustrated by shorter time spent in TUGT (mean change = 13%; p=0.003), better trunk elongation in FR (mean change = 24.3%; p=0.001), and longer duration of SLS for both dominant leg (mean change = 41.7%; p=0.001) and non-dominant leg (mean change = 104.9%; p=0.001). Besides, those elderly also showed greater happiness level from OHQ (mean change = 25 %; p=0.007). Previous studies reflected the supportive trend of findings from technology-based exercises.

Games selected in our pilot study not only challenged the capacity of functional balance and weight shifting of those elderly but also on their competence for coordination, agility or even cognitive functions like concentration, short-term memory. For the game "Color Race", participants stepped on the correct tile as quickly as possible according to the colour. The Elderly operated their abilities on short-term memory in "Concentration Color". They needed to match tiles in pair with the same color.

Lund and Jessen (2013) implemented modular interactive tiles for playful balance training on 12 community-dwelling elderly with balancing problems. Significant improvement of 12.3% on the Dynamic Gait Index (DGI) was resulted after 2 months of training.

Ehrari *et al* (2020) did a 10-week Moto Tiles program on 26 independent living elderly. The program was offered in the form of 12-minute, 2 sessions weekly of playful exercises. The modest gain in balance among these elderly was concluded. Moreover, the elderly showed with joyous social atmosphere during the program. Their good motivation and adherence were also recognized.

Glanngjord *et al* (2017) adopted Wii Sports Bowling on 8 older adults aged over 60. Older adults could play this bowling game in various positions like standing or sitting. Good engagement among these participants was observed with enjoyable expressions. Frequent social interactions were demonstrated.

Kosse *et al* (2011) reported improvement on both static and dynamic balance on 9 elders after 6-week weight shifting games with the technology-based wobble board. Statistical significant changes were evaluated from Berg Balance Scale.

Young *et al* (2010) implemented Wii balance board with various games for 6 healthy elders. Significant improvement in sway variability resulted among these participants after 10 sessions of a 20-minute session in 4 weeks.

All these positive feedbacks and results encourage the corporation of technology-enhanced exercises to promote the physical status, mood and social interactions enhancement for the elderly in the community.

Conclusion

Significant improvement in the elders' functional balance and happiness statuses could be attained by short-duration Moto Tiles program in this pilot study. Risk of fall could be minimized with substantial ability in functional balance.

Furthermore, the Moto Tiles was noticed to be well accepted by those elderly. They showed enjoyment with good adherence, active group dynamics among elders and us were observed during each session.

The feasibility of implementing of shorter duration of technology-enhanced exercise program on fall prevention for elders in the community setting could be considered to enhance cost-effectiveness. In fact, community-dwelling elderly can also benefit from independence in daily functions, better self-confidence

with good social support. Despite ageing, the elderly should also deserve autonomy in living, considerable life quality and better well-being.

Further investigation on the effects of Moto Tiles or other technology-enhanced exercise on cognitive functions and other physical abilities such as agility, coordination could be evaluated. If the results were convincing, implementation of these playful exercises could be considered as an element in the rehabilitation areas. In addition, specific conditions of individuals such as dementia, stroke, autism spectrum disorder and developmental coordination disorder etc could be potential targets for this playful training.

Acknowledgement

We express our sincere thanks to those social workers and staff from the Christian Family Service Centre (Kwun Tong) who assisted to recruit the elderly for our program. They also provided the venue for the Moto Tiles programme.

Besides, we also make our special thanks to all those elderly who had voluntarily participated in the Moto Tiles exercise programme.

References

Centre of Health Protection (2013). NCD watch 2013_Falls in the elderly. Retrieved from https://www.chp.gov.hk/files/pdf/ncd_watch_nov2013.pdf.

Collado-Mateo, D., Lavin-Perez, AM., Penacoba, C., Del Coso, J., Leyton-Roman, M., Luque-Casado, A., Gasque, P., Fernanez-del-Olmo, MA., Amado-Alonso, D.(2021).
Key factors associated with adherence to physical exercise in patients with chronic diseases and older adults: an umbrella review. International Journal of Enviornmental Research and Public Health, 18, 1-24.

Chu, LW., Chi, I., Chiu, AY. (2007). Falls and fall-related injuries in community-dwelling elderly persons in Hong Kong: a study on risk factors, functional decline, and health services utilisation after falls. *Hong Kong Medical Journal*, 13: S8-12.

Duncan, PW., Weiner, DK., Chandler, J., Studenski, S. (1990). Functional reach: a new clinical measure of balance. *Journal of Gerontology*, 45(6), 192-197.

Ehrari, H., Larsen, RT., Lamgberg, H., Andersen, HB. (2020). Effects of playful exercise of older adults on balance and physical activity: a randomized controlled trial. *Journal of Population Aging*, 13:207-222.

Fong, KNK.,Siu, AMH., Au Yeung, K., Cheung, SMS., Chan, CCH. (2001). Falls among the community-living elderly people in Hong Kong: A retrospective study. *Hong Kong Journal of Occupational Therapy*, 21(1), 33-40.

Glannfjord, F., Hemmingsson, H., Ranada, AL.(2017). Elderly people's perceptions of using Wii sports bowling- qualitative study. *Scandinavian Journal of Occupational Therapy*, 24(5): 329-338.

Hadinezhad, H. & Zaree, F. (2009). Reliability, validity and normalization of the Oxford Happiness Questionnaire. *Psychological Research*, 12(1-2), 62-77.

Hills, P & Argyle, M. (2002). The Oxford Happiness Questionnaire: a. compact scale for the measurement of psychological well-being. P*ersonality and Individual Differences,* 33(7),1073-1082.

Kosse, N., Caljopuw, S., Vuijk, P., CJC, L. (2011). Exergaming: interactive balance training in healthy community- dwelling elderly. *Journal of Cyber Therapy & Rehabilitation*, 4, 399-407.

Lund, HH., Jessen, JD. (2013). Effect of playful balancing training- a pilot randomized controlled trial. In *Proceedings of 18th International Symposium on Artificial Life and Robotics*.

Lund, HH. & Jessen, JD.(2014) Effects of short-term training of community-dwelling elderly with modular interactive tiles. *Games of Health Journal*, 3(5), 277-283.

Mailloux, J., Finno, M., Rainville, J. (2006). Long term exercise adherence in the elderly with chronic low back pain. *American Journal of Physical Medicine & Rehabilitation*, 85(2), 120-126.

Mancini, M., Salarian, A., Carlson-Kuhta, P., Zampieri, C., King, L., Chiari, L., Horak, FB. (2012). ISway: a sensitive, valid, and reliable measure of postural control. *Journal of Neuro Engineering and Rehabilitation*, 9(59).

Michikawa, T., Nishiwaki, Y., Takebayashi, T., Toyama, Y. (2009). One-leg standing test for elderly populations. *Official Journal of the Japanese Orthopaedic Association*,14(5), 675-685.

Mittaz Hager, AG., Mathieu, N.,Lenoble-Hoskovec, C., Swanenburg, J., De Bie, R., Hilfiker, R. (2019). Effects of three home-based exercise programmes regarding falls, quality of life and exercise-adherence in older adults at risk of falling: protocol for a randomized controlled trial. BMC Geriatrics, 19(13), 1-11.

Shumway-Cook, A., Brauer, S., Woollacott, M. (2000). Predicting the probability for falls in the community-dwelling older adults using the Timed Up & Go Test. *Physical Therapy*, 80 (9), 896-903.

Smaerup, M., Gronvall, E., Larsen, SB., Laessoe, U., Henriksen, JJ., Damsgaard, EM. (2017). Exercise gaming- a motivational approach for older adults with vestibular dysfunction. *Disability and Rehabilitation: Assistive Technology*, 12(2), 137-144.

Springer, BA., Marin, R., Cyhan, T., Roberts, H., Gill, NW. (2007). Normative values for the unipedal stance test with eyes open and closed. *Journal of Geriatric Physical Therapy*, 30, 8-15.

World Health Organization (2012). Fall Prevention in Older Age. Retrieved from *https://www.who.int/ageing/projects/falls_prevention_older age/en.*

Young, W., Ferguson, S., Brault, S., Craig, C. (2010). Assessing and training standing balance in older adults: a novel approach using the "Nintendo Wii" Balance Board. *Gait & posture*, 33, 303-305.

Consideration of Tablet Application for Special Needs Children with Multiple Support Functions

S. Akiguchi[*,a], C. Ohashi[b]

[a] National Institute of Technology, Toyama College / Department of Electronics and Computer Engineering, Toyama, Japan
[b] National Institute of Technology, Toyama College / General Education, Toyama, Japan

*akiguchi@nc-toyama.ac.jp

Abstract

In this paper, we report on a tablet application for special needs children with multiple support functions. The functions included in this application are based on the requests from the special school. We explain each support function, the graph display function for the status of efforts, and the prototype function for individual settings. We also report an example of each of the personal settings and the operation of the collected data.

Keywords: *Tablet Application, Special Needs Children, Assistive Technology, Technical Aids*

Introduction

In recent years, there is a growing need for tablet applications. Tablet devices, such as the iPad, have various features: Its lightweight and small size make it highly portable, and its intuitive operation requires no expertise in operation (e.g., Hamka, F. H., Bouwman, H., de Reuver, M., & Kroesen, M, 2014; Lin, K. Y, 2016). The characteristics of tablet devices match well with the characteristics of special needs children. Therefore, opportunities for using tablet devices in special needs education are increasing. However, there are several problems in the use of tablet devices by children with special needs (e.g., Khan S, Tahir MN, Raza A, 2013; N. M. Sofian, A. S. Hashim, W. F. W. Ahmad, 2018). Each child has different characteristics, but typical tablet applications cannot adjust. Therefore, it is necessary to find one that fits the characteristics of the user from among many tablet applications. In addition, most tablet applications have a single support function. Special needs children with various characteristics may need many applications. Each application is easy to operate, but as the number of applications to be used increases, the number of operations must also be remembered since different producers produce them.

Therefore, we studied a tablet application for children with special needs that has multiple support functions. Each support function has its settings for special needs children. In addition, by registering multiple support functions on a single tablet application, we consider it possible to obtain information such as the usage status of each function, which cannot be obtained with a conventional application with a single support function.

Tablet Application for Children with Special Needs

This chapter describes a tablet application for special needs children with multiple support functions that we created. This time, eleven functions were implemented, and each briefly described. Each of these functions was created based on requests from teachers and parents of special needs schools. Figure 1 shows the application launch screen.

Figure 1. Launch Screen

Press the right button to move to the screen for selecting various tools. The left button is for displaying graphs and making settings. This will be explained later.

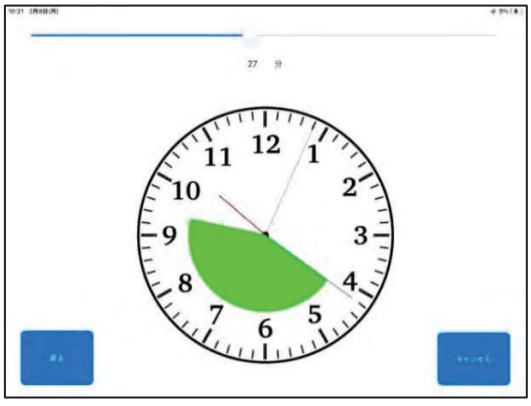

Figure 2. Time Timer (Display Screen)

The first function is a timer (Fig. 2). It visually displays the working time as a fan shape on a clock. This is effective for visually dominant children.

Fig. 3 and 4 show an application that displays the work time in segments. In this application, the user can select the number of divisions, display shapes and colors. It can visually display how much work time has progressed.

Figure 3. Shape Timer (Setting Screen)

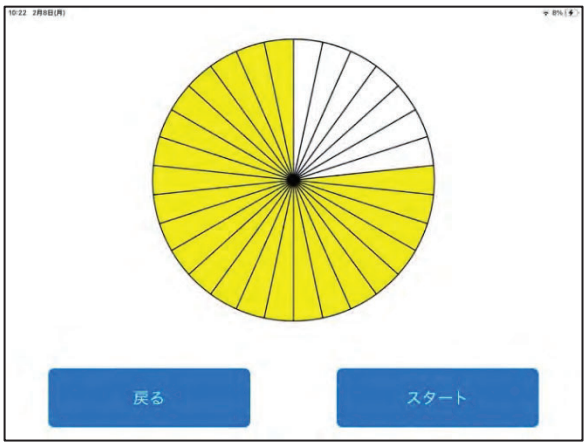

Figure 4. Launch Screen

The following is a modification of the Shape Timer to use images (Fig. 5 and 6).

Figure 5. Image Timer (Setting Screen)

Figure 6. Image Timer (Display Screen)

By tapping on the image area in Fig. 5, the user can freely select any image from the photo library. Images are displayed on the screen for the number of hours determined by the set time, and the number of images displayed decreases as time progresses. These timer-based applications were developed based on the requests of supporters who wanted their children to acquire a sense of time.

The following is a voice recognition application (Fig. 7 and 8).

Figure 7. Voice Recognition App (Run Screen)

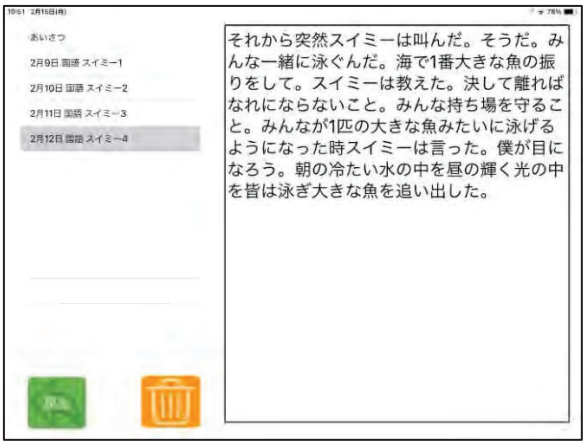

Figure 8. Voice Recognition App (Log Screen)

Tap the red button to start recognition, and the recognition result is displayed in the box on the left. Tapping the red button again stops the recognition, and the recognition result is displayed in the right box. The right box shows the history so far. Tap the Save button to save the history. By tapping the history button, the user can check the saved history. Most speech recognition applications for the visually impaired are mainly for one-on-one communication support. We developed this application based on the request of supporters who wanted to use such a tool in lectures.

The garbage separation learning application is shown in Figure 9.

Figure 9. Garbage Separation Learning App

It is necessary to learn how to separate garbage, as the method of garbage separation is determined in detail by each region. The application was developed based on the supporters' request to make learning fun by using illustrations. The trash is shown as an illustration, and the correct answer is given when the image is moved over the correct trash can.

Next is a manner learning application (Fig. 10-12). We have prepared manners for transportation, public facilities, and eating. It was developed based on the request of the supporters who wanted to learn the manners necessary in daily life in an easy-to-understand manner with illustrations. An example of the learning screen for transportation is shown in the figure.

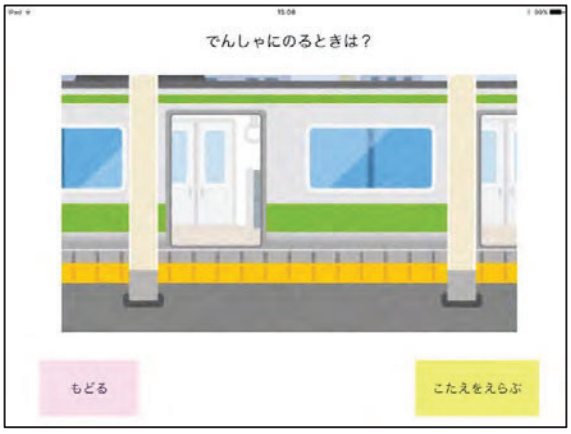

Figure 10. Manners Learning App (Question Screen)

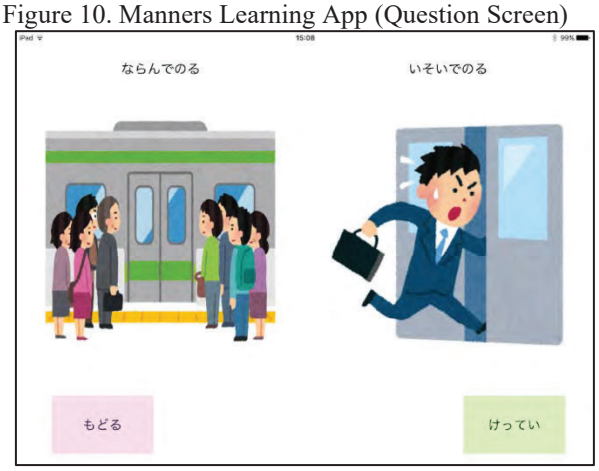

Figure 11. Manners Learning App (Selection Screen)

Figure 12. Manners Learning App (Answer Screen)

Next is a schedule-making application (Fig. 13 and 14). It was created based on a request from a supporter who wanted to support children who can be calm and active when they have a set schedule. When the image corresponding to the schedule is selected on the image selection screen (Fig. 13), the images are displayed in the order selected on the execution screen (Fig. 14). This is used by children who are good at following a schedule in order.

Figure 13. Schedule App Type1 (Setting Screen)

Figure 14. Schedule App Type1 (Run Screen)

Children who want to do their schedules in the order of their choice can use the application shown in Fig. 15.

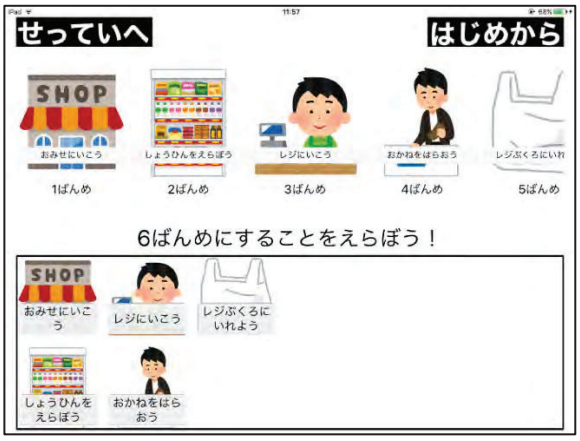

Figure 15. Schedule App Type2

In this app, the user first registers a schedule. Then, by tapping on the image that shows the schedule that has been completed, the app makes that image disappear. Children can do their schedules in any order they want, and by tapping and erasing the ones they have accomplished, they can keep track of the rest of their schedules.

Next is the tooth brushing application (Fig. 16, 17).

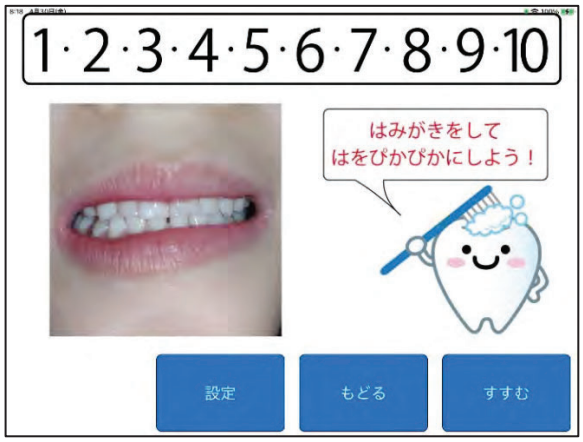

Figure 16. Tooth Brushing App (Display Screen)

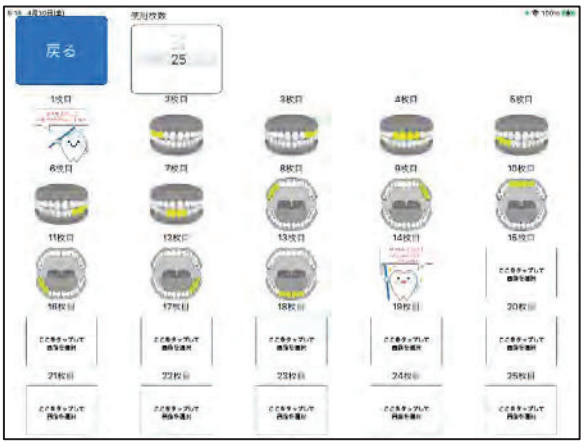

Figure 17. Tooth Brushing App (Setting Screen)

In Fig. 17, the user can select up to 25 images from the photo library displayed on the right screen of Fig. 16.

The following is a number concept understanding and calculation aid application (Fig. 17(a), (b)).

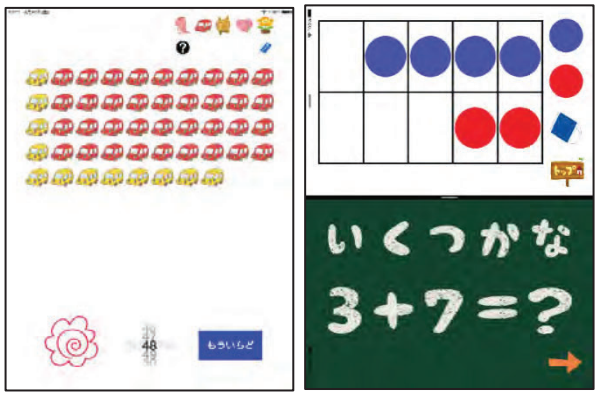

(a) Number Concept (b) Calculation Aid

Figure 18. Number Learning App

Fig. 17 shows an application that allows users to practice summarizing things in tens. Fig. 18 shows an application for practicing calculations using "Ohajiki."

In this way, we have developed various applications for special needs education based on supporters' requests. In addition, by consolidating multiple applications into one, there were requests to store data of each tool usage and change part of the interface. Therefore, in this study, by combining multiple tools into one, we developed a prototype that collects and graphs the usage status of each tool and a function to change the button interface for children who are not good at tapping buttons. Fig. 19-21 shows an example of a graph of the tool usage status.

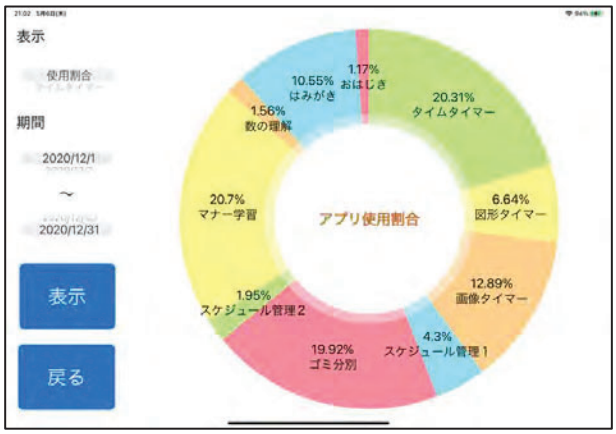

Figure 19. Usage Conditions

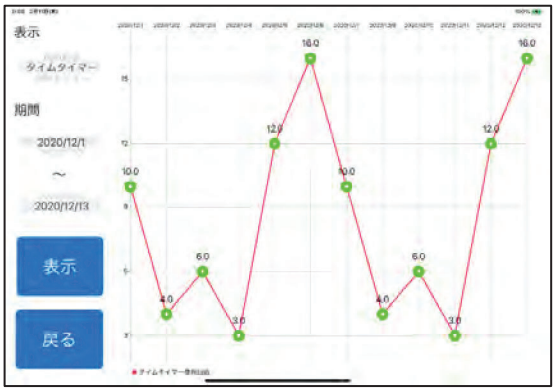

Figure 20. Usage Rate

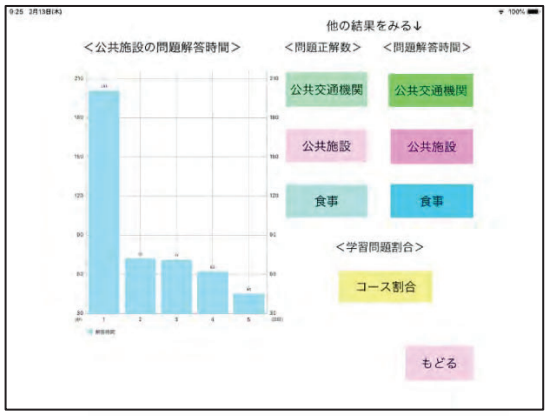

Figure 21. Number of Correct Answers (Manners)

Example of Using Application

This section will show an example and briefly report on the button adjustment for special needs children, the comparison results between the application and paper media, and the identification of child characteristics using the collected data. In this application, a prototyped function that can change the size, color, image, and text of the buttons as an adjustment function for special needs children is created. The button setting screen is shown in Figure 22. The developed prototype is based on the request that a certain number of children cannot tap the buttons well due to physical disabilities or cannot engage in interesting activities if the buttons are only the same color or text.

Figure 22. Button Setting Screen

There was a case where a child with a hand disability tried to use the application shown in Fig. 2-6 but could not tap the buttons properly due to their small size. Therefore, we adjusted the size of the buttons from the settings screen (Fig. 23).

Figure 23. Button Resizing

This is just an example. However, there was an example where this operation improved the false tap rate from 56% to 98%. Fig. 24 shows the comparison results between using the manner learning app and learning on paper. Create three groups: a group that learns using the application (Group A), a group that learns using a sorting chart on paper (Group B), and a group that does not do any prior learning (Group C). A total of 37 students, 16 general students (average age: 20.5 years), and 21 special needs children (average age: 11.7 years) will be assigned to these groups. Except for Group C, the students will study in advance using the respective media and then answer ten questions. These problems were common to all three groups. A t-test was conducted on these results. The test results showed that the p-value was 16 [%] for the general students and 0.01 [%] for the special needs children. The results show that the number of correct answers was higher using the app than using paper. The effect was better for the special needs children.

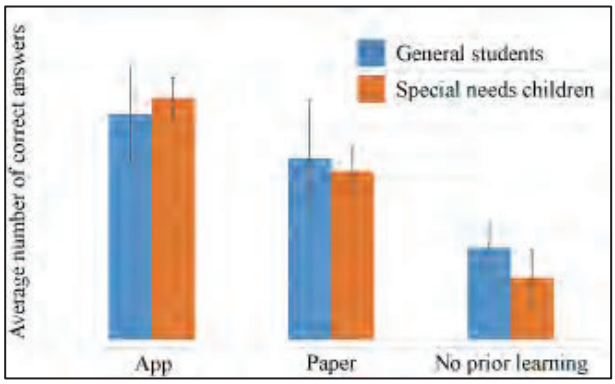

Figure 24. Experiment Comparing Manners Learning App and Paper Media Learning

While some of the supported children are more efficient in using the app, others are not as affected. A graph of usage for two students is shown in Fig. 25.

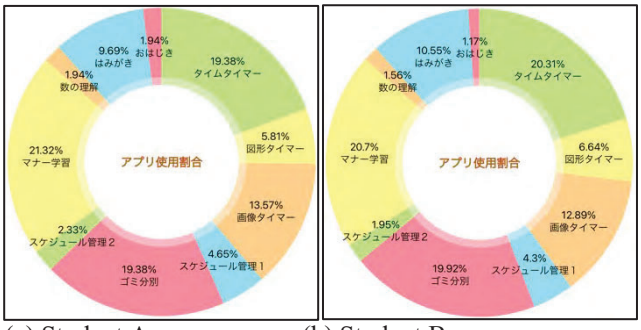

(a) Student A (b) Student B

Figure 25. App Usage by Two Students

From this graph, it appears that they are learning in the same way. However, the graph of the number of correct answers for the manner learning application shows a different result (Fig. 26).

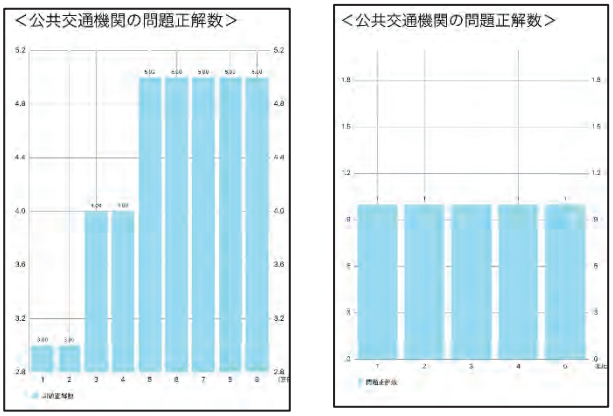

(a) Student A (b) Student B

Figure 26. Number of Correct Answers

For student A, the number of correct answers increased as the number of times they studied increased, but the number remained constant for student B. Each time, the setting of the manner learning application in this example was such that the same question was presented, but student B answered in the same pattern. The number of correct answers for the garbage separation learning application was also constant, and the student answered in the same pattern each time. The student was able to use the timer application and the tooth brushing application correctly.

Discussion

Some students were able to improve their use of the application by using individual settings.

In the experiment shown in Fig. 24, students who could not use the app in its normal state were excluded from the target, but the individual setting function may loosen the restriction of users. Regarding Fig. 25-26, this is an example of how the students use the app without any problem at first glance, but by checking multiple data, a problem was found. Tablet apps have a high affinity with special needs children, but not all patterns are effective. While it is imperative to make them easy to use through settings, it is also essential to choose tools other than apps according to the characteristics of students. If students' characteristics, strengths, and weaknesses can be extracted by collecting data through the aggregation of multiple tools, it will be effective for student guidance.

Conclusions

In this study, we examined a tablet application for children with special needs with multiple support functions. The possibility of easing the user limitation by the individual setting function was examined. In addition, the possibility of deriving the characteristics of users from the collected data was presented.

Acknowledgements

The Japan Society for the Promotion of Science through Kakenhi Grants (JP 19K11316).

References

Hamka, F. H., Bouwman, H., de Reuver, M., & Kroesen, M. (2014). Mobile customer segmentation based on smartphone measurement. *Telematics and Informatics*, 31(2), 220-227.

Lin, K. Y. (2016). User communication behavior in mobile communication software. *Online Information Review*, 40 (7), 1071-1089.

Khan S, Tahir MN, Raza A. (2013) . Usability issues for smartphone users with special needs—Autism. *Open Source Systems and Technologies (ICOSST)*, 2013 International Conference on; 2013: IEEE.

N. M. Sofian, A. S. Hashim, W. F. W. Ahmad. (2018). A review on usability guidelines for designing mobile apps user interface for children with autism, *AIP Conference Proceedings 2016*, 020094(1)-020094(6).

CASE STUDY OF CURRICULUM DESIGN OF COMPUTER PROGRAMMING RELATED TO ASSISTIVE TECHNOLOGY

M. Shimakawa[*,a], C. Okuma[a], K. Kiyota[a]

[a] National Institute of Technology (KOSEN), Kumamoto College, Kumamoto, Japan

[*] shimakawa@kumamoto-nct.ac.jp

Abstract

Assistive technology utilizing IT can widen the range of support for handicapped people. It is predicted that the needs for assistive technologies will increase in the future. In order to provide assistive devices, it is necessary to train engineers who are familiar with computer programming and also related IT field and can develop them. This paper introduces the curriculum design of computer engineering, especially computer programming, of an IT department in National Institute of Technology (KOSEN), Kumamoto College.

The department is named "Department of Human-Oriented Information Systems Engineering", aims to train IT engineers who are familiar with IT fields with having creativity and rich emotion. The computer programming education is in a five-year consistent curriculum and is structured so that students can acquire programming skills from the 1st grade to the 3rd grade and apply them into specialized subjects in the 4th and 5th grades. In addition to the general subjects found in the fields of information science and computer engineering, it has it includes distinctive specialized subjects such as "Human and Environmental Engineering", "Assistive Engineering", "Human Information Processing", and so on. Furthermore, laboratory experiments and exercises have themes that treat biometric information signals. Some students conduct study and development of assistive devices for people with disabilities in their graduation research. Computer programming education is positioned as a fundamental and important part of this curriculum.

The 1st graders begin programming with Processing language, and the 2nd and 3rd graders use the C language and Python to acquire programming skills. In addition, as advanced acquisition of programming skills, there are also subjects using Java, JavaScript, and R language in the 4th and 5th grades. This paper shows that the curriculum of the department fits to curriculum standard in computer engineering, and introduces such subjects related to computer programming, their relevance to other subjects, and specific examples.

Keywords: *curriculum design, computer programming, programming education, computer engineering, assistive technology*

Introduction

Supporting people with disabilities and elders is a major public issue. The fact sheet of WHO (2020) said,

> *"Over 1 billion people are estimated to live with some form of disability. This corresponds to about 15% of the world's population, with up to 190 million (3.8%) people aged 15 years and older having significant difficulties in functioning, often requiring healthcare services. The number of people living with disability is increasing, in part due to ageing populations and an increase in chronic health conditions."*

Assistive technology can widen the range of support for such people. For example, Kiyota, K., et al (2017) developed a note-taking system that recognizes Japanese character hand-written by visually impaired. Shibasato, K., et al (2017) have proposed RFID-implemented teaching materials such as picture matching games for challenged students with disabilities in special schools. Shimakawa, M., et al (2020) developed a smartphone app that detects obstacles and alert dangerous situation to visually impaired user. Like these studies, it is expected furthermore that assistive technologies utilizing IT will support handicapped people. In order to provide useful assistive devices, it is necessary to train engineers who are familiar with computer programming and also related IT field and can develop them.

National Institute of Technology (NIT) is a higher education institution that provides consistent engineering education for five years from the age of 15. It is a characteristic education system that originated in Japan and is neither high school nor university. NIT organizes 51 colleges (a.k.a. KOSEN) that are scattered all over Japan. Kumamoto College, to which the authors belong, is one of them. Each NIT college has 3 to 6 departments in technology, and some college has also a maritime technology department. The departments of each college educate students on their own curriculum, but it satisfies the model core curriculum (MCC) that is defined as minimum standard in which the graduates should achieve

in each major field. Aburatani, H. (2019) introduced the MCC and compared with CDIO Standard and Syllabus.

This paper introduces the curriculum design of computer engineering, especially computer programming, of an IT department in Kumamoto College. The department is named "Department of Human-Oriented Information Systems Engineering" (abbreviated as HI department), aims to train IT engineers who are familiar with IT fields with having creativity and rich emotion. This department was established in 2010 by the department reorganization due to the integration of two colleges.

Curriculum of HI department

First, here introduces about categories of subjects in the HI department. Figure 1 shows subject categories and their credits for each grade. The number of credits for liberal subjects is highest in the first grade and decreases as the grade goes up. On the conversely, the credits of major subjects increase. Students are required to earn at least 167 credits to graduate. Graduates are given the title of associate bachelor degree.

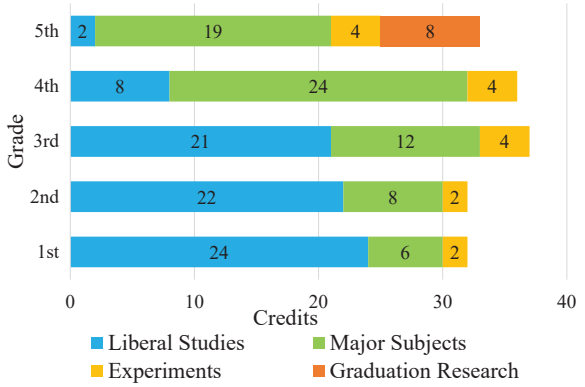

Figure 1. Subject categories and credits.

When the HI department was established in 2010, specialized subjects were selected with reference to the computing curriculum standard J07 formulated by Information Processing Society of Japan, IPSJ. (2008). J07 was based on the Computing Curricula of ACM/AIS/IEEE-CS (2005). that was a world standard. IPSJ reviewed them according to the situation of information technology education in Japan, and defined five disciplines of computing:

- Computer Science (J07-CS),
- Information System (J07-IS),
- Software Engineering (J07-SE),
- Computer Engineering (J07-CE),
- Information Technology (J07-IT),

and

- General Education in Information (J07-GE).

After that, the Computing Curricula has been revised by ACM/IEEE-CS and related societies. The task forces of each discipline had revised curriculums, like CS2001, CS2008 to CS2013 in Computer Science, and CE2004 to CE2016 in Computer Engineering, ACM/IEEE-CS (2016). ACM/IEEE-CS. (2020) released the Computing Curricula CC2020 as the latest version. On the other hand, IPSJ also revised the computing curriculum standard from J07 to J17, IPSJ (2017).

Figure 2 shows a framework to illustrate the commonalities and differences among computing disciplines. The horizontal range runs from Theory, Principles, Innovation on the left, to Application, Deployment, Configuration on the right. The vertical range runs from Computer Hardware and Architecture at the bottom, to Organizational Issues and Information Systems at the top. Each of the five computing disciplines is located on the framework.

The curriculum of the HI department is well aligned with Computer Engineering (CE) because it referred to the model curriculum of J07-CE/CE2004. This model curriculum was developed by first defining the primary disciplines that make up the body of knowledge for computer engineering. In CE2004, the computer engineering body of knowledge was divided into 18 areas. However, in CE2016, the areas that contain material that should be included in all computer engineering curricula are rearranged 12 knowledge areas as follows:

- Circuits and Electronics (CAE),
- Computing Algorithms (CAL),
- Computer Architecture and Organization (CAO),
- Digital Design (DIG),
- Embedded Systems (ESY),
- Computer Networks (NWK),
- Preparation for Professional Practice (PPP),
- Information Security (SEC),
- Signal Processing (SGP),
- Systems and Project Engineering (SPE),
- System Resource Management (SRM),
- Software Design (SWD),

and then J17-CE added more

- Innovation and Venture (JIV).

Table 1 shows specialized subjects of the HI department and comparison with knowledge areas in J17-CE/CE2016. It is found that the specialized subjects satisfy the computer engineering knowledge areas moderately well as a whole, even if each subject does

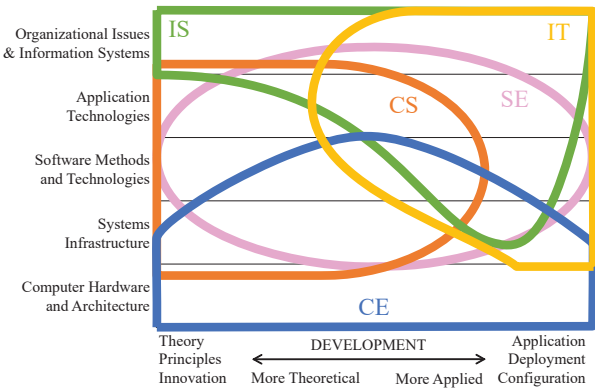

Figure 2. Five disciplines on the problem space of computing (cited from CC2005 overview).

Table 1. Specialized subjects of HI department and comparison with knowledge area in J17-CE/CE2016.

Grade	Specialized Subjects	J17-CE/CE2016												
		CAE: Circuits and Electronics	CAL: Computing Algorithms	CAO: Computer Architecture and Organization	DIG: Digital Design	ESY: Embedded Systems	NWK: Computer Networks	PPP: Preparation for Professional Practice	SEC: Information Security	SGP: Signal Processing	SPE: Systems and Project Engineering	SRM: Systems Resource Management	SWD: Software Design	JIV: Innovation and Venture
1st	Basic Electricity I	●												
	Computer Engineering I				●									
	Computer Literacy		●											
	Basic Exercises for IT I	●	●		●									
2nd	Basic Electricity II	●												
	Computer Engineering II				●									
	Computer Programming I		●											
	Basic Exercises for IT II	●	●		●									
3rd	Electrical Circuits	●												
	Electronic Circuits	●												
	Computer Architecture			●										
	Human and Environmental Eng.													
	Computer Programming II		●											
	Experiments in Info. and CS I	●	●		●								●	
4th	Applied Mathematics I													
	Applied Physics													
	Electromagnetism													
	Embedded System					●								
	Numerical Computation		●											
	Signal Processing									●				
	Data Structure and Algorithms		●										●	
	Information Network						●							
	Operating System											●		
	Experiments in Info. and CS II	●	●		●								●	
	Assistive Engineering													
	Object Oriented Programming												●	
	Engineering English I													
	Internship							●						●
5th	Applied Mathematics II													
	Systems Engineering		●								●			
	Information Mathematics		●											
	Information Theory								●					
	Information Security								●					
	Engineering Ethics							●						
	Experiments in Info. and CS III		●		●								●	
	Graduation Research	●	●	●	●	●	●	●	●	●	●	●	●	●
	Database												●	
	Mathematical Information Eng.		●											
	Visual and Speech Processing									●				
	Human Information Processing													
	Engineering English II													

not completely match the knowledge area. Some subjects colored in gray are not directly related to the CE knowledge areas, however among them include the subjects that characterize this HI department, such as

- Human and Environmental Engineering (3rd grade),
- Assistive Engineering (4th grade),
- Human Information Processing (5th grade).

The HI department curriculum, which consists of such specialized subjects, also satisfy the model core curriculum (MCC) that is formulated by National Institute of Technology as minimum standard in which the graduates should achieve in their major field. The MCC (2017) presented the learning items shown in Table 2 as the specialized abilities for IT engineers.

Table 2. Learning items as the specialized abilities for IT engineers in MCC (2017).

V-D-1. Programming - Programming Elements - Programming - Programming Language Processing - Computing Model - Practical Programming	V-D-2. Software - Algorithms - Data Structure - Software Engineering - Program Analysis
V-D-3. Computer Engineering - Numbers - Binary Logic - Logic Circuits - Sequential Logic - Computer Hardware - Hardware Design	V-D-4. Computer Systems - Computer System - System Design
V-D-5. System Programming - Operating System - Compiler	V-D-6. Information Communication Network - Network Layer Protocol - LAN and Internet - Network Application
V-D-7. Information Math and Information Theory - Discrete Mathematics - Discrete Mathematics Application - Numerical Processing and Error - Numerical Computation - Information Theory	V-D-8. Other Related Items - Fundamentals of Electronic and Electronics - Information Literacy - Information Security - Database - Media Processing
VI-D. Experiments and Practical Exercises - Programming - Logic Circuit Design - Software Development Environment - Application Design and Development	

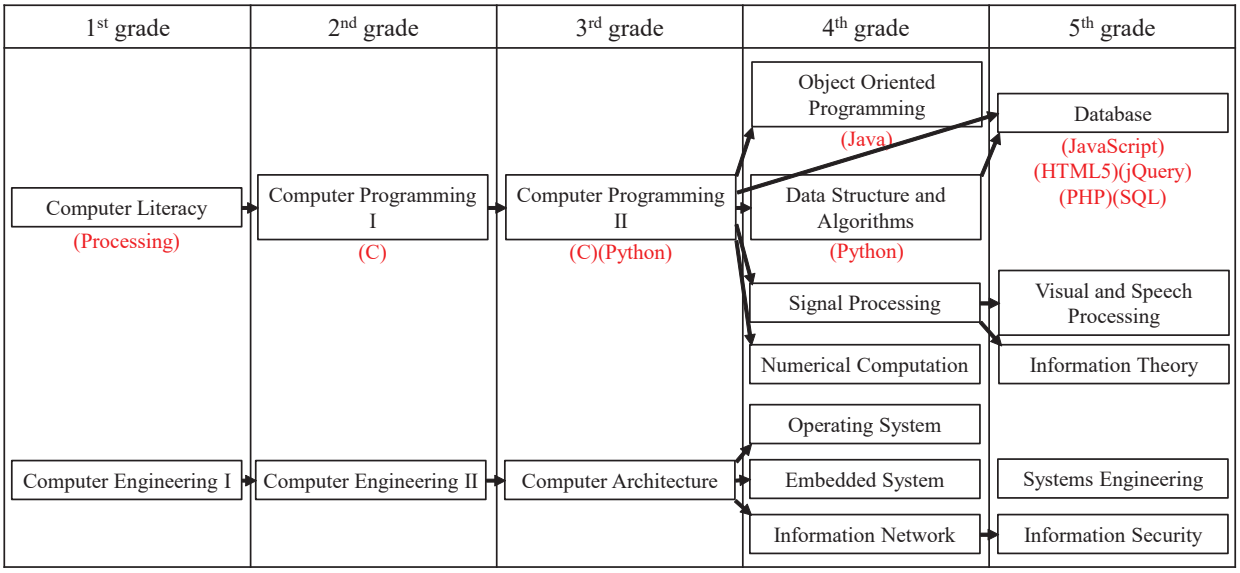

Figure 3. Genealogy of specialized subjects in HI department related to computer programming and computer engineering.

Relationship with Assistive Technology

Figure 3 shows a genealogy of specialized subjects in HI department related to computer programming and computer engineering. Students in this department begin programming with Processing language in Information Literacy class in their first grade. Then, they learn C language for two years in Computer Programming class and acquire basic skills firmly. In 4th and 5th grades, furthermore, they learn other programming languages and apply them to other fields. While they learn about programming, they also acquire the knowledge related to human informatics.

For example, when learning about file I / O and graph display, they use Electroencephalography (EEG) data. 5th-grade students experiment there is a theme of brain waves measured. It is to observe the change in brain activity using an EEG shown in Figure 4(a). Students make a program that read a file of the EEG data and display a graph of its moving average using Python in 3rd grade, Figure 4(b). It not only learns programming skills, but also gives them an interest in human informatics.

(a) EMOTIV® EPOC+

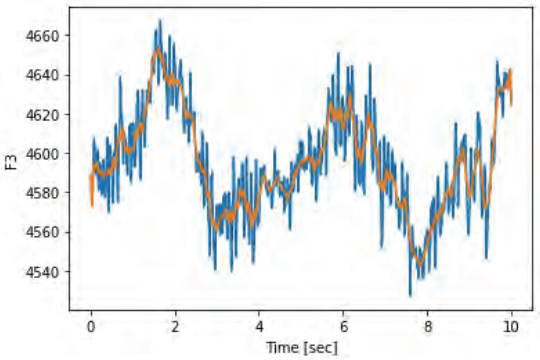

(b) Moving average of an EEG data

Figure 4. Python programming using EEG data.

In Embedded System in 4th grade, students learn the fundamentals of human interaction using microcontroller Arduino. Figure 5 shows a circuit for checking the operation of a motion sensor light using PIR (Passive Infrared Ray) sensor. This is a very simple example, but understanding human characteristics is important for assistive technology.

Here, we would like to introduce two cases related to assistive technology that students conducted as graduation research. First one is a smartphone application for visually impaired, Shimakawa, M., et al. (2019). This app uses CNN, a one of Deep Learning, to

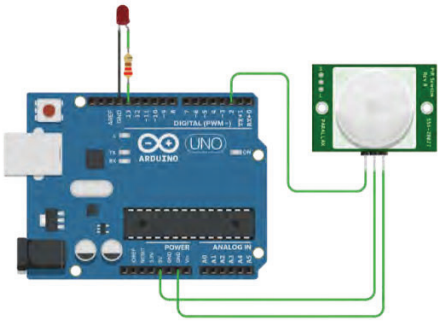

Figure 5. A circuit using Arduino for checking the operation of a motion sensor light.

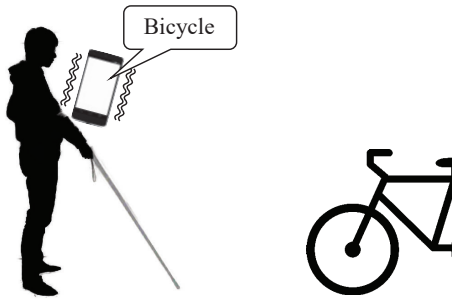

(a) Concept image

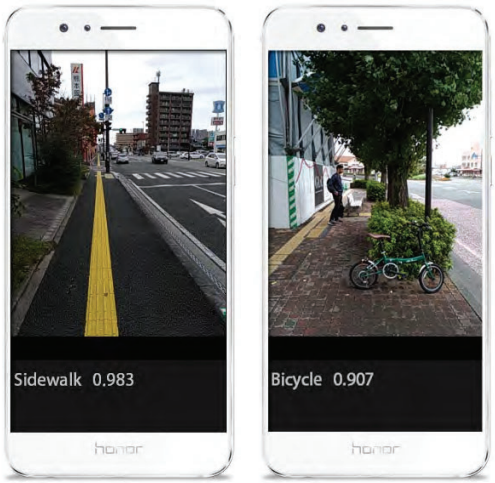

(b) Experimental results of obstacle detection

Figure 6. Smartphone application of obstacle detection for visually impaired.

detect obstacles that prevent walking, and alert the situation in dangerous. Figure 6(a) shows the concept of this app, and Figure 6(b) shows partial results of obstacle detection experiment.

Second one is a pen-based memorandum system named "*Pen-Talker*" for blind user. People with acquired blindness know how to write characters, however, it was difficult to recognize because the character structure tended to be broken as shown in Figure 7(a). This system allowed the input of such handwritten characters directly, Figure 7(b). It makes blind user easy to input Japanese characters instead of a keyboard without well training in this system.

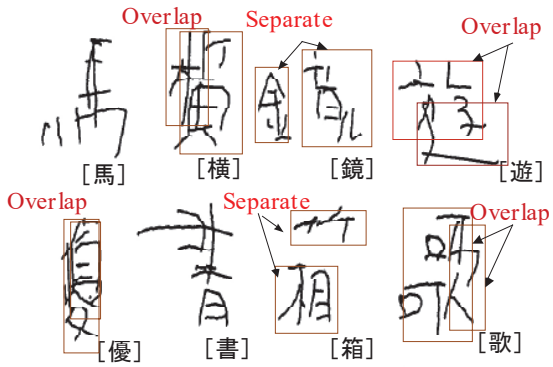

(a) Examples of Japanese handwriting character written by acquired visually disabled person.

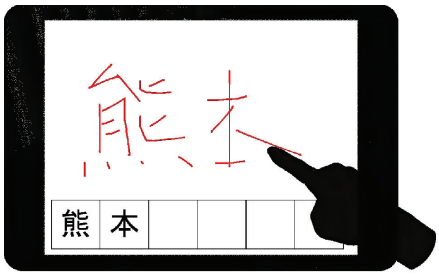

(b) Handwritten character recognition

Figure 7. Pen-based memorandum system "*Pen-Talker*" for blind user.

Conclusions

In this paper, we introduced the curriculum of the HI department of NIT (KOSEN), Kumamoto College and showed that it complies with the Computing Engineering Curricula CE2016 formulated by ACM/IEEE and the Computer Engineering Curriculum Model J17-CE formulated by IPSJ. We also showed that the curriculum meets the model core curriculum (MCC) formulated by NIT. It can be seen that the HI department curriculum, if not perfect, fits to the field of computer engineering from these facts.

We showed two examples of student graduation research related to assistive technology. Like this way, assistive technologies utilizing Information Technology are expanding the scope of support for people with disabilities. The HI department curriculum is not specialized in assistive technologies. However, there are some specialized subjects related to human informatics, and computer programming classes dealt with biometric information while learning programming skill. It is believed that such attempts have motivated students' interest in assistive technology.

The most important thing when applying assistive technology to people with disabilities is to clarify what they are looking for. The ability to analyze and to correctly define what their requests are is required. The same is true for development of software and computer system.

In future works, we should like to examine the adequacy of the curriculum more deeply and present curriculum standards in the field of computer engineering related to assistive technologies.

References

Aburatani, H. (2019). Comparison between NIT KOSEN Curriculum and CDIO Standards and Syllabus. *Proc. of the 15th International CDIO Conference*. Retrieved from http://www.cdio.org/files/document/file/118.pdf

ACM/AIS/IEEE-CS (2005). Computing Curricula CC2005. The Overview Report. *The Joint Task Force for Computing Curricula 2005*. Retrieved from https://www.acm.org/binaries/content/assets/education/curricula-recommendations/cc2005-march06final.pdf

ACM/IEEE-CS. (2016). Computer Engineering Curricula CE2016. Retrieved from https://www.acm.org/binaries/content/assets/education/ce2016-final-report.pdf

ACM/IEEE-CS. (2020). Computing Curricula CC2020. Retrieved from https://www.acm.org/binaries/content/assets/education/curricula-recommendations/cc2020.pdf

EMOTIV. Mobile EEG EPOC+ Retrieved from https://www.emotiv.com/epoc/

IPSJ. (2008). Overview of Computing Curriculum Standard J07. IPSJ Magazine, Vol.49, No.7, pp.721-727. (*in Japanese*)

IPSJ. (2017). Computing Curriculum Standard J17. Retrieved form https://www.ipsj.or.jp/annai/committee/education/j07/curriculum_j17.html (*in Japanese*)

Kiyota, K., et al. (2017). Practical Application of a Pen-based Notepad System for the Visually Disabled. *Proc. of the 5th IIAE International Conference on Intelligent Systems and Image Processing 2017* (ICISIP2017), pp.496-499.

MCC. (2017). Model Core Curriculum Guideline for National Institute of Technology (KOSEN) (in Japanese), retrieved from NIT Website: https://www.kosen-k.go.jp/Portals/0/MCC/mcc2017all.pdf

Shibasato, K., et al (2017). Development of Picture Matching Material using RFID for Challenged People. *Proc. of the 5th IIAE International Conference on Intelligent Systems and Image Processing 2017* (ICISIP2017), pp.479-485.

Shimakawa, M., et al. (2019). Smartphone Application Program of Obstacle Detection for Visually Impaired People. *ICIC Express, Part B: Applications*, Vol.10, No.3, pp.219-226.

WHO (2020). Disability and health. *Fact sheet*. Retrieved from https://www.who.int/news-room/fact-sheets/detail/disability-and-health/

CDIO Approach based Educational Project of Sensor Fusion for Assistive Technology

Kosei Nojiri*[,a], Hirofumi Ohtsuka[a], Daichi Arai[a] and Etsuo Horikawa[b]

[a] National Institute of Technology (KOSEN), Kumamoto College, Koshi, Japan
[b] Fukuoka International University of Health and Welfare, Fukuoka, Japan

*nojiri@kumamoto-nct.ac.jp

Abstract

National Institute of Technology (KOSEN), Kumamoto College has been accepted to join the "CDIO Initiative" in 2019. While our educational curriculum had established with several subjects and practices, including conceiving/design/implement via active learning, taking this opportunity, we started the project development for the comprehensive technical training that covers the operation stage. That is, it is an effort to educate engineers through social implementation-type research and development that allows them to experience a series of processes of idea creation, design, development, implementation, and operation for actual social needs. The specific example to be reported is the result of the implementation in the final grade of the 5-year course. The task set for the target students is to build a platform that integrates and synchronously collects data groups output from image sensors, mechanical sensors, and so on, which are often used in the field of welfare support equipment development. The purpose of the development is to simplify the analysis by sensor fusion. It is based on the needs of medical personnel who have abundant medical judgment experience regarding driving a car for the elderly. By carrying out the project with the advice and feedback from him, we could repeat the CDIO process based on practical stage issues after proceeding to the implementation stage. A time-synchronized data set is created by simultaneously collecting output data from multiple cameras that capture the person's physical behaviour to be measured and multiple mechanical sensors attached to the person or the device to be operated. It is necessary to deal with the data collection work even if it is performed indoors / outdoors or inside a moving vehicle. Considering these conditions, the students prepared multiple Raspberry Pis, which are cheap and easy to obtain, and conceived and realized a system to link them. Moreover, the user interface system was developed to improve the operation convenience, and the set task was almost completed. This report presents this initiative's effectiveness by introducing the results in detail while also showing the progress of this project.

Keywords: *CDIO, time-synchronized data collecting system, Sensor Fusion, Assistive Technology*

Introduction

In June 2019, National Institute of Technology (KOSEN), Kumamoto College, to which the authors belong, has been accepted to join the "CDIO Initiative". CDIO stands for Conceive, Design, Implement and Operate, a concept developed to reform engineering education, and is the trademark of Conceive Design Implement Operate. The "CDIO Initiative" is an innovative educational framework for producing the next generation of engineers. The framework provides students with an education stressing engineering fundamentals set in the context of Conceiving, Design, Implement and Operate (CDIO) real-world systems and products. Throughout the world, the "CDIO Initiative" collaborators have adopted CDIO as the framework of their curricular planning and outcome-based assessment. CDIO collaborators recognize that an engineering education is acquired over a long period and in a variety of institutions, and that educators in all parts of this spectrum can learn from practice elsewhere[1].

In the past, in the curriculum for engineer training, we had prepared active learning and practice subjects including design and implementation to improve the creation ability. When we joined the "CDIO Initiative", we started to develop a project for fostering comprehensive technological skills, including operation. In other words, we have accelerated our efforts to educate engineers through research and development of a social implementation type that allows students to experience a series of processes from idea generation, design, development, and implementation operation in response to actual social needs.

The first and second authors are collaborating with Prof. Horikawa et al. of Fukuoka International University of Health and Welfare to develop a system for allowing or disallowing driving for elderly people and people recovering from brain function diseases. In order to develop the system, information on the front and rear of the vehicle, the driver's situation, i.e., gaze, face direction and steering wheel operation, the driver's gas/brake pedal operation and vehicle behaviour, in other words, the position and posture of the vehicle, is essential. Before

the joint research, Prof. Horikawa et al. had been collecting such information using commercially available video cameras and drive recorders developed by several manufacturers. However, since it was necessary to use a combination of different devices to collect the desired data, the cost of installing the devices in the vehicle and the cost of analysis after collecting the various data was high, and a considerable amount of time and effort was required to compile the analysis results.

We consider this joint research to be a social implementation type of research and development, and as an example of our approach to engineer education, we had the students experience the series of processes of idea generation, design, development, and implementation operation in response to the needs of Prof. Horikawa and others. The specific case reported here is the result of a project conducted in the final year of a five-year course at a technical college.

The task set was to build a platform for integrated synchronous collection from image sensors and mechanical sensors, which are frequently used in the field of welfare support equipment development. The objective of this project is to simplify the analysis by sensor fusion by using multiple cameras to capture video of the person's physical behaviour to be measured and simultaneously acquiring data sets from multiple mechanical sensors attached to the person himself and the device he is operating. With his advice and feedback, we carried out the project and advanced to the implementation phase, and then repeated the CDIO process based on the issues presented in the practical phase.

Since existing multi-sensor data synchronous collection systems are very expensive and rare on the market, and since data collection work needs to be done indoors, outdoors, and even inside a moving car, the students took these conditions into consideration and developed a system that uses multiple small microcomputers The system was designed and realized by linking multiple Raspberry Pi computers. Furthermore, a user interface system for data collection was additionally developed to improve the convenience of operation, and an integrated multi-data synchronous collection platform was almost completed.

In this report, we will show the effectiveness of our efforts by introducing the implementation results in detail while also presenting the results of this project in the middle.

Proposal multi-data synchronous collection platform

The overall configuration of the proposed system is shown in Figure 1.

This system consists of one or more Raspberry Pi 4, one M5 Stack Core2 to control Pi4, a camera and various sensors connected to Pi4 by USB, and a USB memory for data collection. Pi 4 and M5 Stack Core2 are connected to Wi-Fi. The Wi-Fi router needs to be connected to the Internet in order to acquire the time of the devices.

The Operating system of the proposed system is in the Micro SD card installed in the Raspberry Pi 4. The USB memory has a recording program, setting files for various sensors and Wi-Fi connections, and folders for saving acquired data and logs.

As the controller of the system, M5 Stack Core2 equipped with a small display and a microcomputer that can connect to Wi-Fi is used, and the user can operate Pi 4 and check the logs after starting data acquisition. There is the setting program in a Micro SD card.

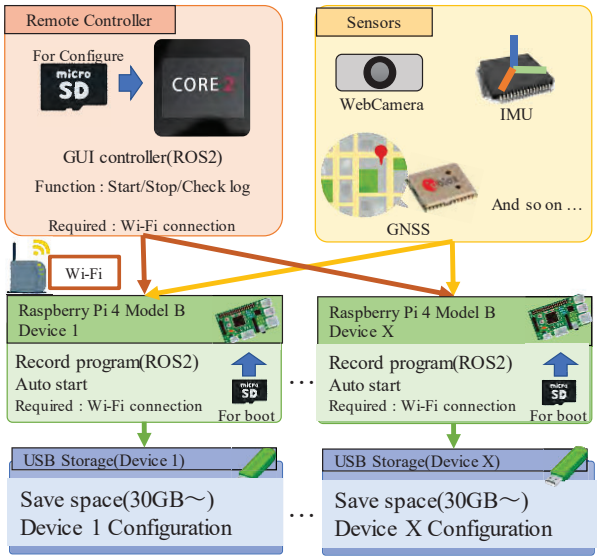

Figure 1. Data acquisition system diagram.

The operation of the system will be explained using one Raspberry Pi 4 as an example. The green frame in Figure 2 shows the operation order.

First, the operation of the controller will be explained. The controller starts by pressing the power switch on the left side and turns it off by pressing and holding for about 6 seconds. When it starts up, it first reads the information in the configuration file on the SD card and tries to connect to Wi-Fi. After connecting to Wi-Fi, gets the time from the NTP server. Then, try to connect to Raspberry Pi 4 based on the IP address of Raspberry Pi 4 described in the configuration file. Once the connection is complete, recording can be started by performing a recording start/end operation. During operation, the scheduled start time is always sent and log data is received by the controller.

Operation display of the controller is shown in Figure 3.

Next, the operation of Raspberry Pi 4 will be explained. Raspberry Pi 4 starts automatically when a 5V power supply is applied. At present, the power is applied manually, but by creating a power supply system using relays, it can be started with a single switch. A shutdown of Raspberry Pi 4 is performed by pressing and holding the red switch of "Reboot / Shutdown button" in Fig. 2 for 5 seconds after starting the system. After Raspberry Pi 4 starts up, it reads the settings from the USB memory and sets Wi-Fi and each sensor. When all the settings are

applied, launch the ROS2 recording program. This program receives the scheduled start time "/start_time" sent from the controller and the data sent from the sensor driver and sends the log "/log_at2" to the controller.

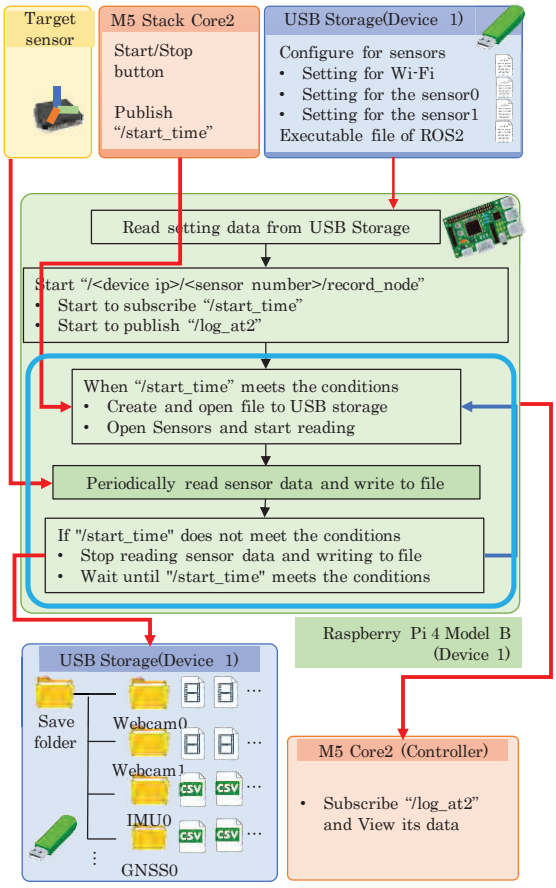

Figure 2. Software diagram.

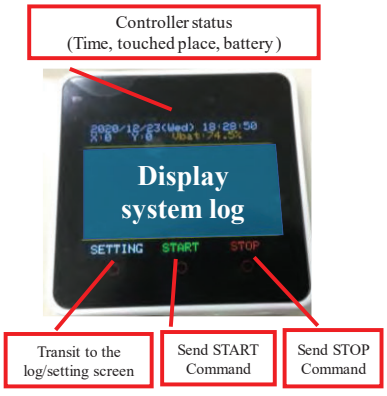

Figure 3. Operation display of the controller.

The recording start timing is determined by comparing the scheduled recording start time transmitted by the controller with the current time. When the user presses the start button of the controller, the update of the scheduled recording start time is stopped and recording is started. Also, the recording is ended by press the end button.

The save destination folders are divided for each sensor, and the video and CSV format save files are saved separately according to the recording start time. Fig. 4 shows the system connection.

For Proposal platform

We conducted an evaluation experiment of the platform developed by the students in this project.
The evaluation experiment was limited to a straight driving path, and the driving behaviour under the following conditions was analysed.
(a). overtaking a pedestrian
(b). One pedestrian is coming from the opposite side of the vehicle.
(c). A pedestrian jumps out from the left side of the vehicle.
(d). A pedestrian jumps out from the right side of the vehicle.
(e). A pedestrian overtakes a stopped vehicle on the left side as seen from the vehicle.
(f). A pedestrian jumps out from the left side after overtaking a stopped vehicle on the left side as seen from the vehicle.

The vehicle used in the evaluation experiment was a single-seater electric vehicle, COMS, manufactured by Toyota Auto Body. The subjects, or drivers, were two men, one in his early 40s and one in his early 20s.

The data to be collected are images of the front and rear of the vehicle, the driver's face and arms, and the driver's feet taken by each of the four webcams, as well as the vehicle's longitudinal and lateral acceleration and yaw angle using Realsense's T265 tracking camera.

Results and Discussion

The images from the four webcams and the vehicle's longitudinal and lateral velocity and yaw angle were displayed and analyzed as shown in Figure 4 through 9.

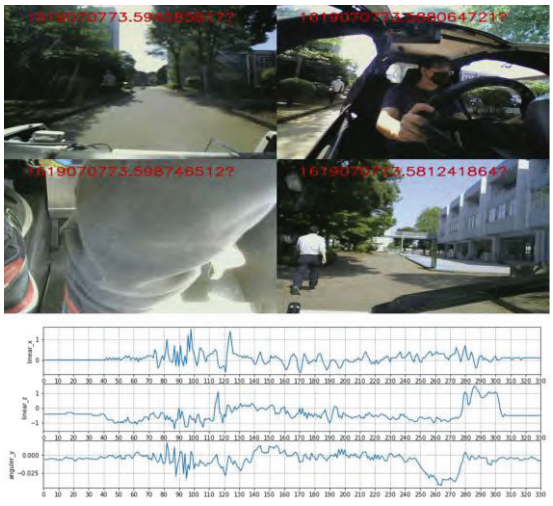

Figure 4. Example of a driver in his early twenties in experiment (a).

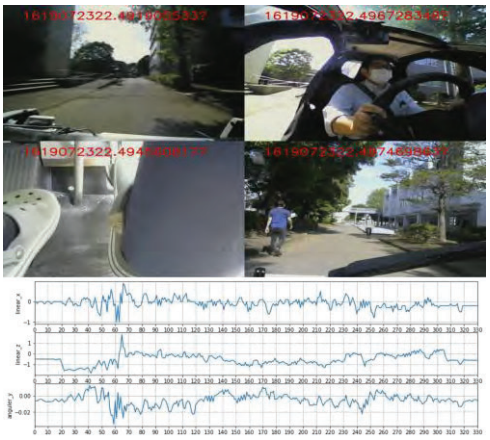

Figure 5. Example of a driver in his early 40s in experiment (a)

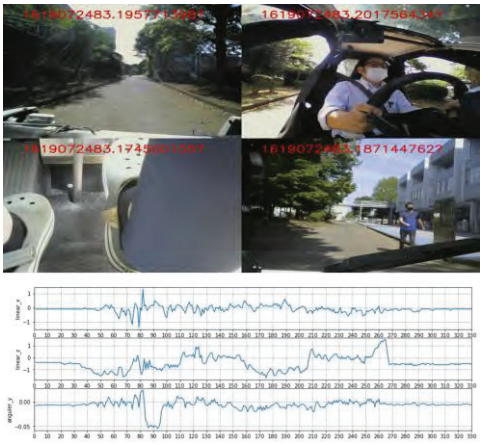

Figure 6. Example of a driver in his early 40s in experiment (b)

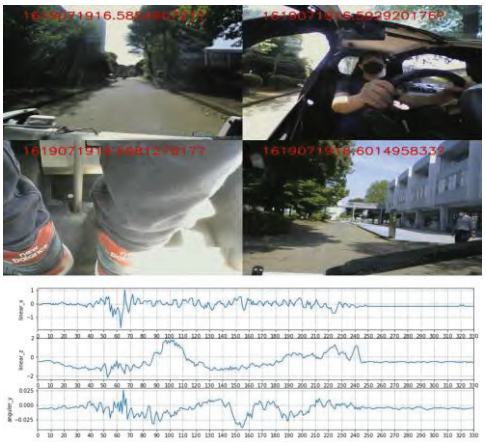

Figure 7. Example of a driver in his early twenties in experiment (d).

From the results shown in Figure 4 to 8, we believe that it is possible to evaluate the synchronous collection of camera and sensor data and the differences caused by the driver and driving conditions.

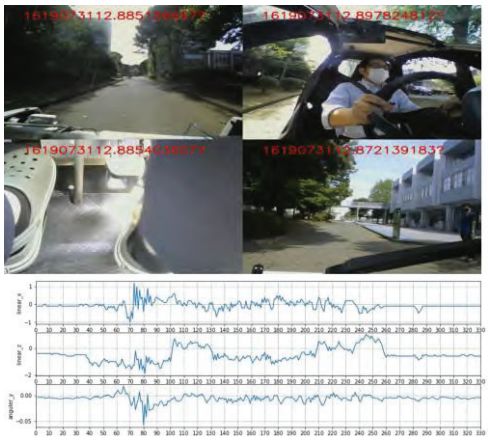

Figure 8. Example of a driver in his early 40s in experiment (d).

Figure 9. Example of a driver in his early twenties in experiment (e).

Conclusions

This report presented this initiative's effectiveness by introducing the results in detail while also showing the progress of this project.

Future works include further data collection and stabilization of data collection, such as increasing the number of subjects, as well as improving the platform and display for analysis based on feedback from Professor Horikawa and others.

References

"CDIO", http://www.cdio.org/

Daichi Arai, Kosei Nojiri, and Hirofumi Ohtsuka : “Basic Design of Integrated Data Collection Platform for Drive Assistant System Development”, Proceeding of Japan Society for Welfare Engineering, Kyushu Branch, pp.32-33, 2020

"ROS2 documentation", 2020, https://index.ros.org/doc/ros2/

Image Correction Methods of Cirrhosis Liver Classification on CNNs

Yoshihiro Mitani[*,a], Robert B. Fisher[b], Yusuke Fujita[c], Yoshihiko Hamamoto[c], and Isao Sakaida[c]

[a] National Institute of Technology, Ube College, Ube, Japan
[b] Edinburgh University, Edinburgh, UK
[c] Yamaguchi University, Ube, Japan

*mitani@ube-k.ac.jp

Abstract

We examine the effect of the image quality of the region of interest(ROI) image by image correction methods on a convolution neural network(CNN) in classifying a cirrhosis liver on B-mode ultrasound images. The experimental results show the effectiveness of the image correction methods by improving the image quality of ROI images. By ignoring the intensities less than a thresholding value of ROI images, the image quality improves and then the generalization ability of the CNN improves.

Keywords: *image correction, tone curves, image quality improvement, B-mode ultrasound images, cirrhosis liver classification, convolution neural networks*

Introduction

In a medical imaging field, a computer-aided diagnosis(CAD) (e.g., Doi, 2007) system which gives a second opinion is strongly needed. Ultrasound imaging is non-invasive and widely used for diagnosis of liver cirrhosis (Huber, 2015). The cirrhosis liver will be expected to progress to liver cancer in the worst case. Therefore, we are investigating a CAD system to diagnose a cirrhosis liver sooner (Sasaki, 2015; Mitani, 2020). In this study, we focus on classifying regions of interest(ROIs) on B-mode ultrasound images. Fig. 1 shows examples of ROI images. The ROI images are manually cut out from the liver areas, by the physician. Fig. 1 (a) and (b) show normal and cirrhosis livers. The size of ROI image is 32 by 32 pixels. The gray level is 8 bits. Thus, the value is ranging from 0 to 255. This is a typical 2-class problem, normal or cirrhosis. From this figure, it seems difficult to classify normal or cirrhosis by naked eyes of not physician because of noisy ultrasound images. In a previous study (Sasaki, 2015), we explored cirrhosis liver classification using a higher order local auto-correlation(HLAC) feature based approach which is known as a hand-crafted feature in the pattern recognition field. The HLAC feature approach produced the best performance among our experimental results. However, this experimental result showed that the average error rate was over 40%. Even the best performance conventional approach was not so good.

(a)Normal (b)Cirrhosis

Figure 1 ROI images.

Convolution neural networks(CNNs) are reported to be used widely in the medical imaging field (e.g., Litjens, 2017). We are expecting that the deep neural nets will be able to yield a good performance in this cirrhosis liver classification problem. One of defects of CNNs needs a lot of training samples. This leads to an over-training problem. In a previous study, we showed the effectiveness of the ROI image augmentation method by a perspective transformation. Apart from the ROI image data augmentation, we would also like to tackle a cirrhosis liver classification problem to improve the error rate on CNNs better.

Different from the conventional pattern recognition system, the CNN could work well by learning a combination of input images and output labels or class names. Thus, we may overlook the importance of obtaining the better image quality. In the pattern recognition field in general, the richer features we get, the better the performance of the pattern recognition system is. Any classifier could work well only if the features we get are better. Therefore, the amount of efforts has been devoted to get the better features. However, we have missed the efforts because the CNN learns automatically by feeding up a combination of input images and output labels. Therefore, we will focus on improving the image quality of ROI images to classify the cirrhosis liver. The cirrhosis liver is known to be harder. In this case, the brightness of ultrasound image of the cirrhosis liver could be lighter. Therefore, we are expecting that lighter regions of ROI images will have richer features in classifying cirrhosis liver. In order to highlight lighter regions of ROI images, we adopt the approach to cut the dark intensities. The image quality is expected to be better by using the image correction methods of tone curves (e.g., Raman, 2010). We are hoping that the improvement of the image quality leads to the decrease of the error rate of the cirrhosis liver classification on CNNs. In the experiments, we use some gray-level transformation functions, i.e., tone curves as the image

quality improvement. In this study, we used the tone curves which include 2 line-typed and 1 curved line-typed tone curves.

In this paper, we examine the effect of the image quality by image correction methods on CNNs in classifying a cirrhosis liver on B-mode ultrasound images. The experimental results show the effectiveness of the image correction methods by improving the image quality of ROI images. From the result, by ignoring the intensities less than a thresholding value of ROI images, the image quality improves and then the generalization ability of the CNN improves.

Methods

The performance of CNNs depends on its network structure and the parameters to be determined. First, we show the CNN architecture which is the same as Mitani (2020). The input of the CNN is the ROI image of size 32 by 32. Firstly, we convolve the ROI image by using 32 filters with a 3 by 3 filter size. And by 2 by 2 maxpooling, we reduce the ROI image size to a half-sized image, 16 by 16. Secondly, we repeatedly convolve and do max-pooling in the same manner. Then, we get 32 8 by 8 sized images. Thirdly, we flatten this image into 2,048(=32 by 8 by 8) dimensional data. Finally, we make a fully connected artificial neural network. The network has one hidden layer. The number of the neurons also depends on the classification performance. In the experiment, we used 100. Then we used dropout. The rate of dropout is 0.5. The number of the outputs of the CNN is 2. Therefore, the structure of the fully connected artificial neural network is 2,048-100-2. All the activation functions are ReLU except for the output. In the output, we used softmax. The learning optimizer is adam. The epochs and batch size are 100 and 400, respectively.

Second, we show image correction methods we used. We are expecting that lighter regions of ROI images will have richer features in classifying cirrhosis liver. Thus, we adopt the approach to cut the dark intensities. In this study, we used 2 line-typed and 1 curved line-typed tone curves as image correction methods (Raman, 2010). Fig. 2 shows tone curves we used. The notations *f* and *g* are intensities of input and output images, respectively.

Type I linear line

Type I linear line behaves the same as a linear line except for less than a thresholding point. When it comes to be less than a thresholding point, intensity values will be zero. That means they turn black and will be ignored.

$$g = \begin{cases} 0, & f < t \\ f, & otherwise \end{cases} \quad (1)$$

A thresholding value *t* is a cutting point. If *f* is less than *t*, the intensity of input image turns into 0. The intensities will disappear. We could change values *t* among from 0 to 255. If the value of *t* is 0, this means the intensities of input and output images are the same.

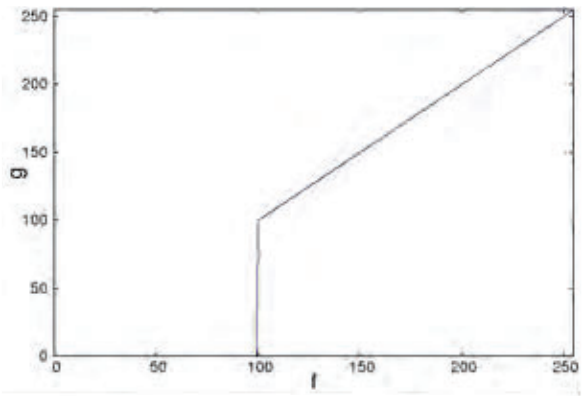

(a) Type I linear line (t = 100)

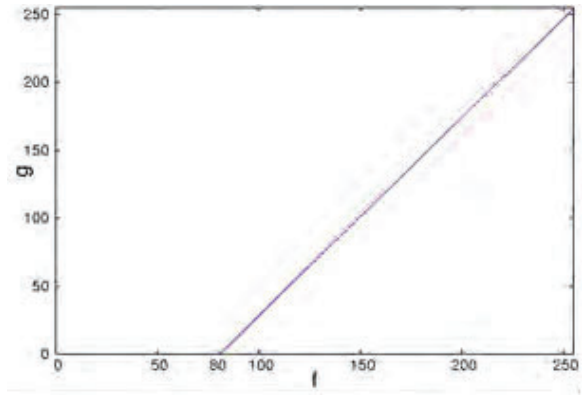

(b) Type II linear line (t = 80)

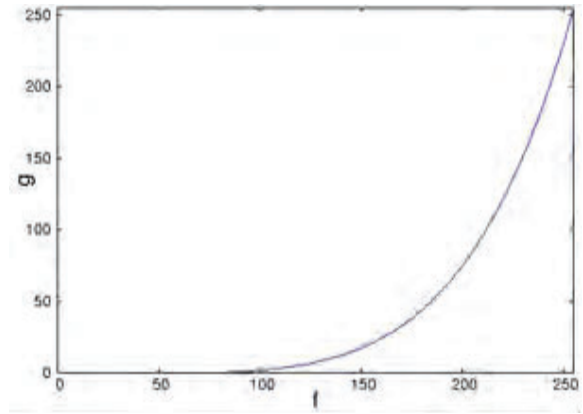

(c) Type III Gamma curve ($\gamma = 1/5$)

Figure 2 Tone curves we used.

Type II linear line

Type II linear line is alike Type I. When it comes to be equal to or more than a threshold, values of intensity will linearly increase. Otherwise, intensities will be zero.

$$g = \begin{cases} 0, & f < t \\ 255(f-t)/(255-t), & otherwise \end{cases} \quad (2)$$

A thresholding value *t* is a cutting point. If *f* is less than *t*, the intensity of input image becomes 0. The intensities

will disappear. We could change values t among from 0 to 255. If the value of t is 0, this means the intensities of input and output images are the same. These are the same of Type I.

Type III Gamma curve

Gamma curve is known as one of curved line-typed tone curves. It draws as not a linear line but a non-linear curve.

$$g = 255\left(\frac{f}{255}\right)^{\frac{1}{\gamma}} \quad (3)$$

We could control a degree of non-linearity by a value of γ. When a value of γ is equal to 1, the intensities of input and output images are the same. If a value of γ is less than 1, the image is getting dark. Otherwise, the image turns light.

In the experiments, we used ROI images made by these image correction methods. We tried investigating the effectiveness of with and without the image correction methods on CNNs in terms of the average error rate.

Results and Discussion

We used 500 available ROI images: 200 normal images and 300 cirrhosis images. The effectiveness of with and without the image correction methods on CNNs is examined in terms of the error rate. The error rate is defined as a ratio of the number of test images misclassified to the number of all test images.

$$\text{Error rate} = \frac{\#test\ images\ misclassified}{\#all\ test\ images} \times 100(\%) \quad (4)$$

For error rate estimation, the holdout method has been successfully used, because it maintains the statistical independence between the training and test images (Fukunaga, 1990). To evaluate the generalization ability of the CNN, the average error rate was obtained by the holdout method. Fig. 3 shows the flow of the error rate estimation. First, we randomly divided the 500 available ROI images into 400 training ROI images and 100 test ROI images. The 400 training ROI images consist of 160 normal and 240 cirrhosis ROI images. The 100 test ROI images consist of 40 normal and 60 cirrhosis ROI images. Second, we corrected the training and test images by the use of tone curves as described above, respectively. Third, we train the CNN using the training images and compute the error rate using the test images. Finally, by 5 repetitions, the average error rate and 95% confidence interval were obtained.

The purpose of the experiment is to investigate the generalization ability of the CNN without and with image correction methods of ROI images in terms of the average error rate. For Type I and Type II linear lines, values of t were varied from 20 to 160 every 20. For Type III Gamma curve, values of gamma were ranged among 1/10, 1/5, 1/3, 1/2, 1, 2, 3, and 5. Table 1 shows the

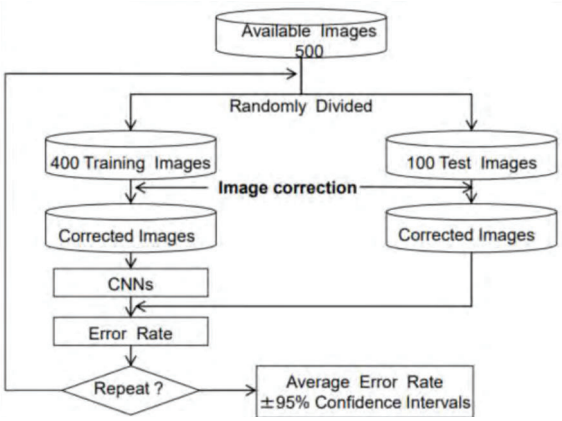

Figure 3 Error rate estimation by the holdout method.

Table 1 Generalization ability of the CNN without and with image correction methods, Type-I, II, and III.

CNN	Type-I	Type-II	Type-III
37.6	32.5	31.7	33.1
±4.1	±3.7	±5.2	±4.5

Upper: Average error rate(%), Lower: 95% confidence

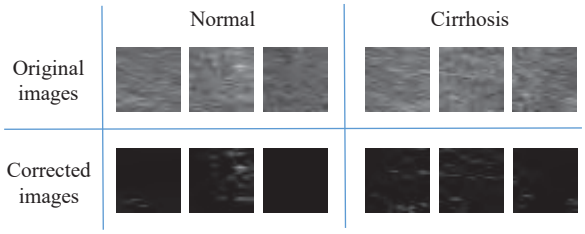

Figure 4 Difference between original and corrected ROI images for normal and cirrhosis liver using Type II(t=100).

generaliation ability of the CNN without and with image correction methods, Type-I, II, and III. From the results, we chose values which gave the minimum average error rates. Then the optimal values of Type I, II, and III are t=140, t=100, and γ=1/5, respectively. When it comes to use the image correction methods, Type I, II, and III, we see these methods are superior to that without image correction. In particular, Type II method shows the minimum error rate 31.7% and is most effective for classifying cirrhosis liver.

From the experimental results, the average error rate of Type II method shows the best. We need to evaluate the image quality by Type II method when t=100. We should be noted ignoring the intensities less than 100. Therefore, we tried observing the corrected ROI images by this image correction method. Fig. 4 shows the difference between original and corrected ROI images for normal and cirrhosis liver using Type II(t=100). From this appearance of corrected images and the experimental results, we conclude as below.

1. The corrected ROI images get much darker.

2. There seems no difference between normal and cirrhosis liver ROI images of image correction by a look, as well as original ROI images.

For Type II method(t=100), the corrected ROI images are much darker because the intensities less than 100 will be ignored. By cutting darker regions, we could obtain richer features for classifying cirrhosis liver. Consequently, we see the darker regions may be useless. By ignoring these regions, features will be richer and the generalization ability of the CNN is considered to improve. As we tried looking at another image correction methods of Type I(t=140) and Type III(γ=1/5), these corrected ROI images also get much darker like Type II(t=100). As we expected, lighter regions of ROI images could have richer features in classifying cirrhosis liver. Interestingly, there seems no difference between normal and cirrhosis liver of the corrected ROI images by a look. The image correction leads to improve image quality and then the generalization ability of the CNN improves.

Conclusions

In this paper, we have examined the effect of the image quality of the ROI image by image correction methods on the CNN in classifying a cirrhosis liver on B-mode ultrasound images. The experimental results showed the effectiveness of the image correction methods by improving the image quality of ROI images. By ignoring the intensities less than a thresholding value of ROI images, the image quality has improved and then the generalization ability of the CNN has improved. As we mentioned above, the darker images are effective. This means the lighter regions of ROI images may have richer features for classifying cirrhosis liver.

In the future, we explore another type of image correction methods. Apart from this approach, we try highlighting darker regions of ROI images. Perhaps, features of normal liver could be emphasized, and the generalization ability of the CNN may be improved. Moreover, in order to improve the generalization ability of cirrhosis liver classification, we develop a hybrid approach to use both darker and lighter regions of ROI images.

References

Doi, K. (2007). Computer-aided diagnosis in medical imaging: Historical review, current status and future potential. *Computerized Medical Imaging and Graphics*, 31, 198-211.

Fukunaga, K. (1990). Introduction to statistical pattern recognition. Second Edition, *Academic Press*.

Huber, A. Ebner, L. Heverhagen, J. T. & Christe, A. (2015). State-of-the art imaging of liver fibrosis and cirrhosis: A comprehensive review of current applications and future perspectives. *European Journal of Radiology Open*, 2, 90-100.

Litjens, G. Kooi, T. Bejnordi, B. E. Setio, A. A. A. Ciompi, F. Ghafoorian, M. Laak, J. A. W. M. van der. Ginneken, B. van. & Sanchez, C. I. (2017). A survey on deep learning in medical image analysis. *Medical Image Analysis*, 42, 60-88.

Mitani, Y. Fisher, R. B. Fujita, Y. Hamamoto, Y. & Sakaida, I. (2020). Effect of an augmentation on CNNs in classifying a cirrhosis liver on B-mode ultrasound images. *Proc. 2020 IEEE 2nd Global Conference on Life Sciences and Technologies*. 253-254.

Raman, M. & Himanshu, A. (2010). A comprehensive review of image enhancement techniques. *Journal of Computing*. 2, 3, 8-13.

Raudys, S. J. & Jain, A. K. (1991). Small sample size problems in designing artificial neural networks. *Machine Intelligence and Pattern Recognition*. 11, 33-50.

Sasaki, K. Mitani, Y. Fujita, Y. Hamamoto, Y. & I. Sakaida, I. (2017). A liver cirrhosis classification on B-mode ultrasound images by the use of higher order local autocorrelation features. *Proc. SPIE10225, 8th International Conference on Graphic and Image Processing.* 102250U.

Development of a High Repetition Impulse Power Supply for Sterilization by High Electric Fields

Takahisa Ueno[*,a], Kyohei Asami[a], Takashi Furukawa [b] and Takashi Sakugawa [c]

[a] National Institute of Technology, Oita College, Department of Electrical and Electronic Engineering, Oita, Japan
[b] Kitasato University, Department of Health Science, School of Allied Health Sciences, Kanagawa, Japan
[c] Kumamoto University, Faculty of Advanced Science and Technology, Kumamoto, Japan

*ueno@oita-ct.ac.jp

Abstract

This study developed an impulse power supply for applying impulse high voltage to low impedance loads. The application of high voltage technology has been widely used in fields, such as exhaust gas treatment and semiconductor lithography equipment. It has also been explored in the biological field for sterilization. However, due to their low impedance, it is not easy to apply high impulse high voltage to liquids containing many impurities, such as sewage and domestic wastewater. Thus, the impulse power supply was optimized by improving the circuit configuration, selecting magnetic materials, and preventing magnetic saturation. First, inexpensive Mn–Zn magnetic materials were selected to replace the expensive iron-based nanocrystalline alloys used for SI. Then, three types of Mn–Zn magnetic materials were evaluated from SI characteristic tests. The result shows that even inexpensive Mn–Zn magnetic materials can play the role of SI. Additionally, an impulse generator without SI was created to increase the energy transfer rate. By replacing the semiconductor switches from Si type to SiC type, the generator can be operated with semiconductors connected in parallel without using SI. At the maximum operating frequency of 100 Hz, an output voltage, V_{out}, of 8.0 kV was applied to a resistor, R, of 47 Ω at charging voltage, V_1, of 2.0 kV.

Keywords: *Impulse generator, Pulsed power, Si-semiconductor, SiC-semiconductor, Saturable Inductance*

Introduction

Pulsed power technology has been applied to basic technologies, such as laser oscillation (Melville, 1951) and plasma generation (Sakugawa et al., 2002), and to the decontamination of concrete rubble and exhaust gas treatment (Namihira et al., 2000). Recently, research on applications to living organisms, such as bacterial inactivation(Samaranayake et al., 2001) and plant growth control (Joshi, Locke, & Finney., 1995), has also been conducted.

The semiconductor devices used in the impulse generator power supply for generating pulsed power affect the performance of the power supply. Thyristors, which have excellent withstand voltage and current capacity, have a long turn-on time. However, MOSFETs and IGBTs, which have a short turn-on time, are appropriate for impulse generators that output short pulses. Although Sakugawa et al. (2006) and Akiyama (2000) have reported on the fabrication of impulse generator power supplies using discrete MOSFETs and IGBTs available in the market, it is not easy to create a power supply since the pulse rating using semiconductors is not always clear.

Additionally, when impulsive high voltage is used to inactivate bacteria, it is usually impossible to apply the required high voltage due to the low impedance of the impurities in sewage and domestic wastewater.

In this study, the development of an impulse power supply that can output high voltage and current is reported. Additionally, an impulse generator supply that connects multiple semiconductors in parallel and uses a transformer to increase the output voltage has been developed.

Target values for the output of the impulse generator power supply

In developing the impulse generator power supply, the required electrical characteristics of the power supply were defined (Table 1). The voltage value was determined to be the voltage that can generate the electric field necessary to sterilize microorganisms (Ueno, Furukawa, Sakugawa, & Katsuki, 2020).
The current value was calculated as the value at which the electric field could be applied to actual wastewater. The reactance of the actual wastewater differs depending on the type of wastewater due to impurity

ionization; however, it is calculated as the resistance value since the resistance component is dominant (Ueno, Furukawa, Sakugawa, & Katsuki, 2019).

Table 1 Electrical characteristics required for the power supplies. These electrical properties were derived from previous electric field sterilization experiments.

Applied voltage	8.0 kV
Resistance	47 Ω
Operating frequency	100 Hz
Rise time	< 10 μs

Creating an impulse generation power supply

Figure 1 shows the circuit diagram of the impulse generation power supply using a transformer. The circuit configuration consists of a primary capacitor C_0 = 1.67 μF, a saturable inductor SI, a transformer, and ten Si-IGBTs (IXYS, IXYL60N447) connected in parallel. The output voltage V_{out} is applied to the load resistor R connected in parallel with the capacitor C_1 = 25 μF.

The Si-IGBT is a discrete type device with a rated voltage (V_{CES}) of 4.5 kV and an instantaneous maximum current (<1 ms) of I_{CM} = 680 A.

SI was used to connect the current to the IGBTs in parallel uniform. SI consists of windings on the iron core. The current switching is performed through the inductance change when the iron core is saturated and unsaturated, called a magnetic switch or saturable inductor. Therefore, the permeability at saturation and unsaturation significantly affect the switching performance. Additionally, high saturation magnetic flux density and slight core loss are required. In this section, the generation of I_1 was delayed using SI, and I_1 flowed after all Si-IGBTs connected in parallel were turned on, making parallelization possible. The saturation time t_s [μs] when a voltage V [V] is applied to a magnetic material with a running cross-sectional area Ae [mm^2], saturation flux density Bs [mT] where the number of turns N follows the equation below (Choi, Namihira, Sakugawa, Katsuki, & Akiyama, 2007).

$$t_s = \frac{N \cdot Ae \cdot Bs}{V} \times 10^{-3} \quad \text{(Equation 1)}$$

From the above equation, the delay time is proportional to the saturation flux density and number of turns of the magnetic material and inversely proportional to the applied voltage. SI used in this study is an iron core made of iron-based nanocrystalline alloy (Hitachi Metals, FT-3H, Bs = 1.23 mT) with a cross-sectional area of 1983 mm^2. The number of turns was set to 15. The primary and secondary windings in the transformer were routed at equal intervals to equalize the magnetic flux distribution in the transformer, prevent leakage inductance, and increase the coupling factor.

Figure 2 shows the gate circuit of the Si-IGBT shown in Figure 1. A pulse signal with a signal voltage of 5 V from a function generator is input to a photocoupler (Toshiba, TLP350(F)); the pulse signal is amplified to 22 V. The amplified pulse signal is transmitted to each Si IGBT through the gate resistor R_g. At this time, R_g was set to 8.0 Ω.

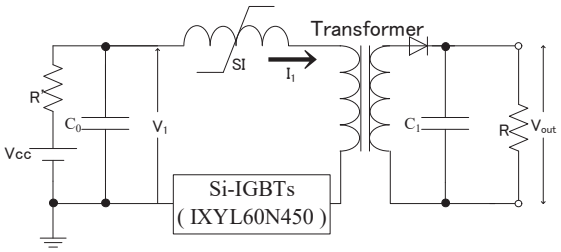

Figure 1 Impulse generation power supply circuit diagram. In this structure, the charged primary capacitor is discharged by a semiconductor, and the voltage is boosted using a transformer.

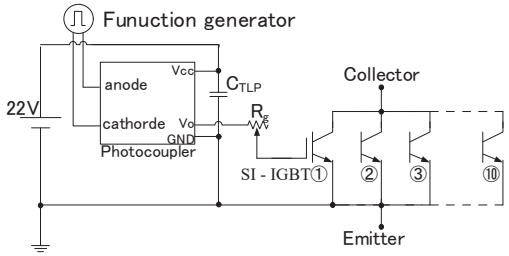

Figure 2 Si-IGBTs gate circuit diagram. The gate signal output from the photocoupler is input to ten IGBTs connected in parallel. At this time, the main current does not flow through the semiconductor since the SI is unsaturated.

Generation of primary-side current

Figure 3 shows the waveform of the primary-side voltage (V_1 = 2.3 kV) and current at this time. The waveform of the primary-side voltage and current is shown in the figure. It was confirmed that I_1 = 728 A was flowing to the Si-IGBTs connected in parallel. The parallel connection of Si-IGBTs enabled the switching of the current exceeding the device's rated current.

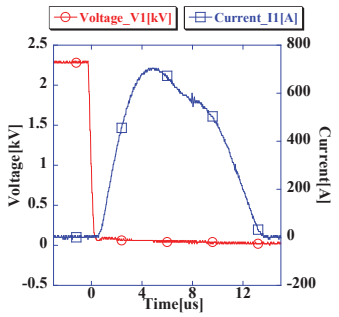

Figure 3 Voltage and current waveforms of the primary side. A current of about 728 A flows through the semiconductor for 0.8 μs after the voltage applied to the semiconductor falls.

Evaluation of magnetic materials by SI characteristic tests

The magnetic material used for SI in the previous section, iron-based nanocrystalline alloy, is costly and difficult to obtain. Therefore, Mn–Zn (manganese-nickel) alloy, which is one of the inexpensive and readily available magnetic materials, was used as a magnetic material to evaluate three types of magnetic materials (No. 1, No. 2, and No. 3) with different dimensions (Table 2). The circuit configuration was the same as in Figure 1. V_1 = 2.0 kV was applied, and switching was performed. The maximum current on the primary side, the current pulse width of the full width at half maximum, and the saturation time were measured. Figure 4 shows the magnetic materials compared in this study. Figure 5 shows the voltage and current waveforms.

Table 2 presents the details of the magnetic materials. The saturation time, pulse width (full width at half maximum) of the primary current, and maximum current value when V_1 = 2.0 kV were used.

The results show that there are differences in the maximum magnetic flux density and current pulse width, although the magnetic materials are the same. No.1 has the longest saturation time but the lowest maximum current value; No. 3 has the shortest saturation time. In this study, No. 2, which has the best balance between the length of the saturation time and the maximum current on the primary side, is used.

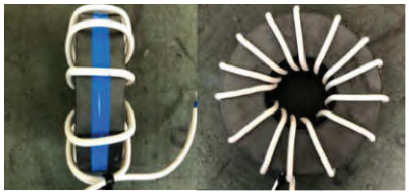

Figure 4 Photograph of magnetic materials (No.1). The other magnetic materials (No.2 and No.3) are wound in the same way as No.1; thus, the windings are evenly distributed.

Voltage application to a resistive load (load resistance R = 47 Ω)

Figure 6 shows the voltage and current waveforms when V_1 = 2.3 kV was applied. The V_{out} = 8.0 kV could be applied at an operating frequency of 100 Hz. It can be seen that I_1 is distorted at t = 8.0 μs. This is due to the saturation of the magnetic material in the transformer, which prevents energy transfer from the primary side to the secondary side.

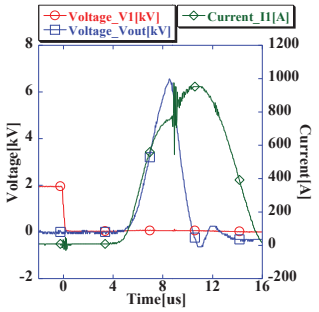

(a) Magnetic material No.1

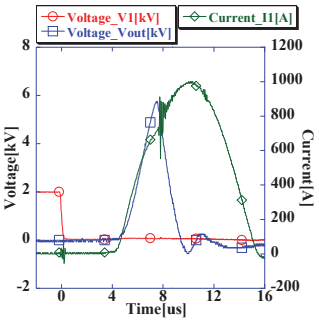

(b) Magnetic material No.2

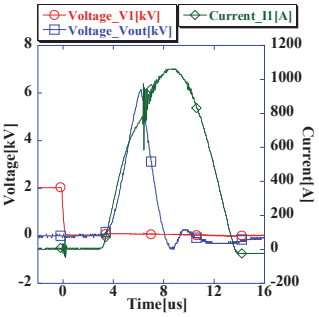

(c) Magnetic material No.3

Figure 5 Voltage and current waveforms of magnetic material numbers 1, 2, and 3 are shown in order from the above figure. For all magnetic materials, the number of turns and magnetic materials was the same, but the current flow and saturation time were different.

Table 2 SI Characteristic Test. The magnetic material and cross-sectional area were also the same

	No.1	No.2	No.3
Magnetic material	Mn–Zn	Mn–Zn	Mn–Zn
Cross-sectional area [mm^2]	1695	1675	1631
Saturation magnetic flux density [mT]	480	490	380
Number of turns [turn]	15	15	15
Saturation time [μs]	4.5	4.0	3.1
Current pulse width [μs]	7.3	7.4	7.1
Maximum primary current [A]	952	1000	1060

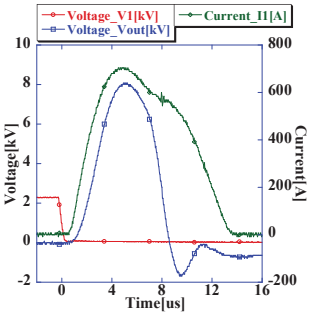

Figure 6 Voltage and current waveforms from impulse generator (load resistance R = 47 Ω). An output voltage of 8.0 kV was achieved, but the voltage waveform dropped sharply, indicating saturation in the transformer.

SI removal from impulse generation power supply

Although the impulse generator described in the previous section could apply an output voltage, V_{out} of 8.0 kV, I_1 is distorted at t = 8.0 μs (Figure 6). This is due to the saturation of the magnetic material of the transformer, which prevents energy transfer from the primary to the secondary side. To prevent magnetic saturation, it is necessary to change the magnetic material of the transformer to one with a higher saturation magnetic flux density. Alternatively, energy can be transferred to the secondary side before magnetic saturation occurs.

In this study, the closed-circuit inductance on the primary side was reduced by short-circuiting the SI; thereby, decreasing the pulse width of the primary side current. Additionally, the number of magnetic materials used in the circuit can be reduced by short-circuiting the SI, which reduces the cost of making the power supply and makes the power supply smaller, making it more portable.

SI removal from impulse generation power supply

In this section, the inductance of the primary circuit was reduced to increase the amount of energy transmission. When the closed-circuit inductance is L, and the capacitor is C, the period T [s] of the current generated in the closed-circuit is given in the following equation.

$$T = 2\pi\sqrt{LC} \quad \text{(Equation 2)}$$

Here, the width of the positive pulse, τ [s], is given by

$$\tau = \pi\sqrt{LC} \quad \text{(Equation 3)}$$

From the above equation, reducing the closed-circuit inductance on the primary side decreases the pulse width of the current and shortens the energy transfer time. By removing the SI, the primary-side current is generated immediately after the semiconductor switch turns on. In the Si-IGBTs used so far, the current concentrates on a specific semiconductor due to the turn-on variation, which may lead to the destruction.

Therefore, the semiconductors made of Si were replaced with those made of SiC to realize high-speed turn-on and eliminate the variation of the turn-on current.

Figure 7 shows the circuit diagram of the main circuit. The circuit configuration is as shown in Figure 1 with the SI removed, the semiconductor replaced with SiC-MOSFETs, and the voltage applied to R = 47 Ω. Figure 8 shows the voltage and current waveforms of impulse generator power supply after removing SI. A high impulse voltage of 8.0 kV was output.

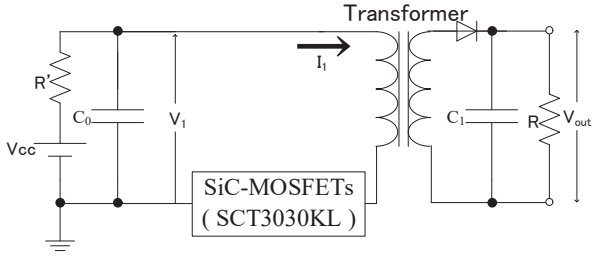

Figure 7 Impulse generator power supply after SI removal. The values of the elements are the same as in Figure 1.

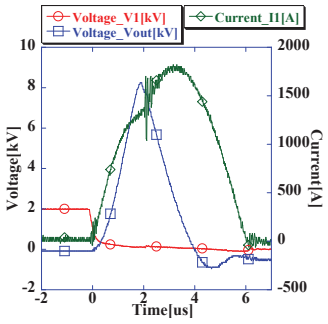

Figure 8 Voltage and current waveforms of impulse generator power supply after removing SI. Parallel switching of semiconductors was achieved without using SI, and a high impulse voltage of 8.0 kV was output.

Discussion

Figure 3 shows that using a saturable inductance SI allowed the Si-IGBTs connected in parallel to operate and switch at a higher current than the single Si-IGBTs. The maximum current flowing through each semiconductor was measured to be in the range of about 65 to 75 A. This difference in current was attributed to the variation in the on-resistance of each semiconductor.

Figure 6 shows that the inexpensive Mn–Zn alloy can replace the magnetic material used in the SI.

The current flowing through each semiconductor was about the same as in the case of the iron-based nanocrystalline alloy. Therefore, time integration of the voltage and current was performed to calculate and compare the losses. Considering that the input energy is

3.34 J, the difference is less than 2%, which can be replaced in terms of loss.

Figure 8 shows that the parallel operation is possible even without SI by replacing the semiconductor switches from Si to SiC. The power dissipation is 0.077 J, which is lower than that using SI. This can be attributed to the low on-resistance of the SiC semiconductor switch.

Conclusions

This study developed an impulse generation power supply for application to a low impedance load. A pulse voltage of 8.0 kV, the target value, could be applied to the load. Additionally, the expensive iron-based nanocrystalline alloy used in the SI was replaced by an inexpensive Mn–Zn alloy, and an impulse generator without SI was realized using SiC semiconductors.

Acknowledgements

This work was supported by JSPS KAKENHI Grant Number 18K04096.

References

A. A. Joshi, B. R. Locke, P. Arce, & W. C. Finney (1995). Formation of Hydroxyl Radicals, Hydrogen Peroxide and Aqueous Electrons by Pulsed Streamer Corona Discharge in Aqueous Solution. *J. Hazardous Materials*, 41, 3-30.

H. Akiyama (2000). Streamer Discharges in Liquids and their Applications. *IEEE Trans. Dielect. Elect. Insulation*, 7, 5, 646-653.

J. Choi, T. Namihira, T. Sakugawa, S. Katsuki, & H. Akiyama (2007). Loss Characteristics of a Magnetic Core for Pulsed Power Applications. *IEEE Trans. Plasma Sci.*, 35, 6, 1791-1796.

T. Namihira, S. Tsukamoto, D. Wang, S. Katsuki, R. Hackam, H. Akiyama, Y. Uchida, & M. Koike (2000). Improvement of NOX Removal Efficiency Using Short-Width Pulsed Power. *IEEE Trans. Plasma Sci.*, 28, No.2, 434-442.

T. Sakugawa, T. Yamaguchi, K. Yamamoto, T. Kiyan, T. Namihira, S. Katsuki, & H. Akiyama (2006). Generation of Streamer Discharge Plasma in Water by All Solid-State Pulsed Power. *IEEJ Trans. FM*, 126, 7, 703-708.

T. Sakugawa, M. Ieda, N. Takada, S. Yamada, K. Kitakizaki, & M. Haba (2002). TEA CO2 Laser Oscillation using an All Solid-State Pulsed Power Generator with a High Energy Transfer Efficiency. *IEEJ Trans. FM*, 122-A, 2, 186-191.

T. Sakugawa & H. Akiyama (2001). An all-solid-state pulsed power generator using a high-speed gate-turn-off thyristor and a saturable transformer. *IEEJ Trans. FM*, 122-A, 4, 51-358.

T. Ueno, T. Furukawa, T. Sakugawa, & S.Katsuki (2020). Inactivation of Vibrio fischeri by the Application of a Pulsed Electric Field. *Transactions on GIGAKU*, 7, 1, 07002-1-9

T. Ueno, T. Furukawa, T. Sakugawa, & S.Katsuki (2019). Using High Electric Filed to Measure Aerosol-based Bacterial Inactivation. *Proceedings of The 11th Asia-Pacific International Symposium on the Basics and Applications of Plasma Technology*, 17, P2

W. J. M. Samaranayake, Y. Miyahara, T. Namihira, S. Katsuki, T. Sakugawa, R. Hackam, & H. Akiyama (2001). Pulsed Power Production of Ozone in O2 / N2 in a Coaxial Reactor without Dielectric Layer. *IEEE Trans. Dielect. Elect. Insulation*, 8, 5, 826-831.

W. S. Melville (1951). The Use of Saturable Reactors as Discharge Devices for Pulse Generators. *Proceedings of IEEE*, 98, 53, 185-207.

Assistive Technology in Education for Self-Monitoring with an Optical Wearable Heart Rate Monitor

M. Nagamori [*, a], M. Fukuda [a], H. Takano [a], N. Shinoda [a], A. Shionoya [a], S. Ohhashi [a, b], T. Susukida [c], M. Nagasawa [d], and H. Miyake [e]

[a] Nagaoka University of Technology, Nagaoka, Japan
[b] National Institute of Technology Tomakomai College, Tomakomai, Japan
[c] Lorem Ipsum Corp., Nagaoka, Japan
[d] Niigata University, Niigata, Japan
[e] Tachikawa Medical Center, Nagaoka, Japan

*E-Mail nagamori@kjs.nagaokaut.ac.jp

Abstract

To assist in the attainment of SDGs3.4 and SDGs4.5, we report on technology (assistive technology) aimed at self-monitoring that supports the education of people with developmental disabilities. The characteristics of developmental disabilities can sometimes hinder self-awareness. Therefore, even if others may think that there is a need for considerations, it may be difficult to expect persons with disabilities to independently request for such considerations. In our university, an e-portfolio system was developed to support self-monitoring and coping for the purpose of providing reasonable accommodation. This system is characterized by the use of heart rate information (Lorenz Plots of heart rate variability) as an objective assessment indicator of stress during activity participation together with International Classification of Functioning: ICF-CY environmental factors as subjective assessment indicators of situations (CY: Disability and Health version for Children and Youth). We employed optical wearable heart rate monitors to store daily heart rate information. Due to their noninvasive characteristic, wearable monitors support daily heart rate variability measurements. Furthermore, these monitors can be worn on different body parts (wrist, ankle, or temple) to meet the diverse needs of different people. This type of assistive technology can support continuous self-monitoring. And, a mobile system was used to store daily records of stress factors. In this system, the input of subjective stress assessments uses icons that correspond to generic terms for onomatopoeic. These enable the simple expression of one's internal emotions and are widely used in sensitivity expression classifications in psychotherapy and tactile perception due to their ease of use. The use of these icons simplifies the storage of stress factors and focuses on supporting the daily archiving of information for the purpose of coping with stress. This paper introduce a concept of engineering-based support for self-monitoring and coping in reasonable accommodation in response to SDG Target 3.4.

Keywords: *Assistive Technology, SDGs, Mental Health, Developmental Disorder, e-Portfolio, Onomatopoeia, Noninvasive, Heart Rate Variability, Wearable Monitor*

Introduction

In September 2015, the United Nations introduced Sustainable Development Goals (SDGs) as targets for all countries, including developed countries. Among the 17 SDGs, one SDG is aimed at the provision of "good health and well-being for all". Specifically, SDG 3 aims "to ensure healthy lives and promote well-being for all at all ages". Among the targets in SDG 3, Target 3.4 is as follows: "By 2030, reduce by one-third premature mortality from non-communicable diseases through prevention and treatment and promote mental health and well-being". Japan has adopted these SDGs, and published the SDGs Implementation Guiding Principles in December 2016.

The "all (people)" described in SDG 3 includes persons with disabilities, who comprise 15% of the world's population (Kobayashi, 2018). Even in Japan's SDGs Implementation Guiding Principles, one of the major principles is "inclusiveness", which contains the key phrase "no one will be left behind" and specifically includes persons with disabilities. In this context, Japan has promoted the implementation of reasonable accommodation based on SDGs (Cabinet Office of Japan, 2015).

The prevention and treatment of "non-communicable diseases" stated in Target 3.4 requires improvements in lifestyle habits. Here, self-monitoring (records of one's own behavior, thoughts, and emotions) and coping (mechanisms to deal with stress) are thought to be useful. In addition, in order to "promote mental health and well-being", self-monitoring and coping are also important

from the perspective of reasonable accommodation. Support for self-monitoring and coping is crucial for assisting persons with disabilities, especially support in education for children with developmental disabilities.

Also, The SDG 4 aims to "Ensure inclusive and equitable quality education and promote lifelong learning opportunities for all". Specifically, Target 4.5 states that "By 2030, eliminate gender disparities in education and ensure equal access to all levels of education and vocational training for the vulnerable, including persons with disabilities, indigenous peoples and children in vulnerable situations". This target is linked with the continuity of education and training, as well as with self-reflection in learning.

In response to Target 3.4 above, we introduce the concept of engineering-based support for self-monitoring and coping with reasonable accommodation. Furthermore, this paper reports on an information system designed to realize Target 4.a, which aims to "Build and upgrade education facilities that are child, disability and gender sensitive and provide safe, non-violent, inclusive and effective learning environments for all". This system was developed to target the vulnerable groups, especially children with developmental disabilities, described in Target 4.5.

Assistive Technology: Support System Concept

In April 2016, Japan passed the Act for Eliminating Discrimination against Persons with Disabilities, which made it compulsory for administrative agencies (including universities) to provide reasonable accommodation. Consequently, there have been advances in the provision of reasonable accommodation for persons with disabilities (including developmental disabilities) in educational institutions. As a general principle of reasonable accommodation provision, support starts when a person with a disability directly states that there is a need to remove social barriers (Ministry of Education in Japan, 2016). However, the characteristics of developmental disabilities can sometimes hinder self-awareness. Therefore, even if others may think that there is a need for considerations, it may be difficult to expect persons with disabilities to independently request for such considerations (Okeya, 2013; Nishimura, 2017).

In our university, an e-portfolio system was developed to support self-monitoring and coping for the purpose of providing reasonable accommodation (Nagamori, 2010; 2018). This system is characterized by the use of heart rate information as an objective assessment indicator of stress during activity participation together with International Classification of Functioning: ICF-CY environmental factors as subjective assessment indicators of situations (CY: Disability and Health version for Children and Youth). To ensure noninvasiveness to meet the diverse needs of users, optical wearable devices (which have poorer accuracy than electrode-based devices) were selected to store and analyze daily heart rate variability measurements. Input on stress using onomatopoeia-based icons can allow for easier records of subjective assessment indicators of stress factors, thereby supporting continuous self-monitoring and coping in users.

ICF-Compliant e-Portfolio

e-Portfolio system's descriptive items provide descriptions of the subject students' own requests

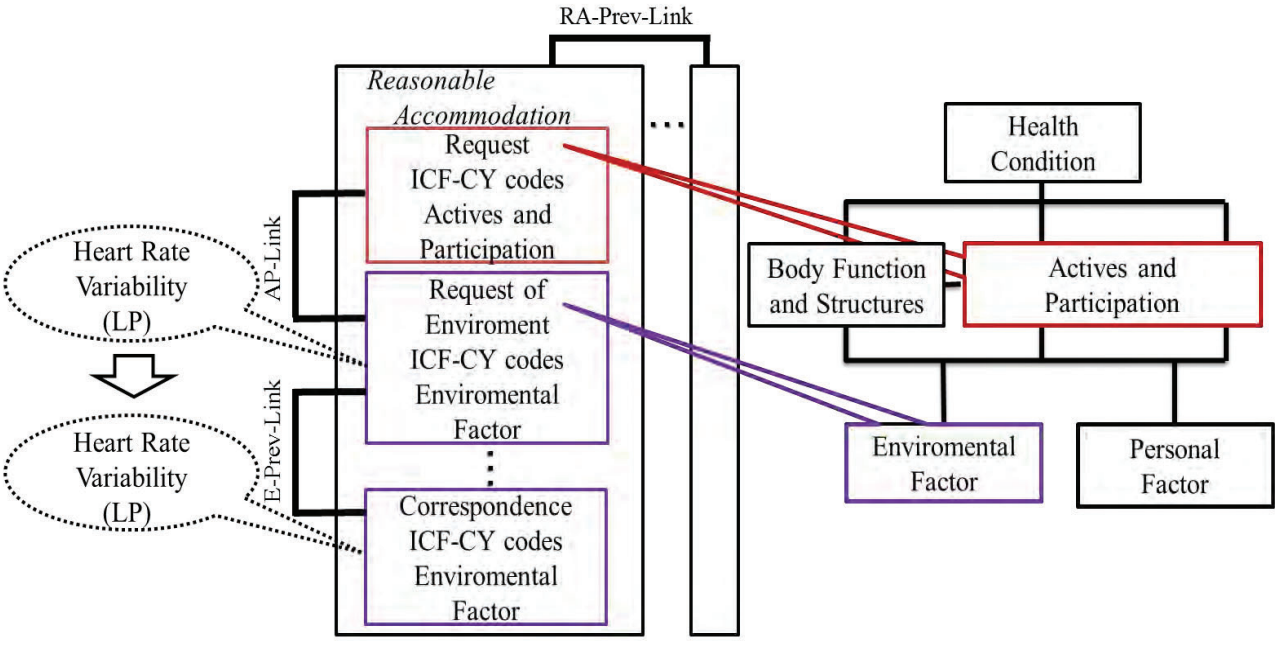

Figure 1 Concept image for DB and ICF in the support process part of e-portfolio system.

(including barriers) as review information, as well as each institution's responses (including facilitators) as decision information; this information is used to support choices on reasonable accommodation. When describing the requests and responses in the system, ICF's activity and participation classifications are added to requests, and specific responses (adjustments and changes) are stored with the ICF-CY (Children and Youth version) environmental factor classifications relevant to the students' institutions as meta-information.

Through these request and response classifications, the difficulties in activities and participation before and after adjustments and changes in environmental factors can be examined in the consensus-building process for reasonable accommodation. The subjects may be encouraged to engage in introspection as they review the support and consensus-building process in their own portfolios. Heart rate information (Lorenz Plots: LPs), as described in the next section, was employed as an objective indicator to support this introspection.

Figure 1 shows the DB of the e-portfolio system's support process and the database structure for ICF. Heart rate information LPs are recorded as objective indicators according to environmental factors. In the figure, LPs are applied to two places: the subject student's conditions in the environment at the time of request and their conditions after the institutions' responses. These responses are not finished after one time. Instead, they are continuously described as the post-response conditions are considered and further requests are made until a consensus on reasonable accommodation is reached. In this consensus-building process, the system measures the daily LPs and supports the continued review of one's own objective indicators according to stress factors in the portfolio.

Wearable Heart Rate Variability Monitors

Heart rate information, which is a physiological indicator that can be easily and noninvasively measured, was examined as an objective indicator to encourage the subject students to review themselves. The LPs of heart rate information were used as assessment indicators of one's stress tendencies during these reviews. An LP refers to a graphical plot of the nth electrocardiogram (ECG) RR interval on the horizontal axis and the n-1th ECG RR interval on the vertical axis. This is a useful method to visually ascertain changes in RR intervals. When a subject is calm, the center of the plot will shift to the upper right side of the graph. When a subject is tense, the plot will start to move toward the lower left side of the graph, and the dispersions at each point will expand in a circular pattern. As the subject becomes increasingly tense, the center of the plot will shift toward the lower left side of the graph and the dispersions will become smaller.

In LPs, the mean distance from the origin is designated "m" and the ellipse area is designated S; these are reported to be alternative assessment indicators to the high-frequency (HF) component that reflects parasympathetic nerve activity (Toyofuku, 2007; Nagamori, 2018). This research was conducted to test the ascertainment of stress tendencies in subjects through the continuous review of their own portfolios with m calculated from the LPs.

Furthermore, even among subjects with the same developmental disability, there are wide variations in the manifestation and extent of symptoms at the individual level. When measuring heart rate information in persons with these disabilities, some may not be able to wear monitoring devices on specific body parts or express

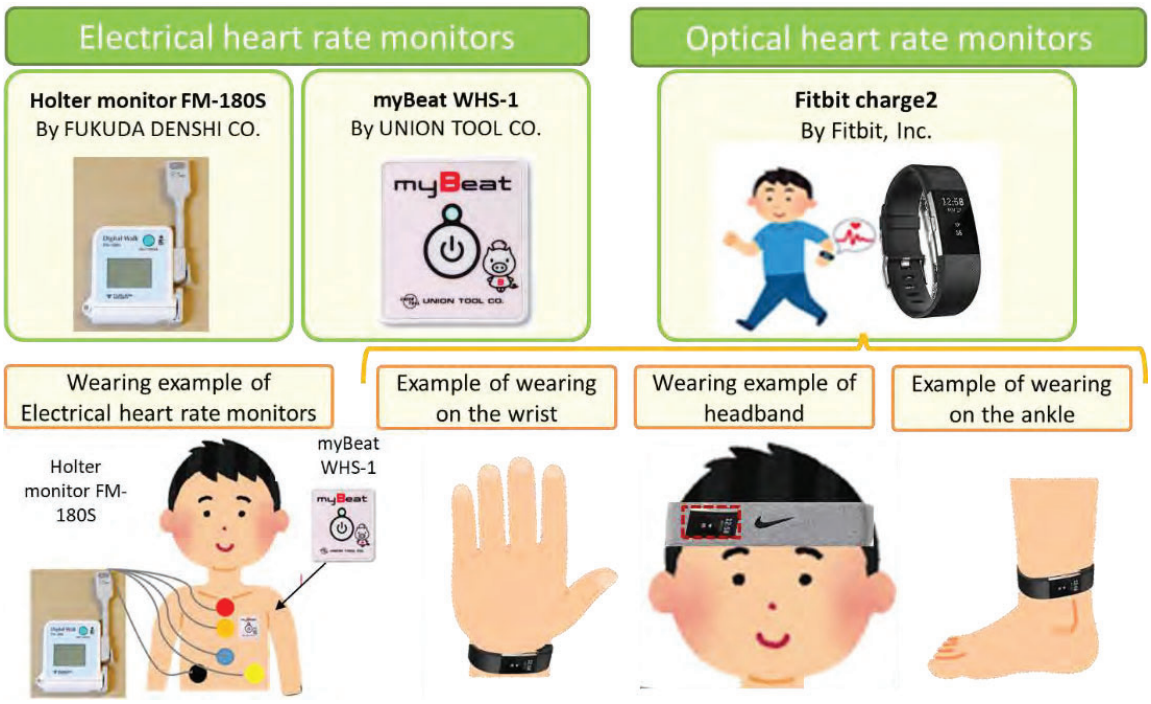

Figure 2 An example of comparing an electric heart rate monitor with an optical heart rate monitor.

Figure 3 Input interface of onomatopoeia-based icons. Eustress and Distress.

discomfort, which could affect stress measurements. With this consideration in mind, optical heart rate monitors were chosen as they are noninvasive and can be worn easily, and are therefore ideal for daily heart rate variability measurements.

However, the use of optical devices may still have limitations, such as workplace regulations or causing dermatitis. It is easy to think of situations where these devices cannot be worn. From the perspective of hygiene, it would also be problematic for subjects to continue wearing the device on their wrists when cooking in daily life. Due to these various situations, other heart rate measurement methods were considered to meet the diverse individual needs (including personal preferences) of the subjects. These included temple measurements using headband-mounted monitors, and ankle measurements using anklet monitors. Figure 2 shows examples of these devices.

Emotion records using onomatopoeia-based icons

A mobile system was used to store daily records of stress factors. In this system, the input of subjective stress assessments uses icons that correspond to eight generic terms for onomatopoeic/mimetic words identified from previous experiments (NOBI NOBI, HETO HETO, etc.). These enable the simple expression of one's internal emotions and feelings, and are widely used in sensitivity expression classifications in psychotherapy and tactile perception due to their ease of use. Furthermore, ICF classifications are also employed as stress factors/icons pertaining to the onomatopoeia-based icons, which are used as meta-records to examine how different scenes and interpersonal relationships can lead to stress conditions. The use of these icons simplifies the storage of stress factors and focuses on supporting the daily archiving of information for the purpose of coping with stress. Figure 3 shows the input interface of onomatopoeia-based icons.

Results and Discussion

In this study, onomatopoeia-based icons were adapted to individual factors that are components of ICF. An individual factor is an individual's psychological qualities, and in this system, this individual factor is defined and accumulated as good or bad in activities / participation in environmental factors. By looking back on the judgment of stress factors by this icon as an e-portfolio, the effect on the reasonable accommodation received can be clarified, and support for the next request for accommodation can be expected. For the input of subjective information in this experiment, we prepared four types of icons (Eustress: UkiUki / NoriNori, Distress: KutaKuta / HetoHeto), which were frequently used in previous studies. The four types of onomatopoeia were selected in consideration of ease of use by children and students.

Since 2017, the author has been holding a computer class for disability support on Saturday in collaboration with local citizens' activities. In this paper, we report the results of requesting cooperation from junior high school boys who participate in this classroom. As an evaluation of daily accumulation using the stem, we compared the subjective information of stress factors (icons according to ICF-CY) and the objective information of stress factors (m value) in the target situation. The practice period was two months from November to December, of which five days were practiced. The target students were made to wear a wearable terminal (Optical Wearable Heart Rate Monitor), and a 60-minute work experience was performed using a personal computer. The target students were asked to input icons, which are subjective information of stress factors, from mobile terminals using the system as appropriate during work. In addition, the practice time was not included in the evaluation because the wearable terminal was installed on a trial basis in order to examine the invasiveness of the target student's terminal installation. Regarding the heartbeat information used in this experiment, we obtained the

Figure 4 The results of objective information on stress factors based on m values.

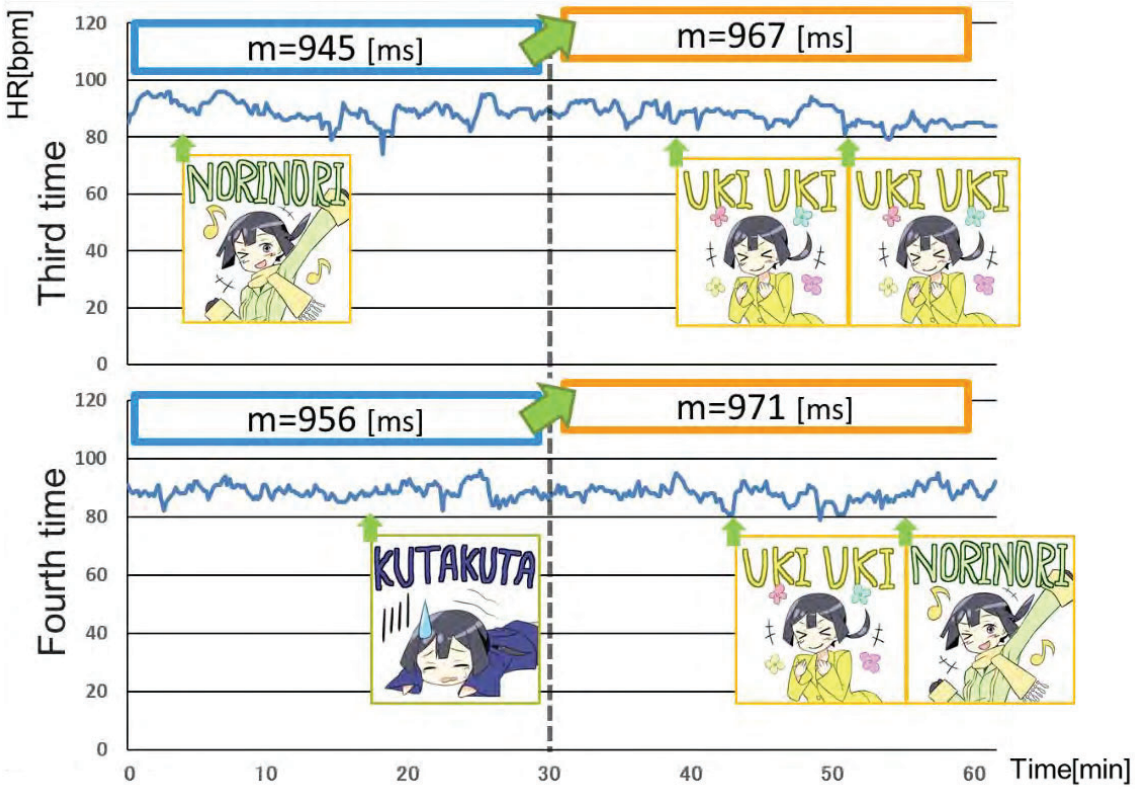

Figure 5 The input results of subjective information for stress factors by icons (only the 3rd and 4th times).

consent of the parents of the children in advance regarding the sharing of the heartbeat information with the concerned parties and the use of the heartbeat information in the study in consideration of personal information.

The experiment was conducted with the approval of the ethics committee of the university to which the researcher belongs.

Figure 4 shows the results of objective information on stress factors based on m values. Comparing the m values in the first half and the second half of all four times, it was found that the m value increased in the second half from all the practices. That is, it is objectively judged to have a eustress tendency.

Figure 5 shows the input results of subjective information for stress factors by icons (only the 3rd and

4th times on paper). Of all four practices, the distress icon was entered only once. In addition, the number of icon inputs increases in the latter half. The number of eustress icon inputs increased in the second half. In other words, it is subjectively judged to have a tendency toward eustress.

From these results, it was confirmed that the transition of heart rate variability, which is a record of objective information on stress factors, and the icon according to ICF-CY, which is a record of subjective information, tend to match. In addition, it was confirmed from each interview that the use of the system did not burden the target person and that the accumulated information was effective in deciding the support policy of the volunteers who are the supporters.

This indicates that the operation of this system is practical in the daily activities and participation of the subjects.

Conclusions

This paper introduced a concept of engineering-based support for self-monitoring and coping in reasonable accommodation in response to SDG Target 3.4.

In SDG 3, Target 3.d aims to "Strengthen the capacity of all countries, in particular developing countries, for early warning, risk reduction and management of national and global health risks". Even in Japan, the need for self-monitoring and coping has become increasingly emphasized, as shown by the introduction of the mandatory stress check program in december 2015. This has led to a demand for various measures (including assistive technology) to support persons with developmental disabilities who have difficulties in being self-aware.

In recent years, a more realistic definition of health has been proposed as "the ability to adapt and to self-manage in the face of social, physical and emotional challenges" (Huber, 2011). Self-monitoring and coping for reasonable accommodation can certainly be thought of as methods to acquire the abilities to make things easier in the context of medical and social disabilities. It is hoped that subjective information using the e-portfolio and objective information from daily physiological measurements can contribute to these abilities, including self-advocacy.

In the presentation, we will report multiple cases of lifelong learning of persons with disabilities as actual measurement cases. In addition, as a basic research of daily accumulation and analysis, we will also report on the one-year record of university students who belong to the Faculty of Engineering in the environment of COVID-19 infection prevention measures.

References

Cabinet Office of Japan, (2015). Guidelines for Promoting the Elimination of Discrimination on the Grounds of Disability in Related Ministries and Agencies.

Kobayashi. M, (2018). Research on Disability and Development, Ajiken World Trend, 269: 68-69.

Machteld Huber, et al., How should we define health ? , British Medical Journal, 343: d4163 (2011)

Ministry of Education in Japan, (2016). Regarding the Second Report of Investigative Commission on Study Support for Students with Disabilities.

Nagamori, M., Morimoto, Y., Ueno, M. (2010). Development of Support System for Creating e-Portfolio for Individualized Educational Support Program, Institute of Electrical Engineers of Japan. IS, Information System Study Group, 50: 13-17.

Nagamori, M., Ando, M., Wakabayashi, A., Hara, S., Shionoya, A., Miyak, H., (2018). Practice of Peer Support with E-portfolio Based on ICF-CY as Basic Environment, AHEAD JAPAN2018, National Council for Supporting Students with Disabilities in Higher Education.

Nishimura, Y. (2017). Building a Support System with Sufficient Structure for University Student with Developmental Disorders, Clinical study of campus life, 16: 15-20.

Okeya, F. (2013). Reasonable Accommodation in the Support for Students with Developmental Disabilities: Current Situations and Issues, Clinical study of campus life, 12: 57-65.

Toyofuku, F., Yamaguchi, K., Hagiwara, H., (2007). Simplified method for estimating parasympathetic nervous activity by Lorenz plot of ECG RR intervals, JAPAN HUMAN FACTORS AND ERGONOMICS SOCIETY, 43(4), 185-192.

IMPROVEMENT OF GAZE INPUT COMMUNICATION SYSTEM WITH PREDICTIVE CONVERSION

K. Hama[*,a], Y. Jia Xin[b], M. Suzuki[a] and T. Nakamura[a]

[a] National Institute of Technology, Hakodate College, Hakodate, Hokkaido, JAPAN
[b] Toyohashi University of Technology, Toyohashi, Aichi, JAPAN

*hama@hakodate-ct.ac.jp

Abstract

Patients with chronic neurological diseases such as cerebral palsy and amyotrophic lateral sclerosis (ALS) have difficulty in speaking due to muscle wasting, which greatly impairs communication. Depending on the progress of the medical condition, switch operation can also prove to be difficult, thus various support methods are being studied to accommodate different kinds of physical conditions. Eye tracking devices are less demanding on the upper body than mouse operation and allow for a more intuitive input. However, clicking method by gaze fixing and blinking can bring about problems like misoperational inputs, huge amount of time consumed in word selection, and eye fatigue due to consistent conscious movement using the eyes. Therefore, it is necessary to find an effective solution to these problems. In a previous research, text input with one single gaze operation was made possible by simultaneously using the movement of the lips. This was achieved while keeping the absolute area of each character on the screen wide, which is one of the features of the two-step input method. However, since the movement of the lips differs depending on the individual, it became necessary to determine the standard value based on the features extracted and to resolve the issue of time-consuming operation learning process. In response to these issues, in this study, we aim to reduce eye muscle fatigue and shorten the input time by taking into consideration the operational efficiency and physical ease of use. Therefore, in addition to reconstituting the screen keyboard, we also introduced predictive conversion, audio output and emoji keyboard into the existing system. Text candidates for predictive conversion are words and phrases that are often used in daily life. When the words a user wants to convey are selected, they will be output in audio form and the communication is then achieved. Furthermore, the system was expanded to reduce the input number of times for diphthongs and geminate consonants, which are features of the Japanese language, shorten the overall input time, promote smoother conversations and let users express their emotions more authentically. The improvement of the system was confirmed through some simple experiments.

Keywords: *gaze input system, screen keyboard, predictive conversion, communication tool, quality of life*

Introduction

Amyotrophic lateral sclerosis (ALS) is a neurodegenerative neuromuscular disease that results in the progressive loss of motor neurons that control voluntary muscles. The disease affects nerve cells in the brain and spinal cord, causing loss of muscle control. ALS often begins with muscle twitching and weakness in a limb, or slurred speech. Eventually, ALS affects control of the muscles needed to move, speak, eat and breathe. There is still no cure for this fatal disease.

It may begin with weakness in the arms or legs, or with difficulty in speaking or swallowing. Eventually both the limbs and mouth become impaired. For people who are affected by such motor neuron disease, it becomes difficult to use keyboards due to limb dysfunction, and dysarthria occurs due to weakening of the throat and tongue, which greatly impairs communication function (Mitsubishi Tanabe Pharma Corp.). Therefore, various support methods are being studied according to the progress of the medical condition and the physical condition (Kobayashi, 2018). Some examples are the use of alphabet board where the patient is required to point to the letters of the words, and of assistive devices like an eye tracker that can help patients type into a screen keyboard by using only their eyes (Sagarifuji, 2015).

Eye trackers, when connected to a device like a computer, can be used easily and mouse pointer can be controlled by using only eye movement. It is therefore less demanding on the physical body for the users than using an alphabet board, which requires to pinpoint and spell the words to determine what the users want to convey (Feit, A. M., et al., 2017). However, frequent input errors and eye fatigue are some of the problems that arise while using the current input system. As input is carried out one character at a time, it can be time-consuming to compose full sentences, which makes smooth communication difficult (Hara, 2020).

In this research, in consideration of system efficiency

and user-friendliness, we aimed to shorten the input time and reduce eye fatigue by modifying the screen keyboard and adding three functions into the existing system, which are the predictive conversion function, audio output, and an emoji keyboard. In this paper, we report the outline of the modified screen keyboard, the processing flow, and the experiments carried out.

System Configuration

The overall system configuration is shown in Figure 1. The eye tracker used in this research is the Tobii Eye Tracker 4C manufactured by Tobii Technology (Figure 2). This device integrates an infrared micro projector, an optical sensor, and an image processor. In the previous research, we used the HD Webcam C270 from Logitech as the Web camera to capture the shape of the mouth. In this research, we used a USB microphone made by Sanwa for sound recording and a compact stereo speaker made by Logitech. The technique used in eye-tracking is the pupil center corneal reflection (PCCR) method. Near-infrared illuminations create the reflection patterns on the cornea and pupil of the user's eye and image sensors capture images of the eyes and the reflection patterns. A sophisticated 3D eye model algorithm is then used to estimate the eyes' position and gaze point in the space with high accuracy. Calibration before use is important to customize the measurement method in consideration of the light conditions and eye characteristics and to calculate the gaze point more accurately.

Gaze Input System

・Existing System

Among the existing systems, the most common input keyboard is the one where all 50 sounds are displayed on the screen. The advantage of this method is that characters can be input with just a single click. Since the required eye movement is relatively small, quick input is possible and the eyes are less likely to feel tired easily. However, by displaying 50 sounds on the screen, the clickable area of each character becomes narrow, which leads to frequent input errors. As input errors increase, the input time also increases as a result.

Aside from this, there is also a method in which the input is carried out in two stages, by firstly selecting the consonant of a character and the vowel afterwards. The advantage of this method is that the clickable area per character is larger than that of the 50 sounds method, so input error is less likely to occur. However, since two clicks are needed for the input of one character, the input time inevitably becomes longer as the amount of eye movement increases.

・Previous Research

In creating new screen keyboard, we will first explain the outline of the system developed in the previous research (Fujita, et al., 2019). As mentioned in the last

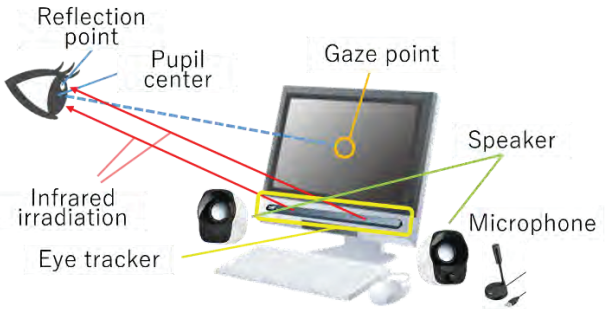

Figure 1. System Configuration.

Figure 2. Tobii Eye Tracker 4C.

section, in the two-step input method, the input time increases due to frequent input errors, which leads to more eye fatigue. This causes more stress to the user. Therefore, in the previous research, we decided to improve the weaknesses while making use of the advantages of the existing method, by also using the movement of the mouth together with gaze input. The gaze point is used to select the consonant, and the movement of the mouth indicates the vowel. With this method, it was made possible to input with only one click while simultaneously maintaining the wide clickable area for each character.

The vowels of the mouth were identified using images captured by the camera. With reference to other research papers, trained data that can detect the coordinates of the eyebrows, eyes, nose, contour of the lower half of the face, inside and outside of the lips at 194 points are used. From these points, 56 points related to the lips are extracted. The vowel is determined by calculating the maximum and minimum of length and width between the points, and comparing with the pre-determined reference values. This reference value refers to the vertical and horizontal lengths for each specific vowel, and the most similar vowel that minimizes the difference between the two is selected. It is therefore necessary to pre-measure the value when the mouth is closed. Since the vowel is shaped by the mouth during input, it gives the user the feeling as if they are speaking the character aloud.

With the created screen keyboard, we were able to retain the wide clickable area for the characters, which is one of the advantages of the two-step input method, and as vowels are determined by using mouth movement, only the consonants were needed to be displayed on the screen. Subsequently, the eye movement required and input errors were decreased. The vowels identified based on the camera image is displayed on the upper right of the screen keyboard, and the current state can also be confirmed on the keyboard. By clicking the Enter key, the words in the text box are moved to the history bar below. This enables user to write long sentences.

Taking the character “ko” as an example, Figure 3 shows the input flow of the character. Firstly, the user

rounds the lips into the vowel “o” shape, while shifting his or her gaze to the consonant, in this case, the “k” button. The gaze position and the shape of the mouth are measured in real time, and when both moves are maintained for a certain period of time, the selection of character will be confirmed and the corresponding character is output. From the experiment results, we were able to confirm improvement in the input time, input error and input accuracy measured. However, since the movement of the mouth varies from one person to another, there were problems that it was time-consuming to standardize the data and to learn operation. Furthermore, plenty of time is also needed to compose a full sentence as the words are input one at a time, thus making it difficult to have a smooth conversation.

Modified Gaze Input System

・Processing Flow

Figure 4 shows the overall processing flow of the system (Yu, et al., 2020). By using the information of the gaze position obtained from the eye tracker, the mouse pointer operation is carried out with the help of an external software, HeartyAi.

In the software, the average position of the gaze is constantly calculated and the mouse pointer is placed at that average position. When the gaze is maintained for a specific amount of time, click action will be performed. As the character is input into the text box, the candidate words that follow the character will also be displayed. By gazing on the word that the user wishes to choose, the word will be selected and entered into the text box. Communication is achieved by clicking the speech icon, which outputs the contents in the text box as audio.

・Screen Keyboard

In this study, we decided to prioritize keeping the clickable area wide for each character and adopted the two-step input method to reduce input error. Because of this, two clicking operations will be required for every input. However, by modifying the input screen and introducing the predictive conversion function, we expected a shortening effect of input time, especially in the case where long sentences are used.

Figure 5 shows the modified screen keyboard used in this study. There is the entry text box at the top, where the words entered are displayed. The speech icon at the bottom right is for playing the text box content in audio form, while the emoji icon on its right opens the emoji keyboard. The blue area in the center of the screen is where the predicted candidate words are displayed. Words are input in two steps by selecting the consonants on the left side and then the vowels on the right side of the keyboard. Table 1 shows the function of each key on the keyboard.

・Input Method

In order to explain the input method using the keyboard, the process of inputting the character “ka” is

Figure 3. Input with gaze and mouth movement.

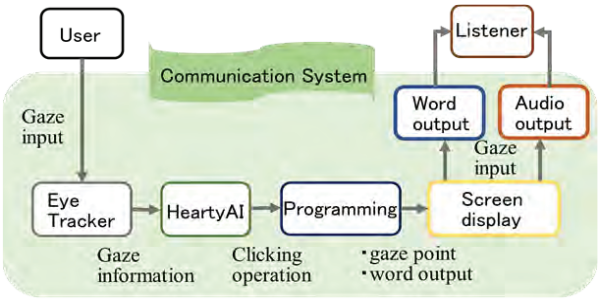

Figure 4. Processing flow.

Figure 5. Modified Screen Keyboard.

Table 1. Function of the keys.

「k」～「w」	to insert consonant
「あ」～「お」	to insert vowel
＊ 「w:い」=「ん」, 「w:う」=「ー」	
「clear all」	to delete all contents in the text box
「数字」	to access the numeric keyboard
「backspace」	to delete the character before the cursor’s current position
「゛゜小」	to add sonant mark (゛) or semi-sonant mark (゜) to the current character , or to convert into a small character

shown through Figure 6 and Figure 7. As shown in Figure 6, the user shifts his or her gaze to the “k” button, which is the consonant of the “ka” character. By maintaining the gaze for a specific period of time, the letter “k” will be output in the text box. At the same time, the “a”, “i”, “u”, “e”, and “o” buttons on the vowel side switch accordingly to “ka”, “ki”, “ku”, “ke” and “ko” respectively. This state of the keyboard is shown in Figure 7. Here, when the user clicks on the “ka” button, the “k” in the text box will be replaced by the character “ka”, and the buttons on the vowel side return to default. Simultaneously, candidate words starting with the character “ka” are displayed in the predictive conversion column. While Japanese characters that have a consonant require two clicks for each input, the “a”, “i”, “u”, “e”, and “o” characters can be input directly with only one click.

Furthermore, one of the advantages of this keyboard is

the soku-on (double consonants, e.g., /ss/, /kk/) and yō-on (hiragana using a kana ending in i, such as ki, plus one small letter of the three y kana, ya, yu or yo) which are specific to the Japanese language, can both be input in three steps. As an example, the yō-on "kya" and the soku-on "kka" can both be input with three clicks on the keyboard, where more may have been required in the other existing keyboard systems. The input process of the yō-on "kya" is shown in Figure 8. As shown in this figure, the clickable area for each button is widened, which was thought to contribute to a reduction in input error.

Using the gaze position obtained from the eye tracker, the gaze control software called HeartyAi under the input software called HeartyLadder is used. With this software, the mouse pointer will be displayed according to the information on the current gaze position. Click operation is possible with gazing, blinking and winking. Because a constant use of the eyelids would fatigue the user easily, the click operation by gazing was chosen in this study. Since the experiment subjects are healthy person and have no trouble moving their gaze accurately, the mouse pointer setting was set to "accurately controllable" from the five levels of gaze control accuracy in the software. Clicking motion is set to be carried out when gaze motion is maintained for 1.0 second. With the help of this software, operations such as moving and clicking the mouse pointer can be performed by gaze. By developing the screen keyboard so that it can used with the mouse pointer, gaze input is made possible in this study.

・New Functions

1) Predictive Conversion Function

Eyestrain is generally a common result of using eye-tracking, regardless of input method, as focusing and use of the eyes are often required. Therefore, it is important to shorten the input time in order to reduce the stress felt by the user. In this research, we introduced the predictive conversion function with the purpose of saving input time, reducing the effort to build a sentence from scratch, and significantly lightening the burden on the user.

It is also more efficient to convey sentences with predictive conversion particularly in the case of standard Japanese greetings and commonly used requests on the user's behalf. The candidate words and phrases are chosen based on estimation of the user's common needs in daily life.

When a character is inserted into the text box, the candidate words starting with the inserted character will be displayed across the screen. By gazing at the candidate word on the screen, the word will be inserted into the text box. For example, the candidate words that are displayed after entering the character "ka" are shown in Figure 9. In addition, Figure 10 shows the candidate words that follow when the word "face" in Figure 9 is selected.

2) Audio Output

Audio output function was added to the existing system with the purpose of conducting a more natural conversation. Once the input is complete, the inserted content can be played by clicking on the speech icon.

Figure 6. Gaze position at consonant "k".

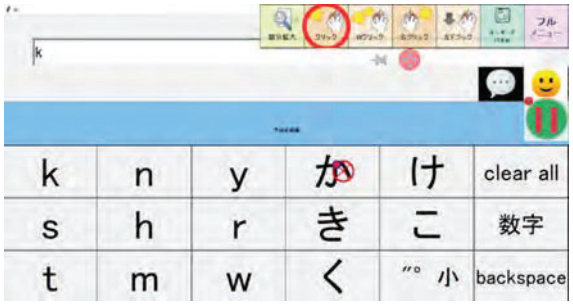

Figure 7. Consonant "k" output and change of vowels.

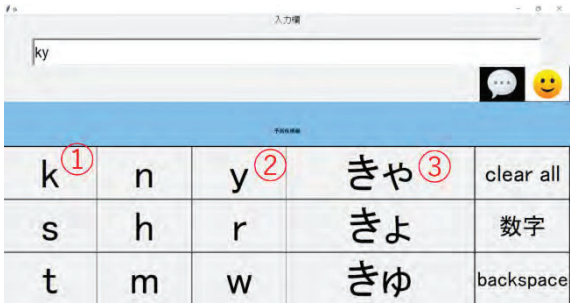

Figure 8. Input flow of the yō-on "kya".

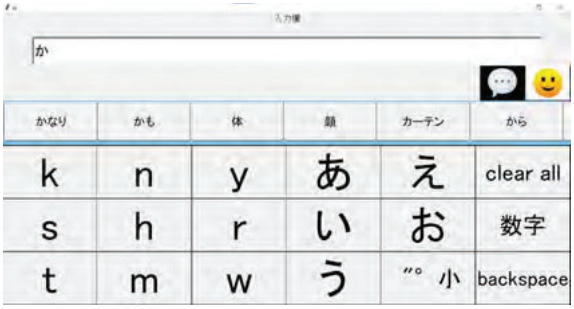

Figure 9. Input of the character "ka" and the suggested words that follow.

Figure 10. Input of the word "face" and the suggested words that follow.

For the programming, a python function called pyttsx3 was used. The voice is taken from HARUKA, one of the speech synthesizers installed within the Microsoft system. With this function, the listener does not have to constantly check on the screen as the user can use this text-to-speech function to communicate. This makes communication possible even when the listener is not nearby. Consequently, this is also thought to be able to reduce the burden on both the user and the listener.

3) Emoji Keyboard

With the widespread application of computing and development of technology, the use of emoji is becoming more and more frequent in network communication. It is irrefutable that emoji plays a vital role in conveying the tone and emotions in a communication. In this study, the emoji keyboard can be accessed by clicking on the emoji icon at the bottom right of the text box.

Evaluations and Considerations

・Evaluation on the new keyboard

The subjects for the experiment are four healthy 20-year-old men. After briefly explaining the mechanism and the input method of the keyboard, each subject trained input both with the mouse and with the eye tracker, for approximately 5 minutes.

Prior to the experiment, the area around the computer was shielded from light in order to prevent any malfunctioning of the eye tracker due to external light. In addition, the subjects also underwent a calibration procedure installed in the HeartyAi software to improve the accuracy and precision of gaze data calculation.

For comparison purposes, the same input text from previous research, “dai 19 kai keisoku jidou seigyo gakkai” was used. This is translated to “The 19th Society of Instrument and Control Engineers” in English. The four subjects input the text twice using the eye tracker. The time taken and the number of input errors for each input were recorded, and the average values calculated. The gaze period for each input was set at 1.0 second.

The average values obtained from the experiment are shown in Table 2. The results from previous researches, the flick method (2018) and the gaze-and-mouth-movement method (2019), were also shown. The input accuracy was calculated using the following formula (1).

$$\text{Input accuracy} = \frac{\text{total input count} - \text{number of input error}}{\text{total input count}} \times 100\ [\%] \quad (1)$$

As shown in Table 2, the improvement of the system created this year can be seen in all the evaluation aspects including the input time, the number of input error, and the input accuracy. From the result, we were able to confirm the effectiveness of the two-step input system developed in this study, even without the use of the predictive conversion function.

Table 2. Comparison with previous research.

Year	2018	2019	2020
Type of input	Gaze input with flick method	Input with gaze and mouth movement	Gaze input with 2-step method
Participants	3 healthy adults	system developer	4 healthy adults
Input time [s]	122.03	108.90	103.96
Input errors [times]	4.3	2.0	0.63
Input accuracy [%]	82.9	93.9	97.8

・Evaluation on the Predictive Conversion Function

Prior to the experiment, we briefly explained the mechanism and input method of the screen keyboard to three 20-year-old healthy subjects. They trained input using the eye tracker for approximately 3 minutes. As in the previous section, we also shielded the environment around the computer from external light and carried out calibration for each subject.

For the experiment, the subjects input the three text examples shown below, by using the predictive conversion function and then without it. The input time for both scenarios were recorded. The texts that were input by using the predictive conversion function are separated into two parts as shown below. The gaze period for each input was set at 1.0 second.

① 「温度下げてください」(Please lower the temperature.)
→「温度」(The temperature)＋「下げてください」(Please lower)

②「もう一度お願いします」(Please say that again.)
→「もう一度」(Say that again)＋「お願いします」(Please)

③「目が疲れた」(My eyes are tired.)
→「目が」(My eyes)＋「疲れた」(Are tired)

Table 3 shows the average input time of the three subjects. The amount of time reduced and the time reduction rate were calculated by using the following equations (2) and (3), respectively.

$$\text{Time reduced} = \text{Normal input time} - \text{Input time with predictive conversion function } [s] \quad (2)$$

$$\text{Time reduction rate} = \frac{\text{Amount of time reduced}}{\text{Normal input time}} \times 100\ [\%] \quad (3)$$

As a result, the use of predictive conversion function is proven to lead to a reduction in input time, and the effectiveness of this function was confirmed, albeit within a limited range.

Table 3. Evaluation on the predictive conversion function.

Input text	Input time[s]		Amount of time resuced [s]	Time reduction rate [%]
	without predictive function	with predictive function		
″Please lower th temperature″	58.39	7.84	50.55	86.57
″Please say that again″	60.55	9.39	51.16	84.49
″My eyes are tired″	43.11	10.10	33.02	76.58
Average time reduction rate [%]				82.55

・Considerations

In the evaluation experiment of the screen keyboard, the number of subjects is small and as the standard deviation is rather large, it is thought necessary to increase the number of subjects in order to evaluate the system more accurately. One of the reasons estimated to have caused the improvement compared to previous studies is the reduction of number of inputs needed when typing the yō-on and soku-on.

On the other hand, from the experiment results on the predictive conversion function, it was proven that the use of this function had led to a reduction in input time. However, since the words inserted have all been inserted into the program in advance, the effectiveness of the function in real life is yet to be confirmed. In order to have a true evaluation of the function, it is necessary to increase the number of candidate words in the dictionary and re-evaluate the mechanism of the predictive function.

To address this issue, we need to look at the various predictive text systems currently used in the numeric keypads of mobile phones and in accessibility technologies. While predictive text systems may differ from one keyboard to another - from ones that curate predictions on texts that the user uses over time, building their own glossary of words, to ones that utilize internal dictionaries and external databases – the common feature in most systems is the use of natural language processing and machine learning. On the other hand, the candidate words in the predictive function of this study are prepared and added into a dictionary in the program in advance. Therefore, there is a limit to the number of words. Moreover, because typing habits also differ from an individual to another, it is necessary to improve the mechanism of the predictive function used in this study in order to achieve a more accurate and efficient way of communication.

For the predictive function used in this study, words and phrases are initially prepared and stored in a nested dictionary. Every time a character is inserted into the text box, words that match the character will be displayed across the screen as candidates. However, enough space to display candidate words was not secured in the predictive text column.

One of the solutions to cope with these problems is to save the input history, and build a glossary of words based on words and phrases that the user types repeatedly. The system will then work to score these words by the probability of when the user will use it again, so that the candidate words will be arranged and presented to the user in order of frequency of use.

Conclusions

In this study, the screen keyboard used in the conventional gaze input system for people with chronic neurological disorders such as ALS was modified with the purpose of improving operability and efficiency. We also introduced three new functions into the system – predictive conversion function, audio output, and an emoji keyboard – to shorten the input time, reduce the probability of eye fatigue and the burden on the users.

From the results of the evaluation experiments, we could confirm the effectiveness of the modified screen keyboard in improving the input time, input efficiency and input error, as compared to other existing input systems. Furthermore, although it was only a simple experiment, we were also able to confirm that the predictive conversion function plays a vital role in shortening the input time. Therefore, it could be said that improvement was achieved.

However, the predictive conversion function of this system is no more than a dictionary of words prepared in advance, and the range of word candidates that can be handled is limited. Therefore, in order to more efficiently and accurately predict intended words in a conversation, and to also build a more useful dictionary of word candidates, it is deemed necessary to consult the opinions of experts and patients in the fields related and analyze the daily conversation patterns of the parties concerned.

In the future, we aim to do more research on the existing predictive text systems currently used in smartphones and hopefully apply machine learning and natural language processing skills for improving and developing a more efficient input system.

References

Feit, A. M., Williams, S., Toledo, A., Paradiso, A., Kulkarni, H., Kane, S. and Morris, M. R., (2017). Toward Everyday Gaze Input: Accuracy and Precision of Eye Tracking and Implication for Design. *Proceedings of the 2017 CHI Conference on Human Factors in Computing Systems*, 1118-1130.

Fujita, T., Hama, K., Suzuki, M. and Nakamura, T. (2019). Gaze Input System for communication used mouth movement. *Proceedings of 2019 Japan Society for Precision Engineering Hokkaido Branch Office Meeting*, 41-42.

Hara, S. (2020). Gaze-input electric communication device for amyotrophic lateral sclerosis patient improved social participation. *Journal of Kyushu University of Health and Welfare*, 21, 87-93.

Kobayashi, H. (2018). Communication Aids for Amyotrophic Lateral Sclerosis. *The Japan Journal of Rehabilitation Medicine*, 55, 8, 564-572.

Mitsubishi Tanabe Pharma Corporation. ALS station, forefront of ALS, Vol.6 Communication disorder due to ALS, https://als-station.jp/recent_situation_06.html

Sagarifuji, N. (2015). Chapter 2 Eye-Gaze Input Interface for People with Severe Disabilities. *The Journal of the Institute of Image Information and Television Engineers*, 69, 6, 530-534.

Jia Xin, Y., Hama, K., Suzuki, M. and Nakamura, T. (2020). Development of gaze input system for communication using predictive conversion. *Proceedings of 2020 Japan Society for Precision Engineering Hokkaido Branch Office Meeting*, 39-40.

DEVELOPMENT OF SMARTPHONE OPERATION SUPPORT SYSTEM BASED ON INCLUSIVE DESIGN

Yeoh Wei Loon[a], Ryuto Handa[a], Isamu Matsuno[a], Hidetoshi Nakayama[*,a] and Shinya Suzuki[a]

[a] National Institute of Technology (KOSEN), Nagano College

*nakayama@nagano-nct.ac.jp

Abstract

In this study, based on the design process of "inclusive design", we developed a prototype system that can reply with a message template without character input on a smartphone. This is to solve a problem for people with diabilities like those we met at "the Japan AT Forum 2018 in Tokuyama". Character input by smartphone is still a big problem for a person with disabilies and the elderly. This research aims to make messaging even more accessible for those who have difficulty using hands. We have used the switch input device "MESH made by Sony" and the web service "IFTTT" to solve this problem. Our system can reply to a message by just using three buttons without the need to take out one's smartphone. Although three buttons definitely limit how we are going to reply, it is convenient when we just want to reply to someone with certain messages such as "Thanks". This could also reduce the burden for people with muscle difficulty in messaging as they can use only one or three buttons instead of exhaustingly typing by using the small smartphone keyboard. Not only that, this device is especially useful when the surrounding environment is limiting chances for a reply. For instance, while in a meeting, the cinema or while snowboarding, we can reply to messages without needing to enter the usally required application. Some people have taken this device and tested it out. As a result, they were happy with it because it is convenient and easy to use. Even though this device is good, the cost is still high. Nowadays, AI in smartphones is able to do much more than what we have created it for. In the future, it is expected that we can send more than three messages and make our own hardware which we can use to reduce the cost and expand what we can do instead of using the MESH.

Keywords:

inclusive design, disabled people, smartphone, switch input device, message template

Introduction

With the spread of IT equipment in recent years, the development of IT equipment that can support physically handicapped people is highly expected.

In this research done together with Mr. X (pseudonym), who is a physically disabled perdon that I met in the workshop of the Japan AT Forum 2018 in Tokuyama, we decided to work on the development of a system to support smartphone operation based on the idea of inclusive design that will be described later.

Inclusive design ensures that products and environments are open to all people, regardless of age, disability, and background. With this in mind, we will be able to explore the hidden needs and use them as an idea to improve one's quality of life.

Mr. X, mentioned above, has a physical disability which limits his ability to move his limbs as he wishes, especially his fingers. Therefore, sending messages using smartphones poses many challenges for him due to the small size of the keyboard.

Thus, the purpose of this study was to develop an operation support system (OSS) that enables quick reply without the need to manually type on smartphones.

It is thought that the development of this system will also be able to help those who have difficulty in using their phones temporarily (e.g., while wearing gloves, or with injured fingers, etc). (Figure 1)

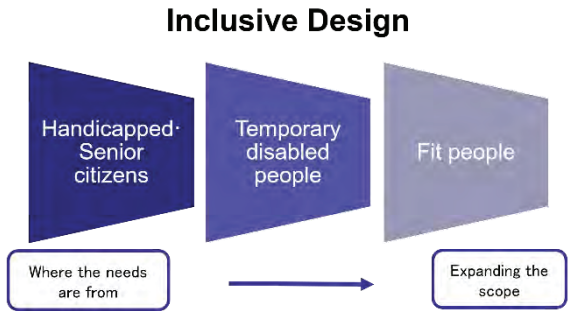

Figure 1. Application of Inclusive Design

Overview of the prototype system

To fully realize the devised device, the following system has been proposed by us.(Figure 2) First, a button-type input device(a) and a smartphone(b) that are wirelessly connected are used to link to the web application(c) on the internet when the button is pressed. Then the message template will be sent by the web application to the receiver in a messaging platform (LINE etc)(d). In order to realize this system, we will create a prototype by using a commercially available IoT kit and verify wheter it can be operated pratically or not. At the same time, we will also ask the targeted user and healthy users to try it and provide us with more information so that it can be improved enough to be implemented in society in the future.

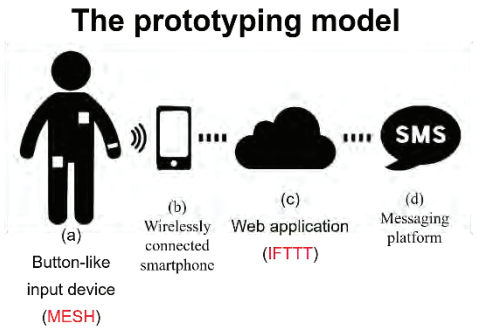

Figure 2. The diagram of the proposed system

In creating the prototype of the system, we used the IoT kit series MESH owned by Sony Corporation. MESH is a block-shaped device equipped with a Bluetooth module, and there are multiple blocks of MESH which are assigned with a single function such as a sensor or button.[1] By wirelessly connecting the block and the smartphone and using a dedicated application, it is possible to program the behaviour of the block. In addition, the function can be greatly expanded by linking with web services such as Google Home and IFTTT through a dedicated application.

Figure 3. MESH

In order to realize the operation of sending a message template to SMS by just pressing a button, we have created a prototype of the system by using the MESH block equipped with a button and the IFTTT linkage function of LINE. As shown in Figure 3, by fixing the button block to the wristband for a wristwatch using Velcro, it is easy to attach the block to the wrist and detach the block during charging.

Figure 4. Button block that is fixed to the wristband

At the Japan AT Forum 2019 in Toyama held in September last year, we asked the participants who mostly consisted of people without disabilities to use the prototype of the created system and we conducted an interview survey to gather data for device performance and usability. As a result, we were able to obtain valuable opinions such as 'I want to register more than one' and 'It is difficult to press because the push button is just too small and has a dented shape'.

Overview of the two improved systems

Based on the feedback received from the participants at the Japan AT Forum 2019 in Toyama held in September last year, we decide to improve the system in terms of multiple registration of the message template and the ease of pressing the button.

The first plan is to improve or add more push buttons. By selecting one with a shape that is easier to push from the ready-made buttons and connecting it with multiple MESH blocks (GPIO blocks) equipped with expansion terminals that can be wired to the outside, it is thought that the two problems that were mentioned above can be solved.

The second plan is to use the NFC reader function of the smartphone. A commercially available NFC tag is used as a trigger for the IFTTT applet, and a message template is sent by holding a smartphone over it. Unlike the first button, since the second plan requires less detailed manipulation and the number of message templates that can be registered can equal the number of NFC tags, it is thought that this will be the solution to the problem.

Figure 5 shows a schematic diagram of a system (system version 2-A) that uses MESH GPIO blocks and multiple buttons. Based on the diagram, we decided to connect multiple buttons to GPIO block and send different fixed phrases to IFTTT from each connected terminal which is pre-set by the button. We also decided to fix the button to the wristband together with the GPIO block so that it can be worn on the wrist.

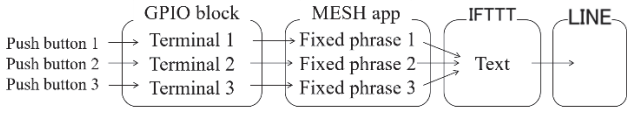

Figure 5. The schematic diagram of system version 2-A

The push button was soldered so that it could be connected in parallel to the GND terminal of the GPIO block and the three digital input terminals, and then connected to the GPIO block. After, we used a glue gun to strengthen the strength of the wires by fixing the soldered part. We fixed it to the band with Velcro so that the position could be adjusted on the wristband. (Figure 6)

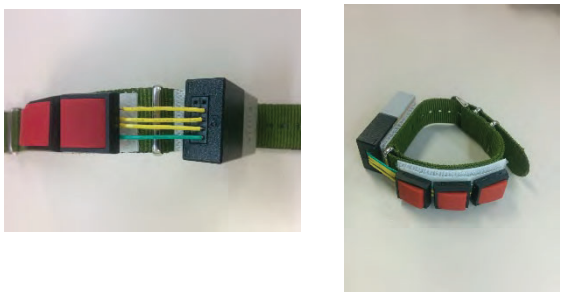

Figure 6. The finished device

Figure 7 shows the screenshot of the entire program created on the MESH application. Here, events are sent from the three digital input terminals of the GPIO block to different IFTTT blocks, respectively. By using IFTTT blocks, we can set a fixed phrase and send it to IFTTT together with the event.

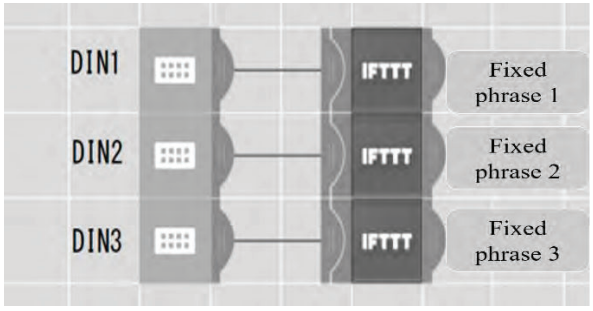

Figured 7. Program on the MESH application

As shown in Figure 7, we set the IFTTT applet so that the text sent from the MESH application of IFTTT block will be sent to LINE Notify.

Figure 8. The setting of IFTTT applet

Figure 9 shows a schematic diagram of the system (system version 2-B) that uses the NFC reader function of the smartphone. A user-definable HTTP callback, Webhook is used as a trigger for the IFTTT applet that sends a fixed phrase to LINE Notify. BY doing this, it will be possible for us to activate the IFTTT applet by sending the POST request to the URL that has been set by the Webhook. The operation of sending a request to the URL is performed by using Trigger, which is a task launcher for smartphones. To set the task execution condition of the Trigger, we used the registered NFC tag, and set the task to send a request to the specific URL after the reading of the NFC tag.

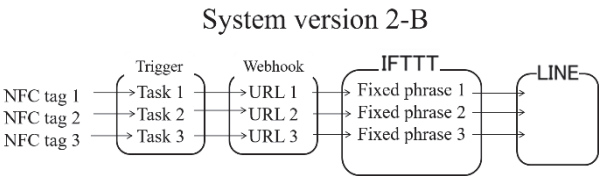

Figure 9. The schematic diagram of system version 2-B

Figure 10 shows the appearance of the NFC Tags (MM-NFCT manufactured by Sanwa Supply) that we purchased this time. It is a circular sticker tag with a diameter of 23mm and a thickness of 0.6mm that can be attached to various things such as clothes, etc. This time, it is used as a task execution condition of the Trigger, which is a task launcher for smartphones that will be described later.

Figure 10. The obverse and reverse of NFC Tags.

Trigger is an Android smartphone's application provided by Coleridge Apps LLC in the United States, and you can combine triggers and actions to create tasks, then activate the tasks that you created with conditions that you set. In addition to the date and time, the reading of the registered NFC tag can also be set as the trigger condition which is what we need.[2] With this, not only can we use NFC Tags to trigger automation on changing the screen brightness and volume, but we can also set it so that a specified URL can be accessed automatically as well.

This time, we created a task called "Open the specified URL when the registered NFC Tags is read". Here the purchased NFC tag seal was registered as a task trigger, and the URL set by the Webhook, which will be described later, was specified as the access destination. In addition to that, "run in the background" is enabled to prevent the browser application screen from appearing when accessing the URL.

(a) Set NFC tags as trigger. (b) Register NFC Tags.

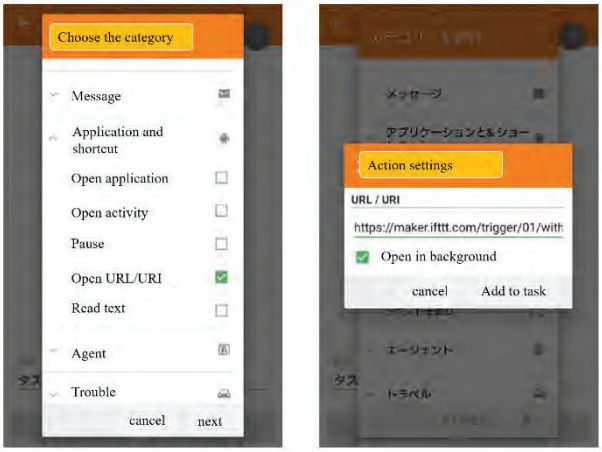

(c) Allow "Open URL/URI" (d) URL from the webhook

Figure 11. Settings of Trigger.

Webhooks are "user-defined HTTP call backs". They are usually triggered by some event and when that event occurs, the source site makes an HTTP request to the URL configured for the webhook.[3] Users can configure them to cause events on one site to invoke behaviour on another. This time with the IFTTT application, the notification from the webhook is set as a trigger and the transmission of the fixed phrase by the LINE Notify is set as an action.

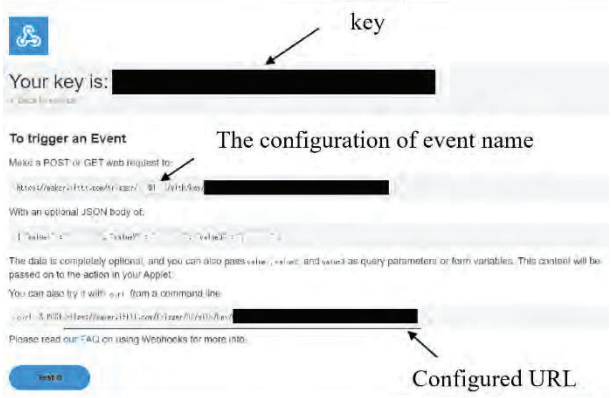

Figure 12. Webhook

Figure 13. The configuration of IFTTT application

Review

After we asked the people without disabilities to try each of the two systems that were described above for a week, this review is what we were able to gather. Among these, some are good reviews such as “You can easily send a message with just a touch of button”, “It was convenient for urgent contact”, etc. Not only that, but there were also bad reviews such as “It is troublesome to create a new MESH and IFTTT account”, “I tend to make sure I didn’t break the input device accidentally when it is attached to my arm which is tiresome,” and “Sometimes the NFC Tags can’t be read properly”.

Not only that, but with new and more attractive technology such as APPLE watch becoming a trend nowadays, it becomes harder for people to use our device just for the sake of replying to a message. Technology such as APPLE watch not only makes replying to the message much more convenient, but also saves people’s lives whenever an abnormal change in the wearer’s health condition is detected. Still, due to an APPLE watch’s high price, our product has received a lot of positive feedback because it is much cheaper and easier to use.

Table 1. Review of each system version

	Good	Bad
System version 2-A	Can use it by intuition due to its simple design	Does not fell right because must bring around with the wristband
System version 2-B	It is easy to bring around due to its small size	Sometimes it does not respond properly

Figure 14. Apple watch

Results and Discussion

System version 2-A is more stable and easier to use for the button operation, but it is inconvenient to install an input device. Compared to that, system version 2-B does not require a large input device, but its button operation is unstable. From here we can learn that each has its own advantages and disadvantages.

In addition, from the review we can found that it was useful not only for replying to a message from the other party but also for urgent contact depending on the fixed phrase that has been set.

On the other hand, there were some people who felt annoyed or felt it was unnecessary when being introduced to the system. In addition, some people also felt it inconvenient to wear an input device when they are already wearing a watch. To solve this problem, it is necessary to simplify the settings and make the input device as small as possible. However, it seems difficult to solve these problems with the current system using the ready-made kits and services.

From the above analysis, it is considered necessary to develop a new hardware and software without using the ready-made kits and services.

Conclusions

In the end, we were able to create a prototype by embodying the idea of a system that can reply quickly without the need to manually input a full answer on smartphones, starting out with the needs of people with physical disabilities in mind. In addition, we were able to create a system that is easier to use based on the user feedback. Furthermore, we were able to summarize the results of reviews of the improved system by the non-disabled users and clarify the new improvements on the device.

In the future, we will try to develop a new hardware and software that does not rely on ready-made kits and services to simplify settings and reduce the size of the input devices. In addition, we will ask potential users as well as people without disabilities to try the product to verify and evaluate the operability of the product.

Not only that, but it is also expected that the concept of inclusive design will spread widely in the future based

on this research. This will greatly lead to support for the independent life of physically handicapped people.

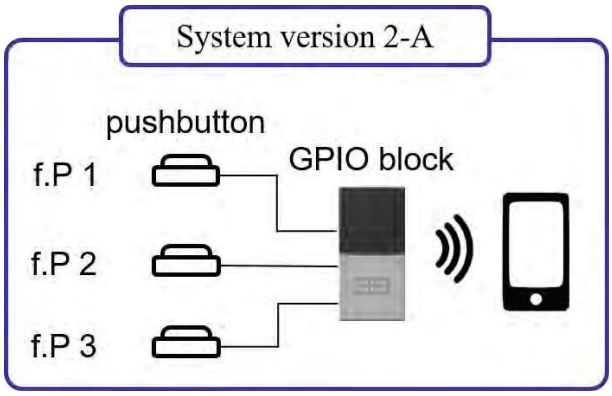

Figure 14. System version 2-A, f.P here means fixed phrase

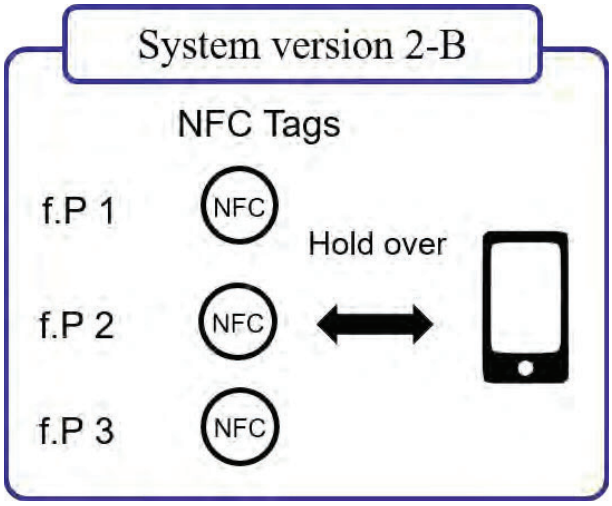

Figure 15. System version 2-B, f.P here means fixed phrase

Acknowledgements

Throughout the writing of this paper, I have received a great deal of support and assistance from others both mentally, and physically.

I would first like to thank my teacher, Professor Nakayama, whose expertise was invaluable in formulating the research questions and solutions. Your insightful feedback pushed me to sharpen my thinking and encourage me to give my best effort to complete this project.

I would like to acknowledge my classmates for sharing my burden whenever difficult questions come up. Without you all, I could not finish this project in time. Also, thanks to my juniors who provided stimulating discussions as well as happy distractions to rest my mind outside of my research.

In addition, I would also like to thank my parents for their wise counsel and sympathetic ear. My parents always accept who I am and readily listen to my problems.

References

With MESH, anything can become a smart device! |Sony. Retrieved from https://meshprj.com/en/

Trigger – Task Launcher – Apps on Google Play. Retrieved from https://play.google.com/store/apps/details?id=com.jwsoft.nfcactionlauncher&hl=en_US&gl=US.

Violet Whitney (2019). Linking IFTTT & Processing with Webhooks. *Measuring the Great Indoors, Medium.* Retrieved from https://medium.com/measuring-the-great-indoors/linking-ifttt-processing-with-webhooks-6b20c6ed722d

Functional Engineering Materials

Mechanical Property of Low-Melting Sn-Bi Lead-Free Solder Alloys

A. Yamauchi[*, a], J. Umeyama[b] and M. Kurose [a]

[a] Mechanical Engineering, Institute of Technology, Gunma College, Maebashi, Japan
[b] Student, Institute of Technology, Gunma College,
Present address: Sumitomo Heavy Industries, Ltd., Chiba, Japan

*ayama@gunma-ct.ac.jp

Abstract

The purpose of this study is to clarify the conditions of Sn-Bi alloy's superplasticity. Sn-Bi-X low-melting lead-free solder alloys were used in this study. Dog bone-type tensile test specimens machined from the cast cylindrical Sn–Bi–X ingot. Tensile tests of Sn-Bi-X alloys were carried out at various temperatures (298, 313, 333, and 353 K) and under various strain rates (from 5.25×10^{-5} to 5.25×10^{-2} s^{-1}). The cross-sectional microstructures and fracture surfaces were observed and analyzed with SEM, EPMA, and EBSD. In this study, superplasticity of Sn-Bi-X alloys was observed at high temperatures (more than 333 K) and low strain rates (under 5.25×10^{-4} s^{-1}). The strain rate sensitivity 'm' value for Sn-Bi-X alloys was less than 0.3. From the results of the microstructure observation after superplasticity, it was showed that the primary crystal Sn grains could not deform along the axial direction and then eutectic microstructure contributed to superplasticity deformation. This result speculated that the deformation mechanism is similar to that of fine-grained superplasticity using boundary sliding.

Keywords: *Lead-Free solder, Sn-Bi based alloy, Superplasticity, Ductility, Strain rate sensitivity*

Introduction

Recently, the use of lead and lead-containing products are banned in many countries because of their harmful effects on the human body and environmental problems (e.g., Suganuma, 2001). Many lead-free solder alloys have been developed to replace Sn-Pb solders in electronic home appliances. Sn-Ag-Cu lead-free solder, for example, Sn-3.0mass% Ag-0.5mass% Cu (SAC305), has spread as the substitute of Sn-Pb lead solder because of the high strength and high joint reliability. However, SAC305 is not easily applied to some low heat-resistance components due to the high melting temperature, about 494 K, higher than that of Sn-Pb eutectic solder, 456 K. The eutectic Sn-58mass% Bi alloy with the lower melting temperature of 412 K has several advantages in low-temperature soldering because it can protect electronic devices from damage under high reflow temperatures. However, Bi-containing solder alloy shows low ductility. Therefore, the use of Bi containing solder alloys in electronic home appliances is limited (e.g., Watanabe, 2005; Nagano et. al., 2006).

Aiming to solve this problem, Takao, Yamada, Hasegawa, and Matsui (2002) reported that Sn–Bi and Sn–Bi–Cu alloys show superplasticity. However, the superplasticity mechanism for Sn-based alloys remains unclear. In this study, we investigate the influence of the strain rate and the testing temperature on Sn–Bi–Cu and Sn-Bi-Sb alloys. Tensile tests are performed under various conditions to clarify the superplasticity behavior.

Experimental Procedure

Sn, Sn57mass% Bi, Sn0.7mass% Cu with 99.5% purity, and Sb with 99.9% purity were used to synthesize Sn-40mass%Bi-0.1mass%Cu and Sn-40mass%Bi-Xmass%Sb (X = 0.1, 0.5,1.0). Hereafter, the composition unit "mass%" is omitted. The synthesized ingots were weighted and fused in Al_2O_3 crucible in an electric furnace at 673 K and left to solidify for 24 h to obtain a homogeneous composition. Then the ingots were remelted at 653 K and cast in an Al mold cooled at 15 $Kmin^{-1}$ to form a cylindrical ingot. Dog bone-type tensile test specimens machined from the cast cylindrical Sn-40Bi based alloys ingot are shown in Figure 1.

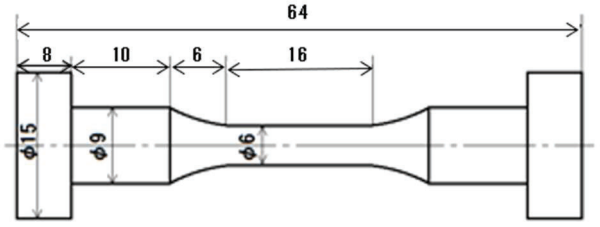

Fig.1 Schematic of tensile test specimen (unit: mm)

Tensile tests were performed on a universal material testing machine at strain rates of 5.25×10^{-2}, 5.25×10^{-3}, 5.25×10^{-4}, and 5.25×10^{-5} s^{-1}. Each test piece was tested at 298, 333, and 353 K using an atmospherically controlled furnace until a complete fracture occurred. The tensile test results were statistically averaged over three trials under each set of conditions.

Specimens before and after tensile testing were embedded in resin and cut for microstructural observation. Their surfaces were polished with SiC papers of up to # 1500-grit and then with a 1-μm diamond abrasive and colloidal silica for mirror finishing. The cross-sectional microstructures and fracture surfaces were observed with a scanning electron microscope (SEM). The crystal orientation was also analyzed by electron backscatter diffraction (EBSD). The elemental distribution was evaluated by electron probe microanalysis (EPMA).

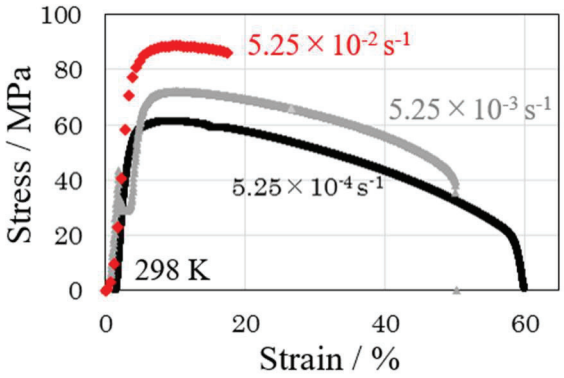

Figure 2 Stress-Strain curves of Sn-40Bi-0.1%Cu at 298 K under various strain rate.

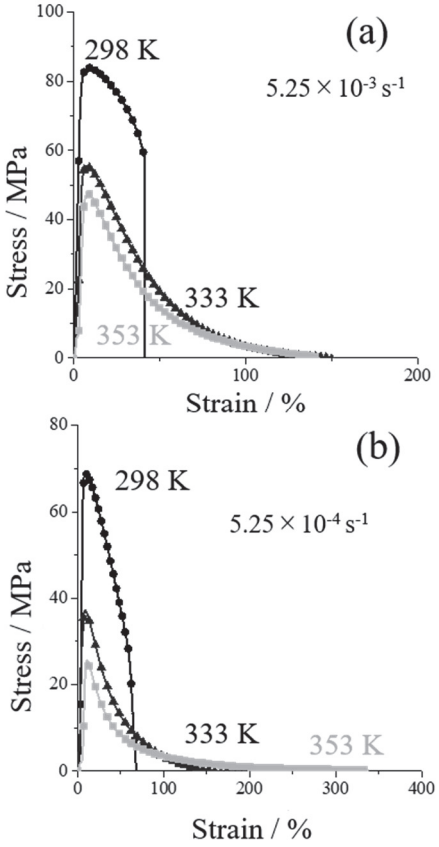

Figure 3 Tensile stress–strain curves of Sn–40Bi–0.1Cu at 298, 333, and 353 K under strain rate of (a) 5.25 × 10^{-3} and (b) 5.25 × 10^{-4} s^{-1}.

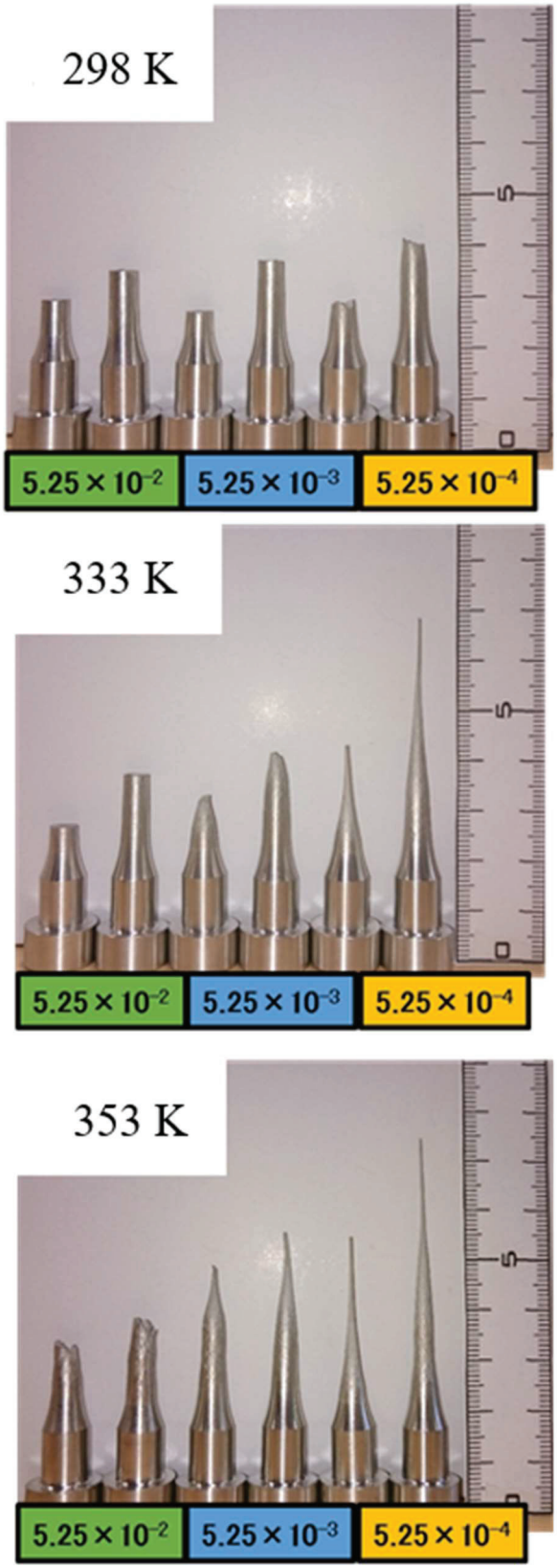

Figure 4 Optical microscope images of fractured specimens after the tensile test.

Results and Discussion

The effect of strain rate on the mechanical properties

of Sn-40Bi-0.1Cu is shown in Figure 2. The tensile strength decreased with a decrease in strain rate. The tensile strength under 5.25×10^{-2} s^{-1} became 0.7 times as large as that of the alloy under 5.25×10^{-4} s^{-1}. On the other hand, the elongation increased with a decrease in strain rate. The specimen elongation is over larger three times as large as that of 5.25×10^{-2} s^{-1}. The tensile behavior of Sn-Bi-Cu at 298 K is different from superplasticity. Figure 3 shows the effect of test temperatures on the mechanical properties of Sn–40Bi–0.1Cu alloy. With decreasing strain rate, the tensile strength is decreased but the elongation is rapidly increased at temperatures of >333K and strain rates of $<5.25\times10^{-3}$ s^{-1}. The highest elongation, under the condition of 353 K and 5.25×10^{-4} s^{-1} is 340%. Superplastic behavior is classified as > 200% strain(e.g., Ohsawa and Nishimura, 1989). Therefore, superplasticity appears at temperatures of > 333 K and strain rates of $< 5.25\times10^{-4}$ s^{-1}. From the stress-strain curves at 298 K, the stress decreases remarkably after the ultimate tensile strength is achieved as the strain rate decreases. This is attributed to the relative strengthening of recovery and recrystallization mechanism in the Sn-40Bi-0.1Cu alloy compared to the work-hardening mechanism. Figure 4 shows OM images of fractured Sn-40%Bi-0.1Cu specimens after the tensile test. Sn-Bi-Cu alloys at 298 K and at 333 K under 5.25×10^{-2} s^{-1} displayed a brittle fracture mode. Sn-Bi-Cu alloys at 333 K under 5.25×10^{-3} s^{-1} and at 353 K under 5.25×10^{-2} s^{-1} displayed a ductile fracture mode. These specimens indicated necking and their fractured surfaces consist of ductile dimples. At remaining specimens chisel point fracture were observed. The tip of the break department was a circular. Based on the obtained stress-strain curves and fractured morphologies, fracture mode can be divided into four classes as shown in Figure 5. The microstructure of Sn–40Bi–0.1Cu shows the hypoeutectic structure comprising primary Sn dendrites with the average diameter of approximately 25 μm and Sn–Bi eutectic phases with the average diameter of approximately 10 μm from the SEM observation. The EPMA results confirm that Cu atoms are dissolved in the Sn–Bi eutectic-phase matrix.

The strain rate sensitivity index "*m*" at various test temperatures is shown in Figure 6. The strain rate sensitivity index "*m*" is defined generally by the equation

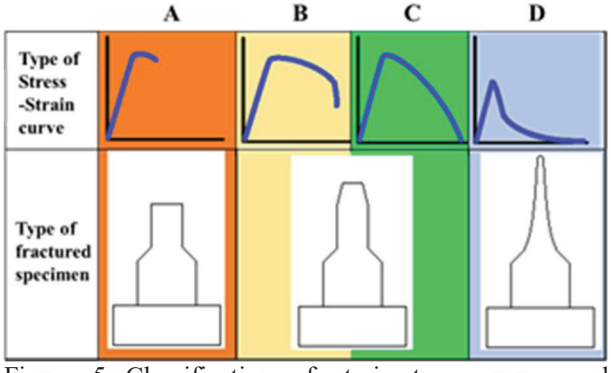

Figure 5 Classification of strain-stress curves and fracture mode of Sn-based alloys.

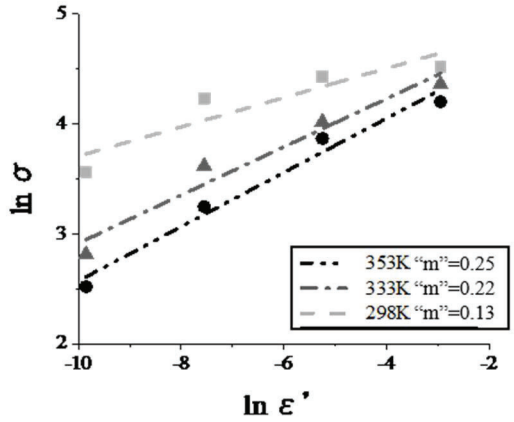

Figure 6 Strain rate sensitivity index "m" of Sn–40Bi–0.1Cu alloy at various test temperatures.

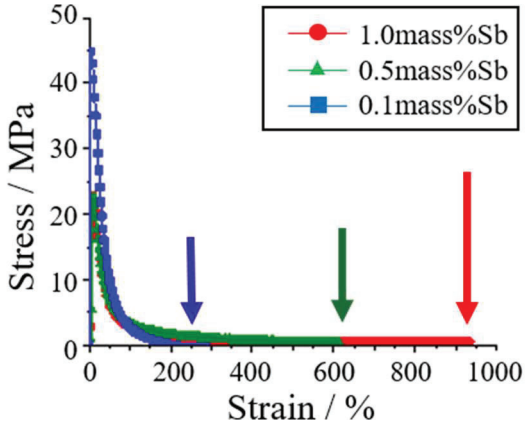

Figure 7 Stress-Strain curves of various Sn-Bi-Sb alloys at 353 K under strain rate of 5.25×10^{-4} s^{-1}.

below.

$$m = \frac{d\ln\sigma}{d\ln\dot{\varepsilon}} \quad \text{equation (1)}$$

The strain rate sensitivity index "*m*" is calculated by the slopes of various temperature's lines. Index "*m*" increases with temperature increase. The strain rate sensitivity index "*m*" for general superplastic materials with fine grains is >0.3 (e.g. JIS H7007, 2002; Ishihara and Kondoh, 1997). From this figure, this value is lower than the critical value of 0.3 indicating fine-grained superplasticity. However, it is close to 0.3.

Next, we investigated the effect of strain rate and test temperature on the mechanical properties of Sn-40Bi-XSb alloys. The stress-strain curves of Sn-40Bi-X%Sb alloys are similar to those of Sn-40Bi-0.1Cu and Sn-40Bi-0.01Ni alloys (e.g. Yamauchi, Ida, Fukuda, and Yamaguchi, 2018). Figure 7 indicates the stress-strain curves of Sn-40Bi-X%Sb alloys at 353 K under 5.25×10^{-4} s^{-1}. In this condition, the highest tensile strength is 45 MPa for Sn-40Bi-0.1Sb alloy. The tensile strength decreased with an increase Sb concentration. The tensile strength of Sn-40Bi-1.0Sb, 23 MPa, became half times as large as that of Sn-40Bi-0.1Sb at 353 K under 5.25×10^{-4}

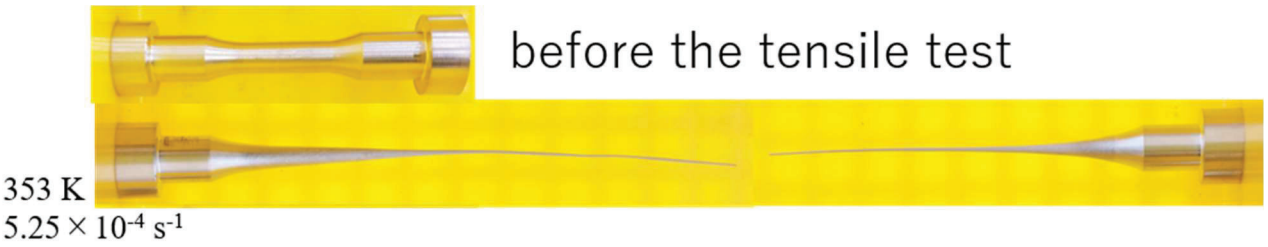

Figure 8 Appearance of the Sn-40Bi-1.0Sb specimen before and after tensile testing at 353 K under 5.25×10^{-4} s^{-1}

s^{-1}. Conversely, the elongation increased with Sb concentration. The highest elongation of Sn-40Bi-1.0Sb, under the condition of 353 K and 5.25×10^{-4} s^{-1} is not less than 900% (Figure 8 shows a photograph of the appearance of the specimen having an elongation of not less than 900%). These specimens observed longer elongation without necking and their fractured mode shows chisel point fracture. The reason for this is that Sb is not only solid-solved in Sn primary crystals, but also solid-solved in Bi at all rates, so unlike the conventional Cu and Ni additions, it is sufficient to add a certain amount of Sb instead of adding a small amount. It is considered that this resulted in superplastic deformation. In addition, from the microstructure observation results, it is considered that superplastic deformation is likely to occur because the eutectic structures of Sn primary crystals and Sn-Bi become finer as the Sb concentration increases.

Figure 9 shows the strain rate sensitivity index "*m*" at various test temperatures. The strain rate sensitivity index of these alloys was lower than the threshold value of 0.3 in general fine-grained superplasticity. This result was the same as the Sn-40Bi-0.1Cu and Sn-40Bi-0.01Ni alloys(e.g. Yamauchi, Ida, Fukuda, and Yamaguchi, 2018). The microstructure and average grain sizes of Sn-40Bi-Sb alloys are similar to those of Sn-40Bi-0.1Cu alloy. From the EPMA analysis, it is indicated that Sb atoms are dissolved in the primary Sn phase preferentially, and then with increasing Sb concentration

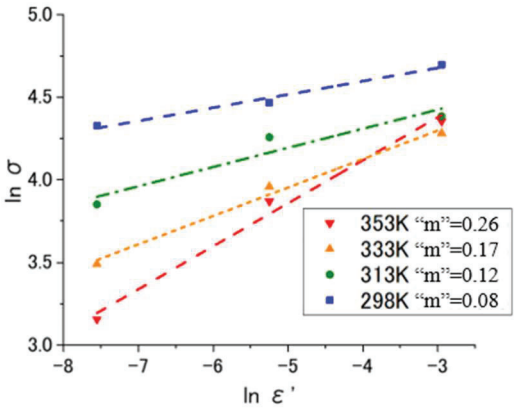

Figure 9 Strain rate sensitivity index (*m*) of Sn–40Bi–1.0Sb alloy at various test temperatures.

Sb atoms are also dissolved in the Sn–Bi eutectic-phase matrix.

Conclusions

In the present study, the tensile behaviors of Sn–40Bi–0.1Cu and Sn-40Bi-X%Sb(X = 0.1, 0.5,1.0) alloys at various test temperatures and strain rates were investigated and observed by OM, SEM, and EBSD. The superplastic deformation mechanism of these alloys was clarified. The following results were obtained.

1. The tensile strength was decreased and the elongation was increased with increasing temperature or decreasing strain rate.
2. Superplasticity of Sn–40Bi–0.1Cu and Sn-40Bi-X%Sb(X = 0.1, 0.5,1.0) alloys was observed at high temperatures and low strain rates, specifically at >333 K and $<5.25 \times 10^{-4}$ s^{-1}.
3. The strain rate sensitivity index *m* was increased with temperature. The strain rate sensitivity index *m* of Sn-based alloys is lower than the critical value of 0.3 indicating fine-grained superplasticity.The maximum *m* of Sn–40Bi–1.0Sb alloy was 0.26.
4. Cu atoms are dissolved in the Sn–Bi eutectic-phase matrix. Sb atoms are dissolved in both the primary Sn phase and Sn–Bi eutectic-phase matrix. The difference of dissolved into the phase caused the disparity of superplasticity elongation between Sn-40Bi-0.1Cu and Sn-40Bi-Sb alloys.

Acknowledgements

This work was supported by JSPS KAKENHI Grant Number 18K03859, ECB Foundation (26A003), and JKA and its promotion funds from Auto race (27-181). This work was partially performed under the inter-university cooperative research program (Proposal No. 20G0041) of the Cooperative Research and Development Center for Advanced Materials, Institute for Materials Research, Tohoku University. The authors would like to thank Chinami Nagata, Masato Fukuda, and Yukihiro Izawa for their support of fabricating test specimens.

References

Nagano, M. Hidaka, N. Watanabe, H. Shimoda, M. Ono M. (2006). Effect of addition elements on creep properties of the Sn-Ag-Cu lead free solder. Journal of Japan Institute of Electronics Packaging, 9, 171-179.

Ohsawa, H. Nishimura, H. (1989). Manufacturing methods of superplastic materials and commercial applications. J. Jpn. Inst. Light Metals, 39, 765-775.

Suganuma, K. (2001). Advances in lead-free electronics soldering. Curr. Opin. Solid State Mater. Sci., 5, 55-64.

Takao, H. Yamada, A. Hasegawa, H. Matsui, M. (2002). Mechanical properties and solder joint reliability of low-melting Sn-Bi-Cu lead free solder alloy. J. Jpn Inst. Electron. Packag., 5, 152-158.

Yamauchi, A. Ida, K. Fukuda, M. Yamaguchi, (2018). T. Tensile properties of Sn-Bi lead-free solder alloys. Solid State Phenomena, 273, 72-76.

Watanabe, H. (2005). The lead-free solder of addition micro-elements in industrial products. Journal of Japan Institute of Electronics Packaging, 8, 183-187.

LOW TEMPERATURE SINTERING OF $ZnAl_2O_4$ CERAMICS CONTAINING $Cu_3Nb_2O_8$ ADDITIVE AND THEIR DIELECTRIC AND THERMAL PROPERTIES

K. Shigeno*, [a], T. Yano[a] and H. Fujimori [b]

[a] National Institute of Technology, Ube College, 2-14-1 Tokiwadai, Ube, Yamaguchi, Japan.
[b] Graduate School of Yamaguchi University, 2-16-1 Tokiwadai, Ube, Yamaguchi, Japan.

*E-Mail: shigeno@ube-k.ac.jp

Abstract

For low temperature co-fired ceramic (LTCC) materials used for compact electronic devices, their low heat dissipation is a problem, hence high heat conduction has been required. Previous studies by the authors have been intended to develop sintering aids that could allow Al_2O_3 (alumina) with high thermal conductivity of approximately 30 W/mK to be sintered at a low temperature with a small quantity. By utilizing $CuO–TiO_2–Nb_2O_5–Ag_2O$ additives, low temperature co-firing with silver electrodes at 900 °C or less was realized and a low temperature co-fired alumina having high thermal conductivity of 20 W/mK was successfully developed. In this study, we focused on $ZnAl_2O_4$ (gahnite) ceramic, which has the potential to exhibit higher thermal conductivity than Al_2O_3 but sinters densely at a moderate temperature of approximately 1,500 °C, has been investigated. When adding only 4 wt% $Cu_3Nb_2O_8$ (copper niobate) additive, the sintering temperature was lowered significantly to 935 °C, which is lower than the melting point of silver of 961 °C. The sample fired at 935 °C for 24 h exhibited a relative dielectric constant (ε_r) of 9.1, a quality factor multiplied by resonant frequency ($Q \times f$) value of 80,000 GHz (at a measurement frequency of approximately 12 GHz), and a temperature coefficient of resonant frequency (τ_f) of –65 ppm/K, being relatively satisfactory values. The thermal conductivity of the sample was 8.7 W/mK, which exceeds that of conventional LTCC materials (~2–7 W/mK). In addition, low-temperature sintering mechanism was also discussed. The melting temperature of the powder mixture consisting of the $Cu_3Nb_2O_8$ additive and $ZnAl_2O_4$ was measured, but no significant changes were observed compared with the melting temperature of the $Cu_3Nb_2O_8$ additive only of approximately 970 °C. These results indicated that the densification of the sample occurred in solid state (solid-state-activated sintering).

Keywords: *Ceramics, $ZnAl_2O_4$ (Gahnite), Low-temperature sintering, Microwave dielectric properties, Thermal conductivity*

Introduction

Low-temperature co-fired ceramics (LTCC) are dielectric materials widely used for small electronic devices such as wiring substrates and integrated circuit packages (e.g., Sebastian, 2008; Imanaka, 2005). However, the low heat dissipation of LTCC materials has been a problem. Aluminum-based oxide ceramics, such as alumina (Al_2O_3) as the base material, have relatively high thermal conductivity. However, it is necessary to add a large amount (approximately 50 % or more of the total amount) of low softening point glass with low thermal conductivity to achieve low-temperature sintering. Consequently, the majority of these conventional LTCC materials exhibit a shortcoming, namely, a low thermal conductivity (approximately 2–7 W/mK) (Sebastian and Jantunen, 2008; Induja et al., 2015). Recently, the heat generation density of semiconductors, such as LEDs mounted on LTCC multilayer devices, has been increasing, and LTCC materials with a high thermal conductivity have been in demand (Shimizu et al., 2015). Therefore, in our previous research, by utilizing alumina as a base material with a high thermal conductivity of approximately 30 W/mK, we developed sintering additives for alumina through which alumina could be sintered at a low temperature, by adding a small amount. As a result, we have developed a $CuO-TiO_2-Nb_2O_5-Ag_2O$ additive that can sinter alumina at a low temperature of 900 °C or less at 5 wt% addition, and have realized low-temperature co-fired alumina (LTCA) with high thermal conductivity of 18 W/mK (Shigeno et al, 2007; Shigeno et al., 2016).

In this study, we focused on gahnite ($ZnAl_2O_4$) (Surendran and Sebastian, 2005) having high thermal conductivity potential exceeding alumina as a base material and examined low temperature sintering by addition of a small quantity of $Cu_3Nb_2O_8$ (Kim et al, 2001), which has been reported to have relatively good dielectric properties as a sintering aid. We also investigated to elucidate a part of the low-temperature sintering mechanism in this system.

Materials and Methods

Commercially available Al_2O_3 and ZnO powder (manufactured by High Purity Chemical Laboratory Co., Ltd., Japan), exhibiting an average particle size of 1 μm, was weighed at a molar ratio of 1:1 and mixed with a ball mill for 16 h, utilizing water as a dispersion medium. The dried powder was calcined at 1100 °C (for 4 h) in an air atmosphere to synthesize gahnite. The synthesized gahnite powder was pulverized by a ball mill for 48 h, utilizing water as a dispersion medium. The dried powder was used as the raw material powder. The specific surface area measured by the BET method was 8.65 m^2/g. Next, 100–95 wt% of gahnite powder and 0–5 wt% of $Cu_3Nb_2O_8$ additive powder were weighed and mixed for 16 h by a ball mill, utilizing water as a dispersion medium. The dried powder was granulated with a PVA binder and formed into a disk through uniaxial pressing at 75 MPa. The green bodies were fired at 685–1535 °C in an air atmosphere, for 10 min.–96 h.

The properties of the obtained sintered bodies were examined by measuring their bulk densities, microwave dielectric properties, and thermal conductivities. Three major parameters that describe dielectric properties, namely, the relative dielectric constant (ε_r), quality factor multiplied by the resonant frequency ($Q \times f$), and temperature coefficient of resonant frequency (τ_f) were measured using a network analyzer (Agilent Technologies, 8720ES), by the Hakki–Coleman method (Hakki and Coleman, 1960). The τ_f values were calculated using the following equation:

$$\tau_f = \frac{f_{80} - f_{20}}{f_{20} \times (80-20)}, \quad (1)$$

where f_{20} and f_{80} are the resonant frequencies at 20 and 80 °C, respectively. The thermal conductivities were measured using the xenon flash method (Netzsch, LFA447). In addition, to further discuss the low-temperature sintering performances of the developed materials, microstructure observation by a transmission electron microscope (TEM), measurement of the gahnite lattice constant and phase identification by X-ray diffraction (XRD) utilizing a Cu Kα radiation source, and melting temperature measurement of the additive by a differential thermal analysis (DTA) were performed.

Results and Discussion

Figure 1 shows the relationship between the firing temperature and the sintered density of the gahnite sample. In order to obtain a dense sintered body, a firing temperature of 1485 °C was required for the gahnite single component. On the other hand, in the gahnite with the $Cu_3Nb_2O_8$ additive, the sintering temperature was significantly lowered. That is, for the sample to which 4 wt% or more of the sintering aid was added, a dense sintered body of 95 % (4.376 g/cm^3) or more of the theoretical density of gahnite (4.606 g/cm^3) was obtained at a firing temperature of 960 °C for 2 h.

Figure 2 depicts TEM photographs of the microstructures of the gahnite sintered bodies containing 5 wt% $Cu_3Nb_2O_8$ additive. For the sample fired at 785 °C, there was almost no necking between the powders, and many pores were present (Fig. 2(a)). On the other hand, for the sample fired at 960 °C, the particles were angular and no pores were observed. Grain growth was also observed as can be seen by comparing with Fig. 2(a). Therefore, we confirmed that it was densified (Fig. 2 (b)).

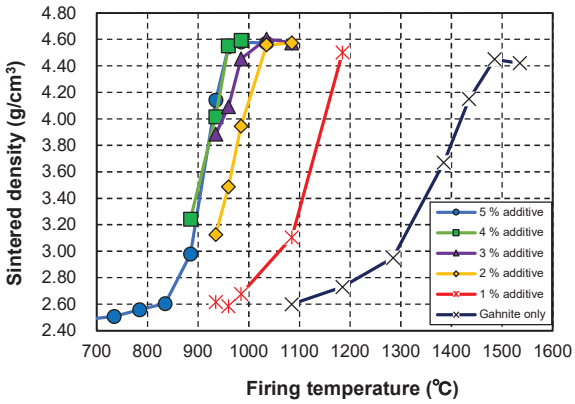

Figure 1 Effect of $Cu_3Nb_2O_8$ additive amount on the relationship between firing temperatures and gahnite sintered densities (holding time: 2h).

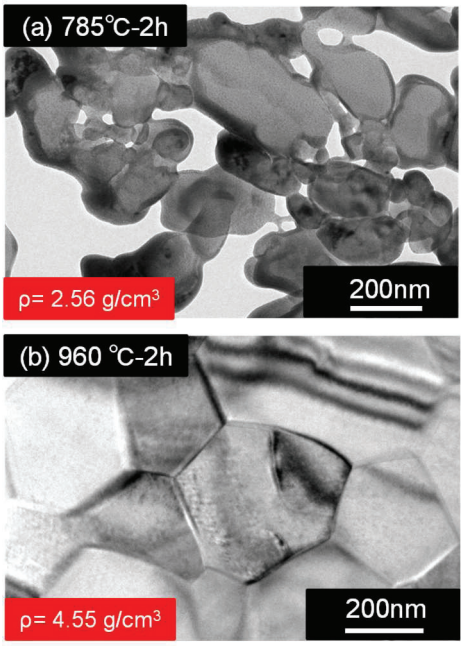

Figure 2 Transmission electron microscopy images of sintered gahnite containing 5 wt% $Cu_3Nb_2O_8$ fired at (a) 785 °C for 2 h; and (b) 960 °C for 2 h.

Furthermore, as shown in figure 3, it was found that the sintered densities of the samples in this system are greatly affected by the holding time at the firing temperature. That is, even if the firing temperature was less than 960 °C, for example, 935 °C, dense sintered bodies were obtained by holding for a long time of 24 h or more.

Table 1 denotes the firing temperature, dielectric properties, and thermal conductivity of the gahnite single component, the conventional LTCC material, and the

gahnite with 4 wt% $Cu_3Nb_2O_8$ additive developed in this study. The relative permittivity (ε_r) of the gahnite with 4 wt% of the above additive is 9.1, the quality factor multiplied by resonant frequency ($Q \times f$) value of 80,000 GHz (at a measurement frequency of approximately 12 GHz), and the temperature coefficient of resonant frequency (τ_f) of –65 ppm/K, being relatively satisfactory values. Although the thermal conductivity was 8.7 W/mK, which was approximately 1/3 of that of the sample without additives (27 W/mK), the value exceeds the highest values of conventional LTCC materials (Induja et al, 2015) other than the low temperature sintered alumina reported by us (20 W/mK) (Shigeno et al, 2021).

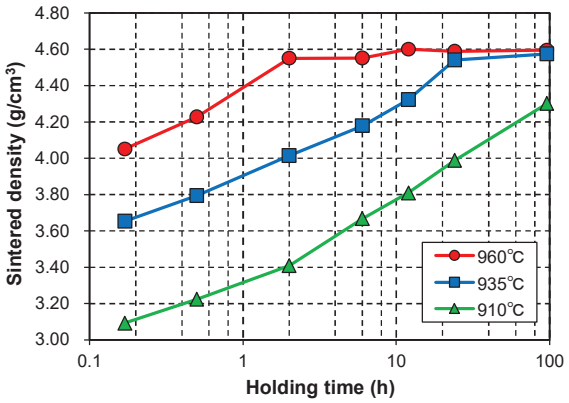

Figure 3 Relationship between holding time and sintered densities of gahnite fired at 910, 935, and 960 °C ($Cu_3Nb_2O_8$ additive amount: 4 wt%).

Table 1 Firing parameters and microwave dielectric, and thermal properties of pure gahnite, conventional low-temperature co-fired ceramic (LTCC) (alumina + glass), and sintered samples from our current study (gahnite + 4 wt% $Cu_3Nb_2O_8$).

Sample		Gahnite	Conventional LTCC [3, 4]	This study
Composition		$ZnAl_2O_4$ only	Al_2O_3 + glass	$ZnAl_2O_4$ + 4 wt% $Cu_3Nb_2O_8$
Firing temperature	(°C)	1485	900	935
Holding time	(h)	2	—	24
Microwave dielectric properties	ε_r (–)	9.0	7.2	9.1
	$Q \times f$ (GHz)	16000	10000	80000
	τ_f (ppm/K)	−73	−55	−65
Thermal conductivity	κ (W/mK)	27	2−7	8.7

In order to elucidate a part of the low temperature sintering mechanism in this system, the melting temperature was measured by DTA. As a result, as shown in figure 4, the melting temperature of $Cu_3Nb_2O_8$ was 967 °C. When gahnite was added into the mixture, the occurrence of melting at a temperature lower than 967 °C was not observed. From these results, it was clarified that the densification of gahnite was completed before the sintering aid became a liquid phase. Thus, data suggesting that "solid-state-activated sintering" proposed by German et al., 1988. occurs in this system was obtained.

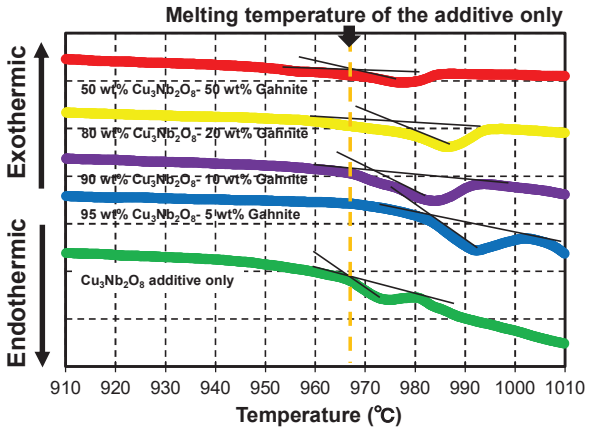

Figure 4 Differential thermal analysis curves of $Cu_3Nb_2O_8$/gahnite mixtures at a heating rate of 10 °C/min.

Conclusions

By an addition of a small amount of $Cu_3Nb_2O_8$ sintering aid to gahnite, which is a high thermal conductive material, we succeeded in low-temperature sintering below the melting point of silver, 961 °C, and obtained good dielectric and thermal properties. Then, it was suggested that "solid-state-activated-sintering" occurs in this system, in which densification is almost completed even when the sintering aid is in the solid state. In the future, the mechanism of solid-state-activated sintering in this system will be elucidated in detail by measuring the change in lattice constant with firing temperature by X-ray diffraction (XRD), elemental analysis of gahnite grains and grain boundaries by energy dispersive spectroscopy (EDS). This study provided an important stepping stone for that.

Acknowledgements

We are indebted to Prof. Akinori Kan of Meijo University for his help with the experiments of dielectric properties. This research was supported by the Electric Technology Research Foundation of Chugoku.

References

German, R.M. Farooq, S. & Kipphut, C.M. (1988). Kinetics of liquid sintering, *Mater. Sci. Eng.*, A105/106, 215-224.

Hakki, B.W. & Coleman, P.D. (1960). A dielectric resonator method of measuring inductive capacities in the millimeter range, *IRE Trans. Microw. Theory Tech*. 8, 402–410.

Imanaka, Y. (2005). *Multilayered Low Temperature Cofired Ceramics (LTCC) Technology*. New York: Springer.

Induja, I.J. Abhilash, P. Arun, S. Surendran, K.P. & Sebastian, M.T. (2015). LTCC tapes based on Al_2O_3–

BBSZ glass with improved thermal conductivity. *Ceram. Int.* 41, 13572–13581.

Kim, D. Kim, I. Park, B. & Hong, K. (2001). Microwave dielectric properties of (1−x) $Cu_3Nb_2O_8$−x $Zn_3Nb_2O_8$ ceramics, *J. Mater. Res.* 16, 1465-1470.

Sebastian, M.T. (2008). *Dielectric materials for wireless communication.* New York: Elsevier.

Sebastian, M.T. & Jantunen, H. (2008). Low loss dielectric materials for LTCC applications, *Int. Mater. Rev.* 53, 58–90.

Shigeno, K. Katsumura, H. Kagata, H. Asano, H. & Inoue, O. (2007). Preparation and characterization of low temperature sintered alumina by CuO-TiO_2-Nb_2O_5-Ag_2O additives. *Ferroelectrics*. 356, 189-196.

Shigeno, K. Asakawa, T. Kuraoka, Y. & Fujimori, H. (2016). Effects of chemical compositions on electrical properties of low temperature co-fired alumina ceramics with built-in silver electrodes, *Trans. Mat. Res. Soc. Japan*. 41, 121-126.

Shigeno, K. Kuraoka, Y. Asakawa, T. & Fujimori, H. (2021). Sintering mechanism of low-temperature co-fired alumina featuring superior thermal conductivity, *J. Am. Ceram. Soc*. 104, 2017-2029.

Shimizu, M. Tomioka, S. Yoshida, N. Kameyama, I. & Okuda, K. (2015). Japanese Patent Application No.2015-156406.

Surendran, K.P. & Sebastian, M.T. (2005). A low loss, dielectric substrate in $ZnAl_2O_4$–TiO_2 system for microelectronic applications, *J. Appl. Phys*. 98, 044101.

FABRICATION OF FLEXIBLE MAGNETO-OPTICAL INDICATOR WITH KOSEN STUDENTS FOR ENGINEERING EDUCATION OF NON-DESTRUCTIVE INSPECTION

R. Hashimoto[*,a], Y. Funaki [a] and T. Itaya[b]

[a] National Institute of Technology, Suzuka College / Department of Electrical and Electronic Engineering, Shiroko-cho, Suzuka, Mie, Japan
[b] National Institute of Technology, Suzuka College / Department of Electronic and Information Engineering

*hashimoto@elec.suzuka-ct.ac.jp

Abstract

Nondestructive inspection technologies are expected to continue to contribute to the safety of life in the manufacturing, infrastructure, and construction industries. However, there is a scarcity of engineers who have expertise in using these inspection technologies. National Institute of Technology, Suzuka College (Suzuka KOSEN) suggests educating through research; engineering education of nondestructive inspection was provided to students in my laboratory through graduation research. Since I was assigned to Suzuka KOSEN, 17 students (including 6 advanced course students) have worked in my laboratory in 5 years. More than 70% of the students had been involved in the R&D of nondestructive inspection technologies, and about 95% of the students had been involved in the study of magnetic materials. In my laboratory, magneto-optical (MO) imaging technologies are studied as nondestructive inspection methods. MO imaging is one of the new attractive methods for nondestructive inspection. The magnetic field distribution corresponding to defects on the surface of a metal specimen can be visualized via MO imaging. Therefore, MO imaging can be used for not only the detection of defects but also the estimation of the shape and depth of defects via magnetic field distribution. Magnetic garnet materials are used for MO indicators of MO imaging. A magnetic garnet thin film is placed on the surface of a metal specimen as a sensor of the magnetic field. The modulation of the direction of magnetization in the thin film by the magnetic field can be visualized using a polarization camera. In this study, flexible MO indicators were fabricated for MO imaging via a spin coating process as a part of engineering education of nondestructive inspection. In addition, seminars were held several times per year jointly with laboratories specializing in nondestructive inspection to deepen student's understanding. As a result of questionnaire survey of students in the last year, this education through graduation research was generally effective. All advanced course students in my laboratory went on to college after graduation, and they are still studying engineering.

Keywords: *engineering education, magnetic materials, magneto-optical imaging, magnetic garnet, nondestructive inspection*

Introduction

Nondestructive inspection technologies are expected to continue to contribute to the safety of life in the manufacturing, infrastructure, and construction industries. However, there is a scarcity of engineers who have expertise in using these inspection technologies. To develop human inspection resources with high expertise, it is necessary to train engineers at a young age. National Institute of Technology, Suzuka College (Suzuka KOSEN) suggests that educating through research provides a good opportunity to develop diverse human resources through graduation research. Therefore, engineering education of nondestructive inspection had been provided to several students in my laboratory through graduation research for five years since I was assigned to Suzuka KOSEN.

This study aims to develop effective educational methods for nondestructive inspection engineer development. Specifically, we focus on the magneto-optical (MO) imaging method as an example of nondestructive inspection to realize experiments by which students obtain the expertise of sensor materials and fundamental knowledge of optical measurement.

There are three steps to this study.

1) Calculation study of magnetic field
2) Fabrication and analysis of sensor materials
3) Development of MO imaging set-up

Each year, we have several students working on one of these steps. A total of 17 students (including 6 advanced course students) had joined my laboratory before now. More than 70% of the students had been involved in the R&D of nondestructive inspection technologies, and about 95% of the students had been involved in the study of magnetic materials.

In this article, we report the results of our efforts so far, including the self-evaluation of students.

Magneto-optical imaging

MO imaging is an advantageous method for the nondestructive inspection. MO imaging can visualize the magnetization distribution in an MO indicator that is magnetized by the stray field leaked from defects on a metal surface. The MO indicator rotates the polarization plane of the linear polarization that passes through a magnetic film via the Faraday effect. The Faraday rotation angle is converted to light intensity using polarizers positioned at the Cross–Nicol alignment. This light intensity is obtained as a photograph using an image sensor, such as a charge-coupled device camera. Therefore, the stray field from defects can be visualized by the two-dimensional image of the converted light intensity via the MO indicator.
The intensity of the converted light can be calculated as follows:

$$I_o = I_i \times \%T \times (\sin^2 \theta_F), \qquad (1)$$

where I_i is the intensity of the light source, $\%T$ is the transmissivity of the MO indicator, and θ_F represents the Faraday rotation angle of the polarization plane.

Calculation study of magnetic field

In MO imaging, it is essential to analyze the intensity distribution of the stray field from a defect because the Faraday rotation angle depends on the stray field intensity. Therefore, as the first step in this study, the intensity distribution of the stray field was calculated to estimate the sensitivity of the sensor. Comsol multiphasic ver.5.3, which is finite element analysis software, was used for the magnetic field analysis.

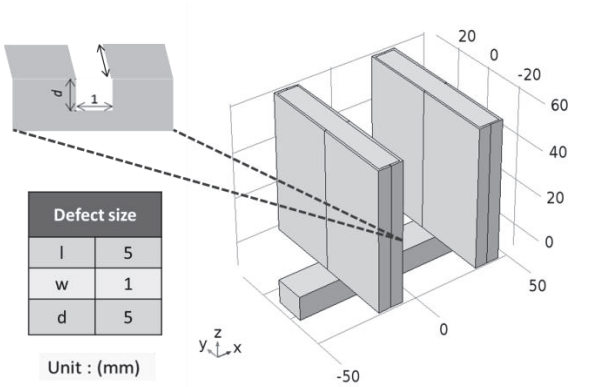

Figure 1. Calculated model developed by a student. Comsol multiphasic ver.5.3 was used for calculation and analysis of the stray field.

Figure 1 shows a model developed by a student. This student built this calculation model in a few months and could analyze the calculated results. The analysis results were used to establish a design for a magnetizer to generate a stray field.

Fabrication and analysis of sensor materials

A thin film of bismuth-substituted yttrium iron garnet (Bi: YIG) was used as a material of the MO indicator because the Bi: YIG indicated a large Faraday rotation angle in the visual light range. In our previous research, MO indicators had been formed via iron beam sputtering. The deposited films were crystallized via heat treatment at approximately 800 degrees. The formed MO indicator was unable to handle the curved surface of specimens, i.e., the inspection was limited to a flat surface of specimens. The substrate of the MO indicator was limited to high-heat resistant materials such as quartz glass because the substrate required high heat resistance to tolerate heat treatment. In the case of a glass substrate, there was a gap between the indicator and the specimen surface. The stray field intensity decreased depending on the distance from a specimen surface. Because of this gap, it was difficult to detect stray fields via the MO indicator. Thus, fabricating an MO indicator on a flexible substrate is required to detect defects on curved surfaces.

Therefore, as the second step in this study, a flexible MO indicator was fabricated to enable nondestructive inspection on curved surfaces. The Bi: YIG as an indicator material was prepared in the particle state. The crystallized Bi: YIG particles were mixed in an organic binder solution. Polyvinyl alcohol (PVA) solution was used as an organic binder to hold the Bi: YIG particles on a substrate. Afterward, this solution was deposited by the spin courter on a flexible plastic substrate. By crystallizing materials before deposition, we fabricated an MO indicator on a flexible substrate.

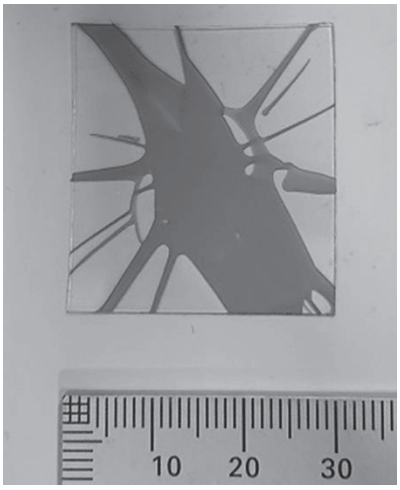

Figure 2 Optical image of the surface of the film in which the mass ratio of PVA and Bi: YIG was 2:3.

Figure 2 shows an optical image of the surface of the film in which the mass ratio of PVA and Bi: YIG was 2:3. It was difficult for students to deposit a uniform film, so the spin coating process was improved.

The spin coating process has three steps with different rotation speeds and times. Table 1 shows the spin coating process conditions before improvement. We extended the rotation time of the first step in Table 1 from 5 to 10 s for a smooth flow of particles. In addition, the Bi: YIG solution was dropped on a substrate after beginning rotation.

Figure 3 shows an optical image of the surface of the film that was deposited via an improved process. Improved condition indicated the good uniform distribution of the Bi: YIG particles; this condition was easier for students to make a film.

Table 1. Spin coating process conditions before improvement.

Step number	Rotation speed [rpm] / time [seconds]
1st	500 / 5
2nd	2000 / 60
3rd	5000 / 1

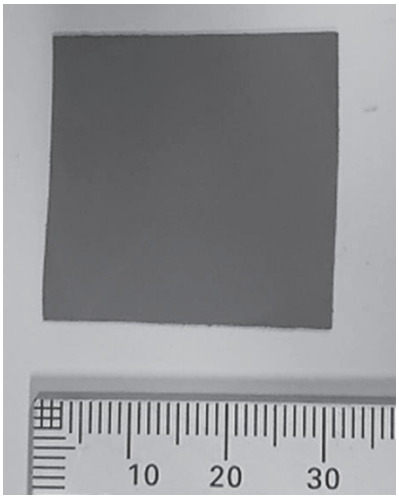

Figure 3. Optical image of the surface of the film that was deposited via an improved process.

Development of MO imaging set-up

To educate students on the application knowledge of MO imaging an optical setup had been built by the students. This optical set-up provides MO images with a smartphone. Since the abovementioned flexible sensor was in the development stage, a commercially available iron garnet film (MO imaging plate manufactured by off-diagonal) was used as the MO indicator.

Figure 4 shows an MO image taken by a student. A carbon steel plate with a slit as a defect of 0.5 mm in width and 9 mm in depth was used as a sample. The plate was a square with a length of 100 × 100 mm^2, and the thickness was 10 mm. The defect corresponding to the stray field had been visualized via MO imaging as the contrast of light and dark of the image. Therefore, the students had succeeded in constructing an MO imaging setup with a smartphone.

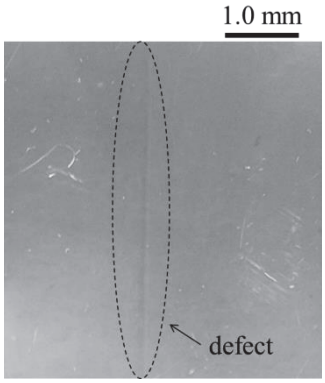

Figure 4. MO image taken by a student. The defect corresponding to the stray field had been visualized as the contrast of light and dark of the image.

Results and Discussion

We conducted a questionnaire survey targeting all students who belonged to my laboratory last year to evaluate the educational effect on the students. The students evaluated the educational effect on a scale of 1 to 5.

Figure 5 shows the results of the questionnaire survey on the level of learned knowledge about nondestructive inspections. A large number of students chose "Excellent," and the response was generally good. In my laboratory, fundamental nondestructive inspection education was conducted in a lecture style over two months from April to June yearly. Afterward, students experience experimental studies on nondestructive inspection, so the results of the questionnaire were high responses.

Figure 6 shows the results of the questionnaire survey on the level of learned knowledge about magnetic materials. A large number of students chose "Excellent," and the response was generally good as before.

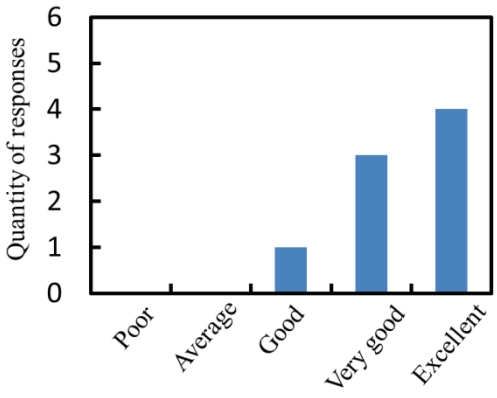

Figure 5. The results of the questionnaire survey on the level of learned knowledge about nondestructive inspections.

Figure 7 shows the results of the questionnaire survey on the level of learned knowledge about fabrication and evaluation of magnetic sensors. The students reacted slightly differently from before, "very good" was the largest number in the responses from students because not all students were involved in the fabrication and evaluation of magnetic sensors.

Figure 8 shows the results of the questionnaire survey on the time spent on graduation research last year. Some students studied beyond the time of the class of graduation research (60 h). Some students studied for several hours almost daily.

Table 2 shows the expertise that students gained, especially in their graduation studies. Students realized that they had learned about "Material analysis" and "Photography of MO image," which had many experiments.

At the end of the questionnaire, we surveyed the degree of satisfaction with my laboratory. The result is shown in Figure 9. As a result of the questionnaire, the students showed a high level of satisfaction with graduation research.

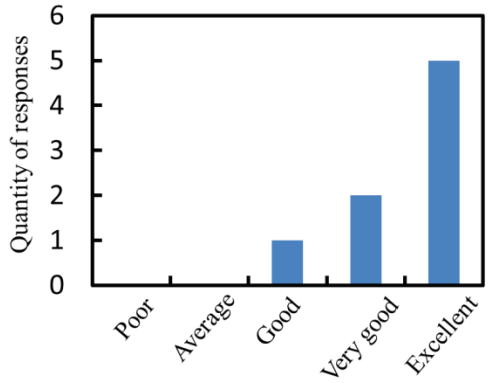

Figure 6. The results of the questionnaire survey on the level of learned knowledge about magnetic materials.

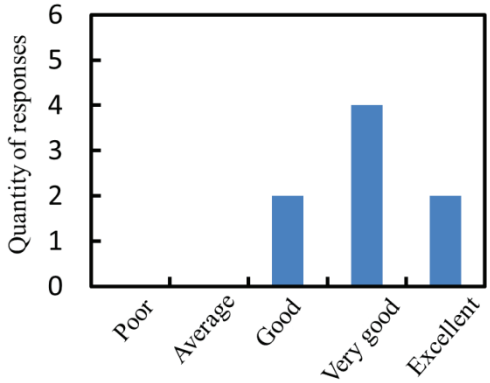

Figure 7. The results of the questionnaire survey on the level of learned knowledge about fabrication and evaluation of magnetic sensors.

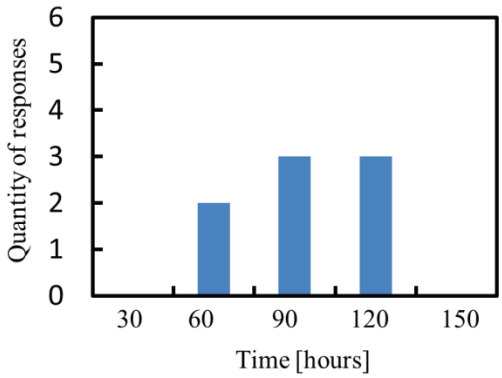

Figure 8. The results of the questionnaire survey on the time spent on graduation research last year.

Table 2 Expertise learned especially in graduation research

Expertise	Number of response
Material development	1
Material analysis	4
Thin film process	1
Photography of MO image	4
Optical equipment	1
Calculation analysis	2
Physics	1

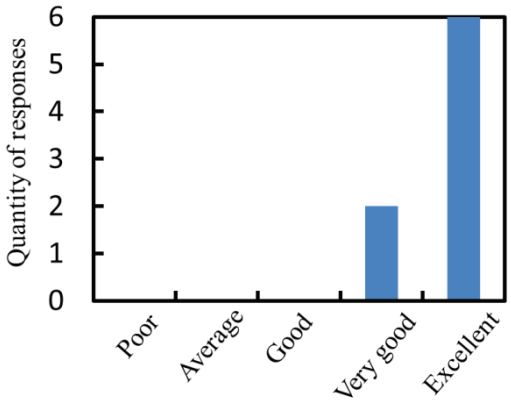

Figure 9. The degree of satisfaction with our laboratory. The students showed a high level of satisfaction with graduation research.

Conclusions

We had provided engineering education of nondestructive inspection to several students through graduation research to develop effective educational methods for nondestructive inspection engineer development in my laboratory.

We focused on the MO imaging method as an example of nondestructive inspection to realize experiments by which students gained the expertise of

sensor materials and fundamental knowledge of optical measurement.

A total of 17 students (including 6 advanced course students) had joined my laboratory before now. More than 70% of the students had been involved in the R&D of nondestructive inspection technologies, and about 95% of the students had been involved in the study of magnetic materials.

We conducted a questionnaire survey targeting all students who had belonged to my laboratory last year to evaluate the educational effect on the students. As a result of the questionnaire, the students generally responded well to this education. All advanced course students in my laboratory went on to college after graduation, and they are still studying engineering.

We would like to continue this education for nondestructive inspection engineer development.

Acknowledgements

This work was supported by JSPS KAKENHI Grant Number JP19K14851.

References

Hanju, L. Taedong, K. Songhui, K. Youngwoon, Y. Seungwhan, K. Arsen, B. Takayuki, I. Barry, F. & Kiejin, L. (2010). Magneto-optical imaging using a garnet indicator film prepared on glass substrates. *Journal of Magnetism and Magnetic Materials*, 322, 2722-2727.

Ryosuke, H. Hiroyuki, T. Takumi, Y. Kazuto, S. & Mitsuteru, I. (2014). Magneto-optical imaging using magnetophotonic crystals. *Journal of Applied Physics,* 115, 17A931-17A933.

Ryosuke, H. Takumi, Y. Hiroyuki, T. Taichi, G. Hisashi, E. Akira, N. & Mitsuteru, I. (2015). Defect depth estimation using magneto optical imaging with magnetophotonic crystal. *Journal of the Magnetics Society of Japan,* 39, 213-215.

QUANTITATIVE EVALUATION OF BIOFILMS FORMED ON VARIOUS MATERIALS USING CRYSTAL VIOLET

H. Kanematsu [*,a], K. Sakurai[a] , R.Satoh[b] and D.M. Barry [c,d], R.Kawai[a], T.Kogo[a], A.Ogawa[a], N.Hirai[a], M.Yoshitake[e], Toshihiro Tanaka[f]

[a] National Institute of Technology (KOSEN), Suzuka College, Suzuka, Mie, Japan
[b] National Institute of Technology（KOSEN）Tsuruoka College, Tsuruoka, Yamagata
[c] Dept. Electrical and Computer Engineering, Clarkson University
[d] Science / Math Tutoring Center, the State University of New York at Canton in Canton, NY, U.S.A.
[e] National Institute of Materials Science
[f]Dept. Materials Science and Engineering, Graduate School of Engineering, Osaka Unviersity, Suita, Osaka, Japan

*kanemats@mse.suzuka-ct.ac.jp

Abstract

Biofilms form on materials' surfaces and affect components, products, facilities, etc. in various ways. It is important to evaluate biofilm appropriately to establish proper countermeasures. However, there is no common standard test at this point. Therefore, various evaluation methods have been proposed so far and are now being investigated from various viewpoints. In this experiment, we evaluated biofilms formed on various materials using crystal violet. Biofilms were formed on metallic, polymeric, and ceramic materials (in bacterial solutions) within a flow type laboratory biofilm reactor or static plastic wells. Then specimens were stained by 0.1% crystal violet. After washing the specimens with pure water three times, stained biofilms were extracted by using alcohol or 10% SDS. And the absorbance was measured with a plate reader. By using this process, we quantified biofilms formed on materials's surfaces. For this study, the suitability, applicability, merits, and demerits of our process are discussed.

Keywords: *biofilms, quantification, laboratory biofilm reactors, crystal violet, absorbance, E.coli, S.epidermidis*

Introduction

Biofilms form on materials' surfaces and affect them negatively in various ways. Fig.1 shows the mechanism of biofilm formation on materials' surfaces.

Bacteria exist everywhere, but for some bacteria, they individually exist and are floating in oligotrophic environments. Such bacteria are called "planktonic bacteria". Planktonic bacteria in oligotrophic environments seek nutrients at any time to survive. Nutrients for bacteria are carbon compounds in most cases. Therefore, bacteria tend to attach to materials to get nutrients. However, bacteria have electric double layers around them. On the other hand, materials also have electric double layers on them. When the two electric double layers approach each other, then the osmotic pressure would cause repulsive forces between them. This is the usual case. However, sometimes another attractive force overcomes the repulsive one. Therefore, the number of bacteria finally begins to increase. When the number of bacteria (on a local area of materials' surfaces) reach a threshold value, the signal deduction process called quorum sensing works so polysaccharides are excreted simultaneously from

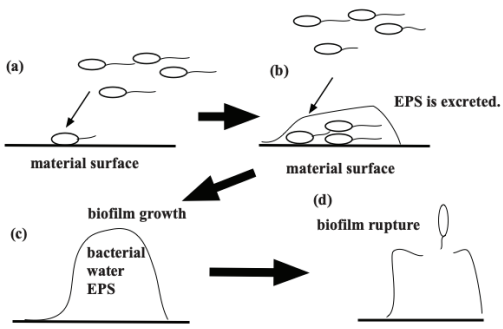

Fig.1 Schematic illustration of biofilm formation and growth.

bacteria in the area. Then biofilms form on materials' surfaces.

The produced biofilms continue to grow, incorporating various organic and inorganic substances into the biofilms. The components of biofilms change with time. In some cases, biofilms grow to a solid scale product containing no water.

Produced biofilms influence materials in various ways. We could mention four main problems that materials scientists and engineers often encounter in their daily lives.

One of them is corrosion problems. When biofilms form on materials, the geographical patterns on materials' surfaces become inhomogeneous. Then the oxygen concentration cells are produced. As a result, the anodic sites (where biofilms form.) corrode. And in addition, biofilms provide materials' surfaces water components as thin water film. Therefore, the corrosion reaction is promoted. Due to the two reasons, corrosion is accelerated on materials' surfaces. Biofilms promote corrosion as a result.

The second problem is the deterioration of hygiene conditions caused by biofilms. Biofilms are composed of bacteria and those within biofilms are generally resistant to drugs. Therefore, biocides and antibiotics in general conditions do not work. The concentrations should be increased to control biofilms for example. The problems are encountered in food industries, sanitary parts in our daily lives and the medical fields including (hospitals), etc. Generally, the problem leads to sickness. Sticky matter (from biofilm) is found in toilets, bathrooms, kitchens and on walls, floors, and other sections of a house, as well as in public swimming pools.

The third problem is scale problems in pipe works. Inside walls of pipes, where liquids flow, are places where biofilms develop (whatever the pipes might be). Before the concept of biofilm was proposed, people didn't realize the close relation between scale products on the inside walls of pipes and biofilms at all. However, we already know the scale products are the developed biofilms themselves. Therefore, the scale products start to form with bacteria.

The fourth problem is ships and other marine structures. In marine environments, biofouling has caused serious problems so far. Biofouling is the general phenomenon where organisms attach to materials. Ships and parts of marine structures suffer from the problems seriously. Biofouling is generally classified into microfouling and macrofouling. For the latter, oysters, barnacles and other relatively large marine creatures attach to materials' surfaces, while bacteria and other microbes attach to materials' surfaces in the case of microfouling. Both are related in series with each other. It means that microfouling by bacterial activities would occur first of all. Then macrofouling would occur after that.

The topics described above are only representative of four. We authors have also investigated many problems caused by biofilms. However, the problems are seen in addition to the four cases everywhere on a regular basis since bacteria exist everywhere. Whenever bacteria might exist, biofilms always form and bring about problems. That could be attributed to that most of bacteria in nature exist not as planktonic bacteria, but rather in biofilms. Biofilms are the usual existence forms of bacteria.

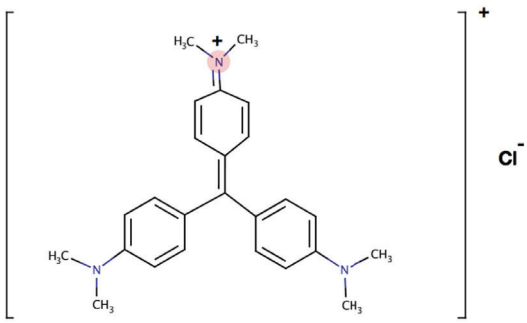

Fig.2 The structure of crystal violet

Biofilms affect many materials and their structures in various ways. Since many of those problems are detrimental and negative, it is very important to develop antibiofilm materials. However, we have to prepare the suitable evaluation systems, first of all. At this time, we don't have any standard quantitative methods which people in industrial fields can use. They should be user-friendly, rapid and cost effective.

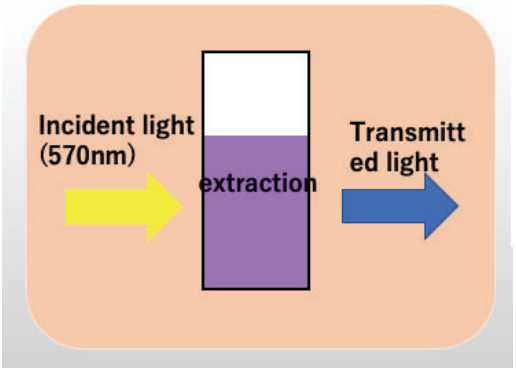

Fig.3 Schematic principle of absorbance measurement.

Proposed standard method using Crystal Violet

Usually, anti-infectious materials should be evaluated from the viewpoints of anti-bacterial, anti-viral, anti-fungal and anti-biofilm characteristics. Fortunately, the first three anti-properties for materials except the anti-biofilm property could be evaluated by using international standards. However, only the anti-biofilm property of materials doesn't have any international standard at all. In fact, there are some standards for anti-biofilm properties. However, all of them are established for chemicals, biocides, and drugs.

As for the standard, SIAA and some of the authors have tackled with the topic together. The draft has been established. Now the ISO committee began their first voting for the proposed standard. In this paper, it could not be publicized yet. However, the basic concept can be introduced.

The basic concept is the utilization of staining by crystal violet. Crystal violet is an organic chloride composed of cations having triphenylmethane structure and chloride anions. The chemical structure is shown in Fig.2. After biofilms are produced by various methods, the specimens or products are stained by immersing in 0.1% crystal violet solution. Usually, crystal violet solution is used for Gram stain. In that case, crystal violet stains the outer part of bacteria in various ways. However, this is not the case for the current purpose. To evaluate biofilms, we focus on EPS, external polymeric substances derived from bacteria. Biofilm contains lots of EPS. Since EPSs are polymeric substances, they have polar characters to a greater or lesser extent. Depending on the extent, the cationic part of crystal violet adsorbs to the negative polarized local parts. Then the parts are shown in blue or violet colours. The extent of violet colours should correspond to the amount of biofilm. Since biofilms contain versatile and complicated substances the polarizable polymers must be stained to some extent. Bacteria themselves are also stained. However, all of them must be components of biofilms. From the viewpoint, such a tendency should be welcomed. The stained crystal violet is extracted by alcohol or some other appropriate surface acting agent. Since crystal violet absorbs the light of 570 nm selectively, the optical characteristics are used for the evaluation. The light of 570nm is irradiated to the extracted solution. Then the absorbance is measured. The absorbance should correspond to the amount of crystal violet existing on materials' surfaces. Fig.3 shows the process schematically.

Experimental

Three kinds of commercial polymeric materials (PP, PS, Silicone), carbon steel (SS400), glass slides and the newly developed polymer (Polymer A) were used as specimens. They were prepared as sheets (10x10mm) and the surfaces were cleaned by alcohol.

Escherichia coli (*E.coli*, K12 G6) were used as model bacteria for this experiment. E.coli was cultured with vibration in LB liquid culture at 37 degrees Celsius in 24 hrs in advance. This was used as the bacterial solution for this study.

The bacterial solution was dispensed (1.6ml) into each well of 12 plastic wells where the specimen was put in advance. And the plastic wells were put in the incubator at 25 degrees Celsius for 24 hours to form biofilms. For each material, 6 specimens were used. Then the results were averaged.

0.1 % crystal violet solution was prepared in advance. Using the solution, specimens were put in 12 plastic wells again. 1.5ml CV solution was poured into each well and the static immersion was kept for 30 minutes. Then, each specimen was washed by distilled water three times.

The stained specimens were extracted by 10% SDS (dodecyl sodium sulfate solution) into a centrifugal tube for 30 minutes. Then the solution of 200 micro litters was dispensed into each of 96 plastic wells and the absorbance at 570nm was measured, using a plate reader (FC-multi scan, Thermo Fisher).

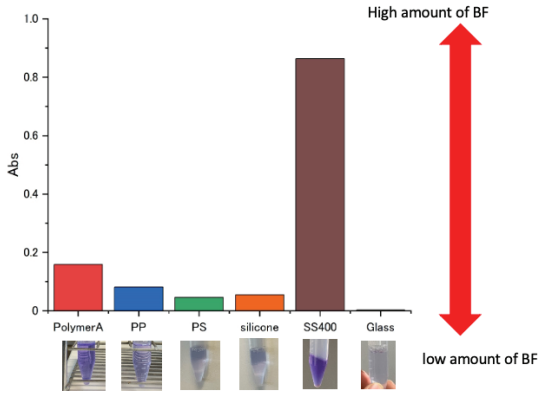

Fig.4 Absorbance of crystal violet extracted from a material's surface by SDS.

Results and Discussion

The absorbance of light at 570 nm was measured for the extracted solution by 10% SDS. The result is shown in Fig. 4.

The upper bar graph shows the average of absorbance values. The horizontal axis corresponds to the absorbance value obtained by the plate reader. The higher the absorbance value is, the higher the amount of biofilm formed on materials' surfaces.
The photos below the bar graph show the appearance for each corresponding extract solution.
The results obtained for this experiment show that the absorbance decreased in this order.
SS400 > Polymer A > PP > Silicone> PS > glass.

The results were obtained by the combination of materials and bacteria. The result would differ usually, depending on the combinations. However, this method makes it possible for us to evaluate the amounts of biofilms concretely and quantitively.

Conclusions

The quantitative, user-friendly, rapid, and cost-effective evaluation method for biofilms was introduced. Also, an example of analysis was shown for the reference. Basically, the method is a staining process that

uses crystal violet. However, this method can be utilized soon for the industrial evaluation purposes. It is very natural that the conventional analyses using expensive analytical apparatus and microscopes still visualize biofilms. Information and knowledge from them are still informative and effective. In the future, the combination of many methods will be used to answer industrial and academic questions. Biofilm analyses are difficult and always need multiple analyses from various approaches.

Acknowledgments

This work was supported by JSPS KAKENHI (Grants-in-Aid for Scientific Research from Japan Society for the Promotion of Science, Grant Number 20K05185 and 21K12739. A part of this work was supported by GEAR 5.0 Project of the National Institute of Technology (KOSEN) in Japan.

References

Characklis, W.G. Fouling biofilm development: a process analysis. *Biotechnology and bioengineering* **1981**, *23*, 1923-1960.

Characklis, W.G. Fouling biofilm development: a process analysis. *Biotechnology and bioengineering* **1981**, *23*, 1923-1960.

J.W.Costerton; K.J.Cheng; Geesey, G.G.; I.Timothy; J.Ladd; Nckel, C.; Dasgupta, M.; Marrie, T.J. Bacterial biofilms in nature and disease. *Annual reviews in Microbiology* **1987**, *41*, 435-464.

Lappin-Scott, H.M.; Costerton, J.W. Bacterial biofilms and surface fouling. *Biofouling* **1989**, *1*, 323-342, doi:https://doi.org/10.1080/08927018909378120.

Characklis, W.G.; Marshall, K.C. *Biofilms*; John Wiley & Sons, Inc., New York, the USA: New York, 1990.

Lawrence, J.; Korber, D.; Hoyle, B.; Costerton, J.W.; Caldwell, D. Optical sectioning of microbial biofilms. *Journal of bacteriology* **1991**, *173*, 6558-6567.

Lewandowski, Z.; Walser, G.; Characklis, W.G. Reaction kinetics in biofilms. *Biotechnology and bioengineering* **1991**, *38*, 877-882.

Mattila-Sandholm, T.; Wirtanen, G.J.F.r.i. Biofilm formation in the industry: a review. **1992**, *8*, 573-603.

Lappin-Scott, H.M.; J., J.; Costerton, J.W. Mmicrobial biofilm formation and characterisation. *Society for Applied Bacteriology technical series, Society for Applied Bacteriology Symposium* **1993**, *30*.

Lee, W.; Lewandowski, Z.; Morrison, M.; characklis, W.G.; Avci, R.; Nielsen, P.H. Corrosion of mild steel underneath aerobic biofilms containing sulfate - reducing bacteria part II: at high dissolved oxygen concentration. *Biofouling* **1993**, *7*, 217-239, doi:0.1080/08927019309386255.

Lewandowski, Z.; Altobelli, S.A.; Fukushima, E. NMR and Microelectrode Studies of Hydrodynamics and Kinetics in Biofilms. *Biotechnology progress* **1993**, *9*, 40-45.

Quesnel, L.B.; Gilbert, P.; Handley, P.S. *Microbial cell envelopes : interactions and biofilms*; Blackwell Sci. Pubs.: Oxford ; Boston, 1993; pp. vii, 160 p.

Stewart, P.S.; Peyton, B.M.; Drury, W.J.; Murga, R. Quantitative observations of heterogeneities in Pseudomonas aeruginosa biofilms. *Appl. Environ. Microbiol.* **1993**, *59*, 327-329.

Beer, D.d.; Stoodley, P.; Roe, F.; Lewandowski, Z. Effects of biofilm structures on oxygen distribution and mass transport. *Biotechnology and bioengineering* **1994**, *43*, 1131-1138.

De Beer, D.; Stoodley, P.; Roe, F.; Lewandowski, Z. Effects of biofilm structures on oxygen distribution and mass transport. *Biotechnology and bioengineering* **1994**, *43*, 1131-1138.

Flemming, H.-C. *Biofilme, Biofouling und mikrobielle Schädigung von Werkstoffen*; Oldenbourg, München, Germany: München, 1994; pp. xvi, 277

Fletcher, M. Bacterial biofilms and biofouling. *Current opinion in biotechnology* **1994**, *5*, 302-306.

Jiang, H.; Bishop, P. Aerobic biodegradation of azo dyes in biofilms. *Water Science and Technology* **1994**, *29*, 525.

Jiang, H.; Bishop, P. Aerobic biodegradation of azo dyes in biofilms. *Water Science and Technology* **1994**, *29*, 525.

Abrahamson, M.T. Development of Artificial Biofilms for Use in Mass Transport Studies. Montana State University, Bozeman, Montana, the USA, 1995.

Busscher, H.; Bos, R.; Van der Mei, H. Initial microbial adhesion is a determinant for the strength of biofilm adhesion. *FEMS microbiology letters* **1995**, *128*, 229-234.

Percival, S.L.; Walker, J.T.; Hunter, P.R. *Microbiological aspects of biofilms and drinking water*; CRC Press: Boca Raton, 2000; pp. 229 p.

Donlan, R.M. Biofilms and Device-Associated Infections. *Emerging Infectious Diseases* **2001**, *7*, 277-281.

Murga, R.; Miller, J.; Donlan, R. Biofilm formation by gram-negative bacteria on central venous catheter connectors: effect of conditioning films in a laboratory model. *Journal of clinical microbiology* **2001**, *39*, 2294-2297.

Harrison, J.J.; Turner, R.J.; Marques, L.L.R.; Ceri, H.

Biofilms - A new understanding of these microbial communities is driving a revolution that may transform the science of microbiology. *American Scientist* **2005**, *93*, 508-515, doi:10.1511/2005.56.977.
Bjarnsholt, T.; Kirketerp-Moller, K.; Kristiansen, S.; Phipps, R.; Nielsen, A.K.; Jensen, P.O.; Hoiby, N.; Givskov, M. Silver against Pseudomonas aeruginosa biofilms. *APMIS* **2007**, *115*, 921-928, doi:10.1111/j.1600-0463.2007.apm_646.x.

Eboigbodin, K.E.; Seth, A.; Biggs, C.A. A review of biofilms in domestic plumbing. *American Water Works Association. Journal* **2008**, *100*, 131.

Shirtliff, M.; Leid, J.G. The role of biofilms in device-related infections. In *Springer series on biofilms v. 3.*, Springer: Berlin, 2009; pp xii, 269 p.

Kurisserya, S.R.; Kanavillila, N.; Leungb, K.T.; Chenc, A.; Daveyb, L.; Schraftb, H. Electrochemical and microbiological characterization of paper mill biofilms. *Biofouling* **2010**, *26*, 799
- 808, doi:10.1080/08927014.2010.519025.

Lobelle, D.; Cunliffe, M. Early microbial biofilm formation on marine plastic debris. *Marine pollution bulletin* **2011**, *62*, 197-200.

Kanematsu, H.; Ikigai, H. Alloy Plating and Biofilm Formation. *Proceedings of 14th International Congress Marine Corrosion and Fouling (ICMCF)* **2008**, 38 (29A-32-33).

Kanematsu, H.; Ikigai, H.; Campbell, S.A.; Beech, I.B. Sn-Ag Alloy Plating Films Mitigating Biofilm Formation. *Sur/Fin 2009* **2009**, 406-415.

Kanematsu, H.; Ikigai, H.; Yoshitake, M. Evaluation of Various Metallic Coatings on Steel to Mitigate Biofilm Formation. *International Journal of Molecular Science* **2009**, *10*, 559-571, doi:10.3390/ijms10020559.

Miyano, Y.; Kanematsu, H.; Hirai, N.; Hirai, T.; Kamiya, O. The Study of Biofilm Formation and the Electrochemical Behavior of Some Metals. In Proceedings of The 15th International Congress on Marine Corrosion and Fouling. 2010, The Sage Gateshead, UK, July 28, 2010; p. 60.

Kogo, T.; Hideyuki, K.; Daisuke, K.; Itoh, H. Biofilm Formation Derived from Ambient Air and the Characteristics of Apparatus. In Proceedings of The Asia-Pacific Interdisciplinary Research Conference (AP-IRC 2012), Irago Sea-Park & Spa Hotel, Tahara, Aichi, Japan; p. 77.

Kanematsu, H.; Hihara, T.; Ishihara, T.; Imura, K.; Kogo, T. Evaluation for Corrosion Resistance of Nano-Cluster Layer and Biofilm Formation. *International Journal of Engineering Sciences & Research Technology* **2013**, *2*, 2424-2432.

Kanematsu, H.; Hirai, N.; Miura, Y.; Itoh, H.; Kuroda, D.; Umeki, S. Biofilm Leading to Corrosion on Material Surface and the Moderation by Alternative Electro-magnetic Field. In Proceedings of Materials Science and Technology (MS & T), Montreal, Quebec, Canada, 0ctober 27-31, 2013; pp. 2761-2767.

Kanematsu, H.; Kogo, T.; Noda, M.; Hirai, N.; Ogawa, A.; Miura, Y.; Itoh, H.; Yoshitake, M. Composite Coating to Control Biofilm Formation and MIC. In Proceedings of 17th International Congress on Marine Corrosion and Fouling (ICMCF). Stephen Riady Centre, National University of Singapore, Singapore, 6-10, July 2014; p. 101.

Barry, D.M.; Kanematsu, H. Physical Removal of Biofilm. In *Biofilm and Materials Science*, 2015; 10.1007/978-3-319-14565-5_20pp 163--167.

Hirai, N.; Mun, M.K.; Masuda, T.; Itoh, H.; Kanematsu, H. Atomic force microscopy analysis of biofilms formed on different plastics. *Materials Technology* **2015**, *30*, 57-60, doi:10.1179/1753555714y.0000000238.

Kanematsu, H.; Barry, D.M. New Evaluation Techniques for Biofilm in Materials Science. In *Biofilm and Material Science*, Kanematsu, H., Barry, D.M., Eds. Springer: New York, 2015; pp. 187-192.

Kanematsu, H., & Barry, D. M. (2015). Conditioning Films. In H. Kanematsu & D. M. Barry (Eds.), *Biofilm and Materials Science* (1st ed., pp. 9-15). New York, USA: Springer.

Kanematsu, H., et al. (2016). Verification of effect of alternative electromagnetic treatment on control of biofilm and scale formation by a new laboratory biofilm reactor. *Ceramic Transactions* **259**: 199-212.

Kanematsu, H. (2017). A New International Standard for Testing Antibacterial Effects. *Advanced Materials & Processing, 175*(4), 26-29.

Hideyuiki, K.; Barry, D.M.; Ikegai, H.; Yoshitake, M.; Mizunoe, Y. Nanofibers and Biofilm in Materials Science. In *Handbook of Nanofibers - Fundamental aspects, experimental setup, synthesis, properties and physicochemical characterization*, Barhoum, A., Bechelany, M., HamdyMakhlouf, A.S., Eds. Springer International Publishing AG: Switzerland, 2018; Vol. 1, pp. 1-21.

Kanematsu, H.; Kanesaki, S.; Kudara, H.; Barry, D.M.; Ogawa, A.; Mizunoe, Y. Biofilm Formation on Titanium Alloy Surfaces in a Laboratory Biofilm Reactor. In *Ceramic Transactions - Advances in Ceramics for Environmental, Functional, Structural, and Energy Applications*, Mahmoud, M.M., Sridharan, K., Colorado, H., Bhalla, A.S., J.P.Singh, Gupta, S., Langhorn, J., Jitianu, A., Manjooran, N.J., Eds. John Wiley & Sons Inc: New York, the United States, 2018; Vol. 265,

pp. 221-228.

Kanematsu, H.; Maeda, S.; Barry, D.M.; Umeki, S.; Tohji, K.; Hirai, N.; Ogawa, A.; Kogo, T.; Ikegai, H.; Mizunoe, Y. Effects of Elastic Waves at Several Frequencies on Biofilm Formation in Circulating Types of Laboratory Biofilm Reactors. In *Ceramic Transactions - Advances in Ceramics for Environmental, Functional, Structural, and Energy Applications*, Mahmoud, M.M., Sridharan, K., Colorado, H., Bhalla, A.S., J.P.Singh, Gupta, S., Langhorn, J., Jitianu, A., Manjooran, N.J., Eds. John Wiley & Sons Inc: New York, the United States, 2018; Vol. 265, pp. 43-51.

Kanematsu, H.; Oizumi, A.; Sato, T.; Kamijo, T.; Honma, S.; Barry, D.M.; Hirai, N.; Ogawa, A.; Kogo, T.; Kuroda, D., et al. Biofilm Formation of a Polymer Brush Coating with Ionic Liquids Compared to a Polymer Brush Coating with a Non-Ionic Liquid. *Coatings* **2018**, *8*, 398-412, doi:http://dx.doi.org/10.3390/coatings8110398.

Kanematsu, H.; Oizumi, A.; Sato, T.; Kamijo, T.; Honma, S.; Barry, D.M.; Hirai, N.; Ogawa, A.; Kogo, T.; Kuroda, D., et al. Polymer Brush Made By Ionic Liquids and the Inhibition Effects for Biofilm Formation. *ECS Transactions* **2018**, *85*, 1089-1095, doi:10.1149/08513.1089ecst.

Kanematsu, H.; Shindo, K.; Barry, D.M.; Hirai, N.; Ogawa, A.; Kuroda, D.; Kogo, T.; Sano, K.; Ikegai, H.; Mizunoe, Y. Electrochemical Responses of Graphene with Biofilm Formation on Various Metallic Substrates by Using Laboratory Biofilm Reactors. *ECS Transactions* **2018**, *85*, 491-498, doi:10.1149/08513.0491ecst.

EVALUATION FOR ANTI-VIRAL CHARACTERISTICS OF VARIOUS METALLIC MATERIALS USING INFLUENZA A AND FELINE CALCIVIRUS

H. Kanematsu[*,a], T. Tamura[a], D.M. Barry[b,c], E.Nakajima[d], T.Kogo[a],
R. Kawai[a], A. Ogawa[a], N.Hirai[a], R.Satoh[e], M.Yoshitake[f], Y.Imoto[d],

[a] National Institute of Technology (KOSEN), Suzuka College, Suzuka, Japan
[b,c] Department of Electrical & Computer Engineering, Clarkson University, Potsdam, NY, 13699, the USA/SUNY Canton, Canton, NY, 13617, the USA
[d] Japan Textile Products Quality and Technology Center
[e] National Institute of Technology（KOSEN）Tsuruoka College, Tsuruoka, Yamagata
[f]National Institute of Materials Science

*E-Mail Address of the corresponding author
kanematsu@mse.suzuka-ct.ac.jp

Abstract

The pandemic was caused by COVID-19 at the end of 2019. Since then, we have suffered from widespread infection. Due to the pandemic, people's interest level in infection increased. We now understand that infection spreads not only from humans to humans, but also from humans to matter to humans. Infections might lead to the outbreak of the disease. Why could viruses maintain their activities on inanimate materials? This question should be answered from the viewpoint of materials science, since the interaction between materials' surfaces and polymeric substances (derived from viruses) should be the key. In this paper, we established an evaluation system for the anti-viral properties of materials, using the standardized evaluation method according to ISO 21702. As for the viruses, influenza A and feline caliciviruses are used. The former has the envelope structure, while the latter doesn't. The general procedure has a solution contact materials' surfaces covered with films for a certain amount of time. After that, the film and specimens are washed into a petri dish, which was put into an incubator at 25 degrees Celsius for 24 hours. Then the extraction solution was applied to host cells. The disrupting behaviors are measured by counting the number of "Plaque". The number of disrupting bacteria corresponds to the period of time that viruses are active on materials' surfaces. We checked a steel specimen for an example.

Keywords: *anti-viral property, influenza A, feline calcivirus, film covering method, viruses*

Introduction

The pandemic was declared on May 11, 2020, by COVID-19. However, it started at the end of 2019. Since then, we have suffered from the widespread infection. Due to the pandemic, people's interest level in infection increased. What is infection? Why are people infected? And how? These fundamental questions have appeared in people's minds. Most of the people in the world are now concerned about the methods to control the disease and ways to protect us from it.

Basically, infection can be defined as the phenomenon involving the invasion and growth of germs in the body. The germs may be bacteria, viruses, yeast, fungi, or other microorganisms [NIH web page], according to NIH. In both cases, the growth of germs is the key point. However, the infection caused by viruses is much different from the type caused by bacteria [Deitch, Edwin A. et al. 1987, Bullock, W. E., et al, 1919, Peracino, B. et al, 2006, Goldenfarb, Paul B.,et al. 1970, Matalonga, J., et al. 2017, McDevitt, A.C., et al. 2011, Hori, K. et al. 2010, Daigneault, M. et al. 2012, Karlsson, F., et al, 2003, Carrasco, L. et al, 1977, Baron, S., et al 1964, Ohnishi, H., 1982].

Bacteria are organisms. They can grow by themselves. If people are infected by bacteria (that excrete poisonous substances), then they become physically ill. On the other hand, viruses are not organisms. They attach and bind to cells (host). Then their parts (nucleotides, etc.) are incorporated into the host cells. Within the host cells, reactions with the components of host cells occur to produce the duplication of nucleic acids and the synthesis of proteins.
Then the host cells die as a result. This is the cause of a virus infection. Fig.1 shows the schematic diagrams for the mechanisms.

As described, infection occurs in organisms. As for human diseases, they occur in human bodies. However, according to our experiences through COVID-19, we know that viruses can remain active. If human beings

touch substances (materials) during that period, they might get viruses from materials' surface and get sick due to the viruses. In such a case, the viral disease can spread from human to human through materials. Fig.2 shows the situation schematically.

Due to the COVID 19 pandemic and the following detailed information, we now understand that infection can spread from human-human and from human-materials-human which might lead to the outbreak of the disease. Why could viruses maintain their activities on inanimate materials? This question should be answered

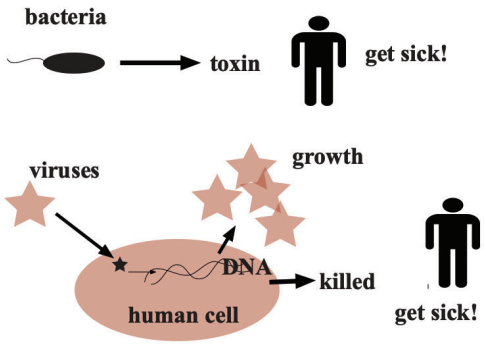

Fig.1 diseases are different depending on the sources.

from the viewpoint of materials science since the interaction between materials' surfaces and polymeric substances (derived from viruses) should be the key.

Before developing anti-virus materials, we have to understand the mechanism of viral infection through materials (the answers for questions described above) and must evaluate the viral activity on materials' surfaces. In this paper, we discuss the mechanism of the relationship between materials and viruses. Then we introduce a method to measure viral activity on materials' surfaces.

Interaction between materials and viruses

There are many types of viruses and there are some classifications for them. However, they have some common characteristics. When we come to think about the physical structures of viruses, viruses have nucleic acids (DNA or RNA) in their centres. The nucleic acids are surrounded by a protein sheath. The sheath is called a capsid. According to the structure and shape of the capsid, viruses are classified into some groups. Some viruses have lipid layers around their capsids. The lipid layer is called an envelope. Therefore, viruses can be classified into DNA types and RNA types depending on the type of nucleic acid is at the centre. They can be also classified into envelope types and non-envelope types.

As for the interaction between viruses and materials' surfaces, we must focus on the surface structures of viruses and materials. The activity of viruses must depend on how viruses can maintain their structures. That is our tentative presumption. Fig.3 shows the schematic concept. As for the envelope types, the lipid outer layer should be the key to maintain their structures. while capsids have protein sheaths. They are the non-envelope type viruses.

According to Japan's copper centre [Japan Copper Development Association web page], copper showed a very high power to decrease viruses' capabilities. According to their results,75% of the virus (Influenza A) touching the copper surface became inactive in one hours. Fig.3 shows the schematic illustration for such an antiviral effect of metallic materials on viruses. Arguably, the metallic materials would produce their cations on the metallic surfaces and the cations could

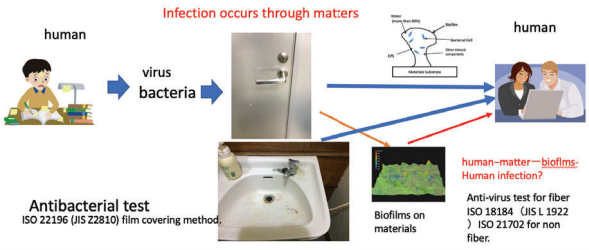

Fig.2 human-substance(materials)-human infections.

interact with lipid layers for envelope type viruses and with the proteins for non-envelope viruses. The affinity of metallic ions with lipids or proteins would determine the viral activities and longevities on various materials.

The description above is restricted to the case of metallic materials. However, the interaction between viruses and materials should vary from material to material. At this point, we don't have any concrete answers for the interaction of viruses with ceramics or polymers. That should be a topic for the near future. However, we could say at this point that the interaction between outer parts of viruses and materials' surfaces should be the key.

Importance of evaluation methods

Based on the proposed mechanism, we can develop antiviral materials further. However, we need a standard evaluation method to achieve the purpose. Fortunately, the standard evaluation method for the anti-viral materials is already fixed by the effort of the Society of International Sustaining Growth for Antimicrobial Articles (SIAA). It is ISO 21702:2019 "Measurements of antiviral activity on plastics and other non-porous surfaces". Originally, the antibacterial standard test for materials and parts came before. It is well- known as Kohkin test (ISO 22196:2007). To understand the antiviral test much better, it is informative for us to investigate the standard test for anti-bacterial materials.

Fig.4 shows the flow chart of the process for the evaluation of anti-bacterial materials. First, bacterial

solutions are prepared in advance, after certain bacteria are chosen as the target. They are cultured at 35 degrees Celsius for about 18 hours (RH90%) for example. Then the bacterial solution is diluted in various ways to make some series of diluted solutions. Then a certain amount of the bacterial solution is put on specimens. Next a polymeric film, e.g polypropylene film, is put on the bacterial solution, so that the three components (the material, the bacterial solution and polypropylene film) are closely attached to each other. The generalized name for the evaluation test is usually called the Film Covering Method. The name comes from the visual situation. After a certain incubation time, the film and the covered specimen are washed out by distilled water or sterilized water. And the washed-out solution is inoculated into solid culture and put in an incubator at a temperature for a certain time interval. Then the colony is formed on the solid culture. The number is measured and calculated. The measured figures correspond to the number of colonies. Therefore, the unit of the number should be the colony formation unit (CFU).

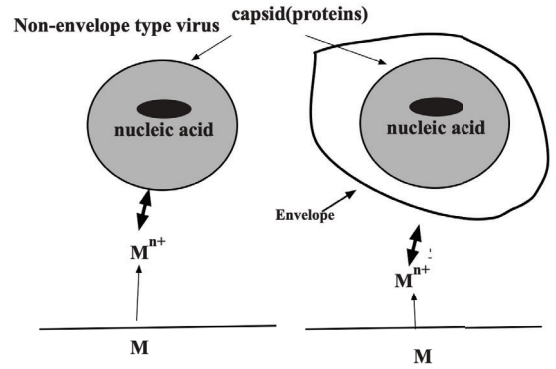

Fig.3 Interaction of metallic materials and viruses.

The antibacterial effect is expressed by the antibacterial activity value, as shown in equation (1).

$$\text{Antibacterial activity value} = (\log \mathrm{Ct} - logC0) - (logTi - logT0) \quad (1)$$

Ct: the number of live bacteria on control material after a certain time passes.
C0: the number of live bacteria on control material just after the inoculation.
Ti: the number of live bacterial on the target material after a certain time passes.
T0: the number of live bacteria on the target material just after the inoculation.

When the value is larger than 2, the antibacterial effect can be confirmed, conventionally.

For the evaluation of anti-viral materials, the concept of the film covering method is applied. In the case of the evaluation for antibacterial materials, the number of colonies could be counted. However, viruses are very small. They belong to the nano world actually. It means we could not count the number of viruses at all. Instead, we count the number of plaque corresponding to the damaged parts of cells. The example is shown in Fig.5. The white particles are plaque. In this case, the counted number is called the plaque formation unit (PFU). A certain virus solution is put on the target specimen. Then a polymer film is put on the solution. After a certain time, the specimen and film are washed out and the solution is collected into a standardized petri dish. Then the virus solution is inoculated into solid cell cultures derived from animals. After a certain time, the plaque appears. They are counted and the PFU is counted to evaluate the antiviral property of materials. Fig.5 shows the flow chart of the standard method. The viral activity is calculated as follows. (equation (2)).

$$\text{Viral activity} = -(\log Pi - \log P0) \quad (2)$$

Pi: the number of plaque on a target material.
P0: the number of plaque on the same material just after the inoculation. As already described, the active virus attacks animal cells. And if the cells are damaged by viruses, they show the while circle. Therefore, the number could lead to the evaluation of viral activity. Usually in Japan, influenza viruses and noroviruses have been issued in every winter. Therefore, Influenza A and feline calcivirus (whose structure is similar to them) are used. However, the choice is usually entrusted to each country.

Concrete examples

We tentatively checked the viral activity of a steel, using this method. The specimen was a carbon steel (SS 400). The test virus was Influenza A (H3N2, A/Hong Kong/8/68; TC adapted ATCC VR-1679) and the concentration of the test virus was 1.8×10^7 PFU/ml. According to the result, the viral activity dropped rapidly, when we used carbon steel as an example. The reason could be attributed to the iron element that has high affinity for lipid. In this case, we didn't carry out the experiment with feline calciviruses. However, we expect to have a similar result in the case, since iron could interact with polymers derived from organisms.

For the future

In this study, most of the investigation was dedicated and spent to establish the system in Kanematsu's Laboratory. At this point, we presume that the antiviral properties of metallic materials are similar to the antibacterial properties, since the interaction between metallic ions and polymeric substances (derived from organisms) seem to be the key. However, the differences

between antibacterial and antiviral properties will be elucidated one by one in the near future.

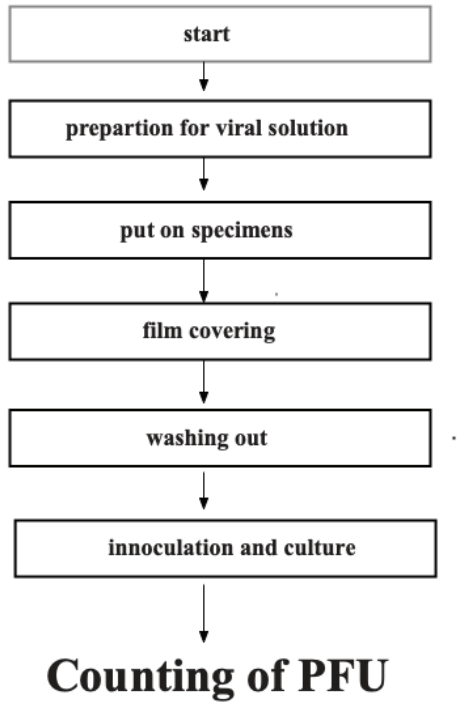

Fig.5 The flow chart of anti-viral test for materials.

Acknowledgements

This work was supported by JSPS KAKENHI (Grants-in-Aid for Scientific Research from Japan Society for the Promotion of Science, Grant Number 20K05185 and 21K12739. A part of this work was supported by GEAR 5.0 Project of the National Institute of Technology. (KOSEN) in Japan. And we also appreciate SIAA (Society of International Sustaining Growth of Antimicrobial Articles) and Advanced Technology R & D Center, Mitsubishi Electric Corporation for their useful advices.

References

www.cancer.gov/publications/dictionaries/cancer-terms/def/infectiona

Deitch, Edwin A., and Rodney Berg. "Bacterial translocation from the gut: a mechanism of infection." *The Journal of burn care & rehabilitation* 8, no. 6 (1987): 475-482.

Bullock, W. E., and W. Cramer. "On a new factor in the mechanism of bacterial infection." *Proceedings of the Royal Society of London. Series B, Containing Papers of a Biological Character* 90, no. 633 (1919): 513-529.

Peracino, Barbara, Carina Wagner, Alessandra Balest, Alessandra Balbo, Barbara Pergolizzi, Angelika A. Noegel, Michael Steinert, and Salvatore Bozzaro. "Function and mechanism of action of Dictyostelium Nramp1 (Slc11a1) in bacterial infection." *Traffic* 7, no. 1 (2006): 22-38.

Goldenfarb, Paul B., Stanley Zucker, James J. Corrigan Jr, and Mary H. Cathey. "The coagulation mechanism in acute bacterial infection." *British journal of haematology* 18, no. 6 (1970): 643-652.

Ocana, Marcos G., Víctor Asensi, Angel H. Montes, Alvaro Meana, Antonio Celada, and Eulalia Valle-Garay. "Autoregulation mechanism of human neutrophil apoptosis during bacterial infection." *Molecular immunology* 45, no. 7 (2008): 2087-2096.

Matalonga, Jonathan, Estibaliz Glaria, Mariana Bresque, Carlos Escande, José María Carbó, Kerstin Kiefer, Ruben Vicente et al. "The nuclear receptor LXR limits bacterial infection of host macrophages through a mechanism that impacts cellular NAD metabolism." *Cell reports* 18, no. 5 (2017): 1241-1255.

McDevitt, Christopher A., Abiodun D. Ogunniyi, Eugene Valkov, Michael C. Lawrence, Bostjan Kobe, Alastair G. McEwan, and James C. Paton. "A molecular mechanism for bacterial susceptibility to zinc." *PLoS Pathog* 7, no. 11 (2011): e1002357.

Hori, Katsutoshi, and Shinya Matsumoto. "Bacterial adhesion: from mechanism to control." *Biochemical Engineering Journal* 48, no. 3 (2010): 424-434.

Daigneault, Marc, Thushan I. De Silva, Martin A. Bewley, Julie A. Preston, Helen M. Marriott, Andrea M. Mitchell, Timothy J. Mitchell, Robert C. Read, Moira KB Whyte, and David H. Dockrell. "Monocytes regulate the mechanism of T-cell death by inducing Fas-mediated apoptosis during bacterial infection." *PLoS Pathog* 8, no. 7 (2012): e1002814.

Karlsson, Fredrik, Carl AK Borrebaeck, Nina Nilsson, and Ann-Christin Malmborg-Hager. "The mechanism of bacterial infection by filamentous phages involves molecular interactions between TolA and phage protein 3 domains." *Journal of bacteriology* 185, no. 8 (2003): 2628-2634.

Carrasco, Luis. "The inhibition of cell functions after viral infection A proposed general mechanism." *FEBS letters* 76, no. 1 (1977): 11-15.

Baron, Samuel. "Mechanism of recovery from viral infection." *Advances in virus research* 10 (1964): 39-64.

Ohnishi, Haruo, Hiroshi Kosuzume, Hitoshi Inaba, Masatsugu Okura, Yasunobu Morita, Hidenori

Mochizuki, and Yasuo Suzuki. "Mechanism of host defense suppression induced by viral infection: mode of action of inosiplex as an antiviral agent." *Infection and immunity* 38, no. 1 (1982): 243-250.

Japan Copper Development Association: http://www.jcda.or.jp/

ON-SITE CHARACTERIZATION OF IMPURITIES IN GYPSUM FROM WASTE PLASTERBOARDS FOR A CIRCULAR ECONOMY SYSTEM

M. Tafu*,[a], J. Nakamura[b], M. Tanii[b], S. Takamatsu[a] and A. Manaka [a]

[a] Department of Applied Chemistry and Chemical Engineering, National Institute of Technology, Toyama College, Toyama, Japan
[b] ECOdesign Engineering Program, Advanced Course, National Institute of Technology, Toyama College, Toyama, Japan
*tafu@nc-toyama.ac.jp

Abstract

Plasterboards consist of solidified gypsum (calcium sulfate dihydrate) between the board papers and are widely used as wallboards. Building demolition generates large amounts of waste plasterboards, which increase every year. In Japan, gypsum powder in waste plasterboards is recycled (recycled gypsum) into ground stabilizers for soft ground and construction sludges. Because gypsum in the plasterboards is obtained through various byproducts from several chemical industries and fuel gas desulfurization in coal-fired power plants, recycled gypsum contains numerous chemical impurities such as fluoride and arsenic that cause soil pollution after ground stabilization. Determination of the impurities in recycled gypsum requires special apparatus and harmful chemicals (such as perchloric acid) for pretreatment because gypsum is stable in water. In this study, we developed a novel pretreatment method to determine arsenic levels in recycled gypsum from waste plasterboards. Applying ion exchange resins in water facilitated the release of fluoride and arsenic in gypsum by shifting the dissolution equilibrium of gypsum in water. By selecting a suitable resin, fluoride and arsenic were successfully released into the extract, and their concentrations were determined using a conventional test method with an arsenic test kit. The results showed that the proposed method facilitates the monitoring of arsenic amounts in gypsum powder from waste plasterboards.

Keywords: *Arsenic, Plasterboard, On-site determination*

Introduction

Plasterboards consist of solidified gypsum (calcium sulfate dihydrate, $CaSO_4 \cdot 2H_2O$) between the layers and are widely used as wall materials in houses constructed using the 2X4 (two-by-four) method. In Japan, the lifespan of such houses is approximately 40 years. Because older houses are built on the ground with a lower ground hardness, demolition and rebuilding of a newer house is preferred rather than renovation. After demolition, large amounts of plasterboards are collected. One of the desirable uses of the waste plasterboard is recycling the gypsum to produce new plasterboards with correcting board paper. However, this type of recycling is not preferred because the gypsum in plasterboards is derived from mining (natural gypsum) and from byproducts of various chemical plant processes (chemical gypsum), such as phosphate and fluoride production, smelting, and flue gas desulfurization (FGD) in thermal power plants by burning coal and heavy oil (FGD gypsum). Hence, reprocessing of recycled gypsum into newer plasterboards is limited.

Gypsum is also utilized in Portland cement, which is widely used in general construction and as a ground stabilizer to improve ground hardness. Based on this background, the utilization of recycled gypsum as a ground stabilizer was investigated (Figure 1).

Because gypsum in plasterboards is supplied from various sources, it potentially contains various chemical impurities derived from the raw materials used in these chemical industries.

In our previous study, we focused on fluoride in waste gypsum, which causes soil pollution after ground stabilization. The fluoride released from chemical gypsum was successfully controlled by the addition of dicalcium phosphate dihydrate (DCPD, $CaHPO_4 \cdot 2H_2O$), which stabilized fluoride ions in gypsum to form stable fluorapatite (FAp, $Ca_{10}(PO_4)_6F_2$) [Tafu & Chohji, 2006, Tafu et al., 2010].

In addition to fluoride, arsenic in waste gypsum poses a serious environmental threat. As a hazardous waste product in the metallurgical industry, arsenic-bearing gypsum (ABG) is derived from the lime neutralization process of waste acid liquor [Li et al., 2018]. Some of the ABG was accidentally used as plasterboards in Japan during 1973–1997. In 2017, approximately 1.5×10^4 tons of ABG were separated from abandoned buildings in Japan [Yang et al., 2019]. Waste plasterboards containing ABG have been collected carefully during the demolition process in Japan.

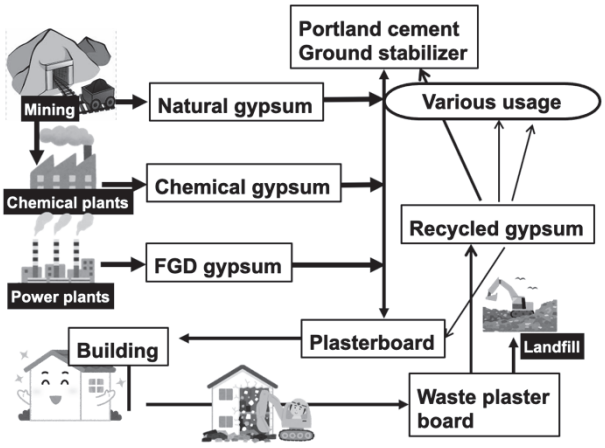

Figure 1 Material flow of gypsum in Japan (FGD: flue gas desulfurization)

However, discrimination of ABG-containing waste plasterboards is an important methodology for the safe use of ground stabilization using recycled gypsum to avoid soil pollution due to arsenic. Application of this concept may lead to the development of a safe circular economy system for recycled gypsum from waste plasterboards.

Determination of arsenic levels in gypsum requires a pretreatment process, wherein gypsum is dissolved into a homogeneous solution through a pyrolysis process involving harmful chemicals (such as perchloric acid) for pretreatment because gypsum is stable in water. We demonstrated that gypsum is easily dissolved in water containing cation and anion exchange resins, and the fluoride content in gypsum can be successfully determined by analyzing the fluoride content in the resulting solution using a simple colorimetric method (Manaka et al., 2011). These findings indicate that arsenic in waste gypsum seems to be released by the pretreatment technique using only a cation exchange resin because arsenic forms arsenate anions.

In this study, we aimed to develop a novel pretreatment method to determine arsenic levels in recycled gypsum for recycling waste plasterboards as a ground stabilizer. We investigated the dissolution of gypsum in water by the addition of a cation exchange resin. The amount of arsenic in the resultant solution was determined using a conventional arsenic determination test kit based on Gutzeit's method. We also attempted to interpret the color change of a test paper from the arsenic test kit based on the concentration of arsenic using data from an image sensor in smart devices, such as smartphones and/or tablets. From the obtained results, we concluded that our proposed method was suitable for determining arsenic amounts in gypsum within a short time period.

Materials and Experimental Methods

1) Materials and reagents

Reagent grade gypsum and sodium arsenite (FUJIFILM Wako Pure Chemical Corp., Osaka, Japan) were used as the starting materials. Simulated arsenic-polluted gypsum was prepared using the following method: Gypsum (10 g) was mixed with arsenite solution (10 mL) containing various amounts of arsenite ions for 5 min. The mixture was dried in a convection oven at 333 K for 24 h. Water was purified via ion exchange and ultrafiltration (Milli-Q A10, Merck-Millipore, Burlington, MA, USA).

2) Dissolution of gypsum using a cation exchange resin

Gypsum (300 mg) was added to water (20 mL) and mixed with various amounts of a cation exchange resin (Amberlite IR120 H, DuPont Water Solutions, Wilmington, DE, USA). The mixture was shaken for 5 min using a reciprocal shaker. The shaking speed was set to 200 stroke per minute, and the temperature was adjusted to 298 K. The liquid phase was separated via pressure filtration through a cartridge membrane filter (pore size: 0.45 μm). The calcium and sulfur concentrations of the obtained solutions were determined using inductively coupled plasma atomic emission spectrometry (ICP-AES, 720ES, Agilent Technologies, Inc., Santa Clara, CA, USA) with argon plasma.

3) Determination of arsenic levels in the simulated polluted gypsum

Simulated polluted gypsum (300 mg) containing various amounts of arsenic ions were mixed with water containing 0.2 g of a cation exchange resin. The mixture was shaken for 5 min using a reciprocal shaker. The shaking speed was set to 1500 rpm, and the temperature was adjusted to 298 K. The liquid phase was separated via pressure filtration through a cartridge membrane filter (pore size: 0.45 μm). The arsenic content of the resultant solutions was determined using an arsenic test kit (MQuant Arsenic Test, Merck KGaA, Darmstadt, Germany) and a tablet (ZenPad 8.0, ASUS, Taiwan).

Results and Discussion

1) Dissolution of gypsum using a cation exchange resin

Figure 2 shows the sulfur and calcium concentrations in water as measured by ICP-AES, after treatment of the gypsum reagent with a cation exchange resin. Owing to the low solubility of gypsum in water, calcium and sulfur concentrations after mixing gypsum into water without a cation exchange resin were lower than the calculated values obtained by dissolving all the gypsum into water (red and blue lines in the figure). The addition of a cation exchange resin increased the sulfur concentration and decreased the calcium concentration.

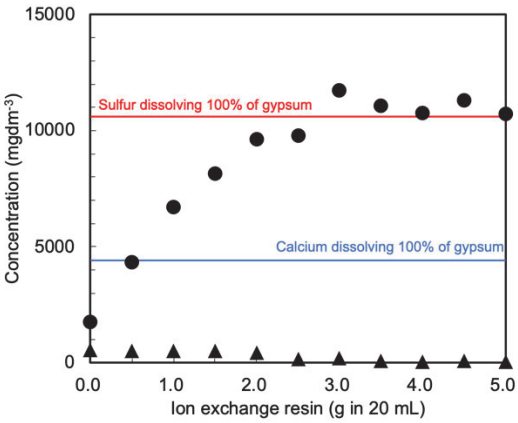

Figure 2 Sulfur and calcium concentrations in the water sample as measured by ICP-AES, after treatment of the gypsum reagent with a cation exchange resin.
Black circle: sulfur, black triangle: calcium
Amount of gypsum amount: 0.3 g
Abbreviation: ICP-AES, inductively coupled plasma atomic emission spectrometry

These phenomena resulted from the adsorption of calcium ions in the cation exchange resin, as shown in Eq. (1), and shifted the solution equilibria to the right, as shown in Eq. (2).

$$R\text{-}H^{+} + Ca^{2+} \Leftrightarrow [R\text{-}Ca]^{+} + H^{+} \quad (1)$$

$$CaSO_4 \cdot 2H_2O \Leftrightarrow + Ca^{2+} + SO_4^{-} + 2H_2O \quad (2)$$

R in the eq. (1) represents the ion exchange resin.

The results in Figure 2 indicate that gypsum was successfully dissolved in water owing to the addition of the cation exchange resin. The dissolution rate of gypsum reached 100% owing to the excess addition of the cation exchange resin.

2) Determination of arsenic concentration in the simulated polluted gypsum

Figure 3 shows the changes in the color of the test paper due to the presence of arsenic in the water sample. Determining the arsenic concentration in the sample requires the comparison of the color change with the color sample; this procedure was difficult as the change in color was not significant.

To avoid observation errors, we investigated the usage of smart devices containing image sensors. Standard solutions containing various amounts of arsenic were applied to the arsenic test kit, and the tablet captured color changes in the test paper. Figure 4 shows the change in the blue value of the image sensor as a function of the arsenic concentration in the solution. From the figure, it appeared that using the tablet, the arsenic concentration in the solution was determined to range from 0.05 to 0.15 $mgdm^{-3}$.

Based on this finding, we further investigated the process for determining arsenic levels in the simulated arsenic-polluted gypsum. The gypsum sample was dissolved in water containing the cation exchange resin, and the obtained sample was applied to the arsenic test kit as described above. The results shown in the figure indicated that the use of the tablet enabled the accurate determination of arsenic concentration in the solution to range of 10–100 $mgkg^{-1}$.

3) Benefits of the study results in gypsum recycling

Gypsum has suitable properties for potential application as a fertilizer [Oster, 1982]. If the impurity concentrations are controlled, recycled gypsum from waste plasterboards can be used in agricultural applications.

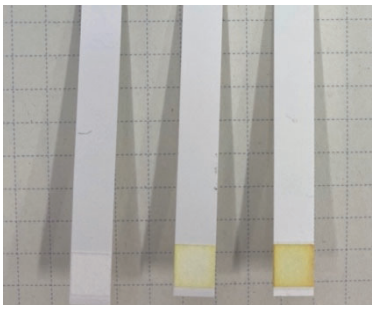

Figure 3 Change in color of test paper due to the presence of arsenic in the water sample

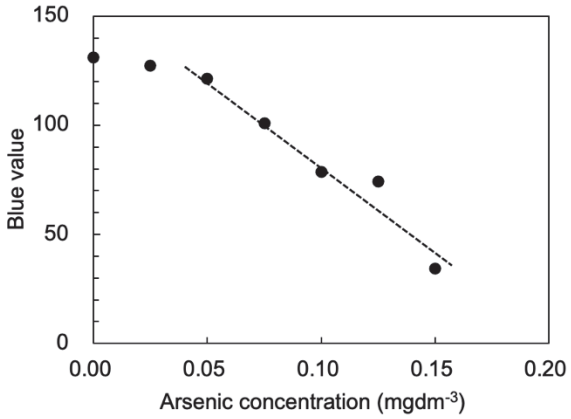

Figure 4 Change in the blue value of the image sensor as a function of the arsenic concentration in the solution

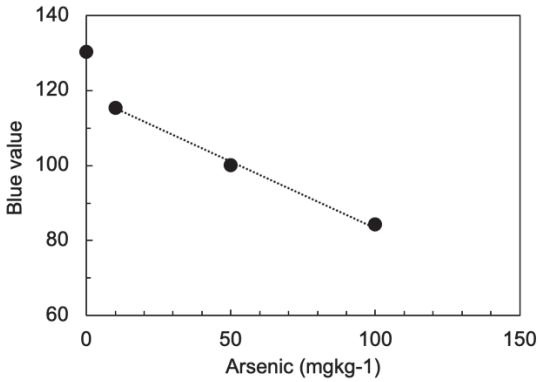

Figure 5 Arsenic levels in the simulated polluted gypsum, as determined using the proposed method

We previously reported the on-site determination of fluoride content in waste gypsum [Manaka et al., 2011]. In this study, we presented a novel and simple method for the on-site determination of arsenic content in waste gypsum. Figure 6 shows the benefits of our findings in terms of the safety of gypsum recycling for various applications. This flowchart indicates that the use of our approach will lead to reduction in the amount of waste gypsum disposed in landfills, safer use of recycled gypsum for agricultural applications, and efficient use of DCPD for stabilization of fluoride in the recycled gypsum, which will inhibit the release of fluoride into the surrounding soil for ground stabilization.

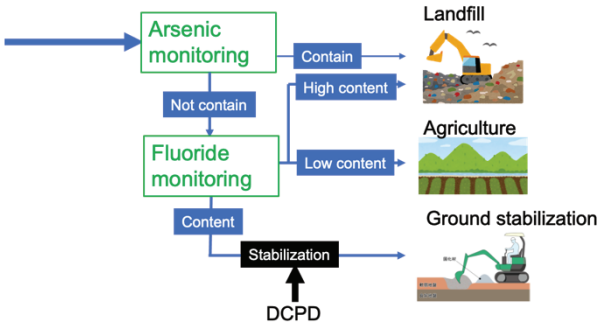

Figure 6 Benefits of our findings for safe reprocessing of recycled gypsum obtained from waste plasterboards
Abbreviation: DCPD, dicalcium phosphate dihydrate

Conclusion

In this study, the arsenic content in recycled gypsum from waste plasterboards was determined by introducing a pretreatment method employing an ion exchange resin, a conventional arsenic test kit, and tablet monitoring. The key points are summarized below.

1) Although gypsum is a stable compound in water, enhanced solubility was obtained by adding the cation exchange resin.
2) The arsenic content in the solution was determined with a conventional arsenic test kit and by capturing the color changes using a tablet, with the blue value being indicated as a function of the arsenic concentration ranging from 0.05 to 0.15 $mgdm^{-3}$.
3) Using our proposed method, we accurately determined the arsenic concentration in the solution to a range of 10–100 $mgkg^{-1}$.

The results of this study can be applied to the construction of a waste plasterboard safety recycling system while adhering to the concept of a circular economy.

Acknowledgements

We are grateful for the support by the Gypsum Board Association of Japan for various suggestions regarding our research and Ms. Haruka Tsunekawa for providing technical support for arsenic monitoring.

References

Li, X, Zhu, X, Qi, X, Li, K, Wei, Y, Wang, H, Hu, X & Zhang X (2018). Pyrolysis of arsenic-bearing gypsum sludge being substituted for calcium flux in smelting process, *Journal of Analytical and Applied Pyrolysis*, 130, 19-28.

Manaka, A, Sawai, H, Tafu, M, Toshima, T, Serikawa, Y & Chohji, Y (2011). A simple preprocessing method using ion exchange resins for the analysis of fluoride content in gypsum, *Journal of Ecotechnology Research*, 16, 47-50.

Oster, J (1982). Gypsum usage in irrigated agriculture: A review, *Fertilizer Research*, 3, 73-89.

Tafu, M & Chohji, T (2006). Reaction between calcium phosphate and fluoride in phosphogypsum, *Journal of the European Ceramics Societies*, 26, 767-770.

Tafu, M, Chohji, T, Morioka, I, Hiwasa, M, Nakano, H & T. Fujita (2010). Stabilization of fluoride in waste gypsum by using surface-modified calcium phosphate particle, *Transactions of the Materials Research Society of Japan*, 35, 377-380.

Yang, D, Atsushi Sasaki, A & Endo, M (2019), Reclamation of a waste arsenic-bearing gypsum as a soil conditioner via acid treatment and subsequent Fe (II) as stabilization, *Journal of Cleaner Production*, 217, 22-31.

A CONCRETE EXAMPLE OF SOCIETAL IMPLEMENTATIONS BASED ON GEAR / MATERIAL PROJECT:"DEVELOPMENT OF SOFT AND RESILIENT TRIBOLOGY (SRT) MATERIALS CONSISTING OF POLYMER / IONIC LIQUID COMPOSITE"

Takaya Sato [*,a], Hideyuki Kanematsu [b] and Hitoshi Wake [a]

[a] National Institute of Technology (KOSEN) / Headquarter, Tokyo, JAPAN

[b] National Institute of Technology (KOSEN) / Department of materials science and engineering, Suzuka, JAPAN

*E-Mail tsato@kosen-k.go.jp

Abstract

Ionic liquids (ILs) are non-volatile, non-flammable, high thermal stability, and have relatively good lubricity. We have introduced an active double bond into the molecule of IL to synthesize an ionic liquid monomer that can be used as a polymerizable monomer. Using this monomer, we have succeeded in preparing low friction surface materials made from an IL type concentrated polymer brush surface and a polymer gel film with tough strength. These new materials have a friction coefficient on the order of 10^{-3}, which is an order of magnitude lower than the ice surface, high wear resistance and load durability. And it has been confirmed that they function as some new sliding materials (SRT materials: Soft and resilient tribology materials) that can be used under high temperature and/or vacuum condition. These researches are currently being carried out continuously on a GEAR project of the National Institute of technology (KOSEN). This paper reports on the synthetic methods and tribology properties of these materials. Additionally, recently, our research group has developed a low-friction surface with regenerative function. It is prepared by growing a polymer brush from the inside of a polymer film coated on a substrate using the phase separation phenomenon of two or more mixed polymers. We will introduce the outline of this new research result.

Keywords: *Ionic liquid, concentrated polymer brush, tribology, low friction, radical polymerization*

Introduction

Since 2019, National Institute of Technology (KOSEN) has been promoting the "Project of human resource development for future society". The project named GEAR is an educational program for students to become independent engineers. KOSEN Students participate in world-leading research and grow as independent engineers and researchers through research practices. Research themes are set for the purpose of implementation in society. They actually perform the research, the development, and compile the results into a journal papers. In this project, we are conducting research and development of new ecological and highly efficient functional materials that will be needed in the future by forming a team of students and faculty members. The research team includes not only faculty members of KOSEN but also many researchers from companies, national research institutes, and universities. KOSEN students grow up as engineers and researchers by practicing research aimed to the social implementation. In this paper, we will introduce the development of low-friction materials centered on ionic liquids that we have been working with students.

Ionic liquids (IL) is a generic term for salts which shows a liquid state at a temperature of 100 ºC or lower. Since they have non-volatility, non-flammable, high thermal and electrochemical stability [T. Sato et al.] and relatively good lubricity, we regard them as important materials for developing some low friction systems. For example, a lubrication system using IL may provide a low friction system that can be used in space in high temperature, high vacuum environments. In the last decade, we developed some kinds of polymerizable ILs and applied a surface initiated living radical polymerization method to those IL

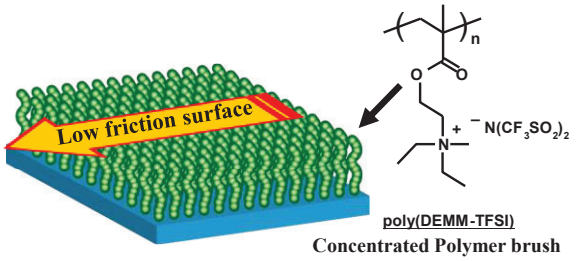

Figure 1. Conceptual diagram of a low friction surface covered with a concentrated polymer brush made from an ionic liquid with a polymerization function.

to construct a surface of a concentrated polymer brush (CPB) having ionic liquid properties. The IL-CPB has highly stretched structure in various ionic liquids, and that it significantly reduces the friction of boundary lubrication even under extremely large compression and low shear rate [H. Arafune et al.].

The second SRT material is a quite novel material, an IL double network gel (IL-DNgel) that has a high softness and low friction properties while having high strength due to the IL-containing double polymer network structure. Some ambitious challenges have been made to use water-based hydrogels as friction materials, however, their industrial uses have been limited because of the hydrogels lose their low friction characteristics and toughness due to hardening by the evaporation of water. We have developed a new material that can stably maintain low friction behavior under harsh conditions such as vacuum and high temperature by using IL as a swelling agent instead of water [H. Arafune et al.]. Their coefficient of friction is as low as about 0.003, and their durability has been shown to be at the application level of some mechanical parts such as sealing and sliding materials.

In the final topic, we will introduce our current development of a novel CPB preparation method. Typically, the CPB is synthesized by the surface-initiated living radical polymerization. Ultra-high pressure polymerization conditions are required in most cases to prepare CPBs with long brush chain lengths, so cost and cumbersome steps hinder industrialization. We have developed a method for manufacturing CPB by a simple coating method, it is an "Inverted grafting to" method (IGT-method) in which a polymer brush is induced interfacial segregation from inside the coated polymer material layer. If the formation of a polymer brush can be induced on the surface of the friction material by the phase separation of polymers, it will be possible to form a self-healing brush. We demonstrate to prepare polymer brushes by IGT-method and their lubricating properties also report. In this paper, we introduce three of the preparation methods and their low friction properties as a practical approach, (1) IL-CPB prepared by In-situ polymerization in IL, (2) ionic liquid double network gel (IL-DNgel) as a practical SRT material, and (3) CPB prepared by the IGT-method as a completely new SRT material.

Materials and/or Methods

All materials, preparation methods of polymer materials [T. Sato et al.] and measurement method used in this paper can be found in the previous paper of the author listed in the reference section of this paper.

Results and Discussion

1. In-Situ polymerization of concentrated polymer brush (CPB) on the material surface

The CPB synthesis is generally carried out by immersing a solid substance having a polymerization initiating group on the surface in a solution containing a monomer and a catalyst on the heating condition. As a CPB formation method that can be produced at low cost, we have established an in-situ brush synthesis method based on liquid film polymerization technology. The CPB film thickness assumed in this study is several hundred nanometers to several tens of micrometers. In other words, the amount of reactant liquid required to form these sizes of CPB is at most about 100 microns in terms of film thickness. It could be thought that a polymer brush can synthesize by the polymerization in a liquid film coating layer on the surface. If an ionic liquid is used as a solvent, it is a non-volatile solvent, so there is no change in film thickness due to heating. We have developed a technology that enables the formation of various CPBs on surfaces of various shapes (curved surfaces, porous inner walls, etc.) simply by applying and heating a polymer solution in which a monomer and catalyst are dissolved in an ionic liquid, and the polymerization process is performed on the heating condition in an argon atmosphere (Figure 2) [5].

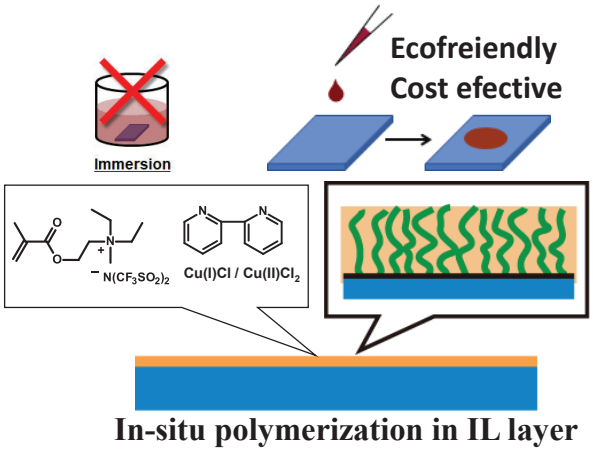

Figure 2. Simple and economically advantageous CPB synthesis in a liquid film by in-situ polymerization

We devised a friction measurement method by using a glass sheet with highly smooth at the level of nanometer as the counter surface to the brush surface, and evaluated the tribology in macroscale. On the surface of IL-CPB, it withstood more than 4000 reciprocating slides even under a load of 400 MPa or more and maintained a low coefficient of friction (μ_k = 0.003) without causing brush breakage. It was confirmed that this method can form an ionic liquid type polymer brush with the same quality as the conventional polymer brush and a swelling film thickness of about 1 micrometer. It can be said that it is an establishment of a general-purpose method for forming a uniform large-area brush surface, and we believe that the manufacturing cost of polymer brushes can be significantly reduced. Figure 3 indicated an EDX

analysis of CPB made in a coated liquid film on a substrate, (It was prepared without a cover glass: Open coat). This is an image obtained by observing the cross section of CPB made on a silicon wafer with a scanning electron microscope attached EDX and analyzing the distribution of atomic species. The image appears to be color coded in two regions, the green color at the bottom suggested to the existence of silicon atoms on the silicon wafer and the red part at the top is the color derived from the carbon atom of CPB. The CPB layer is of uniform thickness and resides on top of the silicon surface, it can be confirmed that CPB was generated on the silicon wafer by the open coating reaction system. The dry film thickness measured by ellipsometry was calculated to be 515 nm in dry state, the graft density and the surface occupancy were 0.15 chains /nm2 and 35%, respectively measured by thermal decomposition analysis. These studies have revealed that CPB has sufficiently large potential for practical use. The discovery of this new soft material with low friction properties might have an impact that brings a paradigm shift from "use of hard surface" to "use of flexible surface" at the research field of low friction materials [T. Sato et al.].

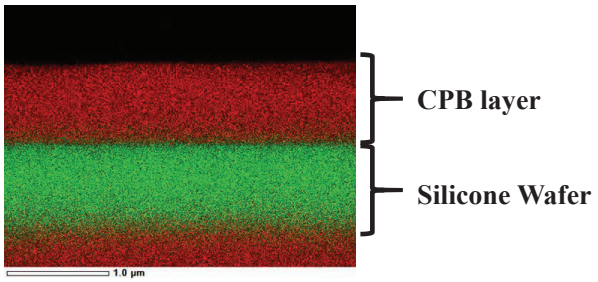

Figure 3. SEM-EDX analyses of the CPB product. Cross-sectional SEM images of the surface of CPB on the Si wafer. Elemental maps about carbon (red) and silicon (green). The thickness measurement of swelled CPB with the IL indicated 747 nm.

2. Preparation and properties of ionic liquid double network gel (IL-DNgel)

Some high-strength gels, which have flexibility, high resilience and exhibit low friction properties, are also promising as SRT materials. Double network gel (DNgel), which is a combination of two types of polymer networks with different properties such as hard and flexible, in an interpenetrating network structure, can exhibit high physical strength and low friction properties ($\mu_k = 10^{-1}$ to 10^{-2}) [3]. Hydrogel, which contains water as a swelling material, has good compatibility with living organisms, and it seems that research is underway to adapt it as a sliding material to replace cartilage in joints. However, on the other hand, when a hydro gel is used as a parts of a machine, the friction coefficient fluctuates greatly due to the volatilization of water, and it is difficult to maintain stable low friction characteristics. Therefore, we have developed a double network gel that incorporates an ionic liquid polymer into the gel framework (IL-DNgel) and uses an ionic liquid that has excellent heat resistance and non-volatility as a swelling agent. The IL-DNgel in this study was made by two-step photoinitiated radical polymerization. For the first network, an ionic liquid polymer was adopted as the electrolyte polymer. Polymethylmethacrylate with non-electrolyte character was used for the second network. An organic solvent containing an MMA monomer and a radical initiator was penetrated perfectly into the first gel, and then a second radical polymerization was carried out in the 1st-gel network. The organic solvent in the resulting gel was replaced with an ionic liquid as a swelling agent to give the final low friction gel.

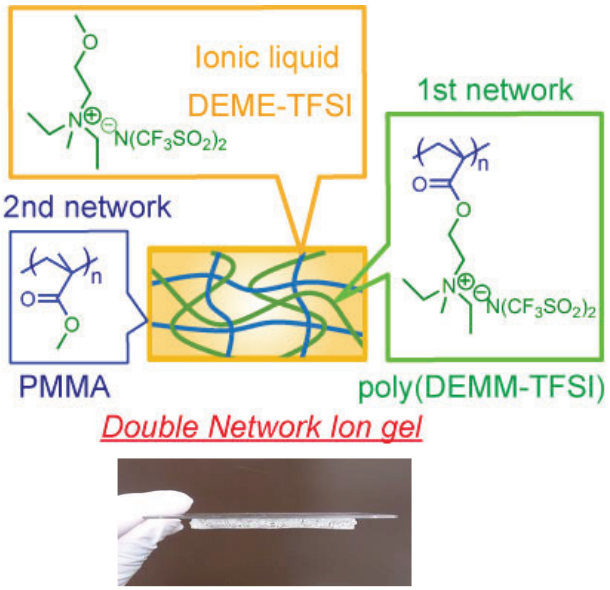

Figure 4. Composition of double network gel consisting of ionic liquid type polymer and neutral polymer and image of the gel fixed to the glass substrate.

The obtained IL-DNgel showed high compression fracture stress (30 MPa), stably exhibited an extremely low coefficient of friction ($\mu_k = 0.007$) not only at room temperature but also at 80 °C, and had similar low friction characteristics even under vacuum conditions. The results obtained in this study shed light on the fabrication of lubricant gels with high mechanical strength and robustness, which are expected to be new candidates for energy conservation.

3. Formation of loop brush by the inverted grafting to method

If it becomes possible to create the low-friction surface of the concentrated polymer brush by a simple process other than the surface-initiated living radical polymerization method, the application fields of the brush will be greatly expanded. We attempted to form a polymer brush by growing the brush from the inside of the polymer layer coated on the surface of the sliding

substrate. This method utilizes the phase separation properties of polymers and is called "inverted grafting to method (IGT-method)". In the IGT-method, the polymer brush is made by mixing the AB type diblock copolymer which is the raw material of the polymer brush, with the polymer C which will form the coating layer, in the solvent and formed a film layer on the substrate by the coating. The mechanism of brush generation is that in the polymer C layer, the A or the B segment having a low affinity for the polymer C is removed from the polymer C layer by phase separation, and the brush appears on the surface. By arranging this method and using an ABA-type copolymer as a brush raw material, it is possible to form a loop-shaped brush which has lower friction compared to the straight brush by the good selecting the B segment having a low affinity to the polymer C as the coating layer. We synthesized an ABA-type triblock copolymer consisting of polybutyl methacrylate (PBMA) as the A block and polyethylene glycol (PEG) as the B block, respectively, by living radical polymerization and introduced into a PBMA thin film. An aqueous glycerol solution was dropped on the surface of the thin film, and the PEG segment of the block copolymer was segregated on the surface to form a brush. The contact angle of water droplets dropped on the surface of the hydrophobic PBMA thin film decreased with time. This phenomenon clearly suggests the formation of hydrophilic PEG brushes on the hydrophobic PBMA film surface.

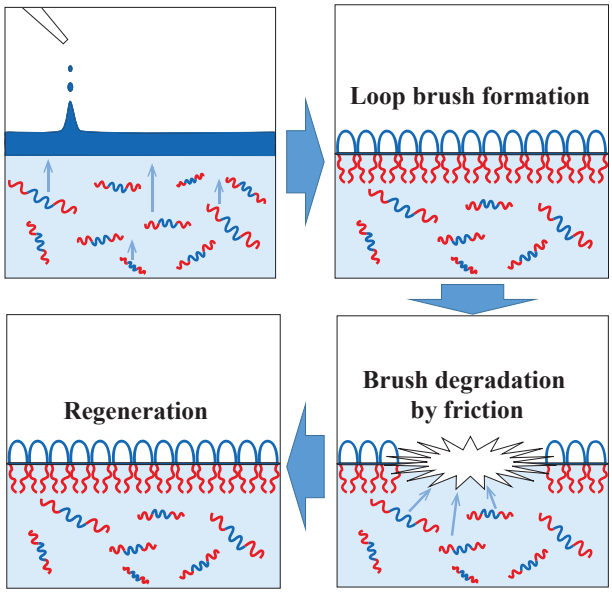

Figure 5. Schematic presentation of the low-friction concentrated polymer brush layer with regeneration function.

The coefficient of friction of the polymer brush surface created by the IGT-method is extremely low compared to the untreated surface in measured by the Ball-on-disk type friction tester using glycerol as a lubricant. In addition, it was confirmed by friction measurement that the friction coefficient of the loop brush was lower than that of the straight brush. And the loop shape was confirmed by comparing the theoretical length expected from the average molecular weight of the PEG segment with the measured value obtained by neutron scattering method. Currently, a confirmation test of self-healing properties is underway. These details will be provided somewhere in the near future. This method is highly practical as a simple brush forming method that does not use surface-initiated living radical polymerization, and at the same time, it is considered that the applicable range of low-friction surfaces using a polymer brush can be greatly expanded. In addition, its self-healing property can be expected to exert a great effect on improving the durability of low-friction surfaces.

Conclusions

We have developed an in-situ polymer brush polymerization method on a sliding surface as a method for improving the practicality of a concentrated polymer brush surface that is a soft material but has a low coefficient of friction and high durability. The brush surface formed by in-situ polymerization showed low friction characteristics that were no different from the surface formed by the conventional surface initiated living radical polymerization in solution method. We have also developed a double network ion gel as a new SRT material. It has been clarified that this gel have been an extremely tough low friction material that can maintain its toughness and low friction characteristics even at high temperature or reduced pressure. The Inverted grafting to method was applied as a method for forming the concentrated polymer brush that does not rely on the living radical polymerization. It was found that the concentrated brush surface could be easily formed by inducing a loop-shaped polymer brush using ABA-type triblock copolymer, and a SRT material and a new low-friction sliding system could be developed.

Acknowledgements

This research was carried out by Prof. Takashi Morinaga, Prof. Toshio Kamijo, Associate Prof. Hiroyuki Arafune, Assistant Prof. Ryo Satoh, Researcher Ms. Shoko Marukane, Ms. Sayaka Homma and many KOSEN students of National Institute of Technology, Tsuruoka College. Part of this research was carried out by the research funding supports of Japan Science and Technology Agency (JST), ACCEL development project "Strengthening resilience of concentrated polymer brushes and applying tribology" and GEAR project by National Institute of Technology, JAPAN.

References

T Sato, G Masuda, K Takagi. (2004). Electrochemical properties of novel ionic liquids for electric double layer capacitor applications. *Electrochimica Acta* 49 (21), 3603-3611.

H Arafune, T Kamijo, T Morinaga, S Honma, T Sato, Y Tsujii. (2015). A robust lubrication system using an ionic liquid polymer brush. *Advanced Materials Interfaces* 2 (15), 1500187.

H Arafune, S Honma, T Morinaga, T Kamijo, M Miura, H Furukawa, T Sato.(2017). Highly Robust and Low Frictional Double-Network Ion Gel. *Advanced Materials Interfaces* 4 (9), 1700074.

T Sato, T Morinaga, S Marukane, T Narutomi, T Igarashi, Y Kawano. (2011). Novel solid-state polymer electrolyte of colloidal crystal decorated with ionic-liquid polymer brush. *Advanced Materials* 23 (42), 4868-4872.

T. Sato, H. Arafune, T. Kamijo, T. Morinaga, S. Honma, K. Nakano, Y. Tsujii. (2019). Preparing method of concentrated polymer brush. *International Patent application*. WO2018/225693.

MORPHOLOGY CONTROL OF MONOMER-POLYMER HYBRID ELECTRON ACCEPTOR FOR BULK-HETEROJUNCTION SOLAR CELL BASED ON P3HT AND TI-ALKOXIDE WITH LADDER POLYMER

T. Kato[*,a,b], Y. Kurokawa[c], K. Nishii[a,b], Y. Ueda[a], F. Imaizumi[a,b], S. Suzuki[a], D. Kawagoe[a], H. Kanematsu[b,d], and T. Fukumoto[e]

[a] NIT, Oyama College, Oyama, Japan
[b] NPO Energy Education, Oyama, Japan
[c] Kyusyu Institute of Technology, Kitakyusyu, Japan
[d] NIT, Suzuka College, Suzuka, Japan
[e] Technical Research Inst., Nishimatsu Construction Co., Ltd., Tokyo, Japan

*kato_t@oyama-ct.ac.jp

Abstract

In 2020, the GEAR5.0 project was started by KOSEN in Japan with an aim to bring the top scientists and engineers together by implementing research and development with KOSEN. In this paper, we report one of our approaches to the GEAR5.0 project for environmental energy conversion device development. In recent years, extensive research on the development of electronic devices such as solar cells, thermal electrical conversion devices, and light-emitting devices comprising hybrid materials was conducted. For these applications, the research targets are efficiency, stability, and function. Hence, morphology control has emerged as an important research topic in many fields such as chemistry, biology, and medicine for the development of highly efficient materials and functional device structures based on organic and inorganic materials and their hybrids. Once developed, these techniques will pave the way for a wide range of possibilities, such as the development of highly efficient novel functional structures in various research fields. Herein, we describe the methods for morphology control of nanophase separation structures in the photoactive layer of organic–inorganic hybrid thin-film solar cell to develop a highly functional electronic device for social implementation. Specifically, organic and organic–inorganic hybrid bulk-heterojunction solar cells have the potential advantages of low manufacturing cost, light weight, and mechanical flexibility. This work demonstrated that it is possible to control the phase-separated structure of a bulk-heterojunction solar cell using a ladder polymer as the carrier manager. Therefore, we obtained higher energy conversion efficiency than the conventional P3HT/Ti-alkoxide system. Titanium is an absorber that harvests light at 500 nm or less; thus, the Ti-alkoxide system is expected to be preferably used for energy harvesting systems in indoor applications because an indoor light source consists of a shorter wavelength component below 500 nm than solar light.

Keywords: *solar cell, energy conversion, organic–inorganic hybrid material, Ti-alkoxide, P3HT*

Introduction

Numerous solar cells such as dye-sensitized solar cells (O'Regan and Grätzel, 1991; Mathew et al., 2014), organic thin-film solar cells, and printable perovskite solar cells (Shuttle et al., 2008; Street et al., 2009; You et al., 2013) have been proposed in recent years. Among these solar cells, the power conversion efficiency (PCE) of perovskite solar cells exceeds 20%, which have demonstrated high-performance using organic–inorganic hybrid materials (Zou et al., 2017). In contrast, organic thin-film solar cells, which have been reported with a PCE of over 10% on a single junction cell (Lingxian et al., 2018), are expected to achieve higher performance for practical applications. It has been reported that the maximum theoretical PCE of organic thin-film bulk-heterojunction solar cells can reach approximately 20% (Seki et al., 2013). The typical photoactive layer of organic thin-film bulk-heterojunction solar cells is composed of a p- and n-type semiconducting material as the electron donor and electron acceptor, respectively. Typically, n-type semiconducting materials used as electron acceptors are fullerene derivatives such as [6,6]-phenyl-C61 or C71-butyric acid methyl ester ([60]PCBM or [70]PCBM). However, fullerene derivatives are air-sensitive after dissolution in some solvents. Therefore, alternative non-air-sensitive electron acceptors are required. Previous studies demonstrated that some metal alkoxides and precursors were available as alternative functional electron acceptor materials (Kato et al., 2016; Kato et al., 2017). In contrast, when using the Ti-alkoxide as the electron acceptor, the PCE was only 0.03% and

short-circuit current density (Jsc) was 191 μA/cm (Kato et al., 2016). Therefore, an increase in Jsc is required. In organic thin-film bulk-heterojunction, the thickness of the photoactive layer is on the order of a few hundred nanometers, and light absorption, charge separation, and transfer occur consecutively within the photoactive layer. Therefore, it is important to consider the light absorption of the photoactive layer in addition to highly efficient charge separation and transfer in parallel (Shuttle et al., 2008; Street et al., 2009). A number of semiconducting polymers with light absorption in the long wavelength range have been developed in recent studies to obtain a higher Jsc (Li et al., 2017); however, device performance has not been improved sufficiently. As one of the factors, it is difficult to simultaneously achieve stable high solubility in a solvent and the control of polymer self-formation for phase-separation structures suitable for charge separation and transfer. In contrast, we indicated that it is effective to control the phase-separation structure of the photoactive layer by using the molecular bulkiness of the electron-accepting materials (Kato et al., 2016; Kato et al., 2017). Furthermore, this proposal is valid using not only one molecular structure but also different molecular structures of the electron-accepting materials for phase-separation structure control. However, both these methods use a monomer with electron-accepting ability. Therefore, these methods are not sufficient for controlling the self-formation of the polymer an electron donor material (Benten et al., 2016). This is because the polymer's ability to self-organization is higher than that of the monomer. Therefore, in this study, we propose a novel method that uses monomers and polymers with different molecular bulkiness and self-organization ability as the electron-accepting material. The photoactive layer is composed of a p-type semiconducting material as the electron donor and two n-type semiconducting materials as the electron acceptor, Ti(IV)-alkoxide as the monomer electron acceptor, and poly(benzimidazobenzophenanthroline) (BBL) as the polymer electron acceptor (Hirvonen and Tenhu, 2015). In particular, a ladder-type polymer is adopted as the electron-accepting material for the formation of consecutive charge transfer pass by the n-type semiconducting material phase for effective electron transportation (Hirvonen et al., 2013). In addition, it has been reported by previous studies that charge separation occurs between poly(3-hexylthiophene-2,5-diyl)(P3HT) as the electron donor material and each electron-accepting material (Manoj et al., 2002). This proposal demonstrates the morphology control of a three-component bulk-heterojunction for highly efficient organic–inorganic hybrid bulk-heterojunction solar cell using a monomer and polymer composite electron-accepting material.

Experimental

The materials used for the photoactive layer, which are poly(3-hexylthiophene-2,5-diyl) (P3HT) as the electron donor material, Titanium(IV) isopropoxide as the monomer electron-accepting material, and poly(benzimidazobenzophenanthroline) (BBL) as the polymer electron-accepting material, were purchased from Sigma-Aldrich. The molecular structures of each material and energy diagram are shown in Fig. 1.

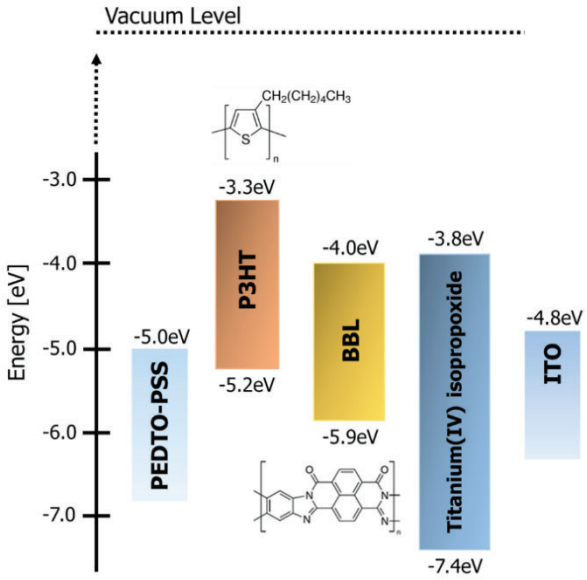

Figure 1. Materials and energy diagram

Indium-tin oxide (ITO)-coated glass substrates (1 5Ω per square) were patterned to fabricate the solar cells. These substrates were successively washed with detergent in water, acetone, and isopropyl alcohol for 15 min each and subsequently dried in a stream of air. The washed substrates were further treated with a UV-O3 cleaner (Filgen, Model UV253E) for 20 min. A functional layer as an electron collecting layer was spin-coated on the ITO substrates from a 0.50 wt% Titanium(IV) isopropoxide solution in isopropyl alcohol at 2000 rpm for 30 s Next, P3HT (3.0 wt%) and Titanium(IV) isopropoxide (6.0 wt%) were separately dissolved in chlorobenzene solution (Babel et al., 2003). These solutions were mixed (1:1 wt%) for the photoactive layer solution of the single-electron accepting system, which was spin-coated on a functional layer at 2000 to 3500 rpm for 60 s. A photoactive layer of monomer-polymer hybrid electron-accepting system was also obtained following the same process. The photoactive layer solution was prepared by dissolving P3HT (3.0 wt%) in chlorobenzene solution (electron donor solution), Ti(IV)-alkoxide (6.0 wt%), methanesulfonic acid (1.2 wt%) and BBL (1.5 wt%) in chlorobenzene solution. The solutions were mixed (1:1 wt%) to obtain the hybrid photoactive layer solution. These photoactive layers were dried at room temperature in an air atmosphere under dark conditions for 10 min, and the thickness of each photoactive layer was approximately 300 nm. Moreover, to promote the hydrolysis of Titanium(IV) isopropoxide, the substrate containing the photoactive layer was placed in a humidistat bath at 80% humidity overnight. An organic

electrode (50 µm) was coated using a screen printer (Mitani Micronics, Model MEC-2400). Poly(3,4-ethylenedioxythiophene)-poly(styrenesulfonate) (PEDOT-PSS, Clevios S V3) was purchased from Baytron and used to form the organic electrodes. Finally, the photoactive layer and organic electrodes were laminated with epoxy resin. The device structure is shown in Fig. 2.

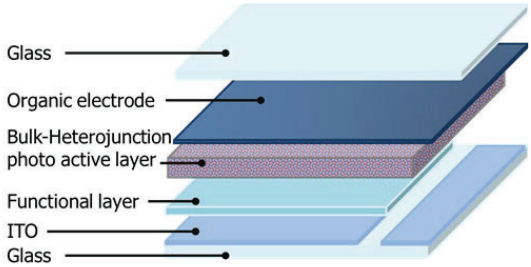

Figure 2. Devise structure for solar cells

The current density–voltage (J–V) characteristics of the solar cells were measured using a direct-current voltage and current source/monitor under illumination with AM 1.5G simulated solar light (San-Ei Electric, XES-40S1) at 100 mW/cm^2. The phase-separated structure of the photoactive layers was investigated by scanning electron microscopy (SEM, JEOL Ltd., JSM-7800). UV-Vis-near-IR spectra of each photoactive layer on a glass substrate obtained by spin coating were measured using a calibrated UV spectrophotometer (Shimadzu, UV-1800).

Results and Discussion

The J–V characteristics of each bulk-heterojunction solar cell based on Ti-alkoxide and P3HT as photoactive layers are shown in Fig. 3. The corresponding performance parameters are listed in Table 1.

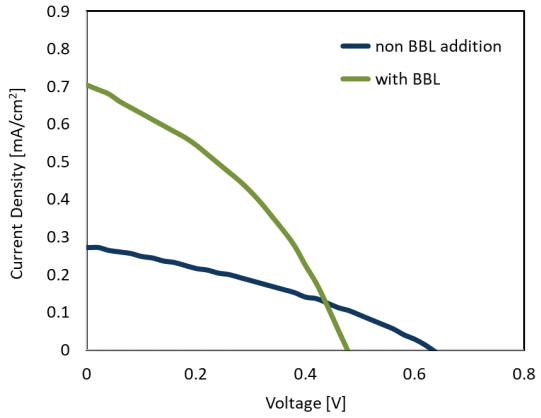

Figure 3. J–V characteristics for solar cells

When using a monomer/polymer hybrid electron acceptor for the photoactive layer, the device exhibited a higher Jsc value than the device using Ti-alkoxide as a single-electron acceptor. In particular, the device with a BBL amount of 0.75 wt% showed the highest Jsc (0.704 mA/cm^2). We will discuss the relationship between the amount of BBL added and Jsc values later in this section. Moreover, almost all hybrid electron-accepting devices exhibited higher fill factor (FF) values than the Ti-electron-accepting devices. In contrast, the open circuit voltage (Voc) decreased from 0.632 to a minimum of 0.451 V when using a hybrid electron acceptor.

Table 1. Solar cell Performances

	Single electron acceptor (non BBL addition)	Hybrid electron acceptor (with BBL)
Jsc [mA/cm^2]	0.272	0.704
Voc [V]	0.632	0.476
Fill Factor	0.336	0.376
PCE [%]	0.057	0.126

This phenomenon is caused because the lowest unoccupied molecular orbital (LUMO) of BBL is deeper than the LUMO of Ti-alkoxide. Therefore, Voc decreased according to the amount of BBL added. As shown in Table 1, the energy conversion efficiency of the solar cell increased from 0.057% to a maximum of 0.126% by improving the Jsc and FF values. To investigate these results, we measured UV-Vis-near-IR spectra (optical absorption spectra) of each photoactive layer. The measurement results of the UV-Vis-near-IR spectra are shown in Fig. 4.

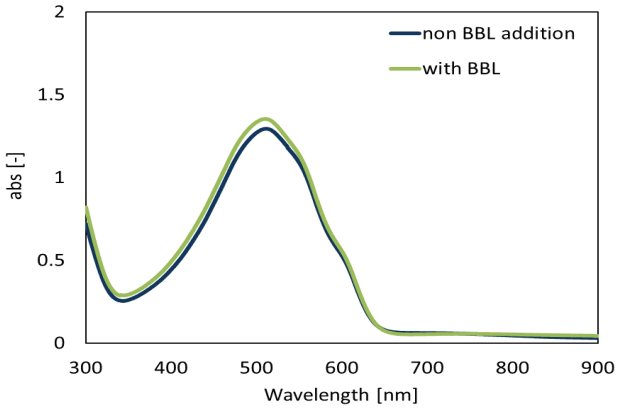

Figure 4. UV-Vis-near-IR spectrum for photoactive layers

Therefore, the optical absorption spectra of each photoactive layer showed almost the same values with the peak value at approximately 550 nm. Accordingly, the improvement in Jsc value was not influenced by the increase in photo absorption in the photoactive layer. The

reason for the high Jsc value of the hybrid electron-accepting material was attributed to the morphology of the photoactive layer. The SEM images of the photoactive layer are shown in Fig. 4.

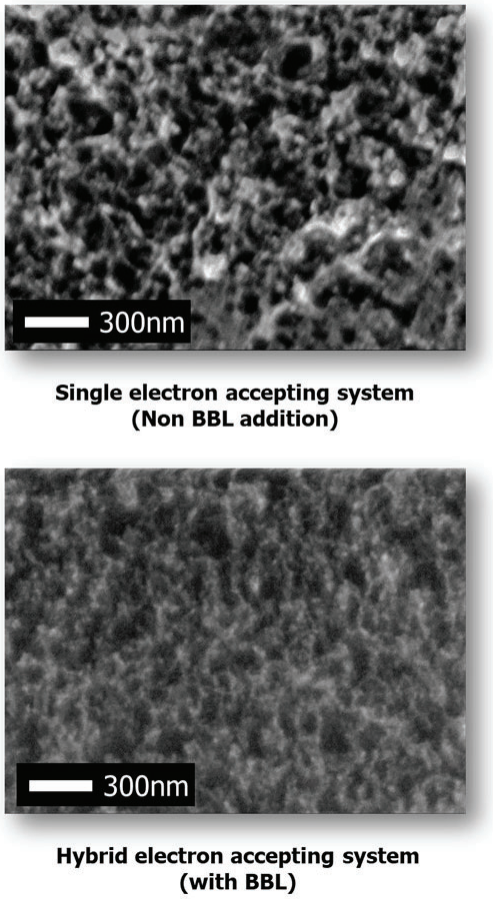

Figure 4. SEM images of photoactive layers

Therefore, the network of Titanium(IV) isopropoxide for carrier transport was improved dramatically without decreasing the p/n interface by using a monomer-polymer hybrid electron acceptor compared with the conventional single-electron acceptor system.

Conclusions

This work demonstrated that possibility of controlling the phase separation using a hybrid electron acceptor as a charge management layer, which consists of a monomer and ladder polymer, thereby improving charge transportation ability for obtaining a high Jsc value without decreasing the charge separation efficiency. When using conventional Titanium(IV) isopropoxide as an electron-accepting monomer and BBL as a ladder polymer, which has the ability to form a mold, the Jsc value improved by approximately 2.2 times in this hybrid electron acceptor system.

Finally, we believe that this research on the environmental energy power generation device will contribute to KOSEN education, which aims to bring up future top scientists.

Acknowledgements

This work was financially supported by JSPS KAKENHI (19H02662). A part of this work was supported by the GEAR 5.0 Project of the National Institute of Technology (KOSEN) in Japan.

References

B. O'Regan & M. Grätzel. (1991). Nature, Vol. 353, pp. 737-740.

Simon Mathew, Aswani Yella, Peng Gao, Robin Humphry-Baker, Basile F. E. Curchod, Negar Ashari-Astani, Ivano Tavernelli, Ursula Rothlisberger, Md Khaja Nazeeruddin & Michael Grätzel. (2014). Dye-sensitized solar cells with 13% efficiency achieved through the molecular engineering of porphyrin sensitizers. Nature Chemistry, Vol. 6, pp. 242-247.

C. G. Shuttle, B. O'Regan, A. M. Ballantyne, J. Nelson, D. D. C. Bradley, J. de Mello & J. R. Durrant. (2008). Experimental determination of the rate law for charge carrier decay in a polythiophene: Fullerene solar cell. Applied Physics Letters, Vol. 92, http://www.ncbi.nlm.nih.gov/pubmed/093311.

R. A. Street, S. Cowan & A. J. Heeger. (2009). Experimental test for geminate recombination applied to organic solar cells. Physical Review B, Vol. 82, http://www.ncbi.nlm.nih.gov/pubmed/82121301.

Jingbi You, Letian Dou, Ken Yoshimura, Takehito Kato, Kenichiro Ohya, Tom Moriarty, Keith Emery, Chun-Chao Chen, Jing Gao, Gang Li & Yang Yang. (2013). A polymer tandem solar cell with 10.6% power conversion efficiency. Nature Communications, Vol. 4, p. 1446.

Lijian Zuo et al. (2017). Polymer-modified halide perovskite films for efficient and stable planar heterojunction solar cells. Science Advance, Vol. 3, p. e1700106, 23, pp.1-11.

Lingxian Meng et al. (2018). Organic and solution-processed tandem solar cells with 17.3% efficiency. Science, Vol. 361, pp. 1094–1098.

K. Seki, A. Furube & Y. Yoshida. (2013). Detailed balance limit of power conversion efficiency for organic photovoltaics. Applied Physics Letters, Vol. 103, http://www.ncbi.nlm.nih.gov/pubmed/253904.

Takehito Kato, Naoki Hagiwara, Eiji Suzuki, Yuki Nasu, Satoru Izawa, Kouichi Tanaka & Ariyuki Kato. (2016). Morphology control for highly efficient organic–inorganic bulk heterojunction solar cell based on Ti-alkoxide. Thin Solid Films, Vol. 600, pp. 98-102.

Takehito Kato, Chihiro Oinuma, Munechika Otsuka & Naoki Hagiwara. (2017). Morphology control for fully-printable organic-inorganic bulk heterojunction solar cells based on a Ti-alkoxide and semiconducting polymer. Journal of Visualized Experiments, Vol. 119, p. e54923

Gang Li, Wei-Hsuan Chang & Yang Yang. (2017). Low-bandgap conjugated polymers enabling solution-processable tandem solar cells. Nature Reviews Materials, Vol. 2, p. 1.

H. Benten, D. Mori, H. Ohkita & S. Ito. (2016). Recent research progress of polymer donor/polymer acceptor blend solar cells. Journal of Materials Chemistry A, Vol. 4, p. 5340-5365.
Sami-Pekka Hirvonen & H. Tenhu. (2015). Modification of naphthalenic unit in BBL main chain. Synthetic Metals, Vol. 207, pp. 87-95.
Sami-Pekka Hirvonen, Mikko Karesoja, Erno Karjalainen, Sami Hietala, Pasi Laurinmäki, Eevakaisa Vesanen, Sarah J. Butcher & Heikki Tenhu. (2013). Colloidal properties and gelation of aqueous dispersions of conductive poly(benzimidazobenzophenanthroline) derivatives. Polymer, Vol. 54, pp. 694-701.
A. G. Manoj et al. (2002). Optical Materials, Vol. 21, pp. 417-420.
Amit Babel & Samson A. Jenekhe. (2003). High electron mobility in ladder polymer field-effect transistors. Journal of the American Chemical Society, Vol. 125, p. 13656-13657.

Development of Biomass-based Plastics with biodegradability and thermoplasticity.

R. Satoh*[,a], M. Konno[a], S. Honma[a], T. Morinaga[a], T. Kamijo[a], and T. Sato[a].

[a] National Institute of Technology, Tsuruoka College, Department of Creative Engineering
Tsuruoka, Yamagata, JAPAN

*r-satoh@tsuruoka-nct.ac.jp

Abstract

The demand for biodegradable bioplastics (BBPs) has been increasing due to the marine plastic pollution problem. In recent years, we have achieved dry molding of natural polymers using ionic liquids (ILs) as a dissolution aid, demonstrating the possibility of creating BBPs from unused biomass. Konjac glucomannan (KGM) is a polysaccharide derived from konjac potatoes and it is a potentially promising candidate for BBPs. However, natural polymers such as KGM generally do not have thermoplasticity, and the cost of equipment and processing is one of the factors that prevent their industrialization as materials. On the other hand, a unique compositing technique that enables natural polymer materials to be given thermoplasticity was found by making effective use of ionic liquids. The goal of our research is to develop a melt-molding method for BBPs, which will contribute to the improvement of social resilience by creating sustainable industrial materials. The flying powder discharged from the konjac flour milling process was used as a raw material. For the plasticizer, not only low-toxicity ionic liquids but also deep eutectic solvents (DESs) were considered as candidates, which are attracting attention for their environmental friendliness. First, fibres and films were fabricated from KGM extracted from flying powder, and the structure-property relationship between the physicochemical properties of the plasticizer and the molecular structure of KGM were analyzed. Finally, ILs or DESs that are suitable for KGM plasticization based on thermogravimetric analysis were systematically identified. In the future, we plan to design and synthesize ILs and DESs as plasticizers which melt various natural polymers and elucidate the correlation between the molecular structures of polysaccharides, ILs/DESs and the structural properties of natural polymers and the thermo-plasticization mechanism by using thermogravimetric analysis and material tests and thermoplasticization mechanism of natural polymers.

Keywords: *konjac glucomannan, ionic liquid, deep eutectic solvent, biomass-based plastic, melt molding*

Introduction

The BBPs has been increasing due to the marine plastic pollution problem. According to the International Union for Conservation of Nature (IUCN), the majority of marine microplastics are generated in people's daily lives; 35% from the washing of synthetic fabrics and 28% from tire wears. Although the health effects of microplastics are still being investigated (Revel *et al*., 2018), they have been found to migrate from the intestinal tract to the skin, muscle, and liver (Abbasi *et al*., 2018) in fish, suggesting bioaccumulation through the food chain (Setälä *et al.*, 2014). In addition, phthalate esters and polychlorinated biphenyls (PCBs) have also been detected (Hardesty *et al*., 2015, Besseling *et al.*, 2013) and can be expected to circulate and threaten human health. The development of BBPs is required from the viewpoints of environmental protection, marine conservation, and health and hygiene.

KGM is a polysaccharide consisting of glucose and mannose which is randomly linked. konjac potato (*Amorphophallus Konjac*) containing KGM undergoes drying and cutting processes to produce a crude powder. The crude powder is further purified to yield about 60% edible purified KGM powder, while the rest is discarded. KGM is a polysaccharide with excellent biocompatibility, similar to cellulose which is composed solely of β-glucose. In contrast to cellulose, KGM has been used as a food product mainly in Asia; the molded konjac.

Our research group has developed natural polymer moldings from silk fibroin extracted from silkworm silk cocoons using ILs and organic solvents. While KGM is a polysaccharide similar to cellulose, it is inherently plastic and biodegradable, as it has already been used as a gel food. If KGM could be processed into fibres and films by industrial processes, it would be possible to implement biodegradable plastics in society along with cellulose. The final goal of this research is to develop biomass-derived plastics that are biodegradable and thermoplastic. Natural polymers have usually no melting point of their own and can only be processed in a limited number of molding processes. Therefore, we expect that ionic ILs or DESs, which can act as melting aids, can be applied to the molding of KGM to produce fibres, films, or resins with excellent processability. In this report, we

constructed a process for extracting KGM from konjac potato and studied the artificial preparation of molded products according to solution molding scheme.

Materials and Methods

Fifty wt% 4-methylmorpholine N-oxide (NMMO) aqueous solution was purchased from Sigma-Aldrich (St. Louis, MO, USA), Dimethyl sulfoxide (DMSO) was purchased from Kanto Chemical (Tokyo, Japan). Ethanol, diethyl ether, 36 wt% hydrochloric acid and sodium hydroxide were purchased from Nacalai Tesque (Kyoto, Japan). All reagents above were used without further purification. Fehling's solution containing sodium hydroxide, copper sulfate, sodium potassium tartrate, and sodium hydroxide was obtained from Nacalai Tesque. The konjac potatoes were produced by overseas farmers and were kindly gifted. All water used in the experiment was ultrapure grade.

KGM was extracted and purified from konjac yams according to the following method (T. Sato, 1992). Briefly, the dried powder was suspended in a 10 wt% sodium hydroxide solution and boiled. After that, the Fehling's solution prepared at the time was added gently and allowed to stand overnight. The precipitates were washed with ultrapure water and ground slightly in a household mixer. One wt% hydrogen chloride/ethanol solution was used for neutralization and washing. Further washing was carried out using aqueous ethanol solution and pure ethanol, and finally with diethyl ether. The resulting powder was vacuum dried overnight.

A suspension containing 2 wt% KGM was prepared by adding 50 wt% NMMO solution to the purified KGM. The solution was evaporated at 80°C. The process was carried out until the entire liquid was infiltrated to the KGM powder. Two-times portion of DMSO for the initial weight of KGM/NMMO mixture was added and the solution was heated at 80°C under ambient pressure. A clear, colorless, viscous liquid was obtained.

Results and Discussion

The obtained colorless and viscous solution (dope) was stable at room temperature. The dope was poured into a Teflon mold and allowed to stand for several hours at room temperature to form a gel-like solid. The compressive properties of the molded product were shown in Figure 1 by mechanical testing equipment. The brittle fracture of the gel was observed at a stress of 8.06 MPa and a strain of 94%. The solvent of the gel seeped out on the specimen table after the test, suggesting that the mechanical relaxation effect of the gel occurred until the brittle failure of the specimen.

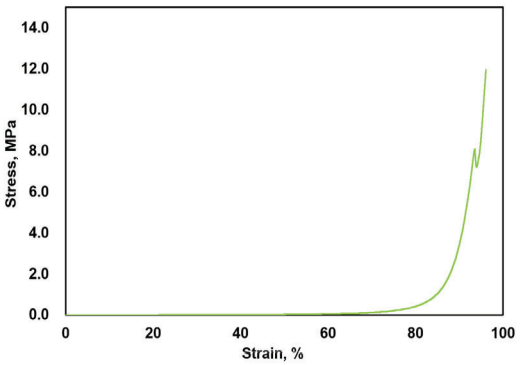

Figure 1 Stress-strain curve of gel moldings derived from konjac glucomannan (KGM).

Conclusions

In this study, we examined the possibility of protocolization of KGM extraction and molding in order to create BBPs using KGM. We achieved to obtain a polysaccharide solution that is stable at room temperature, and achieved the process of molding gel materials from the solution. In the future, we will apply ILs and DESs as plasticizers to verify the reversible melt-solidification process in the temperature range below 200°C, while testing the thermal properties of molded solids obtained from KGM solutions.

Acknowledgements

A part of this work was supported by GEAR 5.0 Project of National Institute of Technology (KOSEN) in Japan.

References

E. Besseling, A. Wegner, E. M. Foekema, M. J van den Heuvel-Greve, A. A. Koelmans (2013). Effects of microplastic on fitness and PCB bioaccumulation by the lugworm Arenicola marina (L.). *Environmental Science & Technology*, 47, 593-600.

J. E. Hardesty, B. Wahlang, K. C. Falkner. B. Clair, B. J. Clark, B. P. Ceresa, R. A. Prough, M. C. Caveh (2015). Polychlorinated Biphenyls Disrupt Hepatic Epidermal Growth Factor Receptor Signaling. *Xenobiotica*, 47, 807-820.

M. Revel, A. Châtel, C. Mouneyrac (2018). Micro(nano)plastics: A threat to human health? *Current Opinion in Environmental Science & Health*, 1, 17-23.

O. Setälä, V. Fleming-Lehtinen, M. Lehtiniemi (2018). Ingestion and transfer of microplastics in the planktonic food web (2018). *Environmental Pollution*. 185, 77-83.

S. Abbasi, N. Soltani, B. Keshavarzi, F. Moore, A. Turner, M. Hassanaghaei (2018). Microplastics in different tissues of fish and prawn from the Musa Estuary, Persian Gulf. *Chemospher*, 205, 80-87.

T. Sato (1992). Preparation and some functional properties of water-soluble cellulose derivatives and branched polysaccharides. *Thesis* (Kyoto University, Japan), pp.-195.

TENSILE EXAMINATION AND STRENGTH EVALUATION OF LATEWOOD IN JAPANESE CEDAR

A. Takahashi[*,a], S. Yuki[b], H. Yamamoto[c], N. Yamamoto[d] and T. Toyohiro[a]

[a] Department of Mechanical Engineering, National Institute of Technology, Miyakonojo College, Miyazaki, Japan
[b] Department of Aerospace Engineering, Tohoku University, Miyagi, Japan
[c] Department of Mechanical Design System Engineering, University of Miyazaki, Miyazaki, Japan
[d] Technical Support Center, National Institute of Technology, Miyakonojo College, Miyazaki, Japan

*akihiro@cc.miyakonojo-nct.ac.jp

Abstract

The role of tree ring location and height within tree are reflected on the properties of earlywood and latewood. Latewood in wood is known to have the role of rigidity of the entire wood, however research of characteristics on strength and fracture is not sufficient. Although there are differences depending on the kind of woods, latewood part is significant thin layer in the wood. Therefore, latewood material testing standard for thin dimension wood are currently not established. In this paper, a new tensile specimens for latewood (Cryptomeria japonica, called Obi in Japanese) is proposed, and it is described to precisely measure the fracture stress and fracture strain of samples even in regions of very small displacements without having to perform machining for measurement. Latewood tensile specimen in growth direction taking from the tree log for tensile testing is cut from wood plate using cutter tool and sandpaper. Quasi-static tensile test of the latewood specimen is performed at initial loading speed of 1.0 mm/min in the atmosphere with universal testing machine.

Keywords: *Japanese cedar, latewood, tensile test, mechanical characteristics, fracture surface*

1. Introduction

Wood has been effectively utilized one of the important materials for furniture and building and also as a fuel material for the warm up in the house. Wood has a valuable feature of absorbing carbon dioxide (CO_2) for own photosynthesis, and the CO_2 stays inside of wood even if it's after they are harvested or burnt up (i.e. carbon neutral) [1-4]. Thus, several wood applications have been expected to be developed to the new productions which woods have not been applied on. An in-depth data on the wood's mechanical property is requested for creating demand and effectively utilizing of wood in the future [5].

It is especially important to predict the strength of laminated wood which has a lots of high production. If it can be achieved, a stable supply and a price stability of wood will be possible at an early stage. In recent years, structural analysis based on finite element method has been widely used to make early prediction of stiffness and deformation of structural members. Outputs by structural analysis is faster than those by experiments. Furthermore, improvement of jointing technology in wood structure can be expected by establishment of structural analysis of wood. Input of highly accurate elastic modulus and mechanical property in major wood structures: earlywood and latewood for the analysis.

All wood plants share similar biological characteristics that produce wood as their structure. As the tree grows, it develops two growth rings in the tree; an earlywood and a latewood as shown in Fig.1. It is understand that the latewood region makes narrow vessels like the degree of thickness of 0.1 to 0.4 mm. However, there is no material testing standards for tensile test using miniature wood test piece. Thus, it is important to preparing of miniature specimen which could be subjected to tensile test. This research is what for the preparation of miniature specimen of a latewood with thin thickness.

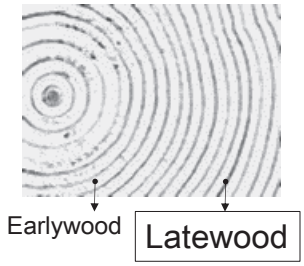

Figure 1. Cross-section of the tree log showing earlywood and latewood.

2. Materials and Methods

2.1 Wood

Latewood was used from a Japanese cedar called Obi-Sugi in an even-aged 40-years old forest stand from Nichinan city, Miyazaki in Japan. Fig.2 shows illustration of the cross section and orientation of the longitudinal latewood sample made from the Obi-Sugi.

2.2 Tensile examination

Fig.3 shows configuration and dimensions of the tensile test pieces prepared in this study. Tensile test piece as shown in Fig.3 (a) is made with reference to the

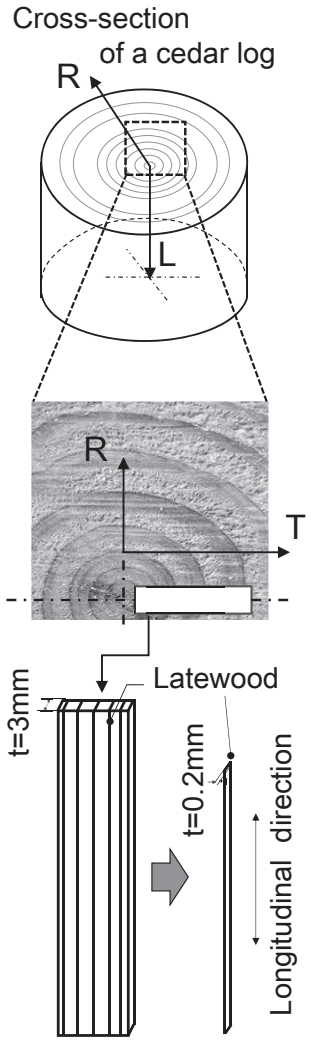

Figure 2. Schematic showing the cross section and orientation for the latewood sample.

tensile testing standard of a natural plant fiber in the previous study [6]. Fig.3 (b) is the test piece in which the grip strength is increased by making the grip dimension is longer than that in Fig.3 (a). Test pieces of Figs.3 (a) and (b) consist of thick paper and two liquid type curing adhesion resin. Fig.3 (c) has the feature of much higher the bonding force by enclosing adhesion resin of the grip. Gage length of Figs.3 (a) to (c) is the same. Fig.4 (a) is a grip structure of the A-A cross section of each test piece in Figs.3 (a) and (b) which is one side bonding by the adhesion. On the other hand, The B-B in Fig.4 (b) means all-around bonding structure by adhesion resin applied to Fig.3 (c). Therefore, the value of bonding force in Fig.3 (c) predicts four times more than that in Fig.3 (a). Experimental tensile tests were conducted to examine success rate of Figs.3 (a) to (c), respectively. The base of the test piece during tensile examination was observed to investigate pull-out of latewood and adhesion failure.

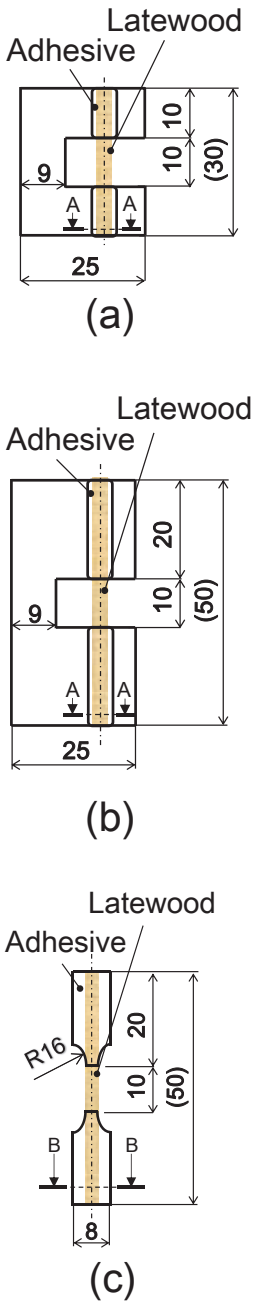

Figure 3. Configuration and dimensions of the several test pieces prepared in this study.

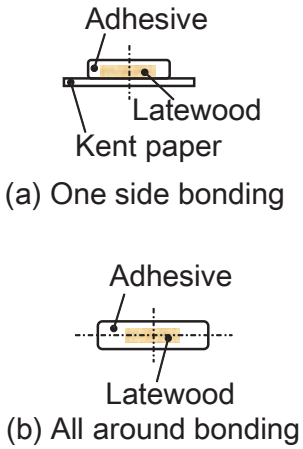

Figure 4. A-A cross section, (a) in Figs.2 (a) and (b) test piece and B-B cross section, (b) in Fig.2 (c) test piece.

Tensile examination was carried out at quasi-static loading speed of 1mm/min under atmospheric pressure. Fig.5 shows schematic illustration of tensile examination apparatus. Load-cell and laser extensometer were used to measure the applied load and tensile deformation, respectively. The latewood sample was glued on the pasteboard with thickness of 0.2 mm. Latewood of moisture content (MC) was 9 % in this study

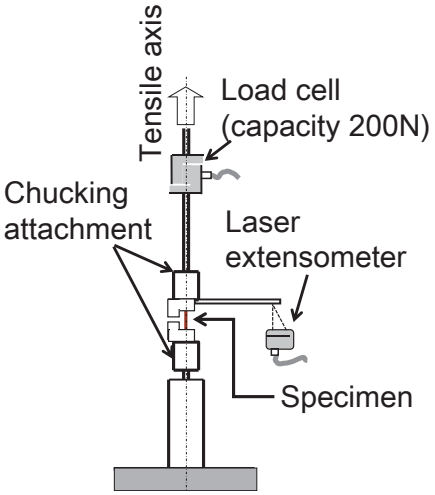

Figure 5. Tensile testing system.

3. Results and Discussion

Fig.6 shows stress-strain curve of the each test piece indicated Figs.3 (a) to (c). Arrow indicates the rapid degradation of applied load and increase of deflection related slip deformation by test piece, only observing in Figs.3 (a) and (b). Fig.7 (a) shows behavior of pull-out and separation of Fig.3 (a) test piece occurred at adhesive layer at the base of a bonded part. A success rate in Fig.3 (a) test piece was less than 20 %. Fig.7 (b) is observation result after tensile examination using Fig.3 (b) test piece. A pu11-out and resin failure

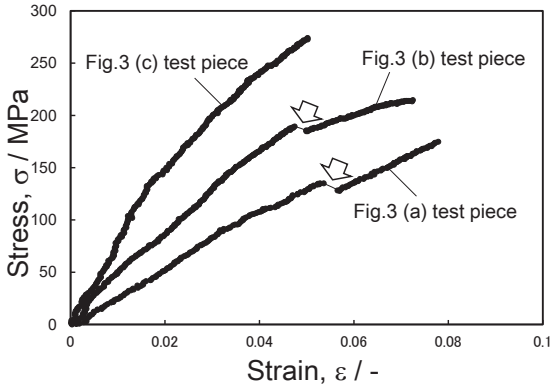

Figure 6. Stress-strain curves.

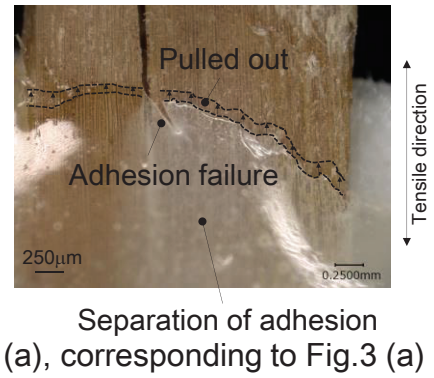

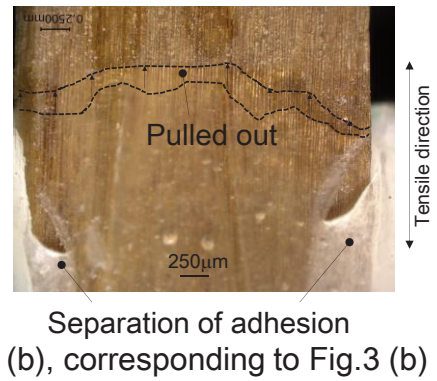

Figure 7. Observation results of the base of each test piece after tensile examination.

similar to that in Fig.3 (a). Success rate of the Fig.3 (b) test piece was approximately 30 %. In the case of one side adhesion, the success rate enhancement was not achieved with twice the bonding length. This finding indicates that the adhesive force was not sufficient to carry out the tensile examination. On the other side, improper pull-out and other damages of the Fig.3 (c) test piece were not confirmed as shown in Fig.7 (c), and the success rate had reached 100 %. The Fig.3 (c) test piece of the cross sectional structure enclosing latewood around adhesion is possible to form higher adhesive force than Figs.3 (a) and (b) [7-9].

Table 1 shows elastic modulus and mechanical property, which are found by using Fig.3 (c) test piece. However, in order to examine reproducibility of the Fig.3 (c) test piece, a lot of experimental examination is required in the future.

Table 1. Elastic modulus and mechanical property of the latewood.

	9% MC
Elastic Modulus, E	8.2 ± 1.9 GPa
Tensile Strength, σ_B	208 ± 56 MPa
Fracture strain, ε_f	0.022 ± 0.001

4. Conclusions

It was recognized that the Fig.3 (c) test piece, which has much higher the bonding force by enclosing adhesion resin of the grip, is one that could carriy out tensile examinatio of thin latewood specimen with significant suitable.

Acknowledgements

This work got supported by the KOSEN 4.0.

References

Livesley, S. J., McPherson, E. G. & Calfapietra, C. (2016). The urban forest and ecosystem services: impacts on urban water, heat, and pollution cycles at the tree, street, and city scale. *Journal of Environmental Quality*, 45, 119-124.

Canadell, J. G & Raupach, M. R. (2008). Managing forests for climate change mitigation. *Science*, 320, 1456-1457

Field, C. B. & Mach, K. J. (2017). Rightsizing carbon dioxide removal. *Science*, 356, 706-707.

Tollefson, J. (2017). The wooden skyscrapers that could help to cool the planet. *Nature*, 545, 280-282.

Toyohiro, T., Takahashi, A. & Yamamoto, N. (2014). Mechanical property and fatigue crack in consolidated wood by hot-pressing. International Journal of Innovations in Engineering and Technology, Special issue – JTL AEME (Japan), 76-82.

Kamimura, K., Takahashi. A., Yamamoto, N. & Toyohiro, T. (2017). Tensile test using strain gage of late wood in Japanese cedar. *The Proceedings of 7th IJSEE 2017*, 16-17.

Yuki, S., Takahashi, A., Yamamoto, N. & Toyohiro, T. (2018). A study on evaluation for tensile properties of latewood in cedar. *The Proceedings of 8th IJSEE 2018*, 111-116.

Yuki, S., Takahashi, A., Yamamoto, N. & Toyohiro, T. (2019). Fracture mode and tensile strength on latewood in Japanese cedar. *The Proceedings of 5th ICAEME 2019*, 39-42.

Yamamoto, H., Yuki, S., Takahashi, A., Yamamoto, N. & Toyohiro, T. (2020). Fracture behaviour and fracture analysis of latewood in Japanese cedar. *The Proceedings of 6th ICSTE 2020*, 6-10.

FRACTURE BEHAVIOR AND STRENGTH DEGRADATION IN OVER-AGED MARAGING STEEL

A. Takahashi[*,a], R. Ichimiya[b], N. Yamamoto[c], T. Toyohiro[a], Y. Segawa[a], M. Kobayashi[d] and H. Miura[d]

[a] Department of Mechanical Engineering, National Institute of Technology, Miyakonojo College, Miyazaki, Japan
[b] Advanced Course of Mechanical and Electrical Engineering, Department, National Institute of Technology, Miyakonojo College, Miyazaki, Japan
[c] Technical Support Center, National Institute of Technology, Miyakonojo College, Miyazaki, Japan
[d] Department of Mechanical Engineering, Toyohashi University of Technology, Aichi, Japan

*akihiro@cc.miyakonojo-nct.ac.jp

Abstract

A number of studies have been carried out in the past on the relationship between mechanical property and aging conditions of different grades of maraging steels. Due to maraging steel is age-hardening type materials, many research efforts have focused on the microstructural development which combined with strength and toughness at the highest hardness. In the future, in order to improve the effective utilization technology of maraging steel as a structural material, it will be required to improve weldability. The heat-affected zone during welding always includes an over-aged region in the vicinity of the welded microstructure. However, investigation has not been conducted on the mechanical property and fracture morphology at over-aged maraging steel. The objective of this paper is to present the results of an investigation whose goal was to study the property of strength and behaviour of fracture in over-aged maraging steel. The heat treatment procedure was selected to be identical to that used in a previous study of other researcher. The samples for heat-treatment test were cut from the bar and solution treated at 1123 K for 5.4 ks, and then cooled in air. They were subsequently aging treated at 753 K for several periods: 150 ks, 550ks and 1100 ks. Vickers hardness test, tensile test and fracture surface observation were carried out at various aging treatment steps. Vickers hardness at peak aged sample (753 K - 150 ks) was approximately 10 % decreased than that at over aged sample (753 K - 1100 ks). Over-ageing caused a loss in strength owing to precipitate coarsening and decomposition of the martensite phase with a reversion back to austenite phase. The feature of mechanical property and fracture behaviour at over-aged specimen were described and discussed on the based on metallurgical side in this paper.

Keywords: *maraging steel, over-aged, mechanical property, deformation, fracture surface*

Introduction

Maraging steels have been intensively researched and developed since 1950s [1]. They belong to the series of high strength with important parts such as aircraft, rocket, metal moulds and so on [2]. Recently, maraging steel would be favourable for the additive manufacturing process with selected laser melting [3,4]. The range of application to the market will be gradually expanded in the future. The good mechanical property of maraging steel could be achieved due to relevant heat treatment. After artificial heat treatment, microstructure in maraging steel is formed second phase precipitation, resulting in enhancement of hardness, strength, ductility and toughness. The main additional element are nickel, cobalt, molybdenum. Maraging steels have a low carbon content so that after austenitisation, quenching results in a microstructure which is predominantly soft-martensite by the solution treatment, which is then hardened by a kinds of the precipitation phase of intermetallic compounds such Ni_3Ti, Ni_3Mo and Fe-Mo system phases after aging treatment. [5]. Among them, because maraging steels are age-hardness type materials, many R&D efforts have increased profusely microstructural development which combined with strength and toughness at highest hardness. Hereafter, in order to improve the effective utilization technology of maraging steel as a structural material, it will be required to improve weldability. The heat-affected zone during welding always includes an over aged region in the vicinity of the welded microstructure [6,7]. However, investigation has not been conducted on the mechanical property, microstructural evolution and fracture morphology at over-aged maraging steel.

The objective of this paper is to present the results of an investigation whose goal was to study the property of strength and fracture surface in over-aged maraging steel.

Materials and Methods

Maraging steel

A commercial 350 grade maraging steel bar made by vacuum arc melted method was used in this study. The chemical analysis of the material is given in Table 1.

Table 1. Chemical composition used in this study.

Element	Composition (mass%)
C	0.001
Ni	18.0
Mo	4.0
Co	12.0
Si	≦0.01
Mn	≦0.01
Others	Ti, Al
Fe	Balance

2.2 Aging treatment

Solution treatment was 1123 K (850 °C) for 5.4 ks (1.5 h) and artificial aging condition was given in Table 2. Aging temperature and keeping time were determined with reference to previous papers [8-10]. Peak aged condition was 753 K for 150 ks, over-aged for 550 ks and 1100 ks were after that. Aging of the tensile specimen was conducted in an electric furnace with a temperature accuracy of 1 K (1 °C). Aging treatment was terminated by air-cooling at 300 K (27 °C).

Table 2. Aging condition.

	Solution Treatment	Temperature	Time
1	1123 K, 5.4 ks	753 K	150 ks
2			550 ks
3			1100 ks

Tensile test and characterization

Cylindrical tensile specimen of 5 mm diameter and 50 mm gage length was machined from the heat-treated bar with its long axis in keeping with the length of the bar. Tensile test was carried out on an Instron-type universal machine with a capacity of 50 kN (Shimadzu Co.) at a constant quasi-static loading speed of 1.0 mm/min which corresponds to a nominal strain rate of 3.3×10^{-4} s^{-1}. Fig.1 indicates a schematic illustration of the tensile testing system. Applied load during tensile test was measured by load-cell. Fig.2 shows overlaying output data from the non-contact extensometer and strain gage. Output result of strain gage lost between ε = 0.020 to 0.023, because strain gage come off during tensile deformation. Thus, the tensile elongation at first stage was used strain gage

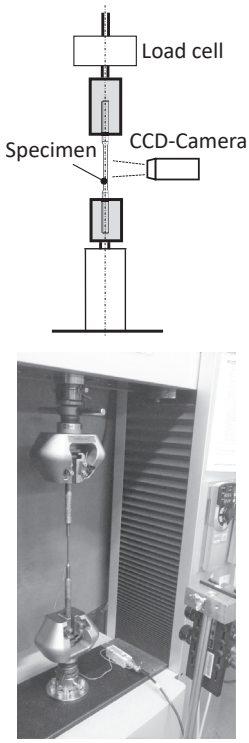

Figure 1. Testing system.

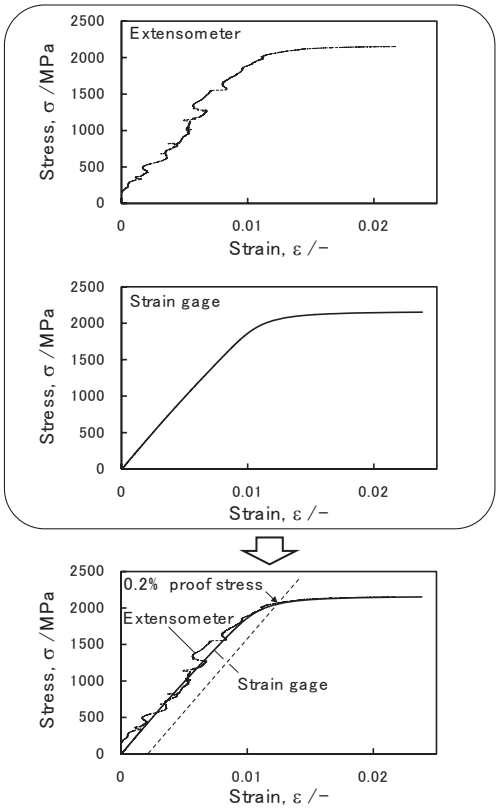

Figure 2. Evaluation of the tensile deformation and 0.2 % proof stress at tensile early stage.

and non-contact extensometer was used to measure the deformation data after the yield point.

Specimens for optical microscopy (OM) and scanning electron microscopy (SEM) were etched in acid.

Fracture surfaces of the tensile samples were examined under scanning electron microscope (SEM), operated 5kV.

Results and Discussion

Table 3 indicates hardness values at several heat treated. By previous study, it was reported that peak hardness of ST and at 753 K for 150 ks was achieved. In present study, although the peak hardness was slightly low value, the aging hardness behaviour was recognized as shown in Table 3, which included over aged behaviour of No.2 and 3.

Table 3. Hardness values at several aging conditions.

	Heat treatment condition	Hardness	Reference
ST	1123 K, 5.4 ks	336 HV	340 HV
1	1123 K, 5.4 ks + 753 K, 150ks	671 HV	705 HV
2	1123 K, 5.4 ks + 753 K, 550 ks	652 HV	-
3	1123 K, 5.4 ks + 753 K, 1100 ks	631 HV	-

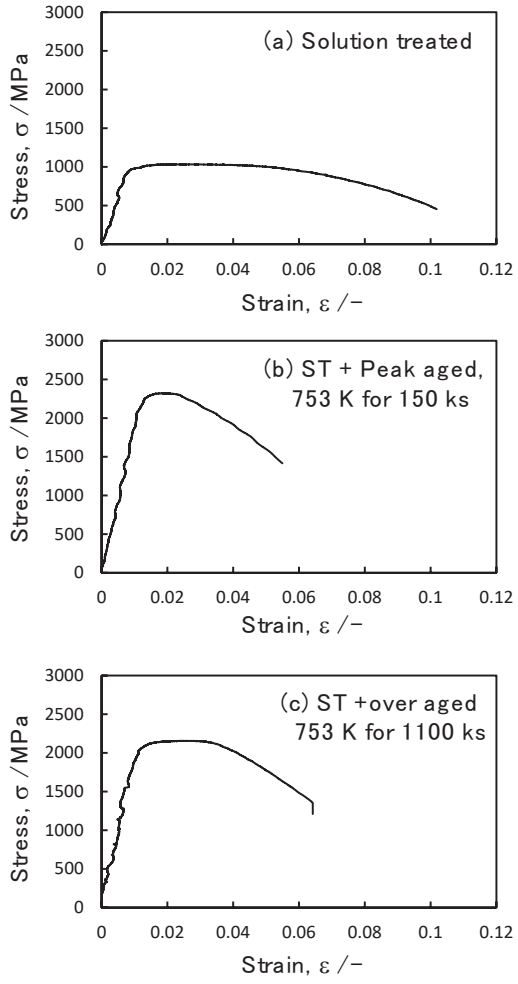

Figure 3. Stress strain curve at several aging conditions.

Table 4. Mechanical properties at several aging conditions.

	Heat treatment condition	0.2% proof stress (MPa)	Tensile Strength (MPa)	Fracture Strain
ST	1123 K, 5.4 ks	958	1033	0.102
1	1123 K, 5.4 ks + 753 K, 150ks	2268	2320	0.055
2	1123 K, 5.4 ks + 753 K, 550 ks	2140	2203	0.057
3	1123 K, 5.4 ks + 753 K, 1100 ks	2073	2154	0.064

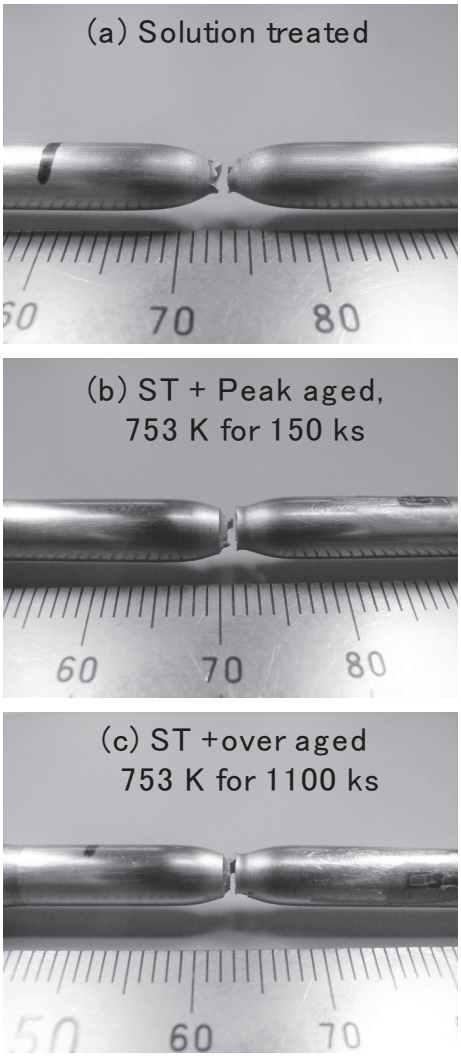

Figure 4. Photographs of the cup and cone fracture behavior at several aging conditions.

Tensile stress-strain curve provides efficient knowledge of material's overall mechanical properties, metallurgical characterization of the grain, grain boundary orientation and other interesting information for better understanding the behaviour of aging. Fig.3 (a) shows stress-strain curve at solution treated specimen. Solution treated specimen represented low strength and high ductility, resulting the volume fraction of austenite phase and unowned precipitation phases. Fig.3 (b) shows the curve at peak aged specimen. High strength was observed, and ductility 50 % decreased than the solution treated specimen, but unequal elongation was grown until fracture point. Fig.3 (c) shows the curve at over aged

specimen at 753 K for 1100 ks. The ductility of the over aged did not decreased significantly than that of the peak aged.

Table 3 shows mechanical properties at several aged condition. It was confirmed that the strength decreased as the aging treatment processed. Nevertheless, over aging treatment generally reduces the tensile ductility, the fracture strain increased with increasing aging time.

Fig.4 shows macroscopic fracture behaviour at several aging conditions. Extremely plastic deformation at fracture region (i.e. necking) was observed at solution treated specimen. The cup and cone fracture was found at all specimens regardless of the aging conditions. Usually, the over aging treatment with degradation of ductility achieves a high temperature solution annealing and/or a treatment at a high aging temperature such around 823 K (550 °C). In present study, the aging temperature at 753 K was determined based on the literature [ ], and the attempt was made to reproduce the over aged state by increasing the keeping time for aging treatment.

For most metals and alloys, the temperature dependence of the diffusion coefficient, D of the solvent element in solid is expressed by the Arrhenius equation [11,12]:

$$D = D_0 exp\left(\frac{-Q}{RT}\right) \qquad (1)$$

where, Q is the activation energy for the mass transport, D_0 is the pre-exponential factor, R is the gas constant and T is the temperature. It is approved that heat treatment temperature as a solution treatment and/or aging treatment has an exponential effect on microstructural evolution such as crystallographic texture, grain size, distribution of intermetallic precipitation particle and so on. In present study, the strength was improved by the peak aging treatment from solution treated. However, the ductility was slightly increased by the over aging treatment comparing with that by peak aging treatment. Future research in an appropriate temperature range for heat treatment will be desired.

Conclusions

In this study, the tensile strength and 0.2 % proof stress were improved by the solution sreatment, 1123 K for 5.4 ks and then the peak aging treatment, 753 K for 150 ks. However, the fracture strain was slightly increased by the solution treatment and then the over aging treatment, 753 K for 1100 ks.

Acknowledgements

We would like to thank Prof. Nagano for providing 350 grade maraging steel.

References

Inco databooks. (1976). 18 per cent nickel maraging steels. NiDI.

Viswanathan, U. K., Dey, G. K. & Sethumadhavan, V. (2005). Effects of austenite reversion during overageing on the mechanical properties 18 Ni (350) maraging steel. *Materials Science and Technology A*, 398, 367-372.

Chadha, K., Tian, Y., Bocher, P., Spray, J. G. & Aranas, Jr, C. (2020). Microstructure evolution, mechanical properties and deformation behaviour of an additively manufactured maraging steel. *Materials*, 12, 2380.

Balan, A. S. S., Chidambaram, K., Kumar, A. V., Krishnaswamy, H., Pimenov, D. Y., Giasin, K. & Nadolny, K. (2021). Effect of cryogenic grinding on fatigue life of additively manufactured maraging steel, Materials, 14, 1245.

Tewari, R., Mazumder, S. Batra, I. S. Dey G. K. & Banerjee, S. (2000). Precipitation in 18 wt% Ni maraging steel of grade 350, Acta Materialia, 18, 1187-1200.

Viswanathan, U. K., Kishore, R. & Asundi, M. K. (1996). Effect of thermal cycling on the mechanical properties of 350-grade maraging steel. *Metallurgical and Materials Transactions A*, 27A, 757-761.

Rajkumar, V., Arivazhagan, N. & Devendranath Ramkumar, K. (2014). Studies on welding of maraging steels. *Procedia Engineering*, 75, 83-87.

Kawagoishi, N., Nakamura, Y., Karita, K., Chen, Q., Nagano, T. & Maeda, Y. (2013).Aging condition for improvement of fatigue properties of maraging steel. Journal of the Society of Materials Science, Japan, 62, 756-763.

Kawagoishi, N., Miyamoto, M., Nagano, T. & Moriyama, M. (2009). Effect of humidity on fatigue strength of maraging steel with different hardness. Journal of the Society of Materials Science, Japan, 58, 787-792.

Nagano, T., Kawagoishi, N., Moriyama, M., Chen, Q. & Magashima E. (2007). Influence of shot peening on fatigue strength of maraging steels with different hardness. Journal of the Society of Materials Science, Japan, 56, 1126-1132.

Shewmon, P. G. (1963). Diffusion in solids. McGraw-Hill Book Company.

Shewmon, P. G. (1969). Transformations in metals. McGraw-Hill.

BEHAVIOUR OF POLYSILOXANE FILMS IN CONTACT WITH WATER OR SOLUTIONS SIMULATING BIOFILMS

N. Hirai[*,a], M. Horii[a], N. Sugawara[a], H. Kato[a], K. Sano[a,b], A. Suzuki[b], Y. Sawada[b], T. Kougo[a], A. Ogawa[a], D. Kuroda[a], and H. Kanematsu[a]

[a] NIT (KOSEN), Suzuka College, Suzuka, Mie, Japan
[b] D&D Corporation, Yokkaichi, Mie, Japan

*hirai@chem.suzuka-ct.ac.jp

Abstract

Currently, there is a problem that cultural properties such as World Heritage Sites and National Treasures, which are built of rocks and wood from, are weathering and creating micro pores over a long period of time, which are deteriorating and collapsing due to the penetration of rainwater into them. One of the candidates to solve this problem is a transparent sealant. If applied to the surface of the target rock or wood, the colour of the rock or wood will remain almost unchanged, and the sealant will penetrate the micro pores on the surface, and harden to prevent rainwater from entering the micro pores. Transparent sealants must not only prevent rainwater penetration, but also inhibit the adhesion of biofilm and other contaminants. Therefore, it is important to investigate how biofilm adheres and what kind of wetting or penetration behaviour of droplet exhibits. In this study, the behaviour of poly-siloxane films, which is one of the transparent sealants, in contact with aqueous solutions or biofilm simulating solutions was evaluated to get knowledge for realizing transparent sealants that sufficiently reduce the adhesion of biofilm and do not deteriorate due to the penetration of aqueous solutions. In addition to pure water, sodium alginate solution (concentration 0.1-5%), as the aqueous solution simulating a biofilm, was used as a droplet to evaluate the wettability. Poly-siloxane films named Permeate (D&D Co.) was used in this paper. For comparison, glass, acrylic, and fluoropolymer were also evaluated. The static contact angles, roll-off angles, *etc.* were measured. It has been found that the poly-siloxane films with a larger percentage of phenyl groups showed a tendency to have a larger contact angle but a smaller roll-off angles, with pure water. It has been also found that the concentration of sodium alginate in the droplets had little effect on the static contact angle, but had a significant effect on the roll-off behaviour.

Keywords: *biofilm, wettability, poly-siloxane films, contact angle, roll-off angle*

Introduction

Currently, there is a problem that cultural properties such as World Heritage Sites and National Treasures, which are built of rocks and wood from, are weathering and creating micro pores over a long period of time, which are deteriorating and collapsing due to the penetration of rainwater into them. One of the candidates to solve this problem is a transparent sealant. If applied to the surface of the target rock or wood, the colour of the rock or wood will remain almost unchanged, and the sealant will penetrate the micro pores on the surface, and harden to prevent rainwater from entering the micro pores. Transparent sealants must not only prevent rainwater penetration, but also inhibit the adhesion of biofilm and other contaminants.

When microorganisms adhere to a material surface, biofilms are formed on solid surfaces, consisting of water, microorganisms, and extracellular polymeric substances (EPS) produced by the microorganisms. Biofilms have sometimes many advantages such as water purification, but they also have many problems such as tooth decay, infectious diseases, food spoilage, and metal corrosion, so they must be removed. When considering the removal of biofilm, information on the adhesion work between biofilm and substrate is necessary, and for this purpose, it is essential to evaluate the wettability of biofilm on the substrate. Wettability of a biofilm on a solid surface can be evaluated by observing the contact angle and behaviour of the biofilm on the substrates. However, natural biofilms are difficult to extract and thus difficult to use for wettability evaluation. One solution to this problem is to use the solution simulating biofilms instead of natural biofilm.

In this study, we have investigated the wetting and roll-off behaviours of water or the solution simulating biofilms in air or in water on various substrates, such as glass, acrylic, fluoropolymer, and poly-siloxane films, which is one of the transparent sealants. In natural biofilms, polysaccharides and proteins are the main components of EPS, however, alginate as a polysaccharide and various amino acids instead of proteins are used for the solution simulating biofilms.

Experimental

In addition to pure water, sodium alginate solution (concentration: 1 to 20 g L^{-1}) and solutions containing 0.7 M of various amino acids (phenylalanine, L-alanine, L-tryptophan, L-arginine) were used as liquids to evaluate the wetting behaviour. In addition to glass, acrylic, fluoropolymer, poly-siloxane films formed on glass were used as substrates. The poly-siloxane films used were prepared by mixing two following oligomers; alkoxysilane oligomer containing methyl and phenyl functional groups (MW 360, D&D Co., Yokkaichi, Japan) and n-2-(aminomethyl)-3-aminopropyltrimethoxysilane, named KBM-603 (MW 222, Shin-Etsu chemical Co., Tokyo, Japan).

Wetting behaviour was evaluated using a contact angle meter DMo-501 (Kyowa Interface Science Co., Ltd.). Surface tension, static contact angle, roll-off angle, *etc*. were measured. Changes over time of wetting behaviours of the solution simulating biofilms in water on the substrate were also observed. These evaluations and observations were carried out at room temperature.

Results and Discussion

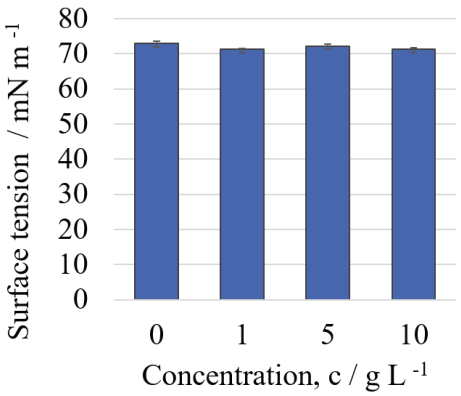

Figure 1 Surface tension of sodium alginate solution (concentration 0 to 10 g/L)

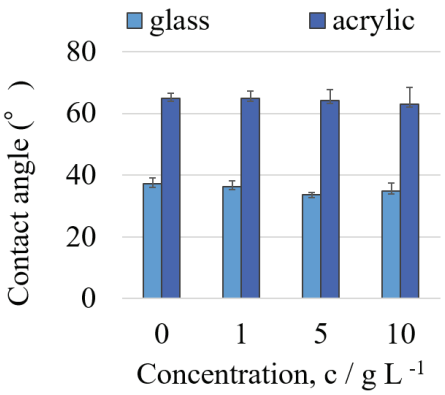

Figure 2 Contact angle of sodium alginate solution (concentration: 0 to 10 g L^{-1}) on glass and acrylic.

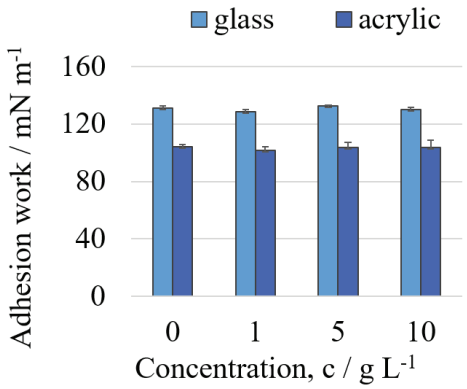

Figure 3 Adhesion work of sodium alginate solution (concentration: 0 to 10 g L^{-1}) on glass and acrylic.

Figure 1-3 show the measured surface tension and static contact angle, and adhesion work of sodium alginate solution (concentration: 0 to 10 g L^{-1}) calculated from the tension and the angle on glass and acrylic. The error bars show the standard deviation. It can be seen from the figures that the adhesion work on the glass is larger than that on the acrylic. The concentration of the sodium alginate solution has little effect on the adhesion work, i.e., surface tension and static contact angle.

Figure 4-6 show the measured surface tension and static contact angle, and the calculated adhesion work of 10 g L^{-1} of sodium alginate solution with 0.7 M of L-phenylalanine, L-alanine, L-tryptophan, and L-arginine on glass, acrylic and fluoropolymer. The error bars show the standard deviation. Figure 4 shows that the addition of amino acids to a 10 g/L sodium alginate solution slightly decreases the surface tension, and the amount of decrease increases in the order of L-phenylalanine, L-alanine, L-tryptophan, and L-arginine. Figure 6 also shows that the adhesion work decreases in the order of glass, acrylic, and fluoropolymer regardless of the

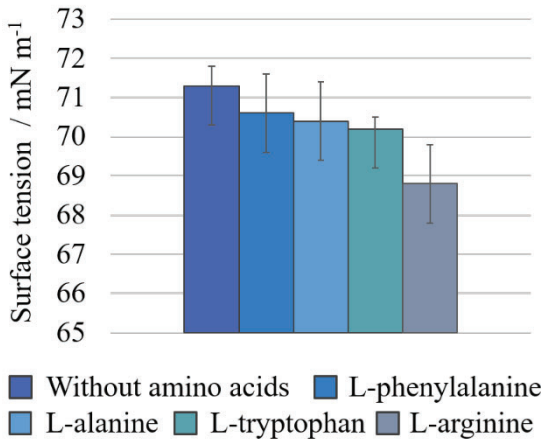

Figure 4 Surface tension of 10 g L^{-1} of sodium alginate solution with 0.7 M of L-phenylalanine, L-alanine, L-tryptophan, and L-arginine

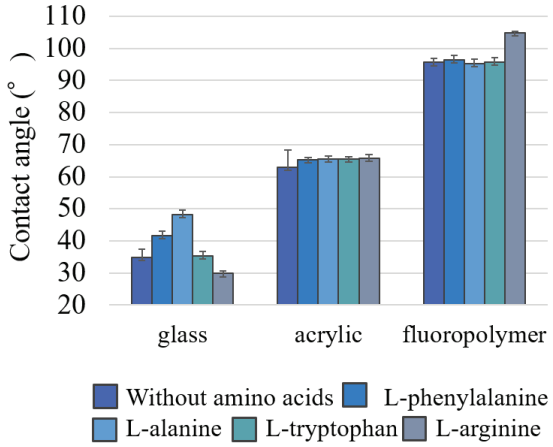

Figure 5 Contact angle of 10 g L^{-1} of sodium alginate solution with 0.7 M of L-phenylalanine, L-alanine, L-tryptophan, and L-arginine on glass, acrylic and fluoropolymer.

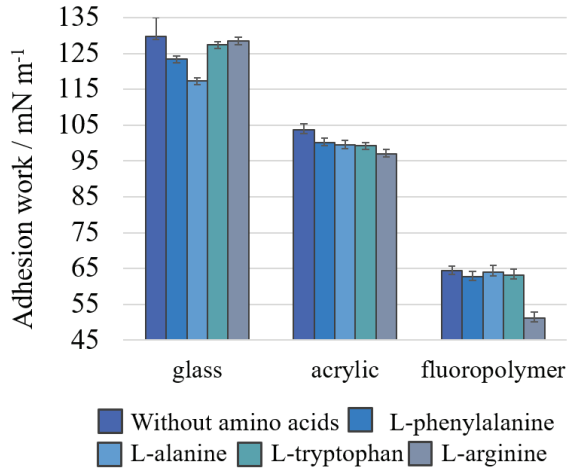

Figure 6 Adhesion work of 10 g L^{-1} of sodium alginate solution with 0.7 M of L-phenylalanine, L-alanine, L-tryptophan, and L-arginine on glass, acrylic and fluoropolymer.

solution type. These results indicate that the effect of surface tension on the adhesion work is large for acrylic, while the effect of contact angle on the adhesion work is large for glass and fluoropolymer when amino acids are added.

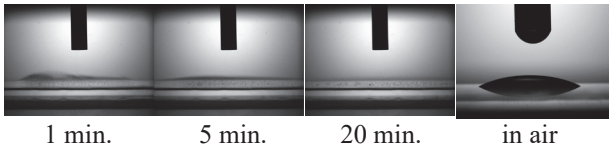

Figure 7 Wetting behaviour of sodium alginate droplets (20 g L^{-1}) on glass 1, 5, and 20 minutes after the droplet attached on each substrate in pure water or in air.

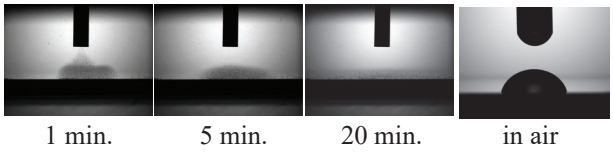

Figure 8 Wetting behaviour of sodium alginate droplets (20 g L^{-1}) on acrylic 1, 5, and 20 minutes after the droplet attached on each substrate in pure water or in air.

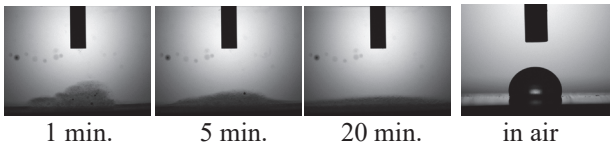

Figure 9 Wetting behaviour of sodium alginate droplets (20 g L^{-1}) on fluoropolymer 1, 5, and 20 minutes after the droplet attached on each substrate in pure water or in air.

Figures 7-9 show the wetting behaviour of sodium alginate droplets (20 g L^{-1}) on glass, acrylic, and fluoropolymer, respectively, 1, 5, and 20 minutes after the droplet attached on each substrate in pure water. The results in air are also shown in the figure for comparison. In water, the droplets spread over a wide area after a certain period of time for all three substrates. In contrast, the droplets shown on the right side of the figure were observed to be stable and did not spread over time in air. The speed of wetting differed depending on the type of substrate, and the speed was found to be faster for glass, acrylic, and fluoropolymer, in that order.

Figures 10-12 show the roll-off behaviour on glass, acrylic, fluoropolymer, respectively, of the droplet of (a) sodium alginate (20 g L^{-1}) and (b) pure water as a function of roll-off angle. Volumes of all droplets are 40 ml. The substrate was tilted by 5° per second. It was found that the droplets of pure water on any substrates rolled off when the substrate was tilted less than 50 degrees, but the droplets of alginate on any substrates did not roll off even when the substrate was tilted up to 90 degrees.

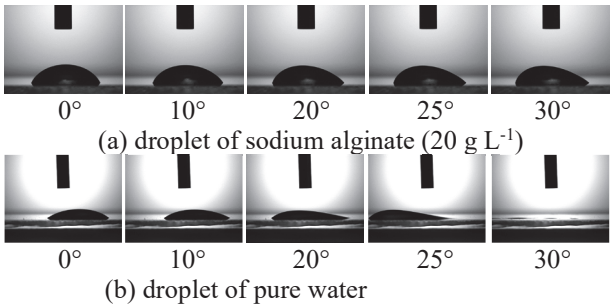

Figure 10 Roll-off behaviour on glass of the droplet of (a) sodium alginate (20 g L^{-1}) and (b) pure water as a function of roll-off angle. Volumes of all droplets are 40 ml. The substrate was tilted by 5° per second.

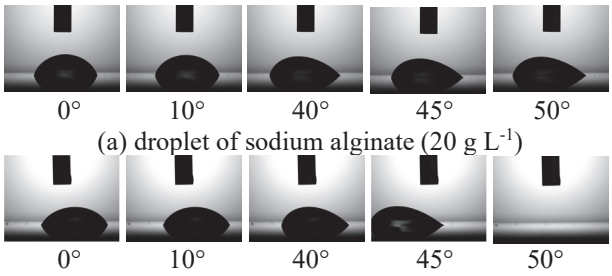

Figure 11 Roll-off behaviour on acrylic of the droplet of (a) sodium alginate (20 g L^{-1}) and (b) pure water as a function of roll-off angle. Volumes of all droplets are 40 ml. The substrate was tilted by 5° per second.

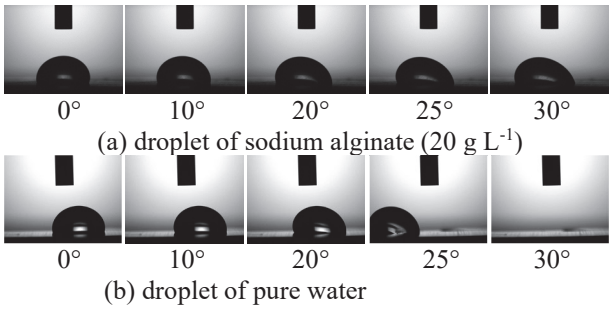

Figure 12 Roll-off behaviour on fluoropolymer of the droplet of (a) sodium alginate (20 g L^{-1}) and (b) pure water as a function of roll-off angle. Volumes of all droplets are 40 ml. The substrate was tilted by 5° per second.

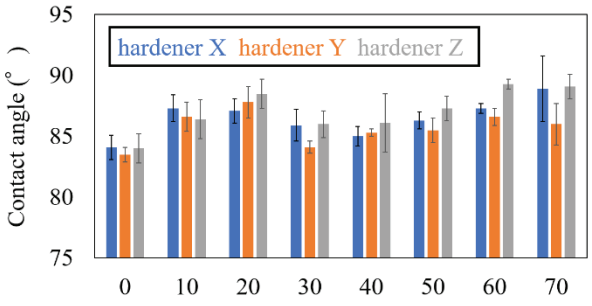

Figure 13 Contact angle of pure water on poly-siloxane films formed on glass substrate as a function of the weight ratio of alkoxysilane oligomer containing methyl and phenyl functional groups. 3 types of hardener (hardener X, Y, Z) were used for hardening the poly-siloxane films. Volumes of all droplets are 30 ml.

Figures 13 shows the contact angle of pure water on poly-siloxane films formed on glass substrate as a function of the weight ratio of alkoxysilane oligomer containing methyl and phenyl functional groups. 3 types of hardener (hardener X, Y, Z) were used for hardening the poly-siloxane films. Volumes of all droplets are 30 ml. The error bars show the standard deviation.It can be seen from the figure that the contact angle of pure water becomes larger with increasing the weight ratio of alkoxysilane oligomer containing methyl and phenyl functional groups. It`s probably because the alkoxysilane oligomer containing methyl and phenyl functional group contains the phenyl functional group, which is hydrophobic.

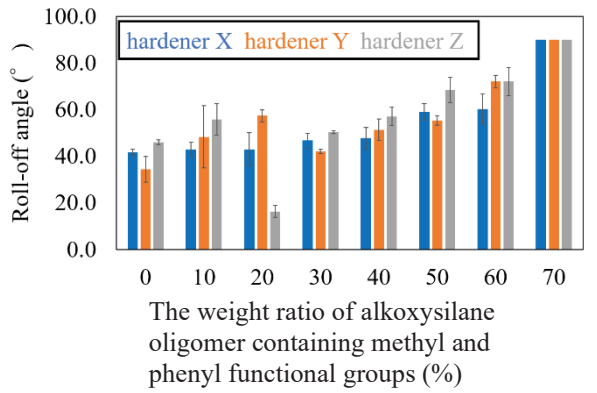

Figure 14 Roll-off angle of pure water on poly-siloxane films formed on glass substrate as a function of the weight ratio of alkoxysilane oligomer containing methyl and phenyl functional groups. 3 types of hardener (hardener X, Y, Z) were used for hardening the poly-siloxane films. Volumes of all droplets are 30 ml. The substrate was tilted by 5° per second.

Figures 14 shows the roll-off angle of pure water on poly-siloxane films formed on glass substrate as a function of the weight ratio of alkoxysilane oligomer containing methyl and phenyl functional groups. Volumes of all droplets are 30 ml. The substrate was tilted by 5° per second. The error bars show the standard deviation. It can be seen from the figure that the roll-off angle of pure water becomes larger with increasing the weight ratio of alkoxysilane oligomer containing methyl and phenyl functional groups.

Conclusions

In this study, we have investigated the wetting and roll-off behaviours of water or the solution simulating biofilms in air or in water on various substrates, such as glass, acrylic, fluoropolymer, and poly-siloxane films. The following conclusions were reached.

1. The adhesion work of sodium alginate solution on the glass is larger than that on the acrylic.
2. The concentration of the sodium alginate solution has little effect on the adhesion work of sodium alginate solution.
3. The addition of amino acids to a 10 g/L sodium alginate solution slightly decreases the surface tension.
4. In water, the droplets of sodium alginate (20 g L^{-1}) spread over a wide area after a certain period of time on glass, acrylic, or fluoropolymer. The speed

of wetting differed depending on the type of substrate, and the speed was found to be faster for glass, acrylic, and fluoropolymer, in that order.

5. The droplets of pure water on any substrates rolled off when the substrate was tilted less than 50 degrees, but the droplets of alginate on any substrates did not roll off even when the substrate was tilted up to 90 degrees.
6. The contact angle of pure water on poly-siloxane films formed on glass substrate becomes larger with increasing the weight ratio of alkoxysilane oligomer containing methyl and phenyl functional groups.
7. The roll-off angle of pure water on poly-siloxane films formed on glass substrate becomes larger with increasing the weight ratio of alkoxysilane oligomer containing methyl and phenyl functional groups.

Synthesis and Properties of Graphene Oxide Composite Electrolyte Membrane with Single Ion Conductivity

R. Shomura[*, ab], R. Tamate[b], T. Morinaga[a], T. Sato[a], and K. Takada[b]

[a] National Institute of Technology (KOSEN), Tsuruoka College, Tsuruoka, Yamagata, Japan
[b] National Institute for Materials Science (NIMS), Tsukuba, Ibaraki, Japan

* shomura@tsuruoka-nct.ac.jp

Abstract

Single ion-conducting polymers show efficient ion conduction because they have an ion transport number of almost 100 %. Therefore, single ion-conducting polymers are garnering significant attention as a candidate material for solid polymer electrolytes in the field of secondary battery electrolyte materials. However, lithium ion conductivity is low because of the strong interaction between anions and cations (such as lithium ions) and high crystallinity. Additionally, physical strength of the electrolyte film is low, and thus difficult to handle as a membrane. Hence, it has not been put into practical use. In this study, we propose a composite electrolyte membrane (LiSTFSI-GO) of a single ion conducting polymer (LiSTFSI) and graphene oxide (GO) to improve the ion conductivity, film strength, and flexibility of the electrolyte membrane. The resistance value of the prepared composite electrolyte membrane was studied by AC impedance measurement, decomposition temperature by thermogravimetric measurement, and glass transition temperature by differential scanning calorimetry (DSC) measurements. The conductivity was calculated from the bulk resistance of AC impedance measurements. However, the conductivity could not be calculated for the electrolyte membrane composed of a single ion conducting polymer alone because the bulk resistance was too high. However, when GO was added, the conductivity was calculated under all conditions. The result with the highest conductivity was obtained when 5 % GO was added to the single ion conducting polymer. Additionally, DSC measurements were performed to investigate the cause of the increase in conductivity. The result indicated that the glass transition point (T_g) was observed at approximately 35 – 40 °C in all samples, and no difference in T_g was observed. In other words, the results suggested that the difference in conductivity is not due to the indirect effect of the added GO as a plasticizer, but due to the direct contribution of GO to lithium-ion conduction.

Keywords: *Graphene oxide (GO), Single ion conductivity, Solid polymer electrolyte (SPE), Secondary battery, Lithium-ion conduction*

Introduction

Solid polymer electrolytes (SPEs) are promising materials in the field of secondary batteries because of their high energy density and safety. A single ion-conducting polymer has an anion skeleton in the main chain and a cation as the free radical. This suggests that the anion is fixed to the main chain of the polymer and only the cation moves during the charge/discharge cycles. Therefore, theoretically, the cation transport number is 100 %, i.e., ion conduction is completely efficient (Zhang, H. et al., 2017). This may lead to a breakthrough in the development of materials for secondary battery technology. However, there are disadvantages, such as low ionic conduction near room temperature and low physical strength. Nevertheless, various methods, such as the use of polymer blends (Pan, Q, et al., 2015), copolymers (Bouchet, R. et al., 2013), and hybrids with inorganic materials (Chereddy, S. et al., 2018), have been reported to overcome these disadvantages. However, they have not yet been put into practical use.

Graphene oxide (GO) is a material in which various oxygen-containing functional groups, such as epoxy, carboxyl, carbonyl, and hydroxyl groups, are bonded to a monolayer of graphite. Recently, it was reported that these oxygen atoms contribute to ion conduction (Gao, Y. et al., 2019). This indicates that GO composite electrolyte materials could have interesting applications as polymer electrolytes. One advantage at the GO composite electrolyte film is that the mechanical strength of the GO composite electrolyte membrane drastically increases because of the toughness of the added graphene. Furthermore, as a filler, GO improves the ion conduction by decreasing the crystallinity of the polymer electrolyte. Therefore, GO composite electrolyte membranes are expected to be a promising material for practical use.

In this study, we focus on polymers with trifluoromethanesulfonimide as the main chain and lithium ions as the counter cations (LiSTFSI). A novel

polymer electrolyte with single ion conduction was synthesized by compositing this type of polymer with GO (LiSTFSI-GO). In this study, we report the synthesis of a LiSTFSI-GO film and the detailed physical properties of polymer electrolytes, such as lithium-ion conduction.

Materials and Methods

General procedures

Trifluoromethanesulfonimide monomer was purchased from Tosoh Finechem Corporation. Graphene oxide, Polyethylene oxide (PEO, M_w = 600,000), polyethylene glycol (PEG, M_w = 300) were purchased from Sigma-Aldrich. DMF was purchased from FUJIFILM Wako Pure Chemical Corporation. All reagents were used without purification. The electrochemical measurements of ionic conductivities were carried out on a Bio-Logic Sciences Instruments, VMP3 using AC impedance technique. The electrolyte films were sandwiched between a pair of stainless steel electrodes made by EC FRONTIER CO., LTD.. The measurements were performed in the temperature range from 30 to 90°C. The AC impedance spectra were recorded over the frequency range from 1 MHz to 100 mHz. Thermogravimetric analysis was performed on a TA Instruments, Discovery TGA. Samples of average weight of approximately 2 mg were placed in a Pt pan and heated at a rate of 20°C min^{-1} from room temperature to 600°C under a flow of argon. The differential scanning calorimetric analysis were performed on a Hitachi, Ltd., DSC-7000X. Samples of average weight of approximately 3-5 mg was hermetically sealed in an aluminum pan. The sample was measured at a rate of 10°C min^{-1} in the range of -40 to 100°C under nitrogen flow.

Preparation of LiSTFSI-GO film

Synthesis of the LiSTFSI was refer to the past report (Feng, S. et al., 2013). LiSTFSI monomer(1.94 g, 6.04 mmol), AIBN (9.9 mg, 0.06 mmol), and DMF (10 mL) were mixed in a Schlenk flask. The solutions were degassed and flushed with dry argon three times, hermetically sealed and were then heated at 60°C for overnight. The raw polymer was precipitated by pouring the solutions into a large volume of diethyl ether, the polymer was further purified two times. The gummy residue obtained was dried for 3 days under high vacuum, LiPSTFSI (1.67 g, yield 86 %) as a white solid. The synthesized LiSTFSI and GO were mixed in water, and the mixed solution was drop-cast onto a Teflon petri dish. The drop-cast solution was dried at 45°C on the hot plate. And then, the film dried under reduced pressure at 60°C was obtained as a sample.

Results and Discussion

In this study, LiSTFSI-GO was prepared and the conductivity was measured. As shown in Figure 1, LiSTFSI-GO was obtained as a self-standing membrane.

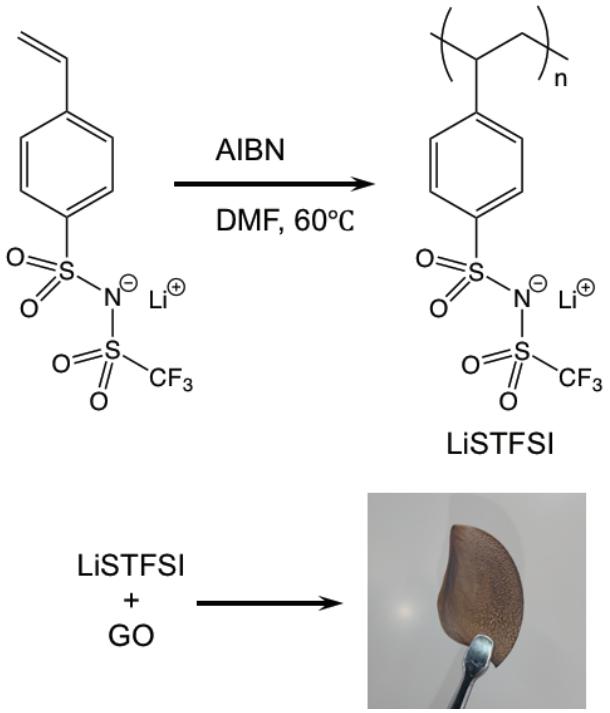

Figure 1. Preparation of self-standing LiSTFSI-GO film.

Using these LiSTFSI-GO films as samples, the conductivity was measured using impedance measurements (Figure 2). The conductivity of LiSTFSI and GO are not shown in the graph because these conductivities could not be calculated owing to high bulk resistance. All samples were measured twice using the same sample. The first measurements were obtained when the cast films were measured immediately after mounting them on the conductivity measurement cell. The second measurements, which were performed without removing the samples after the first measurements, were obtained under the same conditions as the first measurements. In almost all measurements, the conductivity value of the second measurement was higher than that of the first measurement. When the temperature was raised to 90 °C during the first measurement, the adhesion between the LiSTFSI-GO film and electrodes increased. Furthermore, it is considered that the LiSTFSI-GO film was annealed during the first measurement, and the resistance was lower at the time of the second measurement.

By comparing the conductivity when the GO content was 5 %, 10 %, and 30 %, the result showed that the conductivity was the highest when the GO content was 5 %. When the change in the conductivity with respect to the temperature change was compared (Arrhenius equation), the magnitudes of the slopes were different for 10 % and 30 % GO content and for 5 % GO content. In other words, the result suggested that the ion conduction mechanism was different for the case of 5 % GO content and 10 % and 30 % GO content.

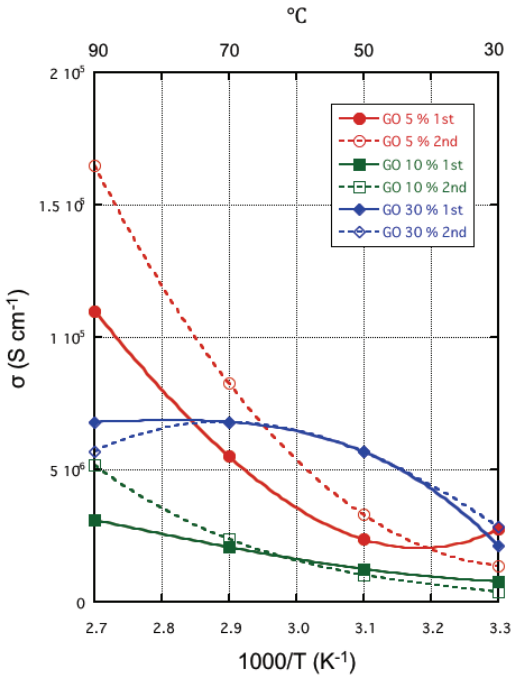

Figure 2. Result of calculating the lithium-ion conduction of LiSTFSI-GO film from the resistance value of impedance measurement. Solid line: results of first measurement. Dotted line: results of secoond measurement.

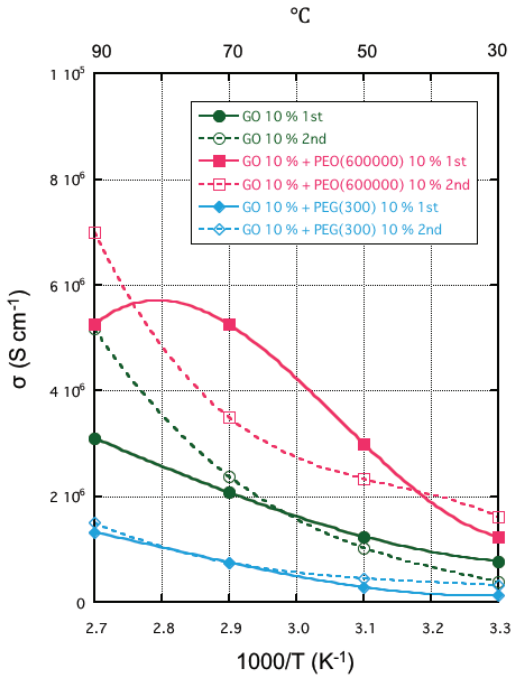

Figure 3. Result of calculating the lithium-ion conduction of LiSTFSI-GO film containing PEO (PEG) from the resistance value of impedance measurement.
Solid line: results of first measurement
Dotted line: results of second measurement

PEO or PEG contributes to lithium-ion conduction in the SPEs. To improve the conductivity of the LiSTFSI-GO composite electrolyte, PEO or PEG was added to LiSTFSI-GO, and the conductivity was measured (Figure 3). The result indicated that when 10 % PEO (average molecular weight 600,000) was added, there was a slight change in conductivity. Additionally, when 10 % PEG (average molecular weight 300) was added, the conductivity decreased. An unexpected result was when the conductivity of LiSTFSI-GO film reduced when liquid PEG was added. It is possible that the miscibility between LiSTFSI-GO and PEG was poor, thereby resulting in phase separation. However, the investigation is still underway.

Thermal analysis by thermogravimetry (TG) and differential scanning calorimetry (DSC) measurements were performed to determine the ion conduction mechanism in LiSTFSI-GO (Figure 4). Three types of samples were measured: LiSTFSI only, LiSTFSI-GO (GO 10 %), and LiSTFSI-GO (GO 10 %) with 10 % PEG.

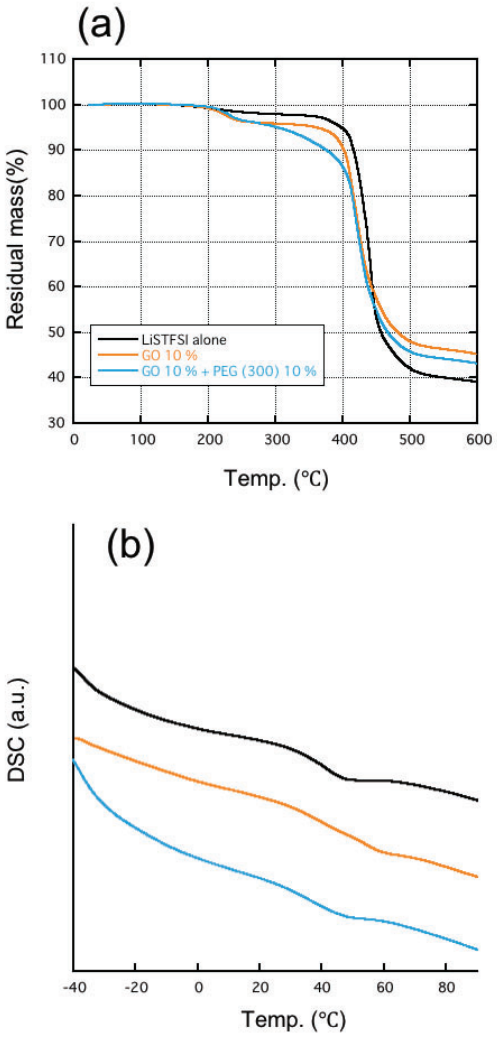

Figure 4. Results of thermal analysis. (a) TG measurements (b) DSC measurements

The TG measurement results suggested that no decomposition behavior was observed below 100 °C; i.e., the sample was stable in the conductivity measurement range (30 – 90 °C). The DSC measurement results suggested that the glass transition temperature (T_g) was observed at approximately 35 – 40 °C in all samples. Initially, it was expected that the change in conductivity would be due to the difference in T_g. However, DSC measurements suggested that the difference in conductivity was not due to T_g, and another factor could be considered. We will consider this in detail in the future.

Conclusions

In this study, the ion conductivity of LiSTFSI-GO, which is a composite electrolyte film of a single ion conducting polymer and GO, was investigated. The results suggested that the conductivity improved significantly when GO was added as compared to LiSTFSI alone. The conductivity was highest when the GO content was 5 %. Furthermore, the conductivity was approximately 40 times higher when measured at 90 °C than when the GO content was 10 % or 30 %. Additionally, when PEO (PEG) was added to LiSTFSI-GO, the conductivity was lower than that without the addition of PEO (PEG). In other words, the results suggested that the added PEO (PEG) became resistant.

The results of the thermal analysis (TG and DSC) showed that there was no significant change in the T_g value of each sample. It is possible that the improvement in conductivity was not due to the plasticizer effect of adding GO, but rather due to the contribution of GO to lithium-ion conduction. The detailed mechanism is currently under investigation. In the future, we aim to further improve the conductivity of LiSTFSI-GO for social implementation.

Acknowledgements

A part of this work was supported by JSPS KAKENHI Grant Number 19K15396 and 19H02783.

References

Heng Zhang, Chunmei Li, Michal Piszcz, Estibaliz Coya, Teofilo Rojo, Lide M. Rodriguez-Martinez, Michel Armand and Zhibin Zhou. (2017). Single lithium-ion conducting solid polymer electrolytes: advances and perspectives. *Chem. Soc. Rev.,* 46, 797-815.

Qiyun Pan, Wenchao Zhang, Meize Pan, Baodan Zhang, Danli Zeng, Yubao Sun and Hansong Cheng. (2015). Construction of a lithium ion transport network in cathode with lithiated bis(benzene sulfonyl)imide based single ion polymer ionomers. *Journal of Power Sources*, 283, 279-288.

Renaud Bouchet, Sébastien Maria, Rachid Meziane, Abdelmaula Aboulaich, Livie Lienafa, Jean-Pierre Bonnet, Trang N. T. Phan, Denis Bertin, Didier Gigmes, Didier Devaux, Renaud Denoyel and Michel Armand. (2013). Single-ion BAB triblock copolymers as highly efficient electrolytes for lithium-metal batteries. *Nature Materials*, 12, 452-457.

Shaowei Feng, Dongyang Shi, Fang Liu, Liping Zheng, Jin Nie, Wengfang Feng, Xuejie Huang, Michel Armand and Zhibin Zhou. (2013). Single lithium-ion conducting polymer electrolytes based on poly[(4-styrenesulfonyl) (trifluoromethanesulfonyl)imide] anions. *Electrochimica Acta*, 93, 254–263.

Sumanth Chereddy, Parameswara Rao Chinnam, Vijay Chatare, Stephen Patrick diLuzio, Mallory P. Gobet, Steven G. Greenbaum and Stephanie L. Wunder. (2018). An alternative route to single ion conductivity using multi-ionic salts. *Mater.Horiz.,* 5,461-473.

Yue Gao, Zhifei Yan, Jennifer L. Gray, Xin He, Daiwei Wang, Tianhang Chen, Qingquan Huang, Yuguang C. Li, Haiying Wang, Seong H. Kim, Thomas E. Mallouk and Donghai Wang. (2019). Polymer–inorganic solid–electrolyte interphase for stable lithium metal batteries under lean electrolyte conditions. *Nature Materials*, 18, 384–389.

Characterization of a Double Network Ion gel Formed By One Pot Synthesis

H. Arafune[*,a], K. Miura[a], S. Inoue[a], Y. Tsuchida[a], Y. Watarai[a], T. Morinaga[a], T. Kamijo[a] and T. Sato[a]

Department of Creative Engineering, National Institute of Technology, Tsuruoka College, Tsuruoka, Japan

*harafune@tsuruoka-nct.ac.jp

Abstract

Reducing friction is important to develop mechanical systems with high energy efficiency and long lifetime. Since human joints with gel-like structure show low friction for several decades, gel materials are known to be useful for developing low frictional materials. Double network ion gels (DN ion gel) composed of hard but brittle 1st network, soft 2nd network and ionic liquids possess high mechanical strength and low friction under high temperature or vacuum are one of candidates for robust lubricant gels. For their industrial application, development of one pot synthesis process is effective due to its simplicity and low cost, opening up the way to form thin film coating of gel lubricants. However, radical polymerization of 1st and 2nd network at same time results in formation of random polymer to lose characteristics of DN ion gels. In this study, we examined one pot synthesis of DN ion gels by combining polycondensation and radical polymerization to develop simple and facile fabrication process for gel lubricant coating.

Tetraethoxysilane (TEOS) and methylmethacrylate (MMA) were chosen as a 1st and 2nd monomer of a DN ion gel, respectively. 1-Butyl-3-methylimidazolium triflate (BMIm-Otf) was chosen as swelling agent of a DN ion gel due to its compatibility for both network. Polycondensation of TEOS progressed with oxalic acid as a catalyst. Radicial polymerization of MMA progressed with azobis(isobutyronitrile and triethyleneglycol dimethacrylate as an initiator and cross linker, respectively. The mixed solution of these reagents was poured into the 2 mm thick reaction cell by using an injection syringe under argon atmosphere. It was heated at 50 °C for 24 hours to obtain DN ion gel.

From thermogravimetry analysis, vacuum heating was effective to promote polymerization of gel network. Obtained DN ion gel didn't showed any fracture under maximum stress of our device (32 MPa), which is higher than the fracture stress of conventional ion gels. As obtained onepot synthesis method can be applied for thin gel film, obtained DN gel is expected to be applied for gel lubricant under harsh condition like heat or vacuum, which is difficult for conventional DN hydrogels.

Keywords: *double network gel, ionic liquid, one pot synthesis*

Introduction

Reducing friction is important to develop mechanical systems with high energy efficiency and long lifetime. Since human joints with gel-like structure show low friction for several decades, gel materials are expected as a candidate for low frictional materials (Holmbeg *et al*., 2012). Double network hydrogels (DN hydrogels) composed of hard but brittle 1st network and ductile 2nd network possess high water content (>80 wt%) , high mechanical strength and low frictional properties, which is a candidate for strong but lubricious soft materials (e.g. Kaneko *et al.*,2005). Such properties are useful as lubricant gels such as artificial joints or vessels in human body where gels can obtain enough amount of water. However, hydrogels are easily dried under heat, vacuum or long time exposure, which have been a task to overcome for industrial usage.

Recently, our research group have develped DN ion gles incorporating ionic liquids as swelling agent (Arafune *et al.*, 2017). Ionic liquids (ILs) are liquid salts wholly composed of anions and cations whose melting temperature is lower than 100°C. Because ILs possess high thermal stability and negligible volatility, DN ion gels can maintain lubricious surface under high temperature (80°C) or vacuum (2.4×10^{-4} Pa) . Thus, DN ion gels are expected as robust lubricant gel materials under harsh condition where DN hydrogel cannnot be applied. Instead of these advantages, fabrication process of DN ion gels is complex and time-consuming because we adopted conventional stepwise photoradical polymerization. In addition, stepwise polymerization of DN gels include swelling process of brittle 1st gel network. This process prevent to achieve thin film fabriction of DN gels because brittle first network collapsed by extension by immdiate swelling caused by rapid diffusion of swelling agents (Wu *et al*., 2011).

For their industrial application, development of one pot synthesis process is effective due to its simplicity and low cost, opening up the way to form thin film coating of gel lubricants. However, radical polymerization of 1st and 2nd network at same time results in formation of random

polymer to lose characteristics of DN ion gels. In this study, we examined one pot synthesis of DN ion gels by combining polycondensation and radical polymerization to develop simple and facile fabrication process for gel lubricant coating.

Materials and Methods

DN ion gel was synthesized by onepot synthesis combining polycondensation of 1st network and radical polymerization of 2nd network. Tetraethoxysilane (TEOS) and methylmethacrylate (MMA) were chosen as a 1st and 2nd monomer of a DN ion gel, respectively. 1-Butyl-3-methylimidazolium triflate (BMIm-Otf) was chosen as polymerization solvent and swelling agent of a DN ion gel due to its compatibility for both network. Polycondensation of TEOS progressed with oxalic acid as a catalyst. Radicial polymerization of MMA progressed with azobis(isobutyronitrile (AIBN) and triethyleneglycol dimethacrylate (TEGDMA) as an initiator and cross linker, respectively. Typically, the mixed solution of oxalic acid (0.35g), water (0.02 g), BMIm-Otf (0.5 g), TEOS (0.098g), MMA (0.8 g), azobis-isobutylyronitrile (0.021 g), TEGDMA (0.0087 g) was poured into the 2 mm thick reaction cell by using an injection syringe under argon atmosphere. Then, it was heated at 50 °C for 24 hours (DNIG-50) to promote polycondensation and radical polymerization of gel networks, then followed by vacuum heating at 50 °C for 24 hours (DNIG-50-V)

The mechanical properties of obtained DN ion gels was examined by compressive stress-strain test by using a universal testing system (Instron 3342, Instron) The cylindrical samples of 3 mm diameter and 2 mm thickness of a gel sample was set on the lower anvil, and the upper anvil was compressed at 10% strain/min. The thermogravimetry analysis (TGA) was performed to examine thermal properties of DN ion gels by using a TGA system (TG8120, Rigaku Co.) under a nitrogen atmosphere to measure the weight loss from room temperature to 500°C with a heat rate of 10°C /min.

Results and Discussion

1. Effect of heat temperature on a gel formation

Figure 1 and 2 show TGA curve of DNIG-50 and derivative of TG curve of DNIG-50, oxalic acid and BMIm-Otf normalized by peak value of each curves, respectively. Sample showed 25% weight loss in 100-200°C, indicating the thermal decomposition of oxalic acid or water and ethanol from residual TEOS. Polycondensation of TEOS with acid catalyst starts from hydrolysis of ethoxy group (Si-OEt) to form silanol group (Si-OH), and then dehydration condensation of silanol proceeds to form siloxane bonding (Si-O-Si). Thus, polycondensation of TEOS generate EtOH and water as by-product. Broad peak from 30-200°C of DNIG-50 in Figure 2 compared with that of oxalic acid indicates that not only thermal decomposition of oxalic acid but that of water and ethanol from residual TEOS were included in this temperature range. Secondary weight loss from 300°C and 400°C were attributed to the thermal decomposition of PMMA and BMI-Otf, where PMMA in IL was thermally stable compared with bulk PMMA.

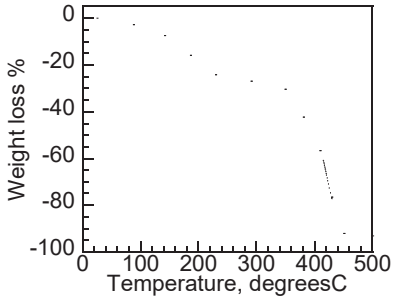

Figure 1 TG curve of DNIG-50

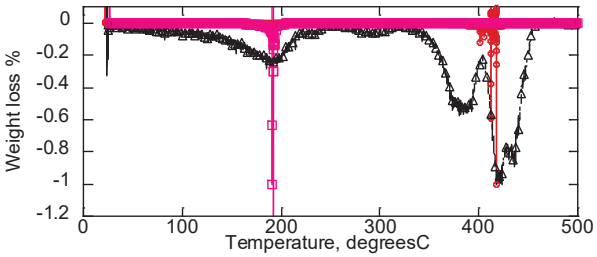

Fig. 2 Normalized DTG curves of DN ion gel(triangle), oxalic acid(square) and BMI-Otf(circle)

2. Effect of vacuum heating on a gel formation

We next examined the vacuum heating to promote polycondensation of TEOS. Figure 3 shows TGA curves of DNIG-50 and DNIG-50-V. Weight loss at 100-200°C was clearly decreased after vacuum heating, indicating that vacuum promoted the polycondensation of TEOS by removing volatile water and ethanol to shift chemical equilibrium.

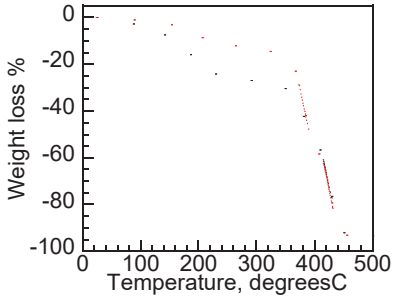

Figure 3 TG curves of DNIG-50 (black line) and DNIG-50-V (red line)

Figure 4 shows the stress-strain curves of DNIG-50 and DNIG-50-V. DNIG-50-V showed high mechanical strength, which sustained a compressive stress of more than 35 MPa, reached to the maximum value of our deviec. It also showed high elasticity which restored quickly after compression. In contrast, DNIG-50 showed low elasticity and compressive fracture stress (20 MPa). Additionally, it showed yield point at 6 MPa with 80% strain. As DNIG-50 showed crack in the central part

inside gel, such difference are supposed to be insufficient polymerization of TEOS network.

It should be noted that compressive fracture stress was higher than that of conventional ion gels. Fujii *et al* (2012) fabricated a tetra-poly(ethylene glycol) gels combined with ionic liquids ethylmethylimidazolium bis(trifluoromethylsulfonylimide) (C_2C_1Im-TFSI). This ion gel showed a high mechanical strength of 20 MPa, due to its homogeneous network structure synthesized from the symmetrical structure of tetra-arm PEG macromers. Kamio *et al.* (2017) have developed DN ion gel combining TEOS, dimethylacrylamide and amino acid based ionic liquid, which sustain more than 28 MPa of compressive fracture stress. As obtained onepot synthesis method can be applied for thin gel film, obtained DN gel is expected to be applied for gel lubricant under harsh condition like heat or vacuum, which is difficult for conventional DN hydrogels.

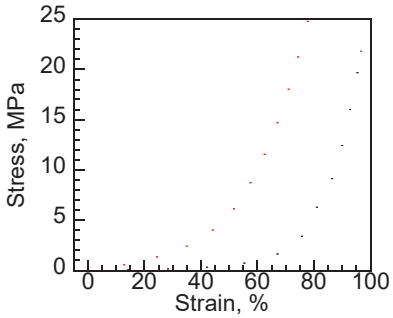

Figure 4 Compressive stress-strain curves of DNIG-50 (black line) and DNIG-50-V (red line)

Conclusions

We applied onepot synthesis combining polycondensation and radical polymerization to develop fast and effective way to form DN ion gel. Vacuum heating was effective to promote polycondensation of gel network. Obtained DN ion gel with onepot synthesis showed high mechanical strength and quick restoration compared with conventional DN ion gel obtained from stepwise radical polymerization. As onepot synthesis is effective to form thin film coating of DN ion gel, obtained DN ion gel is expected to be applied for gel lubricant under harsh condition like heat or vacuum, which is difficult for conventional DN hydrogels.

Acknowledgements

This research was funded by Grant-in Aid for Scientific Research (No. 20K04249 and 20H02060) from the Ministry of Education, Science, Sport, and Culture, Japan.

References

Arafune, H., Kamijo, T., Morinaga, T., Honma, S., Sato, T., & Tsujii, Y. (2015). A Robust Lubrication System Using an Ionic Liquid Polymer Brush. *Adv. Mater. Interfaces*, *2*, 1500187.

Fujii, K., Asai, H., Ueki, T., Sakai, T., Imaizumi, S., Chung, U., Watanabe, M., & Shibayama, M. (2012). High-performance ion gel with tetra-PEG network. *Soft Matter*, *8*, 1756.

Kamio, E., Yasui, T., Iida, Y., Gong, J. P., & Matsuyama, H. (2017). Inorganic/Organic Double-Network Gels Containing Ionic Liquids. *Advanced Materials*, *29*(47).

Kaneko, D., Tada, T., Kurokawa, T., Gong, J. P., & Osada, Y. (2005). Mechanically Strong Hydrogels with Ultra-Low Frictional Coefficients. *Advanced Materials*, *17*(5), 535–538.

Liang, S., Wu, Z. L., Hu, J., Kurokawa, T., Yu, Q. M., & Gong, J. P. (2011). Direct Observation on the Surface Fracture of Ultrathin Film. *Macromolecules*, *44*, 3016–3020.

CHARACTERISTICS OF POWDER DISCHARGE BY VIBRATING FLUIDIZATION

Koichiro Ogata[*,a], Tsutomu Harada [a], Riho Abe [a], Hideo Kawahara [b], Eiji Mitani [c] and Koji Mitani [c]

[a] Department of Mechanical Engineering, National Institute of Technology, Oita College
1666 Maki, Oita, Oita 870-0152 Japan
[b] Department of Shipping Technology, National Institute of Technology, Oshima College
1091-1 Komatsu, Suo-Oshima, Oshima, Yamaguchi 742-2193 Japan
SSC Company Limited
[c] Tomomachi Ushiroji 26-216, Fukuyama, Hiroshima 720-0202 Japan

*k-ogata@oita-ct.ac.jp

Abstract

The cohesive powder is widely used in various industries such as material production and pharmaceutical development. Recently, functional materials such as ceramic powder have been produced in the engineering fields of semiconductors, automobiles, and medical fields, and then the handling of cohesive powders is increasing in these processes. However, the handling of cohesive powder is extremely difficult by the influence of cohesive force which is relatively strong against the gravity force when the particle diameter is decreased. Especially, the steady powder discharge is very important in these powder handling processes. Therefore, the purpose of this study is to achieve a steady powder discharge for cohesive powder.

We have experimentally investigated the characteristics of powder discharge using vibrating fluidization. The particle used is the alumina powder that has a mean particle size of 2.9μm and particle density of 3808 kg/m^3. This powder belongs to the C particle in the classification of the Geldart diagram. That means the fluidization is extremely difficult to the powder in the classification of the diagram. For this reason, the vertical vibration was applied simultaneously to obtain the fluidization of the cohesive powder.

The experimental apparatus consists of the vibrating fluidization vessel, the air distributor at the bottom of the vessel, the venturi feeder above the fluidizing vessel, the powder discharge tube, and the cyclone of collecting powder. The fluidizing vessel has an inner diameter of 50 mm and a height of 300 mm. The polyurethane tube of the inner diameter of 4.32 mm is connected between the feeder and the cyclone for particle discharge. As the experimental condition, the supplying air velocity of feeder u_f=3.03 m/s and the vibration strength Λ=8.18 were fixed and the fluidizing velocity to powder bed was changed.

The result obtained that good fluidization of cohesive powder was achieved when the fluidization velocity was increased. Then, it is found the powder was also dispersed in the vessel, and the discharge mass of powder against the time took a linear profile. It means the steady powder discharge was obtained by using this system. Besides, the mass flow rate of powder was related to the increased fluizing velocity.

Keywords: *Cohesive powder, Vibrating fluidization, Dispersion, Powder discharge, Fluidizing air velocity*

Introduction

Currently, ceramics are widely used from structural materials to various functional materials because ceramic products have excellent heat resistance, corrosion resistance, and wear resistance (e.g., Naito, 2011). In recent years, ceramic materials with particle sizes from micron size to nano-size have been developed and used in various products such as semiconductors, automobiles, and medical fields.

However, when handling micron-sized particles in a gas, it is well known that the particles form agglomerates due to the influence of cohesive force, making it difficult to handle and control the powder. The reason is that as the particle size becomes smaller, the cohesive force increases relative to the gravity acting on the particles (e.g., J. Soc. Powder Technol., Japan Eds., 2006).

Generally, particles are treated as aggregates, that is, powders, and are handled in liquids and gases. While the operation in the liquid requires a drying process and the treatment of the liquid used, the operation in gas has the advantage that it can be used without changing the composition of the material. For this reason, powder handling in a gas in which the composition of the material does not change is required at the production site. In particular, the development of technology for stable handling and quantitative discharge of micron-sized powder, which is greatly affected by cohesive force, in gas is very important because it can be applied in various production processes.

From the above background, this research focuses on the elucidation of the dispersion and stable discharge

characteristics of micron-sized cohesive ceramic powder. Additionally, it is considered that the vertical vibrating fluidization operation is applied at the stable supply of the cohesive powder to the HVAF spraying device (Mitani, 2012 & 2015). As the powder used, alumina powder classified into Group C in the Geldart diagram (Geldart, 1973) was used.

As experimental conditions, the vibration intensity in the vertical direction and the secondary air velocity to the powder feeder were made constant, and the fluidized air velocity to the bottom of the powder bed was changed. In this paper, we report the results obtained for the fluidization characteristics, powder dispersion state, and powder discharge characteristics of the powder bed during vertical vibrating fluidization.

Experiment

Figure 1 shows the outline of the experimental apparatus. The apparatus consists of a powder dispersion vessel, a venturi-type powder feeder, and a powder receiving part of a cyclone and a tank. The powder dispersion vessel was an acrylic cylindrical vessel with an inner diameter of 50 mm, a height of 300 mm. The polyurethane tube with an inner diameter of 4.23 mm was used for the transportation of the powder in the system. A porous membrane was installed at the bottom of the dispersion vessel to supply uniform air for fluidization. Additionally, two vibration motors were connected to the bottom of the dispersion vessel for giving vertical vibration. A venturi-type feeder was installed above the powder dispersion vessel, where the secondary air sent from the upstream side of the feeder for the powder transportation. The transported powder was collected at a cyclone and receiving tank with a bug filter.

In this study, a fluidization experiment and powder discharge experiment was conducted. It adopted a de-fluidization experiment, which is said to be less susceptible to intermolecular forces as well as Mawatari (2002). The pressure drop of the powder bed ΔP was estimated as the difference of the air pressure with and without powder in a dispersion vessel.

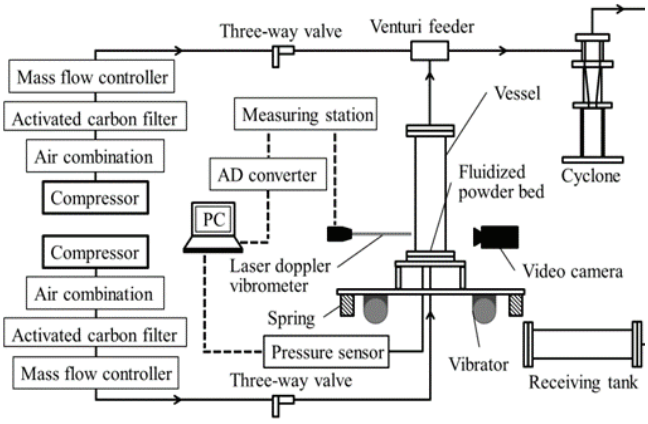

Figure 1 Experimental apparatus

The fluidization characteristics were evaluated from the pressure drop and the fluidization state of the powder bed in the dispersion vessel when the fluidization air velocity to the vessel was reduced. A digital video camera was used to visualize the fluidized state.

As the experimental conditions for the vibrating fluidization, the fluidized air velocity at the bottom of the dispersion vessel u_b was from 1.70×10^{-3} m/s to 55.02×10^{-3} m/s. Also, the secondary air velocity on the upstream side of the venturi type feeder u_t was 3.03 m/s, and the vibration intensity Λ was 8.18. The vibration intensity was calculated by the measured vibration amplitude, gravitational acceleration and the frequency of 60 Hz. In this study, Λ was fixed as 8.18 to obtain a good fluidization state.

In the powder discharge experiment, the particle mass per minute was measured to estimate the mass flow rate of powder G_s. The precision electric balance was used to measure the particle mass M_p at the elapsed time T in the experiment.

Regards with the experimental conditions for the powder discharge experiment using vibrating fluidization, the experiment was conducted with fluidized air velocity that enables powder discharge. The velocity u_b was from 0.068 m/s to 0.510 m/s. The secondary air velocity and the vibration intensity were the same as the case of the fluidization experiment. The alumina powder used in these experiments has an average particle size of 2.92 μm, a true density of 3808 kg/m^3, and an initial filling mass of powder of 100 g.

Results and Discussion

Vibrating fluidization characteristics

The alumina powder used in this study belongs to the Geldart C particle. Generally, the Geldart C particle has a poorly flowability by high cohesiveness. It is therefore necessary to confirm the fluidization state in the vibrating fluidization. Figure 2 shows the relationship between the pressure drop ΔP inside the powder bed and the fluidized air velocity u_b when Λ=8.18. In the experiment, the powder bed was vibrated and fluidized for 5 minutes at a fluidized air velocity of u_b=0.051 m/s, and then the air velocity was gradually reduced from the fluidized air velocity at the start of measurement u_s=0.047 m/s. From the figure, when the fluidized air velocity was decreased, the pressure drop increased and took the maximum value at any fluidized air velocity.

It is speculated that this is because the powder bed formed a stirring and an expanding state from the fluidized state as the fluidized air velocity decreased. Afterwards, as the fluidized air velocity decreased more, the pressure drop also decreased, and the state of the powder bed became close to that of the fixed bed.

Figure 3 shows the relation of the dimensionless pressure drop $\Delta P/\Delta P_i$ and the dimensionless fluidized air velocity u_b/u_c when Λ=8.18, the fluidized air velocity at the start of measurement u_s was changed. The procedure was the same as the reported for the vibrated fluidization

for adhesive fine particles by Mawatari (2005). Here, the critical fluidized air velocity u_c is defined as the fluidized air velocity at which the maximum pressure drop of the pressure drop curve in Figure 2, and ΔP_i is the initial pressure drop which estimated by the gravity force of the initial filling of the powder bed and the cross-sectional area.

From the figure, $\Delta P/\Delta P_i$ increased sharply as u_b/u_c decreased, regardless of the fluidized air velocity at the start of measurement. Also, $\Delta P/\Delta P_i$ has a peak value at all experimental conditions near u_b/u_c=1. Afterwards, $\Delta P/\Delta P_i$ decreased gradually with decreasing the fluidizing velocity. Regarding the reduction of pressure drop when u_b/u_c was over 1, it is inferred that the inter-particle and particle-wall forces were reduced by applied the vertical vibration and fluidizing air. At this time, it is considered that the powder bed is transferred from the fixed bed to the fluidized bed.

From the above results, it is necessary to confirm the state of the powder bed in a powder dispersion vessel by the applied vibrating fluidization. Figure 4 shows the transition of the state of the powder bed due to the decrease in the fluidized air velocity u_b at the bottom of the dispersion vessel in the present experimental conditions as a schematic diagram. The evaluation criteria for the flow state in the figure are as follows. When the fluidized air velocity was low, the bed expansion has appeared as the diagram (I). Afterwards, it was observed the fluidized bed in case of the increased air velocity of the diagram (II). Finally, the powder bed was fluidized well, and then the particle could be dispersed and transported upward.

Powder discharge characteristics

Figure 5 shows the relationship between the discharge mass of the powder M_p and the elapsed time T when A=8.18 and the fluidized air velocity u_b was changed. As above mentioned, the velocity u_b was from 0.068 m/s to 0.510 m/s. The result shows that the powder could not transport almost with the lower fluidizing velocity in the present experimental condition. This is because the powder bed in a dispersion vessel did not obtain well fluidization state. When the fluidized air velocity is increased, the discharge mass of the powder also increased gradually as u_b=0.127-0.17 m/s. Furthermore, the discharge mass of the powder increased drastically with increasing the fluidized air velocity, and then the flow pattern of the powder bed became in the state of the dispersion bed as shown in Figure 4 (III). In addition, it seems that the profiles of the discharge mass of the powder indicated almost linearly with the elapsed time. This means that the steady transport of powder was realized in this system.

Figure 6 shows the results of the mass flow rate of the powder G_s when A=8.18 and the fluidized air velocity u_b was changed. Here, the mass flow rate of the powder was averaged for 5 minutes by the amount of increase in the mass of the powder per minute. From the figure, when the vibration intensity was constant, the amount of mass flow rate of the powder was increased as the increasing fluidized air velocity. It is thought that this is because the powder was dispersed and transported well in the experimental condition of the increased fluidizing air velocity.

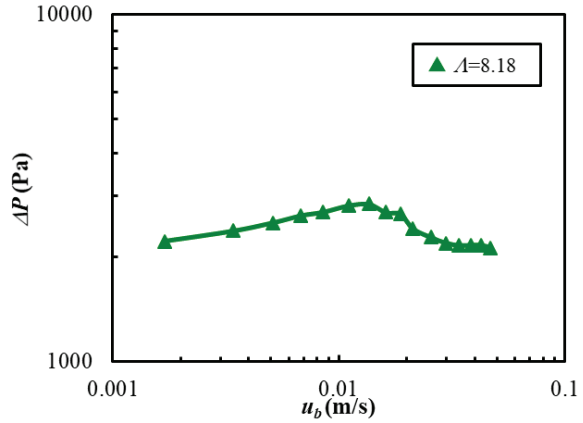

Figure 2 Relationship between pressure drop of powder bed and fluidizing air velocity where vibration strength was changed

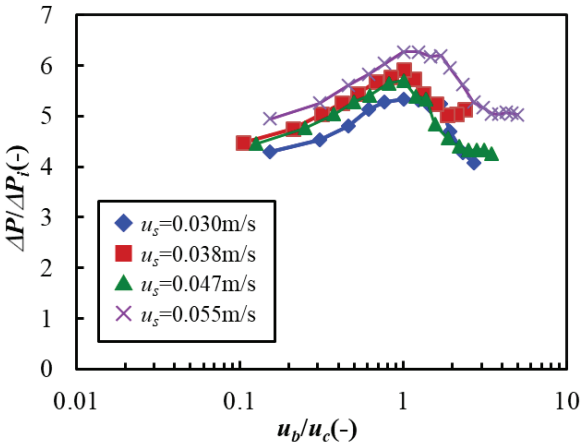

Figure 3 Relationship between dimensionless pressure drop and dimensionless fluidizing velocity where vibration strength A=8.18

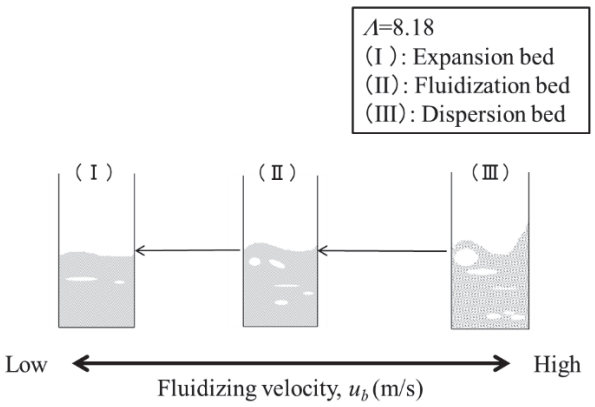

Figure 4 Typical flow pattern by vibrating fluidization

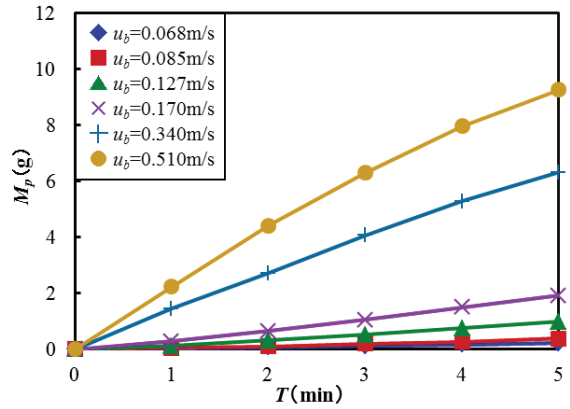

Figure 5 Discharge mass of powder against elapsed time

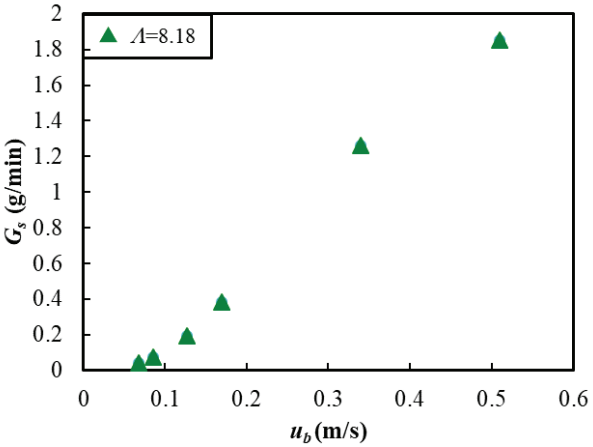

Figure 6 Relationship between mass flow rate and fluidizing velocity at the bottom of dispersion vessel

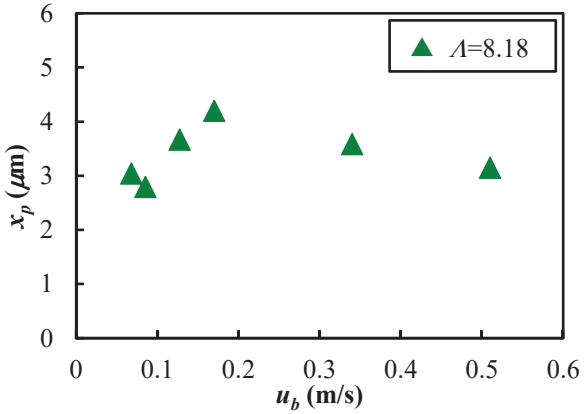

Figure 7 Relationship between average particle size and fluidizing velocity at the bottom of dispersion vessel

Figure 7 shows the relationship between the particles size and the fluidizing air velocity when Λ=8.18. The average particle size is about 3 to 4 μm. As described in the experimental condition, the average particle size of the alumina powder used in this study is 2.92 μm. Compared with this value, it is considered that the alumina powder is supplied while being dispersed by the vibrating fluidization.

Conclusions

In this study, we experimentally investigated the vibrating fluidization characteristics and the powder discharge characteristics of alumina powder. The results obtained are shown below.

(1) It was confirmed that alumina powder who is belonging to Group C particles in the Geldart diagram could be fluidized well by the applied vibrating fluidization in the present study when the fluidized air velocity was exceeded the critical fluidizing velocity. Then, the dimensionless pressure drop was also decreased greatly because the inter-particle force and the particle-wall force on the powder bed in a dispersion vessel were reduced with an external force based on the vibrating fluidization. In addition, it was found that the state of the powder bed such as the fluidization and the dispersion has appeared with increasing fluidized air velocity.

(2) From the powder discharge experiment, it was indicated that the steady discharge of alumina powder was realized by using vertical vibration and fluidization operation. Then, the mass flow rate of the powder increased with increasing the fluidized air velocity. It was found that the fluidizing velocity to supply to the bottom of the powder bed influenced strongly the discharge and the transport of cohesive powder.

Acknowledgements

A part of this work was supported by the GEAR5.0 project for the education and advanced resource in the National Institute of Technology, KOSEN.

References

Geldart, D. (1973). Types of gas fluidization, *Powder Technology*, 7, 285 - 292.

Mawatari, Y., Koide, T., Tatemoto, Y., Uchida, S. & Noda, K. (2002). Effect of particle diameter on fluidization under vibration. *Powder Technology*, 123, 69-74.

Mawatari, Y., Tsunekawa, M., Tatemoto, Y. & Noda, K. (2005). Favorable vibrated fluidization conditions for cohesive fine particles. *Powder Technology*, 154, 54-60.

Mitani, K & Mitani, E. (2012). Powder central axis HVAF thermal spraying device, JP 2012-92391

Mitani, K & Mitani, E. (2015). HVAF thermal spraying device for low temperature spraying, JP 2015-127126

Naito, M. & Makino, H. (2011). *Shoho kara manabu Funtaigizyutsu* (in Japanese), Morikita shuppan.

The Society of Powder Technology, Japan Eds. (2006). *Kisoutyuu no Ryuushi Bunsan Bunkyuu Buri Sousa* (in Japanese), Nikkan Kogyo Shinbunsha.

MECHANICAL JOINING OF TWO ULTRA-HIGH-STRENGTH STEEL AND ONE ALUMINIUM ALLOY SHEETS USING PRE-PUNCHED MIDDLE SHEET

Y. Abe* and K. Mori

Department of Mechanical Engineering, Toyohashi University of Technology, Toyohashi, Japan

*abe@plast.me.tut.ac.jp

Abstract

As functional engineering materials, ultra-high-strength steel sheets and aluminium alloy sheets are effective for lightweight sheet materials in the automobile body parts. To increase the application of these materials for the parts, the development of joining methods for joining the ultra-high-strength steel and aluminium alloy sheets is attractive. In addition, not only joining two sheets, but also joining of three sheets is desired for improving the body structure. In this study, a cold joining process of two ultra-high-strength steel and one aluminium alloy sheets using a pre-punched middle sheet was developed. The thicknesses of the sheets were 1 mm each, and the sheet configuration was two ultra-high-strength steel and one aluminium alloy sheets for assuming the structure and roof panels. This sheet configuration was not easy to join by conventional mechanical clinching because of the low ductility of the ultra-high-strength steel sheets. In the joining process of three sheets using the pre-punched middle sheet, the sheets are joined by formation of an interlock between the upper and lower sheets in the hole of the middle sheet the using the high ductility of the lower aluminium alloy sheet. The lower sheet bottom joined by this process has a flat, whereas the bottom joined by the conventional mechanical clinching protrudes. Because these sheets are generally stamped including punching before the joining process, the punching the middle sheet is possible in the stamping process. The effect of the hole diameter in the pre-punched middle sheet was investigated and the joint strength was measured. Finally, the two 980 MPa ultra-high-strength steel and one 5000 series aluminium alloy sheets were successfully joined using the joining process using the pre-punched middle sheet with the optimum hole diameter. It is found that the joining process of three sheets using the pre-punched middle sheet was effective for joining two ultra-high-strength steel and one aluminium alloy sheets.

Keywords: *Joining, mechanical joining, three sheets, ultra-high-strength steel sheets, aluminium alloy sheets*

Introduction

As functional engineering materials in automobile body parts, high-strength steel sheets, ultra-high-strength steel sheets and aluminium alloy sheets are effective. The thin high-strength steel sheets having the tensile strength up to 780 MPa and aluminium alloy sheets tend to use as lightweight sheet materials. The ultra-high-strength steel sheets having the tensile strength over 780 MPa and high-strength steel sheets tend to use as impact protection materials. These sheets usually are stamped and assembled to the automobile body parts. In the steel body parts, the properties of steel sheets are designed for the required strength and ductility in the final products including the stamping ability and joining ability with steel sheets. However, the some steel parts are replaced to aluminium alloy parts, the joining of steel and aluminium alloy sheets is required.

In the steel sheets, resistance spot welding is used for overlap joints. The joining of steel and aluminium alloy sheets by resistance spot welding is not easy because of the different melting points of the materials, the intermetallic layer in the interface and the oxidation layer of aluminium (Watanabe, 2005). Although friction stir welding with a lower temperature process is possible to join the aluminium alloy and steel sheets, the tool is only possible to stir in the aluminium alloy side. Therefore, the mechanical fastening such self-pierce riveting, flow drill screwdriving and mechanical clinching tends to use in the actual joining process (Sakiyama et al., 2013).

The high joint strength tends to obtain by uses of a rivet and a screw, whereas the joining costs of rivets and screws increase (Varis, 2006). Although the joint strength of mechanical clinched sheets without rivets is usually lower (Abe et al., 2020), the joining cost in the mechanical clinching is lower because the sheets are joined without rivets. In the automobile body parts, not only two sheets but also three sheets are joined. The self-pierce riveting (Han et al., 2006) and mechanical clinching (Kaðèák et al., 2017) are possible. The joining abilities of a sheet configuration of two ultra-high-strength steel and one aluminium alloy sheets for assuming the structure and roof panels are investigated by self-pierce riveting and mechanical clinching, and then one aluminium alloy and two ultra-high-strength steel, was possible to join by conventional mechanical

clinching and self-pierce riveting (Abe et al., 2020). However, joining of two ultra-high-strength steel and one aluminium alloy sheets was difficult by mechanical clinching. To reduce the joining cost, the development of mechanical fastening for two ultra-high-strength steel and one aluminium alloy sheets without rivets is required.

In this study, a cold joining process of two ultra-high-strength steel and one aluminium alloy sheets using a pre-punched middle sheet was developed. The effect of the hole diameter of middle sheet on the material flow was investigated. And then, the joint strength was measured.

Mechanical Joining of Three Sheets Using Pre-Punched Middle Sheet

There are many sheet configurations in the joints of automobile body parts (Martin et al., 2020). In this study, the structure and roof panels were selected as shown in **Figure 1**. The thicknesses of the sheets were 1 mm each, and the sheet configuration was two ultra-high-strength steel and one aluminium alloy sheets for assuming the structure and roof panels. Abe et al. (2020) showed the opposite sheet configuration, one aluminium alloy and two ultra-high-strength steel, was possible to join by conventional mechanical clinching and self-pierce riveting. However, joining of the sheet configuration of two ultra-high-strength steel and one aluminium alloy sheets is difficult. In addition, the bottom of joint by the conventional mechanical clinching and self-pierce riveting protrudes, thus the bottom is not flat.

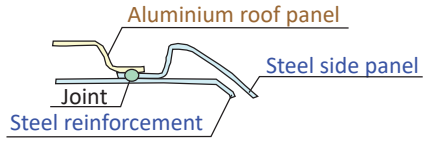

Figure 1 An example of joining of three sheets in automobile body parts.

Mechanical joining of three sheets using the pre-punched middle sheet is shown in **Figure 2**. This process consists of the punching and joining stages. In the punching stage, a sheet for the middle sheet was punched to form a hole having a diameter d by a pair of a punch and a die. In the joining stage, the three sheets set on an anvil under holding by a sheetholder were formed by a punch. The material of the upper sheet flows the lower sheet through the hole in the middle sheet. The compressed material of the lower sheet flows into the cavity between the outer upper sheet and the hole. Finally, the mechanical interlock between the upper and lower sheets are formed, thus, three sheets are joined. In the deformed shape of the cross section, the interlock, the lower neck thickness t_u and the upper neck thickness t_u are formed. Although the bottom protrudes joined by the conventional mechanical clinching process, the lower sheet bottom joined by this process is flat.

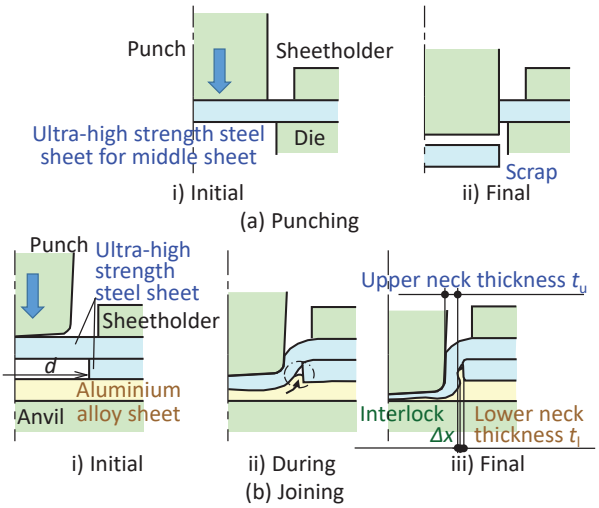

Figure 2 Mechanical joining of three sheets using pre-punched middle sheet for two ultra-high-strength steel and one aluminium alloy sheets.

In mechanical joining of three sheets using the pre-punched middle sheet under the sheet configuration, the process parameters are the punch shape, the punch stroke and the diameter of middle sheet. In this study, the shape of the punch is same in the mechanical clinching process (Abe et al. 2020). Although the long punch stroke is required to increase the material flow, the maximum stroke is given by the allowance compressive load of the punch. The effect of the hole diameter on the material flow in mechanical joining of three sheets using the pre-punched middle sheet is shown in **Figure 3**. In the small hole diameter, necking occurs because of the severe deformation of the upper sheet. In the excessive hole diameter, the interlock is not formed because of the insufficient material flow to the large cavity.

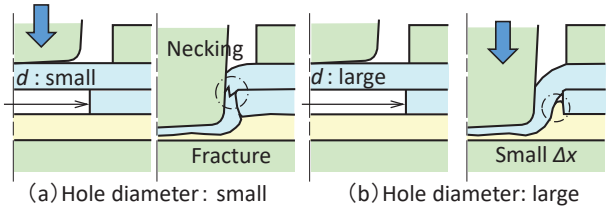

Figure 3 Effect of hole diameter on material flow in mechanical joining of three sheets using pre-punched middle sheet.

The mechanical joining conditions of three sheets using the pre-punched middle sheet are shown in **Figure 4**. In the punching stage, the ultra-high-strength steel sheet for the middle sheet was punched by a pair of a punch and a die. The diameter of the punch d was 5.5 to 7.5 mm to find joining the three sheets without defects. The clearance between the punch and die is d + 0.1 mm, thus the clearance ratio of the clearance and thickness was 10%. In the joining stage, the sheets were set on the anvil, and then the punch travelled into the sheets up to 65 kN.

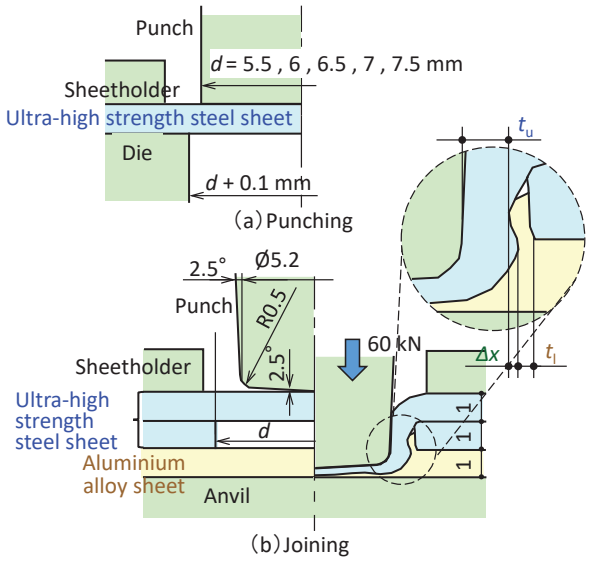

Figure 4 Mechanical joining conditions of three sheets using pre-punched middle sheet.

The material properties of the sheets are shown in **Table 1**. The properties were measured by a uni-axial tension test. The 980 MPa steel sheet has the high strength and low ductility.

Table 1 Material properties of sheets.

Sheet	Thickness [mm]	Tensile strength [MPa]	Elongation [%]
980 MPa steel	1.0	1002	14
A5052	1.0	275	25

The deformed shapes of the sheets were calculated by a finite element simulation. The finite element simulation code was the commercial finite element code LS-DYNA and JVISION (JSOL Corp., Tokyo, Japan). In the simulation, an axisymmetric deformation model was used. The sheets and tools were elastic-plastic and rigid bodies, respectively. The flow stresses of the sheets were used in Table 1. The frictional condition was assumed as coulomb friction, the frictional coefficient was 0.2 equivalent to the contact without lubrication. The adaptive remeshing for the elements of the sheets was automatically performed, and fracture criteria was not used.

Joined Three Sheets

The effect of the hole diameter on the calculated interlock and neck thicknesses is shown in **Figure 5**. The upper and lower neck thicknesses increase with increasing of the hole diameter because of the large cavity. In the experiment, fracture may occur by severe thinning in the upper neck portion. On the other hand, the interlock is formed from d = 6 to 7 mm, has a peak at d = 6 mm.

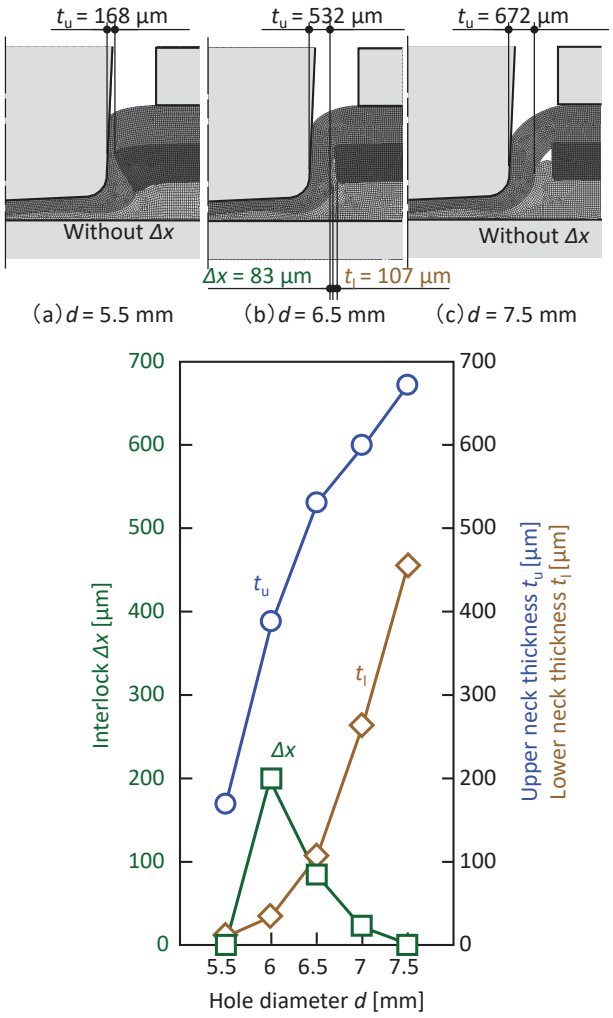

Figure 5 Effect of hole diameter on calculated interlock and neck thicknesses.

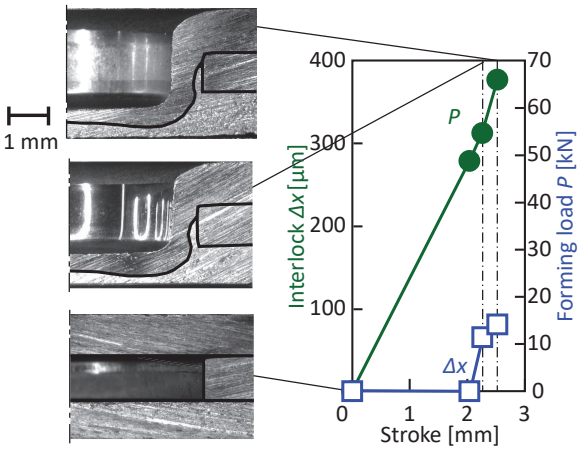

Figure 6 Deforming behaviours of sheets in joining for d = 6.5 mm.

In the calculation, the sheets were joined without defects for d = 6 to 7 mm. The deforming behaviours of sheets in the joining experiment for d = 6.5 mm are shown in **Figure 6**. After 2 mm in stroke, the interlock

increases with increasing of the stroke. The sheets are joined without defects in the experiment.

The cross-sectional shapes of the formed sheets are shown in **Figure 7**. In the small hole diameter, the fracture occurs in the upper neck portion because of the severe deformation. In the excessive hole diameter, the interlock is not formed because of the insufficient material flow to the large cavity. It seems that the punch was out of alignment with the hole. In d = 6.5 mm, the sheets are joined without defects.

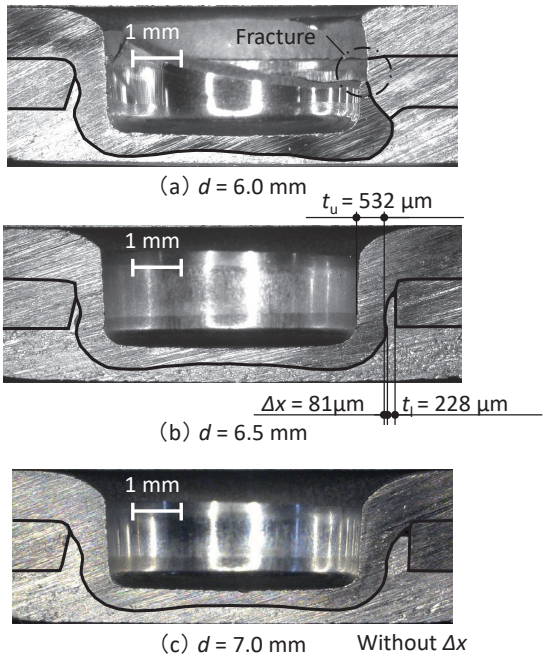

Figure 7 Cross-sectional shapes of formed sheets.

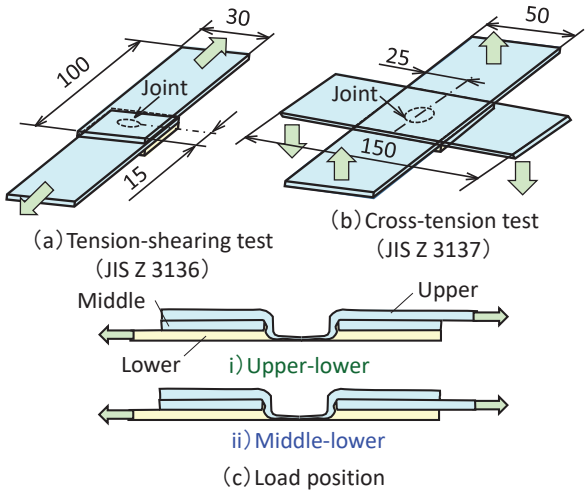

Figure 8 Measurement of joint strength of sheets.

Joint Strength of Joined Sheets

The joint strength was measured by the tension-shearing and cross-tension tests. These tests are generally used for the measurement of the welded joint strength. The tension-shearing and cross-tension tests are shown in **Figure 8**. Because the three sheets were joined, the loads of the configurations including the lower aluminium alloy sheet were measured.

The tension-shearing loads of joints are shown in **Figure 9**. The fracture occurs around the neck thickness of aluminium alloy sheet in both the load positions. The load of welded two aluminium sheets for the JIS class B (average) is also shown. The maximum load for the load position of the middle and lower sheets is higher than those for the load position of the upper and lower sheets and the JIS class B.

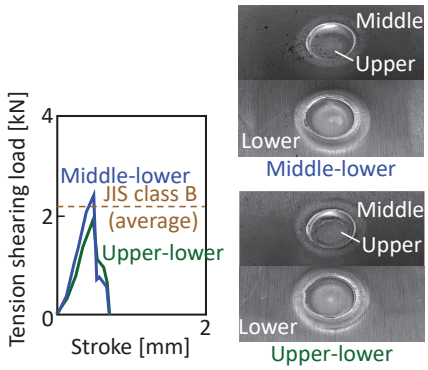

Figure 9 Tension-shearing loads of joints.

The cross-tension loads of joints are shown in **Figure 10**. The fracture occurs around the neck thickness of aluminium alloy sheet in both the load positions. The maximum loads for both the load positions are similar, and are smaller than those in the tension-shearing test.

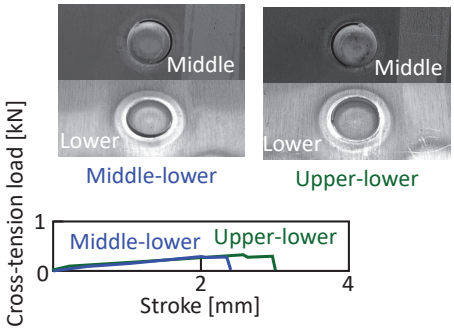

Figure 10 Cross-tension loads of joints.

Conclusions

In this study, a cold joining process of two ultra-high-strength steel and one aluminium alloy sheets using a pre-punched middle sheet was developed. Using the middle sheet with an optimum hole diameter, the three sheets having a flat bottom of the lower sheet were joined without defects. In the future, the robustness for the alignment of punch, the hole diameter, the deviation of sheet thickness and flow stress are required for application to the actual joining process.

References

Abe, Y., Maeda, T., Yoshioka, D. & Mori, K. (2020) Mechanical clinching and self-pierce riveting of thin three sheets of 5000 series aluminium alloy and 980 MPa grade cold rolled ultra-high strength steel. *Special Issue of Materials*, 13–21, 4741.

Han, L., Chrysanthou, A. & Young, K.W. (2007) Mechanical behaviour of self-piercing riveted multi-layer joints under different specimen configurations. *Material and Design*. 2007, 28, 2024–2033.

Kaðèák, L., Spiðák, E., Kubík, R. & Mucha, J. (2017) Finite element calculation of clinching with rigid die of three steel sheets. *Strength of Materials*, 49, 488–499.

Martin, S., Alan M., Camberga, A. & Tröstera, T. (2020) Probability distribution of joint point loadings in car body structures under global bending and torsion, *Procedia Manufacturing*, 47, 419–424.

Sakiyama, T., Naito, Y., Miyazaki, Y., Nose, T., Murayama, G., Saita, K. & Oikawa, H. (2013) Dissimilar metal joining technologies for steel sheet and aluminum alloy sheet in auto body. *Nippon Steel Technical Report*, 103, 91–98.

Varis, J. (2006) Economics of clinched joint compared to riveted joint and example of applying calculations to a volume product. *Journal of Materials Processing Technology*, 172, 130–138.

Watanabe, T., Doi, Y., Yanagisawa, A. & Konuma, S. (2005) Resistance spot welding of mild steel to Al-Mg alloy, *Quarterly Journal of the Japan Welding Society*, 23-3, 491–495.

BROAD EXCITATION BAND OF SPIN WAVE USING MICROSTRIP LINE FOR MAGNONIC DEVICE

Kanta Mori[a], Taichi Goto[a,*], Toshiaki Watanabe[b], Pang Boey Lim[a], and Mitsuteru Inoue [a,c]

[a] Toyohashi University of Technology, Toyohashi, Aichi, Japan
[b] Shin-Etsu Chemical Co., Ltd., Annaka, Gunma, Japan
[c] National Institute of Technology, Hachioji, Tokyo, Japan

*goto@ee.tut.ac.jp

Abstract

Spin wave devices attract many interests of researchers as next-generation computing devices instead of semiconductor-based computing devices because of their low loss and wave functionalities. To realize the spin wave devices, controlling the propagation of the spin waves is a key technology. The propagation properties of spin waves can be controlled by magnonic crystals comprising artificial periodic magnetic structures. Recently, we demonstrated a magnonic crystal comprising periodic metal structures deposited on a spin-wave waveguide, and the waveguide was composed of yttrium iron garnet film epitaxially grown on gadolinium gallium garnet substrate. This magnonic crystal showed a clear magnonic bandgap (stopband) at a frequency of 1.5 GHz. To increase the dimension of the periodicity of the magnonic crystal from one to two, a broad excitation band of a spin wave is essential. However, the broad excitation band of the spin waves was not reported so far. Hence, in this paper, to obtain the broad excitation band, the structure of microstrip line antennas exciting spin waves was investigated using a high-frequency simulator based on finite integration technique. The microstrip line antenna was located onto the yttrium iron garnet film. The thickness of the yttrium iron garnet film was 1 μm. This yttrium iron garnet was put onto a 100 nm thick copper film deposited on a silicon substrate. The copper layer worked as an electrical ground. The thickness of the silicon substrate was 380 micro-meter. The thickness and width of the microstrip line antenna and the thickness of the yttrium iron garnet film were varied in the simulator. The figure of merits was defined as the multiplication of the spin-wave intensity at the frequency of 4 GHz and the frequency bandwidth at half of the maximum value. As a result, the largest figure of merit was 24 Oe GHz, 1.87 times larger than the conventional antenna. In the symposium, the details of the method and results would be discussed.

Keywords: *spin wave, microstrip line, magnonics, magnonic crystal, yttrium iron garnet*

Introduction

Spin wave (SW) devices attract many interests of researchers as next-generation computing devices instead of semiconductor-based computing devices because of their low loss and wave functionalities (Chumak, Vasyuchka, Serga & Hillebrands, 2015; Goto, 2021; Goto et al., 2019; Serga, Chumak & Hillebrands, 2010). To realize the SW devices, controlling the propagation of the SWs is a crucial technology. The propagation properties of SWs can be controlled by magnonic crystals comprising artificial periodic magnetic structures (Chumak, Serga & Hillebrands, 2017). Recently, we demonstrated a magnonic crystal comprising periodic metal structures deposited on an SW waveguide, and the waveguide was composed of yttrium iron garnet film epitaxially grown on gadolinium gallium garnet substrate (Goto, Shimada, Nakamura, Uchida & Inoue, 2019; Shimada et al., 2017). This magnonic crystal showed a clear magnonic bandgap (stopband) at a frequency of 1.5 GHz (Goto, Shimada, Nakamura, Uchida & Inoue, 2019). To increase the dimension of the periodicity of the magnonic crystal from one to two, a broad excitation band of SW is essential. Simultaneously, the excitation antenna needs to be integrated into the same substrate. However, such an SW spectrum and antenna have not been reported because of the fabrication difficulty.
Hence, this paper suggests the new structure of microstrip line (MSL) antennas, and its performance was calculated.

Calculation Model

An MSL antenna comprises a dielectric layer sandwiched by a signal line (SL) and a ground plane (GP). To broaden the excitation spectrum, the width of the SL should be decreased because of their Fourier-transformable relationship (Goto et al., 2019). However, simultaneously, the distance between the SL and GP becomes so large, decreasing the antenna output and the SW magnitude drastically. Hence, we suggest using the SW waveguide as a dielectric layer in MSL, as shown in Figure 1. The SW waveguide is composed of a magnetic

insulator, a yttrium iron garnet (YIG). A bias magnetic field was applied perpendicular to the plane in order to excite the forward volume SWs. The conductivity of both SL and GL was 5.97×10^7 S/m. The relative permittivity and saturation magnetization, the magnetic damping constant, and the gyromagnetic ratio of YIG were 15.3, 1800 G, 2.4×10^{-4}, and 2.8 MHz/Oe, respectively. The relative permittivity of the Si substrate was 12. The working frequency was set as 4 GHz. The Si substrate size was 100 μm × 100 μm × 380 μm, sufficiently larger than the wavelength of SWs.

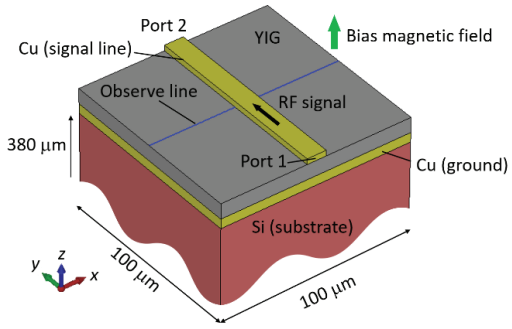

Figure 1. Calculation model of the MSL. SW waveguide (YIG) layer was sandwiched by SL and GP.

Calculation Procedure

And RF electrical signal was incident on port 1, and the RF response was calculated using the finite integration technique (Shimada et al., 2017). The *x*-component of the RF magnetic field distribution along the blue line in Figure 1 bisecting SL on the YIG surface was obtained. This distribution was Fourier transformed, and we obtained the SW's wavelength spectrum. Using this spectrum and dispersion curve (Goto, Shimada, Nakamura, Uchida & Inoue, 2019) of the propagating SW, the frequency spectrum of the excited SW was obtained, as shown in Figure 2. The bias field was adjusted so that the wavelength of the SW was 8.9 μm at a frequency of 4 GHz. The figure of merit (FOM) was defined as the multiplication of the spin-wave intensity at the frequency of 4 GHz and the frequency bandwidth at half of the maximum value.

The thickness and the width of SL, the thickness of YIG were varied, and FOMs were calculated.

Results and Discussion

First, the thickness of SL was varied 0.1–10 μm while fixing the YIG thickness to 1 μm and the width of SL to 1 μm. A 0.1-μm-thick SL showed the largest FOM because of the increase of *x*-component of RF signal compared with *y*-component of that.

Second, the width of SL was varied 0.4–10 μm while fixing the YIG thickness to 1 μm and SL thickness to 0.1 μm. The largest FOM was obtained when the SL width was 0.6 μm.

Third, the YIG thickness was varied 0.1–10 μm while fixing the thickness and width of SL to 0.1 μm and 0.6 μm, respectively. The optimal YIG thickness was 1 μm because of the increase of distance between SL and GP and the narrowing of the bandwidth.

Therefore, we determined the MSL antenna structure, showing the spin-wave intensity of 15.3 Oe, the bandwidth of 1.62 GHz, and the FOM of 24.9 OeGHz.

Conclusions

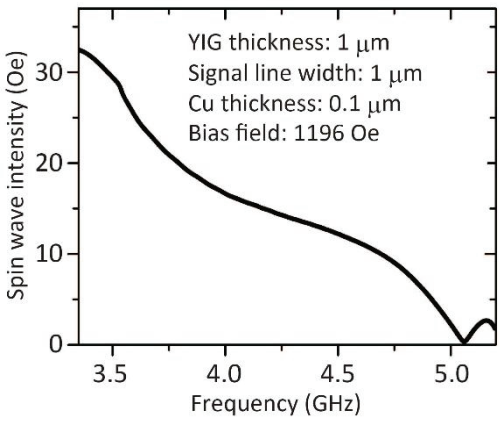

Figure 2. SW intensity spectrum excited by the MSL antenna sandwiching YIG film. The thickness and width of SL were 0.1 μm and 1 μm, recpectively. The YIG thickness was 1 μm, and the bias field was 1196 Oe.

The SW spectra generated by the MSL antenna sandwiching the YIG layer were calculated using a finite integration technique with various structural parameters. The optimum thickness and width of SL were 0.1 μm and 0.6 μm, respectively, when the thickness of YIG was 1 μm. This MSL antenna showed 0.533 times higher SW intensity, 3.52 times broader bandwidth, and 1.87 times larger FOM compared with the conventional antenna. This paper showed a potential planar antenna structure for exciting broadband SW, essential for demonstrating two-dimensional magnonic crystals.

Acknowledgements

This work was partly supported by Grants-in-Aid for Scientific Research (KAKENHI) Nos. 20H02593, 19H00765, 20K20535 from the Japan Society for the Promotion of Science (JSPS), the Research Foundation for the Electrotechnology of Chubu, and the Foundation for Technology Promotion of Electronic Circuit Board. We also acknowledge Prof. Hironaga Uchida, and Prof. Yuichi Nakamura for their support.

References

Chumak, A. V., Serga, A. A., & Hillebrands, B. (2017). Magnonic crystals for data processing. *Journal of Physics D: Applied Physics*, 50, 244001.

Chumak, A. V., Vasyuchka, V. I., Serga, A. A., & Hillebrands, B. (2015). Magnon spintronics. *Nature Physics*, 11, 453.

Goto, T. (2021). Logic device using spin wave interference propagating in a magnetic insulator (Review). *Oyo Buturi*, 90, 172.

Goto, T., Shimada, K., Nakamura, Y., Uchida, H., & Inoue, M. (2019). One-dimensional magnonic crystal with Cu stripes for forward volume spin waves. *Physical Review Applied*, 11, 014033.

Goto, T., Yoshimoto, T., Iwamoto, B., Shimada, K., Ross, C. A., Sekiguchi, K., Granovsky, A. B., Nakamura, Y., Uchida, H., & Inoue, M. (2019). Three port logic gate using forward volume spin wave interference in a thin yttrium iron garnet film. *Scientific Reports*, 9, 16472.

Serga, A. A., Chumak, A. V., & Hillebrands, B. (2010). YIG magnonics. *Journal of Physics D: Applied Physics*, 43, 264002.

Shimada, K., Goto, T., Kanazawa, N., Takagi, H., Nakamura, Y., Uchida, H., & Inoue, M. (2017). Extremely flat transmission band of forward volume spin wave using gold and yttrium iron garnet. *Journal of Physics D: Applied Physics*, 50, 275001.

Development of multiferroic composite films for voltage-driven magneto-optic special light modulators

Y. Nakamura*,[a], N. Kamada [a], R. Hasumi[a], T. Goto[a], P. B. Lim[a], H. Uchida[a], and M. Inoue[b]

[a] Electrical and Electronic Information Engineering, Toyohashi University of Technology, Aichi, Japan
[b] National Institute of Technology, Tokyo, Japan

* nakamura.yuichi.go@tut.jp

Abstract

With the progress in optical information processing and communications, high speed light modulation devices are eagerly desired. A magneto-optical spatial light modulator (MOSLM) that can operate at a speed higher than conventional SLMs such as digital mirror device is a device that modulates the intensity and phase of light using the magneto-optical effect. For the development of voltage driven MOSLMs, a multiferroic composite film in which magnetic columns are embedded in a piezoelectric matrix is desired. To realize such the structure, the fabrication method to grow aligned $BaTiO_3$ (BTO) and bismuth substituted rare earth iron garnet (Bi:RIG) on the same substrate was investigated. In a preliminary work, $CoFe_2O_4$ (CFO) was found to be aligned both on the $SrTiO_3$ (100) and GGG (111) substrates, while BTO and Bi:RIG can only grow epitaxially on the substrate with the same crystal structure. This suggests the use of CFO as a buffer layer may give us the aligned BTO and Bi:RIG on the GGG (111) substrate. Based on this result, the effect of CFO thickness on the alignment of BTO was investigated. The preferential growth of BTO (111) was observed on the CFO buffered GGG (111) substrate, and the (111) oriented BTO was obtained on the 2500 pulsed CFO layer. From pole figure analysis of the sample, it was found there are two-sets of orientation groups tilted by 20 ° to the left and right in the plane probably due to the relaxation of the lattice mismatch at the interface between CFO and BTO layers. This suggests that the use of CFO buffer layer is effective to grow BTO and Bi:RIG simultaneously with a certain crystal relationship on the GGG (111) substrate and is an important breakthrough for obtaining multiferroic composites using Bi:RIG for light modulation.

Keywords: *multiferroic composites, $CoFe_2O_4$ buffer layer, GGG substrate, crystal alignment*

Introduction

With the remarkable progress in the fields of optical information processing and communications, optical modulation devices that can be driven at high speed are eagerly desired. Spatial light modulator (SLM) is an element that controls light intensity, phase, and polarization in two dimensions. We have investigated to realize a magneto-optical SLM (MOSLM) that can operate at a speed higher than conventional SLMs such as liquid crystal on silicon (LCOS) and digital mirror device (DMD). The MOSLM is a device that modulates the intensity of light using the magneto-optical effect in which the polarization plane of light rotates depending on the direction of magnetization by inserting an analyser on the output side. This MOSLM can modulate light in nanosecond order in principle by controlling the direction of magnetization and is expected to be applied to next-generation devices such as optical communication and optical computing.

We developed current driven MOSLM (*i*-MOSLM) that uses a magnetic garnet thin film to modulate the magnetization direction of arbitrary pixels arranged two dimensionally with a magnetic field by a current (Takagi et al., 2006). In this *i*-MOSLM, it was difficult to increase the scale because the Joule heat was large due to the current for magnetization reversal. So, the voltage driven MOSLM (*v*-MOSLM) in which a piezoelectric material was formed on the magnetic garnet layer was developed (e.g., Takagi et al., 2006 & 2009; Mito et al., 2011). This *v*-MOSLM controls the magnetization direction through the inverse magneto-strictive effect by applying voltage to piezoelectric layer. However, since the strain generated in the piezoelectric material is applied only near the interface with the magnetic material, the amount of modulation cannot be increased above a certain value even if the magnetic material is thickened. Therefore, the structure that can apply a large and uniform stress in thick magnetic material is desired.

The 1-3 type multiferroic composite film in which magnetic columns are embedded in the piezoelectric material may be a strong candidate (e.g., Ma et al. (2011)). In this structure, stress can be applied uniformly to the magnetic material even if the film is thickened, so the increase in the modulation is expected in proportion to the film thickness. It has been reported that many

combinations of materials such as $BiFeO_3$ (BFO) and $BaTiO_3$ (BTO) as perovskite and $CoFe_2O_4$ (CFO) as spinel form this 1-3 type self-assembled perovskite-spinel nanostructure. (e.g., Zavaliche et al. (2005); Zheng et al. (2006); Ma et al. (2011)). Zavaliche et al. (2005) reported that a large electromagnetic effect of 10^{-2} G·cm/V is exhibited at room temperature in the epitaxially grown composite structure in which CFO pillars are embedded in BFO matrix. In addition, Aimon et al. (2015) reported that magnetization of CFO embedded in BFO matrix was reversed by applying a voltage with a microprobe to a multiferroic composite film prepared by simultaneously growth with the PLD method. The *v*-MOSLM is expected to realize by using a rare earth magnetic garnet (Bi:RIG) as a magnetic material in this structure. However, typical piezoelectric materials such as PZT and BTO have a perovskite structure that is different from the garnet structure. There were several reports (e.g. Dong et al. (2017); Jung et al. (2021)) in which yttrium iron garnet (YIG) and BTO were deposited by sputtering on $SrTiO_3$ (STO) single crystal substrate. In these reports, the YIG crystal was polycrystalline and did not grow epitaxially on STO substrate, while the BTO showed epitaxial growth. In order to grow piezoelectric and the magnetic materials simultaneously, it is reported that both of them should keep a crystal orientation (Zheng et al. (2006)). However, it is not easy because of the difference in crystal structures between garnet and perovskite. In this work, we found that CFO could be aligned and grown on the (111) plane of the $Gd_3Ga_5O_{12}$ (GGG) single crystal substrate, that is usually used for the deposition of single crystal garnet film, and investigated the growth conditions using this thin film as the buffer layer for obtaining a BTO film oriented on the GGG substrate.

Experimental

A pulsed laser deposition (PLD) method was used to prepare the sample. First, BTO, CFO, and Bi:RIG were deposited on the STO (100) and $Gd_3Ga_5O_{12}$ (GGG) (111) substrates to check the crystal alignment on these substrates with X-ray diffraction (XRD) analysis. Based on this result, the effect of CFO thickness on the crystal alignment of BTO deposited on GGG (111) substrate. Table 1 shows the fabrication conditions of the samples. The CFO layer was deposited with various pulse numbers between 50 and 2500 pulses, and then the BTO was formed with 2500 pulses with the substrate temperature of 750 °C. The crystal orientation of these BTO / CFO / GGG (111) samples was evaluated by XRD, and the pole figure analysis was also performed on the sample with BTO deposited 15000 pulses.

Table 1 Experimental conditions

Substrate	GGG (111)	
Target	$CoFe_2O_4$	$BaTiO_3$
Distance between target and substrate	5 cm	
Substrate temperature	750 ºC	
Oxygen partial pressure	7.0 Pa	
Laser condition	360 mJ/pulse， 10 Hz	
Pulse number	50 ~ 2500	2500, 15000

Results and Discussion

Figure 1 shows the XRD patterns of the samples deposited on STO (100) and GGG (111) substrates with the target of BTO, CFO or Bi:RIG. As shown in this figure, BTO and Bi:RIG can grow epitaxially only on STO and GGG substrates that has the same crystal structure, respectively. On the other hand, CFO can grow with the same crystal alignment on both of STO and GGG substrates. This suggests that BTO may grow hetero-epitaxially on the CFO layer deposited on GGG substrate since both BTO and CFO can grow epitaxially on the STO substrate.

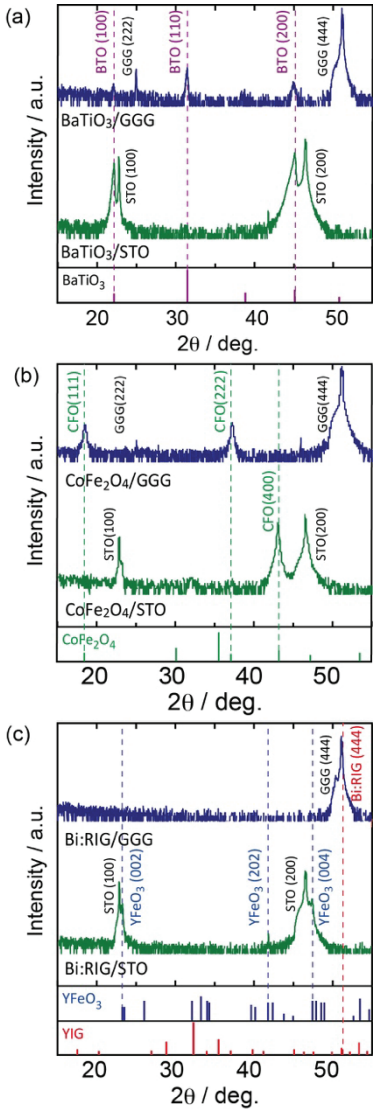

Figure 1 XRD patterns of the samples deposited on STO (100) and GGG (111) substrates with the targets of (a) BTO, (b) CFO and (c) Bi:RIG.

Figure 2 shows the XRD patterns of multilayer films in which the BTO layer was deposited on CFO layer with different thicknesses formed on GGG (111) substrate. As shown in this figure, when the deposition pulse number of CFO film is less than 100 pulse, the strength of the (110) face, which is the strongest peak of BTO, is strong. However, when the deposition pulse number of CFO exceeds 200 pulses, the strength of the (111) face became relatively strong, and those of the other faces became weak. When the deposition pulse number of CFO was 2500, the intensity of BTO (111) face became dominant, and CFO {111} peaks were also detected.

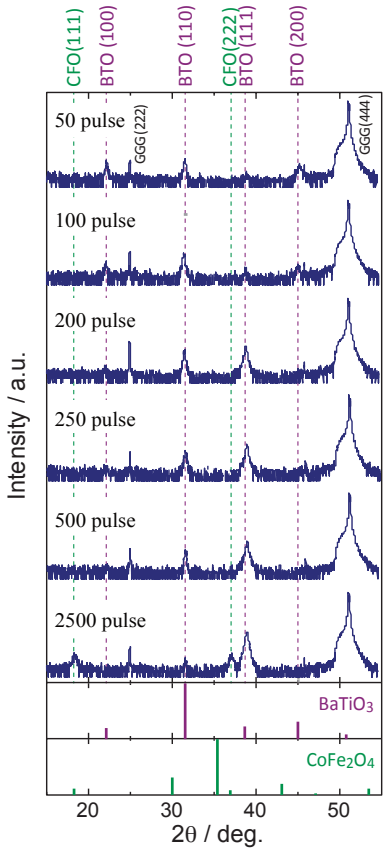

Figure 2 XRD results of BTO deposited on CFO buffer layer with various thickness on GGG (111) substrate.

In order to evaluate the effect of the thickness of the CFO buffer layer on the BTO orientation quantitatively, the ratio of the intensity of BTO (111) face to the sum of (111) and (101) faces, $I_{(111)} / (I_{(111)} + I_{(101)})$, are plotted in Fig. 3 against the deposition pulse number of CFO. As shown in this figure, the intensity ratio of the BTO (111) which was about 0.1 at 100 pulses of less, became about 0.65 when the CFO layer was deposited by 200 pulses. This ratio increased to about 0.8 at the CFO deposition pulse numbers of 500 and finally reached 0.98 in the sample deposited on the CFO layer deposited with 2500 pulses, and the preferential orientation of (111) was recognized. Since the deposition rate of the CFO film was about 0.02 nm/pulse, the thickness of about 10 nm of the CFO layer is thought to be needed to achieve the (111) oriented BTO film.

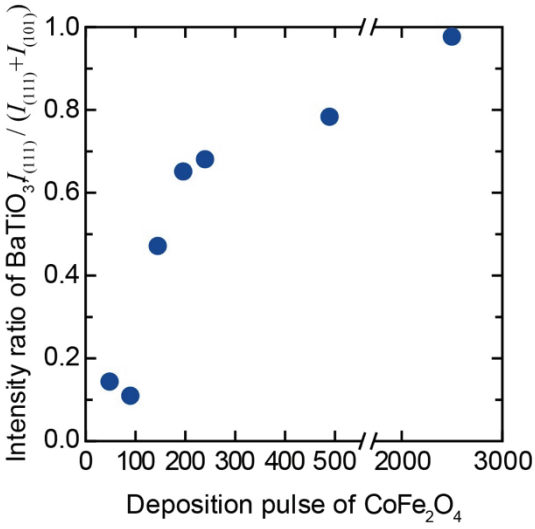

Figure 3 Intensity ratio of BTO (111) face against the thickness of CFO buffer layer.

To see the in-plane orientation of the BTO film deposited on the GGG (111) substrate, the pole figure analysis was carried out for the sample with 15000 pulse of BTO layer on the 2500 pulses of CFO buffer layer, that showed the strongest BTO (111) peak. Figure 4 shows a cross-sectional SEM image of this layered sample. The thickness of the BTO layer was about 630 nm, and that of the CFO layer was about 50 nm, respectively. Figure 5 shows the evaluation results of the XRD pole figure for the BTO {100} and {221} planes of this sample. As shown in this figure, two sets of three-fold symmetric peaks were obtained for the {100} and {221} planes, while the thickness of the CFO layer was too thin to confirm in-plane orientation. That is, the BTO had a uniaxial orientation in which the [111] direction was perpendicular to the substrate surface, while unfortunately it was found that there were two different sets of orientation groups in the in-plane direction rather than biaxial orientation. Considering that the CFO (lattice constant of 0.840 nm) has a lattice constant about twice that of the BTO (lattice constant of 0.404 nm), the lattice mismatch between them is about 4 %. This misfit is relaxed to about 1.5 % through the rotation of the BTO by 20 degree in the plane. On the other hand, since the CFO has a lattice constant about 2/3 of GGG (lattice constant of 1.238 nm), the lattice mismatch between them is about 1.5%. Hence the BTO is thought to growth with the rotation by 20 ° in the plane to relax the lattice misfit at the interface between CFO and BTO if the CFO shows biaxially oriented growth on the GGG (111) substrate.

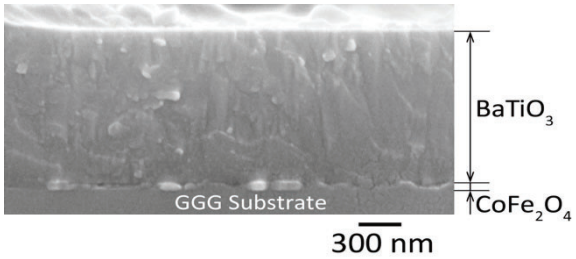

Figure 4 Cross sectional view of the BTO/CFO layered sample deposited on GGG (111) substrate.

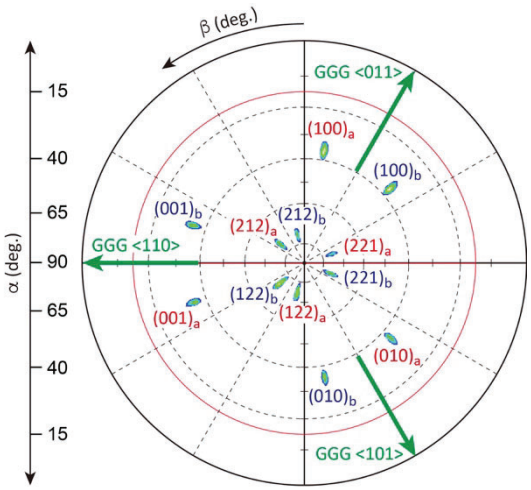

Figure 5 XRD pole figure of the BTO deposited on CFO buffer layer on GGG (111) substrate.

In order to grow BTO and Bi:RIG simultaneously on the GGG substrate, it is desirable that there is a certain crystal relationship between the BTO and the Bi:RIG crystals. In this work, the BTO grown on the CFO buffer layer did not show complete in-plane alignment, but the alignment was limited to two groups, and it would be expected to grow with maintaining some crystal relationship in each alignment group. So, the use of CFO buffer layer is considered to be an important breakthrough for obtaining multiferroic composites using Bi:RIG for light modulation.

Conclusions

To realize the light control multiferroic composite for MOSLM, the method for obtaining aligned BTO and Bi:RIG on the same single crystal substrate was investigated using PLD method. The CFO was found to be aligned both on the STO (100) and GGG (111) substrates, and this suggests that the use of CFO as buffer layer leads the aligned growth of BTO on GGG substrate. So, the effect of CFO buffer thickness on the alignment BTO layer deposited on the GGG (111) substrate was investigated. The preferential growth of BTO (111) was observed on the CFO layer with the deposition of 200 pulses or more, and the (111) oriented BTO was obtained on the 2500 pulsed CFO layer. From the pole figure analysis, it was found there are two-sets of orientation groups tilted by 20 ° to the left and right in the plane probably due to the relaxation of the lattice mismatch at the interface between CFO and BTO. This suggests that the use of CFO buffer layer is effective to grow BTO and Bi:RIG simultaneously with a certain crystal relationship for obtaining multiferroic composites using Bi:RIG for light modulation.

Acknowledgements

This work was supported in part by the Grants-in-Aid for Scientific Research (S) 26220902, (B) 16H04329 and Strategic international research network promotion program No. R2802.

References

Aimon, N.M., Kim, D.H., Sun, X.Y., & Ross, C.A. Multiferroic behavior of templated $BiFeO_3$-$CoFe_2O_4$ self-assembled nanocomposites. (2015) *ACS Appl. Mater. Interfaces*, 7, 2263-2268.

Dong, G, Zhou, Z., Xue, X., Zhang, Y., Peng, B., Guan, M., Zhao, S., Hu, Z., Ren, W., Ye, Z.-G., & Liu, M. (2017). Ferroelectric phase transition induced a large FMR tuning in self-assembled $BaTiO_3$:$Y_3Fe_5O_{12}$ multiferroic composites. *ACS Appl. Mater. Interfaces*. 9, 30733-30740.

Jung, H.K., Mun, J.H., Lee, H.J., Song, J.M., & Kim, D.H. (2021). Magnetic property modulation in sputter-grown $BaTiO_3$–$Y_3Fe_5O_{12}$ composite films. *Ceram. Int.*, 47, 7062–7068.

Mito, S., Takagi, H., Lim, P.B., Baryshev, A.V., & Inoue, M. Spatial light phase modulators with one-dimensional magnetophotonic crystals driven by piezoelectric films. (2011). *J. Appl. Phys.*, 109, 07E313-1-3.

Takagi, H., Tsuzuki, A., Iwasaki, K., Imura, T., Umezawa, J., Uchida, H., Shin, K.H., & Inoue, M. (2006). Multiferroic magneto optic spatial light modulator with sputtered PZT film. *J. Magn. Soc. Jpn.*, 30, 581-583.

Takagi, H., Takahashi, K., Mito, S., Kawanishi, F., Chung, K.H., Heo, J., Kim, J., Lim, P.B., & Inoue, M. (2008). Theoretical Analysis of Voltage-Driven MOSLM with 1-D Magneto Photonic Crystal. *J. Magn. Soc. Jpn.*, 32, 120-123.

Takagi, H., Kim, J., Chung, K.H., Mito, S., Umezawa, H., & Inoue, M. (2009). Magneto-optical spatial light modulators with magnetophotonic crystals driven by PZT films. *J. Magn. Soc. Jpn.*, 33, 525-527.

Ma, J., Hu, J., & Nan, C.-W. (2011) Recent progress in multiferroic magnetoelectric composites: from bulk to thin films. *Adv. Mater.*, 23, 1062-1087.

Zavaliche, F., Zheng, H., Mohaddes-Ardabili, L., Yang, S.Y., Zhan, Q., Shafer, P., Reilly, E., Chopdekar, R., Jia, Y., Wright, P., Schlom, D.G., Suzuki, Y., & Ramesh R. (2005). Electric field-induced magnetization switching in

epitaxial columnar nanostructures. *Nano Lett.*, 5, 1793-1796.

Zheng, H., Straub, F., Zhan, Q., Yang, P., Hsieh, W., Zavaliche, F., Chu, Y., Dahmen, U., & Ramesh, R. (2006) Self-assembled growth of $BiFeO_3$-$CoFe_2O_4$ nanostructures. *Adv. Mater.*, 18, 2747-2752.

Zheng, H., Zhan, Q., Zavaliche, F., Sherburne, M., Straub, F., Cruz, M.P., Chen, L.-Q., Dahmen, U., & Ramesh, R. (2006). Controlling self-assembled perovskite-spinel nanostructures. *Nano Lett.*, 6, 1401-1407.

MAGNETOOPTICAL PROPERTIES OF CERIUM SUBSTITUTED YTTRIUM IRON GARNET FILMS FOR SPIN CONTROLLED LASERS

Yuki Yoshihara[a], Pang Boey Lim[a], Mitsuteru Inoue[a,b] and Taichi Goto[*,a]

[a] Toyohashi University of Technology, Toyohashi, Aichi, Japan
[b] National Institute of Technology, Hachioji, Tokyo, Japan

*goto@ee.tut.ac.jp

Abstract

We developed the spin-controlled laser using a magnetooptical Q-switch comprising a magnetic garnet film and a magnetic field pulse generator. This laser showed high-power pulses, and its cavity length was short, ~10 mm. To integrate this laser into a microchip, we fabricated a cerium substituted yttrium iron garnet (Ce:YIG) film with various thicknesses. A 338 nm thick Ce:YIG showed the Faraday rotation angle of –0.95° at a wavelength of 1064 nm. The figure of merit was 67 °/dB. These values were larger than that of previous reports. We also observed the thickness dependence of the magnetooptical properties. These results showed the high potential of Ce:YIG film for magnetooptical Q-switch used in a spin-controlled laser.

Keywords: *spin controlled laser, Q-switch, magnetooptics, yttrium iron garnet, ion beam sputtering*

1. Introduction

Compact and high-power lasers are used in various fields, like manufacturing and medical industries. A Q-switching technique can enhance the pulse power of the laser while keeping the size of the laser small[1,2]. The electro-optical (EO) effects[3], the acousto-optical (AO) effects[4], and the saturable absorption effects[5] are widely used in Q-switches. These can show high-power pulses but cannot be integrated into microchips in principle. In contrast, the magnetooptical (MO) Q-switch can be integrated into microchips because of its small thickness, approximately 190 μm[6-8]. The laser using the MO Q-switch was called the spin-controlled laser[6], showing interesting properties not available with other lasers. In theory, the thickness of the MO Q-switch can be decreased when we use cerium substituted yttrium iron garnets (Ce:YIG)[9,10] film. However, the Ce:YIG has never been considered for use in the MO Q-switch because of the fabrication difficulty of ~10-μm-order-thick Ce:YIG film. To fabricate such a film, in this study, we prepared Ce:YIG films with various thicknesses and measured the crystalline, magnetic, optical, and MO properties.

2. Film Preparation

Ce:YIG films were deposited by radio-frequency (RF) ion beam sputtering (RMTech RM17-0010) on synthetic fused silica substrates. A sintered target comprising $Ce_{1.0}Y_{2.5}Fe_5O_{12-\delta}$ was used for the deposition. The deposition rate and chamber oxygen flow were varied. Working pressure of ~9×10^{-2} Pa with an oxygen flow of 8 sccm, an ion beam voltage of 800 V with a maximum RF power of 75 W was used. The temperature and rotation speed of the substrates were 200°C and 4.2 rpm, respectively. The deposited samples were diced into 5 mm × 5 mm, and annealed in a glass chamber (Ulvac SSA-P610CP) pumped down at ~2 Pa. Annealing temperature and time were 800°C and 20 minutes, respectively. The color of the prepared samples was yellow-green (Figure 1 inset).

3. Characterization and Discussion

The film thickness was varied from 51 nm to 2056 nm, measured by a stylus profilometer (Kosaka Laboratory ET4000M). The composition of the film was measured using an energy dispersive x-ray spectroscopy system (Hitachi High-Technologies SU3500 and AMETEK EDAX Genesis APEX2 Octane), showing

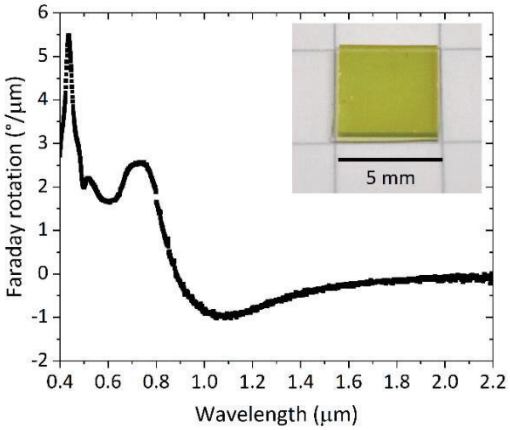

Figure 1. Faraday rotation angle spectrum of a 338 nm thick Ce:YIG film deposited on the synthetic fused silica substrate. The inset shows the top view of Ce:YIG film.

$Ce_1Y_2Fe_5O_{12-\delta}$. Crystalline properties were characterized by out-of-plane x-ray diffraction (XRD, Rigaku Smartlab). The samples thicker than 177 nm showed polycrystalline garnet phases. The strongest (420) XRD peak shifted to the lower angle as the sample become thicker, showing the expansion of the out-of-plane lattice constant because of the lattice relaxation. The estimated lattice constants were between 1.242 nm and 1.244 nm.

The samples' transmissivity was measured in a range of 200–3000 nm using a spectrometer (Shimadzu UV-3150). The transmissivity of a 338 nm thick sample at a wavelength of 1064 nm was 70.6%. The complex refraction index was obtained using these transmission spectra and the software SCOUT based on the Fresnel equation, showing the refractive index of 2.205 and the extinction coefficient of 2.774×10^{-4} ($= -1.424 \times 10^{-2}$ dB/μm).

The Faraday rotation angle was measured using the MO measurement system (JASCO J-1700FK). The range of the wavelength was 200–2200 nm. The temperature of the sample was 40°C. The Faraday rotation angle was a sum of two spectra measured at two magnetic fields of +0.5 T and –0.5 T, Figure 1. The Faraday rotation angle at a wavelength of 1064 nm was –0.95 °/μm. This value is 1.08 times larger than the previous value of –0.88 °/μm[9]. The figure of merit (FOM) is defined as the multiplication of Faraday rotation angle, and the transmissivity was 67 °/dB, 1.06 times larger than the previous value of 63 °/dB[9]. This FOM was not constant when the thickness was changed because of the change of surface roughness of the samples. The surface roughness defined as the root mean square R_q was measured by the stylus profilometer. The value of R_q was increased with increasing the film thickness by $R_q = 1.2$ μm, caused by surface cracks of the samples. The cracks occurred because of the difference in the thermal expansion coefficients between the Ce:YIG films and the synthetic fused silica substrates.

4. Conclusion

We fabricated polycrystalline Ce:YIG films with various thicknesses for the development of an integrated MO Q-switch. Crystalline, optical, the Faraday rotation angle, and surface roughness of Ce:YIG films deposited on the synthetic fused silica substrates were characterized. Thickness dependence of the Faraday rotation angle and FOM was observed. The 338 nm thick Ce:YIG film showed the FOM of 63 °/dB, 1.06 times larger than the previous value. However, this value was limited because of the cracks of the samples. Hence, to further improvement, epitaxial growth of a single crystalline Ce:YIG is needed. These results are a good milestone for the development of integrated spin-controlled lasers.

Acknowledgments

This work was partly supported by Grants-in-Aid for Scientific Research (KAKENHI) Nos. 20H02593, 19H00765, 20K20535 from the Japan Society for the Promotion of Science (JSPS) and the Research Foundation for the Electrotechnology of Chubu. We also acknowledge Prof. Hironaga Uchida, Prof. Yuichi Nakamura, Mr. Naohide Kamada, Cooperative Research Facility Center (CRFC), and Shin-Etsu Chemical Co., Ltd. for their support.

References

1 Taira, T. & Kobayashi, T. (1994). Q-switching and frequency doubling of solid-state lasers by a single intracavity KTP crystal. *IEEE Journal of Quantum Electronics*, 30, 800.

2 Zayhowski, J. J. & Dill, C. (1994). Diode-pumped passively Q-switched picosecond microchip lasers. *Optics Letters*, 19, 1427.

3 Velsko, S. P., Ebbers, C. A., Comaskey, B., Albrecht, G. F., & Mitchell, S. C. (1994). 100 W average power at 0.53 μm by external frequency conversion of an electro-optically Q-switched diode-pumped power oscillator. *Applied Physics Letters*, 64, 3086.

4 Ray, A., Das, S. K., Mukhopadhyay, S., & Datta, P. K. (2006). Acousto-optic-modulator-stabilized low-threshold mode-locked Nd:YVO_4 laser. *Applied Physics Letters*, 89, 221119.

5 Pavel, N., Saikawa, J., Kurimura, S., & Taira, T. (2001). High average power diode end-pumped composite Nd:YAG laser passively Q-switched by Cr^{4+}:YAG saturable absorber. *Japanese Journal of Applied Physics*, 40, 1253.

6 Goto, T., Morimoto, R., Pritchard, J. W., Mina, M., Takagi, H., Nakamura, Y., Lim, P. B., Taira, T., & Inoue, M. (2016). Magneto-optical Q-switching using magnetic garnet film with micromagnetic domains. *Optics Express*, 24, 17635.

7 Morimoto, R., Goto, T., Pritchard, J., Takagi, H., Nakamura, Y., Lim, P. B., Uchida, H., Mina, M., Taira, T., & Inoue, M. (2016). Magnetic domains driving a Q-switched laser. *Scientific Reports*, 6, 38679.

8 Morimoto, R., Goto, T., Taira, T., Pritchard, J., Mina, M., Takagi, H., Nakamura, Y., Lim, P. B., Uchida, H., & Inoue, M. (2017). Randomly polarised beam produced by magnetooptically Q-switched laser. *Scientific Reports*, 7, 15398.

9 Goto, T., Eto, Y., Kobayashi, K., Haga, Y., Inoue, M., & Ross, C. A. (2013). Vacuum annealed cerium-substituted yttrium iron garnet films on non-garnet substrates for integrated optical circuits. *Journal of Applied Physics*, 113, 17A939.

10 Yoshimoto, T., Goto, T., Isogai, R., Nakamura, Y., Takagi, H., Ross, C. A., & Inoue, M. (2016). Magnetophotonic crystal with cerium substituted yttrium iron garnet and enhanced Faraday rotation angle. *Optics Express*, 24, 8746.

SPIN CONTROLLED LASER USING MAGNETIC GARNET FILM

Taichi Goto[*,a], Ken Aoki[a], Hibiki Miyashita[a], Yuki Yoshihara[a], Takumi Koguchi[a], Pang Boey Lim[a] Mani Mina[b], and Mitsuteru Inoue[a,c]

[a] Toyohashi University of Technology, Toyohashi, Aichi, Japan
[b] Iowa State University, Ames, Iowa, USA
[c] National Institute of Technology, Hachioji, Tokyo, Japan

*goto@ee.tut.ac.jp

Abstract

High power lasers are used in many applications, e.g., medical instruments, laser machining, laser ignition. Recently, we reported a spin-controlled laser comprising a diode-pumped solid-state laser and a magnetooptical (MO) Q-switch, irradiating high-power optical pulses. The MO Q-switch is composed of an 0.1-mm-thick magnetic film and a coil. The size of the MO Q-switch is smaller than other Q-switches, and this can be integrated onto laser crystals in principle, but this integration has not been reported so far. Hence, we combined the MO Q-switch with a laser crystal using optical glue and demonstrated a short laser cavity and high-power optical pulses.

Keywords: *laser, magnetics, optics, fabrication, film*

1. Introduction

High-power lasers have been implemented as essential components of various applications, e.g., laser machining devices[1,2], vehicle ignition plugs[3], mass spectrometers[4], satellite propulsion device[5], medical instruments. In these lasers, Q-switching optical component is widely used because of its ability to enhance the power of laser pulses. Recently, we reported a spin-controlled laser using magnetooptical (MO) Q-switches[6-8]. This spin-controlled laser used a magnetic film showing large magnetooptical (MO) effects and magnetic domains, as shown in Figure 1. The MO device was notably thin, compared with other Q-switches using electro-optical (EO) effects and acousto-optic (AO) effects. In general, the pulse width of the output of a Q-switched laser became shorter when the cavity length of the laser is shorter. Hence, the MO Q-switch can shorten the pulse width of output and increase the output power. However, the shortest cavity length of the spin-controlled laser was 10 mm, even the total thickness of all component within a cavity was ~4 mm because of the difficulty of optical alignment of these optical elements. To overcome this issue, we used optical glue and deposition technique to integrate all optical elements in the laser cavity in this study.

2. Laser Preparation

We fabricated the spin-controlled laser using MO Q-switch and laser cavity comprising a 3 mm × 3 mm × 4 mm laser crystal: neodymium (1 atomic percent)-doped gadolinium vanadium oxide (Nd:$GdVO_4$) and two dielectric mirrors. Figure 1 showed the sketch of the fabricated spin-controlled laser. A diode laser generating light at 808-nm wavelength was used to pump the Nd:$GdVO_4$ using lenses. The repetition rate was 10 Hz, the pumped current was 20 A, the pulse width of the pump light was 100 μs. The dielectric mirrors were fabricated on the Nd:$GdVO_4$ crystal using ion beam evaporation. The mirror on the input side of the crystal had high reflectance at the wavelength of 1064 nm. On the output side, the mirror had high transmission at the wavelength of 1064 nm and high reflection at the wavelength of 808 nm. A 3 mm × 3 mm MO film was prepared and used in the laser cavity. The Faraday rotation angle at the wavelength of 1064 nm was 45°. The output coupler was fabricated on the output side of the MO film using a dielectric mirror comprising a structure of MO film/183-nm-thick SiO_2/ 123-nm-thick Ta_2O_5/ 183-nm-thick SiO_2/ 69-nm-thick-Ta_2O_5. This dielectric mirror showed a reflectivity of 50% at the wavelength of 1064 nm to the light incident from the input side. The input side of the MO film was not coated by any dielectric

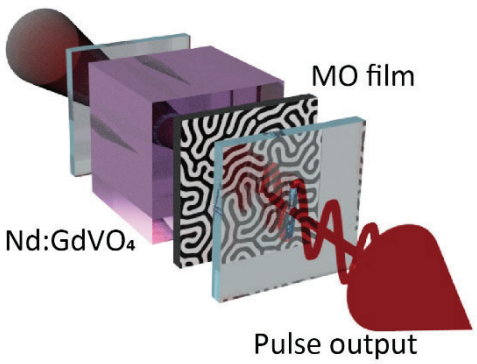

Figure 1. A sketch of a spin-controlled laser. The MO film was contacted to the laser crystal using an optical glue.

mirrors. This MO film was fixed on Nd:$GdVO_4$ crystal directly using optical glue. The MO sample had no substrate, and the thickness was about 0.2 mm. Thus, the total length of the laser cavity was approximately 4 mm.

Magnetic-field pulses were applied to the MO film using a 5-turn solenoid coil connected to the handmade-electrical pulse generator. Trigger signals were generated by a function generator (Tektronix, AFG3022), and a bias voltage was applied using Takasago ZX-S-800MA. The coil diameter was 5 mm, and the diameter of the Cu wire used in the coil was 0.5 mm.

The position of the lens for the pump light was varied, and the output pulses were measured. The magnitude of the magnetic field pulse was also varied. The output pulses were measured using an InGaAs-based fast-response optical photodetector (Thorlabs, DET10C) and a digital oscilloscope (Keysight Technology DSO80804B.

3. Optimization of Pumping Laser

Q-switched pulse was obtained, like Figure 2. The shape and number of the pulse were varied when the position of the lens was shifted. The largest single pulse was obtained when the distance between the lens and the lasing crystal was 14 mm.

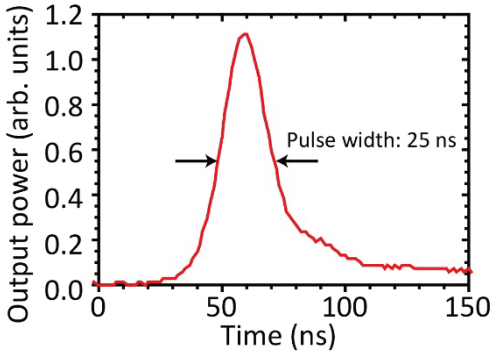

Figure 2. The obtained output pulse generated by the fabricated spin-controlled laser. The pulse width was about 25 ns.

4. Oscillation with Various Magnetic Field Pulses

The intensity of the magnetic field pulse applied to the magnetic garnet film was varied by changing a bias voltage applied to a transistor in the electrical pulse generator. The intensity was varied from 0 to 450 Oe. The Q-switching was observed when the magnetic field was larger than 250 Oe. Single pulses were obtained only at the magnetic field of 250 Oe. The larger magnetic field pulses as >300 Oe generated multiple pulses, probably showing the residual accumulated energy in the cavity not extracted by MO Q-switch. Therefore, a further change of the Q-factor would increase the pulse intensity. In particular, the improvement of the transmissivity at the boundary of the laser crystal/the optical glue and the glue/the MO film would enhance the output.

5. Conclusion

We demonstrated the spin-controlled laser using Nd:$GdVO_4$ and a magnetic garnet film. The laser crystal and the MO Q-switch were contacted via an optical glue. The cavity length was 4 mm. This demonstration was the shorted cavity length of the active Q-switched laser. Further improvement of the bonding technique would increase the pulse power.

Acknowledgments

This work was partly supported by Grants-in-Aid for Scientific Research (KAKENHI) Nos. 20H02593, 19H00765, 20K20535 from the Japan Society for the Promotion of Science (JSPS), the Research Foundation for the Electrotechnology of Chubu, and the Foundation for Technology Promotion of Electronic Circuit Board. We also acknowledge Prof. Hironaga Uchida, Prof. Yuichi Nakamura, Cooperative Research Facility Center (CRFC), and Shin-Etsu Chemical Co., Ltd. for their support.

References

1 Li, Q., Zheng, Y., Wang, Z., & Zuo, T. (2005). A novel high-peak power double AO Q-switches pulse Nd:YAG laser for drilling. *Optics & Laser Technology*, 37, 357.

2 Taira, T. & Kobayashi, T. (1994). Q-switching and frequency doubling of solid-state lasers by a single intracavity KTP crystal. *IEEE Journal of Quantum Electronics*, 30, 800.

3 Zayhowski, J. J. & Mooradian, A. (1989). Single-frequency microchip Nd lasers. *Optics Letters*, 14, 24.

4 Martens, J., Grzetic, J., Berden, G., & Oomens, J. (2016). Structural identification of electron transfer dissociation products in mass spectrometry using infrared ion spectroscopy. *Nature Communications*, 7, 11754.

5 Phipps, C., Birkan, M., Bohn, W., Eckel, H.-A., Horisawa, H., Lippert, T., Michaelis, M., Rezunkov, Y., Sasoh, A., Schall, W., Scharring, S., & Sinko, J. (2010). Review: Laser-Ablation Propulsion. *Journal of Propulsion and Power*, 26, 609.

6 Goto, T., Morimoto, R., Pritchard, J. W., Mina, M., Takagi, H., Nakamura, Y., Lim, P. B., Taira, T., & Inoue, M. (2016). Magnetooptical Q-switching using magnetic garnet film with micromagnetic domains. *Optics Express*, 24, 17635.

7 Morimoto, R., Goto, T., Pritchard, J., Takagi, H., Nakamura, Y., Lim, P. B., Uchida, H., Mina, M., Taira, T., & Inoue, M. (2016). Magnetic domains driving a Q-switched laser. *Scientific Reports*, 6, 38679.

8 Morimoto, R., Goto, T., Taira, T., Pritchard, J., Mina, M., Takagi, H., Nakamura, Y., Lim, P. B., Uchida, H., & Inoue, M. (2017). Randomly polarised beam produced by magnetooptically Q-switched laser. *Scientific Reports*, 7, 15398.

SIMULATION OF MAGNETIC DOMAIN FOR SPIN WAVE LOGIC DEVICE

Takumi Koguchi[a], Tadashi Ataka[b], Pang Boey Lim[a], Mitsuteru Inoue [a,c], and Taichi Goto[*,a]

[a] Toyohashi University of Technology, Toyohashi, Aichi, Japan
[b] Fujitsu Ltd., Minato, Tokyo, Japan
[c] National Institute of Technology, Hachioji, Tokyo, Japan

* goto@ee.tut.ac.jp

Abstract

Spin wave devices are attractive for next-generation information processing. Recently, the spin-wave propagating through magnetic domains or domain walls attract many interests in the field of magnetics because of interesting propagation properties unavailable in uniformly-magnetized spin-wave waveguides. Such spin-wave propagation in magnetic domains or domain walls should occur in any magnetic media, and this is useful for spin-wave logic devices. However, the calculation of magnetic domains in a magnetic garnet, which is the most general magnetic material used as the spin-wave waveguide, has not been reported so far because of the limitation of calculation time and/or speed determined by computational resources. The general size of the magnetic domains in the magnetic garnet is over 1 micron. Thus the amount of mesh, cell, and calculation time is significantly large. To overcome this issue, we used a parallel computing technique for calculating the magnetic domains in the magnetic garnet film. The magnetization state of the magnetic garnet was calculated using a micromagnetic simulator (Fujitsu, EXAMAG). In this study, we calculated the steady magnetization state of magnetic garnet films and the magnetic hysteresis loop. The calculation model was 20 μm × 20 μm × 2 μm and 10 μm × 10 μm × 2 μm for each calculation. The cell size was 80 nm × 80 nm × 80 nm. We used five parallel calculations, and the total core number was 128. The steady magnetization state of magnetic garnet films at zero magnetic fields was calculated using the energy minimization method. Then, the magnetic hysteresis loop of the magnetic garnet film was calculated. The external magnetic field applied perpendicular to the magnetic garnet films was varied from ±50 mT. The total magnetization was calculated with the various external magnetic field, showing a clear magnetic hysteresis loop. The calculated results showed the maze-shaped magnetic domains and the magnetic hysteresis loop, similar to the experiments.

Keywords: *Micromagnetic, Magnetic garnet, Domain, Parallel computing*

Introduction

The information processing technology is developing with complementary metal-oxide-semiconductor (CMOS)-based computing devices, but the speed of the development is decreasing in recent years. Thus, other devices replaceable with the CMOS, so-called beyond CMOS devices, are developing widely. Spin-wave device (e.g., Goto, 2021; Goto et al., 2019) is promising among the beyond CMOS devices because of low heating property and interesting wave functionalities. A spin wave is a collective wave composed of magnetic moments in a magnetic material. Most spin-wave devices have been used uniformly magnetized materials for waveguides. In contrast, recently, the spin-waves propagating in nonuniformly-magnetized materials showing magnetic domains attract many interests because of their functionalities (e.g., Wagner et al., 2016; Wojewoda et al., 2020). However, there is a few reports of the calculation of magnetic domains. In particular, magnetic domains in an iron garnet, which is the promising magnetic material used as the spin-wave waveguide, have not been reported so far. To simulate the magnetic domains in the iron garnets, we used micromagnetic simulation, calculating the motion of magnetic moments. The magnetic domains occur only in the sufficiently large model compared with the domain size. Thus the amount of mesh or cell is significantly large, and the calculation takes a long time. Hence, we used parallel computing.

Calculation Method

We used the micromagnetic simulator (Fujitsu EXAMAG version 2.2.4) with a parallel computing technique. The parallel computer (TUT HPC cluster system) is composed of 128 cores (Intel Xeon Gold 6132 processor) with a memory of 960 GB.

Calculated Magnetic Domains

The model has assumed a typical iron garnet film, but the size was reduced because of the preparation difficulty of the mesh model. The dimension of the calculation model was 20 μm × 20 μm × 2 μm. The model size was

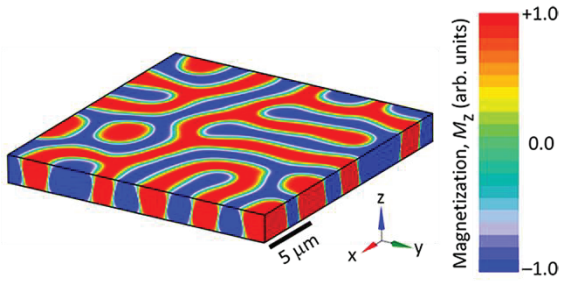

Figure 1. Calculated magnetization state of a iron garnet film. The *z*-component of the magnetization was shown in the contour style. The calculated width of the magnetic domain was about 3 μm.

sufficiently larger than the domain size observed in the experiment. The cell size was 80 nm × 80 nm × 80 nm, the number of cells was 4.770 × 10^6. Saturation magnetization was 40 mT. The exchange coupling constant was 7 pJ/m. The anisotropic magnetic field was 31.35 mT (= 2.5 × 10^4 A/m). The steady magnetization state of this film at zero magnetic fields was calculated using the energy minimization method (Tanaka et al., 2017). This method determined the magnetization states in which the magnetic energy is locally minimized.

This calculation took about 30 minutes. Figure 1 shows the result of the steady state simulation. The z-component of magnetization was shown as contour style. The maze-type magnetic domains were generated. The width of the calculated magnetic domains was ~3 μm. The size of the domain wall was ~0.3 μm, and the type of domain wall was Bloch. The widths of the domain wall were defined as the distance between two points showing the magnetization of +1/e and –1/e. The remanent area was defined as the domain. A similar maze-type domain was also observed in experiments using iron garnet films (Goto et al., 2016), but the width of the domain and the domain walls were different because of the difference in the magnetic properties of the film.

Calculated Magnetic Hysteresis Loop

A magnetic hysteresis loop was calculated by changing the applied field in order to obtain the measurable magnetic parameters from this simulation. In this simulation, the model size was reduced to 10 μm × 10 μm × 2 μm for speeding up without changing the results. Other parameters were the same as the previous calculation. A bias magnetic field was applied perpendicular to the garnet plane. The field intensity was varied from –50 to +50 mT. The initial magnetization curve was also calculated.

This calculation took about 1.5 hours. Figure 2 showed the calculated magnetic hysteresis loop of the iron garnet film. The coercivity was 3 mT. The remanent magnetization was 0.96. In the range of 3–15 mT, the magnetic domain walls were moved, and magnetic domains were disappeared at the magnetic field of 20 mT. In the range of 20–50 mT, the in-plane directions of

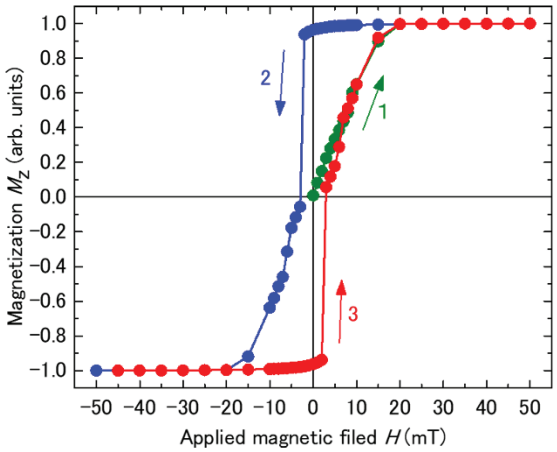

Figure 2. Calculated magnetic hysteresis loop of the iron garnet film. The magnetic field was applied perpendicular to the film plane.

magnetization were rotated, and these were oriented to the *z*-direction. These phenomena were also observed in experiments (Morimoto et al., 2017). The difference would be reduced by using the measured magnetic parameters.

Conclusions

The maze-type magnetic domains in the iron garnet films were calculated using micromagnetic simulation with parallel computing technique. And the magnetic hysteresis loop was also calculated. These results were qualitatively similar to the experiment, but further optimization of the calculation model is required. Spin-wave propagation properties would be calculated using these magnetic domain patterns. Therefore, this study becomes an important milestone for developing spin-wave devices.

Acknowledgements

This work was partly supported by Grants-in-Aid for Scientific Research (KAKENHI) Nos. 20H02593, 19H00765, 20K20535 from the Japan Society for the Promotion of Science (JSPS), the Research Foundation for the Electrotechnology of Chubu, and the Foundation for Technology Promotion of Electronic Circuit Board. We also acknowledge Prof. Hironaga Uchida, Prof. Yuichi Nakamura, Toyohashi University of Technology Information Media Center (IMC), and Shin-Etsu Chemical Co., Ltd. for their support.

References

Goto, T. (2021). Logic device using spin wave interference propagating in a magnetic insulator (Review). *Oyo Buturi*, 90, 172.

Goto, T., Morimoto, R., Pritchard, J. W., Mina, M., Takagi, H., Nakamura, Y., Lim, P. B., Taira, T., & Inoue,

M. (2016). Magneto-optical Q-switching using magnetic garnet film with micromagnetic domains. *Optics Express*, 24, 17635.

Goto, T., Yoshimoto, T., Iwamoto, B., Shimada, K., Ross, C. A., Sekiguchi, K., Granovsky, A. B., Nakamura, Y., Uchida, H., & Inoue, M. (2019). Three port logic gate using forward volume spin wave interference in a thin yttrium iron garnet film. *Scientific Reports*, 9, 16472.

Tanaka, T., Furuya, A., Uehara, Y., Shimizu, K., Fujisaki, J., Ataka, T., & Oshima, H. (2017). Speeding Up Micromagnetic Simulation by Energy Minimization With Interpolation of Magnetostatic Field. *IEEE Transactions on Magnetics*, 53, 1.

Morimoto, R., Goto, T., Taira, T., Pritchard, J., Mina, M., Takagi, H., Nakamura, Y., Lim, P. B., Uchida, H., & Inoue, M. (2017). Randomly polarised beam produced by magnetooptically Q-switched laser. *Scientific Reports*, 7, 15398.

Wagner, K., Kákay, A., Schultheiss, K., Henschke, A., Sebastian, T., & Schultheiss, H. (2016). Magnetic domain walls as reconfigurable spin-wave nanochannels. *Nature Nanotechnology*, 11, 432.

Wojewoda, O., Hula, T., Flajšman, L., Vaňatka, M., Gloss, J., Holobrádek, J., Staňo, M., Stienen, S., Körber, L., Schultheiss, K., Schmid, M., Schultheiss, H., & Urbánek, M. (2020). Propagation of spin waves through a Néel domain wall. *Applied Physics Letters*, 117, 022405.

Mechanical Property Changes of Austenitic Stainless Steels by Severe Plastic Deformation and Subsequent Aging

F.J. Mweta, Y. Todaka * and N. Adachi

Department of Mechanical Engineering, Toyohashi University of Technology, Toyohashi, Aichi, Japan

* E-Mail Address of the corresponding author: todaka@me.tut.ac.jp

Abstract

In this study, high-pressure torsion (HPT) straining, which can effectively induce grain refinement into nanometer regime of bulk metals and alloys, and subsequent aging were performed to investigate the strengthening limit of SUS316LN austenitic stainless steel (ASS). An HPT disk was held between two anvils and was torsion-strained under the compressive stress of P = 5 GPa at the rotation speed of ω = 0.2 rpm at room temperature by using HPT apparatus. After HPT straining, the aging process was performed in the salt bath at 500 °C. The Vickers hardness, HV, in the sample processed by HPT straining and the increment of HV, ΔHV, by aging were measured by Vickers hardness test.

The SUS316LN ASS (316LN) after HPT straining has a homogeneous nanostructure with a grain size of several tens of nanometers. No martensitic transformation was detected even after HPT straining because of high N concentration (0.18 mass%N). While, in the SUS316L ASS (316L) without N, the martensite phase was seen after HPT straining. It was found that the deformation induced phase transformation occurred from austenite to martensite.

The HV of the HPT-processed 316LN samples (HPT) increased with the increase in the Hencky equivalent strain, ε_{eq}, and reached the value of 5.2 GPa. The maximum HV of the sample after HPT straining and subsequent aging (HPT+A) was the value of 6.4 GPa. The ΔHV by aging also increased with the increase in ε_{eq}. It is noteworthy in the age-hardenability that the HV of HPT-processed sample reached its almost maximum value after aging for just 1 min. The HPT sample exhibited the high tensile strength of 2.0 GPa and the large fracture elongation of 17 %. The tensile strength increased by ageing up to 2.5 GPa with the fracture elongation of 6 %.

From the results of small-angle X-ray and neutron scattering (SAXS and SANS) experiments, it seems that the formation off-stoichiometric chromium nitrides by HPT straining and subsequent aging plays the important roles in the development of superior mechanical properties.

Keywords: *SUS316LN austenitic stainless steel, high-pressure torsion (HPT) straining, aging, Vickers hardness, tensile property*

Introduction

Austenitic stainless steels (ASSs) are one of the most important materials and widely utilized as basic a structural material. However, the low mechanical strength of the ASSs is the main obstacles hindering its application. Much attention has been drawn in the past decades to strengthen the ASSs and various approaches have been developed, such as varying its chemical compositions to induce solid solution hardening and grain refinement.

Nitrogen is used instead of carbon as an austenite stabilizer and solution hardener in the ASSs. The ASSs with higher concentration of nitrogen show superior hardness after cold-working and subsequent aging (Narita (2016)), such as SUS316LN ASS.

Recent studies have reported that the heavy cold rolling of SUS316LN ASS produced characteristic heterogeneous nanostructure composed of twin domains, shear bands and low-angle lamellae (Miura, Kobayashi, Todaka, Watanabe, Aoyagi, Sugiura, and Yoshinaga (2017), Watanabe, Kobayashi, Aoyagi, Todaka, Kobayashi, Sugiura, Yoshinaga, and Miura (2020), Koga, Suzuki, Jiang, Watanabe, Aoyagi, Kobayashi, and Miura (2020)). The SUS316LN ASS with such heterogeneous nanostructure produced by heavy cold-rolling and subsequent aging exhibited high tensile strength and large ductility (Miura, Kobayashi, Todaka, Watanabe, Aoyagi, Sugiura, and Yoshinaga (2017)).

To achieve grain refinement down to nanometer-size, various severe plastic deformation (SPD) processes have been developed, such as accumulative roll bonding (ARB), equal channel angular pressing (ECAP) and high-pressure torsion (HPT) straining (Valiev, Islamgaliev, and Alexandrov (2000), Saito, Tsuji, Utsumoniya, Sakai, and Hong (1998)). HPT process can be attained extreme grain refinement compared with other SPD processes.

In this study, the mechanical property changes of SUS316LN ASS (316LN) by HPT straining and subsequent aging were investigated. Small-angle X-ray and neutron scattering (SAXS and SANS) experiments

were performed to clarify the origin of the superior mechanical properties.

Experimental Procedure

The experiments were conducted using SUS316LN ASS (316LN, 0.18 mass%N). For comparison, SUS316L ASS (316L) without nitrogen was also used. The materials were cut and polished into disks (diameter: 10 or 15 mm, thickness: 0.85 mm) for HPT process. The HPT process was carried out using the anvils with the depression of 0.25 mm in depth and 10 or 15 mm in diameter. The disk was held between the two anvils and was torsion-strained (number of revolutions, n : $\leq$ 20 turns, compressive pressure, P : 5 GPa, rotation speed, ω : 0.2 rpm, room temperature). The shear strain, γ, and the equivalent strain of the Hencky strain, ε_{eq}, for HPT straining are given by the following equations:

$$\gamma = \frac{2\pi\, n\, l}{t} \qquad \text{(Eq. 1)}$$

$$\varepsilon_{eq} = \frac{1}{\sqrt{3}} \ln\left(\frac{2+\gamma^2+\gamma\sqrt{4+\gamma^2}}{2} \right) \qquad \text{(Eq. 2)}$$

where l is the distance from the HPT disk center and t is the disk thickness (Onaka (2010)). The HPT disk flowed to a radial direction during HPT straining due to lack of side constraint, resulting in the reduction of thickness to 0.5 mm. After HPT straining, the aging was performed in the salt bath at 500 °C for 1 h.

Microstructure of the HPT-processed sample was observed by transmission electron microscopy (TEM).

The Vickers hardness, HV, in the sample processed by HPT straining and the increment of HV, ΔHV, by aging were measured by Vickers hardness test (load: 4.9 N, holding time: 10 s).

The tensile test (initial strain rate: 1×10^{-3} s^{-1}) was carried out using the sample with gauge dimensions of width × length × thickness = 0.6 × 2.0 × 0.45 mm^3 at l = 3 mm. The tensile direction is parallel to shear direction applied in the HPT process. An elongation during the tensile test was in-situ measured by charge-coupled device (CCD) camera.

Small-angle X-ray and neutron scattering (SAXS and SANS) experiments were performed to characterize microstructure of the samples. The SAXS experiments were performed using Mo-$K\alpha$ radiation (Rigaku Nano-Viewer), with the incident X-rays being focused using a two-dimensional confocal mirror (beam size: < 1 mm). A two-dimensional detector (Rigaku PILATUS 1π00k) was positioned ~1360 mm away from the samples. The SAXS samples were prepared by cutting the HPT-processed disks into disk-shaped samples with a diameter 4 mm centered at l = 3 mm and polishing them to a thickness of approximately 30 μm. The thicknesses of the SAXS samples were estimated from their X-ray transmission rates and line absorption factors. The measured SAXS intensities were converted into absolute units using glassy carbon samples provided by Argonne National Laboratory as a secondary standard (Zhang, Ilavsky, Long, Quintana, Allen, and Jemian (2010)). The data processing software Irena, which was developed by Ilavsky *et al.* at Argonne National Laboratory, was used for the purpose (Ilavsky, and Jemian (2009)). The SANS measurements were performed using the BL-20 iMATERIA beamline of the Materials and Life Science Experimental Facility at the Japan Proton Accelerator Research Complex (J-PARC) (Ishigaki, Hoshikawa, Yonemura, Morishima, Kamiyama, Oishi, Aizawa, Sakuma, Tomota, Arai, Hayashi, Ebata, Takano, Komatsuzaki, Asano, Takano, and Kasao (2009)). The samples for the SANS were prepared by stacking four HPT-processed disks to a total thickness of 2 mm. The neutron beam size of 8 mm was used. The SANS intensities obtained were all converted into absolute units.

Results and Discussion

Figure 1 shows the TEM image of the 316LN after HPT straining. The area about l = 5 mm away from the HPT disk center was observed from the direction parallel to the shear direction of HPT straining. A homogeneous nanostructure with a grain size of several tens of nanometers was observed. No martensitic transformation was detected even after HPT straining. While, in the 316L after HPT straining, the martensite phase was seen in X-ray diffraction measurement. It was found that the deformation induced phase transformation occurred from austenite to martensite. (Wang, Umemoto, Shuro, Todaka, and Kuo (2011), Wang, Shuro, Umemoto, Kuo, and Todaka (2012)) Hereafter, the investigation is focused on the 316LN because of its highly stability of austenite phase.

Figure 2 shows the Vickers hardness, HV, of the 316LN after HPT straining and subsequent aging as a function of Hencky equivalent strain, ε_{eq}. The HV of the as-HPT samples (HPT) increased with the increase in ε_{eq}, and showed the constant value of about 5.2 GPa with ε_{eq} > 5 (n = 20, l > 0.5 mm). The homogeneous nanostructure shown in Fig. 1 seems to form in the region of ε_{eq} > 5. The maximum HV of the sample after HPT straining and subsequent aging (HPT+A) was the value of 6.4 GPa. The increment in HV, ΔHV, by aging also increased with the increase in ε_{eq}. Figure 3 shows the HV of the HPT-

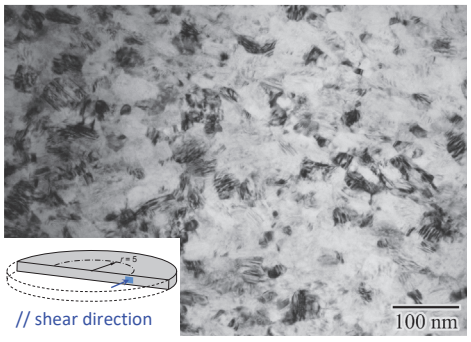

Figure 1 TEM image of 316LN after HPT straining (n = 20, P = 5 GPa, ω = 0.2 rpm).

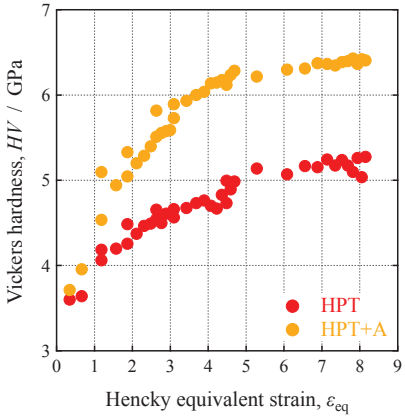

Figure 2 Vickers hardness, *HV*, of 316LN after HPT straining ($P = 5$ GPa, $\omega = 0.2$ rpm) and subsequent aging (500 ℃, 1 h) as a function of Hencky equivalent strain, ε_{eq}.

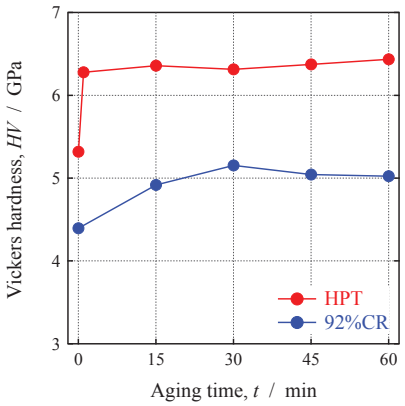

Figure 3 Vickers hardness, *HV*, of HPT-processed ($n = 20$, $P = 5$ GPa, $\omega = 0.2$ rpm) and 92% cold-rolled 316LN after aging at 500 ℃ as a function of aging time, *t*.

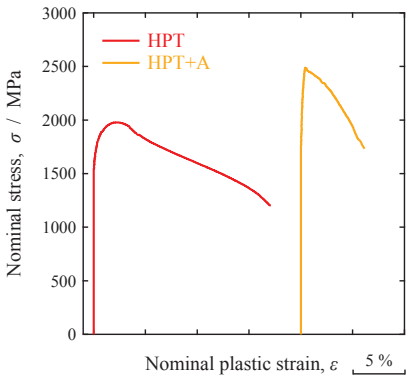

Figure 4 Nominal stress, σ, and nominal plastic strain, ε, curves of 316LN after HPT straining ($P = 5$ GPa, $\omega = 0.2$ rpm) and subsequent aging (500 ℃, 1 h).

processed and 92% cold-rolled samples after aging at 500 ℃ as a function of aging time, *t*. In the both samples, the large ΔHV can be seen. It is noteworthy that the *HV* of HPT-processed sample reached its almost maximum value in just 1 min. The superior age-hardenability seems to be affected by severely deformed nanostructure induced by HPT straining.

Figure 4 shows the nominal stress, σ, and nominal plastic strain, ε, curves of the 316LN after HPT straining and subsequent aging. The HPT sample exhibited the high tensile strength of 2.0 GPa and the large fracture elongation of 17 %. The tensile strength increased by ageing up to 2.5 GPa with the fracture elongation of 6 %, as shown in the HPT+A sample.

Small-angle X-ray and neutron scattering (SAXS and SANS) experiments were performed to clarify the origin of the superior mechanical properties. Figure 5 shows small-angle X-ray and neutron scattering intensity profiles of ND (non-deformed sample before HPT straining), HPT and HPT+A samples of 316LN as a function of a magnitude of q vector which is defined as

$$q = \frac{4\pi \sin(\theta)}{\lambda} \qquad \text{(Eq. 3)}$$

where θ and λ denote half the scattering angle and wavelength, respectively. The difference of scattering intensity between reference and the samples is important to identify the nanostructure introduced by HPT straining and subsequent aging. The small-angle scattering profiles of reference sample (the ND sample) were also shown in the figure. The SAXS intensities $I_X(q)$ of the HPT and HPT+A samples remained almost unchanged comparing with the ND sample. On the other hand, in the SANS experiment, the SANS intensity $I_N(q)$ increased after HPT straining, and the aging after HPT straining caused further increase in $I_N(q)$. Namely, the experimentally obtained $(I_X/I_N)_{exp}$ values in this study are located between 1 and 0. If inhomogeneous bodies such as precipitates in the samples are single phase, small-angle scattering intensity $I(q)$ is theoretically expressed by

$$I(q) = \Delta\rho^2 d \int_0^R N(r)[V(r)F(q,r)]^2 \, dr \qquad \text{(Eq. 4)}$$

where d is the number density of the inhomogeneous bodies, $N(r)$ is the normalized size distribution, $V(r)$ is the volume, and $F(q, r)$ is the form factor of the inhomogeneous bodies with the radius r distributed in the matrix. The value $\Delta\rho$ represents the difference between the scattering length density of the matrix, ρ_m, and that of the inhomogeneous body such as precipitates distributed in the matrix, ρ_i (*i.e.*, $\Delta\rho = \rho_i - \rho_m$). As the $I(q)$ is directly proportional to the square of $\Delta\rho$, the magnitude of $\Delta\rho$ is important to be detected in the small angle scattering experiment. It is well known that scattering length of elements for X-ray increase proportionally with atomic number whereas that for neutron changes complicatedly with atomic number, as shown in Fig. 6. Except for $\Delta\rho$, the parameters in Eq. 4 should be the same irrespective of probe (*i.e.*, X-ray or neutron) because the condition for sample preparation is maintained; the difference between

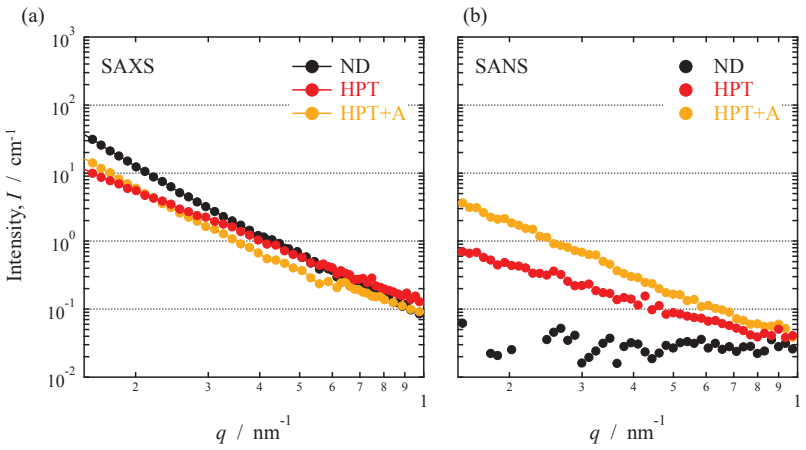

Figure 5 Small-angle scattering profiles of 316LN before/after HPT straining (n = 20, P = 5 GPa, ω = 0.2 rpm) and subsequent aging (500 ℃, 1 h) obtained using (a) X-ray and (b) neutron beams.

$I_X(q)$ and $I_N(q)$ reflects the difference between $\Delta\rho_X$ and $\Delta\rho_N$. Therefore, small-angle scattering intensity ratio $I_X(q)/I_N(q)$ becomes

$$\frac{I_X(q)}{I_N(q)} = \frac{\rho_{X,i} - \rho_{X,m}}{\rho_{N,i} - \rho_{N,m}} = \frac{\Delta\rho_X^2}{\Delta\rho_N^2} \qquad \text{(Eq. 5)}$$

where the subscripts X and N shows X-ray and neutron, respectively. The almost the same $I_X(q)$ between the samples (Fig. 5 (a)) shows that the inhomogeneous bodies formed by HPT straining and subsequent aging have similar ρ with the matrix. Therefore, it can be expected that the formed inhomogeneous bodies mainly consist of the element(s) with similar atomic number (*i.e.*, scattering length) to the matrix. Considering the previous reports and the composition of 316LN, it can be seen that chromium nitride (CrN and Cr_2N) is possible composite detected in the SANS experiment. Assuming that CrN or Cr_2N precipitates in the 316LN matrix, $\Delta\rho_X^2$ and $\Delta\rho_N^2$ were calculated and theoretical small-angle scattering ratios $(I_X/I_N)_{theo}$ was estimated. For the calculation, the density values of CrN and Cr_2N were taken from data base; the densities of CrN and Cr_2N are 6.19 and 6.71 g·cm^{-3}, respectively. The $\Delta\rho_X^2$ and $\Delta\rho_N^2$ of CrN were calculated to be 171.3 × 10^{20} and 50.48 × 10^{20} cm^{-4}. In the case of Cr_2N, $\Delta\rho_X^2$ and $\Delta\rho_N^2$ were 87.4 × 10^{20} and 29.7× 10^{20} cm^{-4}, respectively. From the calculation, it was found that the precipitation of chromium nitride leads to $(I_X/I_N)_{theo}$ value higher than 1, indicating that these phases are not formed in the samples after HPT straining and subsequent aging. The calculation assuming the precipitation of chromium carbide also showed similar trend. While the above calculation assumed the precipitation of stoichiometric chromium nitrides, an off-stoichiometric chromium nitrides are expected to be formed because of the limited diffusion of Cr under the relatively low aging temperature of 500 °C, as shown in Fig. 3. Here, we considered the possibility of the segregation of Cr and N in Fe matrix having a composition of $Cr_{2-X}Fe_XN$ as a precursor of

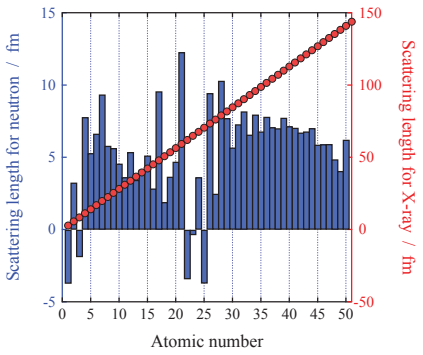

Figure 6 Scattering length of elements for X-ray and neutron plotted as a function of atomic number.

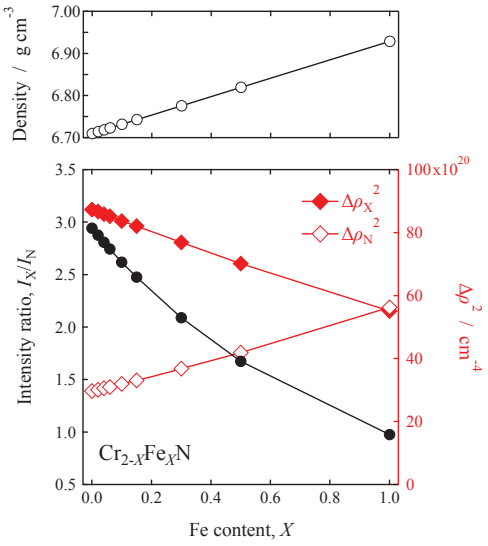

Figure 7 Calculated $\Delta\rho_X^2$, $\Delta\rho_N^2$, and I_X/I_N assuming segregation of Cr and N in Fe matrix. The upper graph of the figure shows the variation of density with composition change.

stoichiometric chromium nitride during HPT straining and aging. As the atomic radii of Fe and Cr are almost the same, variation of lattice constants was assumed to be zero, and variation of density with segregation was considered based on the atomic weight. Figure 7 summarizes the $\Delta\rho^2$ and $(I_X/I_N)_{theo}$ values as a function of Fe content X calculated considering the formation of $Cr_{2-X}Fe_XN$. It can be clearly seen that the increase in X causes increase in $\Delta\rho_N^2$ and decrease in $\Delta\rho_X^2$, and the $(I_X/I_N)_{theo}$ becomes < 1 at around X = 1.

Conclusions

The mechanical property changes of 316LN by HPT straining and subsequent aging were investigated.

The 316LN after HPT straining has a homogeneous nanostructure with a grain size of several tens of nanometers. The *HV* of the HPT-processed 316LN increased with the increase in the ε_{eq}, and reached the value of 5.2 GPa. The maximum *HV* of the 316LN after HPT straining and subsequent aging was the value of 6.4 GPa. The ΔHV by aging also increased with the increase in ε_{eq}. The HPT-processed 316LN exhibited the high tensile strength of 2.0 GPa and the large fracture elongation of 17 %. After aging, the tensile strength increased up to 2.5 GPa with the fracture elongation of 6 %. From the results of SAXS and SANS experiments, it seems that the formation off-stoichiometric chromium nitrides by HPT straining and subsequent aging plays the important roles in the development of superior mechanical properties.

Acknowledgements

The authors thank Prof. Shigeo Sato, Dr. Yohei Noda, Dr. Yojiro Oba, Prof. Hiromi Miura, Prof. Masakazu Kobayashi, Prof. Chihiro Watanabe and Prof. Yoshiteru Aoyagi for fruitful discussions. The neutron diffraction experiment was performed at J-PARC. The SAXS measurements were conducted by using the facilities of the Institute for Integrated Radiation and Nuclear Science, Kyoto University.

This study was conducted under the financial supported by the Japan Science and Technology Agency (JST) under Collaborative Research Based on Industrial Demand "Heterogeneous Structure Control: Towards Innovative Development of Metallic Structural Materials" (Grant No. JPMJSK1413).

References

Ilavsky, J. & Jemian, P.R. (2009). Irena: tool suite for modeling and analysis of small- angle scattering. *Journal of Applied Crystallography*, 42, 347-353.

Ishigaki, T., Hoshikawa, A., Yonemura, M., Morishima, T., Kamiyama, T., Oishi, R., Aizawa, K., Sakuma, T., Tomota, Y., Arai, M., Hayashi, M., Ebata, K., Takano, Y., Komatsuzaki, K., Asano, H., Takano, Y. & Kasao, T. (2009). IBARAKI materials design diffractometer (iMATERIA) - Versatile neutron diffractometer at J-PARC. *Nuclear Instruments and Methods in Physics Research Section A: Accelerators, Spectrometers, Detectors and Associated Equipment*, 600, 189-191.

Koga, N., Suzuki, S., Jiang, H., Watanabe, C., Aoyagi, Y., Kobayashi, M. & Miura H. (2020). Characterization of heterogeneous-nano structure in austenitic stainless steel: crystal orientations and hardness distribution. *Journal of Materials Science*, 55, 9299-9310.

Miura, H., Kobayashi, M., Todaka, Y., Watanabe, C., Aoyagi, Y., Sugiura, N. & Yoshinaga, N. (2017). Heterogeneous nanostructure developed in heavily cold-rolled stainless steels and the specific mechanical properties. *Scripta Materialia*, 133, 33-36.

Narita, S. (2016). Stainless steels and precipitation hardening Ni-based alloy with high strength and high corrosion resistance. Materia Japan, 55, 464-467.

Onaka, S. (2010). Equivalent strain in simple shear deformation described by using the Hencky strain, *Philosophical Magazine Letters*, 90, 633-639.

Saito, Y., Tsuji, N., Utsumoniya, H., Sakai, T. & Hong, R.G. (1998). Ultra-fine grained bulk aluminum produced by accumulative roll-bonding (ARB) process, *Scripta Materialia*, 39, 1221-1227.

Valiev, R.Z., Islamgaliev, R.K. & Alexandrov, I.V. (2000). Bulk nanostructured materials from severe plastic deformation, *Progress in Materials Science*, 45, 103-189.

Wang, H., Shuro, I., Umemoto, M., Kuo, H. & Todaka, Y. (2012). Annealing behavior of nano-crystalline austenitic SUS316L produced by HPT, *Materials Science & Engineering A,* 556, 906-910.

Wang, H., Umemoto, M., Shuro, I., Todaka, Y. & Kuo, H. (2011). Magnetic characterization of SUS316L deformed by high pressure torsion, *Advanced Materials Research*, 239-242, 1300-1303.

Watanabe, C., Kobayashi, S., Aoyagi, Y., Todaka, Y., Kobayashi, M., Sugiura, N., Yoshinaga, N. & Miura, H. (2020). Heterogeneous nano-structure and its evolution in heavily cold- rolled SUS316LN stainless steels. *ISIJ International*, 60, 582-589.

Zhang, F., Ilavsky, J., Long, G.G., Quintana, J.P.G., Allen, A.J. & Jemian, P.R. (2010). Glassy carbon as an absolute intensity calibration standard for small-angle scattering. *Metallurgical and Materials Transactions A*, 41A, 1151-1158.

Formation mechanism of micro-arc and coating by plasma electrolytic oxidation of titanium

Toshiaki Yasui[*,a], Katsuki Hayashi[a] and Masahiro Fukumoto[a]

[a] Department of Mechanical Engineering, Toyohashi University of Technology, Toyohashi, Japan

*yasui@tut.jp

Abstract

Plasma electrolytic oxidation (PEO) of titanium alloy is useful for application of implant due to its porous oxide coating on it. PEO is a kind of anodizing process with accompanying generation of small and minute spark discharge (micro-arc) on the anode surface. The micro-arc forms the oxide coating on the anode surface through the processes of melting, oxidation, and solidification. From the observation of single discharge crater and the behaviour of micro-arc, ejected material and bubble during PEO, formation mechanisms of PEO coating for Ti was investigated. Ejection of anode metal by micro-arc fabricate a central hole and petal shape burr around the hole. However, there is no bubble burst during PEO for Ti. Thus, the ejected metal is not pressed and flattened on the anode, and the central hole remains as porous structure in the coating of PEO for Ti.

Keywords: *plasma electrolytic oxidation, PEO, micro-arc, discharge crater, titanium*

Introduction

Plasma electrolytic oxidation (PEO) is a kind of anodizing process with accompanying generation of small and minute spark discharge (micro-arc) on the anode surface. The process fabricates oxide coating on light metals, such as aluminum and titanium, and greatly improves the anti-wear and corrosion resistance of the metals. The fabricated coating structures differ with metals and process. Thus, active research has been conducted for effective process control and improvements (e.g., Clyne and Troughton, 2019).

Titanium alloys are light weight, high strength, and high biocompatibility, and applied to medical application such as implants. PEO process is applied for fabrication of functional coating on the implant. (e.g., Kazek-Kęsik, Krok-Borkowicz, Pamuła and Simka, 2014; Wang, Chen, and Zhao, 2015). In the PEO process, micro-arc melt, vaporize and eject metals from the anode. The ejected metals are cooled and oxidized by electrolyte solution, form discharge craters, and fabricate coating on the anode. The discharge features are different in metals and process conditions, and affect coating microstructures. In case of Ti alloy, a porous oxide coting is fabricated on the anode. However, the discharge and coating formation mechanisms are not clear. It is important to understand the mechanisms for control of microstructure and function of coating. In this study, the formation mechanism of micro-arc and coating by PEO for Ti alloy was investigated. The discharge features of micro-arc were observed with high-speed camera. The coating was evaluated with the morphology observation, the surface roughness and the friction coefficient.

Experimental Methods

Figure 1 shows the experimental apparatus of PEO for Ti and micro-arc observation. Table 1 shows the experimental conditions. A rectangular β-titanium alloy plate was used as a specimen and an anode. A rectangular SUS410 plate was used as a cathode. The anode and the cathode were immersed in the electrolyte solution of phosphoric acid and sulfuric acid. Outside the treatment area of the anode was masked with fluorine resin tape. DC power source was connected between the anode and the cathode for generation of micro-arc on the anode. The micro-arc behaviour was observed from the front of the

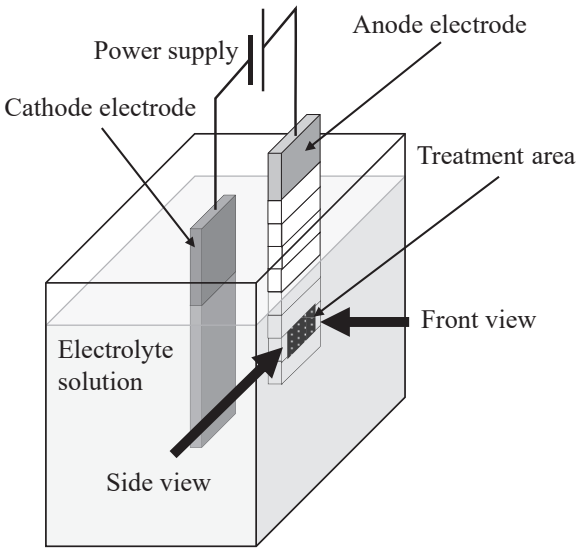

Fig.1 Experimental apparatus of PEO for Ti and observation direction of micro-arc, ejected materials and bubbles.

anode by a high-speed camera (Photron, FASTCAM Mini AX200) at 100,000 fps. The behaviour of ejected materials and generated bubbles by micro-arc was observed from the side edge of anode by high-speed camera at 25,000 fps.

Effect of voltage and current on micro-arc and coating were investigated with three patterns of operating conditions of DC power supply as shown in Table 2. In order to understand the formation mechanism of coating, it is necessary to observe a single discharge crater. the discharge current was supplied from a capacitor bank for short treatment time less than 0.1 s at small treatment area of 1 mm^2 as a single pulse operation.

Table 1 Electrode materials and electrolyte solution for PEO of Ti

Anode electrode	β-titanium alloy (Ti-15V-3Cr-3 Sn-3Al)
Cathode electrode	SUS410
Electrolyte solution	H_2PO_4 (0.1mol/L) + H_2SO_4 (0.1mol/L)

Table 2 Operating conditions of power supply

Operating condition	Voltage (V)	Current density (kA/m^2)	Treatment area(mm^2) / time(s)
Constant voltage (CV)	200, 500	-	50 / 60
Constant current (CC)	-	1.0, 3.0	50 / 60
Single pulse	Charge voltage: 500	-	1 / <0.1s

The morphology of coating and discharge crater were observed with scanning electron microscope. The surface roughness of the coatings was measured with laser microscope (OLYMPUS, OLS31-SU). The friction coefficient of coatings at dry condition was evaluated with friction test by surface property tester (SHINTO Scientific, TYPE:14FW). The experimental setup and test conditions are shown in Fig.2 and Table 3.

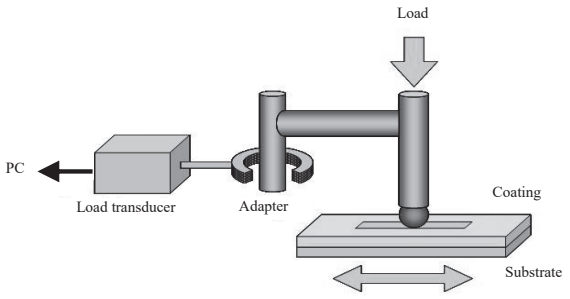

Fig. 2 Experimental setup for friction test.

Table 3 Friction test conditions

Counterpart	SUJ2 (ϕ3mm)
Load	0.98 N
Friction speed	5 mm/s
Friction distance	5 mm
Number of repetitions	30
Ambient	No lubricant

Results and Discussion

Figure 3 shows the cross section and surface morphology of PEO coating with different operating conditions of power supply. As for constant voltage (CV) operation, discharge current increased with time and reached at maximum current density of 7.83 kA/m^2 for 200 V and 10.6 kA/m^2 for 500 V. The coating thickness increases with voltage. However, the discharge craters on the surface becomes small and increases with voltage. At 200V, a number of discharge craters form short strings on the anode. At 500V, the discharge craters join with neighboring craters, and form a coating. It is difficult to distinguish each discharge crater.

As for constant current (CC) operation, discharge voltage gradually increased with time and reached at a maximum voltage of 233 V for 1.0 kA/m^2 and 249 V for 3.0 kA/m^2. There is no obvious change of morphology and thickness of coating for CC operation. Although, the discharge crater join with neighboring craters, it is possible to distinguish each discharge crater. The size of each discharge crater for CC operation is lager than that for CV operation.

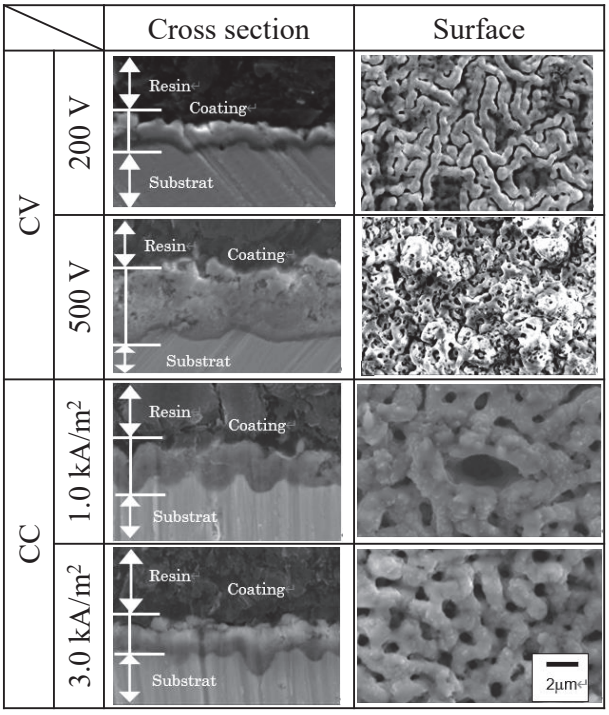

Fig. 3 Cross section and surface morphology of PEO coating by CV operation and CC operation.

Table 4 shows the surface roughness and friction coefficient of coatings. As for CV operation, surface roughness increase with discharge voltage. However, the firiction coefficient decrease with discharge voltage. At CV operation of less than 400V, the coating is easily damaged and peal off. As for CC operation, the roughness and friction coefficient are low and decrease with discharge current. At CC operation of 1.0 kA/cm^2, the coating is damaged and peal off. Thus, the coating damage is small for CV operation for 500V and CC operation for 3.0 kA/m^2 achieved low friction coefficient.

Table 4 Surface roughness and friction coefficient of treated surface

		Roughness (μm)	Friction coefficient
No treatment		-	0.315
CV	200 V	0.3641	0.196
	500 V	0.9875	0.082
CC	1.0 kA/m^2	0.2642	0.197
	3.0 kA/m^2	0.2591	0.144

Figure 4 show the micro-arc on the anode surface by different operating condition with elasped time. As for CV operation of 500 V, the micro-arc is widely distributed on the anode surface. The emission intensity of micro-arc becomes strong with the time. On the other hand, the micro-arc are small and weak for CC operation. During the PEO for CC operation, the voltage increases with the time and drop after This leads to change of surface morphology as shown in Fig.3.

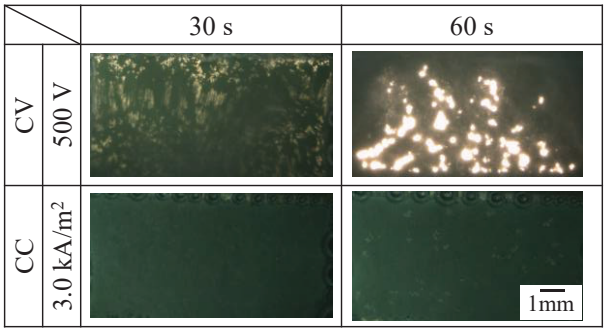

Fig. 4 Observation of micro-arc from front during PEO by CV operation and CC operation.

Figure 5 shows the high-speed camera observation of micro-arc from front during PEO by single pulse operation for the first 110 μs. The peak voltage was 492 V and the peak current was 0.354 A. Small and minute spark discharge (micro-arc) are generated on the anode. Although the discharge diameter ranges from about 8 to 100 μm, it is difficult to distinguish the individual discharges due to the limitation of resolution of the observation system. The discharge time of micro-arc is less than 40 μs.

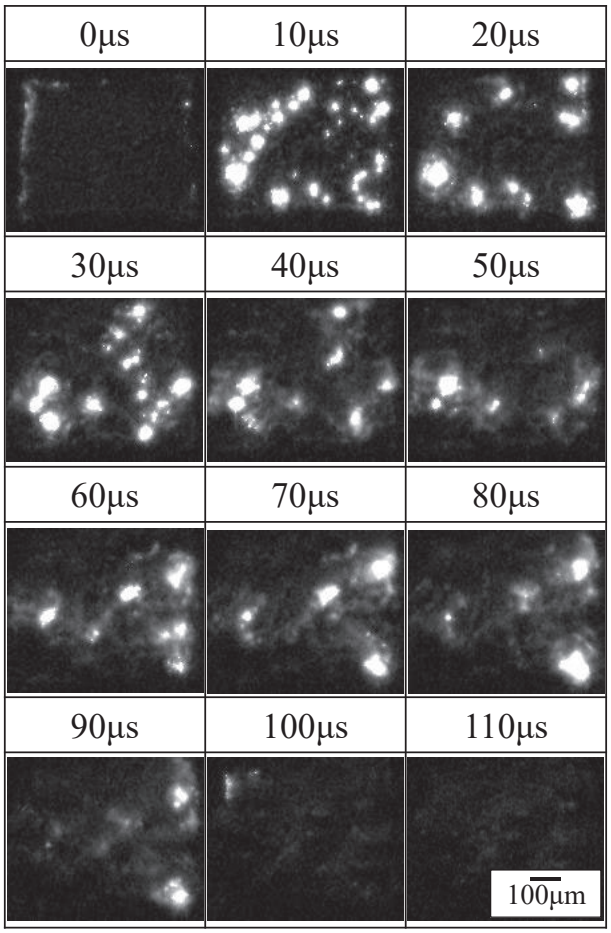

Fig.5 High-speed camera observation of micro-arc from front during PEO by single pulse operation.

Figure 6 shows the single discharge crater on the anode surface fabricated by single pulse operation of power supply. The discharge craters have a central hole of about 0.3 μm in diameter and petal shape burr of 1 μm in diameter around the hole. It is considered that the burr was fabricated by the ejected metals from the hole on the center.

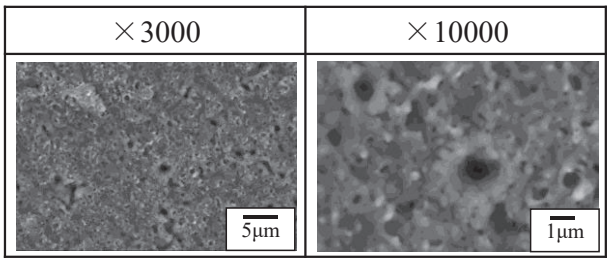

Fig. 6 Discharge crater of Ti fabricated by single pulse operation.

Figure 7 shows the high-speed camera observation of ejected materials and generated bubble by micro-arc for PEO by single pulse operation. The ejected materials and generated bubbles were observed from the side edge of anode as shown in Fig.1. The anode with uneven surface

is in the bottom of each photo. A small ejection from anode surface is observed at 40 μs and moves upwards at 80 μs. This is thought to be the effect of ejected metals from the anode. This ejection expands and changes the morphology of the anode surface from 120 to 160 μs. The discharge time of each micro-arc is less than 40 μs as shown in Fig.5. Thus, this change is the effect number of micro-arc. After that, the ejection spread over the anode surface, destruct the former surface structure, and reconstruct the surface structure.

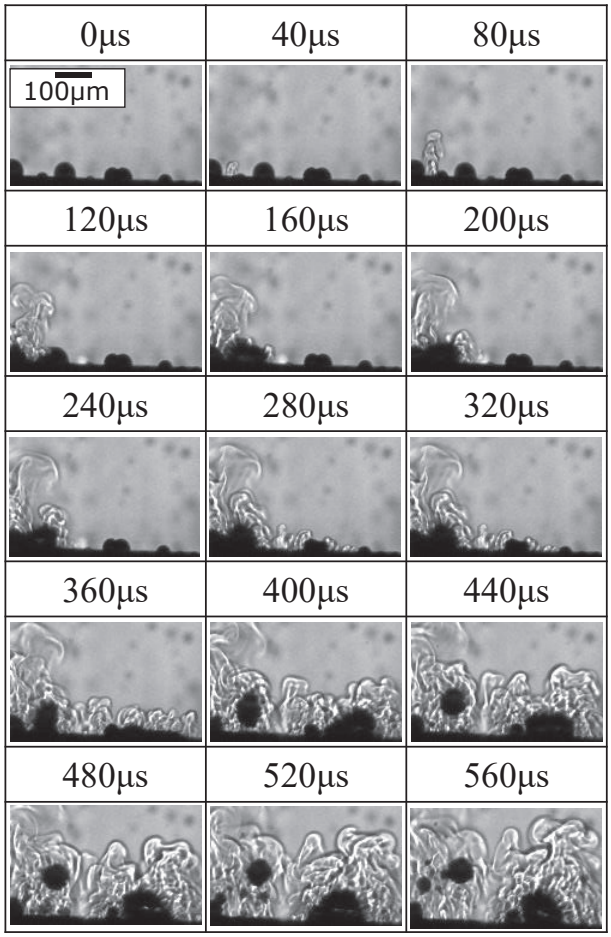

Fig. 7 High-speed camera observation of ejected materials and generated bubbles from the side edge of anode for PEO by single pulse operation.

In case of PEO for Al, the ejected metal from the anode was pressed onto the anode surface by bubble burst around the micro-arc as shown in Fig.8 (Nishikawa, Yasui and Fukumoto, 2012). The shape of discharge crater is similar to a flattening shape of thermal sprayed splat (Fukumoto, Yamaguchi, Yamada and Yasui, 2007). However, the morphology of discharge crater for Ti (Fig.6) differ with the discharge crater for Al. As shown in Fig.7, there is no bubble burst in this experiment. The ejected metals from the anode were not pressed and flattened on the anode. Thus, the central hole remains as porous structure in the coating of PEO for Ti.

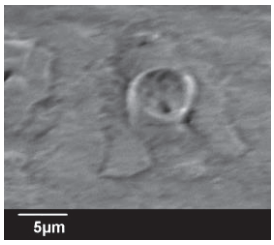

Fig.8 Discharge crater of Al fabricated by single pulse operation. (Nishikawa, Yasui and Fukumoto, 2012)

Conclusions

In this study, the formation mechanism of micro-arc and coating by PEO for Ti alloy was investigated and following results are obtained.

1) As CV operation, discharge craters on the surface becomes small and increases with voltage. surface roughness increase with discharge voltage. However, the firiction coefficient decrease with discharge voltage.
2) As for CC operation, there is no obvious change of morphology and thickness of coating for current density. The roughness and friction coefficient decrease with current density.
3) From the single pulse operation, the discharge craters have a central hole and petal shape burr around the hole. However, there is no bubble burst during PEO for Ti. Thus, ejected metals from the anode were not pressed and flattened on the anode, and the central hole remains as porous structure in the coating of PEO for Ti.

Acknowledgements

Author would like to thank to Prof. Yanada of Toyohashi University of Technology for cooperation of friction test.

References

Clyne, T. W. & Troughton, S. C. (2019). A review of recent work on discharge characteristics during plasma electrolytic oxidation of various metals. *International Materials Review*, 64, 127-162.

Fukumoto, M., Yamaguchi, T., Yamada, M. & Yasui, T. (2007). Splash splat to disk splat transition behavior in plasma-sprayed metallic materials. Journal of Thermal Spray Technology, 16, 905-912.

Kazek-Kęsik, A., Krok-Borkowicz, M., Pamuła, E., & Simka, W. (2014). Electrochemical and biological characterization of coatings formed on Ti–15Mo alloy by plasma electrolytic oxidation. *Materials Science and Engineering C,* 43, 172-181.

Nishikawa, R., Yasui, T., & Fukumoto, M. (2012). Influence of micro-arc and bubble on film formation by

plasma electrolytic oxidation. Proc. of 5th International Conference on Plasma Nanotechnology and Science (IC-PLANTS2012), P-15.

Wang, Y., Yu, H. Chen, C. & Zhao, Z. (2015). Review of the biocompatibility of micro-arc oxidation coated titanium alloys. Materials and Design, 85, 640-652.

Evaluation of Electrode Design of a Microfluidic Impedance Biosensor for DNase Assay

Kanta Nishibayashi[a], Seimei Oku[a] , Takahiro Himuro[a] and Masanori Eguchi[*, a]

[a] Department of Electrical Engineering and Information Science, National Institute of Technology, Kure College, Kure, Japan

*m-eguchi@kure-nct.ac.jp

Abstract

A deoxyribonuclease (hereinafter, this is called "DNase") is a protein found in blood and other body fluids. DNase is deeply involved in deoxyribonucleic acid metabolism in the cell. DNA is known to be dissolved by DNase. It is also known that the activity of DNase differs depending on the disease. In recent years, this DNase characteristics have been studied as a diagnostic biomarker for various diseases. Our group has developed a device to detect DNase using a pair of electrodes and a microfluidic channel. The tip shape of the paired electrodes is triangular to immobilize DNA by generating a non-uniform electric field. DNase is detected by the difference in impedance of the electrodes before and after DNA immobilization. In this paper, a model of DNA (width: 1 µm, height: 1 µm, length: 16 µm, dielectric constant: 8, conductivity: 2.89mS/m) is used for analysis. The complex impedance locus was drawn as a semicircular arc (Cole-Cole plot). From the results, it was found that the equivalent circuit of DNA and electrodes can be represented by a parallel circuit of resistance and capacitance. The impedance of the electrodes after DNA dissolution is larger than the impedance of the electrodes after DNA immobilization. The more the DNA is dissolved, the larger the impedance becomes. We also measured the change in impedance depending on the shape of the electrode. The impedance of the electrodes before DNA immobilization decreased as the surface area increased. The number of needles (triangular electrodes) had no significant effect on the impedance. On the other hand, after DNA immobilization, the impedance decreased as the number of needles increased. And changes of surface area did not significantly affect the impedance. The ideal electrode is the one that shows significant changes before and after the DNA immobilization. Therefore, the ideal electrode shape was found to be the one with a small surface area and a large number of needles.

Keywords: *DNase, Biomarker, DNA immobilization, Impedance biosensor, Complex impedance plot*

Introduction

DNase is a protein which found in blood and other body fluids. It is deeply involved in intracellular DNA metabolism. It plays an important role in vivo. When we suffer from gastric, colorectal, and pancreatic cancer, they show lower DNase activity than healthy person. On the other hand, patients with breast cancer, oral cancer (Lauková, 2020) and acute myocardial infarction (Yasuda, 2005) have been reported to show high DNase activity. Therefore, it has been suggested that DNase may be one of the susceptibility genes for both the former and the latter.

In recent years, DNase biosensors have been studied for diagnosis of various diseases. We have proposed DNase-detecting method using immobilized DNA for measuring DNase activity (Himuro, 2019). The purpose of this study is to demonstrate the usefulness of the proposed method of DNase detection. In addition, the sensitivity of DNase detection is improved by the shape of the electrode. A calculation model of DNA is indispensable for electromagnetic calculation. However, the actual DNA is a double-helix structure consisting with long, thin, and flexible molecules. Since it is difficult to accurately model DNA, it was hypothesized that the DNA is stretched and immobilized in bundles between the electrodes. It has also been known that DNA can conduct electric current under certain conditions, but its electrical characteristics have not yet been specified in detail. Therefore, the electrical characteristics were assumed by previous studies and analyzed.

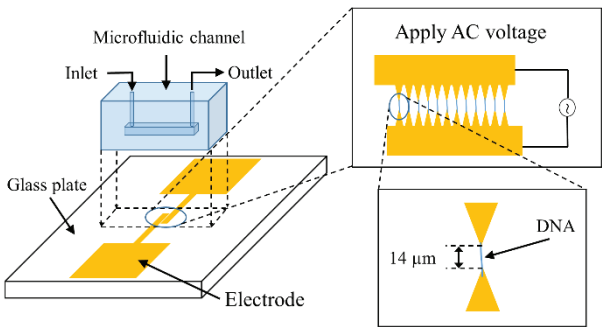

Figure 1. Device structure

Method and device structure

The device for DNase detection used in the proposed method is shown in Figure 1. The device consists of a pair of aluminum electrodes and a microfluidic channel (PDMS, width: 500 µm, height: 50 µm, length: 10 mm) on a glass plate. The tip of the electrodes consists of 12 needles. When an AC voltage is applied to the electrodes, high electric field is produced around the needle tip. Therefore, DNAs in the solution injected into the microchannel can be immobilized between the needles due to electrostatic-orientation, as shown in Figure 2. After that, the impedance between electrodes with immobilized DNAs changes due to dissolving or them by injecting DNase included solution through microfluidic channel. Furthermore, if the number of dissolved DNA changes due to the difference in DNase activity of the solution, it is expected that the impedance change.

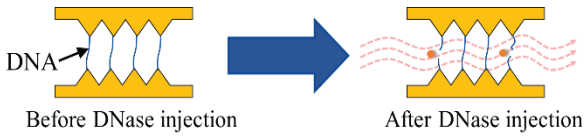

Figure 2. Before and after DNase injection

Experiments and results

In this study, calculation model of DNAs (width: 1 µm, height: 1 µm, length: 16 µm, relative permittivity: 8, conductivity: 2.89 mS/m) is used (Yamahata, 2008, Cuervoa 2014, Oku, 2021). The microfluidic channel was filled with distilled water (relative permittivity: 81, conductivity: 1.0 mS/m). The needles (width: 36 µm, length: 42 µm, thickness: 0.3 µm) used were all the same. Frequency band of analysis was 1 kHz to 5 MHz.

The calculation model of the electrode is shown in Figure 3. In order to detect DNase, these models were used to calculate the electrode and DNA after immobilization. The results are shown in Figure 4.

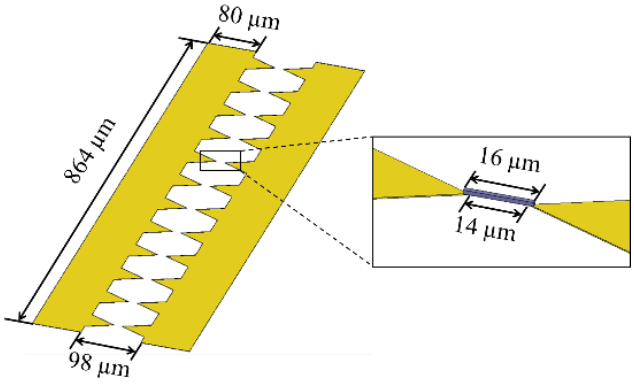

Figure 3. The calculation model of the electrode and DNA

Complex impedance locus of semicircular arc is plotted in the 4th quadrant. It was found that the impedance was substantially reduced because the diameter of the semicircular arc was shortened, when DNAs were immobilized on the electrode.

In order to detect the difference in the activity of DNase, calculation was performed by changing the number of immobilized DNAs. The results are shown in Figure 5. The impedance changes step by step depending on the number of DNAs immobilized.

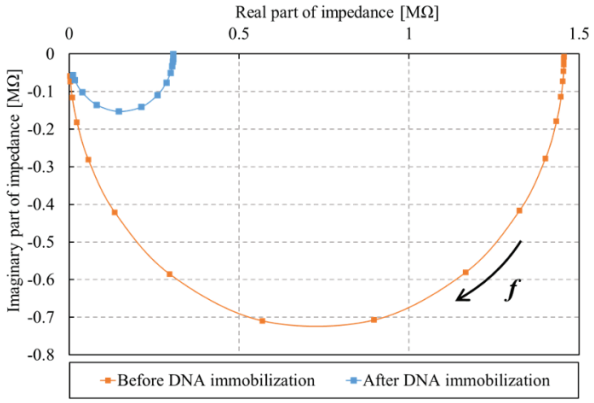

Figure 4. Complex impedance locus of the electrodes before and after DNA immobilization

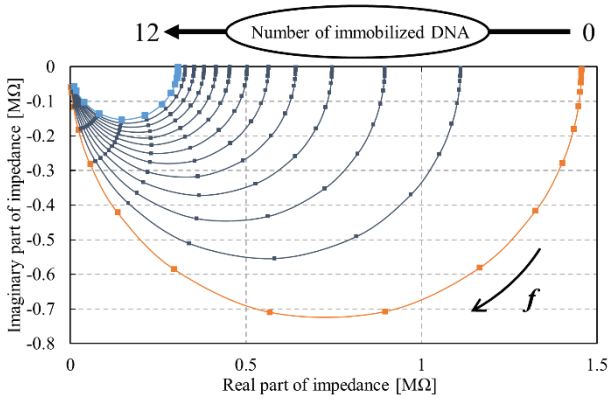

Figure 5. Change in number of DNAs

We also calculated the change in impedance depending on the shape of the electrode. The shapes of the electrode were changed in terms of surface area and the number of needles.

The model of the electrode with changing surface area (length direction) and results of the calculation are shown in Figure 6 and 7, respectively.

The model of the electrode with changing surface area (width direction) and results of the calculation are shown in Figure 8 and 9, respectively. From Figure 7 and Figure 9, the impedance decreases as the surface area increases.

The model of the electrode with changing number of needles is shown in Figure 10. The results of the analysis using this model are shown in Figure 11. The impedance decreases as the number of needles increases.

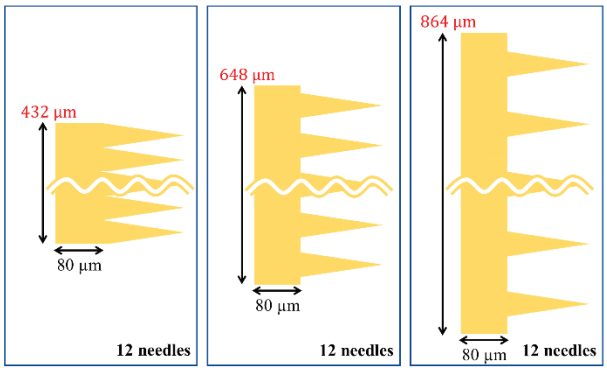

Fig. 6. Model of surface area (length direction) change

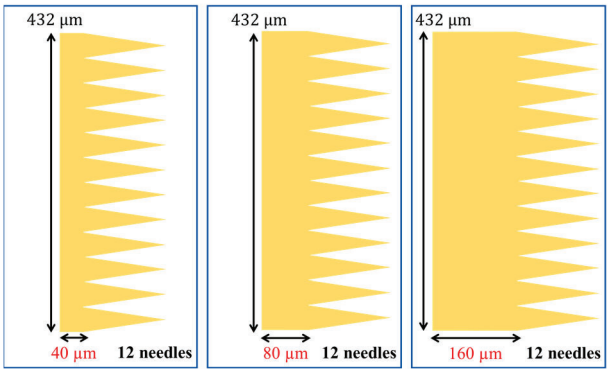

Fig. 8. Model of surface area (width direction) change

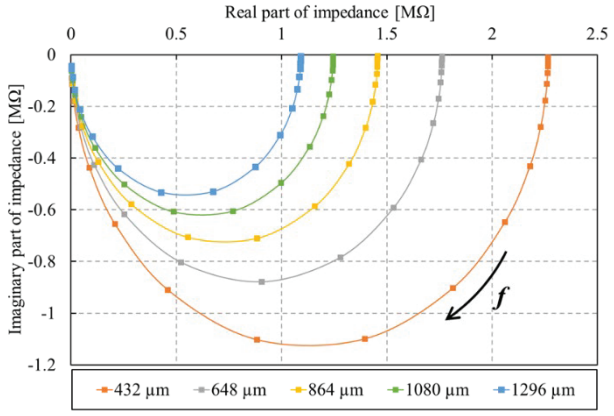

(a) Before DNA immobilization

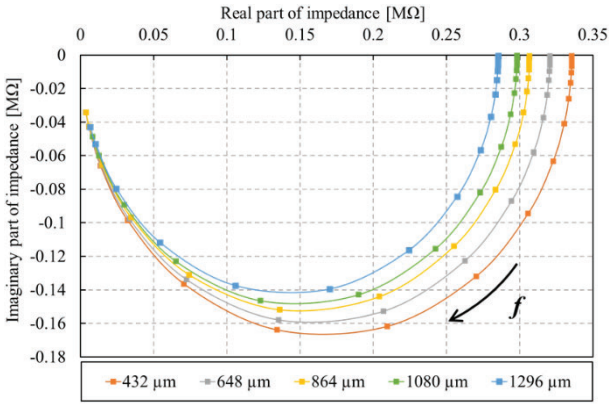

(b) After DNA immobilization

Figure 7. Change in surface area (length direction)

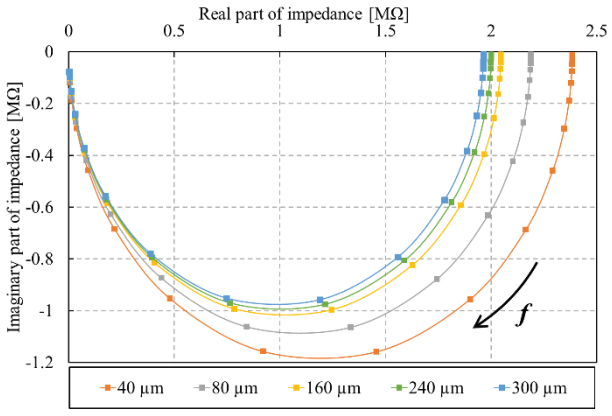

(a) Before DNA immobilization

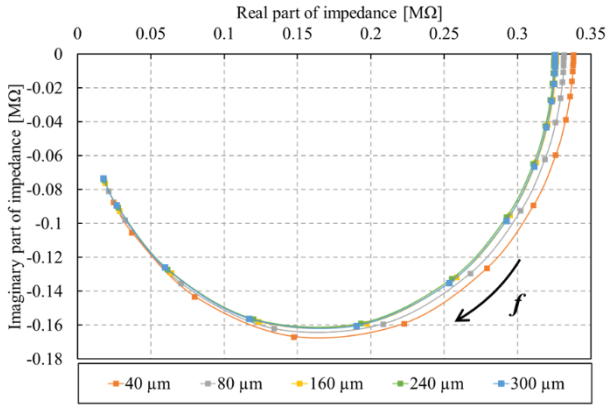

(b) After DNA immobilization

Fig. 9. Change in surface area (width direction)

Discussion and conclusion

The complex impedance locus of electrodes before and after DNA immobilization were calculated. As a result, the complex impedance locus of a semicircular arc is plotted in the 4th quadrant. The equivalent circuit of the electrode and the electrode with immobilized DNAs are presumed to be a parallel circuit of resistance and capacitance.

From Figure 4, the impedance changes of the electrode depending on DNA immobilization were confirmed. Figure 5 indicate that the impedance change of the electrode were confirmed depending on the amount of DNA. From these results, DNases are detectable, as well as differences in DNase activity. Therefore, disease type identification might be expected.

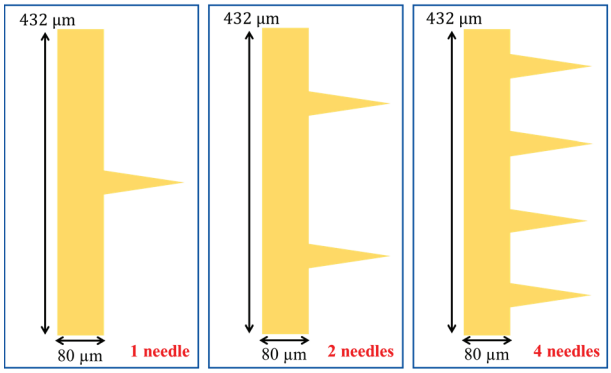

Figure 10. Model of number of needles change

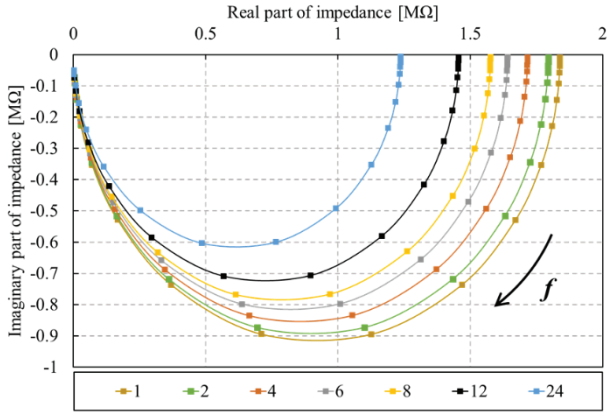

(a) Before DNA immobilization

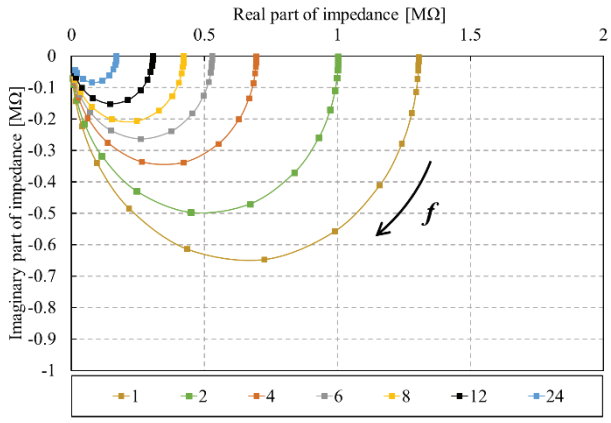

(b) After DNA immobilization

Figure 11. Change in number of needles

The impedance before DNA immobilization was substantially dependent on the surface area, as shown in Figures 7(a), 9(a). The impedance after DNA immobilization was slightly dependent on the shape of the electrode (Figure 7(b), 9(b)). Since the conductivity of DNA is higher than that of water in the microchannel, the impedance of electrodes with immobilized DNA is determined by amount of DNA.

The impedance before DNA immobilization was slightly dependent on the number of needles, as shown in Figure 11(a). This is because the surface area of the electrode increases slightly with the number of electrodes. The impedance after DNA immobilization was substantially dependent on the number of needles (Figure 11(b)). This is because the number of DNA increases with the number of triangular electrodes.

To improve DNase detection sensitivity, there must be a substantial difference between before and after DNA immobilization. Based on the above, we conclude the ideal electrode shape is smaller in surface area and thickness, and larger in the number of triangular electrodes. In future work, we will fabricate the device with ideal electrode and measure DNase activity.

Acknowledgements

This work was supported in part by JSPS KAKENHI grant number JP17H04704.

References

Cuervo, A., Dans, P. D., Carrascosa, J. L., Orozcob, M., Gomilae, G. & Fumagalli, L. (2014). Direct measurement of the dielectric polarization properties of DNA. *PNAS*, 111, 3624-3630.

Himuro, T., Tsukamoto, S. & Saito, Y. (2019). Electrical Evaluation of DNA Stretched and Immobilized Between Triangular-Shaped Electrodes. *journal of Electronic Materials*, 48, 1562-1567.

Lauková, L., Konečná, B., Janovičová, L., Vlková, B. & Celec, P. (2020). Deoxyribonucleases and Their Applications in Biomedicine. *Biomolecules*, 10, 1036.

Oku, S., Nishibayashi, K., Himuro, T. & Eguchi, M. (2021). Electrical Characteristic of Triangular-Shaped Electrodes with Immobilized λDNAs, *Proceedings of the 2021 IEICE General Conference*, C-2-59 (in Japanese).

Yamahata, C., Collard, D., Takekawa, T., Kumemura, M., Hashiguchi, G. & Fujita, H. (2008). Humidity Dependence of Charge Transport through DNA Revealed by Silicon-Based Nanotweezers Manipulation. *Biophysical Journal*, 94, 63-70.

Yasuda, Y., Kawai, Y., Ueki, M. & Kishi, K. (2005). Clinical applications of DNase I, a genetic marker already used for forensic identification. *Legal Medicine* 7, 274–277